ADA 278695

UNITED STATES AIR FORCE

SUMMER RESEARCH PROGRAM -- 1993

SUMMER RESEARCH PROGRAM FINAL REPORTS

VOLUME 4

ROME LABORATORY

RESEARCH & DEVELOPMENT LABORATORIES

5800 Uplander Way

Culver City, CA 90230-6608

Program Director, RDL
Gary Moore

Program Manager, AFOSR
Col. Hal Rhoades

Program Manager, RDL
Scott Licoscos

Program Administrator, RDL
Gwendolyn Smith

Program Administrator, RDL
Johnetta Thompson

Submitted to:

AIR FORCE OFFICE OF SCIENTIFIC RESEARCH

Bolling Air Force Base

Washington, D.C.

Decmeber 1993   DTIC QUALITY INSPECTED 3
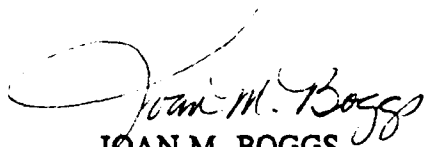
MEMORANDUM FOR DTIC (Acquisition)
(Attn: Pat Mauby)

SUBJECT: Distribution of USAF (AFOSR Summer Research Program (Air Force
Laboratories) and Universal Energy Systems, Inc., and the Research Initiation Program

FROM: AFOSR/XPT
Joan M. Boggs
110 Duncan Avenue, Suite B115
Bolling AFB DC 20332-0001

1. All of the books forwarded to DTIC on the subjects above should be considered
Approved for Public Release, distribution is unlimited (Distribution Statement A).

2. Thank you for processing the attached information.

JOAN M. BOGGS
Chief, Technical Information Division

1993 SRP Vol 1, 2, 3, 4, 5A, 5B, 6, 7, 8, 9
(10 Books)

Master Index for Faculty Members

Abbott, Ben
Research, MS
Box 1649 Station B
Vanderbilt University
Nashville, TN 37235-0000

Field: Electrical Engineering
Laboratory: AEDC/

Vol-Page No: 6- 1

Abrate, Serge
Assistant Professor, PhD
Mechanical & Aerospace En
University of Missouri - Rolla
Rolla, MO 65401-0249

Field: Aeronautical Engineering
Laboratory: WL/FI

Vol-Page No: 5-15

Almallahi, Hussein
Instructor, MS
P.O. Box 308
Prairie View A&M University
Prairie View, TX 77446-0000

Field: Electrical Engineering
Laboratory: AL/HR

Vol-Page No: 2-25

Anderson, James
Associate Professor, PhD
Chemistry
University of Georgia
Athens, GA 30602-2556

Field: Analytical Chemistry
Laboratory: AL/EQ

Vol-Page No: 2-18

Anderson, Richard
Professor, PhD
Physics
University of Missouri, Rolla
Rolla, MO 65401-0000

Field: Physics
Laboratory: PL/LI

Vol-Page No: 3- 7

Ashrafiuon, Hashem
Assistant Professor, PhD
Mechanical Engineering
Villanova University
Villanova, PA 19085-0000

Field: Mechanical Engineering
Laboratory: AL/CF

Vol-Page No: 2- 6

Backs, Richard
Assistant Professor, PhD
Dept. of Psychology
Wright State University
Dayton, OH 45435-0001

Field: Experimental Psychology
Laboratory: AL/CF

Vol-Page No: 2- 7

Baginski, Thomas
Assoc Professor, PhD
200 Broun Hall
Auburn University
Auburn, AL 36849-5201

Field: Electrical Engineering
Laboratory: WL/MN

Vol-Page No: 5-40

Baker, Suzanne
Assistant Professor, PhD
Dept. of Psychology
James Madison University
Harrisonburg, VA 22807-0000

Field:
Laboratory: AL/OE

Vol-Page No: 2-36

Baker, Albert
Assistant Professor, PhD

University of Cincinnati
,   -   0

Field: Electrical Engineering
Laboratory: WL/MT

Vol-Page No: 5-53

Balakrishnan, Sivasubramanya
Associate Professor, PhD

University of Missouri, Rolla
,   -   0

Field: Aerospace Engineering
Laboratory: WL/MN

Vol-Page No: 5-41

Bannister, William
Professor, PhD

Univ of Mass.-Lowell
Lowell, MA   1854-0000

Field: Organic Chemistry
Laboratory: WL/FI

Vol-Page No: 5-16

Barnard, Kenneth
Assistant Professor, PhD

Memphis State University
,   -   0

Field: Electrical Engineering
Laboratory: WL/AA

Vol-Page No: 5- 1

Bayard, Jean-Pierre
Associate Professor, PhD
6000 J Street
California State Univ-Sacramen
Sacramento, CA 95819-6019

Field: Electrical/Electronic Eng
Laboratory: RL/ER

Vol-Page No: 4- 7

Beardsley, Larry
Research Professor, MS

Athens State College
,   -   0

Field: Mathematics
Laboratory: WL/MN

Vol-Page No: 5-42

Beecken, Brian
Assoicate Professor, PhD
3900 Bethel Dr.
Bethel College
St. Paul, MN 55112-0000

Field: Dept. of Physics
Laboratory: PL/VT

Vol-Page No: 3-23

SFRP Participant Data

Bellem, Raymond
Dept, CEM. EE cs, PhD
3200 Willow Creek Road
Embry-Riddle Aeronautical Univ
Prescott, AZ 86301-0000

Field: Dept. of Computer Science
Laboratory: PL/VT

Vol-Page No: 3-24

Bellem, Raymond
Dept, CEM. EE cs, PhD
3200 Willow Creek Road
Embry-Riddle Aeronautical Univ
Prescott, AZ 86301-0000

Field: Dept. of Computer Science
Laboratory: /

Vol-Page No: 0- 0

Bhuyan, Jay
Assistant Professor, PhD
Dept. ofComputer Science
Tuskegee University
Tuskegee, AL 36088-0000

Field: Computer Science
Laboratory: PL/WS

Vol-Page No: 3-33

Biegl, Csaba
Assistant Professor, PhD
 Box 1649 Station B
Vanderbilt University
Nashville, TN 37235-0000

Field: Electrical Engineering
Laboratory: AEDC/

Vol-Page No: 6- 2

Biggs, Albert
Professor, PhD
Electrical Engineering
Univ. of Alabama, Huntsville
Huntsville, AL 35899-0000

Field:
Laboratory: PL/WS

Vol-Page No: 3-34

Blystone, Robert
Professor, PhD
Trinity University
715 Stadium Drive
San Antonio, TX 78212-7200

Field: Dept of Biology
Laboratory: AL/OE

Vol-Page No: 2-37

Branting, Luther
Assistant Professor, PhD
PO Box 3682
University of Wyoming
Laramie, WY 82071-0000

Field: Dept of Computer Science
Laboratory: AL/HR

Vol-Page No: 2-26

Bryant, Barrett
Associate Professor, PhD
115A Campbell Hall
University of Alabama, Birming
Birmingham, AL 35294-1170

Field: Computer Science
Laboratory: RL/C3

Vol-Page No: 4- 1

Callens, Jr., Eugene
Assocition Professor, PhD
Industrial
Louisiana Technical University
Ruston, LA 71270-0000

Field: Aerospace Engineering
Laboratory: WL/MN

Vol-Page No: 5-43

Cannon, Scott
Associate Professor, PhD
Computer Science
Utah State University
Logan, UT 84322-0000

Field: Computer Science/Biophys.
Laboratory: PL/VT

Vol-Page No: 3-25

Carlisle, Gene
Professor, PhD
Dept. of Physics
West Texas State University
Canyon, TX 79016-0000

Field: Killgore Research Center
Laboratory: PL/LI

Vol-Page No: 3- 8

Catalano, George
Associate Professor, PhD
Mechanical Engineering
United States Military Academy
West Point, NY 10996-1792

Field: Department of Civil &
Laboratory: AEDC/

Vol-Page No: 6- 3

Chang, Ching
Associate Professor, PhD
Euclid Ave at E. 24th St
Cleveland State University
Cleveland, OH 44115-0000

Field: Dept. of Mathematics
Laboratory: WL/FI

Vol-Page No: 5-17

Chattopadhyay, Somnath
Assistant Professor, PhD

University of Vermont
Burlington, VT 5405-0156

Field: Mechanical Engineering
Laboratory: PL/RK

Vol-Page No: 3-14

Chen, C. L. Philip
Assistant Professor, PhD
Computer Science Engineer
Wright State University
Dayton, OH 45435-0000

Field: Electrical Engineering
Laboratory: WL/ML

Vol-Page No: 5-26

Choate, David
Assoc Professor, PhD
Dept. of Mathematics
Transylvania University
Lexington, KY 40505-0000

Field: Mathematics
Laboratory: PL/LI

Vol-Page No: 3- 9

SFRP Participant Data

Chubb, Gerald
Assistant Professor, PhD
164 W. 19th Ave.
Ohio State University
Columbus, OH 43210-0000

Field: Dept. of Aviation
Laboratory: AL/HR

Vol-Page No: 2-27

Chuong, Cheng-Jen
Associtae Professor, PhD
501 W. 1st Street
University of Texas, Arlington
Arlington, TX 76019-0000

Field: Biomedical Engineering
Laboratory: AL/CF

Vol-Page No: 2- 8

Citera, Maryalice
Assistant Professor, PhD
Department of Psychology
Wright State University
Dayton, OH   4-5435

Field: Industrial Psychology
Laboratory: AL/CF

Vol-Page No: 2- 9

Collard, Jr., Sneed
Professor, PhD
Ecology & Evolutionary Bi
University of West Florida
Pensacola, FL 32514-0000

Field: Biology
Laboratory: AL/EQ

Vol-Page No: 2-19

Collier, Geoffrey
Assistant Professor, PhD
300 College St., NE
South Carolina State College
Orangeburg,, SC 29117-0000

Field: Dept of Psychology
Laboratory: AL/CF

Vol-Page No: 2-10

Cone, Milton
Assistat Professor, PhD
3200 Willow Creek Road
Embry-Riddel Aeronautical Univ
Prescott, AZ 86301-3720

Field: Electrical Engineering
Laboratory: WL/AA

Vol-Page No: 5- 2

Cundari, Thomas
Assistant Professor, PhD
Jim Smith Building
Memphis State University
Memphis, TN 38152-0000

Field: Department of Chemistry
Laboratory: PL/RK

Vol-Page No: 3-15

D'Agostino, Alfred
Assistant Professor, PhD
4202 E Fowler Ave/SCA-240
University of South Florida
Tampa, FL 33620-5250

Field: Dept of Chemistry
Laboratory: WL/ML

Vol-Page No: 5-27

Das, Asesh
Assistant Professor, PhD
Research Center
West Virginia University
Morgantown, WV 26505-0000

Field: Concurrent Engineering
Laboratory: AL/HR

Vol-Page No: 2-28

DeLyser, Ronald
Assistant Professor, PhD
2390 S. York Street
University of Denver
Denver, CO 80208-0177

Field: Electrical Engineering
Laboratory: PL/WS

Vol-Page No: 3-35

DelVecchio, Vito
Professor, PhD
Biology
University of Scranton
Scranton, PA 18510-4625

Field: Biochemical Genetics
Laboratory: AL/AO

Vol-Page No: 2- 1

Dey, Pradip
Associate Professor, PhD

Hampton University
,   -   0

Field: Computer Science
Laboratory: RL/IR

Vol-Page No: 4-16

Ding, Zhi
Assistant Professor, PhD
200 Broun Hall
Auburn University
Auburn, AL 36849-5201

Field: Electrical Engineering
Laboratory: WL/MN

Vol-Page No: 5-44

Doherty, John
Assistant Professor, PhD
201 Coover Hall
Iowa State University
Ames, IA 50011-1045

Field: Electrical Engineering
Laboratory: RL/OC

Vol-Page No: 4-21

Dolson, David
Assistant Professor, PhD

Wright State University
,   -   0

Field: Chemistry
Laboratory: WL/PO

Vol-Page No: 5-56

Dominic, Vincent
Assustant professor, MS
300 College Park
University of Dayton
Dayton, OH 45469-0227

Field: Electro Optics Program
Laboratory: WL/ML

Vol-Page No: 5-28

SFRP Participant Data

Donkor, Eric
Assistant Professor, PhD
Engineering
University of Connecticut
Stroes, CT   6269-1133

Field: Electrical Engineering
Laboratory: RL/OC

Vol-Page No: 4-22

Driscoll, James
Associate Professor, PhD
3004 FXB Bldg 2118
University of Michigan
Ann Arbor, MI   48109-0000

Field: Aerospace Engineering
Laboratory: WL/PO

Vol-Page No: 5-57

Duncan, Bradley
Assistant Professor, PhD
300 College Park
University of Dayton
Dayton, OH   45469-0226

Field: Electrical Engineering
Laboratory: WL/AA

Vol-Page No: 5- 3

Ehrhart, Lee
Instructor, MS
Communications & Intellig
George Mason University
Fairfax, VA   22015-1520

Field: Electrical Engineering
Laboratory: RL/C3

Vol-Page No: 4- 2

Ewert, Daniel
Assistant Professor, PhD
Electrical Engineering
North Dakota State University
Fargo, IN   58105-0000

Field: Physiology
Laboratory: AL/AO

Vol-Page No: 2- 2

Ewing, Mark
Associate Professor, PhD
2004 Learned Hall
University of Kansas
Lawrence, KS   66045-2969

Field: Engineering Mechanics
Laboratory: PL/SX

Vol-Page No: 3-22

Foo, Simon
Assistant Professor, PhD
College of Engineering
Florida State University
Tallahessee, FL   32306-0000

Field: Electrical Engineering
Laboratory: WL/MN

Vol-Page No: 5-45

Frantziskonis, George
Assistant Professor, PhD
Dept of Civil Engrng/Mech
University of Arizona
Tuson, AZ   85721-1334

Field: College of Engrng/Mines
Laboratory: WL/ML

Vol-Page No: 5-29

Frenzel III, James
Assistant Professor, PhD
Dept of Electrical Engnr
University of Idaho
Moscow, ID 83844-1023

Field: Electrical Engineering
Laboratory: WL/AA

Vol-Page No: 5- 4

Fried, Joel
Professor, PhD
Chemical Engineering
University of Cincinnati
Cincinnati, OH 45221-0171

Field: Polymer Science
Laboratory: WL/PO

Vol-Page No: 5-58

Friedman, Jeffrey
Assistant Professor, PhD
Physics
University of Puerto Rico
Mayaguez, PR   681-0000

Field: Physics/Astrophysics
Laboratory: PL/GP

Vol-Page No: 3- 1

Fuller, Daniel
Dept. Chairman, PhD
Chemistry & Physics
Nicholls State University
Thibodaux, LA 70310-0000

Field: Chemistry
Laboratory: PL/RK

Vol-Page No: 3-16

Gao, Zhanjun
Assistant Professor, PhD
203 W. Old Main, Box 5725
Clarkson University
Potsdam, NY 13699-5725

Field: Mechanical/Aeronautical E
Laboratory: WL/ML

Vol-Page No: 5-30

Gavankar, Prasad
Asst Professor, PhD
Campus Box 191
Texas A&I University
Kingsville, TX 78363-0000

Field: Mech & Indust Engineering
Laboratory: WL/MT

Vol-Page No: 5-54

Gebert, Glenn
Assistant Professor, PhD
Mechanical
Utah State University
Logan, UT 84339-0000

Field: Aerospace Engineering
Laboratory: WL/MN

Vol-Page No: 5-46

Gerdom, Larry
Professor, PhD
Natural Science
Mobile College
Mobil, AL 36663-0220

Field: Chemistry
Laboratory: AL/EQ

Vol-Page No: 2-20

Ghajar, Afshin
Professor, PhD
Mech. & Aerospace Enginee
Oklahoma State University
Stillwater, OK 74078-0533

Field: Mechanical Engineering
Laboratory: WL/PO

Vol-Page No: 5-59

Gopalan, Kaliappan
Associate Professor, PhD
Dept of Engineering
Purdue University, Calumet
Hammond, IN 46323-0000

Field:
Laboratory: AL/CF

Vol-Page No: 2-11

Gould, Richard
Assistant Professor, PhD
Mechanical & Aerospace En
N.Carolina State University
Raleigh, NC 27695-7910

Field: Mechanical Engineering
Laboratory: WL/PO

Vol-Page No: 5-60

Gowda, Raghava
Assistant Professor, PhD
Dept of Computer Science
University of Dayton
Dayton, OH 45469-2160

Field: Computer Information Sys.
Laboratory: WL/AA

Vol-Page No: 5- 5

Graetz, Kenneth
Assistant Professor, PhD
300 College Park
University of Dayton
Dayton, OH 45469-1430

Field: Department of Psychology
Laboratory: AL/HR

Vol-Page No: 2-29

Gray, Donald
Associate Professor, PhD
PO Box 6101
West Virginia Unicersity
Morgantown, WV 20506-6101

Field: Dept of Civil Engineering
Laboratory: AL/EQ

Vol-Page No: 2-21

Green, Bobby
Assistant Professor, MS
Box 43107
Texas Tech University
Lubbock, TX 79409-3107

Field: Electrical Engineering
Laboratory: WL/FI

Vol-Page No: 5-18

Grubbs, Elmer
Assistant Professor, MS
Engineering
New Mexico Highland University
Las Vegas, NM 87701-0000

Field: Electrical Engineering
Laboratory: WL/AA

Vol-Page No: 5- 6

Guest, Joyce
Associate, PhD
Department of Chemistry
University of Cincinnati
Cincinnati, OH 45221-0172

Field: Physical Chemistry
Laboratory: WL/ML

Vol-Page No: 5-31

Gumbs, Godfrey
Professor, PhD
Physics & Astronomy
University New York Hunters Co
New York, NY 10021-0000

Field: Condensed Matter Physics
Laboratory: WL/EL

Vol-Page No: 5-12

Hakkinen, Raimo
Professor, PhD
207 Jolley Hall
Washington University
St. Louis, MO 63130-0000

Field: Mechanical Engineering
Laboratory: WL/FI

Vol-Page No: 5-19

Hall, Jr., Charles
Assistant Professor, PhD
Mech & Aerospace Engr.
North Carolina Univ.
Raleigh, NC 27695-7910

Field:
Laboratory: WL/FI

Vol-Page No: 5-20

Hancock, Thomas
Assistant Professor, PhD

Grand Canyon University
,   -   0

Field: Educational Psychology
Laboratory: AL/HR

Vol-Page No: 2-30

Hannafin, Michael
Visiting Professor, PhD
305-D Stone Building,3030
Florida State University
Tallahassee, FL   3-2306

Field: Educational Technology
Laboratory: AL/HR

Vol-Page No: 2-31

Helbig, Herbert
Professor, PhD
Physics
Clarkson University
Potsdam, NY 13699-0000

Field: Physics
Laboratory: RL/ER

Vol-Page No: 4- 8

Henry, Robert
Professor, PhD
Electrical Engineering
University of Southwestern Lou
Lafayette, LA 70504-3890

Field: Electrical Engineering
Laboratory: RL/C3

Vol-Page No: 4- 3

Hong, Lang   Field: Electrical Engineering
Assistant Professor, PhD   Laboratory: WL/AA
Dept of Electrical Engin
Wright State University   Vol-Page No: 5- 7
Dayton, OH 45435-0000

Hsu, Lifang   Field: Mathematical Statistics
Assistant Professor, PhD   Laboratory: RL/ER

Le Moyne College   Vol-Page No: 4- 9
,   - 0

Huang, Ming   Field: Mechanical Engineering
Assistant Professor, PhD   Laboratory: AL/CF
500 NW 20th Street
Florida Atlantic University   Vol-Page No: 2-12
Boca Raton, FL 33431-0991

Humi, Mayer   Field: Applied Mathematics
Professor, PhD   Laboratory: PL/GP
Mathematics
Worchester Polytechnic Institu   Vol-Page No: 3- 2
Worchester, MA   1609-2280

Humi, Mayer   Field: Applied Mathematics
Professor, PhD   Laboratory: /
Mathematics
Worchester Polytechnic Institu   Vol-Page No: 0- 0
Worchester, MA   1609-2280

Jabbour, Kamal   Field: Electrical Engineering
Associate Professor, PhD   Laboratory: RL/C3
121 Link hall
Syracuse University   Vol-Page No: 4- 4
Syracuse, NY 13244-1240

Jaszczak, John   Field:
Assistant Professor, PhD   Laboratory: WL/ML
Dept. of Physics
Michigan Technological Univers   Vol-Page No: 5-32
Houghton, MI 49931-1295

Jeng, San-Mou   Field: Aerospace Engineering
Associte, PhD   Laboratory: PL/RK
Mail Location #70
University of Cincinnati   Vol-Page No: 3-17
Cincinnati, OH 45221-0070

SFRP Participant Data

Johnson, David
Associate Professor, PhD
Dept of Chemistry
University of Dayton
Dayton, OH 45469-2357

Field: Chemistry
Laboratory: WL/ML

Vol-Page No: 5-33

Karimi, Amir
Associate, PhD
Division Engineering
University of Texas, San Anton
San Antonio, TX   7824-9065

Field: Mechanical Engineering
Laboratory: PL/VT

Vol-Page No: 3-26

Kheyfets, Arkady
Assistant Professor, PhD
Dept. of Mathematics
North Carolina State Univ.
Raleigh, NC 27695-7003

Field:
Laboratory: PL/VT

Vol-Page No: 3-27

Koblasz, Arthur
Associate, PhD
Civil Engineeing
Georgia State University
Atlanta, GA 30332-0000

Field: Engineering Science
Laboratory: AL/AO

Vol-Page No: 2- 3

Kraft, Donald
Professor, PhD
Dept. of Computer Science
Louisiana State University
Baton Rouge, LA 70803-4020

Field:
Laboratory: AL/CF

Vol-Page No: 2-13

Kumar, Rajendra
Professor, PhD
1250 Bellflower Blvd
California State University
Long Beach, CA 90840-0000

Field: Electrical Engineering
Laboratory: RL/C3

Vol-Page No: 4- 5

Kumta, Prashant
Assistant Professor, PhD
Dept of Materials Science
Carnegie-Mellon University
Pittsburgh, PA 15213-3890

Field: Materiels Science
Laboratory: WL/ML

Vol-Page No: 5-34

Kuo, Spencer
Professor, PhD
Route 110
Polytechnic University
Farmingdale, NY 11735-0000

Field: Electrophysics
Laboratory: PL/GP

Vol-Page No: 3- 3

Lakeou, Samuel   Field: Electrical Engineering
Professor, PhD   Laboratory: PL/VT
Electrical Engineering
University of the District of   Vol-Page No: 3-28
Washnington, DC 20008-0000

Langhoff, Peter   Field: Dept. of Chemistry
Professor, PhD   Laboratory: PL/RK

Indiana University   Vol-Page No: 3-18
Bloomington, IN 47405-4001

Lawless, Brother   Field: Box 280
Assoc Professor, PhD   Laboratory: AL/OE
Dept. Science /Mathematic
Fordham University   Vol-Page No: 2-38
New York, NY 10021-0000

Lee, Tzesan   Field:
Associate Professor, PhD   Laboratory: AL/OE
Dept. of Mathematics
Western Illinois University   Vol-Page No: 2-39
Macomb, IL 61455-0000

Lee, Min-Chang   Field: Plasma Fusion Center
Professor, PhD   Laboratory: PL/GP
167 Albany Street
Massachusetts Institute   Vol-Page No: 3- 4
Cambridge, MA   2139-0000

Lee, Byung-Lip   Field: Materials Engineering
Associate Professor, PhD   Laboratory: WL/ML
Engineering Sci. & Mechan
Pennsylvania State University   Vol-Page No: 5-35
University Park, PA 16802-0000

Leigh, Wallace   Field: Electrical Engineering
Assistant Professor, PhD   Laboratory: RL/ER
26 N. Main St.
Alfred University   Vol-Page No: 4-10
Alfred, NY 14802-0000

Levin, Rick   Field: Electrical Engineering
Research Engineer II, MS   Laboratory: RL/ER
EM Effects Laboratory
Georgia Institute of Technolog   Vol-Page No: 4-11
Atlanta, GA 30332-0800

Li, Jian
Asst Professor, PhD
216 Larsen Hall
University of Florida
Gainesville, FL 32611-2044

Field: Electrical Engineering
Laboratory: WL/AA

Vol-Page No: 5- 8

Lilienfield, Lawrence
Professor, PhD
3900 Reservoir Rd., NW
Georgetown University
Washington, DC 20007-0000

Field: Physiology & Biophysics
Laboratory: WHMC/

Vol-Page No: 6-14

Lim, Tae
Assistant Professor, PhD
2004 Learned Hall
University of Kansas
Lawrence, KA 66045-0000

Field: Mechanical/Aerospace
Laboratory: FJSRL/

Vol-Page No: 6- 8

Lin, Paul
Associate Professor, PhD
Mechanical Engineering
Cleveland State University
Cleveland, OH   4-4115

Field: Associate Professor
Laboratory: WL/FI

Vol-Page No: 5-21

Liou, Juin
Associate Professor, PhD
Electrical & Computer Eng
University of Central Florida
Orlando, FL 32816-2450

Field: Electrical Engineering
Laboratory: WL/EL

Vol-Page No: 5-13

Liu, David
Assistant Professor, PhD
100 Institute Rd.
Worcester Polytechnic Inst.
Worcester, MA   1609-0000

Field: Department of Physics
Laboratory: RL/ER

Vol-Page No: 4-12

Losiewicz, Beth
Assistant Professor, PhD
Experimental Psychology
Colorado State University
Fort Collins, CO 80523-0000

Field: Psycholinguistics
Laboratory: RL/IR

Vol-Page No: 4-17

Loth, Eric
Assistant Professor, PhD
104 S. Wright St, 321C
University of Illinois-Urbana
Urbana, IL 61801-0000

Field: Aeronaut/Astronaut Engr
Laboratory: AEDC/

Vol-Page No: 6 4

Lu, Christopher
Associate Professor, PhD
300 College Park
University of Dayton
Dayton, OH 45469-0246

Field: Dept Chemical Engineering
Laboratory: WL/PO

Vol-Page No: 5-61

Manoranjan, Valipuram
Associate Professor, PhD
Neill Hall
Washington State University
Pullman, WA 99164-3113

Field: Pure & AppliedMathematics
Laboratory: AL/EQ

Vol-Page No: 2-22

Marsh, James
Professor, PhD
Physics
University of West Florida
Pensacola, FL 32514-0000

Field: Physics
Laboratory: WL/MN

Vol-Page No: 5-47

Massopust, Peter
Assistant Professor, PhD

Sam Houston State University
Huntsville, TX 77341-0000

Field: Dept. of Mathematics
Laboratory: AEDC/

Vol-Page No: 6- 5

Miller, Arnold
Senior Instructor, PhD
Chemistry & Geochemistry
Colorado School of Mines
Golden, CO 80401-0000

Field:
Laboratory: FJSRL/

Vol-Page No: 6- 9

Misra, Pradeep
Associate Professor, PhD

University of St. Thomas
,   - 0

Field: Electrical Engineering
Laboratory: WL/AA

Vol-Page No: 5- 9

Monsay, Evelyn
Associate Professor, PhD
1419 Salt Springs Rd
Le Moyne College
Syracuse, NY 13214-1399

Field: Physics
Laboratory: RL/OC

Vol-Page No: 4-23

Morris, Augustus
Assistant Professor, PhD

Central State University
,   - 0

Field: Biomedical Science
Laboratory: AL/CF

Vol-Page No: 2-14

Mueller, Charles
Professor, PhD
W140 Seashore Hall
University of Iowa
Iowa City, IA 52242-0000

Field: Dept of Sociology
Laboratory: AL/HR

Vol-Page No: 2-32

Murty, Vedula
Associate Professor, MS

Texas Southern University
,   - 0

Field: Physics
Laboratory: PL/VT

Vol-Page No: 3-29

Musavi, Mohamad
Assoc Professor, PhD
5708 Barrows Hall
University of Maine
Orono, ME   4469-5708

Field: Elect/Comp. Engineering
Laboratory: RL/IR

Vol-Page No: 4-18

Naishadham, Krishna
Assistant Professor, PhD
Dept. of Electrical Eng.
Wright State University
Dayton, OH 45435-0000

Field: Electrical Engineering
Laboratory: WL/EL

Vol-Page No: 5-14

Noel, Charles
Associate Professor, PhD
151A Campbell Hall
Ohio State University
Columbus, OH   43210-1295

Field: Dept of Textiles & Cloth
Laboratory: PL/RK

Vol-Page No: 3-19

Norton, Grant
Asst Professor, PhD
Mechanical & Materials En
Washington State University
Pullman, WA 99164-2920

Field: Materials Science
Laboratory: WL/ML

Vol-Page No: 5-36

Noyes, James
Professor, PhD
Mathematics & Computer Sc
Wittenberg University
Springfield, OH 45501-0720

Field: Computer Science
Laboratory: WL/FI

Vol-Page No: 5-22

Nurre, Joseph
Assistant Professor, PhD
Elec. & Computer Engineer
Ohio University
Athens, OH   45701-0000

Field: Mechanical Engineering
Laboratory: AL/CF

Vol-Page No: 2-15

SFRP Participant Data

Nygren, Thomas
Associate Professor, PhD
1885 Neil Ave. Mail
Ohio State University
Columbus, OH 43210-1222

Field: Department of Psychology
Laboratory: AL/CF

Vol-Page No: 2-16

Osterberg, Ulf
Assistant Professor, PhD
Thayer School of Engrg.
Dartmouth College
Hanover, NH 3755-0000

Field:
Laboratory: FJSRL/

Vol-Page No: 6-10

Pan, Ching-Yan
Associate Professor, PhD
Physics
Utah State University
Logan, UT 84322-4415

Field: Condensed Matter Physics
Laboratory: PL/WS

Vol-Page No: 3-36

Pandey, Ravindra
Assistant Professor, PhD
1400 Townsend Dr
Michigan Technological Univers
Houghton, MI 49931-1295

Field: Physics
Laboratory: FJSRL/

Vol-Page No: 6-11

Patton, Richard
Assistant Professor, PhD
Mechanical&Nuclear Engine
Mississippi State University
Mississippi State, MS 39762-0000

Field: Mechanical Engineering
Laboratory: PL/VT

Vol-Page No: 3-30

Peretti, Steven
Assistant Professor, PhD
Chemical Engineering
North Carolina State Univ.
Raleigh, NC 27695-7905

Field:
Laboratory: AL/EQ

Vol-Page No: 2-23

Petschek, Rolfe
Associate Professor, PhD
Department of Physics
Case Western Reserve Universit
Cleveland, OH 44106-7970

Field: Physics
Laboratory: WL/ML

Vol-Page No: 5-37

Pezeshki, Charles
Assistant Professor, PhD

Washington State University
Pullman, WA 99164-2920

Field: Mechanical Engineering
Laboratory: FJSRL/

Vol-Page No: 6-12

Piepmeier, Edward
Assistant Professor, PhD
College of Pharmacy
University of South Carolina
Columbia, SC 29208-0000

Field:
Laboratory: AL/AO

Vol-Page No: 2- 4

Pittarelli, Michael
Associate Professor, PhD
PO Box 3050, Marcy Campus
SUNY, Institute of Technology
Utica, NY 13504-3050

Field: Information Sys & Engr.
Laboratory: RL/C3

Vol-Page No: 4- 6

Potasek, Mary
Research Professor, PhD

Columbia University
,   - 0

Field: Physics
Laboratory: WL/ML

Vol-Page No: 5-38

Prasad, Vishwanath
Professor, PhD

SUNY, Stony Brook
Stony Brook, NY 11794-2300

Field: Mechanical Engineering
Laboratory: RL/ER

Vol-Page No: 4-13

Priestley, Keith
Research Scientist, PhD

University of Nevada, Reno
,   - 0

Field: Geophysics
Laboratory: PL/GP

Vol-Page No: 3- 5

Purasinghe, Rupasiri
Professor, PhD
5151 State Univ. Dr.
California State Univ.-LA
Los Angeles, CA 90032-0000

Field: Dept of Civil Engineering
Laboratory: PL/RK

Vol-Page No: 3-20

Raghu, Surya
Assistant Professor, PhD
Mechanical Engineering
SUNY, Stony Brook
Stony Brook, NY 11794-2300

Field: Mechanical Engineering
Laboratory: WL/PO

Vol-Page No: 5-62

Ramesh, Ramaswamy
Associate Professor, PhD
School of Management
SUNY, Buffalo
Buffalo, NY 14260-0000

Field: Magement Science/Systems
Laboratory: AL/HR

Vol-Page No: 2-33

SFRP Participant Data

Ramm, Alexander
Professor, PhD
Mathematics
Kansas State University
Manhattan, KS 66506-2602

Field:
Laboratory: AL/CF

Vol-Page No: 2-17

Ray, Paul
Assistant Professor, PhD
Box 870288
University of Alabama
Tuscaloosa, AL 35487-0288

Field: Industrial Engineering
Laboratory: AL/OE

Vol-Page No: 2-40

Reimann, Michael
Assistant Instructor, MS
Information Systems
The University of Texas-Arling
Arlington, TX 76019-0437

Field: Computer Science
Laboratory: WL/MT

Vol-Page No: 5-55

Rodriguez, Armando
Assistant Professor, PhD

Arizona State University
Tempe, AZ 85287-7606

Field: Electrical Engineering
Laboratory: WL/MN

Vol-Page No: 5-48

Rohrbaugh, John
Research Engineer, PhD
347 Ferst St
Georgia Institute of Technolog
Atlanta, GA 30332-0800

Field: Sensors & Applied Electro
Laboratory: RL/ER

Vol-Page No: 4-14

Roppel, Thaddeus
Associate Professor, PhD
200 Broun Hall
Auburn University
Auburn, AL 36849-5201

Field: Electrical Engineering
Laboratory: WL/MN

Vol-Page No: 5-49

Rosenthal, Paul
Professor, PhD
Mathematics
Los Angeles City College
Los Angeles, CA 90027-0000

Field: Mathematics
Laboratory: PL/RK

Vol-Page No: 3-21

Rotz, Christopher
Associate Professor, PhD

Brigham Young University
Provo, UT 84602-0000

Field: Mechanical Engineering
Laboratory: PL/VT

Vol-Page No: 3-31

Rudolph, Wolfgang
Associate Professor, PhD
Dept of Physics and Astro
University of New Mexico
Albuquerque, NM 84131-0000

Field: Physics
Laboratory: PL/LI

Vol-Page No: 3- 0

Rudzinski, Walter
Professor, PhD
Dept. of Chemistry
Southwest Texas State Universi
San Marcos, TX 78610-0000

Field: Professor
Laboratory: AL/OE

Vol-Page No: 2-41

Rule, William
Asst Professor, PhD
Mechanical Engineering
University of Alabama
Tuscaloosa, AL 35487-0278

Field: Engineering Mechanics
Laboratory: WL/MN

Vol-Page No: 5-50

Ryan, Patricia
Research Associate, MS
Georgia Tech Research Ins
Georgia Institute of Tech
Atlanta, GA 30332-0000

Field: Electrical Engineering
Laboratory: WL/AA

Vol-Page No: 5-10

Saiduddin, Syed
Professor, PhD
1900 Coffey Rd
Ohio State University
Columbus, OH 43210-1092

Field: Physiology/Pharmacology
Laboratory: AL/OE

Vol-Page No: 2-42

Schonberg, William
Assoc Professor, PhD
Engineering Dept.
University of Alabama, Huntsvi
Huntsville, AL 35899-0000

Field: Civil & Environmental
Laboratory: WL/MN

Vol-Page No: 5-51

Schulz, Timothy
Assistant Professor, PhD
1400 Townsend Dr
Michigan Technological Univers
Houghton, MI 49931-1295

Field: Electrical Engineering
Laboratory: PL/LI

Vol-Page No: 3-11

Shen, Mo-How
Assistant Professor, PhD
2036 Neil Ave.
Ohio State University
Columbus,, OH 43210-1276

Field: Aerospace Engineering
Laboratory: WL/FI

Vol-Page No: 5-23

Sherman, Larry
Professor, PhD
Dept. of Chemistry
University of Scranton
Scranton, PA 18510-4626

Field: Analytical Chemistry
Laboratory: AL/OE

Vol-Page No: 2-43

Shively, Jon
Professor, PhD
Civil & Industrial Eng.
California State University, N
Northridge, CA 91330-0000

Field: Metallurgy
Laboratory: PL/VT

Vol-Page No: 3-32

Snapp, Robert
Assistant Professor, PhD
Dept of Computer Science
University of Vermont
Burlington, VT 5405-0000

Field: Physics
Laboratory: RL/IR

Vol-Page No: 4-19

Soumekh, Mehrdad
Associate Professor, PhD
201 Bell Hall
SUNY, Buffalo
Amherst, NY 14260-0000

Field: Elec/Computer Engineering
Laboratory: PL/LI

Vol-Page No: 3-12

Spetka, Scott
Assistant Professor, PhD
PO Box 3050, Marcy Campus
SUNY, Institute of Technology
Utica, NY 13504-3050

Field: Information Sys & Engrg
Laboratory: RL/XP

Vol-Page No: 4-26

Springer, John
Associate Professor, PhD

Fisk University
,   - 0

Field: Physics
Laboratory: AEDC/

Vol-Page No: 6- 6

Stevenson, Robert
Assistant Professor, PhD
Electrical Engineering
University of Notre Dame
Notre Dame, IN 46556-0000

Field: Electrical Engineering
Laboratory: RL/IR

Vol-Page No: 4-20

Stone, Alexander
Professor, PhD
Mathematics & Statistics
University of New Mexico
Alburquerque, NM 87131-1141

Field:
Laboratory: PL/WS

Vol-Page No: 3-37

Sveum, Myron
Assistant Professor, MS
Electronic Engineering Te
Metropolitan State College
Denver, CO 80217-3362

Field: Electrical Engineering
Laboratory: RL/OC

Vol-Page No: 4-24

Swanson, Paul
Research Associate, PhD
Electrical Engineering
Cornell University
Ithaca, NY 14853-0000

Field: Electrical Engineering
Laboratory: RL/OC

Vol-Page No: 4-25

Swope, Richard
Professor, PhD
Engineering Science
Trinity University
San Antonio, TX 78212-0000

Field: Mechanical Engineering
Laboratory: AL/AO

Vol-Page No: 2- 5

Tan, Arjun
Professor, PhD
Physics
Alabama A&M University
Normal, AL 35762-0000

Field: Physics
Laboratory: PL/WS

Vol-Page No: 3-38

Tarvin, John
Associate Professor, PhD
800 Lakeshore Drive
Samford University
Birmingham, AL 35229-0000

Field: Department of Physics
Laboratory: AEDC/

Vol-Page No: 6- 7

Taylor, Barney
Visiting Assist Professor, PhD
1601 Peck Rd.
Miami Univ. - Hamilton
Hamilton, OH   4-5011

Field: Dept. of Physics
Laboratory: WL/ML

Vol-Page No: 5-39

Thio, Y.
Associate Professor, PhD

University of Miami
Coral Gables, FL 33124-0530

Field: Physics Dept.
Laboratory: PL/WS

Vol-Page No: 3-39

Tong, Carol
Assistant Professor, PhD
Electrical Engineering
Colorado State University
Fort Collins, CO 80523-0000

Field:
Laboratory: WL/AA

Vol-Page No.   5-11

Truhon, Stephen   Field: Psychology
Associate Professor, PhD   Laboratory: AL/HR
Social Sciences
Winston-Salem State University   Vol-Page No: 2-34
Winston-Salem, NC 27110-0000

Tzou, Horn-Sen   Field: Mechanical Engineering
Associate Professor, PhD   Laboratory: WL/FI
Mechanical Engineering
University of Kentucky   Vol-Page No: 5-24
Lexington, KY 40506-0046

Vogt, Brian   Field: Pharmaceutical Sciences
Professor, PhD   Laboratory: AL/EQ

Bob Jones University   Vol-Page No: 2-24
,   -   0

Wang, Xingwu   Field: Physics
Asst Professor, PhD   Laboratory: WL/FI
Dept. of Electrical Eng.
Alfred University   Vol-Page No: 5-25
Alfred, NY 14802-0000

Whitefield, Philip   Field: Chemistry
Research Assoc Professor, PhD   Laboratory: PL/LI
Cloud & Aerosol Sciences
University of Missouri-Rolla   Vol-Page No: 3-13
Rolla, MO 65401-0000

Willson, Robert   Field: Physics and Astronomy
Research Assoc Professor, PhD   Laboratory: PL/GP
Robinson Hall
Tufts University   Vol-Page No: 3- 6
Medford, MA 2155-0000

Witanachchi, Sarath   Field: Department of Physics
Assistant Professor, PhD   Laboratory: FJSRL/
4202 East Fowler Avenue
University of South Florida   Vol-Page No: 6-13
Tampa, FL 33620-7900

Woehr, David   Field: Psychology
Assistant Professor, PhD   Laboratory: AL/HR
Psycholoogy
Texas A&M University   Vol-Page No: 2-35
College Station, TX 77845-0000

SFRP Participant Data

Xu, Longya
Assistant Professor, PhD
Electrical Engineering
The Ohio State University
Columbus, OH 43210-0000

Field: Electrical Engineering
Laboratory: WL/PO

Vol-Page No: 5-63

Yavuzkurt, Savas
Associate Professor, PhD

Pennsylvania State University
University Park, PA 16802-0000

Field: Mechanical Engineering
Laboratory: WL/PO

Vol-Page No: 5-64

Zhang, Xi-Cheng
Associate Professor, PhD
Physics Department
Rensselaer Polytechnic Institu
Troy, NY 12180-3590

Field: Physics
Laboratory: RL/ER

Vol-Page No: 4-15

Zhou, Kemin
Assistant Professor, PhD
Dept. of Elec & Comp. Eng
Louisiana State University
Baton Rouge, LA 70803-0000

Field:
Laboratory: WL/MN

Vol-Page No: 5-52

Zimmermann, Wayne
Associate Professor, PhD
P.O. Box 22865
Texas Woman's University
Denton, TX 76205-0865

Field: Dept Mathematics/Computer
Laboratory: PL/WS

Vol-Page No: 3-40

OBJECT-ORIENTED FORMAL SPECIFICATION USING REFINE:
A FEASIBILITY STUDY

Barrett R. Bryant
Associate Professor
Department of Computer and Information Sciences

The University of Alabama at Birmingham
1300 University Boulevard
Birmingham, Alabama 35294-1170

OBJECT-ORIENTED FORMAL SPECIFICATION USING REFINE: A FEASIBILITY STUDY

Barrett R. Bryant
Associate Professor
Department of Computer and Information Sciences
The University of Alabama at Birmingham

Abstract

This paper proposes object-oriented extensions to the REFINE specification language which will facilitate transformation of REFINE specifications into C++ programs. The advantages of this approach are: 1) existing REFINE specifications may be enhanced through interfaces with C++ applications, 2) an integration of object-oriented, logic and functional specification methodologies is achieved, and 3) object-orientation provides support for parallel execution in a natural manner which will allow REFINE specifications to be transformed into parallel programs where appropriate.

OBJECT-ORIENTED FORMAL SPECIFICATION USING REFINE: A FEASIBILITY STUDY

Barrett R. Bryant

1 Introduction

The Knowledge-Based Software Assistant (KBSA) [Whit91] was developed at Rome Laboratory to automate the development of software systems throughout their entire software life-cycle. KBSA is unique in that it provides knowledge-base support for the software development process undertaken by the software development team. The specification language used in KBSA is REFINE™ [Reas90], developed by Reasoning Systems, Inc., which is an integration of set theoretic constructions, logical rules, transformation rules, pattern matching, and procedural structures in a knowledge-base system framework. REFINE is executable through program transformation methodology and hence allows the construction of executable specifications.

Current software development methodology has been heavily influenced by the object-oriented programming paradigm [Booc90]. This paradigm is characterized by the representation of a software system as a set of classes, each of which defines an abstract data type and its corresponding set of operations. Object-orientation would exist in the specification, design, and implementation phases of the software system's life cycle. Reuse of existing classes for a wide variety of applications would reduce the amount of time required for software validation and maintenance. Unfortunately, the existing version of REFINE does not support object-orientation.

In this paper, we propose object-oriented extensions to REFINE to facilitate reuse at the specification level. These extensions will be modelled after C++ [Stro86] for the pragmatic reason that it is the most widely used object-oriented programming language in commercial environments. It is hoped that the relationship to C++ will facilitate the

acceptance of object-oriented REFINE among software developers, allow REFINE programs to interface with the large number of existing applications developed in C++, and will enhance C++ itself by providing an interface with an executable specification language featuring a number of powerful tools not currently available in the C++ language. The new specification language will be upwardly compatible with the current version of REFINE, and is especially intended to preserve properties of the original REFINE language which allow reasoning about programs.

The paper is organized as follows. Section 2 discusses object-oriented software specification. In section 3, we evaluate the issues involved in extending REFINE to be object-oriented. Automatic parallelization of object-oriented specifications is discussed in section 4. Finally, we conclude with section 5.

2   Object-Oriented Software Specification

Object-orientation is the concept of modelling real-world entities as *objects* and characterizing the behavior of objects through the definition of *classes* [Wegn87]. The fundamental properties of objects belonging to a certain class are defined by *methods* and the components of objects, called *instance variables*, along with the associated methods form an *abstract data type*. Since the details of the various methods need not be known, only their behavior being necessary, objects may be reasoned about abstractly [Dahl87]. This is further facilitated by the fact that the names of instance variables and methods in each class are local to that class and hence lexical scoping enforces the encapsulation of the data type. A further fundamental property of object-orientation is the notion of *inheritance* whereby a class is denoted as being a *subclass* of another class and thereby inherits all instance variables and methods of the parent class. This allows for further specialization of object behaviors. Inheritance serves to structure the objects into members of a *class hierarchy* which is well founded in type theory [Dahl90]. The development of methods into implementations may conveniently

follow stepwise refinement principles [Lano92, Saak92].

Current efforts at object-oriented specification include FOOPS [Gogu87], an algebraic specification language supporting the definition of classes by describing the algebraic properties of their members, and object-oriented extensions to the Z specification language [Cusa91, Lano91]. Some of the difficulties in making such extensions to Z are the need for universal and existential quantification of types to provide polymorphism as well as high-order operations such as the application of quantification to object methods [Whys90].

Since objects are independent entities which communicate through message passing, concurrency is natural to object-orientedness [Yone87]. There are many forms of concurrency possible within an object-oriented system. Inter-object concurrency refers to different objects carrying out different activities at the same time. Intra-object concurrency refers to a single object executing several methods simultaneously. Each of these methods could themselves be carrying out several operations concurrently [Nels91]. The objects have different threads of control based on the level of concurrency. The different *styles of interaction* between communicating objects can be classified based on the send-receive mechanism, call-reply mechanism and synchronous or asynchronous or future mechanisms [Toml89]. The main issues in such designs are whether message passing should be synchronous or asynchronous or be in the form of a remote procedure call, and the granularity of parallelism: fine-grained (instruction-level), medium-grained (loop parallelism), or course-grained (object method level).

The various efforts towards concurrent object-oriented programming languages have been in extending existing object-oriented languages to support concurrency or developing new languages [Nels91]. For example, Concurrent C++ [Geha88] is one extension of C++. The actor model has been incorporated into C++ in [Kafu90]. These various concurrent object-oriented programming systems provide some explicit concurrency constructs which the programmer has to use to obtain concurrency. In a concurrent object-oriented programming system, the specification of synchronization constraints and its relationship with en-

capsulation is important; and also the relationship between synchronization constraints and inheritance [Nier90]. The different systems realize concurrency over a shared or distributed platform [Bal89, Chin91].

We believe that concurrency can also be conveniently added to object-oriented specification. However, the proposed object-oriented REFINE language has a major advantage over standard C++ with respect to concurrency. The features of the language are sufficiently high-level that they may contain implicit parallelism which may be detected by the specification language compiler and this parallelism may then be explicitly incorporated into the generated code. For example, many of the automatic parallelization techniques described in [Zima90] would be applicable. Furthermore, the exploitation of parallelism in object-oriented languages is based upon formal methods [Amer91].

3   Extending REFINE as a Specification Language

REFINE was designed with the following goals in mind [Reas90]: 1) development of the specification is accompanied by a knowledge-base which stores details of the specification development process, 2) both "wide-spectrum" and "multi-paradigm" programming are supported, 3) the language should be extensible, and 4) there should be language support for stepwise refinement including representations for programs and transformation rules. We believe that each of these goals may be accomplished within the proposed C++ framework. The general strategy is to assume a preprocessor for translating REFINE syntax into the corresponding C++ syntax. REFINE semantics will be defined using a collection of C++ classes, meaning that for every REFINE operation on a data type, there will be a corresponding C++ method for that data type, defined as a class. In the following subsections, we address the different aspects of the REFINE language in turn, discuss how it may be transformed into C++, and identify where parallelism might be exploited.

3.1 Data Types

REFINE provides data types for scalar objects including numbers, characters, symbols, and Booleans, structured objects such as sets, sequences, strings and tuples, as well as binary relations and maps. Undefined and typeless values are also represented and a number of data type conversions are provided.

3.1.1 Scalar Objects

Numbers, characters, symbols and Booleans, and most of their associated operations may be trivially defined using C++. This is true also of universal and existential quantification and nondeterminism because of the limitations REFINE places on the bound variables to ensure finiteness. These may be implemented using an iterator construction in C++. In a parallel implementation, such quantifications ranging over a large number of values may also be considered for possible partitioning into different computational threads.

For an example of representing a REFINE quantification in C++, consider the specification:

ex (x, y) (y * x = 420000 & x in [1 .. 1000] & y in [1 .. 1000])

which evaluates to true because x = 600 and y = 700 is one such solution. A corresponding C++ iteration is:

```
for (x = 1; (x <= 1000) && !exists; x++)
    for (y = 1; (y <= 1000) && !exists; y++)
        exists = y * x == 420000;
```

Using loop parallelization transformations, this could be transformed into equivalent code which executes all iterations of the outer loop in parallel, as in:

```
doall (x = 1; x <= 1000; x++)
    for (y = 1; (y <= 1000) && !xexists [x]; y++)
        xexists [x] = y * x == 420000;
exists = any (xexists);
```

The results of each iteration of x are tallied in the xexists array. A standard function **any** is then used to verify if any element of the xexists array is true. This function may be implemented in parallel as well.

3.1.2 Sets, Sequences, Strings and Tuples

As is the case with scalar objects, these structured objects and most of their operations are easily defined using C++. Sets may be implemented using either bit vectors for dense sets or hash tables for sparse sets. Sequences may be represented using list data structures. Strings are directly representable as well. Tuples correspond to C++ structures.

Similar to Boolean quantification, constructions such as the set former and sequence former and operations based on these may be implemented using iterators with parallel execution feasible for very large sets or sequences. Complexities are introduced by set and sequence operations which require references to functions, such as **filter**, **image**, and **reduce**. In the case where function names are passed as arguments to these operations, the "values" of these arguments may be pointers to the appropriate C++ functions. REFINE also allows functions to be represented by lambda abstractions which are not directly executable in C++. During the course of the preprocessing from REFINE into C++, some of these abstractions may be converted into standard functions in cases where the lambda abstraction is applied to exactly the correct number of arguments. However, if the number of arguments is different from the number of variables bound by the lambda abstraction, then some additional techniques need to be used. One possibility is to convert the resulting function expressions into *supercombinators* [Peyt87]. In this approach, lambda abstractions are translated into standard functions which have exactly the required number of formal parameters to match the number of arguments, either by adding additional formal parameters or by recognizing that the result of the function may be another function and hence require further applications. Supercombinator generation may not always be possible during preprocessing time in which case there must exist methods in lambda abstraction classes to

generate the supercombinator expressions dynamically. This will be facilitated by defining a class for functions and manipulating functions, including lambda abstractions, as first-class objects.

As an example of where parallelism may occur, consider the image of a sequence under a map, image (f, S), where f is a mapping function and S is a sequence. Represented in C++, this might be treated as a message image (f) being sent to S (i.e. S . image (f)). The C++ code to implement this must traverse the sequence S, applying the function f to each member of S. If S is represented as a structure with a length attribute and the individual elements are stored in an array, then the code might be as follows:

```
for (i = 0; i < length; i++)
    new_sequence . element [i] = f (element [i]);
```

Now the code may be parallelized to execute each iteration of the loop in parallel. Similar parallelizing transformations may be applied to the **reduce** and **filter** operations.

Sets, sequences and tuples have pattern and elliptical constructions. During preprocessing, such constructions can be converted into more basic operations using the standard REFINE semantics.

3.1.3   Binary Relations and Maps

Binary relations are essentially implemented in REFINE as sets. Hence, set operations cover binary relation operations with the exception of transitive closure. Maps are function objects which have been described somewhat in the previous section. As mentioned there, difficulties arise in manipulating functions that must be represented dynamically. Either supercombinator reduction or graph reduction may be implemented in the C++ function class to allow function operations to proceed with good efficiency. Functions are among the least natural REFINE structures to represent using C++ since there is no existing support for higher-order functions. However, as mentioned earlier, a class can be constructed to

represent such functions which would then allow higher-order functions to manipulate C++ objects. This could become the framework of a powerful integration of functional and object-oriented programming methodologies.

3.1.4   Knowledge-Base Objects

REFINE provides full support for the construction of an object-oriented knowledge-base system. This means that objects may be created which represent some knowledge about the specification development process. Furthermore, these objects form a hierarchy thereby facilitating the reuse of components. The REFINE "knowledge-base" may be represented by a global object in C++ capable of storing and manipulating the tree-structured hierarchy in response to REFINE statements. In a sense, the maintenance of this knowledge-base is an object-oriented system embedded within and implemented by a C++ object-oriented program.

3.2   Control Constructs

Many control constructs found in REFINE are similar to those in most conventional languages, including C++. Here we concentrate on the unusual ones. The translations of assignment statements, statement sequencing, conditional statements, enumeration, while statements, and function definitions are straightforward. Some parallelism is possible during enumeration and while-iteration as analysis might allow for the bodies of these statements to be executed in parallel across different iterations.

3.2.1   Variables

A **let** statement is used to introduce bindings for local variables. The scoping rules of **let** statements are similar to C++ blocks so a one-to-one translation between the two would be the simplest approach. This would not be possible if there were a "parallel" assignment of

the form:

```
let (x = 1, y = 2)
    let (x = y, y = x)
        . . .
```

In this case, the innermost x is to receive the value 2 and the innermost y the value 1. The simplest solution to this is to substitute the values assigned to the outer variables for those variables within the parallel assignment so as to break the parallelism. As long as there is an order to the variable assignments, this order may be followed in the C++ block in making the assignments. For example, if we have:

```
let (x = 1)
    let (x = 2, y = x)
        . . .
```

we may always translate this into:

```
{ int x = 1
    { int y = x; int x = 2;
        . . .
    }
}
```

where the initializations are performed in order. In performing this translation, some optimizations of the let-block may also be done to eliminate unnecessary variable assignment and redundant computation of common subexpressions. Note that a type analysis is required of the values being assigned to let-variables so that the appropriate declarations in C++ can be made.

3.3 Knowledge-Base Object Replacement and Transforms

As mentioned earlier, the REFINE knowledge-base should be accessible through a global object with methods defined for knowledge-base operations. One such operation is the **replace** statement which replaces one knowledge-base object by another. We assume that the

knowledge-base class has been defined with appropriate methods to perform such replacements.

Transform statements are one of the most unique aspects of the REFINE language in that they provide rules through which the underlying knowledge-base should be updated. In effect, they may be used to specify the replacement of program constructs by other program constructs. In another sense, transformation rules may be thought of as declarative interpretations of program constructions. The implementation of transforms in C++ is similar to that of replacements except that it happens at the global knowledge-base object level rather than in a particular specified object. There are a number of complicated semantic rules pertaining to the implementation of transforms but all may be expressed through appropriate C++ methods.

REFINE permits a form of declarative logic programming through the presence of assertion rules. They are typically used within functions to give a declarative specification of the function semantics. These assertion rules may then be used by the REFINE compiler to produce program code for that function. The methods used to manipulate the global knowledge-base may be used to interpret logical assertions as well. These would include an extensive array of theorem-proving axioms to symbolically manipulate or verify the assertions.

3.4   C++ Infrastructure

The target code of the preprocessor we have been describing will be embedded within an established C++ infrastructure of existing classes and their associated methods. We envision a multiple-inheritance class hierarchy providing a wide range of abstract data types for the target program to draw upon. As has been seen from the discussion, this will include classes for manipulating functions as first-class objects, classes for evaluating declarative specifications of logical rules, and classes for maintaining a separate object-oriented knowledge-base. In this sense, the implementation combines implementation technologies for functional, log-

ic, and object-oriented programming paradigms. We envision that REFINE statements will be directly embedded into C++ functions and class definitions and the preprocessor will distinguish the REFINE code and make the appropriate translations. This embedding of REFINE into C++ will allow the REFINE specification being developed to interface with existing C++ classes, thereby facilitating reuse of developed code at the specification level. Furthermore, it serves to extend C++ with the very advanced and powerful features of the REFINE language, meaning that applications under development in C++ can be "coded" at the specification level rather than the program level, with the preprocessor and associated transformation rules in REFINE doing the program level coding.

In addition to implementing the features of REFINE which will be translated, this underlying C++ infrastructure also introduces some additional semantic complexities. These are enumerated by [Budd91] as follows:

1. C++ does not maintain complete run-time information about the types of objects. On the other hand, objects are often assigned values through pointers. An erroneous assignment of an object reference may not be detected by the C++ compiler. In order to be used as a specification language, this situation must be avoided in the REFINE/C++ interface.

2. In multiple inheritance, the same name may be inherited from two different parents and hence have different semantics. This may be solved using *redefinition* which overrides the ambiguous methods or *renaming* which changes the name of the method. However, the system must ensure that the ambiguity is resolved.

3. If a child has two parents, each of which has a common parent, then the child inherits from the grandparent along two paths, creating ambiguity. This may be solved by declaring the inheritance of the parent classes from the grandparent classes as *virtual*. Again, the system should ensure that this is done.

4. When an overloaded name is used in C++, the inheritance mechanism is first used to

find a name scope in which the function is defined. Parameter types are then used to disambiguate the function name within that scope. Sometimes the ambiguity cannot be resolved due to the types being convertible (e.g., an integer may be converted into a floating point type).

4   Automatic Parallelization of Object-Oriented Specifications

A major advantage of C++ (or the object-oriented framework in general) is the fact that there are a number of techniques for mapping the interacting objects into parallel and distributed execution models. We believe that a good parallelizing compiler can detect interdependencies among objects and map them onto the appropriate processors so as to have effective performance enhancement.

The basic structure of a parallelizing compiler for object-oriented languages would be similar to that for more conventional languages (e.g. see [Zima90]). However, there are some major differences in the nature of the components, caused by object-orientation. The primary components of the parallelization of object-oriented programs are flow analysis, dependence analysis, and parallel code generation.

Flow analysis begins with intermediate code structures produced by a suitable front-end and constructs a flow graph showing the flow of control throughout individual methods, a collection of methods within a class or object, and all the methods of a program. While there are similarities between this flow analysis and that for conventional programming language compilers, it is made considerably more complex by the presence of polymorphism and multiple inheritance. The exact details for solving these problems are currently under investigation.

Dependence analysis uses the control flow information to determine all the data de-

pendencies between the different objects. The primary dependencies in an object-oriented program result from message passing among objects. To determine the degree of interconnectedness between the different objects and the flow of data between different objects, we may construct a message flow graph. We may also construct a standard dependence graph for the code within each method.

Parallel code generation will use the flow and dependence information to partition the objects into processes so as to reduce communication costs. This includes the determination of whether an object process should be synchronous or asynchronous. Furthermore, we may generate code with the necessary process model calls to automatically control communication between processes so as to reduce the number of messages that must be sent while increasing the amount of data transferred in a single message. This would include, for example, the restructuring of iterative constructions involving message passing of individual data structure elements (e.g. sequences) to instead send a single message of the entire structure to a newly created method which then iterates over the structure.

The design of the REFINE language itself facilitates such automatic parallelization. There are no pointers or call by reference to create aliasing in method calls and all object modification may therefore be done explicitly. The fact that most computation takes place using itertive constructions would allow the compiler to take advantage of the many existing parallelization techniques that have been developed for such a control structure.

5   Conclusions

We have presented an analysis of the feasibility of translating REFINE into C++ to support object-oriented specification of software systems under the C++ model. The project is generally feasible with several main tasks required to accomplish the implementation:

1. C++ classes must be defined for all existing REFINE data structures. Many of these are straightforward with the exception of those outlined below.

2. REFINE is currently implemented in and translated into Lisp. There are a number of functional language features supported by REFINE/Lisp that are not directly present in C++, including the ability to manipulate functions as first-class objects by passing them as arguments to various other functions. The inclusion of lambda abstractions is an embodiment of this idea. A C++ class for functions must be defined with an extensive set of methods to support the needed operations. The task is somewhat analogous to constructing a small Lisp interpreter in C++.

3. There are assertions and transformation rules present in REFINE which specify information declaratively. C++ does not have an inherent capability to manipulate declarative information so a class would need to be added for logical rules with methods included for the associated proof theory. The construction of such a class would be relatively complex and essentially embeds a Prolog interpreter into C++.

4. REFINE maintains a separate object-oriented knowledge-base of information about the development of the specification. Some logical aspects of this knowledge-base may be implemented using the logical rule class described previously. However, a class hierarchy must be maintained within the program and the implementation of this will require additional classes.

5. There are several aspects of C++ that hinder its effectiveness as a specification language. These have to do mainly with ambiguities caused by multiple inheritance and polymorphism. The specification environment must ensure that such ambiguities are not created in the specification or that they are effectively resolved prior to invoking the C++ compiler.

There are a number of places within the existing REFINE language where parallelism may be detected and exploited in the target program. However, most parallelism will likely come from the interaction of the objects themselves as defined in C++.

Our future work is to develop a complete implementation of object-oriented extensions to REFINE described in this paper. The result will be a translation from REFINE to C++ which allows REFINE specifications to interface with C++ classes and objects. Furthermore, we will develop parallelizing transformations which allow the resulting C++ programs to be executed in parallel under both shared-memory and distributed models of computations. This will allow not only automatic program generation from specifications but automatic *parallel* program generation from specifications.

References

[Amer91]   America, P., "Formal Techniques for Parallel Object-Oriented Languages," in [Toko91], pp. 119-140.

[Bal89]   Bal, H. E., Stiener, J. G., and Tanenbaum, A. S., "Programming Languages for Distributed Computing Systems," *ACM Computing Surveys 21*, 3 (September 1989), 261-322.

[Booc90]   Booch, G., *Object-Oriented Design*, Benjamin/Cummings, Menlo Park, CA, 1990.

[Budd91]   Budd, T., *An Introduction to Object-Oriented Programming*, Addison-Wesley, Reading, MA, 1991.

[Chin91]   Chin, R. S. and Chanson, S. T., "Distributed Object-Based Programming Systems," *ACM Computing Surveys 23*, 1 (March 1991), 91-124.

[Cusa91]   Cusack, E., "Inheritance in Object-Oriented Z," *Proceedings of ECOOP '91, 5th European Conference on Object-Oriented Programming*, Springer-Verlag LNCS 512, Berlin, 1991, pp. 167-179.

[Dahl87]   Dahl, O.-J., "Object-Oriented Specification," in [Shri87], 1987, pp. 561-576.

[Dahl90]   Dahl, O.-J., "Object-Orientation and Formal Techniques (Extended Abstract)," in *Proceedings of VDM "90, VDM and Z - Formal Methods in Software Development*, eds. D. Bjorner, C. A. R. Hoare, and H. Langmaack, Springer-Verlag LNCS 428, Berlin, 1990, pp. 1-11.

[Geha88]   Gehani, N. H. and Roome, W. D., "Concurrent C++: Concurrent Programming with Class(es)," *Software - Practice and Experience 18*, 12 (December 1988), 1157-1177.

[Gogu87]   Goguen, J. E. and Meseguer, J., "Unifying Functional, Object-Oriented and Relational Programming with Logical Semantics," Technical Report, SRI International, Menlo Park, CA, 1987.

[Kafu90]   Kafura, D. G. and Lee, K. H., "ACT++: Building a Concurrent C++ with Actors," *Journal of Object-Oriented Programming 3*, 1 (May 1990).

[Kim89]   Kim, W. and Lochovsky, F. H., eds., *Object-Oriented Concepts, Databases, and Applications*, Addison-Wesley, Reading, MA, 1989.

[Lano91]   Lano, K., "Z++, An Object-Orientated Extension to Z," *Proceedings of the Fifth Annual Z User Meeting*, 1991, pp. 151-172.

[Lano92]   Lano, K. and Haughton, H., "Reasoning and Refinement in Object-Oriented Specification Languages," *Proceedings of ECOOP '92, 6th European Conference on Object-Oriented Programming*, Springer-Verlag LNCS 615, Berlin, 1992, pp. 79-97.

[Nels91]   Nelson, M. L., "Concurrency & Object-Oriented Programming," *Proceedings of OOPSLA '91, the 1991 Conference on Object-Oriented Programming, Systems, Languages, and Architectures*, 1991, pp. 63-72.

[Nier90]   Nierstrasz, O. M. and Papathomas, M., "Viewing Objects as Patterns of Communicating Agents," *Proceedings of OOPSLA/ECOOP '90, the 1990 Conference on Object-Oriented Programming, Systems, Languages, and Architectures, and European Conference on Object-Oriented Programming*, 1990, pp. 38-43.

[Peyt87]   Peyton Jones, S., *The Implementation of Functional Programming Languages*, Prentice-Hall International, Englewood Cliffs, NJ, 1987.

[Reas90]   Reasoning Systems, Inc., *REFINE User's Guide*, Reasoning Systems, Inc., Palo Alto, CA, 1990.

[Saak92]   Saake, G., Jungclaus, R., and Ehrich, H.-D., "Object-Oriented Specification and Stepwise Refinement," *Open Distributed Processing*, eds. J. de Meer, V. Heymer, and R. Roth, North-Holland, Amsterdam, 1992, pp. 99-121.

[Shri87]   Shriver, B. and Wegner, P., eds., *Research Directions in Object-Oriented Programming*, MIT Press, Cambridge, MA, 1987.

[Stro86]   Stroustrup, B., *The C++ Programming Language*, Addison-Wesley, Reading, MA, 1986.

[Toko91]   Tokoro, M., Nierstrasz, O., and Wegner, P., eds., *Object-Based Concurrent Computing*, Springer-Verlag, Berlin, 1991.

[Toml89]   Tomlinson, C. and Scheeval, M., "Concurrent Object-Oriented Programming Languages," in [Kim89], pp. 79-124.

[Wegn87]   Wegner, P., "The Object-Oriented Classification," in [Shri87], pp. 479-560.

[Whit91]   White, D. A., "The Knowledge-Based Software Assistant: A Program Summary," Technical Report, Rome Laboratory, Griffiss Air Force Base, NY, 1991.

[Whys90]   Whysall, P. J. and McDermid, J. A., "An Approach to Object-Oriented Specification Using Z," *Proceedings of the Fourth Annual Z User Meeting*, 1990, pp. 193-215.

[Yone87]   Yonezawa, A. and Tokoro, M., eds., *Object-Oriented Concurrent Programming*, MIT Press, Cambridge, MA, 1987.

[Zima90]   Zima, H. and Chapman, B., *Supercompilers for Parallel and Vector Computers*, Addison-Wesley, Reading, MA, 1990.

INTEGRATING MULTIMEDIA INFORMATION FOR THEATER-LEVEL COMMAND AND CONTROL

Lee Scott Ehrhart

Center of Excellence in

Command, Control, Communication and Intelligence (C³I)

School of Information Technology and Engineering

George Mason University

4400 University Drive

Fairfax, Virginia 22030

Abstract

The modern command center must support force-level data fusion (the integration and display of information from a range of sources) to meet the needs of contingency operations. Furthermore, the effectiveness of the information use depends upon improving the integration of information processing capabilities with the cognitively-demanding team planning and decision making tasks of the joint force senior command. Thus, "having the most data" is not an assurance of success in warfare. The leveraging factors in information technology for command support are the ability to present the commander with the *right information* at the *right time* with the *right level of detail*. The user-computer interaction (UCI) design goal is an information interaction concept that balances maximal use of the positive characteristics of the various information presentation and interaction technologies to meet requirements, while minimizing the potential for distractions from the primary tasks. Achieving this balance requires understanding not only the cognitive requirements of the task and the characteristics of the individual UCI technologies, but also the interaction of technologies and the additional cognitive requirements imposed by the introduction of new technological capabilities into the operational environment. One of the principal goals of cognitive systems engineering research is the identification and exploration of these relationships. Ultimately, this research should not only guide the design of new systems, but also provide feedback to drive the development of the next generation of technological resources. In direct contrast to the tendency for "technology push" in advanced systems development, this feedback loop supports *requirements-driven design* and reinforces the links to the human user.

This report investigates the "Data Wall" information presentation concept and its associated interface technologies with respect to their potential contributions to the critical requirements associated with theater-level command and control (C^2) decision making. The paper further highlights the pivotal technological issues and emphasizes the importance of context-specific research to support successful design and development to meet the operational requirements of C^2 decision making.

INTEGRATING MULTIMEDIA INFORMATION FOR THEATER-LEVEL COMMAND AND CONTROL

1. Introduction

1.1. THE CHANGING CONTEXT OF MODERN WARFARE

In recent years, the rapid evolution of both the international political environment and innovations in technology have combined to produce dramatic changes in the context of modern warfare. In addition to the possibility of conventional modes of warfare with well-understood adversaries, military forces must now prepare for contingency operations involving limited-objective or low-intensity warfare in relatively novel situations. These new modes of warfare are characterized by shorter warning times, greater ambiguity and a requirement to plan and execute responses in a greatly reduced time frame. To meet the range of operational requirements, the quest for and capability of acquiring more and better intelligence on evolving situations has resulted in a flood of complex data that often overwhelms rather than informs. Information overload is further compounded by the requirement for shorter decision cycles due to dramatic increases in speed and accuracy of weapon systems .

Current doctrine from the Joint Chiefs of Staff (JCS) on the employment of US Armed Forces emphasizes the role of joint (multi-service) forces in modern warfare (JCS, Nov. 1991). Additionally, recent operations in Southwest Asia, Somalia, and Bosnia have involved combined (multinational) forces. Both operational modes of warfare require the capability to rapidly deploy contingency forces into regional conflicts, often without the benefit of previously deployed forward bases of operation. These factors impose additional requirements to quickly assemble a focused, integrated operational picture for situation assessment and planning. The information technology aspects of rapid response are echoed in the JCS mandate for "flexible and adaptive decision support for modular, highly mobile contingency forces" (JCS, Oct. 1991).

Emerging in these models is the notion of *effective* and *efficient* command and control process as a "force multiplier" with the potential to impact battle outcome as significantly as advanced weaponry. However, Coakley (1991) points out that the potential of C^2 process as a force multiplier is dependent upon the organization's ability to employ C^2 technology effectively. Thus, "having the most data" is not an assurance of success in warfare. The leveraging factors in information technology for command support are the ability to present the commander with the right information at the right time with the right level of detail.

1.2. LEVERAGING INFORMATION PRESENTATION TECHNOLOGY TO SUPPORT COMMAND AND CONTROL

The modern command center must support force level data fusion (the integration and display of information from a range of sources) to meet the needs of contingency operations. The joint, interoperable architecture supporting "all media transmission systems -- voice, data, message, and video, as well as imagery" currently envisioned by the C^4I for the Warrior Program carries with it the implicit requirement to effectively integrate and display information drawn from these sources. Furthermore, the effectiveness of the information use depends upon improving the integration of information processing capabilities with the cognitively-demanding team planning and decision making tasks of the joint force senior command. The US Air Force's Air Combat Command is currently pursuing a layered approach to information presentation whereby battle information presented at the senior command level is generally at a high level with minimal detail, tailorable to match decision requirements and individual preference (USAF HQ ACC, 1993). This approach is intended to promote increased access to and use of time-sensitive information by allowing the commander to focus on (or "pull") detailed information only when required for the current decision. In this model, information is "pushed" to the commander based on its value in maintaining situational awareness and relevancy to the operational decisions rather than data availability.

In response to these changes, C^2 systems researchers are exploring innovative concepts in all aspects of user-computer interaction (UCI) and information presentation. New developments in computer architectures have made technologically and economically feasible a variety of UCI approaches previously thought exotic (e.g., natural language interfaces and multimedia information display). Enthusiasm for these new technologies can result in their premature introduction into systems without a clear understanding of the potential impacts. On the other hand, certain technologies may be *under*-exploited when designers are unaware of their potential advantages. The communication of information is not a neutral transfer; the display and interaction design employed in any system *transforms* information, emphasizing certain aspects and de-emphasizing others. The user-computer interaction (UCI) design goal is an information interaction concept that balances maximal use of the positive characteristics of the various technologies to meet requirements, while minimizing the potential for distractions from the primary tasks. Achieving this balance requires understanding not only the cognitive requirements of the task and the characteristics of the individual UCI technologies, but also the interaction of technologies and the additional cognitive requirements imposed by the introduction of new technological capabilities into the operational environment.

Cognitive systems engineering involves the application of research findings, drawn from the fields of cognitive science and engineering, to guide the matching of user, task, and organizational-environmental requirements to available tools and techniques for the design of interaction. Thus, one of the principal goals of cognitive systems engineering research is the identification and exploration of these relationships. Ultimately, this research should not only guide the design of new systems, but also provide feedback to drive the development of the next generation of technological resources [Figure 1]. In direct contrast to the tendency for "technology push" in advanced systems development, this feedback loop supports *requirements-driven design* and reinforces the links to the human user.
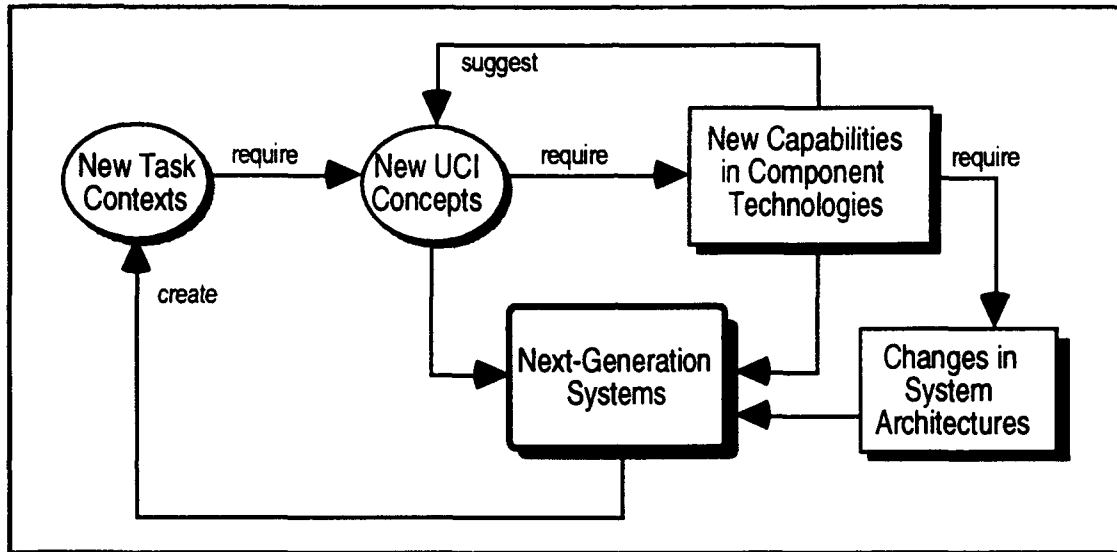
Figure 1: Interaction of Task Requirements and UCI Technology

This report investigates the "Data Wall" information presentation concept and its associated interface technologies with respect to their potential contributions to the critical requirements associated with theater-level command and control (C^2) decision making.

2. Cognitive Task Requirements:
Supporting Decision Processes at the Senior Command Level

2.1. MODELING COGNITIVE TASK REQUIREMENTS

In the simplest terms, what we are trying to do with technology (the task requirements) should define what we want technology to do (the interaction design). Andriole (1989) emphasizes the importance of defining requirements for decision support systems in terms of the users, their tasks, and the organizational and doctrinal context in which decisions are made. The user profile helps to place the user as a member of the larger organization; the task and environmental analyses identify the system's external links and the conditions under which the system operates. It is also necessary to understand the organiza-

tional culture and how it directly, or indirectly, impacts and is impacted by the user and the tasks. Organizational doctrine, whether implicitly or explicitly communicated to the user, may provide not only procedural guidelines for structured tasks, but also a conceptual view and global goals which must be considered. Finally, in the course of evolutionary design and implementation, the designer must be sensitive to the re-definition effects of the new system on the organization and its doctrine.

In systems designed to support planning and decision making, it is important to identify the requirements associated with higher-order cognitive processes involved in these tasks. These *cognitive task requirements* (CTRs) provide a focal point for integrating the user profiles, problem solving tasks, and the decision environments. In addition, cognitive task requirements (CTRs) strongly impact design considerations involving interaction control and focus of attention. The system designer must use information from the requirements analysis to minimize system interference with task performance and direct the user's attention to critical information. This requires understanding which cues will be most effective under specific conditions. Particularly in cases where the tasks are complex and must be performed in a dynamic, time-stressed environment, the designer needs such information to determine optimal display formatting, information representation, and data presentation rates.

Currently, there are no prescriptive means of matching of requirements to design features. Nevertheless, efforts in cognitive systems engineering research have yielded some promising approaches to help bridge the requirements to design gap. For example, Andriole (1989) employs a three-dimensional matrix to represent requirements dimensions and suggest a mapping to the UCI design. The matrix model makes use of a variety of taxonomic approaches to the classification of users and tasks and is readily extensible to a wide range of system contexts. In related work, Andriole, Ehrhart and Aiken (1991) apply this method to the design of a large-screen display for theater-level battle management. Their research provides a hierarchical listing of user, task, organizational-doctrinal requirements subsequently used to define a hierarchical listing of user interface design features. For the purpose of this study, the CTRs were captured using a combination of Andriole's matrix approach and other task profiling techniques that captured the domain-dependent characteristics of theater battle management.

2.2. COGNITIVE TASK REQUIREMENTS FOR THEATER BATTLE MANAGEMENT

2.2.1. The User/Task/Organizational-Doctrinal Requirements

User Profile. Theater commanders are called into situations involving either joint (multi-service) and/or combined (mixture of allies) operations in both limited and conventional warfare. Despite extensive domain experience, their interaction with command support systems may be infrequent and varied across a range of operational experience. For example, a given command support system used in one theater might have a moderate to high frequency of use; however, normal manpower rotation within the services might limit individual hands-on experience with the system. This lack of uniform, frequent experience with computer-based decision support is further compounded by interface designs that focus on the delivery of analytical performance at the expense of user awareness and comprehension. The result is what Lt. Gen. Michael Nelson decries as the technologist's tendency toward a "blizzard of options -- with complex selection trees -- and not towards simplicity at the point of employment" (Nelson, 1993).

Task Overview. Military decision making hinges on situation assessment and option generation. The senior command team begins with some degree of uncertainty and seeks to reduce that uncertainty with additional information and evaluations. Based on the assessment of both the allied and enemy situations, alternative courses of action (COAs) are generated and inferences drawn regarding the possible outcomes of each. Built-in iteration loops feed demands for additional information and refinement of the assessment and option generation phases. An essential aspect of this planning process is the development of a shared situational image. The commander's *image* of the evolving situation and battle plan is a key component of information communicated as the commander's "intent". In pursuit of this shared understanding, planners use wall-size maps and moveable icons, charts, and 3-D representations to focus their discussions, interacting with these displays and each other by drawing courses of action or moving symbols. In studies of US Army corps-level planning groups, Andriole discovered that their methods were highly graphic and non-numeric (Andriole, 1986). In addition, planners incorporate analogs from previous battles fought in the same or similar situations and tactics employed in the past. Information for situation assessment (i.e., weather and terrain data, bomb damage assessment, textual evaluations, photographs, and numerical analyses) are provided by support teams in documents which may be so large as to preclude rapid review under pressure.

Task Environment. The theater-level planning environment involves decision making on a crisis and non-crisis (strategic planning and exercise) basis. In crisis mode, this environment is characterized by very high stakes and the requirement for a short decision cycle.

Since an independently operating adversary is involved. the planners' decision cycle must be shorter than that of the adversary to ensure campaign success. Combined operations present new and unique problems in command and control. Relationships with allies and host nations limit the strength of US forces through political agreements, stationing restrictions, force ceiling restrictions, and budgetary constraints, etc. Decision support systems in this domain must assist this process, promote and facilitate group interaction, and aid the generation and evaluation of alternative courses of action (COAs).

Doctrinal and Organizational Considerations. Any profile of military planning requires an understanding of command, both the theoretical definitions and command as defined by the current doctrine of the organizations involved. This doctrine constitutes the organized knowledge of strategy and tactics employed to achieve a military goal. High-level goals and objectives are determined by orders from the Commander-in-Chief and are further defined within the context of guidelines / restrictions from Congress and the allied governments. While most of these relationships are fixed and formal, doctrine is a dynamic and evolving theory on the command of military forces.

Planning and decision making for modern warfare require the integration of multiple (often overlapping) information sources developed independently with varying degrees of relevance, precision, and timeliness. The resolution of uncertainty is not uniquely a function of intelligence fusion; it requires a combination of information processing, intelligence analysis, and the collaboration among a team of highly experienced senior officers. The hierarchical structure of military organizations plays a major role in the dynamics of the group interactions. Each level in the organization serves as a filter to synthesize, summarize and present information upward to the next level. Traditional information processing approaches to command and control tend to focus on computational tasks without integrating the input of team interaction on the problem. Naturally enough, these systems do not provide any means for facilitating team dialogue. This segregation tends to result in the relegation of computer-based support to lower echelons or limited use as briefing support.

2.2.2. CTR Summary

Based upon the assessment of the user, task, organizational-doctrinal requirements, it is possible to summarize the cognitive task requirements to include the following:

- *Support for infrequent, non-uniform system experience* -- highly transparent, "natural" interaction, permitting users to literally walk-up and use the system.
- *Support for planning and decision making tasks at the most meaningful level of abstraction* -- the right information at the right time in the right form.

- *Support for sharing images* -- facilitating collaboration on situation assessment, understanding and evaluating options, communicating the commander's intent to operational forces, and incorporating feedback on progress of operations.

- *Support for handling information overload* -- relief from the burden of manually reviewing detail without sacrificing awareness of critical factors and developments;

- *Support for mediating the potential errors associated with planning and team decision making* -- cues to the accurate interpretation of information that take into account the degree of certainty, precision, and completeness associated with the information source.

- *Support for integrating the collaborative nature of battle planning with the support system interaction requirements.*

The next section examines the potential application of information presentation and interaction technologies to meet these high-level requirements.

3. Technology Resources for Information Presentation and Interaction in the Theater Command Center

Since the earliest writings on command in warfare, military strategists attempted to characterize the commander's information requirements with respect to dimensions such as timeliness, degree of certainty, level of detail, etc. One of the most promising generic models categorizes C^2 information in terms of pipelines, alarms and trees (Kahan et al, 1989). **Pipelines** present information in set order, set format, and set level of detail as a one-way "push." This mode trades off lower timeliness (i.e., slower delivery) against the value of a lower degree of uncertainty. Thus, its principal advantage lies in its uniformity and consistency as a baseline. Since the information variables must be known in advance, this mode is inadequate when the information needs are context-dependent or the input variables are unknown. At the opposite end of the spectrum, **alarms** (or interrupts) balance high timeliness and detail against highly uncertain information. Some alarms may be set in advance; others must be tailored to suit contingencies. Highly context-dependent situations require demand-driven, branching inquiry -- or **trees**. Trees involve varying degrees of timeliness and detail, but are usually pulled from more certain sources. Effective support for information interaction in each of these modes requires the identification of UCI concepts that facilitate more direct image sharing and provide the capability to mix supply-push and demand-pull interaction.

3.2. MULTIMEDIA INFORMATION PRESENTATION RESOURCES

A comprehensive body of research in memory and learning supports the value of multiple communication modes and presentation media. The theoretical literature extended many of these concepts to a larger model of human information processing. From the perspective of the UCI designer, the utility of multiple information presentation media may be viewed in terms of an expansion of the information communication bandwidth between the computer-based support system and the human user. At each level in the command and control hierarchy, command decision makers develop their situational images from multiple views of the battlefield (i.e., tabular data, mission flow charts, maps, sensor displays, etc.). In addition to the more traditional presentation media, there is a growing interest in exploring the value of incorporating high resolution visual information, sound, speech, and video. Each of these capabilities support the senior command's information access requirements (pipelines, alarms, trees) in varying degrees. Moreover, information that must be "pulled" in tree inquiries by one level in the hierarchy becomes part of the information that is "pushed" to the next level in the form of briefings or situation updates. For example, high resolution photographic imagery, a critical part of the intelligence input for targeting and bomb damage assessment, is pulled by tasking resources to collect it then pushed to the next decision making level as part of the intelligence assessment.

In addition to more traditional non-text media such as photographic imagery, the capability currently exists to communicate information to the senior command in real time or from recorded sources using speech, sound, and video and graphics. Although research tends to focus on speech as an input medium, live or recorded speech may provide out put as verbal communication from field units to supplement both standard (pipeline) and emergency (alarm) communication. Speech may also be a part of human intelligence information (e.g., recorded statements from adversaries) or supplementary verbal explanation attached to graphic and photographic data. In addition, synthesized speech is an effective feedback mechanism for certain interaction tasks (e.g., notification of the completion of a background process). Sound is often associated with system alarms; moreover, sound in the form of auditory icons (Gaver's "earcons") supports the perceptual integration of multiple processes in the form of a single audio cue (Gaver, 1991). Similarly, audio feedback incorporated into visualization routines provides additional cues to assist in the comprehension of complex, multidimensional data.

Video combines a wide range of still and motion visual imagery with speech and sound to provide multimodal communication of complex information. Graphic simulation and multidimensional information visualization project dynamic, evolving representations of highly complex fused data in a form more readily comprehensible to human decision

makers. Information presentation techniques such as stereoscopic 3-D projection and holographic imagery allow users to "view" the battlefield (including aerospace dimensions) in ways previously limited by human perceptual capabilities. Similarly, the multidimensional display of typically non-visible data (e.g., sensor data) permits users to explore relationships and discover meanings in highly complex situations.

These technologies, employed separately and combined, provide a potential enhancement to situational awareness in the command center. Although electronic transmission bandwidth and throughput continues to present problems for theater-wide dissemination of multimedia information, a variety of sampling and compression schemes exist which considerably reduce the bandwidth requirements associated with information-rich media. Much of this technology exists today in a "fieldable" form suitable for use in the theater and force-level command centers.

3.3. REAL-TIME INTERACTIVE INFORMATION RESOURCES

The various multimedia resources also support two-way, or interactive, information communication. Speech and video facilitates distributed team decision making with real-time communication between and among the upper levels of joint and/or combined forces. Interactive simulation allows the commander to explore not only the current situation and recent history, but also to project the consequences or effects of the various courses of action available. Animated graphics, for example, provide the dimension of time to unfolding events. Multidimensional visualization permits the decision maker to "tweak" problem parameters and view the subsequent effects on other factors.

Virtual reality, although still earliest phases of development, constitutes the most dramatic advance in interacting with situational information. Current technology allows a wide range of interaction levels from full sensory emersion in the artificial environment to non-emersive manipulation of virtual objects. Through the use of this technology, decision makers may examine courses of action without risk (i.e., route planners may pre-fly strike routes through threat zones in unfamiliar territory) or explore situations at distant and/or dangerous locations (e.g., commanders may "tour" the target area to understand the contingent targets). Additional possibilities exist for allowing humans to "visit" or interact with environments unavailable to human beings by compressing or expanding the level of detail in a multidimensional information set to facilitate the decision maker's understanding of trends or patterns in data.

Most of these capabilities exist today in standalone prototype form. Research to evaluate their use and impact on task performance typically is conducted without the context of a larger interaction design incorporating various information presentation media and inter-

action modes. There is a critical need for integrative research to investigate the impacts of combining technologies and interaction concepts in specific task environments.

4. The Data Wall:
Integrating Multimedia Information for Theater Battle Management

4.1. THE "DATA WALL" CONCEPT

The Advanced Displays and Intelligent Interfaces Laboratory (ADII) in the C3 Division at Rome Laboratory is currently engineering an integrated environment to explore the design possibilities afforded by combining multimedia information and multimodal UCI technologies to meet the requirements of theater battle management. The "Data Wall" is actually a seamless wall-size display created using multiple high-resolution monitors individually driven by separate processors controlled in a locally distributed architecture. This design permits the direct display (without intermediate frame buffering) of a single image across all of the monitors and the ability to open multiple windows for individual or combined processes.

The Data Wall will support a full range of information presentation media (e.g., photographic imagery, sound, speech, video, graphics, alphanumeric, etc.) and permit the command decision team to interact with each other and the information through the use of gesture and speech. These interaction modes all the more natural interaction the users experience with more traditional information displays such as wall-size maps. In addition, the transparent interaction (that is, without requiring an understanding of system interaction routines or the use of keyboards, etc.) permits the first-time user "walk up and use" access to the system. This is particularly important, since the Data Wall is intended to be a theater-tailorable system and may vary widely in input and output configuration based upon the resources afforded by the contingent operational environment. The Data Wall in the ADII Laboratory will permit the investigation of the individual and combined effects of various modes of interaction and information presentation within the context of team decision making.

4.2. USER INPUT: ADDRESSING THE DATA WALL

The introduction of computer-based decision aids often results in the redirection of much of the effort of individual team members from interaction with each other and the decision information to interaction with the computer support tool. One of the goals of the Data Wall's "transparent interaction" paradigm is to permit the user to focus attention on the tasks and the team rather than the system. This is accomplished by allowing the user to address the Data Wall using the natural communication methods of speech and gesture

which normally accompany interpersonal interaction. The specific means and devices for supporting multimodal communication in a team context introduces one of the pivotal research and design issues for the Data Wall.

The most readily available mechanism for gestural interaction is the direct touch (or touch screen) interface. The obvious disadvantages of direct touch interaction are the requirement to operate "within arms reach" and the potential for masking portions of the display during input with the hand or pointer. The former may be addressed with the use of a long pointer; however, in team activities, this raises the additional issues of who will have pointers. Either passing a single pointer among participants or having each participant use a separate pointer seems likely to interfere with both the team interaction and problem solving processes. Most of the non-touch activated pointing devices (i.e., light beam, glove, etc.) carry with them similar limitations. It would seem desirable to retain the naturalness of direct touch while extending the "reach" and incorporating more of the expressive vocabulary inherent in hand motions. Device-free gestural interaction using video camera recognition of user gestures is under development; however, the current prototypes are limited to single, stationary users operating in extremely close proximity to the camera.

Gestural interaction would appear to reduce cognitive workload in two ways. First, it reduces short term memory requirements in that input and output are accomplished almost simultaneously at the same location. Second, it reduces the requirement for recall of commands or interaction sequences from long-term memory by permitting direct interaction through natural gesture. However, gestural interaction shares one of the principal limitations of the most mundane direct manipulation interfaces: in order to act on an object, the object must be visible. For example, to select a menu item, the user may have to proceed sequentially through a series of menus or traverse a layered hierarchy of menu options. The direct access afforded by command interaction is not available, except as explicitly designed into iconic functions. None of the purely gestural interaction paradigms surmounts this issue.

The addition of speech to gestural interaction permits a more robust specification of the object(s) of interest and action(s) required. Speech-based interaction permits the commander or staff officer to address the Data Wall as they would another team member. The decision maker can ask directly for information (e.g., "Where are the active SAM sites?") and probe for explanations of computer-generated options. Currently, practical application of speech understanding is limited to non-continuous (or discrete) speech. The command center tasks, organization and environment mandate input modes that will accommodate multiple users working together and independently. The users' tasks, situational environ-

ment and organizational structure significantly impacts the determination of an appropriate mode of communication and interaction. Further research is required in a variety of input methods to ascertain their suitability to tasks and user preference under task conditions.

4.3. SYSTEM OUTPUT: INFORMING THE USER

The Data Wall concept involves the capability to present and interact with information through multiple windows. This feature will allow the command team to work individually and together with reference to task specific information while maintaining a situational overview through maps and detail displays. There are a variety of configuration options for windows and multiple displays. Multiple windows may be used to display temporal or spatial ordering and provide comparisons to system generated models. Users may also zoom windows in and out to facilitate examination of detail. The use of multiple, synchronous windows can also serve to provide insights to the effects on one model based on changes in another. Intelligent windows are a powerful way to organize the display of multiple processes. The development of techniques to relate windows and create dependencies within contexts may result in a dramatic change in the way users interact with computers. In the 1970's the Architecture and Machine Group Laboratory (now known as the Media Lab) at MIT developed an entirely new dimension in user interface built upon concepts of spatial articulation of data. The user interacts with a wall-size display incorporating traditional alphanumeric displays, still frames, video, and computer animation in window-like formats. A variety of interaction devices allow the user to 'turn' pages of text, zoom in on information, and access information within the data base. Current research is focusing on new technology which will allow the user to interact with the system through speech gestures, eye movements, voice commands, and similar non-mechanical means to achieve a higher degree of interface transparency.

In a literal interpretation of human-computer communication or human-computer interaction, Bødker (1991) suggests that designers consider human-computer communication in terms of interpersonal communication. This approach conceptualizes the computer as an active partner in task performance and is reflected in research efforts to develop associate technologies (e.g., Pilot's Associate) and intelligent agents that track activities and perform tasks individualized to the context and the operator they "represent." The intelligent multi-agent model bears some resemblance to the blackboard paradigm in which multiple processes contribute problem solving input from their assigned areas. The use of agents to support decision tasks will most likely require the means (similar to the blackboard manager) to assess the various contributions from multiple agents. In lieu of such management

paradigms, the user is once again faced with an onslaught of information from the various agents competing for attention.

Clearly, this paradigm is not appropriate for all applications. Furthermore, conceptualization of the computer as a human-like partner may actually limit the full realization of the technological advantages. However, the intelligent agent need not take on excessively human characteristics. The principal goal of intelligent associate or agent paradigms is the delegation of certain tedious, repetitive tasks to the system in order to free the user to pursue higher-order cognitive activities. The potential for their use in a team decision environment depends upon a better understanding of the role(s) agents may play, how they will be linked to individual users or user tasks, and how multiple agents may communicate with the decision making team without creating chaos in the command center.

5. UCI Research Directions: Exploring the Potential Impacts of Data Wall Technologies on the Command Process

5.1. ENHANCING C^2 DECISION PROCESSES

In the rush to bring new support technology to the users, system designers should take care to retain and extend technological support to those aspects of the C^2 decision process that work well today. The UCI design for the Data Wall must facilitate the team interaction critical to successful campaign planning. For example, while workstation-based high-definition maps are useful for analysts, the command team use the wall map as a frame of reference and communication tool in group discussions. The Data Wall enhances interaction with the static map to permit dynamic mapping capabilities while retaining the discussion and gestural modes of communication. Furthermore, the Data Wall enhances information presented through the map by using the map as a spatial reference and access point to situational detail in the form of simulation, imagery, fused intelligence, etc. Real-time video and/or audio further enhances distributed team interaction by allowing the senior command face-to-face communication with in-theater command posts.

In addition to enhancing current capabilities, the Data Wall has strong potential to address some of the current problems in information presentation for command decision making. The multimodal interaction and multimedia information presentation architecture of the Data Wall design incorporates the layered information access concept endorsed in the *C⁴I for the Warrior* objectives. Windowing against a geographic reference permits the decision maker to control the level of detail desired without sacrificing awareness regarding the situational context. Thus, alarms and updates relevant to background processes can be presented on the large map to reference context.

Research indicates that overloading the human decision maker with information re-sults in decisions based on the evaluation of only a portion of the available information. Filtering (screening out everything except what is relevant to current decision) and fusion (aggregating data to appropriate level of abstraction for problem) may result in several sources for decision error. For example, pieces that don't fit tend to tending to get reshaped or dropped. Inconsistencies disappear and quantitative discrepancies get averaged out. Information displays may suppress or mask uncertainty resulting from such factors as sen-sor range/resolution limitations, environmental constraints, human assumptions and bias, imprecise or ambiguous language, interference, enemy deception and countermeasures. The Data Wall's application of intelligent agents provides the means to both buffer the user from detail and maintain a less biased appraisal of situational data. For example an agent which has been "trained" to consider the impacts of imprecision or completeness in evaluat-ing data will "remember" to annotate the presentation of situational displays with qualify-ing information for evaluation by the decision maker. Furthermore, the agent presents ad-vice unaffected by the impacts of time pressure or perceptual bias within the constraints of its programming.

5.2. SPAWNING NEW COGNITIVE TASK REQUIREMENTS

The introduction of multimedia information presentation and multimodal interaction into the current command and control decision environment will effect the team decision making process. Design and development of the Data Wall system concept must incorpo-rate the assessment of *new* cognitive requirements potentially imposed by the various ad-vanced technologies and interaction designs considered. For example, the simple use of multiple windows central to the Data Wall concept has several implications for individual and team use in the command center environment. Improperly designed, windowing and hierarchical menu structures can result in the user "getting lost" in a multiple display s s-tem (Woods, 1984). Woods has coined the term, *visual momentum*, to describe the measure of the user's ability to draw out and synthesize information across a series of displays. Low visual momentum results in a decrease in the field of attention or cognitive 'tunnel vision' resulting the failure to process important information and a potential for getting lost in the network of displays, menus, and windows. These problems are linked to a further increase in mental workload and degraded problem solving performance.

There are several techniques for improving visual momentum. The concept of an 'establishing shot' or 'long shot' from motion visual communication can be applied in the form of process or system overviews. Successive displays can also be linked perceptually through the use of fixed screen formats, perceptual landmarks, and display overlays. Over-

lays, commonly used in map displays permit the introduction of new information without changing the basic display. Spatial formats can provide information similar to the long shot by displaying temporal or hierarchical relationships in data elements. Moreover, spatial displays have analogical aspects which can significantly reduce the mental workload of the user.

In addition to the cognitive issues associated with the interaction concept, the Data Wall design must address the issues of communication and interaction control arising from having multiple users at a common display. The team members must have a clearly defined and understood ability to control and direct the activities of the Data Wall. Furthermore, output directed toward the group must be discriminated from process output from team members' individual inquiries. These requirements imply an intelligent interaction design that is "aware" of the individual users. Finally, the Data Wall design must also consider the learning and training requirements for system use -- including initial learning, retention, and extension of skills. Each is impacted by the nature of the users, the tasks performed, and the frequency and circumstances of use. Additional tradeoffs exist between ease of learning and usability versus problem solving power and task utility. Research with operationally qualified users performing representative tasks will permit exploration to determine the kinds of learning and performance aids required.

5.3 EXPLORING & EVALUATING NEW INTERACTION CONCEPTS

The Data Wall is a high-risk, investment-intensive concept. Multimedia/multimodal interfaces integrate input modes and information representations which were previously unavailable to users. Design decisions regarding the Data Wall's information presentation and interaction technologies must be based on their potential contribution to improved communication with the user, rather than their novelty appeal. The effectiveness of technology in an organization is often limited by a tendency to plan new systems solely in terms of existing systems or manual procedures. At best, this results in incremental changes, often only "patching" the old systems rather than any true innovation in technological support. To fully exploit the capabilities of new technology, an effective systems planning methodology must overcome these more limited visions. For example, Curtice's (1987) Strategic Value Analysis (SVA), focuses on the organization's functional requirements and the technological opportunities for supporting those requirements, rather than narrowly viewing new systems in terms of problems with existing systems. The design and development process should incorporate guidance from technological forecasting, theoretical literature, and context-specific research findings.

As presented in this paper, the Data Wall's multimedia/multimodal architecture depends upon several pivotal technological issues. In addition to the computational architecture requirements, the Data Wall designers must explore the requirements and implications of the following:

- *Multimodal Input* - Identification and evaluation of speech and gestural input modes with reference to the team environment and decision making tasks in dynamic, complex environments.

- *Multimedia Output* - Identification and evaluation of "user-aware" modes of providing feedback on processes and presenting user-controlled information.

- *Intelligent Interaction* - Preserving user control in a team environment, while providing support for robust situational awareness.

Increasing the synergy between technology development and organizational task requirements is key to leveraging advanced interface technology against the changing requirements in command and control. The successful development of advanced technological concepts such as the Data Wall depend upon a comprehensive, requirements-driven design approach. Guidelines, standards and research on individual components are insufficient for answering the key questions. The successful development of the next generation of command and control support systems will require a better understanding of the interactions and interdependencies between technologies, users, organizations, and tasks. This understanding must be based in part on findings from context-specific research. The ADII Data Wall Laboratory affords the exploration of these issues by facilitating context-specific research on the application of a wide range of advanced UCI technologies and interaction concepts to a variety of military and non-military operational contexts.

9. Bibliography

Andriole, S. J. *Handbook of Decision Support Systems*. Blue Ridge Summit, PA: Tab Books, Inc., 1989.

Andriole, S. J., H. H. Black, G. W. Hopple, and J. R. Thompson. "Intelligent Aids for Tactical Planning," *IEEE Transactions on Systems, Man, and Cybernetics*, 1986, 16(6), 854-864.

Andriole, S. J., L. S. Ehrhart & P. H. Aiken. "Group Decision Support System Pr., types for Army Theater Planning & Counter-Terrorism Crisis Management," in Stephen J. Andriole (Ed.) *Advanced Technologies for Command and Control Systems Engineering*. Fairfax, VA: AFCEA International Press, 1990.

Bødker, Susan. *Through the Interface: A Human Activity Approach to User Interface Design*. Hillsdale, NJ: Lawrence Erlbaum, 1991.

Coakley, T. P. *Command and Control for War and Peace*. Washington, D.C.: National Defense University Press, 1989.

Curtice, Robert M. *Strategic Value Analysis: A Modern Approach to Systems and Data Planning*. Englewood Cliffs, NJ: Prentice-Hall, 1987.

Cutaia, Al. *Technology Projection Modeling of Future Computer Systems*. Englewood Cliffs, NJ: Prentice-Hall, 1990.

Ehrhart, L. S. *Tasks, Models & Methods: System-Level Evaluation of Human-Computer Interaction (HCI) for Command & Control Decision Support*. (R&D Interim Technical Report #MISE-3-1-3. Rome Laboratory/C^{3}AA, Contract #F30602-92C-0119). Fairfax, VA: C^{3}I Center, George Mason University, 1 March 1993.

Gaver, William W., Randall B. Smith and Tim O'Shea. "Effective Sounds in Complex Systems: The ARKola Simulation," *Proceedings of ACM SIG-CHI '91*, New York: ACM, 1991, 85-90.

Joint Chiefs of Staff. *Joint Warfare of the US Armed Forces*. (Joint Pub 1). Washington, DC: Joint Chiefs of Staff, 11 November 1991.

Kahan, J. P., D. R. Worley & C. Stasz. *Understanding Commanders' Information Needs*. Santa Monica, CA: RAND Corporation, June 1989.

Nelson, Lt. Gen. M. A. "Combat Requirements for C^2" Plenary Address, 1993 BRG Symposium on Command and Control Research, June 28-29, 1993, National Defense University, Washington, D.C.

USAF HQ ACC. *Air Force Concept for Theater C^{4}I*. Langley AFB, VA: USAF Headquarters ACC, Director of Requirements, September 1993.

Woods, D. D. "Visual Momentum: A Concept to Improve the Cognitive Coupling of Person and Computer." *International Journal of Man-Machine Studies*, 1984, *21*, 229-244.

A FAST ATM ROUTING ALGORITHM
FOR THE DYNAMIC THEATER ENVIRONMENT

Robert R. Henry
Professor

and

Claud K. Jones

Department of Electrical & Computer Engineering

University of Southwestern Louisiana
P.O. Box 43890
Lafayette, LA 70504-3890

A FAST ATM ROUTING ALGORITHM
FOR THE DYNAMIC THEATER ENVIRONMENT

Robert R. Henry
Professor

and

Claud K. Jones

Department of Electrical & Computer Engineering
University of Southwestern Louisiana

ABSTRACT

Traditional tactical and theater military communication networks are characterized by relatively low bandwidth links. The environment is dynamic in the sense that the links are subject to jamming and the nodes to destruction by the enemy. Modern and future military equipment and tactics require the use of wideband links to exchange bandwidth-intensive information such as video and images. However, current and proposed wideband networks such as ATM have been designed for peacetime, i.e. well-behaved operation. The research described herein proposes and develops an original Fast ATM Routing (FAR) protocol which adapts wideband ATM networks for operation in the dynamic theater environment. It is shown that the FAR protocol provides robust performance in such an environment.

A FAST ATM ROUTING ALGORITHM
FOR THE DYNAMIC THEATER ENVIRONMENT

Robert R. Henry and Claud K. Jones

INTRODUCTION

The research performed this summer by the authors consists of the development and evaluation of a protocol to suitably adapt the Asynchronous Transfer Mode (ATM) implementation of integrated broadband networking to the requirements of a Theater Environment Network (TENet). This research area was previously studied [1] to identify ways in which the advantages of highly adaptable dynamic routing protocols could be combined with the broadband capacity of ATM. This report is divided into four parts. The first describes the relationship between this research effort and other research efforts now being conducted or recently completed at Rome Labs. The second describes the protocol developed by the authors this summer. The third presents the results of a deterministic performance analysis of the protocol, and the fourth describes and presents the results of a detailed simulation of the protocol using the OPNET simulator.

RELATIONSHIP TO CURRENT PROJECTS

Current Projects

The research performed by the authors this summer was chosen to complement and support current research efforts undertaken by Rome Labs. One such project is the Evaluation and Development of Multimedia Networks Under Dynamic Stress (EDMUNDS) project [2]. It is an ongoing effort to develop Secure Tactical Internet Protocols (STIP) that respond well to a stressed tactical environment. Such an environment is characterized by communication

links subject to jamming and nodes subject to destruction by the enemy. The assumption is that the links have relatively low bandwidth, and that there is sufficient time to perform sophisticated processing to determine optimal datagram routing.

The Secure Survivable Communication Network (SSCN) project [3] was initiated in an effort to utilize the emerging Broadband Integrated Services Digital Network (B-ISDN) for military applications. This network relies on the Asynchronous Transfer Mode (ATM) to provide rapid multiplexing and routing of data over wide bandwidth links. Due to high data rates there is relatively little time to determine the optimal route of each packet (cell). Therefore connection oriented services have been selected to provide routing that is fixed for the call duration. This is in direct contrast with the STIP routing protocol.

Two other projects, the Media Resource Controller (MRC) [4] and the Multimedia Communication Capability (M2C2) [5], are similar to the EDMUNDS project in the sense that the routing is adaptive and the links are low bandwidth. However, these projects have actually been implemented and demonstrated in the laboratory. Another laboratory oriented project is the Advanced Multi-Media Information Distribution System (AMIDS) [6] in which a distributed Tactical Air Control Center (TACC) is interconnected by fixed wideband links.

ATM and AMIDS have high capacity links in contrast with the lower capacity MRC and STIP links. Each may be classified into one of two groups based on link capacity and the ability to adapt to a stressed environment as follows:
- ATM/AMIDS: high capacity, low adaptability
- STIP/MRC/M2C2:   low capacity, high adaptability.

Interconnection between these two dissimilar groups requires careful consideration so that performance does not revert to the least common denominator, i.e. low capacity and low adaptability.

3-4
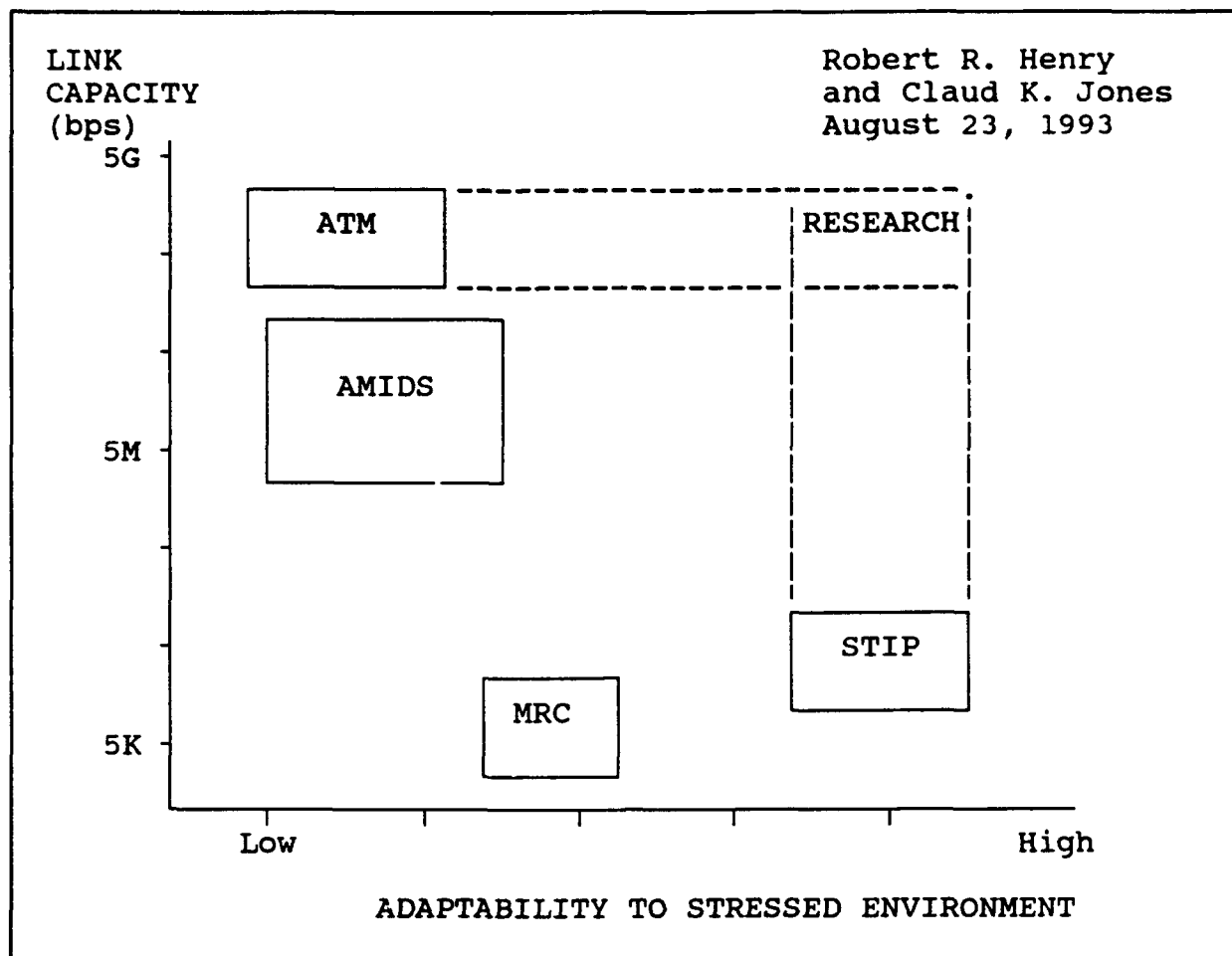
Figure 1. Network Protocol Dynamics.

Figure 1 illustrates the networks in these two groups in more detail. As can be seen ATM represents the highest in link capacity, while STIP represents a high degree of adaptability to a stressed environment.

This Research

An underlying concept of the global grid concept is that the National Command Authority (NCA) will be able to communicate directly with personnel in the tactical environment. In order that graphics and video information be delivered in a timely manner, high capacity links are essential. ATM is a candidate for the wide-area part of this network since it is wideband, is being

developed commercially, and is being standardized in international forums. However, since ATM is designed for peacetime (well-behaved) use, adaptive protocols, such as those incorporated into STIP, must also be incorporated into ATM-based networks to provide for survivability in the tac ical area. This report document: research by the authors that formulates a protocol which combines the advantages of both the ATM and adaptive (i.e. STIP-like) protocols into a network suitable for the military environment. This is the "RESEARCH" area indicated in Figure 1.

THE FAST ATM REROUTING PROTOCOL

Commercial broadband networks are expected to use very reliable, extremely low noise optical fiber links. Given this assumption, error recovery may feasibly be removed from the internal operation of the network to the network edges. Military networks operating in a theater environment cannot make this assumption. The US military may be called upon to operate in areas far removed from modern networks and so will continue to rely upon links, characterized by high bit error rates, for its communication requirements. Military communication networks are subject as well to the fluid nature of combat as exemplified by frequent network reconfiguration and hostile action.

The thrust of this research is to find ways in which broadband networks based on ATM may be adapted to the dynamic theater environment. The authors assert that fault recovery should not be removed to the network edges in the theater environment but must remain internal to the network. It will be shown that the Fast ATM Rerouting (FAR) protocol proposed by the authors reduces the disruption to the network users due to failure. It does so by automatically rerouting to an alternate virtual path connection (VPC) route in a way that is functionally compliant with ATM standards.

3-6

ALGORITHM DESCRIPTION

The purpose of FAR is to overcome some of the problems associated with high speed networks when disruptions in the network occur. Unlike today's relatively low speed networks, propagation delay dominates in broadband networks. This latency means that a very large amount of data (on the order of 10^6 bits per 1000 km, or about 1500 ATM cells) may be in transit from source to destination. In-theater networks must be prepared for frequent disruptions, or rapid and unpredictable changes in their state, resulting in large losses of data. FAR is a step towards minimizing the potential loss of data by allowing the network to sense and react as quickly as possible to these disruptions. This paradigm places in each node, or strategically selected nodes, the ability to assess the quality of its communication with its neighbors and to automatically reconfigure appropriate VPCs.

The FAR Paradigm

When a node determines that its ability to communicate with a neighbor, i.e. the quality of service (QOS), has degraded below some threshold (a "fault" occurs), it will take prompt action to activate an alternate path. The QOS could involve parameters such as bandwidth, latency, security, etc.

The method proposed here maintains alternate standby paths (either hot standby or dormant) that can be activated and used very quickly when a fault is observed. Figure 2 illustrates one such primary VPC with one, pre-defined alternate path branching from node I. Other alternate paths may exist in addition to this one but are not shown in order to simplify the diagram. This representative VPC is also shown in isolation from other VPCs
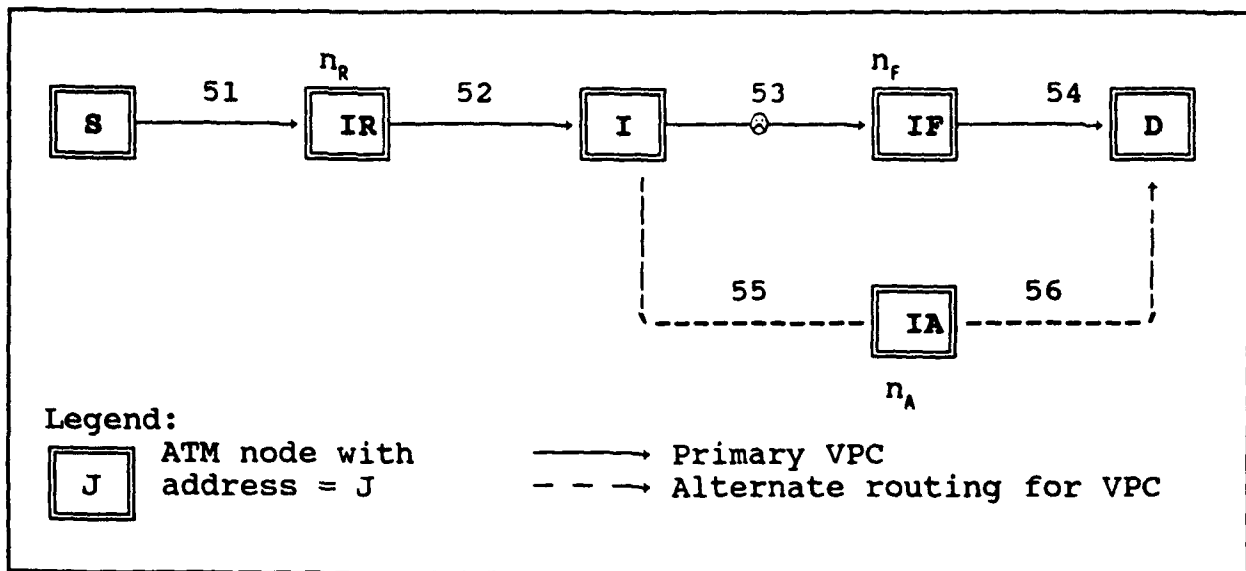
Figure 2. Primary VPC and alternate for node I.

traversing the same nodes. It is defined by source node **S**, destination node **D**, intermediate node **I** , n_R upstream (relative to node **I**) intermediate nodes **IR**, n_F downstream intermediate nodes **IF**, and n_A alternate path intermediate nodes **IA**. It is also assumed that reverse VPCs exist from node **D** to node **S** along the primary and alternate paths.

The typical intermediate node **I** has detected a fault immediately downstream of itself. In response, node **I** takes the necessary steps to reestablish the VPC to **D** along the n_A alternate set of nodes **IA**. The new route continues to use the n_R **IR** nodes upstream from the failure, but bypasses the n_F downstream forward path nodes **IF** downstream of the failure.

In addition to the rerouting mechanism to be described in this paper, it is assumed that there are two other processes running asynchronously in the background at each node. One is the fault detection/reporting function mentioned in the previous paragraph. The second provides the alternate route to be used when a link failure is detected. Such routes may be updated relatively slowly compared to the time in which the node is required to switch to the

alternate route. The selection of the alternate routes is an area for future study and is beyond the scope of this paper.

An advantage of FAR is that most resources are consumed only when needed, with VPI resources being consumed to maintain alternate paths. Bandwidth remains available to other, active VPCs. FAR is also distributed with each node taking action based on OAM (Operation and Maintenance) cells exchanged with its neighbors allowing it to recover from a fault in any link or node. A two-way handshake is provided from the intermediate node I to D and back. However, node I may opt for an early reroute immediately upon detection of the fault before confirmation is received from the handshake as to the availability of resources on the alternate path.

Assumptions for Protocol Implementation

The goal of the research performed in the summer of 1993 at Rome Labs was to fully implement and test a portion of the FAR protocol. The limitation of time dictated that we adopt simplifying assumptions to enable us to reach this goal. First only one alternate path branching at the node just upstream of the fault is assumed. A hard, yes/no decision is made on QOS parameters, ie there is an abrupt transition from acceptable to non-acceptable QOS. Only one try is made at rerouting with the source being notified of the attempt and the status of the attempt. No timeouts are provided for lost OAM cells. A two-way handshake is used from the node initiating recovery to the destination node. No handshake is used upstream from the initiating node but notification of action taken is sent. We stress that these assumptions are not inherent to the FAR protocol but were made only in the interest of reducing the time to achieve measurable results from the protocol.

OAM Cells

Node **I** could assess a fault through the use of F1, F2 and F3 (OAM) cells as defined by the Consultative Committee on Telephony and Telegraphy (CCITT) [7]. Further definition by the CCITT and other standards bodies is required before the suitability of using these OAM cells can be ascertained. Therefore, we have formulated generic type 0, 1, 2 and 3 cells that perform specific functions required of the FAR. Type 0 cells detect and report fault conditions between ATM devices. Cell types 1, 2 and 3 are used to recover from the fault condition. The functions of each cell type are described below:

- **Type 0** Detects faults and reports on the status of the VPC between nodes **I** and **IF**.

- **Type 1** Sent to node **IA** along the alternate route (downstream of **I** and bypassing the fault) and forwarded until **D** is reached or the alternate path also fails. It changes the alternate path to primary route status for the VPC in question.

- **Type 2** Sent to node **S** to inform it of the VPC status, "rerouti "rerouted", or "alt_path_fail".

- **Type 3** Sent to node **I** by node **D** upon receipt of a type 1 cell or by one of the intermediate alternate path nodes **IA** if the alternate path can not be activated for some reason. It informs **I** if the alternate path was successfully activated.

Protocol Description

The FAR protocol can be viewed as a Finite State Machine (FSM) residing at or contained within an ATM node. Seven high level states are presently specified as shown in Figure 3. Lower level states may be contained within each high level state.
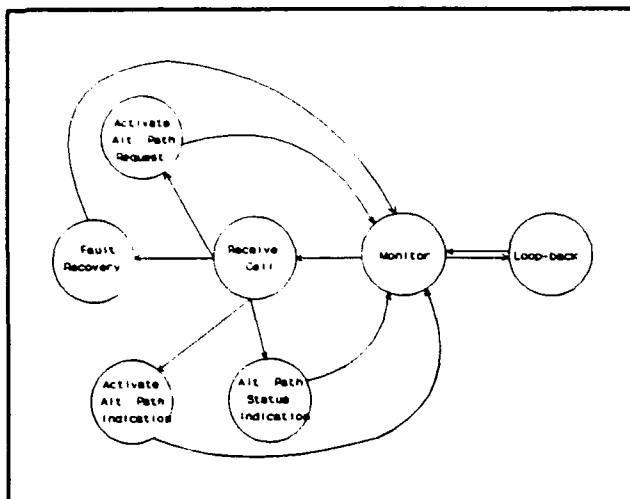
Figure 3. Current FSM for the FAR Protocol.

The loop-back state consists of the exchange of type 0 cells with each neighboring node. Faults are indicated by status conditions returned from downstream or by a timeout. The exact operation in this state is not yet defined pending further definition of standards. Only faults immediately downstream of the subject node are currently detected.
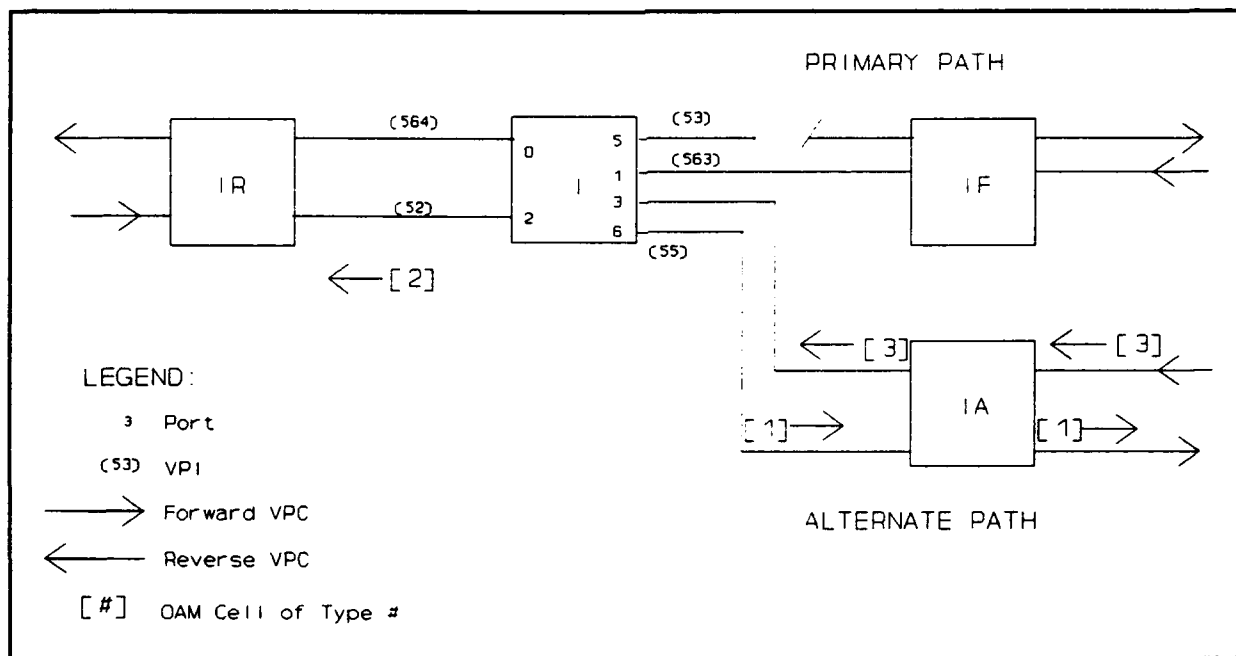
Figure 4. VPC schematic and OAM cell activity.

Figure 4 illustrates the VPCs in the vicinity of node **I** and the **OAM** cell traffic generated as a result of the fault. The outgoing port and VPI to route cells along the alternate path are contained in the alternate path output port/VPI table entry for that VPC as shown in Figure 5. In the <u>fault</u> <u>recovery</u> <u>state</u> the FSM first checks to see if adequate resources, (ie bandwidth) is available to begin the activation of the alternate path. If so, a type 1 cell is sent to the next downstream node **IA**, which then forwards the cell to the next node **IA** and so on until node **D** is reached. A type 2 cell is sent directly to the source node **S** indicating that the network is attempting to reroute the VPC.

VPC Index	CURRENT VPC			ALT PATH VPC		VPC PARAMETERS		Rev. VPC
	IN	OUT	BW	OUT	BW	Src_addr	Dest_addr	OUT
:	:	:	:	:	:	:	:	:
I(f)	2/52	5/53	Bc	6/55	Ba	S	D	0/564
I(r)	1/563	0/564	Bc	--	--	D	S	5/53

Legend:
#/###	port/VPI entry for a VPC
I(f)	forward VPC index
I(r)	reverse VPC index
Bc	Bandwidth parameters set for the current VPC
Ba	Bandwidth parameters acceptable if alternate path is activated
Src_addr	Address of node connected to source
Dest_addr	Address of node connected to destination

Figure 5. Expanded VPC table.

If the resources are not available, a type 2 cell only is sent, again to node **S**, indicating the failure of both the primary and alternate paths. In the representative situation shown in Figure 2, node **I** has entered the fault recovery state, transmitted a type 1 and type 2 cell and has returned to the monitor state. At

a later time a type 3 cell will return to node **I** from node **D** or one of the nodes **IA** causing it to enter the alternate path indication state. Node **S** enters the alternate path status indication state on receiving the type 2 cell. The actions that may be taken by the source could include temporarily suspending transmission, preparing for retransmission of possibly lost data, or any other number of actions.

An "early reroute" option is available in the fault recovery state to reroute the VPC immediately after the type 1 cell is sent. Doing so has the advantage of potentially reducing the number of cells buffered or lost. The disadvantage is that if resources are not available downstream congestion problems may occur for other VPCs traversing the same nodes. Evaluating the ramifications of this option is beyond the scope of this paper and is for future research. By contrast the "late reroute" option waits on the acknowledgement from the destination before rerouting.

The activate alternate path request state is entered upon receipt of a type 1 OAM cell. The type 1 cell arrives over the user VPC but is distinguished by a reserved VCI or cell type indicator or both [8]. The receiving node activates the resources requested by the type 1 cell if possible and checks the destination address contained in the data field of the cell to see if it is the end node for that VPC. If it is the destination node and successfully allocated resources to the VPC, it issues a type 3 cell along the reverse VPC defined in Figure 5. If is not the destination node, it sends the cell along the next link in the alternate, forward VPC. If it can not allocate the requested resources to the alternate VPC, it will issue a type 3 cell along the reverse, alternate VPC with an indication that the alternate path has also failed. Figure 4 shows node **IA** entering the activate alternate path request state, successfully allocating bandwidth, and sending the type 1 cell along the alternate, forward VPC.

3-13

When a node receives a type 3 cell, it enters the <u>activate</u> <u>alternate</u> <u>path</u> <u>indication</u> <u>state</u>. Figure 4 shows node **IA** receiving a type 3 cell from downstream, which would occur at some time after forwarding the original type 1 cell on to node **D**, and forwarding the cell to node **I**. If the data field of the cell contains an indicator that the alternate, forward VPC was successful node **I** immediately sends a second type 2 cell to node **8** indicating that the alternate, forward path was successful. If any node receives a type 3 cell with an indication that the alternate VPC failed, it immediately deallocates the alternate VPC and sends the cell back along the reverse alternate VPC. The type 3 cell contains the destination address of node **I** so that node **I** will know the status of the alternate path and will not forward the cell.

DETERMINISTIC PERFORMANCE ANALYSIS

Parametric equations of performance of the FAR protocol have been derived for the representative environment depicted in Figure 2. Two performance metrics are determined, the time to affect early reroute and the time to affect late reroute. A discussion of the resulting equations is beyond the scope of this paper. For this analysis, a VPC 5000 km long was assumed consisting of six, equally spaced ATM nodes. Node one is the source end-point, node 6 is the destination end-point. The VPC fails 3500 km from node 1 placing the fault 500 km downstream of node 4, or half-way between nodes 4 and 5. This makes node 4 responsible for recovery. A reverse direction VPC is assumed between node 1 and node 6. An alternate path consists of node 7 being equidistant between nodes 4 and 6. All links are equidistant at 1000 km. An estimate is made of the number of clock cycles required to perform the protocol operations, and the propagation speed is assumed to be 0.8c. All links assume OC-3 capacity yielding 148.608 Mbps and a cell transmission delay of 2.853 μsec. Propagation delay between switches is 4.167 msec.

Table I. **Table I.** Selected results of deterministic analysis.

VPC Length	# Nodes	Fault Location	Xmt Speed	Clock Speed	Early Reroute	Late Reroute	ETE Reroute early	ETE Reroute later
km		km	Mbps	MHz	msec	msec	msec	msec
5000	6	3500	148	20	9	25	42	84
5000	6	3500	148	1	9	25	42	84
5000	6	3500	10	10	9	26	43	86
5000	6	0	148	10	9	50	42	84
5000	0	3500	148	10	21	42	42	84
5	6	3.5	148	10	.02	.04	.07	.14
77000	3	53900	148	10	350	620	620	1290
5000	20	3500	148	10	2	16	42	84

The results of the FAR analysis are compared with the end-to-end (ete) protocol that relies on the end-points only to recover. The nominal case assumed two forward VPCs, both 5000 km long with one designated as the alternate path. Various parameters were varied and the results are shown in Table I. In short, the FAR protocol (internal rerouting) performs significantly better than rerouting performed at the network edges. The protocol is insensitive to processing time unless the nodes are very close together as in a LAN configuration.

For VPC lengths ranging from 5 km to 77000, the FAR protocol performs two to three times faster than end-to-end recovery. The distance from a node to a fault is one of the prime determinants in

time to reroute. The closer the node spacing, the faster the fault will be detected. The end-to-end and the FAR protocols converge when a VPC consists only of the two endpoints. Conversely, for a VPC traversing several nodes, the FAR method performs proportionally faster.

Another trend is for the FAR protocol to perform much better if the fault occurs near the downstream end of the VPC rather that the transmitting end. However, if the early reroute option is used, fault location has no effect on performance. Transmission speed was decreased to 10 Mbps having little effect on time to reroute with the exception of short VPCs (LANs). At speeds of 10 Mbps, performance for the FAR protocol remained proportionally faster. All methods had a sharp increase in reroute time due to transmission delay becoming significant relative to propagation delay.

OPNET ANALYSIS

An OPNET simulation of the FAR protocol was implemented to confirm the correctness of the protocol, and to validate the results of the deterministic performance analysis. OPNET is an event driven simulator which provides general purpose routines for creating and destroying packets, determination of time delays, as well as for user defined functions code written in proto-C. Protocols in OPNET are modeled by a FSM, with Figure 3 showing one developed for the

Legend

S	Cell Generator
VPI	VPI Insertion
XMT	Transmitter
RCV	Receiver
PROC	Cell Processing
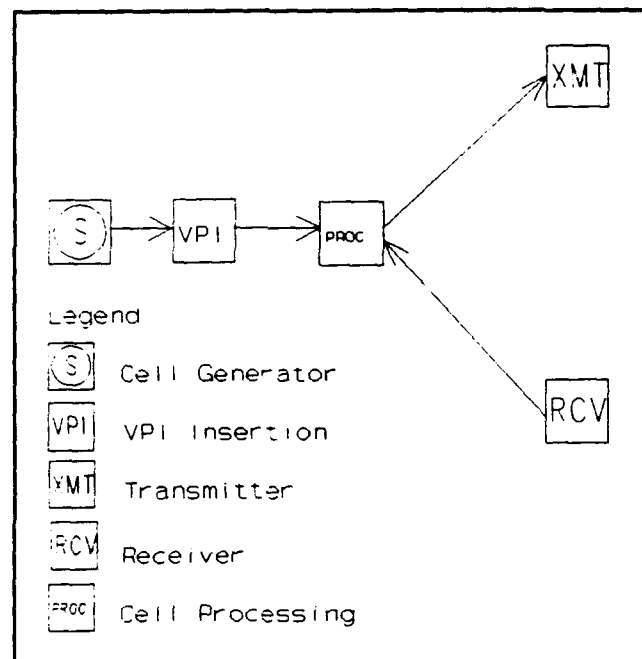
Figure 6. Diagram of OPNET model transceiver.

3-16
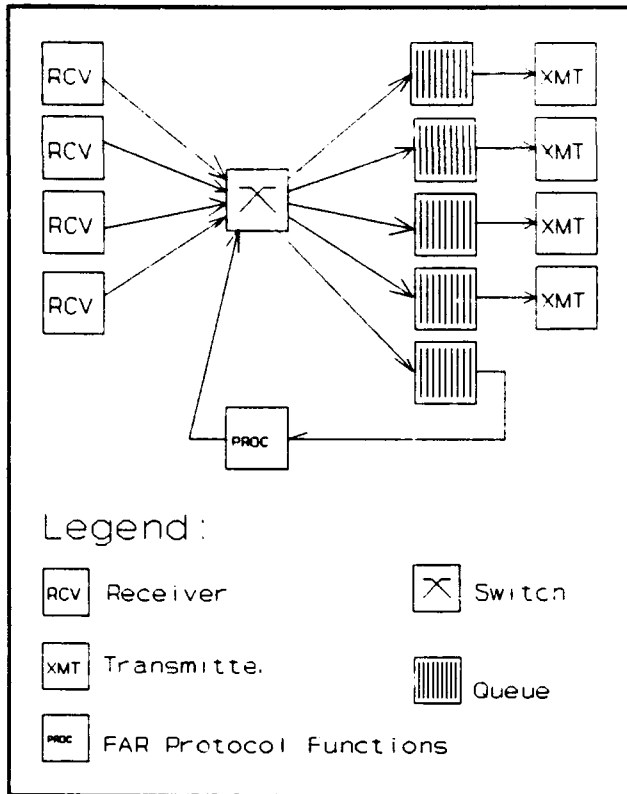
Figure 7. OPNET model of ATM node.

FAR protocol. FSMs are associated with <u>processes</u> which are linked to each other via <u>streams</u> into the next highest level in the OPNET hierarchy, <u>nodes</u>. Figure 6 and Figure 7 show <u>nodes</u> of the FAR transceiver and ATM switch. An OPNET function named **op_pk_send**(<u>index</u>) is available to send a packet over a stream with an identifier of <u>index</u>. OPNET is responsible for delivering the packet to the FSM (process) at the receiving end of the stream. The pre-defined processes Queues, point-to-point transmitters and receivers, and sources are utilized in this simulation.
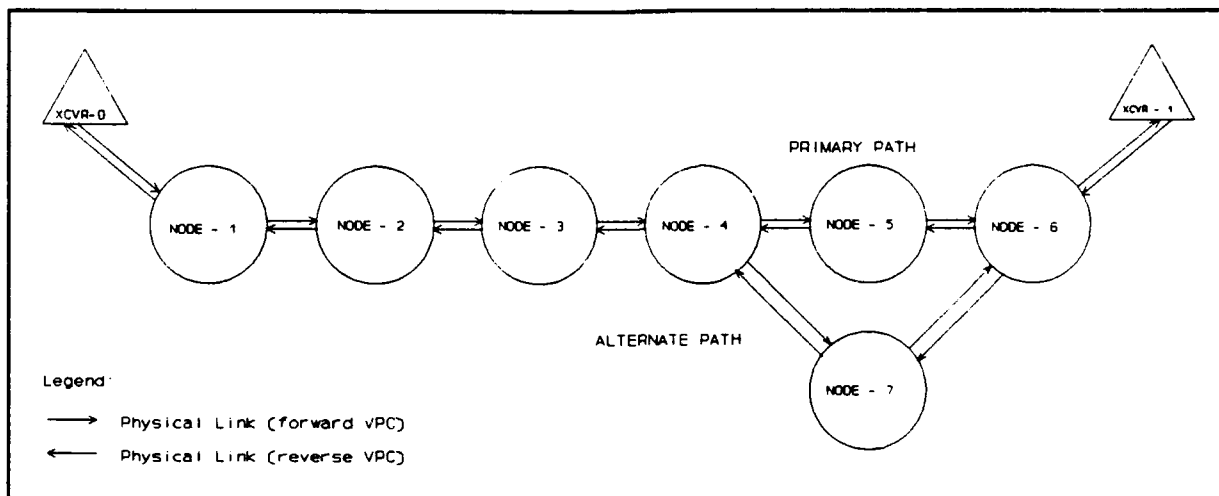
Figure 8. OPNET model of the VPC.

Figure 8 shows the <u>subnet</u> of transceiver and ATM node type

nodes used in the FAR model configuration. The links are representations of physical links for which propagation delay and bit error rate (BER) can be specified. Propagation delay was set at 4.1667 μsec (for a 1000 km link) and BER was not used. Three cases were run, 1 km internodal spacing, 1000 km internodal spacing and 38500 km internodal spacing (3 nodes). These cases emulate a LAN, WAN and satellite system respectively. Delay to reroute once notified of a fault was measured and is in excellent agreement with the analytical results except for the LAN case. This is because the OPNET simulator handles each cell several more times than was assumed in the deterministic analysis. Thus the difference is not noticeable unless propagation delay is very small as in the LAN case. The differences in the to analyses corresponds to the difference in the number of times each cell is handled in the two analyses. Each time a cell is handled adds 2.85 μsec to its total delay and each ATM node in the model handles the cell up to six times (receive, transmit, and 4 queueings) while the deterministic analysis assumed only one handling.

CONCLUSIONS

The authors have developed an original, ATM compliant rerouting protocol, FAR, the Fast ATM Rerouting protocol. It exhibits robust performance over a wide range of parameters such as processing speed, transmission speed, node spacing and VPC length. The protocol has been implemented and verified using the OPNET simulator and compliments and ties together other RL/C3D research efforts.

REFERENCES

1. R.R. Henry, "Wideband ATM Networks with Adaptive Routing for the Dynamic Theater Environment," Final Report AFOSR Summer Research Program, Rome Laboratory, August 1992, page 6-10.

2. "Evaluation and Development of Multimedia Networks in Dynamic Stress," Semiannual Project Report, SRI contract with Rome Laboratory, April 5-9, 1992.

3. "Secure Survivable Communication Network," Users Meeting Report, GTE Government Systems contract with Rome Laboratory, July 15-16, 1992.

4. M.T. Rafter and W.C. Walker, "A Distribution Multiple Media Network Architecture," MILCOM '89 Conference Record, October 15-18, 1989. pp.1-6.

5. "An Overview of the Multimedia Communications Capability Program," Rome Laboratory Telecommunications Division internal report.

6. D.E. Krzysiak, "Advanced Multi-Media Information Distribution System," MILCOM '90 Conference Record, 1990, pp.35.7.1 - 53.7.3.

7. CCITT Recommendation I.610, "OAM Principles of the B-ISDN Access," pp. 12, 14.

8. "ATM User-Network Interface Specification," Version 2.0, The ATM Forum, June 1, 1992, pp 61-63.

EVALUATION OF NETWORK TOPOLOGY IN A DISTRIBUTED PROCESSING ENVIRONMENT

Kamal Jabbour

Associate Professor

Department of Electrical and Computer Engineering

Francis X. Reichmeyer

Graduate Student

Department of Electrical and Computer Engineering

Syracuse University

121 Link Hall

Syracuse, NY 13244-1240

EVALUATION OF NETWORK TOPOLOGY IN A DISTRIBUTED PROCESSING ENVIRONMENT

Kamal Jabbour
Associate Professor

Francis X. Reichmeyer
Graduate Student

Department of Electrical and Computer Engineering
Syracuse University

Abstract

The impact of network topology on the performance of a distributed processing environment was evaluated through experimentation and simulation. Experimental runs of the JDL experiment on Cronus were used to collect traffic data for use in determining the limitations of Ethernet-based networks. Discrete-event simulation and analytical modeling were used to estimate the performance of heavily-loaded Ethernet and FDDI networks.

EVALUATION OF NETWORK TOPOLOGY IN A DISTRIBUTED PROCESSING ENVIRONMENT

Kamal Jabbour and Francis X. Reichmeyer

1. INTRODUCTION

The attractiveness of distributed computing on networks of heterogeneous workstations has created an interesting class of problems. The communications networks and protocols used in such applications were originally designed with a different usage in mind, primarily reliable packet transport over unreliable and low-capacity links. Distributed operating systems, such as BBN's Cronus, use standard technologies like TCP/IP over Ethernet, and as a result suffer from their severe limitations.

In this research we looked at distributed processing over heterogeneous systems and simulated the expected benefit from using new technologies. In particular, we evaluated the performance of the JDL (Joint Director of Labs) experiment over a group of Ethernet networks, characterized its data traffic, and projected the potential improvement from using FDDI networks.

This report starts with a brief introduction to the JDL experiment and the Cronus distributed operating system, followed by an outline of the data collection strategy and a characterization of the JDL traffic. The results are generalized to provide a generic characterization of the packet traffic for typical distributed computing applications. A computer simulation of the performance of an Ethernet-based system under increasingly heavy load is presented next, followed by an analytical model of an FDDI-based system. The report concludes by identifying unanswered questions and topics for future

research, dealing both with the chosen topology and the transport protocol.

2. CRONUS AND THE JDL EXPERIMENT

In this section we introduce briefly the JDL Experiment and the distributed operating system environment, Cronus, on which it runs. The JDL Experiment was used as a sample distributed processing application for the purpose of characterizing network traffic, and subsequently extrapolating such traffic characteristics to other classes of distributed applications.

2.1 Cronus

Cronus is a software environment for the development and operation of distributed computing applications [1]. Cronus was developed by BBN Systems and Technologies of Cambridge, MA, under contract with Rome Air Development Center (Rome Laboratory) in the early 1980s. The Cronus environment runs at the user level, above the operating system, of several different host hardware and operating system combinations. It uses an object-oriented architecture within which every system resource and application-specific resource is viewed as a typed object under the control of an object manager. An object manager implements all the operations that correspond to a particular object type.

In the Cronus environment, client and object managers need not reside on the same machine, and operations can be invoked across machine boundaries. A client process does not need to know the specific locations of objects and managers, as Cronus automatically routes operation invocations to the appropriate manager.

2.2 The JDL Experiment

The Tri-Service Distributed Technology Experiment was initiated as an

unclassified activity by the Distributed Processing Subcommittee of the Joint Directors of Laboratories (JDL) [2]. The concept of the experiment centers around a low-cost distributed computer system application at three sites: Naval Command, Control, Ocean Systems Center RDT&E Division (NRaD), San Diego, CA; Rome Laboratory (RL), Rome, NY; and Communications and Electronics Command (CECOM), Fort Monmouth, NJ. The distributed computing environment Cronus was chosen for the experiment.

The JDL Experiment consists primarily of eight managers, exchanging data in a packet switched mode through Cronus by using UDP and TCP/IP. The operations of these managers is beyond the scope of this report, since our interest lies in characterizing the data traffic generated by the experiment.

The JDL experiment can be run in a one-site (RL), two-site (RL and CECOM), or three-site (RL, NRaD and CECOM) configuration. Computers at these cites are primarily workstations connected locally with Ethernet LANs. The LANs are in turn interconnected through T-1 links over terrestrial wideband links.

3. TRAFFIC CHARACTERIZATION

We conducted local (RL-only) JDL runs separately under light network traffic and under relatively heavy network traffic, as well as multi-site runs under normal prevailing traffic. Etherfind, a network monitoring software provided with the SUN OS, was used to capture the packet headers on the local network for use in traffic characterization. A major limitation of the software/hardware is that workstations keep time to a resolution of 10 msec, thereby preventing more precise measurement of delay.

3.1 Packet Size Distribution

A single-site JDL run generated about 24,137 packets exchanged between the various computers. The majority (23589 or 98%) of these packets used TCP, while the remaining 548 (2%) used UDP. These proportions changed only slightly (94% vs 6%) in multi-site runs. These packets represent collectively fewer than 8,000 transactions. By using TCP, and its inherent inefficiency, each transaction requires a minimum of 3 packets: request, reply, acknowledgement.

A histogram of Ethernet packet size distribution shows a basic tri-modal distribution at 60 bytes (7675 packets) 213 bytes (6971) and 239 bytes (6971) (Fig 4-1). The largest packet is 619 bytes, well below Ethernet's packet size limit. Thus we have observed no fragmentation.

It may be useful at this point to discuss TCP packet structure to put the above packet sizes in perspective. A typical TCP packet consists of a 14-byte Ethernet header, a 20-byte IP header, a 20-byte TCP header, and up to 6 bytes of padding to achieve a 60-byte packet. Thus a 1-byte acknowledgement carries an additional 59 bytes of overhead in a 60-byte packet. Similarly the 239-byte packets consist of 185 bytes of data and 54 bytes of overhead.

In analyzing JDL traffic, we looked at two sample transactions: one dealing with the Timer Manager (running on Mensa), and the second with the Target Filter Manager (running on Orion).

The Timer Manager accounts for the bulk of the network traffic in JDL, namely 20,904 out of 24,137 packets. A typical timing transaction consists of a request (213-byte packet), a reply (239-byte packet) after about 20 ms, and an acknowledgement (60-byte packet):

Time	bytes	source	destination	srcport	dstport
46.72	239	TCP janus.rl.af.mil	mensa.rl.af.mil	1433	2611
46.74	213	TCP mensa.rl.af.mil	janus.rl.af.mil	2611	1433
46.92	60	TCP janus.rl.af.mil	mensa.rl.af.mil	1433	2611

The Target Filter Manager responds to requests for data and accesses the target database. A typical local transaction consists of a request (387 bytes), an ack (60 bytes) after about 80ms, a reply (219 bytes) after about 2.52 sec, and a final ack (60 bytes) after about 80 ms:

Time	bytes	source	destination	srcport	dstport
692.20	387	TCP phobos.rl.af.mi	orion.rl.af.mil	1154	2611
692.28	60	TCP orion.rl.af.mil	phobos.rl.af.mi	2611	1154
694.80	219	TCP orion.rl.af.mil	phobos.rl.af.mi	2611	1154
694.88	60	TCP phobos.rl.af.mi	orion.rl.af.mil	1154	2611

In general, we can characterize JDL traffic as consisting of a series of transactions, each consisting of a request for service, followed by an optional acknowledgement, a reply, and a final acknowledgement. Acks are 60 bytes long, while data packets range from 76 to 619 bytes, with a predominance in the 200-400 byte range.

3.2 Time Domain Characterization

In the time domain, ack packets are generated within 10-100 ms (Fig 4-3), while manager service times range from a few ms to several seconds (Fig 4-4). Service times consist of two components: communication time and processing time. Under very light load conditions, communication times are primarily data transmission times, of the order of 100-500 microseconds. Since a single-site JDL run requires the transmission of about 24,000 packets over a period of an hour, or

less than 7 packets per second, such a run generates a very light network load and has a negligible effect on network performance.

3.3 Additional Data

In addition to the JDL Experiment described above, experimental runs of two other distributed applications were conducted. The Australian Experiment [3] was run at the DISE facility at Rome Lab, and an ISIS run was performed at the Software Engineering Lab at Syracuse University (Fig 4-2). These applications featured a multimedia component and the corresponding large packets for video screen updates. Whereas the JDL Experiment had primarily small packets, multimedia applications require the transfer a large files, resulting in packet fragmentation.

3.4 Background Traffic

As discussed in the previous sections, JDL traffic alone offers a very light load to an Ethernet. Therefore the performance of a JDL run, or any distributed application for that matter, is directly affected by the background traffic on the network. Therefore we have tried to characterize experimentally the background traffic by collecting a significant amount of network traffic data.

Based on the data collected, we have characterized the packet arrival process with an exponential distribution (Fig 4-5). Further, we have observed that the packet size distribution contained a significant peak (about half the packets) at 60 bytes, a small peak at 1514 bytes (fragments at maximum Ethernet packet size), and an otherwise random distribution between 60 and 566, decaying exponentially beyond that (Fig 4-6).

An analysis of the traffic patterns on both the Syracuse University-SELab and

Rome Lab-DISE networks suggests that the majority of the traffic is generated by remote login and telnet users. In a remote login session, each keystroke generates 3 TCP packets, each consisting of 60 bytes (1 packet contains the key stroke, a return packet carries the echo back, and a third ack packet completes the 3-way handshake). At the other extreme, Network File Systems (NFS) traffic consists primarily of large files fragmented into packets of 1500 bytes (unless a lower maximum packet size is set at internet gateways).

4. GENERIC TRAFFIC CHARACTERIZATION

The distributed processing applications described earlier allow us to develop a generic model for characterizing network traffic. Such a generic model will be application-independent and allows a better understanding of the impact of the communications environment. We will assume a packet-switched environment where all communication between processes uses packets (datagrams).

4.1 Basic Transaction

The generic model assumes that a distributed processing application consists of a group of service managers located on various computers. A request for service can originate from any host on the network, and may be preceded by an initial broadcast to locate the server. We will define a transaction as a complete set of packet transmissions consisting of a request for service, an optional acknowledgement, a reply packet, and a final acknowledgement. Acknowledgements are required to complete the 3-way handshake necessary in an unreliable network environment (such as using TCP/IP). The assumption of a reliable (low error rate, eg: optical) network allows the use of a more efficient protocol.

4.2 Packet Generation

We assume that the packet generation intervals are exponentially distributed. In an ideally active network supporting several simultaneous distributed processing applications, we assume that all nodes act as clients as well as servers, therefore all nodes have similar packet generation characteristics. The value of the mean interval determines the loading level of the network. For example, a JDL Experiment generates about 7 packets per second on average.

Similarly, background traffic (generated by non-distributed processing users) can be modeled with an exponential interarrival distribution with a variable mean that determines the background load on the network.

4.3 Packet Size Distribution

The distributed processing applications that we examined rely predominantly on packets of a few hundred bytes (200-600 bytes) for their communication. A handshake packet requires a minimum of 1 byte, burdened by up to 60 bytes of header information (addressing, sequencing, error detection...). Images, high-resolution graphics, and multimedia data require large packets of several kbytes (typically 4-20 kbytes).

To simplify our model, we define packet sizes excluding transport layer headers and independent of network limitations (Ethernet limit is 1,500 bytes, FDDI limit is 4,500 bytes). We assume that distributed processing traffic consists of 3 packet sizes, namely 60 bytes (handshake packets), 300 bytes (requests and replies), and 9,000 bytes (for graphics). The relative distribution of packets among these three sizes is left as a model variable, allowing the specification of a range of applications.

4.4 Packet Transmission Time

Packet transmission time is a primary variable of interest in modeling the communication characteristics of a distributed processing environment. It depends primarily on the type of local area network (Ethernet, FDDI, ATM), the internetworking topology for multi-site applications, and the transport protocol used.

4.5 Processing Time

The final component of the generic traffic model is the remote service time, or manager processing time at a remote site. This is the time it takes a service manager to complete the necessary processing and generate a reply to a request for service. In the above applications, this processing time ranged from sub-millisecond (request for timing information) to several seconds. We assume that the processing time is exponentially distributed, with the mean determining the computational intensity of a given application.

5. COMPUTER SIMULATION OF AN ETHERNET BASED SYSTEM

Currently, the JDL experiment runs on three Ethernet LANs, one at each of the labs involved in the project, as described above. In this section we describe the simulation of the local (RL only) JDL experiment. The simulation was performed to observe the degradation of Ethernet under heavy loads. Since it is not possible to conduct multiple JDL runs simultaneously on the network, and since one JDL experiment by itself does not generate enough network traffic to cause a degradation of the LAN, simulation provides insight that cannot be gained through experimentation alone.

The simulation program is written in C using the SMPL library of subroutines for discrete-event and random variate simulation [4]. We consider an Ethernet LAN of 32 workstations connected with a total cable length of 2.5 kilometers. Each station is considered to be identical in terms of traffic generation. Therefore, LAN access is modeled as a single queue of size 32, which accepts generated packets and releases them on a first in first out (FIFO) basis according to the Carrier Sense Multiple Access with Collision Detection (CSMA/CD) protocol of Ethernet. If the queue is full when a new packet is generated, that packet is discarded. Throughput and average delay are measured as a function of the offered load to the network.

The Ethernet LAN is modeled as an open system, where the total offered load G to the network is the product of the arrival rate L of new packets (for all stations) and the mean transmission time T for a packet, G=LT. The packet length distribution determines the mean transmission time T and the packet interarrival times are obtained from an exponential distribution with mean 1/L. Both packet length distribution and G are supplied as inputs to the simulation by the user.

We considered several different packet length distributions corresponding to different distributed computing applications including JDL, the Australian experiment, and an ISIS run, all three with no background traffic. That is, the only packets on the LAN are those generated by the experiments. For JDL, the packet distribution is as follows:
60% @ 60 bytes, 30 % @ 300 bytes, and 10 % @ 1500 bytes.
The Australian experiment is more computing intensive, having a distribution of:
60% @ 1500 bytes, 30% @ 300 bytes, and 10 % @ 60 bytes.
The 1500-byte packets represent the fragments of the larger packets (mostly 8000 bytes) produced by this application. The ISIS run, simulating an application

4-12

using the ISIS distributed operating system, has the distribution:

57% @ 120 bytes, 32% @ 1500 bytes, and 11% @ 60 bytes.

We also simulated the JDL and Australian experiments with background traffic. In all cases, the interarrival times were computed from offered load and transmission time for the mean packet size (L=G/T).

The attached figures show plots of throughput and delay versus offered load (Fig 4-7, 4-8). Average packet delay is measured from the time a packet is generated to the time it is received. Throughput is defined as the part of the channel utilization used for successful data transmission, based on the total packet length, including the preamble (ethernet header) and data field.

6. PERFORMANCE ANALYSIS OF AN FDDI BASED SYSTEM

An FDDI network was simulated analytically with the same traffic characteristics used above for Ethernet. We assumed a cable length of 2.5 km, 32 stations spaced equally around the ring, and ring access based on the MAC layer. The Target Token Rotation Time was assumed small enough to permit the transmission of only one packet per token acquisition. Finally, large data packets were fragmented to 4500 bytes as opposed to 1500 bytes in the case of Ethernet.

An analytical model of the FDDI ring was developed to estimate network throughput and delay in a simulated distributed processing environment. We assumed that several applications were running simultaneously, with every station hosting a number of managers. Therefore we assumed a homogeneous ring, as far as traffic patterns are concerned [5].

Throughput is shown in Fig 4-9. Offered load refers to the fraction of total network capacity. Since FDDI provide a deterministic data transmission medium,

representing throughput in number of packets per second provides more useful information than presenting it as a fraction of offered load (the latter relationship is linear until maximum load is reached, then flattens out).

Average packet delay is shown in Fig 4-10, and included both the queueing delay inside individual nodes and the transmission delay. The wait queue inside the node was modeled as a M/D/1 queue, assuming a Markov arrival rate, and a deterministic service rate.

Comparing the performance of Ethernet and FDDI shows that FDDI's degradation under heavy loads is more graceful than that of Ethernet. In addition to the obvious order of magnitude in transmission speed (100 Mbps for FDDI vs 10 Mbps for Ethernet), the deterioration in Ethernet's performance is caused by collision, whereas FDDI's deterioration comes from the queueing delays within each node.

At low utilization, such as 10% of offered load, it is not surprising that Ethernet's performance is as good, if not better, than FDDI's. With an estimated 10-bit delay in each FDDI station, it takes a long time for a token to rotate idly around a ring.

7. FUTURE EFFORT

Our work has shown that current technology is well-suited for distributed applications of the class of the JDL or Australian experiment, which offer a small load to an Ethernet. However, multimedia intensive applications generating traffic several orders of magnitude larger than JDL cannot run on existing networks, and necessitate new topologies and transport protocols. In addition, the impact of the network architecture on the traffic characteristics requires

further study. The use of an FDDI network, or an FDDI-ATM interconnection, with the resulting deterministic delay characteristics, will reduce significantly the number of smaller packets and result in a larger number of large packets.

In future effort we propose to examine the performance of two optical networks. The first network uses multiple FDDI rings interconnected with high-speed point-to-point optical links through a single central ATM switch. The second network uses a hierarchical ATM architecture where the computers are connected to local ATM switches which are in turn connected to a central ATM switch. We propose to compare the delay and throughput achieved by these configurations and determine their suitability for distributed processing.

REFERENCES

[1] "Cronus User's Reference Manual", BBN Systems and Technologies, 1991.

[2] "Joint Directors of Laboratories (JDL) Tri-Service Distributed Technology Experiment", Maintenance Manual, 30 Sep 1992.

[3] A.M. Newton et al, "1991 DISE Summary Report", RL-TR-92-302 In-House Report, Rome Laboratory, Griffiss Air Force Base, NY, Nov 1992.

[4] M.H. MacDougall, Simulating Computer Systems. The MIT Press,1987.

[5] Salma Abu Ayyash, Francis Reichmeyer, Salim Hariri, Kamal Jabbour, "Distributed Computing on FDDI-Based Network", Proceedings of the 35th Midwest Symposium on Circuits and Systems, Washington DC, August 9-12, 1992, pp. 1197-1200.

Packet Size Distribution of a JDL Run

Number of Packets x 10^3

Bytes

Fig 4-1

Packet Size Distribution of an ISIS Run

Number of Packets

Bytes x 10^3

Fig 4-2

4-16

Target Filter Manager Service Time

Number of Packets

8.00
7.50
7.00
6.50
6.00
5.50
5.00
4.50
4.00
3.50
3.00
2.50
2.00
1.50
1.00
0.50
0.00

240.00　260.00　280.00　300.00

Time x 10 msec
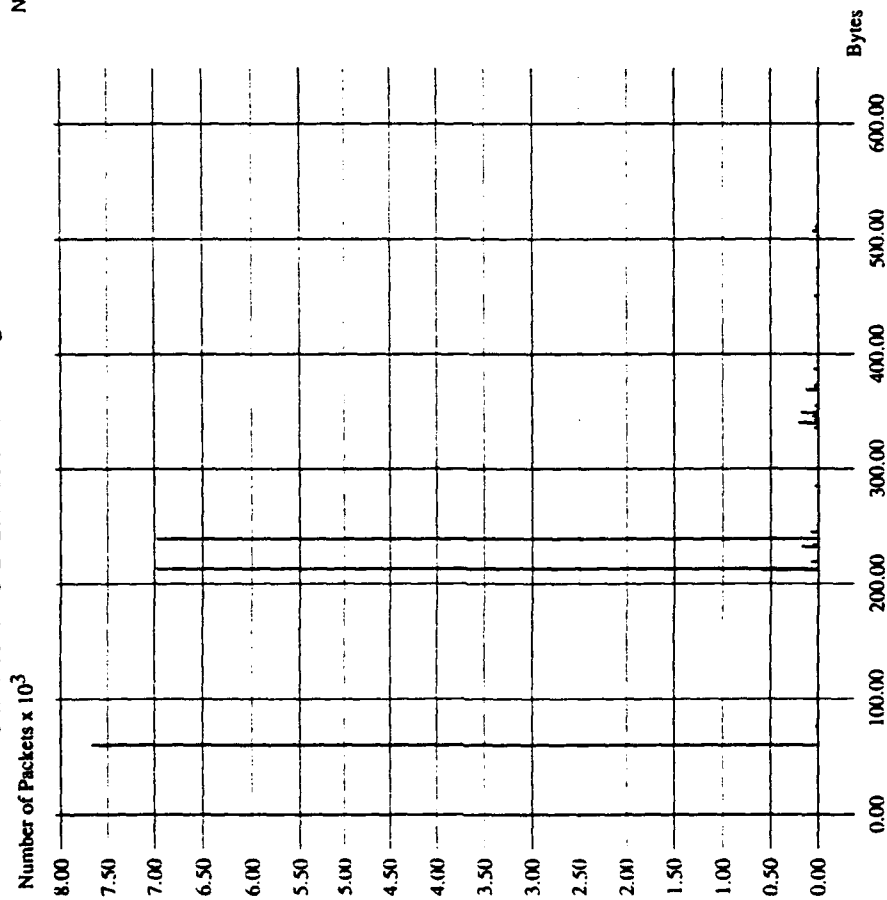
Fig 4-4

ACK Service Time Distribution in JDL Run

Number of Packets

130.00
120.00
110.00
100.00
90.00
80.00
70.00
60.00
50.00
40.00
30.00
20.00
10.00
0.00

0.00　50.00　100.00　150.00　200.00

Time x 10 msec

Fig 4-3

4-17
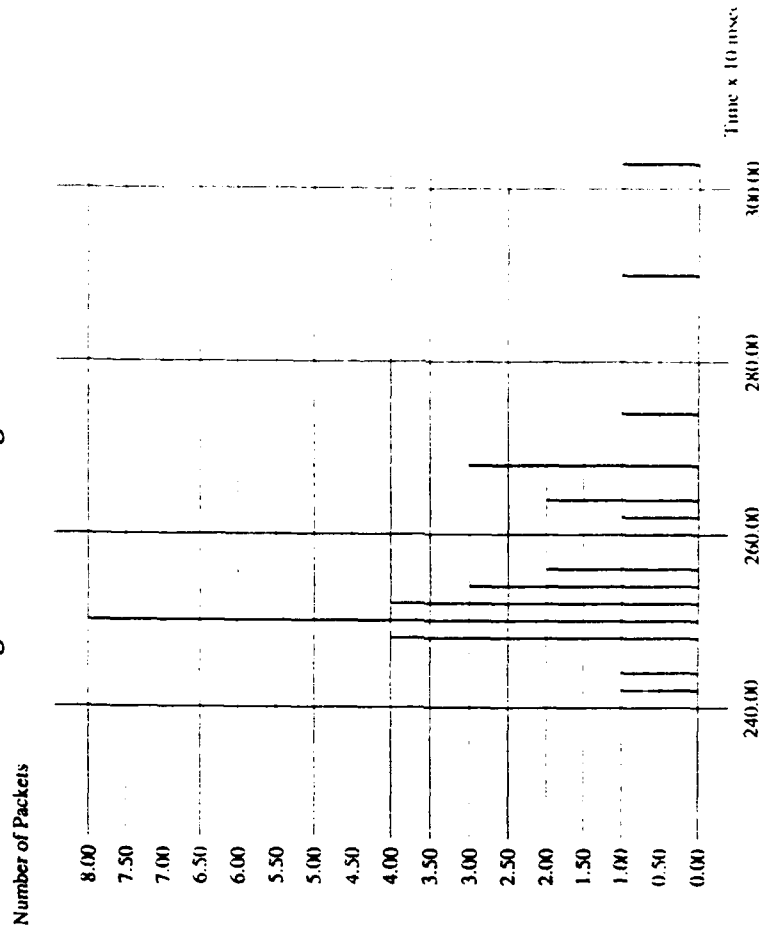
Background Traffic Packet Size Distribution

Number of Packets x 10^3

Fig 4-6

Bytes x 10^3
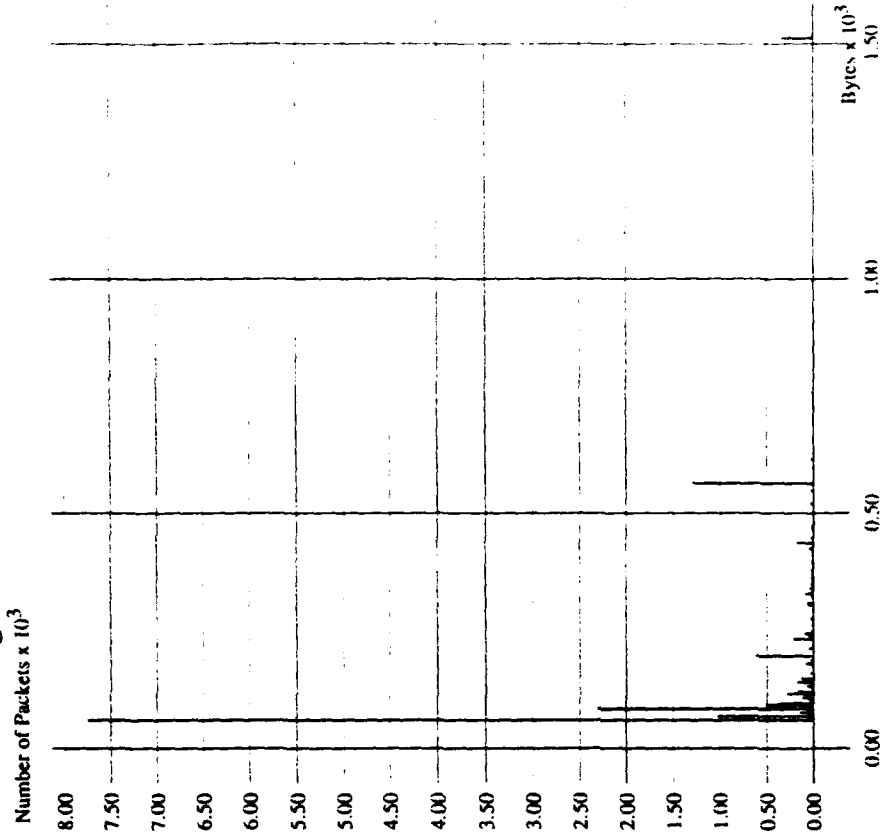
Background Traffic Packet Transmission Interval Distribution
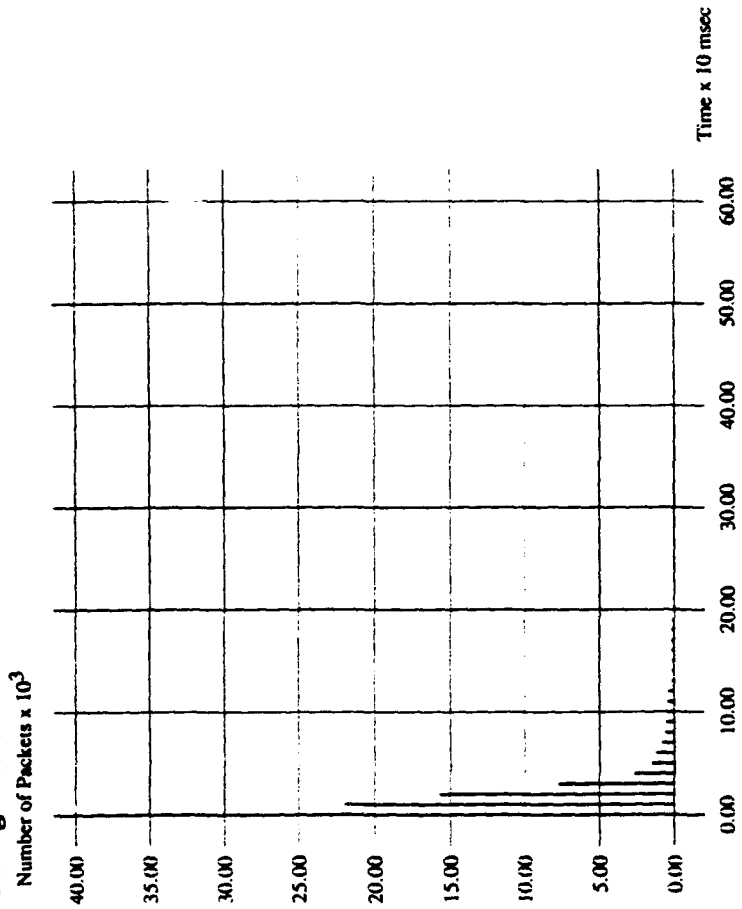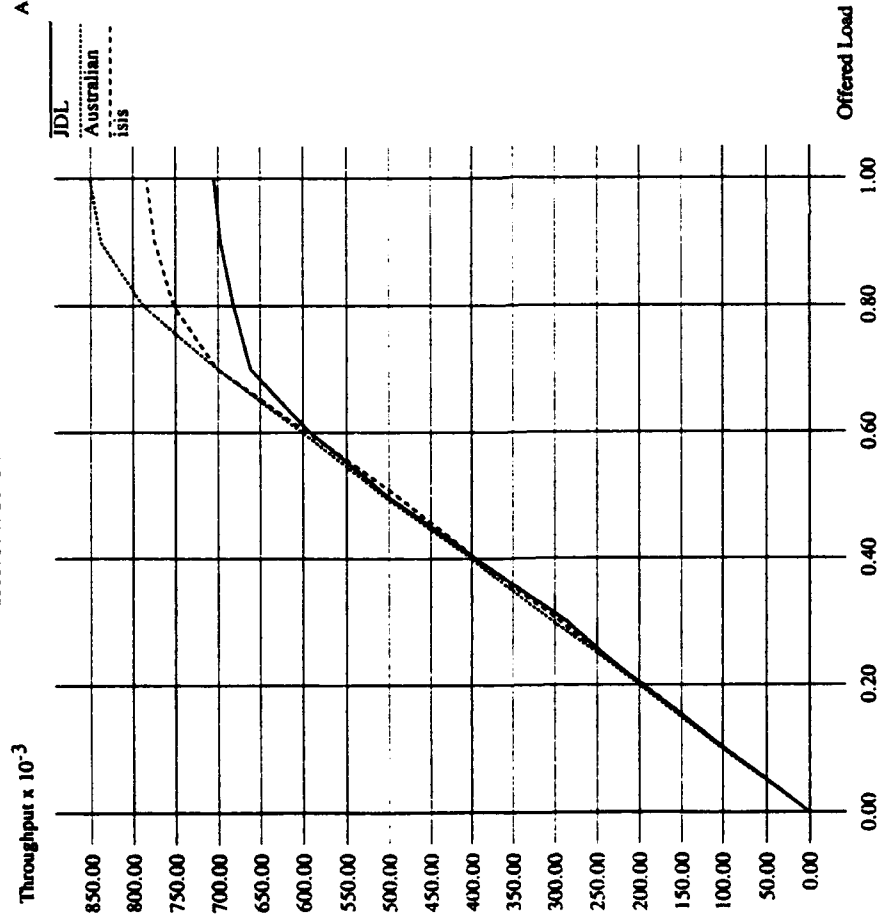
Number of Packets x 10^3

Fig 4-5

Time x 10 msec

4-18

Ethernet Simulation

Throughput x 10⁻³

Fig 4-7

Ethernet Simulation

Average Packet Delay msec

Fig 4-8

4-19

FDDI Simulation

Delay microsec x 10³

JDL ———
Australian ------
isis ············

Offered Load x 10⁻³

Fig 4-10

FDDI Simulation

Throughput packets/sec x 10³

JDL ———
Australian ------
isis ············

Offered Load x 10⁻³
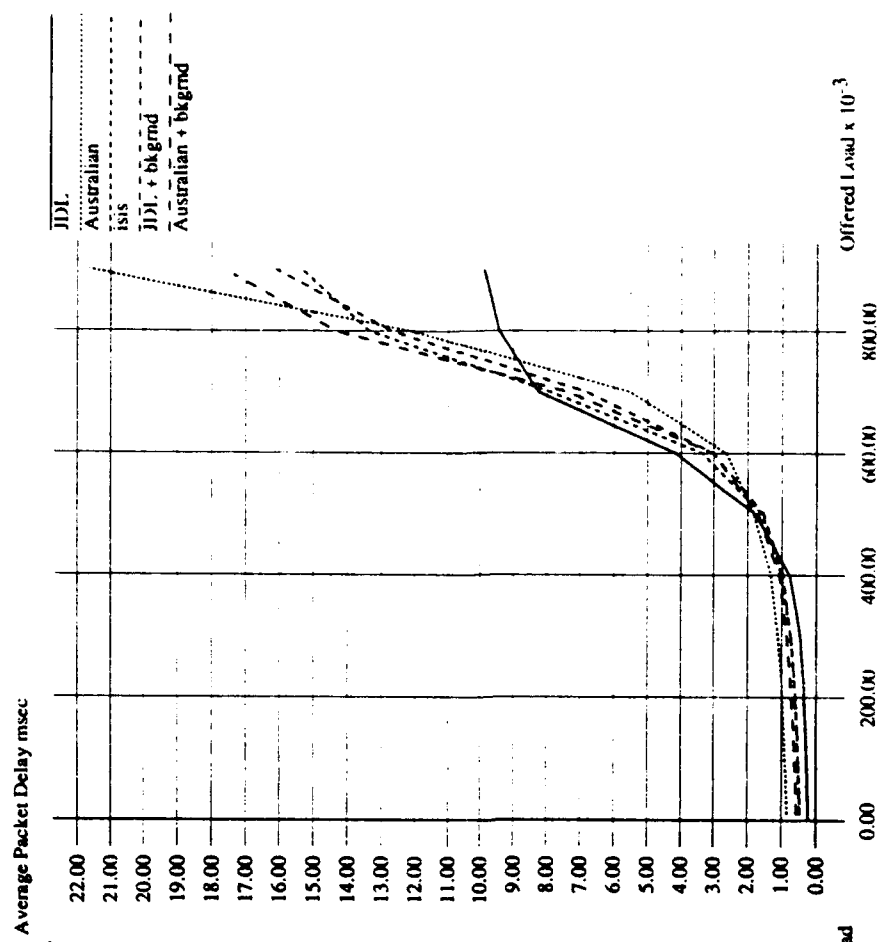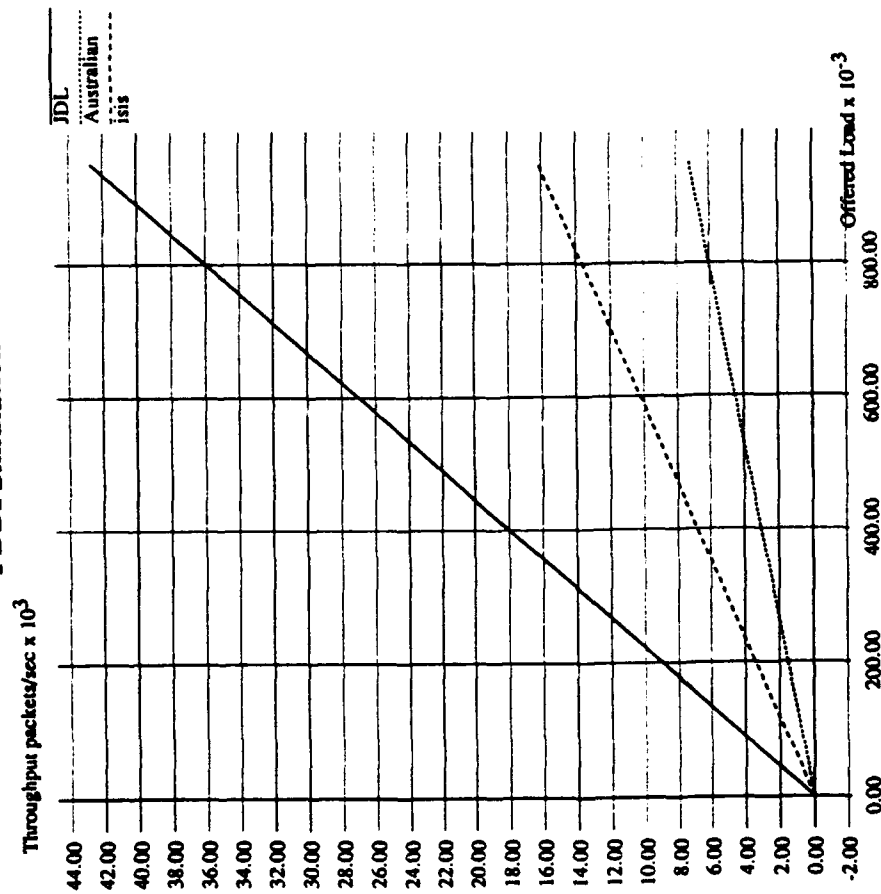
Fig 4-9
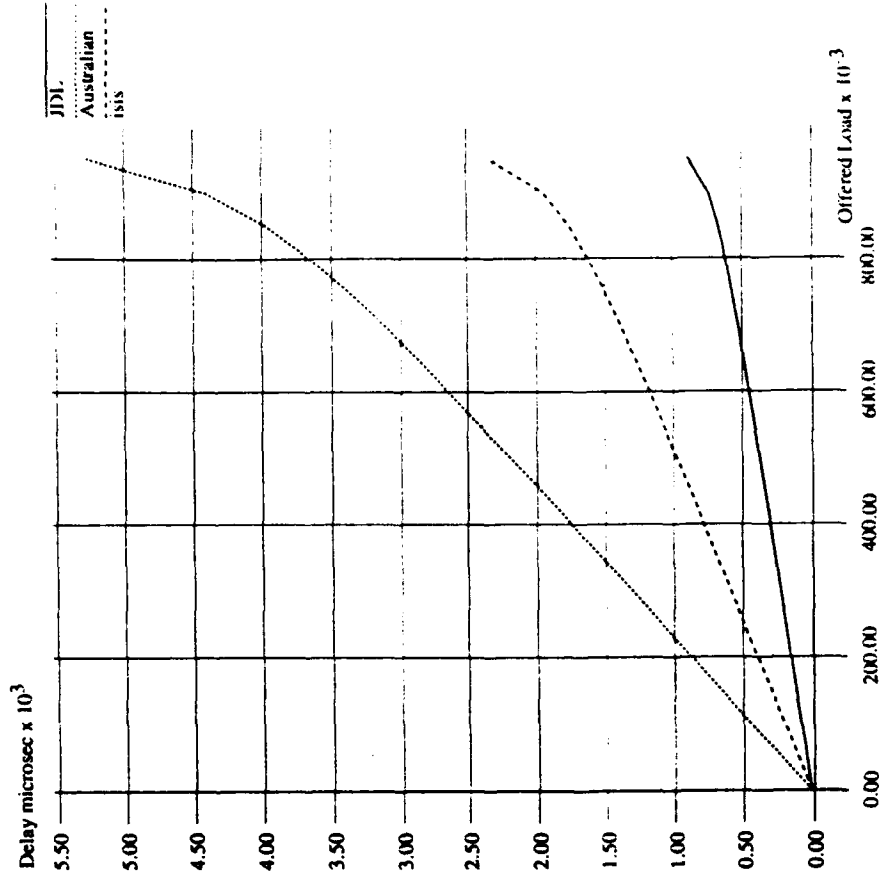
4-20

ADAPTIVE ALGORITHMS FOR ANTENNA
ARRAY SIGNAL PROCESSING

RAJENDRA KUMAR
PROFESSOR
DEPARTMENT OF ELECTRICAL ENGINEERING

CALIFORNIA STATE UNIVERSITY
1250 BELLFLOWER BLVD.
LONG BEACH, CALIFORNIA 90840

FINAL REPORT FOR:
SUMMER FACULTY RESEARCH PROGRAM
ROME LABORATORY

ADAPTIVE ALGORITHMS FOR ANTENNA ARRAY SIGNAL PROCESSING

RAJENDRA KUMAR

PROFESSOR

DEPARTMENT OF ELECTRICAL ENGINEERING

CALIFORNIA STATE UNIVERSITY

Abstract

Quantized-state adaptive algorithms are proposed for adaptive multibeam antenna signal processing and are compared to the known sample matrix inversion and the correlation feedback algorithms of the adaptive antenna signal processing literature in terms of various performance measures of interest. Such performance measures include the interference rejection capability, the computational requirements, convergence rate, numerical robustness for implementation with finite precision arithmetic and fraction of the area coverage lost due to nulling of interference sources. Simulation results show that the quantized state algorithms proposed earlier by the author for somewhat different signal processing problem of adaptive equalization, along with some very significant modifications such as inclusion of an appropriate deadzone in the quantization process, multiple thresholds and a novel method of step size selection etc., constitute powerful algorithms for the multibeam antenna signal processing problems. The proposed schemes are shown to be superior to other known techniques in terms of most of the performance criteria.

ADAPTIVE ALGORITHMS FOR ANTENNA
ARRAY SIGNAL PROCESSING

Rajendra Kumar

1. Introduction

A satellite-based adaptive antenna must be designed to combat interference sources including intentional jammers located anywhere within the desired area covered by the quiescent pattern of the antenna. This is accomplished by the high resolution afforded by a multiple beam antenna with a relatively large aperture size and a significant number of beams (providing the desired number of degrees of freedom)[1]. The outputs of these N beams are linearly combined in an adaptive manner so as to introduce nulls in the direction of interference sources while minimizing the inevitable antenna gain reduction in any other direction within the quiescent beam width. To achieve the desired objectives effectively, the adaptive algorithm must have sufficiently rapid convergence rate to adapt in a dynamic scenario, such as the presence of blinking jammers, have reasonable computational requirements in terms of the actual number of arithmetic operations required per update of the algorithm. Apart from the number of operations, it is equally important that the algorithm be insensitive to arithmetic precision (termed here robustness) so as to be implementable in the DSP chips.

The adaptive algorithms of the literature are based on the constrained optimization of the array gain (signal-to-interference-plus noise ratio) for a signal source in the direction of the peak of the antenna gain as specified by the steering vector[2,3]. The specified steering vector or the quiescent weight vector actually produces 'enough' directive gain to users located anywhere in the specified coverage area in the absence of jammers - essentially a property of the MBA antenna.

However, this may not be the case with the adapted pattern in the presence of jammers and the 'optimal' algorithm termed SMI (sample matrix inversion) [4] may be sub optimum with respect to the criterion of area covered by the adapted beam . In terms of implementation, the SMI algorithm requires order N^2 complex multiplications and additions for each data update and an NxN matrix inversion for each update of the weight vector. For reasonably large value of N (say 91), this may imply about 10,000 multiplications for each data update. In a dynamic scenario involving blinking jammers, it may be necessary to have data update in a fraction of μsec and thus very significant computational requirements are involved. Furthermore, in situations involving multiple jammers of varying power levels, the estimated correlation matrix becomes ill conditioned and high precision arithmetic is required to avoid numerical instability.

A simpler version of this algorithm termed correlation feedback (CF) requires only order N computations. However, for the case of high condition number of the relevant correlation matrix involved, the convergence is very slow and may be unacceptable in some dynamic scenarios . Note that if instead of steering vector, a desired (pilot) signal from the desired direction is given, then the CF algorithm is equivalent to the LMS algorithm of the literature[4].Also both SMI and CF algorithms have their steady-state solutions (under assumed stationarity condition) equal to the steady-state solution of the analog algorithm of Applebaum-Howell [5,6] derived on a more intuitive basis.

A strong motivation therefore exists to explore algorithms which have convergence rates similar to that of SMI algorithm but with much smaller computational requirements, are numerically robust and are capable of providing better coverage area than the SMI algorithm. The quantized state (QS) algorithms proposed earlier by the author for a somewhat different signal processing problem [7], with some very significant modification such as inclusion of an appropriate deadzone in the quantization

5-4

process, multiple thresholds and a novel method of step size selection, etc., are applied here to the MBA signal processing problem. These algorithms only require N^2 increment/decrement operations (as against N^2 complex multiplications and additions required for SMI algorithm), have their convergence rates similar to those of SMI and thus orders of magnitudes faster than CF. Also, the matrix involved in the QS algorithm has a condition number which is approximately equal to the square root of the correlation matrix involved in the SMI algorithm and thus the QS algorithms are much more robust in numerical computations. It may be remarked that much more computationally intensive algorithms are often required to alleviate the matrix ill conditioning problem [8]. These algorithms are based on the update of the square root of the correlation matrix so as to effectively reduce the condition number (CN) to a value equal to the square root of the original matrix but at the cost of order N^3 computations. The QS algorithms in contrast yield the same advantage as afforded by these more computation intensive algorithms, yet at the same time the QS algorithms actually reduce the computational requirement in comparison to the direct SMI algorithm instead of an increase to achieve this CN advantage. The proposed scheme is also superior to the SMI algorithm in terms of antenna pattern area coverage, although there is considerable variability associated with improvement with respect to this criterion.

2.   Adaptive Algorithms

Figure 1 depicts the configuration for the beamformer wherein the amplified rf signals are weighted by complex weights w_1, w_2, ..., w_N, and combined to produce the beamformer output $\{r(t)\}$ whose complex envelope is represented by $z(t)$. The weight vector $w=[w_1,w_2...w_N]'$ is adapted by the adaptive algorithm so as to minimize the residual power at the beamformer output, subject to a constraint on signal response from the desired direction specified by the vector d or more appropriately the signal

response for a specified quiescent weight vector. That is,

$$\text{Min } E\left[|z|^2\right] = w^H R w \; ; \; R = E\left[xx^H\right] \qquad (2.1a)$$

$$\text{Subject to} \quad d^H w = 1 \qquad (2.1b)$$

Here it is implicitly assumed that there are no desired signals
other than in the direction corresponding to the steering vector,
otherwise the algorithm would try to minimize the signal power
from those sources as well. One possible solution to avoid this
problem is to incorporate a "quiet" period during which all
desired signal sources cease transmission and the beamformer
weights are "trained" during this period. This is followed by a
signal transmission period during which the beamformer weights
are not perturbed. The obvious disadvantage of this strategy is
that it may not be possible to null the interference from
blinking jammers. However, as will be seen later, the QS
algorithms can effectively shield the signal sources from the
adaptation algorithm provided that their signal power levels are
smaller than the jammer power levels and, in these situations it
is no longer necessary to have a "quiet" or "training" period
with QS algorithm.   In those situations where power level
constraints are not satisfied, more sophisticated strategies can
be devised to avoid signal cancellation in the absence of a
"training" period as would be the case with blinking jammers.

Another strategy which can reduce the possible signal
cancellation to a limited extent is to impose the following
quadratic constraint

$$w^H w \leq \delta \qquad (2.1c)$$

There are several different but somewhat related ways in which
the quadratic constraint (2.1c) appears in the adaptive antenna
processing literature [2,3,9]. Here, the rationale is that if
the signal covariance matrix R_S is changed by some $\Delta R_S = \xi A$ (for
any arbitrary matrix A of norm 1) then the sensitivity of the
array output signal-to-interference plus noise ratio (SINR) with
respect to ξ is directly dependent on $\|w\|$. Constraint (2.1c)

thus limits the sensitivity of the beamformer output SINR to R_S or equivalently to the distribution of signal sources. Since the beamformer does not distinguish between interference and desired signals except via (2.1b), it is clear that the reduction in SINR sensitivity is achieved at the cost of reduced capability to eliminate the power of (weaker) jammers. Thus, in the selection of δ in (2.1c), there is a tradeoff between these two contradictory requirements. Minimization of the index in (2.1a) subject to (2.1b) and (2.1c) via Lagrangian method yields the following solution:

$$w^0 = \frac{(R + \varepsilon I)^{-1}d}{d^H(R + \varepsilon I)^{-1}d} \qquad (2.2)$$

where ε is an implicit function of δ and a higher value of ε results in reduced interference rejection capability. Since SINR is not changed by an arbitrary scaling of weight vector, the denominator term in (2.2) may be dropped without changing the beamformer output SINR. The solution (2.2) is same as the steady-state solution of the original analog algorithm of Howells-Applebaum [5,6] derived on a more intuitive basis. In practice, R is unknown and (R+εI) may be replaced by the following recursive estimate with R(0)=εI,

$$\hat{R} = \lambda\hat{R}(k-1) + (1-\lambda)x(k)x^H(k) + (1-\lambda)\varepsilon I \ ; \ \ 0 \le \lambda \le 1 \ ; \ k = 1,2,... \qquad (2.3a)$$

$$\hat{w}^{SMI} = \alpha\hat{R}^{-1}(k)\,d \qquad (2.3b)$$

where α is a constant to ensure that $\left\|\hat{w}^{SMI}\right\| = K$ for any constant K independent of k. Note that when R is not a constant (x(k) process is nonstationary) but varies slowly with time, the exponential weighting factor λ in (2.3a) can be appropriately adjusted to track this variation. It may also be noted that within an appropriate (dominant) time constant associated with the variations of R, one needs to compute (2.2) or (2.3b) only once, however, one needs to update (2.3a) many times faster to obtain reliable estimate of R(k). Algorithm (2.3) is referred to

as sample matrix inversion (SMI) algorithm.

Correlation Feedback Algorithm

Correlation feedback algorithm is a simpler reactive version of (2.2) and has been extensively explored in the literature [2-6]. In this procedure, the weight vector w is decomposed as

$$w = w_c + w_u \qquad (2.4)$$

where w_c is the projection of w on the subspace $\mathcal{C}$ of the parameter space wherein the linear constraint (2.1b) is satisfied and w_u is the component in the subspace orthogonal to $\mathcal{C}$. The w_C component corresponding to the solution (2.2) and given by $w_C = d/(d^H d)$ is independent of the process $x(k)$ and thus the optimization is carried out with respect to only w_u. One of the robust versions of the several variations of the resulting algorithm [3,10] has the following form:

$$\hat{w}(k+1) = w_c + \tilde{P}_c[\hat{w}(k) - \mu \hat{R}(k)\hat{w}(k)] \qquad (2.5a)$$

$$\hat{R}(k) = \lambda \hat{R}(k-1) + (1-\lambda)x(k)x^H(k) + (1-\lambda)\varepsilon I \qquad (2.5b)$$

$$\tilde{P}_c = I - d(d^H d)^{-1}d^H \qquad (2.5c)$$

In (2.5), $\tilde{P}_c$ is the projection operator, $\hat{R}(0) = \varepsilon I$ is some non-zero initial estimate of R and the step size μ is selected to be sufficiently small so as to ensure convergence of the algorithm. Note that (2.5) only requires the update of $\hat{R}(k)$ but does not involve a matrix inversion. A computationally simpler version of (2.5) is obtained by substituting $\lambda = o$ and is given by

$$\hat{w}(k+1) = w_c + \tilde{P}_c[(1-\mu\varepsilon)\hat{w}(k) - \mu x(k)z^*(k)] \qquad (2.6)$$

It may be noted that apart from the projection, algorithm (2.6) does not require any matrix operation. However, for a given step size μ (and therefore the convergence rate), (2.6) has higher "algorithm noise" and thus would result in a higher steady-state jammer power at the beamformer output, known as excess mean square error (EMSE) in the literature [11]. Algorithm (2.6) while computationally much simpler compared to (2.2) has the disadvantage of a much slower convergence rate which is a function of μ. It may be shown [11] that for convergence,

$$0 < \mu < \frac{2/3}{\text{Tr}[R] + N\varepsilon}$$

and the EMSE is the weighted sum of the terms $(1 - \mu\varepsilon - \mu\lambda_n)^{2k}$ where λ_n denotes the nth eigenvalue of R. It is easily seen that for high condition number ratio $(\lambda_{max}/\lambda_{min})$ of R (as is the case with the problem under study), the term associated with the minimum eigenvalue λ_{min} will have very slow convergence resulting in an overall slow convergence of the algorithm. For a typical example with $\lambda_{max}=10^5$, $\lambda_{min}=1$, $\varepsilon=1$, and N=7 a conservative estimate of the maximum value of μ is 9.5 x 10^{-7}. With this value of μ, the slow mode will converge as $(1-1.9\times10^{-6})^{2k}$ with the associated time constant $\tau \approx 1/(4\mu\lambda_{min}) = 2.6 * 10^5$ and adaptation time of approximately 10^6 samples. For higher values of N and the condition number, the convergence rate would be even lower. In dynamic scenarios, such low convergence rates may be unacceptable. On the other hand the error in (2.3) is primarily due to estimation error in $\hat{R}$ and thus convergence of MSE to its steady-state value will occur in order $1/(1-\lambda)$ samples. For example, with $\lambda=.95$ this is only about 20 samples. Quantized state schemes are now considered which are computationally very attractive as compared to SMI but have same order of convergence times as for SMI. In the first instance, consider algorithms for the unconstrained minimization problem derived on the basis of geometric projection [12], which are then adapted to the constrained optimization problem under consideration.

A Generalized Adaptive Algorithm - Geometric Approach

Consider the beamformer problem wherein a pilot signal s(k) from the desired signal source is given (instead of the steering vector d) and the weight vector w is selected to minimize the $\text{MSE} = E[|s(k) - w^H x(k)|^2]$. With w^0 denoting the optimum solution, one obtains,

$$s(k) = w^{0H}x(k) + v(k) \qquad\qquad (2.7)$$

where due to the orthogonality principle of minimization, v(k) is

orthogonal to x(k). If it is assumed that x(k) is a Gaussian process, then v(k) is also independent of x(k). Thus, one may consider an equivalent problem of identifying the unknown parameter vector w^0 from the signal model (2.7). In the geometric approach to the solution [12], given an arbitrary initial estimate $\hat{w}$ of w^0, one first projects $\hat{w}$ onto the hyperplane H_k: $s(k) - w^H x(k) = o$; so as to minimize the weighted "norm"

$$\left\| \hat{w} - w_H \right\|_B^2 \qquad ; w_H \in H$$

(the indices of H, w_H, x, and B have been dropped for convenience) with respect to matrices B(k) which satisfy the following conditions:

$$BB^\# x = x \ ; \ x^H B^\# x = 1 \tag{2.8}$$

where $B^\#$ denotes Moore-Penrose pseudo-inverse of matrix B. The optimum projections are simply given by

$$\hat{w}_{H_k} = \hat{w} + B^\#(k)x(k)[s(k) - \hat{w}^H x(k)]^\#$$

$$\left\| \hat{w} - \hat{w}_{H_k} \right\|_{B(k)}^2 = \left| s(k) - \hat{w}^H x(k) \right|^2 \tag{2.9}$$

In the second step, each hyperplane H_k is represented by its respective projection $\hat{w}_{H_k}$ and one then minimizes the following sum to obtain $\hat{w}_m$ termed the "center of the mass" of the hyperplanes. That is

$$\text{Minimize} \ \sum_{k=1}^{m} \left\| \hat{w} - \hat{w}_{H_k} \right\|_{\overline{B}(k)}^2 \tag{2.10}$$

for some appropriate sequence of matrices $\overline{B}(k) > o$. A simpler (recursive) algorithm is obtained if $\hat{w}_{H_k}$ in (2.8) is replaced by $\hat{w}_{H_k}^s$ denoting the projection of $\hat{w}(k-1)$ onto H_k. The resulting recursive solution is given by

$$\hat{w}(k) = \hat{w}(k-1) + \overline{P}(k)\overline{B}(k)B^\#(k)x(k)\xi^{*(k)}$$

$$\xi(k) = s(k) - \hat{w}^H(k-1)x(k)$$

$$\overline{P}^{-1}(k) = \overline{P}^{-1}(k-1) + \overline{B}(k) \ ; \ k = 1, 2, \ldots \tag{2.11}$$

It is easily seen in view of (2.8) that for the case with either

$\overline{B}(k) \equiv B(k)$ or $\overline{B}(k) = x(k) x^H(k)$, the algorithm (2.11) reduces to the recursive least-squares (RLS) algorithm [13,14].

$$\hat{w}(k) = \hat{w}(k-1) + \overline{P}(k) x(k) \xi^*(k)$$

$$\overline{P}^{-1}(k) = \overline{P}^{-1}(k-1) + x(k) x^H(k) \tag{2.12}$$

Also with $\overline{B}(k) = \overline{b}(k)I$ for some scalar sequence $\overline{b}(k)$, (2...) reduces to the following generalized version of the stochastic gradient algorithm (2.6) .

$$\hat{w}(k) = \hat{w}(k-1) + \gamma(k) B^*(k) x(k) \xi^*(k) \tag{2.13}$$

where $\gamma(k)$ is an appropriate scalar sequence related to the $\overline{b}(k)$ sequence. Another solution of most interest here is achieved by the following selection of matrix $\overline{B}(k)$. Note that the term under the summation in (2.10) is required to be some appropriate measure of the distance between a point $\hat{w}$ and the hyperplane containing the point $\hat{w}_{H_k}$ with the property that the distance be non zero if $\hat{w} \notin H_k$ and be zero otherwise. A Hermitian symmetric matrix $\overline{B}(k)$ satisfying this property is given by

$$\overline{B}(k) = x(k) \overline{x}^H(k) + \overline{x}(k) x^H(k)$$
$$Re[\overline{x}_i(k)] = \text{sgn}\{Re[x_i(k)]\}$$
$$Im[\overline{x}_i(k)] = \text{sgn}\{Im[x_i(k)]\}$$

where x_i (resp. $\overline{x}_i$) denote the ith component of the vector x (resp. $\overline{x}$), and $Re(z)$ and $Im(z)$ respectively denote the real and imaginary parts of any complex variable z. It is easily seen for this selection of $\overline{B}(k)$ and any arbitrary vector q, that $q^H \overline{B} q = o$ if q is orthogonal to $x(k)$ i.e., q is parallel to H_k and $q^H \overline{B} q > o$ if q has a component in the direction of $x(k)$. With this selection of $\overline{B}(k)$ and $B(k) = x(k) x^H(k)$, the general algorithm (2.11) reduces to

$$\hat{w}(k) = \hat{w}(k-1) + \overline{P}(k) [\overline{x}(k) + \overline{x}^H(k) x(k) (x^H(k) x(k))^{-1} x(k)] \xi^*(k)$$

$$\overline{P}^{-1}(k) = \overline{P}^{-1}(k-1) + \overline{x}(k) x^H(k) + x(k) \overline{x}^H(k) \tag{2.14}$$

In some situations such as when $x(k)$ is a Gaussian Stationary process (with each of its components having equal variance), it may be shown that $E[\overline{x} x^H]$ is a Hermitian matrix and

therefore, asymptotically the matrix $\bar{P}^{-1}(k)$ in (2.14) is same as that obtained by deleting the last term in its update (ignoring the factor of 2). Moreover, since the two vectors $\bar{x}$ and x will have on the average an small angle between them, one may simplify the algorithm by retaining only the $\bar{x}(k)$ term in the first update of (2.14) giving rise to the following algorithm:

$$\hat{w}(k) = \hat{w}(k-1) + \bar{P}(k)\,\bar{x}(k)\,\xi^*(k)$$

$$\bar{P}^{-1}(k) = \bar{P}^{-1}(k-1) + \bar{x}(k)x^H(k) \qquad (2.15)$$

When compared to the RLS algorithm (2.12), both the algorithms (2.14), (2.15) have the computational advantage in that the update of the matrix $\bar{P}^{-1}(k)$ in (2.14), (2.15) requires only N^2 additions as compared to N^2 complex multiplications and additions in the RLS algorithm. Also, the first update in (2.15) also requires order N^2 additions compared to N^2 multiplications in RLS. However, all three algorithms require a matrix inversion. This problem can be surmounted by updating $\bar{P}^{-1}(k)$ for every k but updating $\bar{P}(k)$ only once in every N iterations, say. This will reduce the computational requirements for the algorithms (2.14) and (2.15) to only order N multiplication and order N^2 additions per update of the weight.

There are equivalent non-recursive forms [11-14] to the RLS algorithm and the QS algorithm (2.15) which under stationarity assumptions approach the following solutions as $k\to\infty$

$$\hat{w}^{LS} = R_{xx}^{-1}\,r_{xs} \quad ; \quad R_{xx} = E[xx^H] \quad ; \quad r_{xs} = E[xs*] \qquad (2.16a)$$

$$\hat{w}^{QS} = R_{\bar{x}x}^{-1}\,r_{\bar{x}s} \quad ; \quad R_{\bar{x}x} = E[\bar{x}x^H] \quad ; \quad r_{\bar{x}s} = E[\bar{x}s*] \qquad (2.16b)$$

With the introduction of a quadratic constraint and replacing r_{xs} or $r_{\bar{x}s}$ term by the steering vector d, (2.16a) reduces to (2.2) while (2.16b) yields

$$\hat{w}^{QS} = (R_{\bar{x}x} + \varepsilon I)^{-1}d \qquad (2.17)$$

To obtain fast algorithms whose computational requirements are even smaller compared to those in (2.15) or (2.17) above, the following transformation in the parameter space is considered next.

Transformation of Parameter Space

If one selects $\gamma(k) \equiv 1$ and $B(k)=I$ in the gradient algorithm (2.13) which corresponds to the selection of $\overline{B}(m)=1$, $\overline{B}(k)=0$, $k<m$ in the optimization index (2.10) and the Euclidean norm in (2.9), the projection operation can be illustrated as in Figure 2 assuming the noise free case. In the presence of noise, γ is less than 1 and the situation will be similar. As is evident from the Figure 2, the algorithm has a faster convergence rate if successive hyperplanes are nearly orthogonal compared to the case when they are not. Near orthogonality of hyperplanes is best achieved when

$$E[x(k)x^H(j)] \cong I\, \delta(k-j) \tag{2.18}$$

Assuming that $\{x(k)\}$ is a nearly independent process, the condition (2.18) can be satisfied for a suitable transformed state $x^n(k)=L\, x(k)$ for some appropriate linear operator L, for example, $L = S^{-1}$ with $SS^H = R_{xx}$ representing square root factorization of the matrix R_{xx}. With a corresponding transformation in the parameter space $w^n = (L^{-1})^H w^0$ one obtains,

$$\hat{w}^n(k) = \hat{w}^n(k-1) + \gamma(k)x^n(k)\xi^*(k) \tag{2.19}$$

Premultiplying equation (2.19) by L^H one obtains the following fast version of the gradient algorithm (2.13):

$$\hat{w}(k) = \hat{w}(k-1) + \gamma(k)L^H L\, x(k)\xi^*(k) \tag{2.20}$$

Similarly if one starts with a quantized state version of (2.13) obtained by replacing $x(k)$ by $\overline{x}(k)$ for computational simplification (which may also be derived directly from (2.9), (2.10) for appropriate selection of the matrices), its corresponding version with accelerated convergence is given by,

$$\hat{w}(k) = \hat{w}(k-1) + \overline{P}(k)\overline{x}(k)\, \xi^*(k)$$

$$\overline{P}^{-1}(k) = \overline{P}^{-1}(k-1) + \overline{x}(k)\overline{x}^H(k) \tag{2.21}$$

The update of $\overline{P}^{-1}(k)$ in (2.21) requires only N^2 increments/decrements as compared to N^2 complex multiplications or full additions in algorithms (2.12) and (2.15) respectively. See also the discussions following (2.15) regarding the update of $\hat{w}(k)$.

Minimization of Power in Clipped Interference Vector

A doubly quantized algorithm can also be obtained as a result of the following minimization problem:

$$\text{Min } E[|\overline{x}^H w|^2] = w^H \overline{R} w \; ; \; \overline{R} = [\overline{x}\,\overline{x}^H] \tag{2.22a}$$

$$\text{Subject to:} \qquad d^H w = 1 \tag{2.22b}$$

$$w^H w = \delta^{-2} \tag{2.22c}$$

The solution to (2.22) is obtained as in terms of an exponential weighting factor λ, as

$$\hat{w}^{QQ}(k) = \hat{\overline{R}}^{-1} d$$

$$\hat{\overline{R}} = \lambda \hat{\overline{R}}(k-1) + (1-\lambda)\overline{x}(k)\overline{x}^H(k) + (1-\lambda)\varepsilon I \tag{2.23}$$

This minimization is meaningful as in the case of MBA beamforming problem, the subspaces spanned by $\{\overline{x}(k)\}$ and $\{x(k\}$ sequence are "nearly" same and thus the weight vector $\hat{w}^{QQ}(k)$ will produce a null in this latter subspace as well.

It is straightforward to obtain constrained recursive versions of the algorithms (2.12)-(2.15),(2.21), and (2.23). The algorithm corresponding to (2.12) is referred to as the constrained version of Newton's or conjugate gradient method. This algorithm is computationally intensive requiring order N^2 multiplications per update and as evidenced by some simulations exhibits poor stability due to the projection operation. In terms of various performance criteria, the constrained version of (2.21) with novel step size selection $\mu(k)$ provides the most attractive algorithm . This novel algorithm will be referred to as conjugate gradient with quantized states (CQ2) and is given below.

$$\hat{w}^{CQ2}(k) = w_c + \tilde{P}_c [\hat{w}^{CQ2}(k-1) - \mu(k)T^{-1}(k)\overline{x}(k)z^*(k)]$$

$$T(k) = \lambda T(k-1) + (1-\lambda)\overline{x}(k)\overline{x}^H(k) + (1-\lambda)\varepsilon I \; ; \; T(0) = \varepsilon I \tag{2.24}$$

Another significant algorithm obtained as a constrained and recursive version of (2.23) and termed conjugate gradient algorithm with quantized states 1(CQ1) is,

$$\hat{w}^{CQ1} = w_c + \tilde{P}_c [\hat{w}^{CQ1}(k-1) - \mu(k)T^{-1}(k)\overline{x}(k)\overline{z}^*(k)] \; ; \; \overline{z}(k) = \overline{x}^H(k)\hat{w}^{CQ1}(k-1) \tag{2.25}$$

with the update for T(k) same as in the algorithm(2.24). As is apparent from the comparison of equations (2.24) and (2.25), the CQ1 and CQ2 algorithms although derived in quite different ways, differ only in terms of the prediction error $\bar{z}(k)$ in CQ1 (resp. z(k) in CQ2). In terms of the computational requirements there is hardly any difference among the two algorithms. However, in terms of other performance criteria, the differences can be significant and it would be of interest to evaluate both of them in terms of simulation and analysis. It is also clear that the dominant computations involved in the parameter update of CQ1 and CQ2 are in the product $\bar{T}^{-1}(k)\bar{x}(k)$ requiring order N^2 additions, while the update of T(k) requires only N^2 increments/decrements. The algorithms do require inversion of a matrix. However, as discussed with reference to equation (2.15), by updating $T^{-1}(k)$ (as against T(k)) once in every N iterations, the computational requirements can be reduced to order N multiplications and order N^2 additions.

Quantization Threshold

From the simulation studies presented in the subsequent section it turns out that the quantized state algorithms derived above and with the quantization defined in terms of the signum function, have relatively poor convergence. The reason for this poor convergence behavior is as follows. Since the observed process x(k) consists of both the noise and interference ,taking sign of the components of x(k) will result in significant loss of information about the interference source. Thus for proper cancellation of the interference only the interference component of x(k) should influence the adaptive algorithm. A simple method to achieve this objective is to place a deadzone (threshold)in the quantization process, that is to replace the signum function in the various quantized state algorithms by the following modified quantization function,

$$\text{quan}(x) = \begin{cases} +1 & ; \ x > th \\ -1 & ; \ x < -th \end{cases}$$

5-15

$$\begin{cases} 0 & ; \text{ otherwise} \end{cases}$$

for an appropriate value of the threshold th. For example, one can simply select th=3σ where σ is the rms value of the receiver noise. Note however that it is possible to optimize the performance of the algorithm to a certain extent with respect to th. More generally at the cost of some additional computations, multiple thresholds may also be incorporated in the quantization process. Such optimizations and extensions will be studied in the subsequent research. In this paper for the sake of simplicity, the notation $\bar{x}$ is used to refer to this modified quantization process as well.

3. Performance Evaluation

In the following, the performance of various algorithms is presented in brief terms. The computational requirements of these algorithms have already been discussed in section 2. For the evaluation of various performance indices, an MBA antenna with 7 beams arranged in a hexagonal geometry as depicted in Figure 3 is considered. Each beam has a 3dB beam width of 2.5^0 with a 3^0 separation among the centers of adjacent beams. With this antenna, two jammer configurations are considered for simulations. In the first configuration, a single jammer is considered located anywhere in the area covered by the MBA beam. The second configuration involves two jammers with various relative power levels. The condition number (CN) of the update matrix was computed by simulations for different algorithms. Note that as for as the condition number is considered, one needs to consider only three cases corresponding to the SMI algorithm, QS algorithm (2.16b) and the QQ (and CQ1 or CQ2) algorithms.

Figure 4 depicts the results when one of the jammers is located at 2 deg azimuth and 2.5 deg elevation with a power level of 28dB above the receiver noise level (corresponding to 70 dBW jammer power for a certain satellite link geometry). The other jammer located at 1.5 deg azimuth and 2.5 deg elevation has

varying power levels between 40 to 90 dBW. The value of ε was selected equal to 1 for SMI and QS algorithms and equal to .01 for the QQ algorithms so as to achieve approximately 0 dB total interference plus noise power level (corresponding to complete interference cancellation) at the beamformer output. As shown in the figure the CN for SMI algorithm is high and is very sensitive to power level difference among jammers (essentially it is equal to the power ratios), while the CN for the QQ algorithm is very low and is least dependent upon the power levels. The results of the figure can be approximated by the following relationships,

$$(CN)_{QQ} \approx (CN)_{SMI}^{1/2}$$

$$(CN)_{QS} \approx \{(CN)_{SMI} \ (CN)_{QQ} \}^{1/2}$$

Since the required arithmetic precision and the resulting numerical stability of the algorithm depends mainly upon the condition number of the matrices involved in the computations, the above result is highly significant clearly delineating the superiority of the proposed quantized state algorithms with respect to these criteria.

Figure 5 plots the convergence results for various algorithms for the case of single jammer. Note that both the SMI and QQ(th=10) achieve complete nulling of the interference in about 4 iterations (data samples) while the QS algorithm requires about 10 iterations. The threshold for the QS algorithm was set to 0 to clearly show the importance of the proposed deadzone in the quantization process. Actually the QQ algorithm with th=0 did not converge as is also evident from the figure. For the correlation feedback algorithm the maximum value of μ is .001 from the previously presented analysis. For this value of μ the convergence rate is rapid but results in about 5 dB residual interference power in steady state. A lower value of μ of course results in much slower convergence. In any case in practice one has to use conservatively low value of μ to ensure convergence. Figure 6 shows the convergence of the conjugate gradient algorithm (CG) for various values of the parameter μ for the case

of single jammer. As is apparent from the figure the CG algorithm exhibits poor convergence behavior even for this relatively simple scenario. An attempt to significantly modify this algorithm was not made as the algorithm is not attractive in terms of other performance criteria as well. The convergence results for the second jammer configuration are plotted in Figure 7 wherein the second jammer has 38 dB relative power level. Clearly while the quantized state algorithms have convergence rates similar to that of the SMI algorithm, these are orders of magnitude faster than the correlation feedback algorithm depending on the value of μ selected for the CF algorithm. Higher value of μ of course results in higher power of the residual interference.

The steady-state weight vector is used to obtain the gain pattern of the adapted MBA antenna beam from which a distribution function of the antenna gain is evaluated both for the SMI (optimal in terms of SINR for a signal source from the specified direction d) and the proposed quantized state algorithms. From some simulations (not reported here due to space limitations), it was observed that considering receivers having antenna gains within 10-15 dB of the maximum gain of the quiescent pattern, the quantized state algorithms can provide much higher percentage of the area covered in the zone surrounding the jammers. In the jammer scenario considered above and evaluating the gain distribution in the upper half of the area under the quiescent beam (0,5.5)deg azimuth, (-5.5,5.5)deg elevation ,the covered area by QQ/QC algorithms was found to be up to 60% higher compared to the SMI algorithm. However there is significant variability associated with this improvement. The improvement is higher for higher power ratios of the jammers and relatively higher link margins. More simulation results are needed to gain further analytical insights and obtain maximum possible improvement in this respect.

4. Conclusions

It has been demonstrated in this report that the quantized state algorithms proposed for the suppression of interference from an MBA antenna exhibit convergence rates similar to that of the sample matrix inversion (SMI) algorithm and the rates are orders of magnitude faster than the correlation feedback algorithm. The computations involved in the quantized state algorithms are dominated by binary operations and thus the algorithms afford very significant computational savings over the SMI algorithm. In fact with simple variations in the update, the computational requirements can be made to be similar to those of correlation feedback algorithm without any significant reduction in the convergence rate. The matrices involved in the doubly quantized algorithms have their condition number approximately equal to the square root of those in the SMI algorithm and thus the proposed algorithms are numerically robust when finite precision arithmetic is used in their implementation using DSP chips. Due to certain inherent detection involved in the quantized state algorithms, they also provide much better resolution capability and thus an increased area coverage in the region surrounding the jammers. In a few simulation examples, the improvement in terms of area coverage turned out to be as much as 60% over the SMI algorithm. Due to considerable variability in this result, more simulation studies are required to gain further analytical insights in order to maximize such improvement. It would also be of considerable significance to evaluate the performance of these algorithms when the adaptation is performed in the presence of desired signal sources. It is anticipated that due to an implicit detection in the proposed algorithms the signal cancellation if any will be much smaller compared to the SMI algorithm. Another very important area of investigation is to consider more sophisticated configurations than just a linear combiner. This would be particularly interesting in view of the computational power released by the quantized algorithms. That is, for a given amount of computational power available much more

sophisticated configurations can be implemented by using quantized state algorithms instead of the SMI algorithm.

Acknowledgment

Reference

[1] J.T. Mayhan,"Area coverage adaptive nulling from geosynchronous satellites: phased arrays versus multiple-beam antennas", IEEE Transactions on Antennas and Propagation, Vol AP34, No.3, pp.410-419, March 1986.

[2] M.H. Er. and A. Cantoni,"A new approach to the design of broad-band element space array processors", IEEE Journal of Oceanic Engineering, Vol OE10, No.3, pp.231-240, July 1985.

[3] H. Cox, R.M. Zeskind and M.M. Owen,"Robust adaptive beamforming", IEEE Transactions on Acoustics, Speech and Signal Processing, Vol ASSP35, No.10, pp.1365-1376, October 1987.

[4] R.A. Monzingo and T.W. Miller, Introduction to Adaptive Arrays, John Wiley and Sons, 1980.

[5] S.P. Applebaum, Adaptive Arrays, Syracuse University Research Corp., Report SPL TR 66-1, August 1966.

[6] P.W. Howells,"Exploration in fixed and adaptive resolution at GE and SURC", IEEE Transactions on Antennas and Propagation, Vol AP24, No.5, September 1976.

[7] R. Kumar and J.B. Moore,"Adaptive equalization via quantized state methods", IEEE Transactions on Communications, Vol COM29, No.10, pp.1492-1501, October 1981.

[8] J. Bierman, Square-Root Factorization, Prentice Hall, Englewood Cliffs, New Jersey.

[9] R. Kumar,"Multi-element array signal reconstruction with adaptive least-squares algorithms", International Journal f Adaptive Control and Signal Processing, Vol 6, pp.561-588, December 1992.

[10] O.L. Frost,"An algorithm for linearly constrained adaptive array processing", Proc. IEEE, Vol 60, pp.926-935, August 1972.

[11] B. Widrow and S.D. Stearns, Adaptive Signal Processing, Prentice Hall, Englewood Cliffs, New Jersey, 1985.

[12] R. Kumar,"State inverse and decorrelated state stochastic approximations", Automatica, Vol 16 ,pp.295-311.

[13] R. Kumar,"Almost sure convergence of adaptive identification, prediction and control algorithms", Proc. 20th IEEE Conf. on Decision and Control, San Diego, pp.1241-46., December 1981

[14] S. Haykin, Adaptive Filter Theory, Prentice Hall, Englewood Cliffs, New Jersey ,1986.
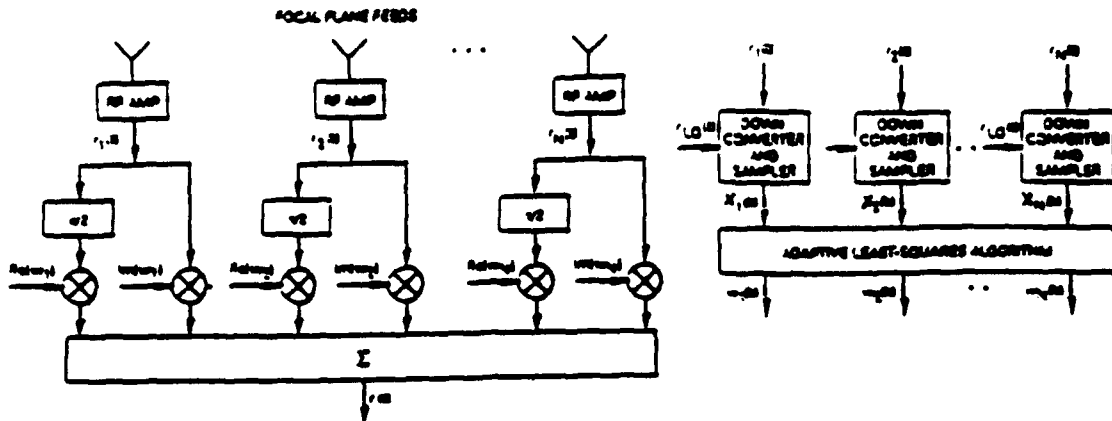
Figure 1. Genaral beamformer configuration

(a)

(b)
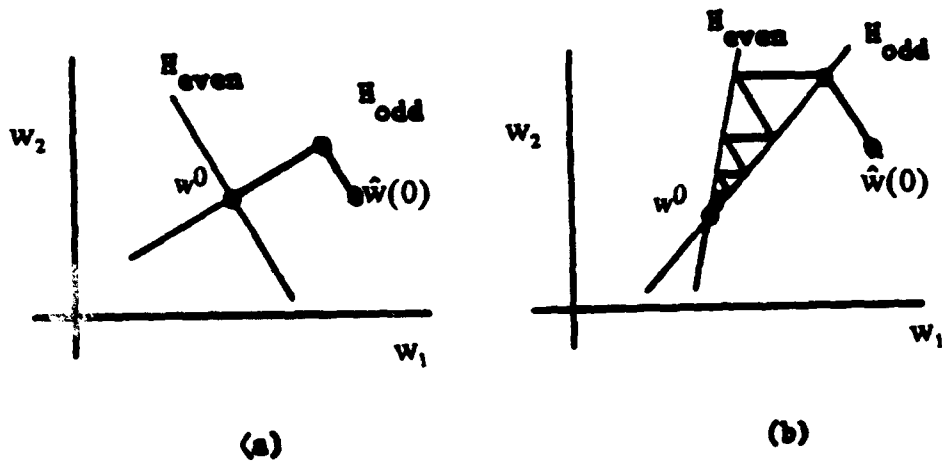
Figure 2. Faster convergence with orthogonal hyperplanes
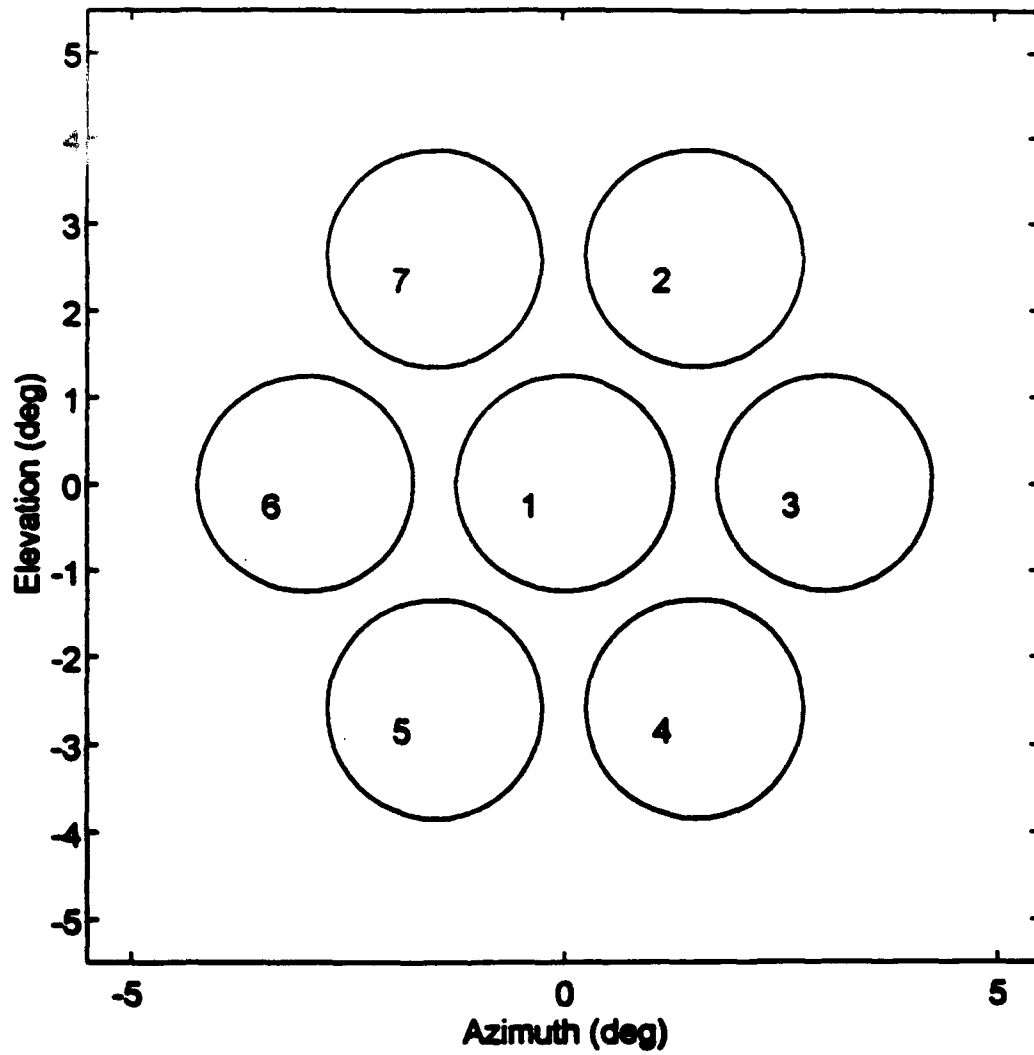
Figure 3. Beam positions of the multiple-beam antenna
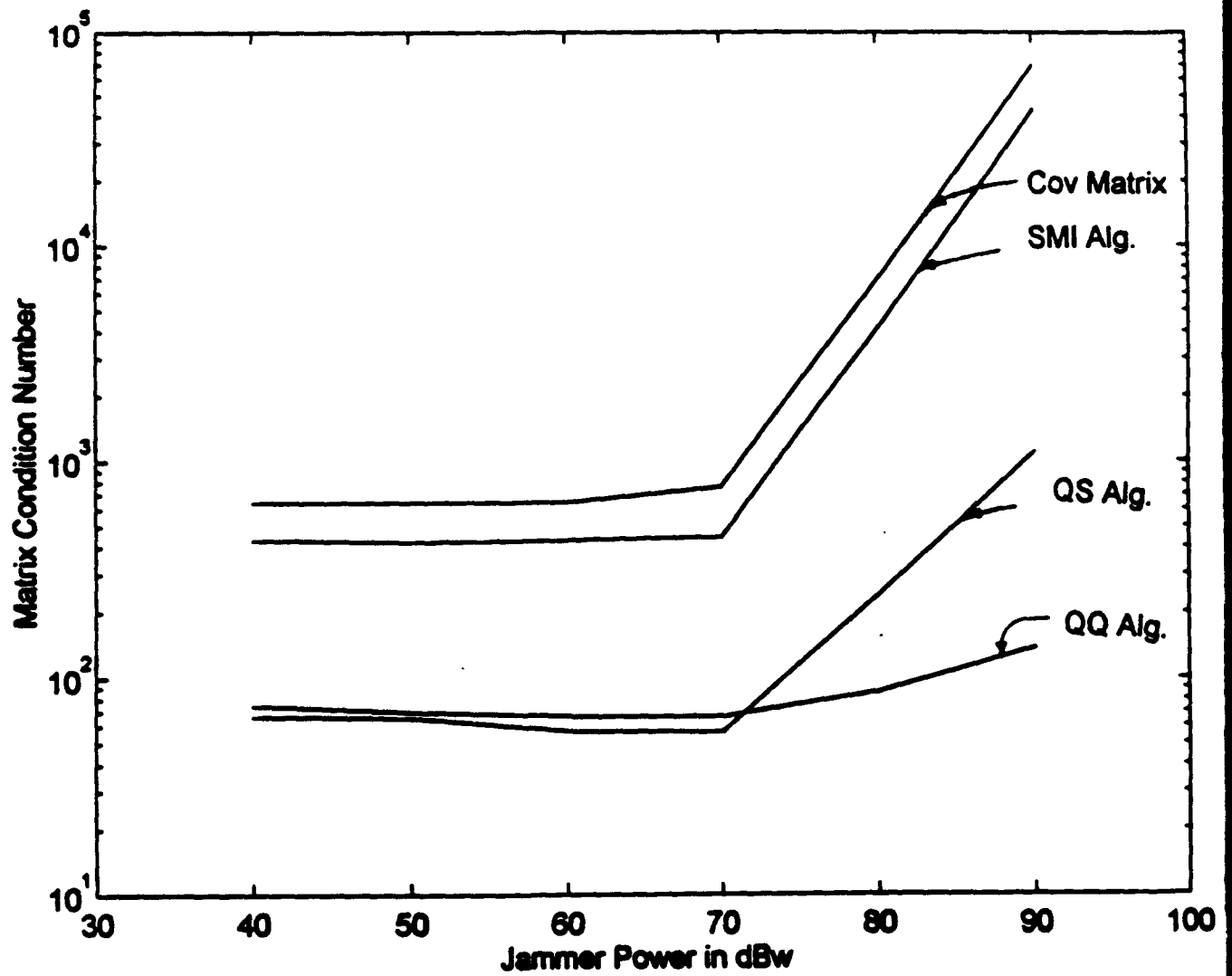
Figure 4. Condition number comparison of various algorithms
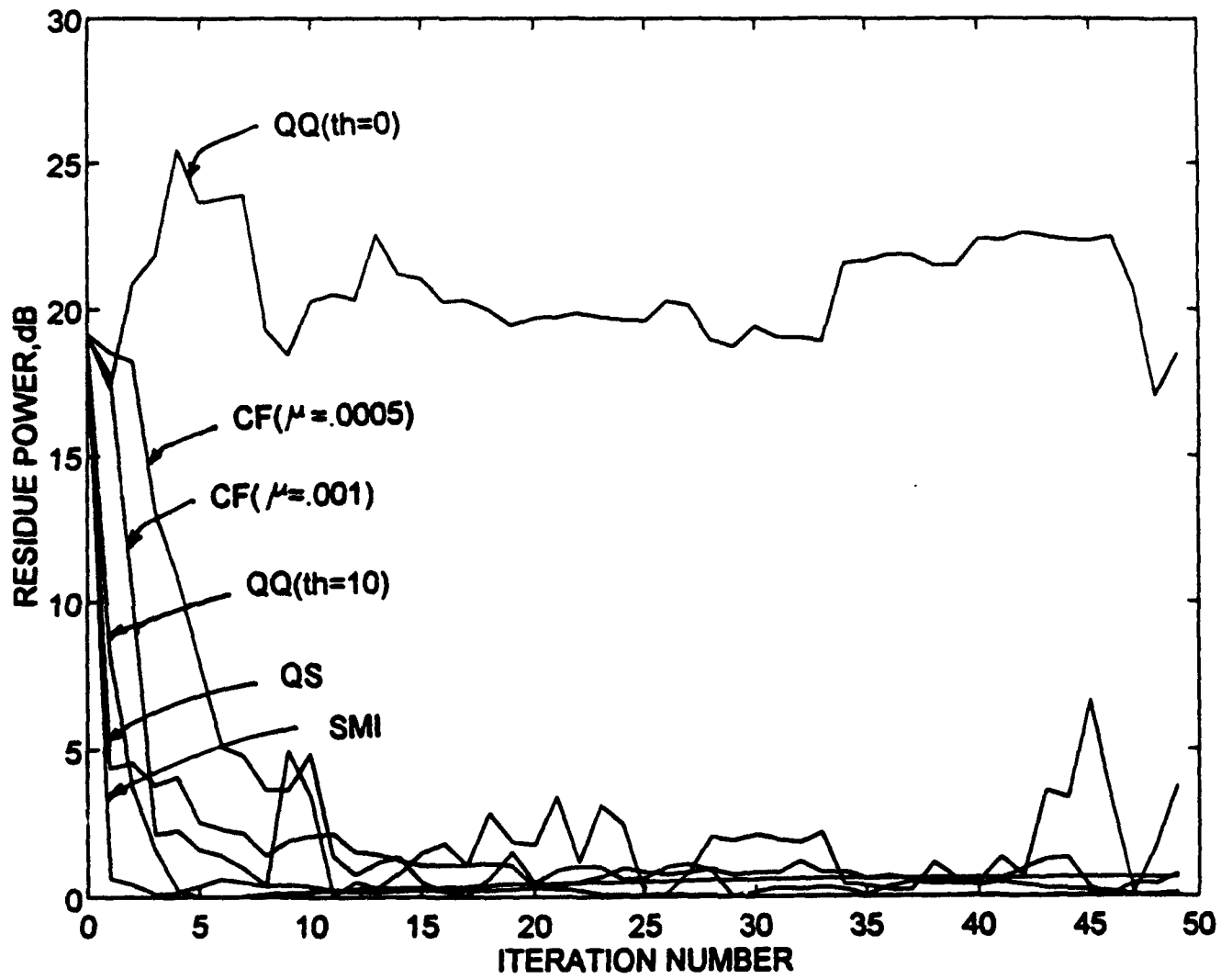
Figure 5. Convergence of various algorithms (single jammer 28 dB above noise)
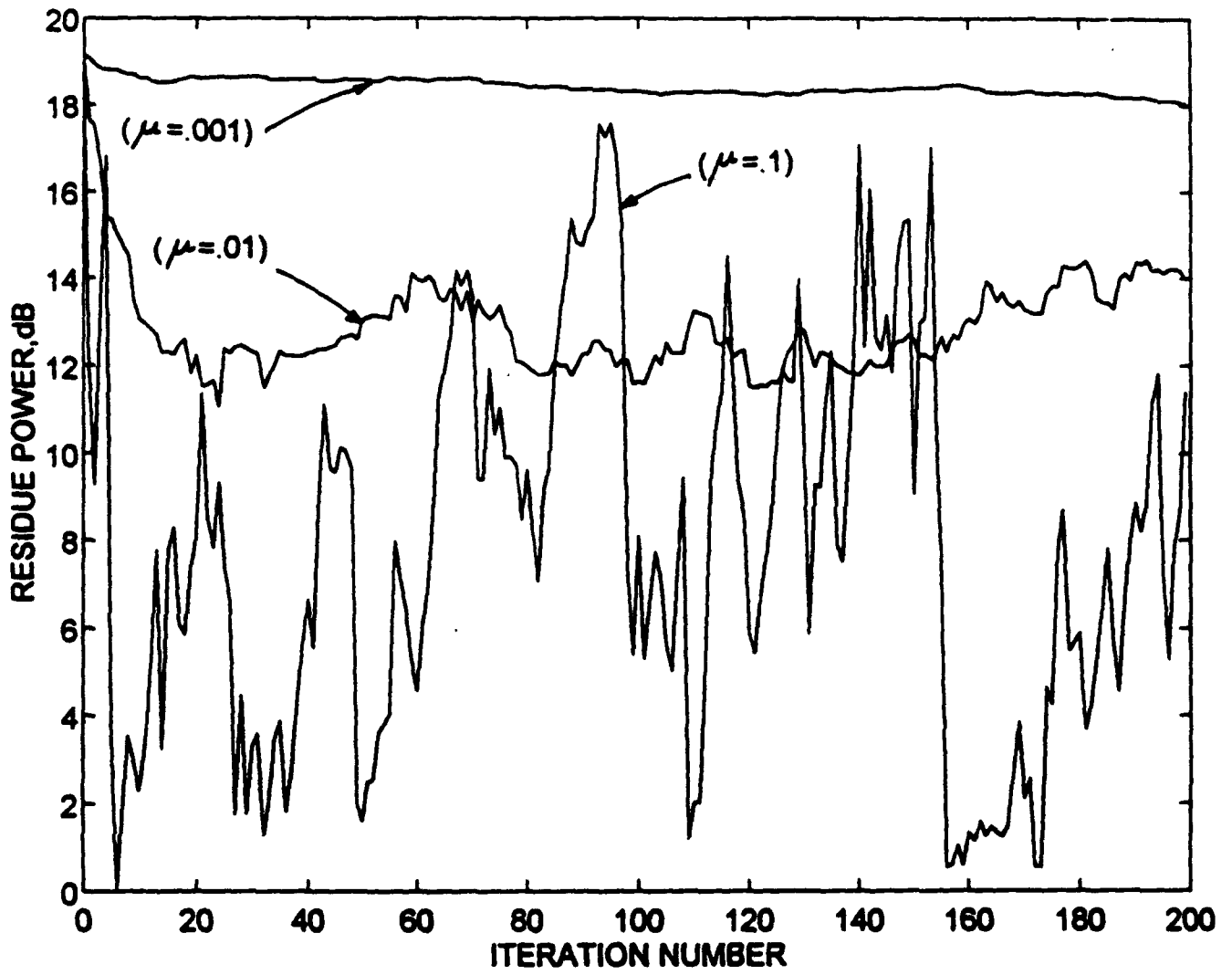
Figure 6. Convergence of conjugate gradient algorithm with projection
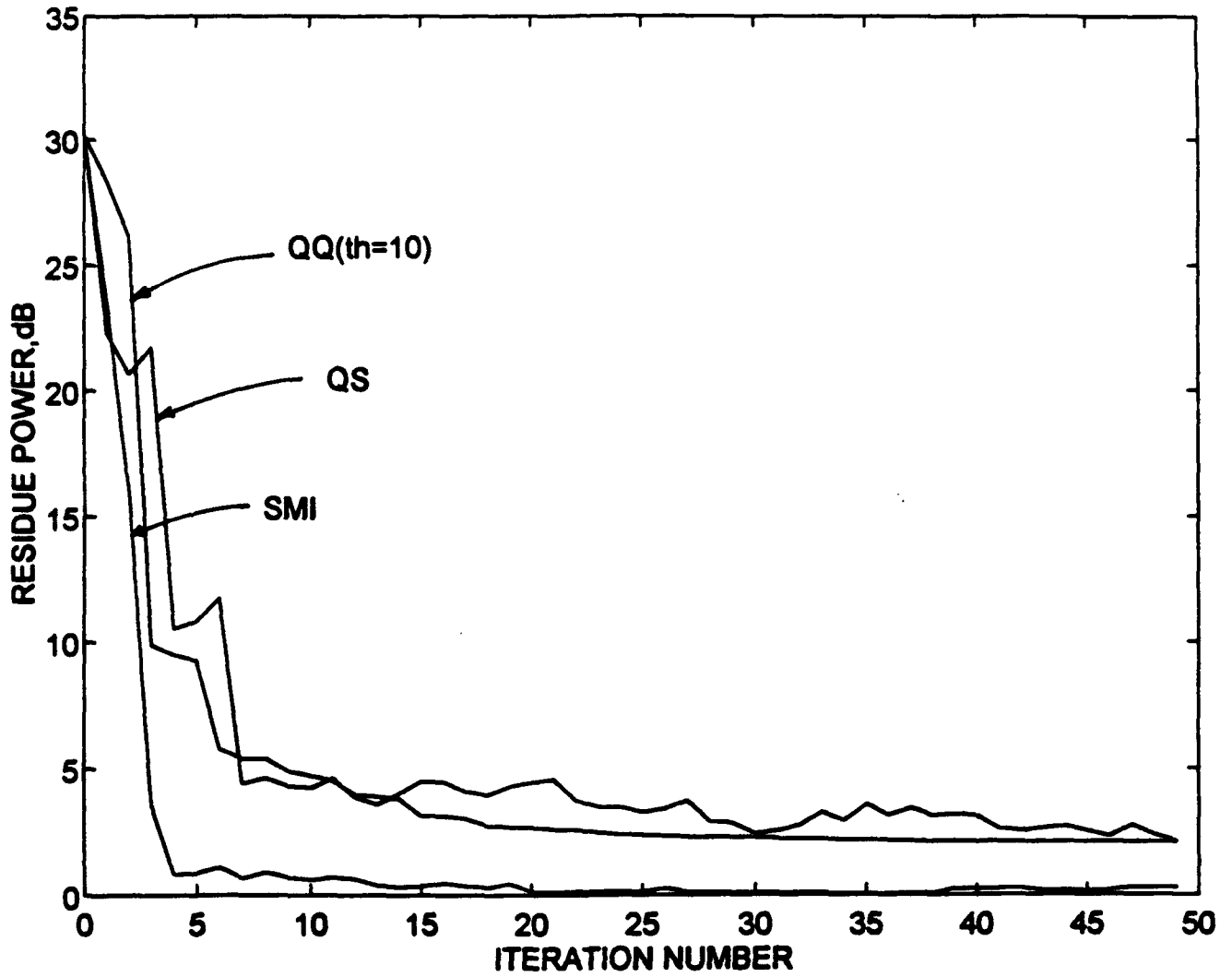
Figure 7. Convergence of various nonrecursive algorithms

(two jammers 28dB and 38dB above noise)
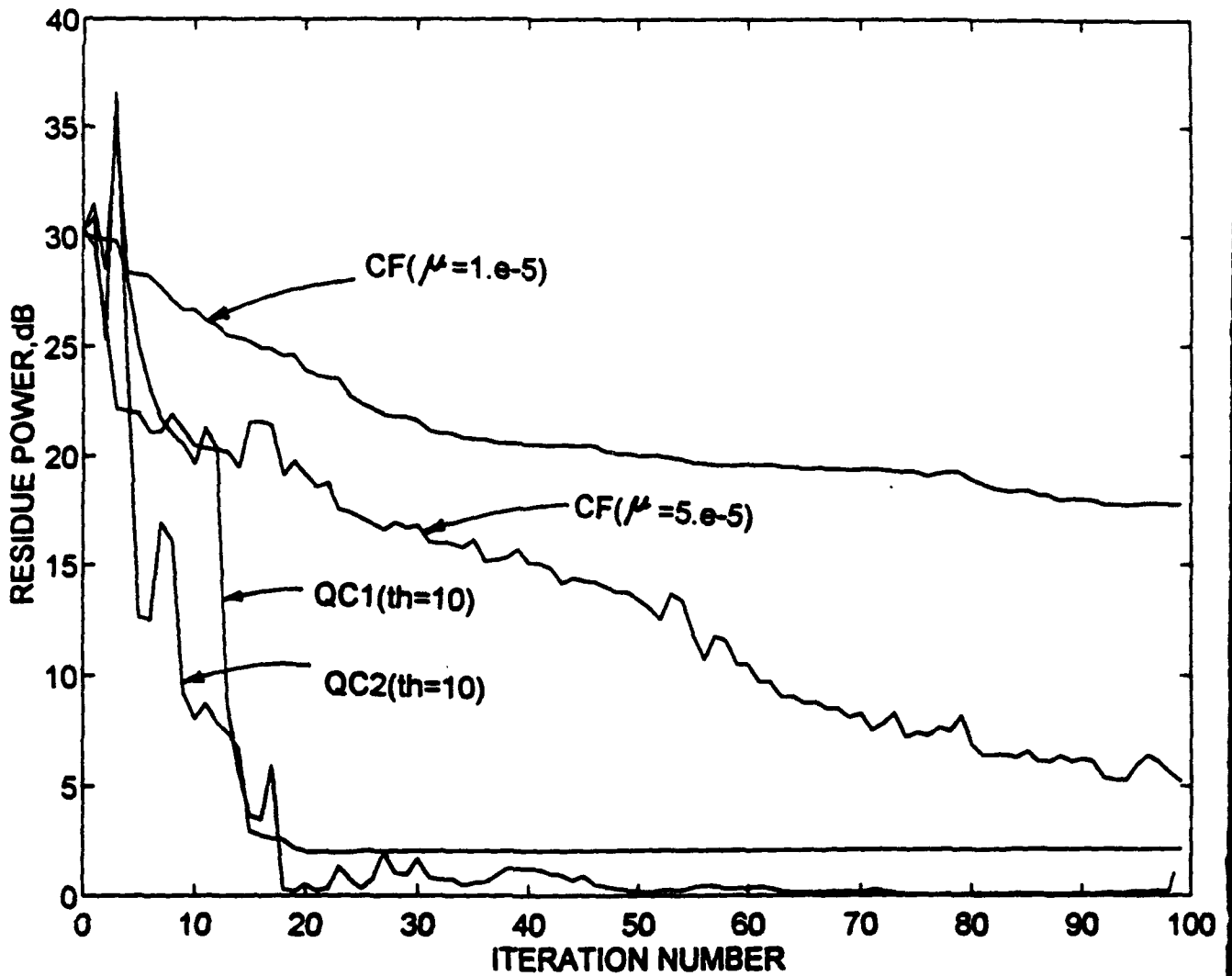
Figure 8. Convergence of various recursive algorithms

(two jammers 28dB and 38dB above noise)
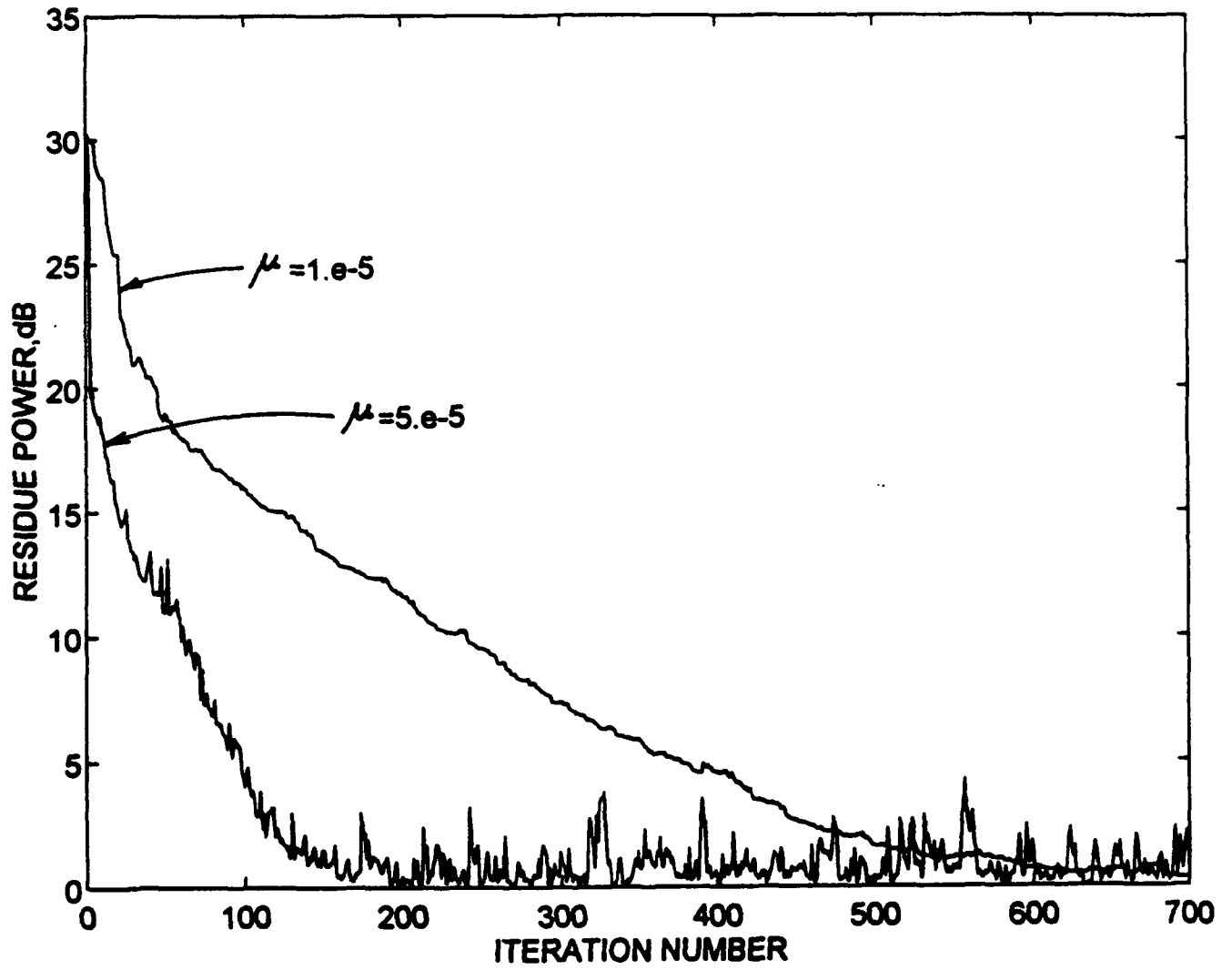
Figure 9. Convergence of correlation feedback algorithm
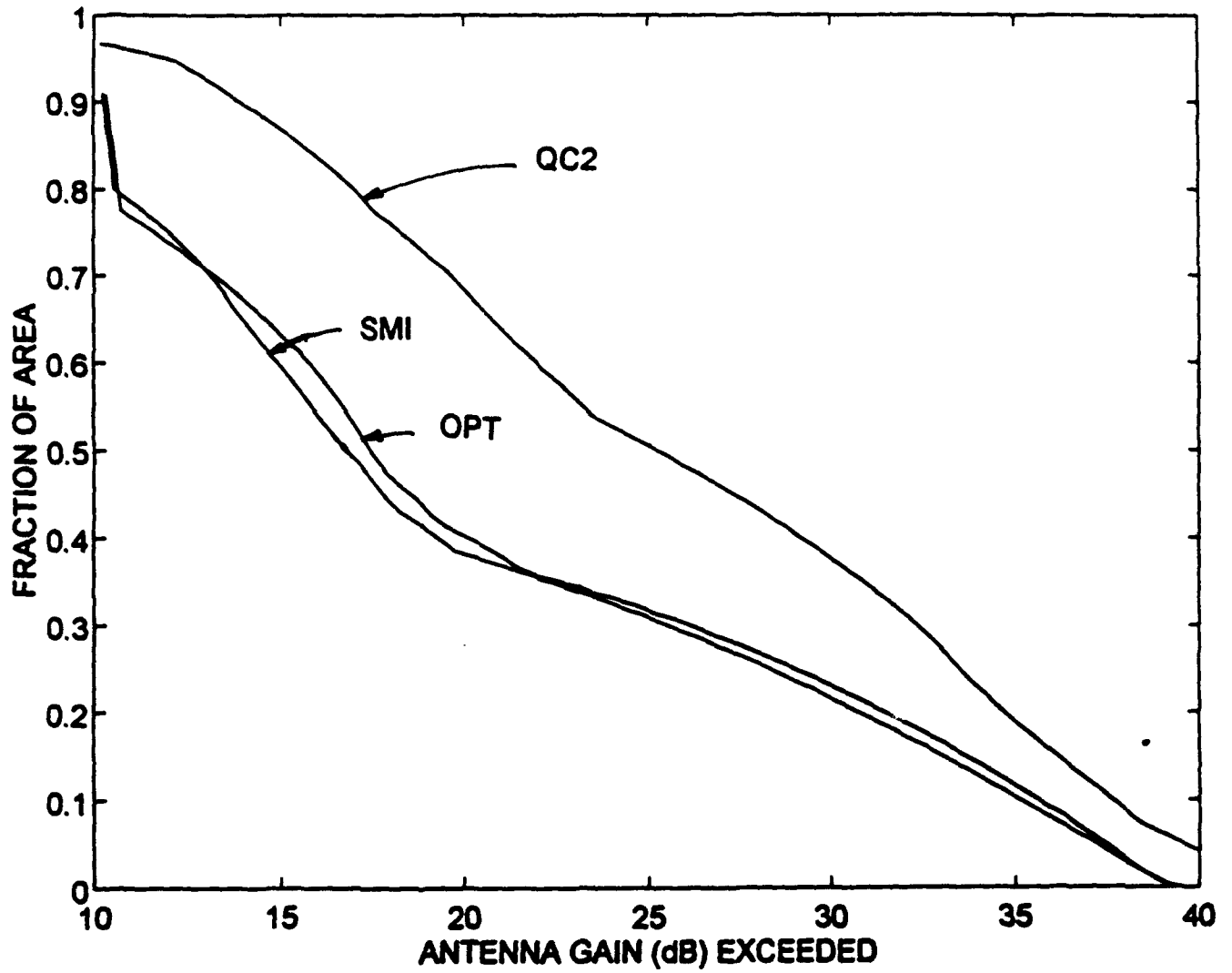
Figure 10. Antenna gain distribution in the region containing jammers
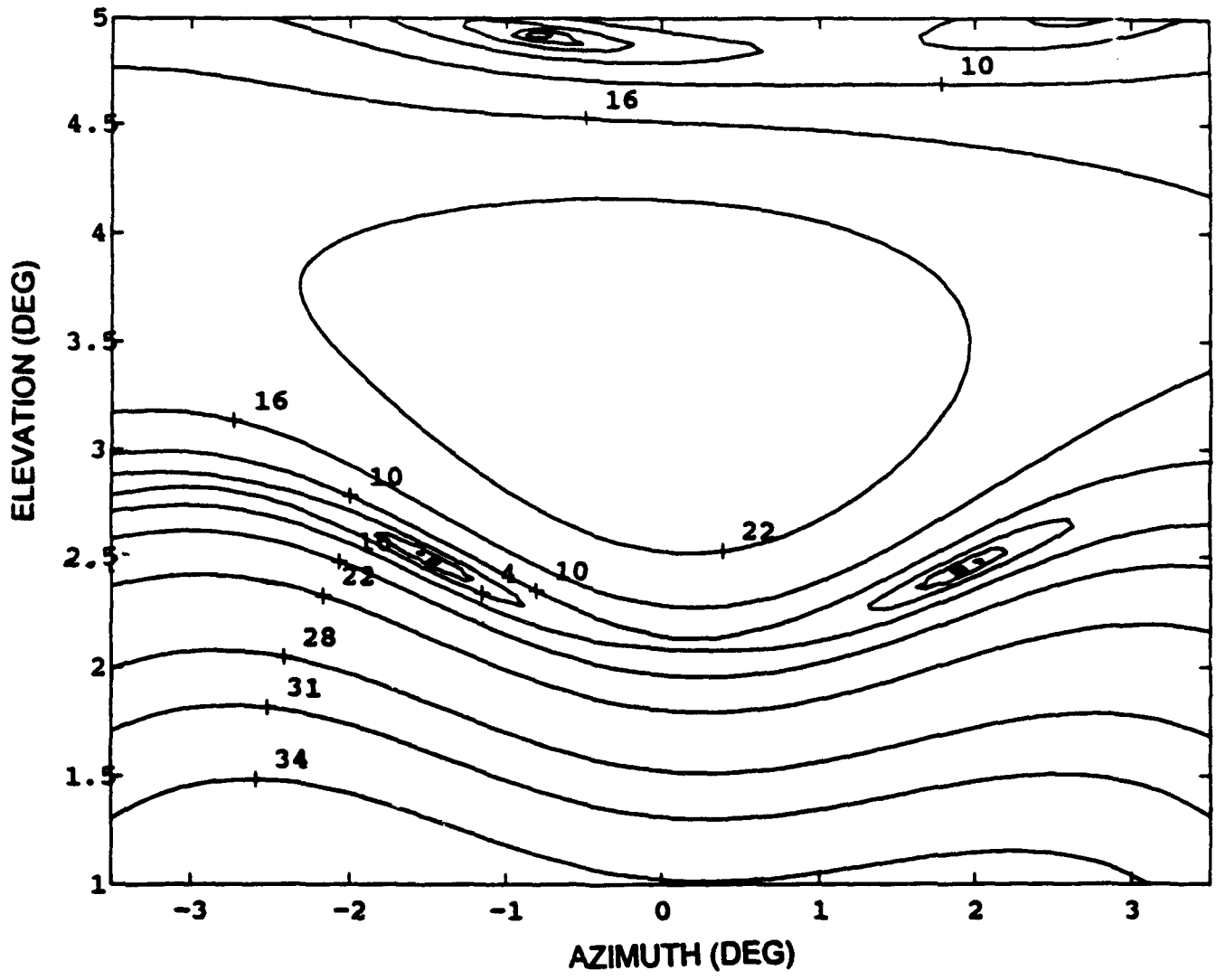
Figure 11. Contour plot of antenna pattern ,SMI algorithm
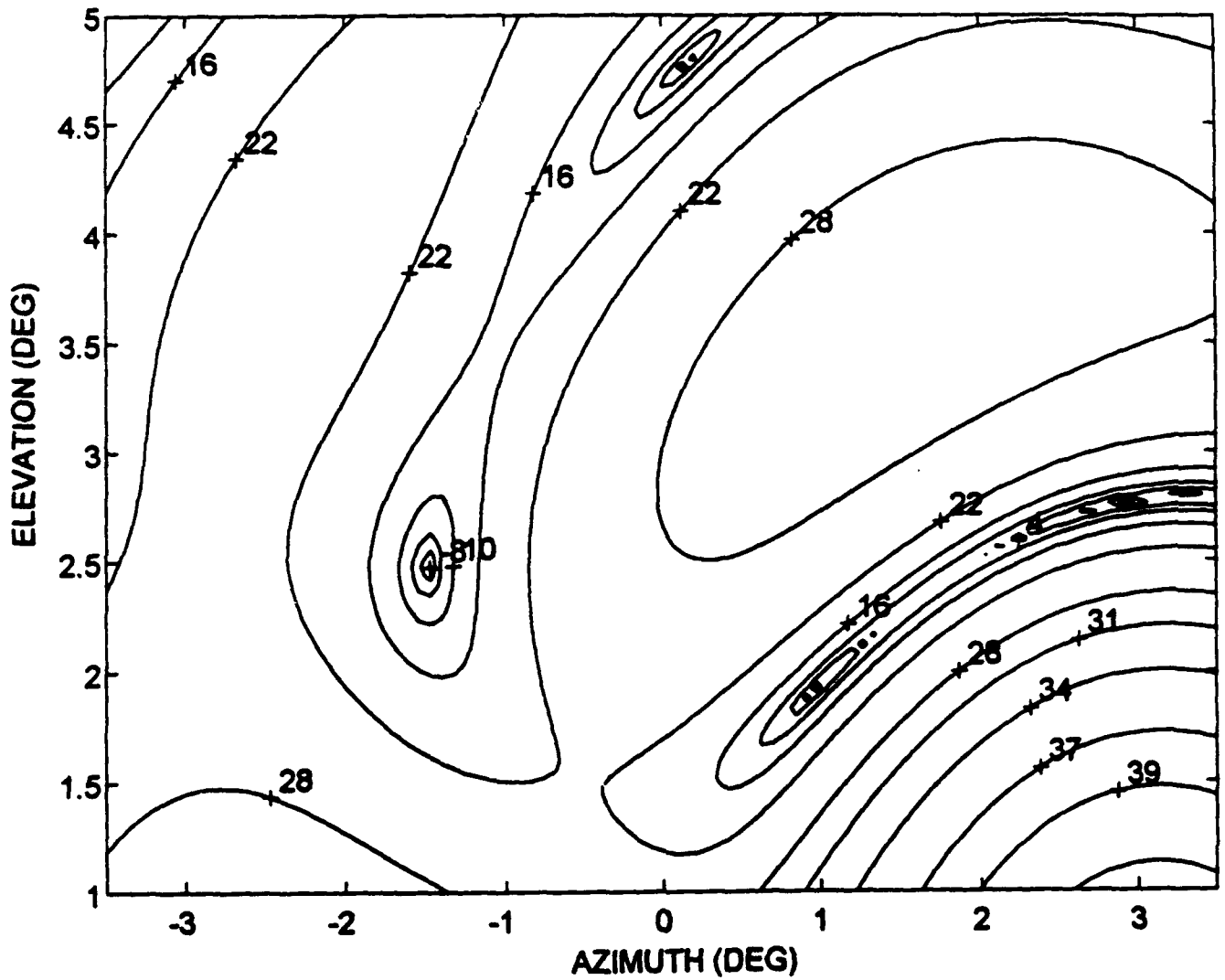
Figure 12. Contour plot of antenna pattern, QC2 algorithm

UPDATING PROBABILISTIC DATABASES

Michael A. Pittarelli

Associate Professor

Department of Computer and Information Science

State University of New York

Institute of Technology at Utica/Rome

P.O. Box 3050

Utica, NY 13504-3050

UPDATING PROBABILISTIC DATABASES

Michael A. Pittarelli
Associate Professor
Department of Computer and Information Science
SUNY Institute of Technology at Utica/Rome

Abstract

A probabilistic database is a generalization of a relational database that replaces the characteristic function of a finite relation with a finite real- or interval-valued probability distribution. In this report, methods are explored for updating real-valued probabilistic databases in response to new information, reassessment by experts of certain probabilities, or in order to smooth a relative frequency distribution based on limited observations. A distinction is made between global updating, which involves selecting a member of the set of joint distributions each member of which has the given database as its projection, updating it appropriately, then projecting; and local updating, in which changes to one distribution are propagated to the others, in order to restore consistency of the database. The appropriateness of Jeffrey's Rule of conditioning for propagating local changes in probability is discussed. Schemes used for updating the probabilities associated with causal, or Bayesian, networks are shown to be applicable to probabilistic databases whose schemes are α-acyclic.

UPDATING PROBABILISTIC DATABASES

Michael A. Pittarelli

I. Introduction and Definitions

Probabilistic data models and their potential for decision support are discussed in [2,6,25,29,30]. In this report, methods for updating probabilistic databases are presented.

Attention will be restricted to the probabilistic model introduced in [6] and elaborated in [30]. Within this model, a probabilistic database instance is a collection of probability distributions over sets of tuples. Formally, let dom(M) denote the finite *domain* of *attribute* M. The set of attributes V_i on which an element p_i of a database $K = \{p_1, \ldots, p_m\}$ is defined is its *scheme*, denoted $s(p_i)$. For a set V of attributes, let $dom(V) = \underset{v \in V}{\times} dom(v)$. Then, for any $p_i \in K$, $p_i : dom(s(p_i)) \rightarrow [0,1]$, where $\sum_t p_t = 1$.

The probabilistic database instance in the tables below might represent uncertainties regarding conditions in Freedonia on a typical August day:

Rain	No_Phones	p_1	No_Phones	Temperature	p_2	Temperature	Late_Trains	p_3
yes	true	3/8	true	high	1/3	high	yes	1/8
yes	false	1/16	true	med	5/36	high	no	3/8
no	true	1/8	true	low	1/36	med	yes	5/18
no	false	7/16	false	high	1/6	med	no	5/36
			false	med	5/18	low	yes	5/72
			false	low	1/18	low	no	1/72

With this model, it would be most natural to maintain separate databases for each month. In the model presented in [2], a single database consisting of individual *probabilistic relations* could be used instead. It is shown in [25] how to translate from either representation to the other. In this report, attention is restricted to the simple model.

Probabilistic data operators and their properties are presented in [30]. We will utilize only three of these: *projection, extension,* and *join.*

Definition Let $A \subseteq s(p)$. Then $\pi_A(p)$ denotes the *projection* of distribution p onto A.

$$\pi_A(p)(x) = \sum_{t \in dom(s(p)),\ t[A]=x} p(t).$$

where, for tuples $w \in dom(W)$ and $b \in dom(B)$, $B \subseteq W$, $w[B]=b$ iff w and b agree on all attributes in scheme B. □

An arbitrary but fixed ordering on the attributes is assumed. To emphasize that a tuple is known to have a particular value, the notation $p(t=x)$ will sometimes be used. The expression $p(t[A])$ will be used to abbreviate $\pi_A(p)(t[A])$, and $p(t[A]|t[B])$ will abbreviate $p(t[A \cup B])/p(t[B])$. Also, where $T \subseteq dom(s(p))$, $p(T)$ will denote $\sum_{t \in T} p(t)$.

Definition A *model* of a scheme V is a set $X = \{V_1, \ldots, V_m\}$ such that $V_j \subseteq V$ and $V_i \not\subseteq V_j$ for

all $i,j\in\{1,...,m\}$. (X will sometimes be referred to as a model of a distribution with scheme V.) □

If X is the set of schemes for the elements of a database K, then the *scheme*, or *structure*, of K is X. Let $s(K)$ denote the structure of K: $s(K) = \{s(p)\,|\,p\in K\}$; and let $dom(s(K)) = dom(\bigcup_{V\in s(K)} V)$. Unless stated otherwise, the structure of a database K will always be taken to be a model, in the above sense, of $\bigcup_{V\in s(K)} V_j$. However, structures that are not models are sometimes useful, for example, when a projection $\pi_A(p_j)$ for some $p_j\in K$ is to be accessed frequently.

A distribution p with scheme V may be projected onto a model $X=\{V_1,\,\ldots,V_m\}$ of V to form a probabilistic database $K = \{p_1,\,\ldots,p_m\}$, where $K = \pi_X(p)=\{\pi_{V_1}(p),...,\pi_{V_m}(p)\}$. A database K formed in this way is guaranteed to exhibit various forms of consistency; e.g., for any p_i and p_j in K, $\pi_A(p_i) = \pi_A(p_j)$, for all $A\subseteq s(p_i)\cap s(p_j)$.

Definition A model X is a *refinement* of model Y (and Y is an *aggregate* or *coarsening* of X), denoted $X\leq Y$, iff for each $V_x\in X$ there exists a $V_y\in Y$ such that $V_x\subseteq V_y$ [5]. □

A database K may be projected onto a refinement X of $s(K)$ in the obvious way to form a database

$$\pi_X(K) = \{\pi_{V_x}(p)\,|\,V_x\in X,\,V_k\in s(K),\,V_x\subseteq V_k,\,p\in K,\,p\in P_{V_k}\}.$$

Definition Let $P_V = \{p\,|\,p:dom(V)\to[0,1],\,\sum_t p(t) = 1\}$. The *extension* of a distribution p with scheme A to the scheme V, $A\subseteq V$, is the set of all preimages p' with scheme V of p under the mapping π_A:

$$E^V(p) = \{p'\in P_V\,|\,\pi_A(p') = p\}.\ \square$$

The extension of a database K is the intersection of the extensions of its elements: $E^V(K) = \cap_{p\in K}E^V(p)$. Thus, $E^V(\pi_X(p))$ is the set of all preimages of the database $\pi_X(p)$ under the mapping π_X; any model X of V partitions P_V into classes $E^V(\pi_X(p))$ equivalent with respect to projections onto X. Any $E^V(p)$ or $E^V(K)$ is a convex polyhedron, the set of solutions to the system of linear equations determined by the projection conditions. (If $s(K)$ is a cover of V, then $E^V(K)$ may be abbreviated $E(K)$.)

Definition The *join*, over a set of variables V, of a database $K = \{p_1,\,\ldots,p_m\}$ is the element $J^V(K)$ of $E^V(K)$ with *maximum entropy*: $J^V(K) = \arg\max_{p\in E^V(K)} -\sum_t p(t)\times\ln(p(t))$. □

(Normally, $s(K)$ is a cover of V. In this case, or when the context makes clear what set of variables is intended, $J^V(K)$ is abbreviated $J(K)$.)

Since $E^V(K)$ is convex, $J^V(K)$ is unique [14]. For a set Q with unique maximum entropy element, let $J(Q)$ denote that element. Determination of $J(Q)$ for arbitrary constraints defining Q is usually a difficult optimization problem. However, this is not the case when the constraints are in the form of a probabilistic database.

Definition The *pairwise join* of two probability distributions is calculated as

$$PJ(p_1,p_2)(t) = p_1(x)\times p_2(y)\Big/ \sum_{z\,|\,z[s(p_1)\cap s(p_2)]=y[s(p_1)\cap s(p_2)]} p_2(z),$$

where $x=t[s(p_1)]$ and $y=t[s(p_2)]$. (The denominator of the above expression equals 1 if $s(p_1)\cap s(p_2) = \varnothing$.) □

Theorem 1 [22] $PJ(p_1,p_2) \in E(\{p_1,p_2\})$ iff $PJ(p_1,p_2) = J(\{p_1,p_2\})$. □

It follows immediately that $p = J(\pi_{\{V_1,V_2\}}(p))$ iff $V_1-(V_1 \cap V_2)$ and $V_2-(V_1 \cap V_2)$ are conditionally independent, given $V_1 \cap V_2$. Note that PJ is not commutative.

When $s(K)$ is α-acyclic [7], $J(K)$ can be calculated as a sequence of applications of pairwise join [30]. $s(K)$ is α-acyclic iff the output Z of the algorithm below (*Graham's algorithm* [7]) is $\{\oslash\}$.

1. $Z := s(K)$
2. Repeat in any order until neither has any effect on the current value of Z:
   a. If v appears in only one element of Z, remove v from that element.
   b. If $V_i \subset V_j$ and $\{V_i,V_j\} \subseteq Z$, then $Z := Z-\{V_i\}$.

If $s(K)$ is not α-acyclic (i.e., is α-cyclic), an iterative proportional fitting algorithm that converges to $J(K)$ must be used instead [5].

II. Updating Databases

In the literature on knowledge bases, a distinction is made between *updating* and *revision* [14,15]. A knowledge base is updated when it is changed in response to a change in the state of affairs it is intended to represent. It is revised when it is altered to represent more faithfully a fixed state of affairs. We will not make this distinction; both types of changes will be referred to here as updates.

In general, an update of a database instance K is any replacement of K with an instance K'. We will consider a variety of types of replacement. For example, $K' = K-\{p\}$ and $K' = K \cup \{p\}$ qualify as updates. Thus, it is not required that $s(K') = s(K)$.

One requirement that will normally be imposed is that the result K' of an update of K be *consistent*, if K itself is. A database K is consistent iff $E(K) \neq \oslash$. A necessary condition for consistency is *local consistency*: K is locally consistent iff for all $p_i, p_j \in K$.

$$\pi_{s(p_i) \cap s(p_j)}(p_i) = \pi_{s(p_i) \cap s(p_j)}(p_j).$$

Local consistency is sufficient for consistency if $s(K)$ is α-acyclic. Consistency corresponds to the existence of a universal instance for a relational database.

Consistent updating consists of two phases (the second of which may be null):

(i) K is replaced by K^{temp}

(ii) K^{temp} is replaced by a consistent K', subject to some additional constraints.

Step (ii) is deliberately vague. For example, suppose $K^{temp} = (K-S) \cup S'$. It might be reasonable to require that

$$K' = \arg \min_{K^* \in C} \sum_{\substack{p^* \in K^*, p \in K^{temp} \\ s(p^*)=s(p), p \notin S}} d(p^*,p).$$

where d is a suitable measure of dissimilarity of probability distributions, and C is the class of consistent K^* such that $s(K^*) = s(K^{temp})$. In other words, the difference between the updated database and the original should be minimized, subject to the constraint that S is replaced by S'.

To illustrate when one might reasonably insist that a $p \in K^{temp}$ be contained in K', consider an update to the database above containing probabilities for conditions on a typical August day in

Freedonia. Suppose that we have become concerned about the likelihood that sharks are present near the shore. and have had an expert assess joint probabilities for temperature and shark activity:

Temperature	Shallow_Sharks	p_i
high	yes	1/8
high	no	3/8
med	yes	1/12
med	no	1/3
low	yes	1/120
low	no	3/40

With $K = \{p_1, p_2, p_3\}$. $K^{temp} = \{p_1, p_2, p_3, p_4\}$. $S = \{p_4\}$ and the minimum distance requirement. $K' = K^{temp}$. since $E(K^{temp}) \neq \emptyset$ and any reasonable distance measure is nonnegative $(d(p,q) \geq 0)$ and nondegenerate $(d(p,q)=0$ iff $p=q)$.

Another type of "wholesale" replacement of a $p \in K$ with $p' \neq p$ occurs in databases of relative frequencies obtained by sampling. A new observation will change all the entries x of an affected distribution p_j to either $\dfrac{Nx}{N+1}$ or $\dfrac{Nx+1}{N+1}$. where N is the number of observations that have already affected p_j. (p_j is affected by observation t if $t[s(p_j)]$ is defined.)

III. Updating Distributions

There are less radical forms of replacement of probability distributions; for example. those arising from constraints of the following types:

(*i*) $t[A]=w$. where $A \subseteq s(p)$

(*ii*) $p(t[A]=w)=x$

(*iii*) $p(t[A]=w | t[B]=u)=x$

Constraint type (*i*) is the special case of (*ii*) in which $x=1$. To illustrate. suppose that we measure the temperature on a typical-seeming August day in Freedonia and find that it is in the high range; where t is the tuple representing this day. we know $t[\text{Temperature}]=\text{high}$. but none of the other components of t. What effect does this information have on p_2? Minimally. p_2 must be changed so that $\pi_{\{Temperature\}}(p'_2)(\text{high})=1$. but there are infinitely many p defined on $s(p_2)$ with this property. With the additional constraint that $p'_2(x | \text{Temperature}=\text{high}) = p_2(x | \text{Temperature}=\text{high})$. p'_2 is uniquely determined and may be calculated by Bayesian conditionalization (which. although it is standard practice. is controversial [1]):

$p'_2(\text{No\_Phones}=\text{true}. \text{Temperature}=\text{high}) = p_2(\text{No\_Phones}=\text{true}. \text{Temperature}=\text{high} \mid \text{Temperature}=\text{high})$

$$= \frac{1/3}{1/3 + 1/6} = 2/3. \text{ etc.}$$

Case (*ii*) when $0<x<1$ is more controversial. If a distribution p has just been replaced with p'. it seems reasonable. *prima facie*. to adopt $\pi_W(p')(w)$. for any $w \in \text{dom}(W)$. $W \subseteq s(p')$. If this policy is followed. it is necessary. after replacing p_2 with p'_2. to replace p_1 with a p'_1 such that

$$p'_1(\text{No\_Phones}=\text{true}) = p'_2(\text{No\_Phones}=\text{true}) = 2/3.$$

Suppose that No_Phones=true means that. at some point during the day. phone service will be

interrupted for at least an hour. and that disruptions in service may be caused by electrical storms. which are likelier on hotter days. Intuitively. then. it is reasonable that our probability for No_Phones=true should increase when we learn that Temperature=high. But the constraint $p'_1(\text{No\_Phones=true})=2/3$ is not sufficient to identify p'_1 uniquely. With only this constraint. values of p'_1 are free to range within the intervals i in the table below.

Adding the information that the probabilities for No_Phones originated in the observation Temperature=high and requiring $p'_1(t) = p(t|\text{Temperature=high})$. for some $p \in E(\{p_1.p_2.p_3\})$ narrows the intervals considerably. to i'.

The stronger constraint $p'_1(\text{Rain=x}|\text{No\_Phones=y}) = p_1(\text{Rain=x}|\text{No\_Phones=y})$. combined with $p'_1(\text{No\_Phones=true})=2/3$ is sufficient to identify p'_1 uniquely. as

$$p'_1(\text{Rain=x.No\_Phones=y}) = p'_1(\text{Rain=x}|\text{No\_Phones=y}) \times p'_1(\text{No\_Phones=y}).$$

Rain	No_Phones	i	i'	p'_1
yes	true	[0.2/3]	[5/12.2/3]	1/2
yes	false	[0.1/3]	[0.1/8]	1/24
no	true	[0.2/3]	[0.1/4]	1/6
no	false	[0.1/3]	[5/24.1/3]	7/24

Updating p_1 to p'_1 in this way is known as *Jeffrey conditionalization* [13]. According to what is referred to as *Jeffrey's Rule* for updating probability. if conditional probabilities $p(A|B_i)$ are unaffected by a change in probabilities for the elements of a partition $\{B_1. \ldots . B_n\}$ of the space on which p is defined. then. in light of these changes. the probability of event A should be updated to

$$p'(A) = \sum_i p'(A|B_i) \times p'(B_i) = \sum_i p(A|B_i) \times p'(B_i).$$

The properties of Jeffrey conditionalization have been studied by a number of authors: the following theorem is a special case of results discussed presented in [19.20.23.35].

Theorem 2 Let p' denote the Jeffrey update of p on the basis of a shift in marginal probabilities from $\pi_A(p)$ to $\pi_A(p)'$. for $A \subseteq s(p)$: $p'(t) = p(t[s(p)-A]|t[A]) \times \pi_A(p)'(t[A])$.

Let $C = E^{s(p)}(\pi_A(p)')$. Let d denote directed divergence (relative entropy. relative information):

$$d(q.p) = \sum_t q(t) \times \log(q(t)/p(t)).$$

Then $p' = \arg\min_{p^* \in C} d(p^*.p)$. □

Of course. Jeffrey conditionalization of a distribution p needn't take place in response to an update to a $q \neq p$. Suppose that we think we have just felt a drop of rain and that Rain=yes means the day's official rainfall total. measured at Freedonia International Airport. is at least 1/8″. We may wish to revise our probability of rain from $\pi_{Rain}(p_1)(\text{yes}) = 7/16$ to $\pi_{Rain}(p_1)'(\text{yes}) = 9/10$. in which case. by Jeffrey's Rule.

$$p''_1(\text{Rain=yes.No\_Phones=true}) = \frac{3/8}{3/8+1/16} \times \frac{9}{10} = \frac{9}{35}. \text{ etc.}$$

To illustrate case (*iii*). suppose that the railroad has replaced all locomotive engines with new ones that are less likely to break down on hot days. Suppose the new *conditional* probabilities $p(\text{Late\_Trains=x}|\text{Temperature=y})$ are:

	yes	no
high	1/2	1/2
med	2/3	1/3
low	5/6	1/6

Since we have no information on the effect of the new trains on Temperature, it seems reasonable to maintain, on grounds of "insufficient reason" to do otherwise. $\pi_{\{Temperature\}}(p'_3) = \pi_{\{Temperature\}}(p_3)$. With this constraint, p'_3 is uniquely determined, as:

Temperature	Late_Trains	p'_3
high	yes	1/4
high	no	1/4
med	yes	5/18
med	no	5/36
low	yes	5/72
low	no	1/72

This is a distance-minimizing update as well, although it is not a Jeffrey update. Van Frassen [33,34] discusses problems with and alternatives to minimum-distance updating. One alternative, applicable in case (iii), is to reduce (and only reduce) joint probability values so they are consistent with the new conditional values, and then normalize them. Van Frassen found that this update rule significantly outperformed minimum (relative information) distance updating and a third method on a test, using simulated data, of the rate at which convergence to an "objectively correct" probability distribution is achieved. Applied to the example, it yields:

Temperature	Late_Trains	p''_3
high	yes	7/32
high	no	7/32
med	yes	5/16
med	no	5/32
low	yes	5/64
low	no	1/64

Notice that $\pi_{\{Temperature\}}(p''_3) \neq \pi_{\{Temperature\}}(p_3)$. Although it is more conservative to assume equality, it may be, for all we know, that the new trains are more efficient and thus generate less heat. Furthermore, *requiring* that marginal probabilities remain unaffected (in this case, that $p(Temperature=high)$ remain 1/2) is incompatible with a policy of updating via standard Bayesian conditionalization whenever it is applicable. (See [33], p. 379.) Suppose that hyper-reliable diesel locomotives that thrive on heat have been acquired and that $p(Late\_Trains=yes|Temperature=high) = 1$. Then $p(Late\_Trains=no|Temperature=high) = 0$, which implies $p(dom(s(p_3)) - \{<high,no>\}) = 1$. Bayesian conditionalization produces the distribution p'''_3, and $\pi_{\{Temperature\}}(p'''_3) \neq \pi_{\{Temperature\}}(p_3)$:

Temperature	Late_Trains	p'''_3
high	yes	9/45
high	no	0
med	yes	20/45
med	no	10/45
low	yes	5/45
low	no	1/45

Much of this controversy can be avoided if we work with only the constraints we do accept. There is widespread agreement that the only reason to be interested in probabilities (as *degrees of belief* versus, e.g., relative intensities in image processing) is to use them to make decisions. A strict Bayesian will want to choose an action that maximizes expected utility relative to a single, known, real-valued probability distribution over the events relevant to the decision. However, there are methods that can be applied to decision making when beliefs are represented by intervals or sets of real-valued probability distributions that reduce to expected utility maximization as a special case [17,28].

Suppose we are trying to decide if we should bicycle to the Freedonia lighthouse this evening. If rain develops we will want to call home for a ride. Also, whether we go or not, we need to contact the neighborhood bookie, by phone or in person, between 6:00 and 7:00 p.m. Utilities for the two actions and immediately relevant states are:

Rain	No_Phones	Go	Don't
yes	true	0	0.8
yes	false	0.2	0.6
no	true	0.1	0.2
no	false	1.0	0.1

We are certain that the temperature is high and we have access to database $K = \{p_1, p_2, p_3\}$. Relative to distribution p'_1, above, "Don't" has higher expected utility: 39/80 versus 19/60. But p'_1 was calculated under an assumption one might wish to reject, viz., that knowledge of Temperature does not affect the conditional probabilities for Rain, given knowledge of No_Phones.

The assumption is unnecessary. For an interval distribution i,

$$R(i) = \{p \in P_{s(i)} | p(t) \in i(t), \text{ for all } t \in dom(s(i))\}.$$

R(i) is the set of solutions of a system of linear inequalities. It can be determined via linear programming whether or not there exists a $p \in R(i)$ relative to which an action a maximizes expected utility (in which case a is said to be E-admissible [21], or a Bayes action).

For the bicycling decision problem, relative to R(i'), "Don't" is a Bayes action and "Go" is not. Two linear programs suffice to determine that "Don't" maximizes expected utility for *all* $p \in R(i')$, including p'_1, which it is therefore unnecessary to calculate.

IV. Restoring Consistency

We now address in greater detail the problem of restoring consistency to a database when one or more of its elements is updated. Recall that the general form of a database update is

$$K \rightarrow K^{temp} \rightarrow K'.$$

Suppose that

$$K^{temp} = (K-S) \cup S'.$$

In our running example, $K = \{p_1, p_2, p_3\}$. Temperature is observed to have the value "high", and p_2 and p_3 are updated via Bayesian conditionalization:

No_Phones	Temperature	p'_2	Temperature	Late_Trains	p'_3
true	high	2/3	high	yes	1/4
true	med	0	high	no	3/4
true	low	0	med	yes	0
false	high	1/3	med	no	0
false	med	0	low	yes	0
false	low	0	low	no	0

$K^{temp} = (K - \{p^2.p^3\}) \cup \{p'_2.p'_3\}$. K^{temp} is inconsistent. $s(K^{temp})$ is α-acyclic, as can be determined by application of Graham's algorithm. Since $s(K^{temp})$ is α-acyclic, it can be made consistent by eliminating all local inconsistencies. There is only one local inconsistency: $\pi_{\{No\_Phones\}}(p_1) \neq \pi_{\{No\_Phones\}}(p'_2)$. Because the update originated in the measurement of a variable in $s(p'_2)$, it seems rational to leave p'_2 fixed and replace p_1 with a p'_1 that is consistent with p'_2. As discussed above, there are infinitely many $p \in E^{s(p_1)}$ such that $\pi_{\{No\_Phones\}}(p) = \pi_{\{No\_Phones\}}(p'_2)$.

Recall that Jeffrey conditionalization on the updated probabilities $\pi_{\{No\_Phones\}}(p'_2)$, which requires the assumption $p'_1(Rain=x|No\_Phones=y) = p_1(Rain=x|No\_Phones=y)$, identifies p'_1 uniquely. Let us define the distribution resulting from Jeffrey conditionalization of q in response to an update of p to p' as follows:

Definition Let $x = t[s(q) - (s(q) \cap s(p'))]$ and $y = t[(s(q) \cap s(p')]$. Then $JC(p'.q) \in P_{s(q)}$ is defined as
$$JC(p'.q)(t) = q(x|y) \times p(y). \ \square$$

In our example, $p'_1 = JC(p'_2.p_1)$, and the database $\{p'_1.p'_2.p'_3\}$ is consistent.

It follows from Theorem 2 that:

Corollary 3 Let $C = E^{s(q)}(\pi_{s(p') \cap s(q)}(p'))$. Then, where d is directed divergence,
$$JC(p'.q) = \arg \min_{q^* \in C} d(q^*.q). \ \square$$

It follows from the definitions of Jeffrey conditionalization and pairwise join that

Theorem 4 $JC(p'.q) = \pi_{s(q)}(PJ(p'.q)). \ \square$

Corollary 5 $s(p') \cap s(q) = \emptyset$ implies $JC(p'.q>) = q. \ \square$

Notice that the Jeffrey update of q by p', the projection onto $s(q)$ of the join of q and p', is analogous to the *semijoin* of one relation by another. The semijoin of a relation r_2 by a relation r_1 is $SJ(r_1.r_2) = \pi_{s(r_2)}(r_1 * r_2)$, where '$\pi$' denotes relational projection and '$*$' denotes natural join [32].

A mapping from a probability distribution to a relation with the same scheme that possesses a number of desirable properties [6,30] is: $t_{pr}(p)(t) = ceil(p(t))$. Let $R_{s(r)}$ denote the set of all non-empty relations over $dom(s(r))$: $R_{s(r)} = 2^{dom(s(r))} - \{\emptyset\}$. It follows from results in [6] that t_{pr} is a homomorphism from $(P_{s(p)} \times P_{s(q)}, P_{s(q)}, JC)$ to $(R_{s(p)} \times R_{s(q)}, R_{s(q)}, SJ)$.

Theorem 6 $t_{pr}(JC(p.q)) = SJ(t_{pr}(p).t_{pr}(q)). \ \square$

Additional forms of replacement may be identified. It is common practice [3] *to adjust* a relative frequency distribution p by replacing it with $p' = J(\pi_X(p))$, where X is a suitable model of $s(p)$. The *primary motivation for such adjustment is the elimination of sampling zeros* (relative frequency values of zero that are due merely to the ratio between sample size and $|dom(s(p))|)$. However, experimental studies [16,27] have shown that, for suitable X, $J(\pi_X(p))$ tends to be closer than the

relative frequency distribution p is to the probability distribution generating the observations from which p is estimated. Identifying an optimal model X is difficult, and involves a tradeoff between the *smoothing* achieved by increasing the refinement of the model and the *loss of information* incurred in doing so; if $X \leq Y$, then, where d is relative information and $u_{s(p)}$ is the uniform distribution over $dom(s(p))$:

Theorem 7 $d(J(\pi_X(p)).u_{s(p)}) \leq d(J(\pi_Y(p)).u_{s(p)})$. $\square$

Theorem 8 $d(p.J(\pi_X(p))) \geq d(p.J(\pi_Y(p)))$. $\square$

An additional consideration, when a relative frequency distribution p to be adjusted is an element of a probabilistic database K, is the additional effort required to resolve inconsistencies in $K^{temp} = (K-\{p\}) \cup \{J(\pi_X(p))\}$. Ways of minimizing this effort are suggested by the following results.

Lemma 9 $A \subseteq B$ implies $\pi_A(\pi_B(p)) = \pi_A(p)$. $\square$

Theorem 10 Let $p' = J(\pi_X(p))$. For all $W \in X$ and $V \subseteq W$, $\pi_V(p') = \pi_V(p)$.

Proof: By the definition of join, $p' \in E(\pi_X(p))$. Then, by the definition of extension, $\pi_X(p') = \pi_X(p)$. By the definition of projection onto a structure, $\pi_W(p') = \pi_W(p)$, for all $W \in X$. If $V \subseteq W$, $\pi_V(\pi_W(p')) = \pi_V(\pi_W(p))$. By Lemma 9, $\pi_V(p') = \pi_V(p)$. $\square$

Let $Y = \{s(p) \cap s(q) | q \in K, q \neq p\}$. It follows from Theorem 10 that if K is consistent and s(K) is α-acyclic, K^{temp} is guaranteed to be consistent if X is a coarsening of the reduction of Y [7], i.e., of $Y - \{V | V \in Y, V' \in Y, V \subset V'\}$. For example, with $K = \{q_1, q_2, q_3\}$, $s(q_1) = \{w, x, y, z\}$, $s(q_2) = \{x, y, u\}$, and $s(q_3) = \{y, v\}$, where q_1 is to be adjusted, if the search is restricted to $\{\{x, y\}\} \leq X \leq \{\{w, x, y, z\}\}$, then $(K - \{q_1\}) \cup \{J(\pi_X(q_1))\}$ will be consistent. Even with this restriction, there remain eight models (other than $\{w, x, y, z\}$, which will yield $q'_1 = q_1$) to choose from.

This form of adjustment is applicable only to p such that $|s(p)| > 1$. For such p, let
$$X = \{W | W \subset s(p), |W| = |s(p)| - 1\}.$$
Then, if K is consistent and s(K) is a model and is α-acyclic, it follows from Theorem 10 that
$$(K - \{p\}) \cup \{J(\pi_X(p))\}$$
is consistent.

This adjustment can be performed in parallel on any number of database elements. From the table below, each of the four databases $\{p_5, p_6\}$, $\{p'_5, p_6\}$, $\{p_5, p'_6\}$, and $\{p'_5, p'_6\}$ is consistent, since the projections onto $\{v_2\}$ of the four distributions are the same.

v_1	v_2	p_5	$p'_5 = J(\pi_{\{\{v_1\},\{v_2\}\}}(p_5))$	v_2	v_3	p_6	$p'_6 = J(\pi_{\{\{v_2\},\{v_3\}\}}(p_6))$
0	0	1/4	3/16	0	0	1/8	3/32
0	1	1/2	9/16	0	1	1/8	5/32
1	0	0	1/16	1	0	1/4	9/32
1	1	1/4	3/16	1	1	1/2	15/32

So, some degree of smoothing can always be achieved, without the need to form scheme intersections and search a (sub)lattice of models. Note, though, that when $|s(p)| > 2$, X as defined above is α-cyclic and iterative proportional fitting is required to calculate $J(\pi_X(p))$.

Not all smoothing procedures in use preserve projections in this way. *Convex smoothing*

replaces p with $\lambda p + (1-\lambda)u_{s(p)}$, where $\lambda \in [0, 1]$. The value of λ may be selected to minimize the expected squared-error distance from the underlying unknown distribution generating the observed frequencies [9]. There is a strong analogy between selecting a $\lambda \in [0, 1]$ and selecting a model $\{\varnothing\} \leq X \leq \{s(p)\}$: when $\lambda = 0$ and $X = \{\varnothing\}$, or when $\lambda = 1$ and $X = \{s(p)\}$, $\lambda p + (1-\lambda)u_{s(p)} = J(\pi_X(p))$; also, corresponding to Theorem 7,

$$\lambda' \leq \lambda \text{ implies } d((\lambda'p + (1-\lambda')u_{s(p)}), u_{s(p)}) \leq d((\lambda p + (1-\lambda)u_{s(p)}), u_{s(p)}).$$

But unlike model-fitting, convex smoothing is not guaranteed to preserve projections even onto single variables. Suppose $p''_5 = 1/2 \times p_5 + 1/2 \times u_{s(p_5)}$, from the table above. Then

$$\pi_{\{v_1\}}(p''_5)(0) = 3/8 \neq 1/4 = \pi_{\{v_2\}}(p_5)(0).$$

Instead of replacing p by $J(\pi_X(p))$, for some X, p may be replaced by the set $\pi_X(p)$ itself. There are two scenarios in which this might be reasonable.

First, it may be determined that p is *reconstructable from* [5] (resp., approximately reconstructable from) X: $p = J(\pi_X(p))$ (resp., $d(p, J(\pi_X(p))) \leq \epsilon$). It is possible to achieve significant data compression by such replacement. Suppose that $X = \{v | v \in s(p)\}$, $|s(p)| = n$, and $|dom(v)| = k$ for all $v \in s(p)$. Then $k^n - 1$ numbers are required to represent p, versus $n(k-1)$ for $\pi_X(p)$.

Second, one may decide that one has insufficient confidence in the assessment or estimation of some $p \in K$. If p is a relative frequency distribution based on N observations, $N/|dom(V)|$ will be larger than $N/|dom(s(p))|$ for each $V \in X \leq \{s(p)\}$. The estimates $\pi_V(p)$ will be more reliable than the estimate p. Or, an expert may have been called upon to assess probabilities over s(p); actions taken based on this assessment turn out badly; when pressed on the matter, the expert admits that she is knowledgeable regarding only the events in certain sets dom(V), where $V \subset s(p)$.

It follows from Theorem 11 below that in each of these cases, if K is consistent then so is $(K - \{p\}) \cup \pi_X(p)$, regardless of the cyclicity of s(K), since, if X is a model of s(p), $(s(K) - \{s(p)\}) \cup X \leq s(K)$.

Theorem 11 [6] $X \leq Y$ implies $E(\pi_Y(p)) \subseteq E(\pi_X(p))$. $\square$

Conversely, $K^* \subseteq K$ may be replaced with $J(K^*)$. One may wish to estimate probabilities for events in dom(V^*), where there is no $V \in s(K)$ such that $V^* \subseteq V$, but $V^* \subseteq \bigcup_{V \in s(K^*)} V$. Since $\pi_{s(K^*)}(J(K^*)) = K^*$, no information is lost by replacing K with $(K - K^*) \cup \{J(K^*)\}$. But for purposes of decision making, there is no need to construct such an estimate unless one is a strict Bayesian [17,28]. Also, unless s(K) is β-acyclic (each submodel of K is α-acyclic [7]), consistency of K does not guarantee consistency of $(K - K^*) \cup \{J(K^*)\}$.

V. Propagating Changes in Probability

We now turn to the problem of updating an entire database K *following receipt of information in one of the forms (i), (ii), or (iii) discussed in Section III.*

How we should proceed seems to depend on our attitude toward K. In the literature on the management of uncertainty, the predominant view is that a single joint probability distribution over dom(s(K)) would be obtained, stored, and updated as appropriate, if it were possible to do so [11,18,24]. There are at least two reasons why it may not be possible.

First. as discussed above. maintaining a joint distribution p will require the determination and storage of exponentially more numbers than a collection $\pi_X(p)$ of marginal distributions. if X is sufficiently refined.

Second. there are many situations in which probabilities can or should be assessed only over subsets of the set of variables over which one would like to have a joint distribution. To illustrate, imagine a study in which probabilities of occupation of the elements of a 3-dimensional grid are to be estimated for an object that can detect other objects only in the $\{X, Y\}$ plane. Therefore. in order not to disrupt the object's usual pattern of movement. frequencies are observed and recorded for the $\{Y, Z\}$ and $\{X, Z\}$ planes only. In general. there will be infinitely many distributions over $\{X,Y,Z\}$ having the estimated distributions as marginals: if no additional information is available (e.g.. location along the X coordinate is probabilistically independent of location along Y. given the location along Z) then it seems that there is no good reason to single out any one of them.

Now. let us distinguish between *local* and *global* database updates. In both cases. the entire database K is updated to K'. But in a *local* update. changes are made to one or more elements of K and these changes are propagated to the other elements. In a global update. some element p of E(K) is selected and updated appropriately to p': K is then updated as $K' = \pi_{s(K)}(p')$.

A global update is always computable. if K is consistent. regardless of the cyclicity of s(K). as follows:

1. Form J(K)

2. Update J(K) to J(K)'

3. Form $K' = \pi_{s(K)}(J(K)')$.

But the reasons that would lead one to maintain a database K of distributions. versus a single distribution whose projection onto s(K) equals K. are reasons for rejecting this global update scheme: computation of J(K). and thus $\pi_{s(K)}(J(K)')$. may be infeasible: K may have the structure s(K) merely because of constraints limiting the sets of attributes over which it is possible to obtain joint probabilities: and the dependency relations from which it may be deduced that the actual distribution over dom(s(K)) is J(K) are either not assumed to hold or are explicitly rejected.

Local updating schemes are discussed in the literature on *causal, or Bayesian, networks* [11.18.24]. These networks are directed acyclic graphs each node of which represents a single variable. and whose arcs represent dependency relations between variables. Associated with each variable v is a matrix containing probabilities

$$p(v=x|t[V]=w)$$

for each x∈dom(v) and w∈dom(V). where V is the set of variables from which there is an arc to v. In combination with the dependency information encoded in the arcs. these matrices determine a single joint distribution over all the variables in the network. Despite this. the schemes in use for updating networks are strictly local.

An early algorithm applicable to databases whose schemes do not reduce to graphs is presented by Lemmer [20]. Although the algorithm has the advantage that it does not need to utilize assumptions of probabilistic independence. the *r-graph* of the database must be a forest. The r-graph of

$K = \{p_1, \ldots, p_n\}$ is an undirected graph with node set $\{s(p_1)\ldots s(p_n)\}$ and edge set

$$\{<V_i, V_j> | V_i \cap V_j \neq \varnothing: [V_k \cap V_i \neq \varnothing, V_k \cap V_j \neq \varnothing, V_i \cap V_j \subseteq V_k] \rightarrow V_k \notin s(K)\}.$$

where V_i, V_j, and V_k are distinct sets of variables. of $s(K)$. To update K in response to an update of $p \in K$ to p':

1. If $s(p')$ is not the root of the tree containing it, then mark $s(p')$ as updated and update its parent, i.e., the distribution q associated with its parent $s(q)$ as $q' = JC(p',q)$, and mark $s(q')$ as updated. Continue until the root is updated.

2. Update each unmarked child c of root r' as $c' = JC(r',c)$, and mark $s(c')$.
   Repeat, recursively, for the subtree rooted at $s(c')$, for each updated child c'.

The resulting database is consistent, if K is consistent.

Although developed for multiply-connected causal networks (where more than one path exists between at least one pair of nodes), there exist local propagation methods applicable to databases whose r-graphs are not forests, but whose schemes are α-acyclic. These are discussed in detail in [18].

For databases whose schemes are not α-acyclic, local updating seems to be out of the question. Consider the consistent, but α-cyclic, database

v_1	v_2	p_9	v_2	v_3	p_{10}	v_1	v_3	p_{11}
0	0	3/8	0	0	3/8	0	0	1/8
0	1	0	0	1	3/8	0	1	1/4
1	0	3/8	1	0	1/8	1	0	3/8
1	1	1/4	1	1	1/8	1	1	1/4

Suppose the information $v_1=1$ is received. Distributions p_9 and p_{11} are updated independently by Bayesian conditionalization:

v_1	v_2	p'_9	v_1	v_3	p'_{11}
0	0	0	0	0	0
0	1	0	0	1	0
1	0	3/5	1	0	3/5
1	1	2/5	1	1	2/5

Depending on whether the (Jeffrey) update of p_{10} is by p'_9 or by p'_{11}, a different result is obtained:

v_2	v_3	$JC(p'_9,p_{10})$	$JC(p'_{11},p_{10})$
0	0	3/10	9/20
0	1	3/10	3/10
1	0	2/10	3/20
1	1	2/10	1/10

Further, as can be determined by linear programming, $E(\{p_9, p_{10}, p_{11}\})$ has a single element; it and its update on the information $v_1=1$ are:

v_1	v_2	v_3	p	p'
0	0	0	1/8	0
0	0	1	1/4	0
0	1	0	0	0
0	1	1	0	0
1	0	0	1/4	2/5
1	0	1	1/8	1/5
1	1	0	1/8	1/5
1	1	1	1/8	1/5

As is easily verified, the projection of p' onto $\{v_2.v_3\}$ is distinct from both $JC(p'_9.p_{10})$ and $JC(p'_{11}.p_{10})$!

VI. A Problem for Enemies of the M.E.P.

There has been much debate regarding whether, when information regarding joint probabilities does not determine those probabilities uniquely, the ambiguity should be resolved by invoking the *maximum entropy principle*. According to Jaynes, its leading proponent:

The MAXENT principle, stated most briefly, is: when we make inferences based on incomplete information, we should draw them from that probability distribution that has the maximum entropy permitted by the information we do have [12, p. 940].

For a consistent database K, the convexity of E(K) guarantees the existence of a unique $p \in E(K)$ with maximum entropy. The arguments for and against maximizing entropy are well-known [12,31]. The present author has sided with the dissenters in this debate, and has advocated methods of inference and decision making with various types of constraints on underdetermined probabilities that do not utilize any particular representative of the set of joint probability distributions satisfying the constraints [17,28]. However, if a database K is updated locally using Bayesian methods, the result is indistinguishable from a global update utilizing the maximum entropy element, J(K), of E(K). Further, it is not the case that for all $p.q \in E(K)$. $\pi_{s(K)}(p') = \pi_{s(K)}(q')$.

To illustrate, recall the example of the object whose movements could be observed only in two planes. Suppose that the true probabilities of location in three dimensions are:

X	Y	Z	p
0	0	0	1/16
0	0	1	0
0	1	0	1/8
0	1	1	3/16
1	0	0	5/16
1	0	1	1/8
1	1	0	1/8
1	1	1	1/16

The 2-dimensional projections of p. i.e., the data actually obtained, are:

Y	Z	p_{12}	X	Z	p_{13}
0	0	3/8	0	0	3/16
0	1	1/8	0	1	3/16
1	0	1/4	1	0	7/16
1	1	1/4	1	1	3/16

It is determined that the probability of Y=0 should be 3/4, not 1/2. The Jeffrey update of p_{12}, p'_{12}, and the Jeffrey update of p_{13} by p'_{12} are:

Y	Z	p'_{12}	X	Z	$JC(p'_{12}.p_{13})$
0	0	9/16	0	0	33/160
0	1	3/16	0	1	5/32
1	0	1/8	1	0	77/160
1	1	1/8	1	1	5/32

The Jeffrey updates, on the information that the probability of Y=0 is 3/4, of p and $J(\pi_{\{\{Y.Z\}.\{X.Z\}\}}(p))$, are:

X	Y	Z	p'	$J(\{p_{12}.p_{13}\})'$
0	0	0	3/32	27/160
0	0	1	0	3/32
0	1	0	1/16	3/80
0	1	1	3/32	1/16
1	0	0	15/32	63/160
1	0	1	3/16	3/32
1	1	0	1/16	7/80
1	1	1	1/32	1/16

Observe that $\pi_{\{\{Y.Z\}.\{X.Z\}\}}(J(\{p_{12}.p_{13}\})') = \{p'_{12}.p'_{13}\}$, but $\pi_{\{\{Y.Z\}.\{X.Z\}\}}(p') \neq \{p'_{12}.p'_{13}\}$, even though we have postulated that $\{p_{12}.p_{13}\} = \pi_{\{\{Y.Z\}.\{X.Z\}\}}(p)$. More generally,

Theorem 12 Where q' is a Jeffrey update of q originating in some $V \subseteq s(q_1) \subseteq s(q)$,

$$\pi_{\{s(q_1).s(q_2)\}}(J(\{q_1.q_2\})') = \{q'_1.JC(q'_1.q_2)\}.$$

for arbitrary distributions q_1 and q_2. □

Remark: Jeffrey updating reduces to Bayesian conditioning as a special case.

This result poses a serious philosophical problem for those maintaining a database K of probability distributions who wish both to reject the assumptions that would pick out the maximum entropy element of E(K) as the joint distribution of which K is a projection and to update the database in response to new information. Local Bayesian updating of K results in the same distribution that results from forming the maximum entropy extension of K, updating the extension, and projecting the update onto s(K).

VII. Conclusion and Open Problems

Probabilistic databases may be updated to accommodate new information, where the new information can take various forms. At one extreme, entire distributions may be added or removed; at the other, the probability of an event in the domain of a single distribution is revised. Databases may also be adjusted to smooth the effects of sample size limitations, for probabilities estimated from frequencies. In each of these cases, local changes must be propagated throughout the database in order to restore consistency.

The method proposed for modifying one distribution in response to changes in another is based on *Jeffrey's Rule* [13]. It is noted that Jeffrey's Rule requires the assumption of constancy in certain conditional probabilities; without this assumption, the update is underdetermined, in general. It is also noted that the use of Jeffrey's Rule to propagate changes in probability is equivalent to projecting

onto the scheme of a database the update of its join. This is troubling for those who are philosophically uncomfortable with the maximum entropy principle.

The distinction in the literature between *updating* and *revising* a knowledge base is mentioned. The distinction seems less critical for probabilistic databases than it does for logical databases [14].

A distinction is made between *local* and *global* updates. Local updating (e.g., by Jeffrey's Rule) appears to be impossible for databases whose schemes are α-cyclic [7]. For such a database, updating by selecting an element of its extension, updating it, then marginalizing, is possible but computationally infeasible.

Methods for updating *interval-valued* probabilistic databases, in which a closed subinterval of [0, 1] is associated with each tuple, remain to be developed. It seems that these should reduce to Bayesian methods in the special case in which all intervals are degenerate. Extension, join and projection operators for such databases are defined in [25,26]. The work of Fertig and Breese on *interval influence diagrams* [8] may be relevant.

Another open problem is to identify *update anomalies* for probabilistic databases analogous to those for relational databases. Probabilistic analogues of relational data dependencies are defined in [6]. There may exist hierarchies of normal forms defined in terms of probabilistic functional, join, and multivalued dependencies whose members possess varying degrees of resistance to whatever meaningful anomalies are discovered.

A third area for future research is the development of ways to coordinate updating with planning and decision making. Not all portions of a database will be relevant to all problems. Identifying relevant subschemes is discussed in [29]. *Anytime* [4,10] methods of decision making with probabilistic databases, in which the number of admissible actions decreases with computing time, should also be explored.

References

1. Bacchus, F., et al., "Against conditionalization", *Synthese*, v. 80, pp. 475-506, 1990.
2. Barbara, D., et al., "The management of probabilistic data", *IEEE Trans. on KDE*, v. 4, pp. 487-502, 1992.
3. Bishop, Y. et al., *Discrete Multivariate Analysis*, MIT Press, 1975.
4. Boddy, M. and T. Dean, "Solving time-dependent planning problems", *Int. J. Conf. on Artificial Intelligence*, Morgan Kaufmann, pp. 979-984, 1989.
5. Cavallo, R. and G. Klir, "Reconstructability analysis of multi-dimensional relations", *Int. J. of Gen. Systems*, v. 5, pp. 143-171, 1979.
6. Cavallo, R. and M. Pittarelli, "The theory of probabilistic databases", *Proc. 13th Int. Conf. Very Large Databases*, Morgan Kaufmann, pp. 71-81, 1987.
7. Fagin, R., "Degrees of acyclicity for hypergraphs and relational database schemes", *J. of the ACM*, v. 30, pp. 514-550, 1983.
8. Fertig, K. and J. Breese, "Interval influence diagrams". In: M. Henrion et al., Eds., *Uncertainty in Artificial Intelligence*, v. 5, North-Holland, 1990.

9. Fienberg, S. and P. Holland, "Simultaneous estimation of multinomial cell probabilities", *J. Am. Stat. Assoc.*, v. *68*, pp. 683-691, 1973.

10. Frisch, A. and P. Haddawy, "Anytime deduction for probabilistic logic", *Artificial Intelligence*, to appear.

11. Heckerman, D. and A. Mamdani, Eds. *Proc. of the 9th Conference on Uncertainty in Artificial Intelligence*, Morgan Kaufmann, 1993.

12. Jaynes, E. T., "On the rationale of maximum-entropy methods", *Proc. of the IEEE*, v. *70*, pp. 939-952, 1982.

13. Jeffrey, R. C., *The Logic of Decision*, 2nd Ed., Univ. of Chicago Press, 1983.

14. Katsuno, H. and A. Mendelzon, "On the difference between updating a knowledge base and revising it". In: P. Gardenfors, Ed., *Belief Revision*, Cambridge University Press, 1992.

15. Keller, A. and M. Winslett-Wilkins, "On the use of an extended relational model to handle changing incomplete information", *IEEE Trans. on Software Eng.*, v. *11*, pp. 620-633, 1985.

16. Klir, G. and B. Parviz, "General reconstruction characteristics of probabilistic and possibilistic systems", *Int. J. Gen. Systems*, v. *25*, pp. 367-397, 1986.

17. Kyburg, H. E., Jr. and M. Pittarelli, "Set-based Bayesianism", TR 407, Computer Science Dept., Univ. of Rochester, 1992.

18. Lauritzen, S. and D. Spiegelhalter, "Local computations with probabilities on graphical structures and their application to expert systems", *J. Royal Statistical Soc.*, ser. B, v. *50*, pp. 157-224, 1988. (With discussion.)

19. Lemmer, J., *Algorithms for Incompletely Specified Distributions in a Generalized Graph Model for Medical Diagnosis*, Ph.D. dissertation, Univ. of Maryland, 1976.

20. Lemmer, J., "Generalized Bayesian updating of incompletely specified distributions", *Large Scale Systems*, v. *5*, pp. 51-68, 1983.

21. Levi, I., *The Enterprise of Knowledge*, MIT Press, 1980.

22. Lewis, P. M., "Approximating probability distributions to reduce storage requirements", *Information and Control*, v. *2*, pp. 214-225, 1959.

23. May, S. and W. Harper, "Toward an optimization procedure for applying minimum change principles in probability kinematics". In W. Harper and C. Hooker, Eds., *Foundations of Probability Theory, Statistical Inference, and Statistical Theories of Science*, Reidel, 1976.

24. Pearl, J., *Probabilistic Reasoning in Intelligent Systems*, Morgan Kaufmann, 1988.

25. Pittarelli, M., "Probabilistic databases for decision analysis", *Int. J. Intelligent Systems*, v. *5*, pp. 209-236, 1990.

26. Pittarelli, M., "Reconstructability analysis using probability intervals", *Int. J. of Gen. Systems*, v. *16*, pp. 215-233, 1990.

27. Pittarelli, M., "A note on probability estimation using reconstructability analysis", *Int. J. Gen. Systems*, v. *18*, pp. 11-21, 1990.

28. Pittarelli, M., "Decisions with probabilities over finite product spaces", *IEEE Trans. SMC*, v. *21*, pp. 1238-1242, 1991.

29. Pittarelli, M., "Probabilistic databases and decision problems: results and a conjecture", *Kyber-netika, v. 29.* pp. 149-165, 1993.

30. Pittarelli, M., "An algebra for probabilistic databases", *IEEE Trans. KDE,* to appear.

31. Seidenfeld, T., "Entropy and uncertainty", *Philosophy of Science, v. 53.* pp. 467-491, 1986.

32. Ullman, J., *Principles of Database and Knowledge-Base Systems, v. 1,* Computer Science Press, 1988.

33. Van Frassen, B., "A problem for relative information minimizers in probability kinematics", *Brit. J. Phil. Sci. v. 32,* pp. 375-379, 1981.

34. Van Frassen, B., *et al.,* "A problem for relative information minimizers, continued", *Brit. J. Phil. Sci., v. 37,* pp. 453-475, 1986.

35. Williams, P., "Bayesian conditionalization and the principle of minimum information", *Brit. J. Phil. Sci., v. 31,* pp. 131-144, 1980.

ANALYSIS OF A GENERALIZED POLARIZER LAYER
FOR INFINITE ARRAYS OF ANTENNAS
ON PROTRUDING DIELECTRIC SUBSTRATES

Jean-Pierre R. Bayard
Associate Professor
Department of Electrical & Electronic Engineering

California State University, Sacramento
6000 J Street
Sacramento, CA 95819-6019

Final Report for:
Summer Research Program
Hanscom Laboratory

ANALYSIS OF A GENERALIZED POLARIZER LAYER
FOR INFINITE ARRAYS OF ANTENNAS
ON PROTRUDING DIELECTRIC SUBSTRATES

Jean-Pierre R. Bayard
Associate Professor
Department of Electrical & Electronic Engineering
California State University, Sacramento

Abstract

In this paper, the solution for a near-field polarizing layer facing an infinite array of antenna elements printed on protruding dielectric substrates is described. The analysis of the polarizer is accomplished by using Floquet expansion modes for expressing the field components, and the method of moments to enforce the conditions on the printed currents. The analysis and code are capable of representing fairly general single-layered polarizer geometries (planar in x and y) with currents printed in both the x and y directions, and with a periodicity identical to that of the array. Numerical values for the element active impedance and axial ratio are presented for a design with circular polarization characteristics positioned on top of arrays of dipoles with straight and bent arms operating in the transmit mode. Reflection coefficients from arrays of dipoles and microstrip patches illuminated by a plane wave are also calculated.

ANALYSIS OF A GENERALIZED POLARIZER LAYER
FOR INFINITE ARRAYS OF ANTENNAS
ON PROTRUDING DIELECTRIC SUBSTRATES

Jean-Pierre R. Bayard

Introduction

Infinite arrays of antennas printed on dielectric walls
protruding from a ground plane have been the focal point of much
research effort related to MMIC and Aerospace applications [1-7].
These antenna elements, whether they are dipoles as in [1-7] or
potentially tapered slots, exhibit because of the array geometry
(radiating currents perpendicular to array face) linear
polarization characteristics. In this paper, a single dielectric
sheet of printed gratings is added in front of the array (see
Figure 1) offering the possibility of altering its polarization
characteristics. This alteration may take the form of a
circularly-polarized (CP) wave, comparable to the performance of
the meander-line polarizer of [8-10], or a purely linearly-
polarized (LP) wave removing the undesirable cross polarization.
The analysis / code for describing the polarizer is the focus of
the effort, and shall be considered a module additive to the work
described in [3-7].

In the section that follows, the analysis of the polarizing
layer is formulated by using the equivalence principle, modal
expansion techniques, and the method of moments. The application
of the equivalence principle at the top and bottom of the layer
follows step identical to those described in [6], thereby
facilitating the integration of this module with the previously
developed code. Since the structure is planar and doubly
periodic in nature, the fields from the equivalent sources, as
well as the Green's function for the printed x and y-directed
electric currents, are expressed using typical Floquet functions.
The method of moments procedure is then used for enforcing the
electromagnetic boundary conditions on the electric currents of
the polarizer. The reader should note that the method can not
presently model a CP-producing meander-line polarizer. In order
to achieve circular polarization from such polarizer, the
gratings ought to be printed oblique to the incoming wave, i.e.,
the y-directed wave emanating from the antenna of Figure 1, and
designed such that the wave components that are perpendicular and
parallel to the meander-line axis are phased 90 degrees apart.
While the present work can not treat polarizer currents printed
on a tapered domain, as would be required by the meander-line
design, it offers a moment-method based approach which, in
conjunction with [6], permits the modeling of a wide variety of
polarizer designs (with currents defined on rectangular domains)
when facing the array.

Lastly, numerical results are presented for infinite arrays
of microstrip-fed dipoles with straight and bent arms. The
physical dimensions of the polarizer and its substrate's
thickness and permittivity are adjusted for achieving circular
polarization near broadside. The active impedance and axial
ratio curves are plotted versus scan and frequency. Plane wave
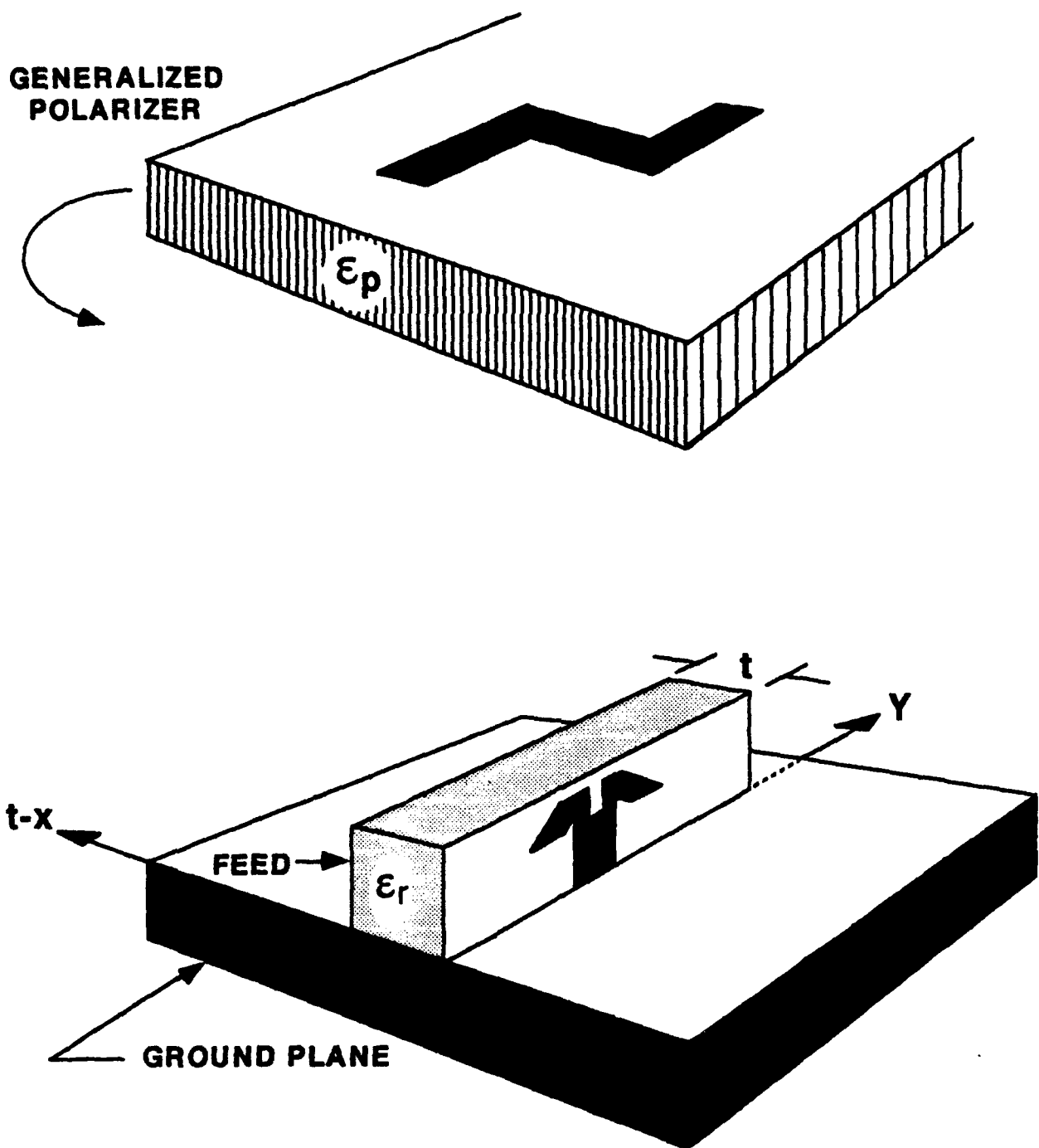
Figure 1. The sketch of the array element.

reflections from dipole and microstrip arrays are also considered as limiting test cases for verification purposes.

FORMULATION

The geometry of the polarizer is shown in Figure 2a. The bottom dielectric layer is a substrate with a relative permittivity ϵ_p, thickness t_p, upon which x and/or y-directed electric currents can be printed. The top layer or superstrate with a permittivity ϵ_d and thickness t_d can serve as a protective radome cover or its permittivity may be set to that of free-space. The goal of the formulation is to determine matrix equations expressing the self and mutual impedances of the electric currents printed a $z=z_p+t_p$, as well as the coupling between these currents and sources located outside the polarizer, i.e., $z<z_p$ and $z>z_p+t_p+t_d$. Applying the equivalence principle at $z=z_p$ and $z=z_p+t_p+t_d$, we set up a model for the regions exterior to the polarizer but included in the unit cell (see Figure 2b). For the purpose of this work, the part of the model represented by the equivalent magnetic sources at $z=z_p-\delta$ and $z=z_p+t_p+t_d+\delta$ (δ indicating a limiting quantity) is assumed known from [6], thus will not be included in the analysis. In order to characterize the region of the model which lies inside the polarizer, the electric current problem and the magnetic current problem are formulated separately using the TM_z and TE_z mode sets. For the electric currents inside the parallel-plate guide of Figure 2b, the first step is to determine the Green's functions for infinitesimal x or y-directed currents printed at (x_o, y_o, z_p+t_p). Let

$$\phi^{pg} = \sum_{n=-\infty}^{+\infty} \sum_{l=-\infty}^{+\infty} E_{nl}^p e^{-jV_n(y-y_o)} e^{-jU_l(x-x_o)} \cos k_z^p (z-z_p)$$

$$\psi^{pg} = \sum_{n=-\infty}^{+\infty} \sum_{l=-\infty}^{+\infty} F_{nl}^p e^{-jV_n(y-y_o)} e^{-jU_l(x-x_o)} \sin k_z^p (z-z_p)$$

where

$$k_z^p = \sqrt{\epsilon_p k_o^2 - U_l^2 - V_n^2},$$

$$U_l = k_o \sin\theta \cos\phi + \frac{l2\pi}{a},$$

$$V_n = k_o \sin\theta \sin\phi + \frac{n2\pi}{b},$$

$\qquad$ (1)

θ, ϕ are the beam steering angles, k_o is the free-space wave number, and a and b are the unit cell dimensions in the x and y directions, be the TM_z and TE_z mode functions for the polarizer substrate ($z_p \leq z < z_p+t_p$). Similarly, let

$$\phi^{dg} = \sum_{n=-\infty}^{+\infty} \sum_{l=-\infty}^{+\infty} E_{nl}^d e^{-jV_n(y-y_o)} e^{-jU_l(x-x_o)} \cos k_z^d (z-z_p-t_d-t_p)$$

$$\psi^{dg} = \sum_{n=-\infty}^{+\infty} \sum_{l=-\infty}^{+\infty} F_{nl}^d e^{-jV_n(y-y_o)} e^{-jU_l(x-x_o)} \sin k_z^d (z-z_p-t_d-t_p)$$

where

$$k_z^d = \sqrt{\epsilon_d k_o^2 - U_l^2 - V_n^2},$$

$\qquad$ (2)

be the TM_z and TE_z functions for the superstrate. The determination of the Green's functions, i.e., the solution for
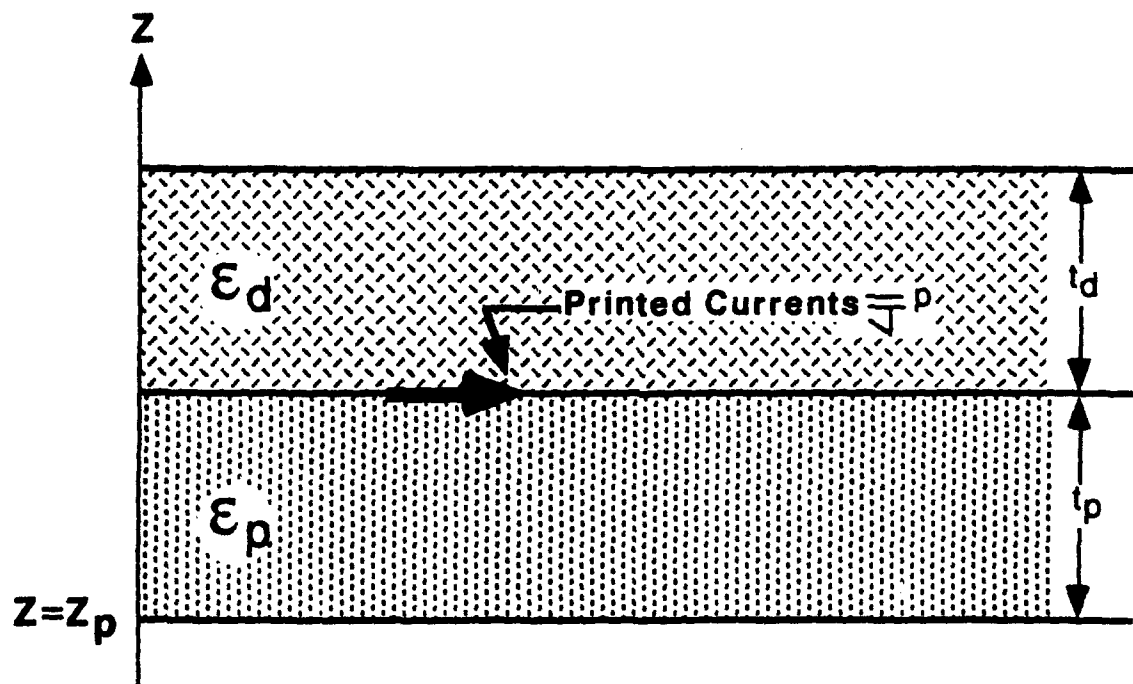
(a) Polarizer geometry
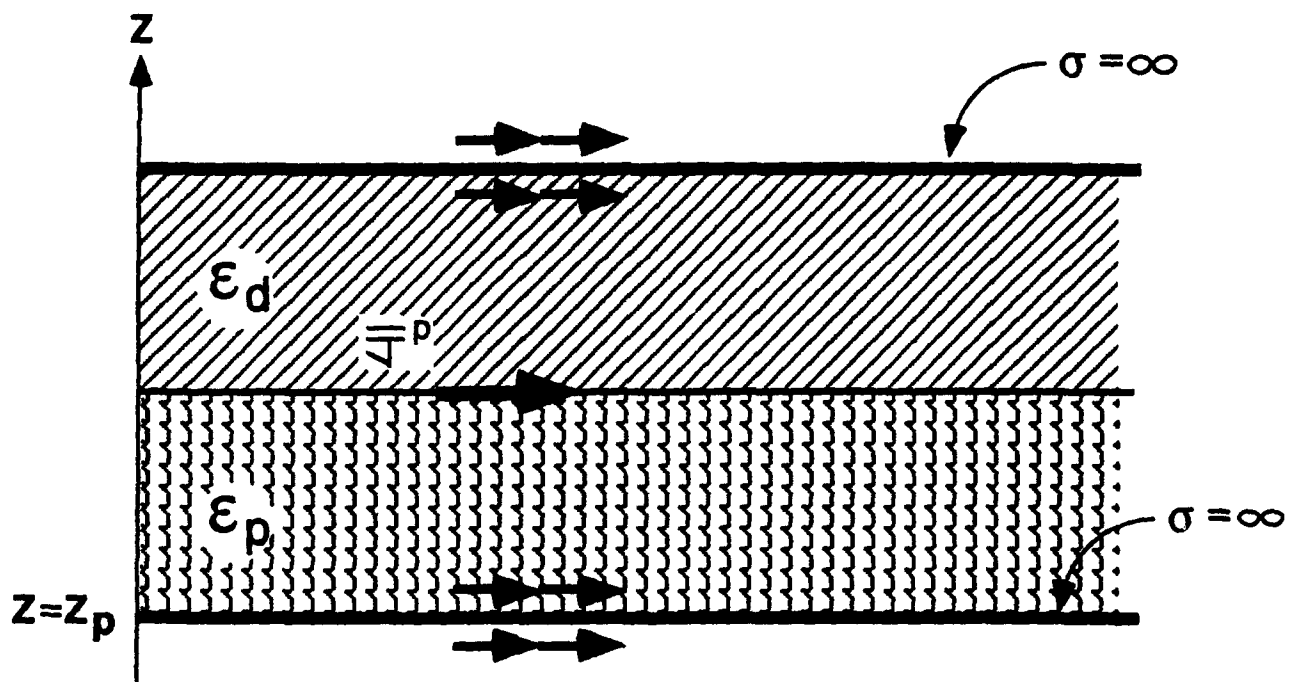
(b) Equivalent model with magnetic sources

Figure 2. The schematic and equivalent model for the polarizing layer.

the modal coefficients E^p_{nl}, F^p_{nl}, E^d_{nl}, F^d_{nl}, is accomplished by enforcing the continuity of the electric field components tangential to the interface at $z=z_p+t_p$, as well as the magnetic field jump discontinuity caused by the delta current sources. The result is given by the following matrix equations:

$$
\begin{bmatrix}
-\frac{1}{\omega\epsilon_o\epsilon_d}U_1k_z^d\sin(k_z^dt_d) & -jV_n\sin(k_z^dt_d) & -\frac{1}{\omega\epsilon_o\epsilon_p}U_1k_z^p\sin(k_z^pt_p) & -jV_n\sin(k_z^pt_p) \\
-\frac{1}{\omega\epsilon_o\epsilon_d}V_nk_z^d\sin(k_z^dt_d) & jU_1\sin(k_z^dt_d) & -\frac{1}{\omega\epsilon_o\epsilon_p}V_nk_z^p\sin(k_z^pt_p) & jU_1\sin(k_z^pt_p) \\
-jU_1\cos(k_z^dt_d) & \frac{1}{\omega\mu}V_nk_z^d\cos(k_z^dt_d) & jU_1\cos(k_z^pt_p) & -\frac{1}{\omega\mu}V_nk_z^p\cos(k_z^pt_p) \\
-jV_n\cos(k_z^dt_d) & -\frac{1}{\omega\mu}U_1k_z^d\cos(k_z^dt_d) & jV_n\cos(k_z^pt_p) & \frac{1}{\omega\mu}U_1k_z^p\cos(k_z^pt_p)
\end{bmatrix}
\begin{bmatrix} E^d_{nl} \\ F^d_{nl} \\ E^p_{nl} \\ F^p_{nl} \end{bmatrix}
=
\begin{bmatrix} 0 \\ 0 \\ G_3 \\ G_4 \end{bmatrix}
\quad (3)
$$

where $G_3 = 1/(ab)$ for x-directed currents, $G_4=1/(ab)$ for y-directed currents, and 0 otherwise. From equations (1-3), any field component produced by an x or y-directed current can be expressed straightforwardly by convolving the current distribution with the appropriate Green's function component.

For the equivalent magnetic sources inside the polarizer, let the TM_z and TE_z mode functions be

$$
\phi^p = \sum_{n=-\infty}^{+\infty} \sum_{n=-\infty}^{+\infty} e^{-jV_ny}e^{-jU_1x}\left\{ A^p_{nl}e^{-jk_z^p(z-z_p-t_p)} + B^p_{nl}e^{jk_z^p(z-z_p)} \right\}
$$

$$
\psi^p = \sum_{n=-\infty}^{+\infty} \sum_{n=-\infty}^{+\infty} e^{-jV_ny}e^{-jU_1x}\left\{ C^p_{nl}e^{-jk_z^p(z-z_p-t_p)} + D^p_{nl}e^{jk_z^p(z-z_p)} \right\}
$$

(4)

for the region defined by $z_p \leq z \leq z_p+t_p$, and

$$
\phi^d = \sum_{n=-\infty}^{+\infty} \sum_{n=-\infty}^{+\infty} e^{-jV_ny}e^{-jU_1x}\left\{ A^d_{nl}e^{-jk_z^d(z-z_p-t_p-t_d)} + B^d_{nl}e^{jk_z^d(z-z_p-t_p)} \right\}
$$

$$
\psi^d = \sum_{n=-\infty}^{+\infty} \sum_{n=-\infty}^{+\infty} e^{-jV_ny}e^{-jU_1x}\left\{ C^d_{nl}e^{-jk_z^d(z-z_p-t_p-t_d)} + D^d_{nl}e^{jk_z^d(z-z_p-t_p)} \right\}
$$

(5)

for $z_p +t_p \leq z \leq z_p+t_p+t_d$. Enforcing the continuity of the tangential electric and magnetic field components at $z=z_p+t_p$ gives

$$
B^d_{nl} = \frac{A^p_{nl}}{2}\left(1 - \frac{\epsilon_d k_z^p}{\epsilon_p k_z^d}\right) + \frac{B^p_{nl}}{2}e^{jk_z^pt_p}\left(1 + \frac{\epsilon_d k_z^p}{\epsilon_p k_z^d}\right)
$$

$$
A^d_{nl} = \frac{A^p_{nl}}{2}e^{-jk_z^dt_d}\left(1 + \frac{\epsilon_d k_z^p}{\epsilon_p k_z^d}\right) + \frac{B^p_{nl}}{2}e^{j(k_z^pt_p-k_z^dt_d)}\left(1 - \frac{\epsilon_d k_z^p}{\epsilon_p k_z^d}\right)
$$

$$
D^d_{nl} = \frac{C^p_{nl}}{2}\left(1 - \frac{k_z^p}{k_z^d}\right) + \frac{D^p_{nl}}{2}e^{jk_z^pt_p}\left(1 + \frac{k_z^p}{k_z^d}\right)
$$

$$
C^d_{nl} = \frac{C^p_{nl}}{2}e^{-jk_z^dt_d}\left(1 + \frac{k_z^p}{k_z^d}\right) + \frac{D^p_{nl}}{2}e^{j(k_z^pt_p-k_z^dt_d)}\left(1 - \frac{k_z^p}{k_z^d}\right)
$$

(6)

reducing equations (4) and (5) to having only four modal coefficients, A^p_{nl}, B^p_{nl}, C^p_{nl}, D^p_{nl}, which will be among the unknowns to be determined in the subsequent moment method formulation.

Method of Moments

At this time, the formulation has accounted for most of the electromagnetic boundary conditions governing the fields produced by the electric and equivalent magnetic sources inside the polarizer. The remaining conditions are those existing on the domains of the sources, i.e., at $z=z_p$, $z=z_p+t_p+t_d$, and on the polarizer conductor printed at $z=z_p+t_p$. Consider a current distribution of the form

$$\vec{J}^P(x,y) = \vec{x} J_x^P(x,y) + \vec{y} J_y^P(x,y) \tag{7}$$

existing on a perfectly-conducting, zero-thickness geometry printed at $z=z_p+t_p$. With the aid of the moment method, the distribution of (7) can be determined by means of a finite sum approximation. Let

$$J_x^P(x,y) = \sum_{n=1}^{NPX} a_n \frac{\sin k_o(h_n^x - |x - x_n^x|)}{W_n^x \sin k_o h_n^x},$$

$$J_y^P(x,y) = \sum_{m=1}^{NPY} b_m \frac{\sin k_o(h_m^y - |y - y_m^y|)}{W_m^y \sin k_o h_m^y}, \tag{8}$$

where x_n, y_n are the coordinates of the mode center, W_n is the mode width, h_n is the mode half-length, and a_n, b_m are the unknown coefficients defining the function. As in [6], adjusting individual mode dimensions and location permits the modeling of a wide variety of polarizer geometries describable in the rectangular coordinate system. With respect to the current distributions at the two apertures at $z=z_p$ and $z=z_p+t_p+t_d$, by expressing their fields as modal sums, we have in effect expanded these currents in terms of Floquet basis functions with unknown coefficients A_{nl}^P, B_{nl}^P, C_{nl}^P and D_{nl}^P. Also, when implementing the formulation numerically, the magnetic current summations are truncated to user-specified integer values, say $-NM \leq n \leq NM$ and $-PP \leq l \leq PP$. As in the Galerkin's procedure, the solution for these 6 unknowns is achieved by testing: a) The x or y-directed electric field at $z=z_p+t_p$ with x or y-directed electric current modes, and b) the x or y-directed electric and magnetic fields at $z=z_p$ and $z=z_p+t_p+t_d$ with the conjugate of the Floquet functions across the apertures. For the conditions at $z=z_p+t_p$, we have:

x-Directed electric field equation

$$[Z^{pxx}][a_n] + [Z^{pxy}][b_m] + [Z^{pxa}]\begin{bmatrix}[A_{nl}^p]\\[B_{nl}^p]\\[C_{nl}^p]\\[D_{nl}^p]\end{bmatrix} = 0 \tag{9}$$

where

$$Z_{mq}^{pxx} = \frac{1}{\omega \epsilon_o \epsilon_p} \sum_{n=-NNP}^{NNP} \sum_{l=-NLP}^{NLP} (U_l k_z^P E_{nl}^P + V_n F_{nl}^P)$$
$$\sin(k_z^P t_p) \, T_1(q) \, T_1^*(m) \, T_2(q) \, T_2^*(m) ,$$

with

$$T_1(q) = \frac{2}{V_n} e^{jV_n y_q^x} \sin\left(V_n \frac{W_q^x}{2}\right),$$

(10)

$$T_2(q) = \frac{2k_o e^{jU_l x_q^x}}{W_q^x \sin k_o h_q^x} \left[\frac{\cos(U_l h_q^x) - \cos(k_o h_q^x)}{k_o^2 - U_l^2} \right],$$

NNP and NLP are user-specified summation limits for the parallel-plate Green's functions, m,q= 1,2, ..., NPX, and the star denoting the complex conjugate of the quantity,

$$Z_{mq}^{pxy} = \frac{1}{\omega \epsilon_o \epsilon_p} \sum_{n=-NNP}^{NNP} \sum_{l=-NLP}^{NLP} (V_n k_z^P E_{nl}^P - U_l F_{nl}^P)$$
$$\sin(k_z^P t_p) \, T_3(q) \, T_1^*(m) \, T_4(q) \, T_2^*(m) ,$$

with

$$T_3(q) = \frac{2}{U_l} e^{jU_l x_q^y} \sin\left(U_l \frac{W_q^y}{2}\right),$$

(11)

$$T_4(q) = \frac{2k_o e^{jV_n y_q^y}}{W_q^y \sin k_o h_q^y} \left[\frac{\cos(V_n h_q^y) - \cos(k_o h_q^y)}{k_o^2 - V_n^2} \right],$$

and q=1,2,...,NPY,

$$Z_{mq}^{pxa} = -\frac{1}{j\omega \epsilon_o \epsilon_p} (U_l k_z^P) \, T_1^*(m) \, T_2^*(m) ,$$
with $-NM \le n \le NM$, $-PP \le l \le PP$, and $q=(l+PP)(2NM+1)+n+NM+1$,
$$Z_{mq}^{pxa} = \frac{1}{j\omega \epsilon_o \epsilon_p} (U_l k_z^P) \, e^{jk_z^P t_p} T_1^*(m) \, T_2^*(m) ,$$
with $q=(2NM+1)(2PP+1)+(l+PP)(2NM+1)+n+NM+1$,   (12)
$$Z_{mq}^{pxa} = (jV_n) \, T_1^*(m) \, T_2^*(m) ,$$
with $q=2(2NM+1)(2PP+1)+(l+PP)(2NM+1)+n+NM+1$,
and
$$Z_{mq}^{pxa} = (jV_n) \, e^{jk_z^P t_p} T_1^*(m) \, T_2^*(m) ,$$
with $q=3(2NM+1)(2PP+1)+(l+PP)(2NM+1)+n+NM+1$.

Realize that the modal coefficients in equations (10) and (11) represent the now known Green's function coefficients for the x-directed source [eq. (10)] and the y-directed source [eq. (11)]. Also, the index q in equation (12) indicates the ordering of the unknowns used in the magnetic current problem.

y-Directed electric field equation

$$[Z^{pyx}]\,[a_n] + [Z^{pyy}]\,[b_m] + [Z^{pya}]\begin{bmatrix}[A_{nl}^p]\\[B_{nl}^p]\\[C_{nl}^p]\\[D_{nl}^p]\end{bmatrix}=0 \qquad (13)$$

where

$$Z_{mq}^{pyx}=\frac{1}{\omega\epsilon_o\epsilon_p}\sum_{n=-NNP}^{NNP}\sum_{l=-NLP}^{NLP}(V_n k_z^P E_{nl}^P - U_l F_{nl}^P)$$
$$\sin(k_z^P t_p)\,T_1(q)\,T_3^*(m)\,T_2(q)\,T_4^*(m)\,, \qquad (14)$$
$$\text{with } m=1,2,\ldots,NPY \text{ and } q=1,2,\ldots,NPX,$$

$$Z_{mq}^{pyy}=\frac{1}{\omega\epsilon_o\epsilon_p}\sum_{n=-NNP}^{NNP}\sum_{l=-NLP}^{NLP}(V_n k_z^P E_{nl}^P - U_l F_{nl}^P)$$
$$\sin(k_z^P t_p)\,T_3(q)\,T_3^*(m)\,T_3(q)\,T_4^*(m)\,, \qquad (15)$$
$$\text{with } q=1,2,\ldots,NPY,$$

$$Z_{mq}^{pya}=-\frac{1}{j\omega\epsilon_o\epsilon_p}(V_n k_z^P)\,T_3^*(m)\,T_4^*(m)\,,$$
$$\text{with } -NM\le n\le NM,\ -PP\le l\le PP,\ \text{and } q=(l+PP)(2NM+1)+n+NM+1,$$
$$Z_{mq}^{pya}=\frac{1}{j\omega\epsilon_o\epsilon_p}(V_n k_z^P)\,e^{jk_z^P t_P}T_3^*(m)\,T_4^*(m)\,,$$
$$\text{with } q=(2NM+1)(2PP+1)+(l+PP)(2NM+1)+n+NM+1, \qquad (16)$$
$$Z_{mq}^{pya}=-(jU_l)\,T_3^*(m)\,T_4^*(m)\,,$$
$$\text{with } q=2(2NM+1)(2PP+1)+(l+PP)(2NM+1)+n+NM+1,$$
$$\text{and}$$
$$Z_{mq}^{pya}=-(jU_l)\,e^{jk_z^P t_P}T_3^*(m)\,T_4^*(m)\,,$$
$$\text{with } q=3(2NM+1)(2PP+1)+(l+PP)(2NM+1)+n+NM+1.$$

For the conditions at $z=z_p$ and $z=z_p+t_p+t_d$, the goal is to simply express in matrix form the fields produced by the sources inside the polarizer at these apertures. Since the x and y-directed electromagnetic fields are tested with $\exp(jV_n y)\exp(jU_l x)$ over $0\le x\le a$ and $0\le y\le b$, the resulting matrices are highly sparse, particularly those coming from the equivalent magnetic sources. The matrix forms of the tangential field components at $z=z_p+\delta$ are given by:

x-Directed electric field

$$[Z^{Lxaa}] \begin{bmatrix} [A_{nl}^p] \\ [B_{nl}^p] \\ [C_{nl}^p] \\ [D_{nl}^p] \end{bmatrix} \qquad (17)$$

where

$Z_{mq}^{Lxaa} = -\dfrac{1}{j\omega\epsilon_o\epsilon_p} (U_l k_z^p) e^{jk_z^p t_p} ab,$

with $-NM \le n \le NM$, $-PP \le l \le PP$, and $m = q = (l+PP)(2NM+1) + n + NM + 1,$

$Z_{mq}^{Lxaa} = \dfrac{1}{j\omega\epsilon_o\epsilon_p} (U_l k_z^p) ab,$

with $q = (2NM+1)(2PP+1) + (l+PP)(2NM+1) + n + NM + 1,$ $\qquad (18)$

$Z_{mq}^{Lxaa} = jV_n e^{jk_z^p t_p} ab,$

with $q = 2(2NM+1)(2PP+1) + (l+PP)(2NM+1) + n + NM + 1,$

$Z_{mq}^{Lxaa} = jV_n ab,$

with $q = 3(2NM+1)(2PP+1) + (l+PP)(2NM+1) + n + NM + 1.$

y-Directed electric field

$$[Z^{Lyaa}] \begin{bmatrix} [A_{nl}^p] \\ [B_{nl}^p] \\ [C_{nl}^p] \\ [D_{nl}^p] \end{bmatrix} \qquad (19)$$

where

$Z_{mq}^{Lyaa} = -\dfrac{1}{j\omega\epsilon_o\epsilon_p} (V_n k_z^p) e^{jk_z^p t_p} ab,$

with $-NM \le n \le NM$, $-PP \le l \le PP$, and $m = q = (l+PP)(2NM+1) + n + NM + 1,$

$Z_{mq}^{Lyaa} = \dfrac{1}{j\omega\epsilon_o\epsilon_p} (V_n k_z^p) ab,$

with $q = (2NM+1)(2PP+1) + (l+PP)(2NM+1) + n + NM + 1,$ $\qquad (20)$

$Z_{mq}^{Lyaa} = -jU_l e^{jk_z^p t_p} ab,$

with $q = 2(2NM+1)(2PP+1) + (l+PP)(2NM+1) + n + NM + 1,$

$Z_{mq}^{Lyaa} = -jU_l ab,$

with $q = 3(2NM+1)(2PP+1) + (l+PP)(2NM+1) + n + NM + 1.$

x-Directed magnetic field

$$[Y^{Lxax}]\ [a_n]\ [Y^{Lxay}]\ [b_m] + [Y^{Lxaa}]\begin{bmatrix}[A_{nl}^p]\\[B_{nl}^p]\\[C_{nl}^p]\\[D_{nl}^p]\end{bmatrix} \tag{21}$$

where

$$Y_{mq}^{Lxax} = (-jV_n E_{nl}^p - \frac{1}{j\omega\mu}jU_l k_z^p F_{nl}^p)\ T_1(q)\ T_2(q)\ ab,$$
with $-NM \leq n \leq NM$, $-PP \leq l \leq PP$, $m = (l+PP)(2NM+1)+n+NM+1$,
and $q = 1, 2, \ldots NPX$, $\tag{22}$

$$Y_{mq}^{Lxay} = (-jV_n E_{nl}^p - \frac{1}{j\omega\mu}jU_l k_z^p F_{nl}^p)\ T_3(q)\ T_4(q)\ ab,$$
with $-NM \leq n \leq NM$, $-PP \leq l \leq PP$, $m = (l+PP)(2NM+1)+n+NM+1$,
and $q = 1, 2, \ldots NPY$, $\tag{23}$

$$Y_{mq}^{Lxaa} = -jV_n e^{jk_z^p t_p}ab,$$
with $-NM \leq n \leq NM$, $-PP \leq l \leq PP$, and $m = q = (l+PP)(2NM+1)+n+NM+1$,
$$Y_{mq}^{Lxaa} = -jV_n ab,$$
with $q = (2NM+1)(2PP+1)+(l+PP)(2NM+1)+n+NM+1$,
$$Y_{mq}^{Lxaa} = -\frac{1}{j\omega\mu}U_l k_z^p e^{jk_z^p t_p}ab,$$
with $q = 2(2NM+1)(2PP+1)+(l+PP)(2NM+1)+n+NM+1$,
$$Y_{mq}^{Lxaa} = \frac{1}{j\omega\mu}U_l k_z^p ab,$$
with $q = 3(2NM+1)(2PP+1)+(l+PP)(2NM+1)+n+NM+1$, $\tag{24}$

y-Directed magnetic field

$$[Y^{Lyax}]\ [a_n]\ [Y^{Lyay}]\ [b_m] + [Y^{Lyaa}]\begin{bmatrix}[A_{nl}^p]\\[B_{nl}^p]\\[C_{nl}^p]\\[D_{nl}^p]\end{bmatrix} \tag{25}$$

where

$$Y_{mq}^{Lyax} = (jU_l E_{nl}^p - \frac{1}{j\omega\mu}jV_n k_z^p F_{nl}^p)\ T_1(q)\ T_2(q)\ ab,$$
with $-NM \leq n \leq NM$, $-PP \leq l \leq PP$, $m = (l+PP)(2NM+1)+n+NM+1$,
and $q = 1, 2, \ldots NPX$, $\tag{26}$

$$Y_{mq}^{Lyay} = (jU_1E_{n1}^P - \frac{1}{j\omega\mu} jV_nk_z^PF_{n1}^P) \, T_3(q) \, T_4(q) \, ab,$$

with $-NM \leq n \leq NM$, $-PP \leq l \leq PP$, $m=(l+PP)(2NM+1)+n+NM+1$, and $q=1,2,\ldots NPY$, **(27)**

$$Y_{mq}^{Lyaa} = jU_1e^{jk_z^Pt_p}ab,$$

with $-NM \leq n \leq NM$, $-PP \leq l \leq PP$, and $m=q=(l+PP)(2NM+1)+n+NM+1$,

$$Y_{mq}^{Lyaa} = jU_1ab,$$

with $q=(2NM+1)(2PP+1)+(l+PP)(2NM+1)+n+NM+1$, **(28)**

$$Y_{mq}^{Lyaa} = -\frac{1}{j\omega\mu} V_nk_z^Pe^{jk_z^Pt_p}ab,$$

with $q=2(2NM+1)(2PP+1)+(l+PP)(2NM+1)+n+NM+1$,

$$Y_{mq}^{Lyaa} = \frac{1}{j\omega\mu} V_nk_z^Pab,$$

with $q=3(2NM+1)(2PP+1)+(l+PP)(2NM+1)+n+NM+1.$

The mathematical representations of the electromagnetic conditions at $z=z_p+t_p+t_d-\delta$ are very much similar to those in equations (17-28), but using the wave functions in equations (2) and (5), and the relationships given in equation (6). For that reason, they are not shown here.

EXAMPLES

The computer code developed from the method described above is applied to a microstrip array, to an array of dipoles printed on a grounded dielectric slab, and to a polarizer design facing arrays of dipoles on protruding dielectric substrates. Aside from these results, the following canonical problems were successfully calculated (but not shown here due to space constraint): 1) Plane wave reflection from a perfectly-conducting surface with and without a dielectric substrate; 2) the element impedance of an infinite array of center-fed and y-directed dipoles inside a free-space parallel-plate guide.

Dipole gratings

In the first example, the plane wave reflection from an infinite array of short-circuit dipoles printed on a grounded dielectric slab is considered. The dipoles are 0.10 cm wide and printed on a 90 mil-Noryl substrate ($\epsilon_p=2.7$) with a 1.3 cm square grid. This geometry can be modeled by simply setting $z_p = 0$ in the present module and d=0 in the work done in [6]. Figure 3a shows the E-plane phase of the reflection coefficient calculated versus dipole length at a frequency of 12 GHz, for normal incidence and with the reference plane at the dielectric - free-space interface. Observe that as the dipole length gets smaller, the phase value approaches 99.6 degrees which is the phase value of a grounded dielectric slab alone. This example serves as an illustration of the versatility of such module whereby plane wave reflection problems from planar geometries with or without a superstrate, and with a one (d=0 case in [6]) or two-layer (d≠0 and t→ a in [6]) substrate can easily be modeled.

Microstrip gratings
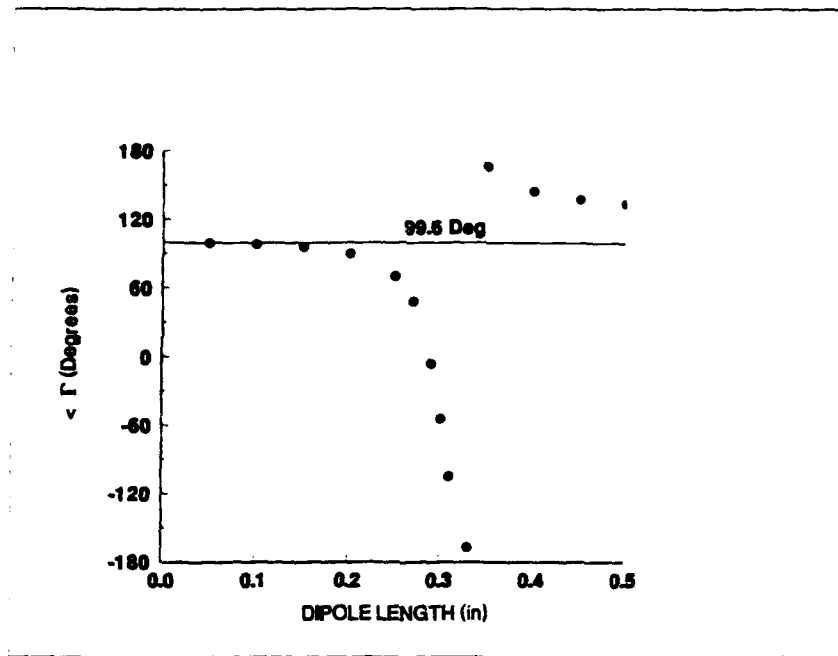
(a) Dipole gratings
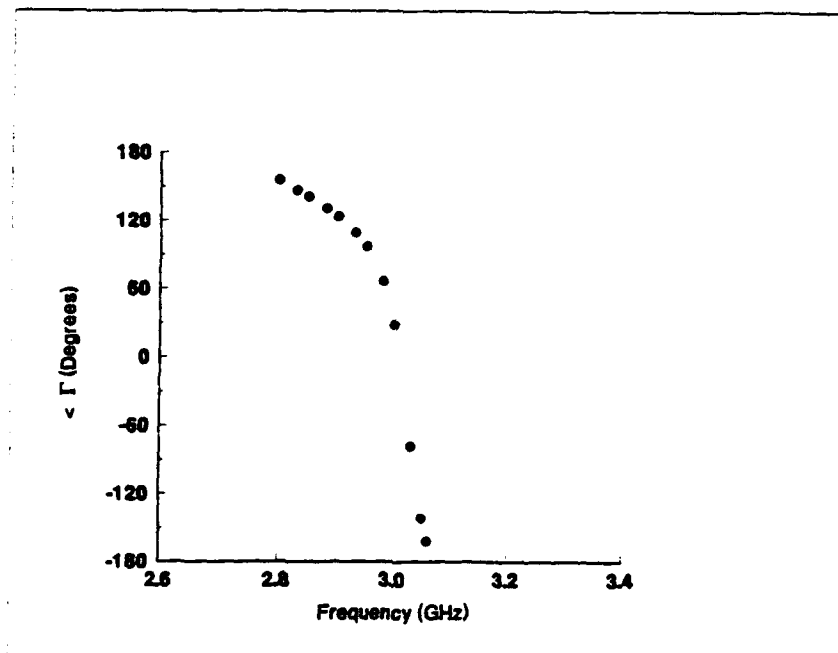
(b) Microstrip gratings

Figure 3.   Reflection coefficient pha   or arrays of dipoles
and microstrip patches printed on a grounded
dielectric slab.

In the second example shown in Figure 3b, the array of open-circuit microstrip patches analyzed and measured in [11] is considered. The square patches are 1.2 in wide, printed on a t_p=0.062 in, ϵ_p=2.47 substrate. The unit cell dimensions are a=1.8 in and b=2.87 in, matching those of the waveguide simulator used in [11]. Unable to determine the reference phase value used for the data of [11], the author selected a reference plane such that his results agree well with those of [11] for 2.8 GHz. Having done so, the frequency is varied (keeping the reference plane constant) and the phase of the reflection coefficient is calculated for several frequencies between 2.8 and 3.1 GHz. Good agreement exists between our calculations and both the theoretical and experimental values shown in [11]. The resonant frequency of the array is located near 3 GHz with a fairly large value of the patch's Q.

Circular polarization gratings

In order to achieve circular polarization from the arrays of microstrip-fed dipoles shown in Figure 4, the polarizer circuit of Figure 5 is considered. Since the dipoles produce a predominantly linearly-polarized wave in the y-direction, it is necessary for the polarizer circuit to couple some of the y-directed radiation into the x-directed component, and provide the 90 degree phase differential between these components. One may view the printed circuit of Figure 5 as a step implementation of an oblique dipole capable of being excited by both x and y-directed electric fields. The polarizer substrate's thickness and permittivity (t_p=0.005m, ϵ_p=6.7) are adjusted so that circular polarization is obtained near broadside. In an attempt to set the phase reference at the dipole's apex, the voltage generator in Figure 4 is moved from the back wall junction (z=0) to the center of the y-directed segment of the microstrip line. Also, to calculate the axial ratio, we express the field radiated from the face of the array to each propagating Floquet mode as:

$$\vec{E} = \hat{\theta} |E_\theta| e^{j\beta_\theta} + \hat{\phi} |E_\phi| e^{j\beta_\phi} \tag{29}$$

Then the axial ratio is found from [12] as:

$$AR = 10 Log_{10}\left(\frac{|E|_+}{|E|_-}\right), \tag{30}$$

where

$$|E|_\pm = \left\{ \frac{1}{2}\left\{ |E_\theta|^2 + |E_\phi|^2 \pm \sqrt{|E_\theta|^4 + |E_\phi|^4 + 2|E_\theta|^2|E_\phi|^2 \cos[2(\beta_\phi - \beta_\theta)]} \right\} \right\}$$

In Figures 6 and 7, the E-plane active impedance (Z=R+jX) is calculated for both configurations of Figure 4 at frequencies f=285, 300 and 315 MHz. Both arrays are capable of radiating a CP wave near broadside (see axial ratio curves in Figure 8). However, the performance is good over a small range, generally less than 30 degrees. Note the presence of a feed anomaly, evidenced in the impedance curves, near the location where the

L_d	0.38λ
W_d	0.05λ
W_c	0.02λ
W_b	0.20λ
L_f	0.255λ
W_f	0.010λ
Y_f	0.0675λ
L_c	0.10λ
L_1	0.065λ
L_2	0.045λ
L_s	0.25λ

GROUND PLANE
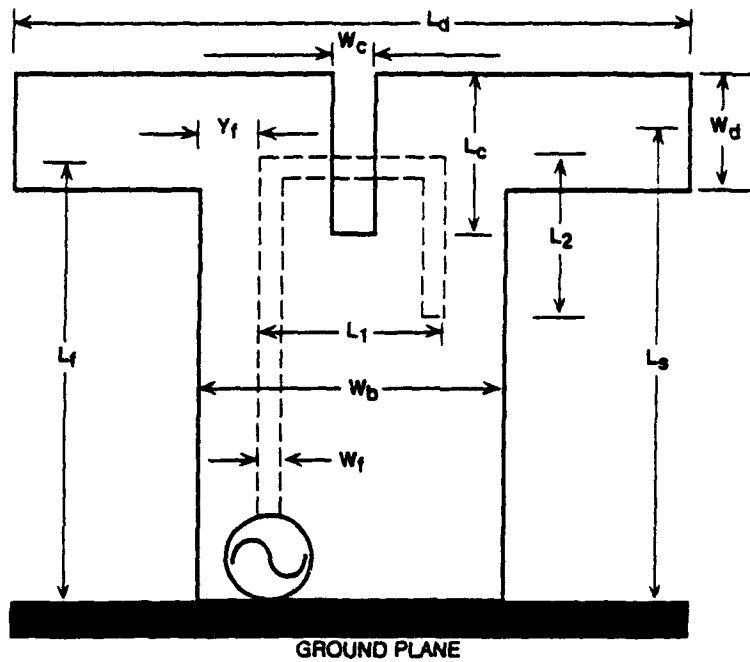
(a) Dipole element with straight arms

L_α	0.16λ
W_α	0.05715λ
W_c	0.02λ
W_b	0.20λ
L_f	0.255λ
W_f	0.010λ
Y_f	0.0675λ
L_c	0.10λ
L_1	0.065λ
L_2	0.045λ
L_s	0.25λ
θ_α	$48.8°$

GROUND PLANE
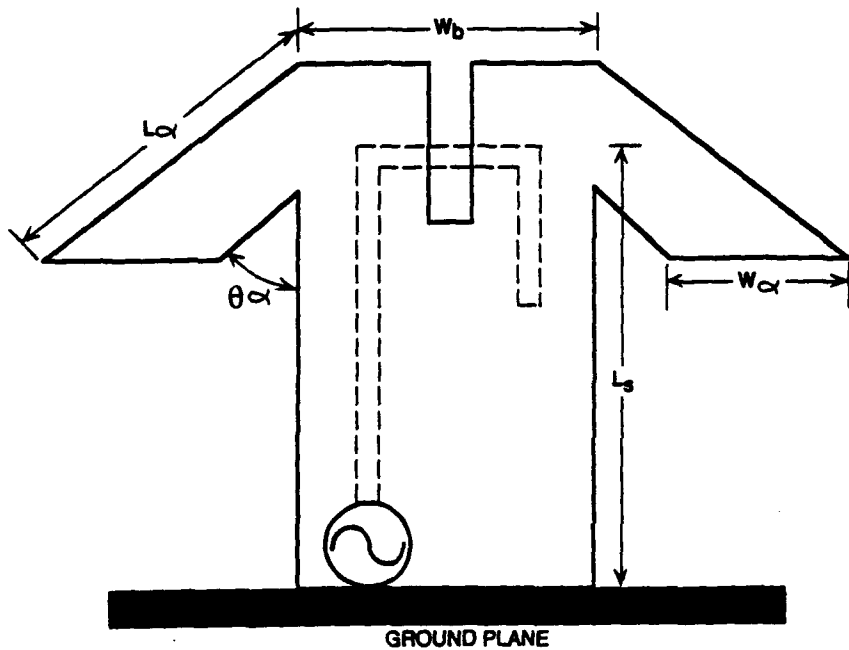
(b) Dipole element with bent arms

Figure 4.   The schematic of the dipole elements fed by coplanar stubs coupled to an excited microstrip line (dashed lines).
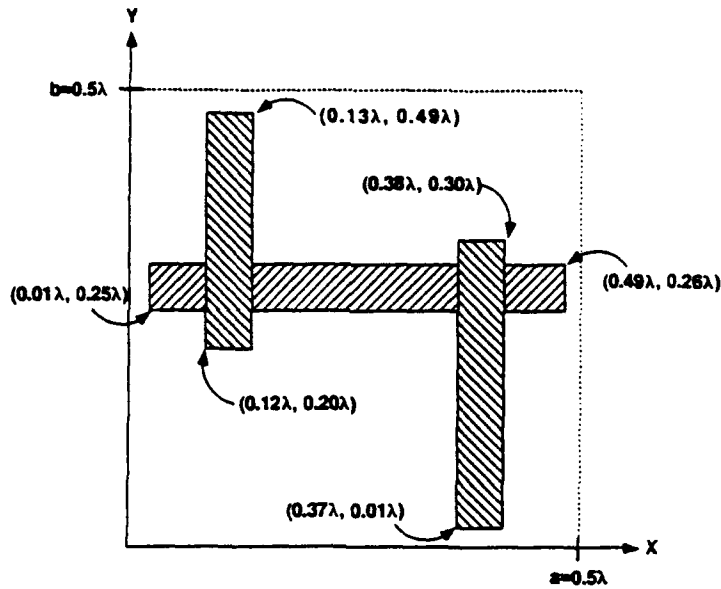
Figure 5.   The sketch of the printed conductors of the polarizer.
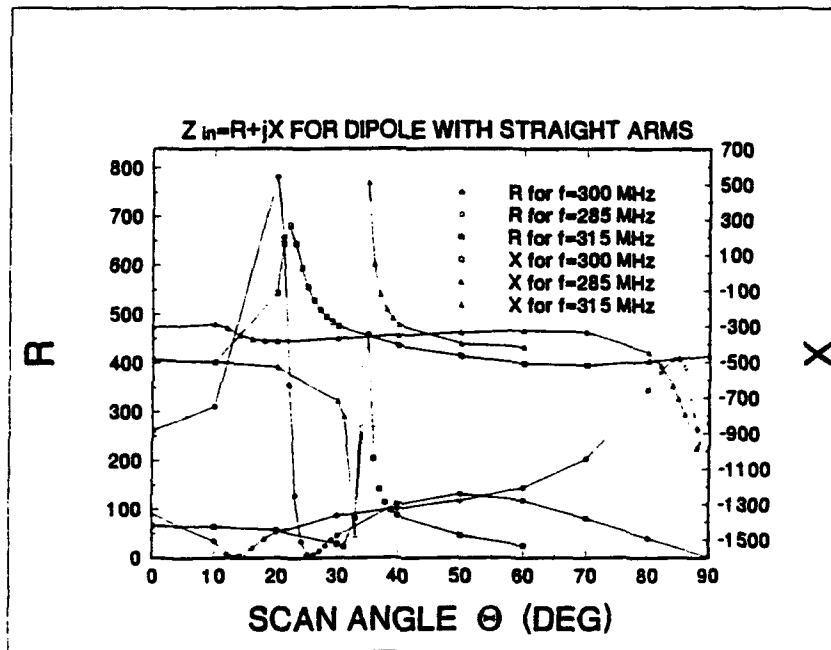
Figure 6.   The element impedance of the array of dipoles with
                 straight arms and covered with a polarizer versus
                 E-plane scan (a=b=0.5λ_o, d=0.3λ_o, t=0.01λ_o, ϵ_r=2.2,
                 f_o=300 MHz).
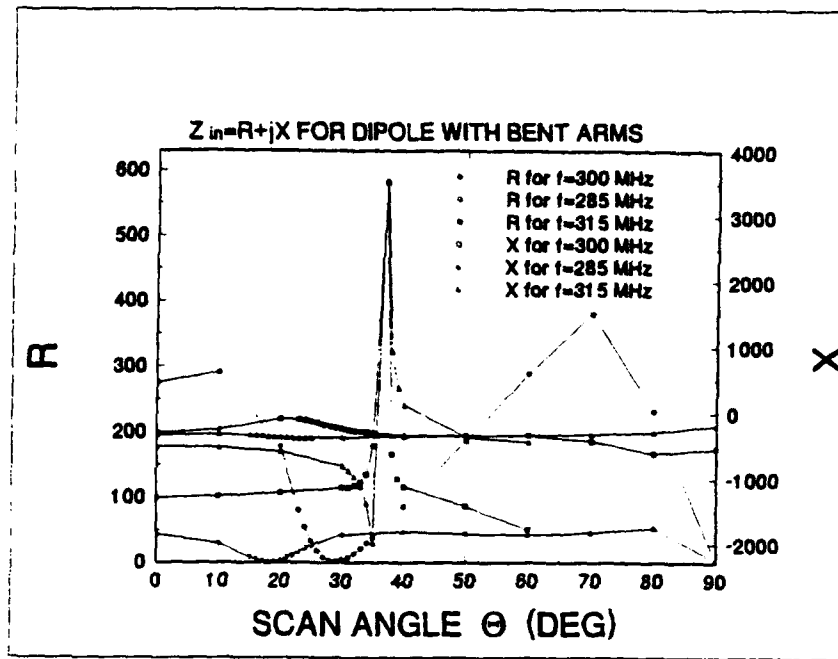
Figure 7.   The element impedance of the array of dipoles with bent arms and covered with a polarizer versus E-plane scan (a=b=$0.5\lambda_o$, d=$0.3\lambda_o$, t=$0.01\lambda_o$, ϵ_r=2.2, f_o=300 MHz).
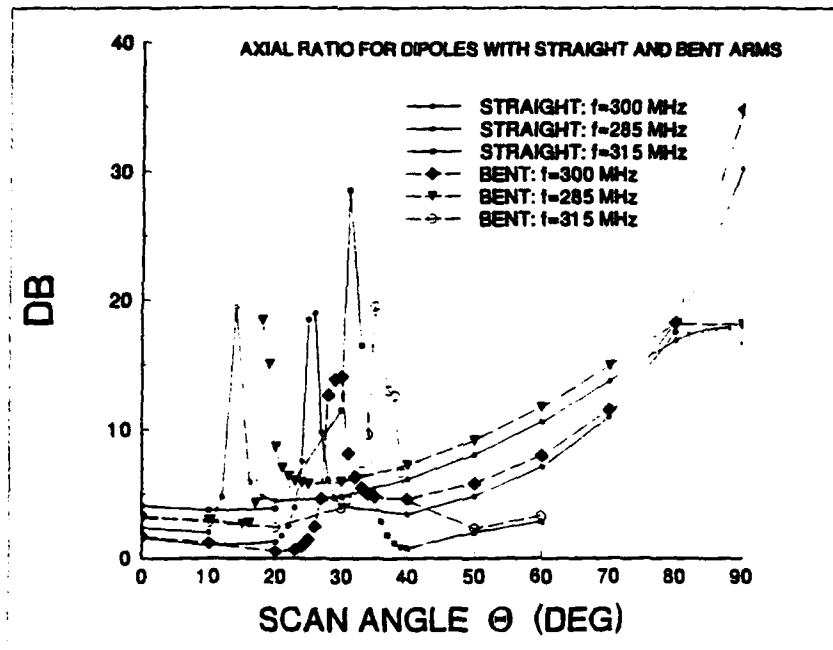
Figure 8.   The axial ratio values of the arrays of dipoles with straight and bent arms and covered with a polarizer versus E-plane scan (a=b=$0.5\lambda_o$, d=$0.3\lambda_o$, t=$0.01\lambda_o$, ϵ_r=2.2, f_o=300 MHz).

axial ratio deteriorates. Because of the feed radiation, both configurations have (at f=300 MHz) an E-plane scan range of about 30 degrees to begin with. The addition of a CP-producing polarizer layer has beneficial effects only within this range. Figure 6, 7 and 8 show also the impedance and axial ratio values for a ±5% shift in frequency.

ACKNOWLEDGEMENT

REFERENCES

[1]   Chu, R-S., and K-M. Lee, "Radiation Impedance of a Dipole Printed on Periodic Dielectric Slabs Protruding over a Ground Plane in an Infinite Phased Array," *IEEE Transactions on Antennas and Propagation*, Vol. AP-35, No. 1, pp. 13-25, January 1987.

[2]   Chu, R-S., "Analysis of an Infinite Phased Array of Dipole Elements with RAM Coating on Ground Plane and Covered with Layered Radome," *IEEE Transactions on Antennas and Propagation*, Vol. AP-39, No. 2, pp. 164-176, February 1991.

[3]   Bayard, J-P. R., M.E. Cooley and D.H. Schaubert, "Analysis of Infinite Arrays of Printed Dipoles on Dielectric Sheets Perpendicular to a Ground Plane," *IEEE Transactions on Antennas and Propagation*, Vol. AP-39, No. 12, pp. 1722-1732, December 1991.

[4]   Bayard, J-P. R., M.E. Cooley and D.H. Schaubert, "A General Method for Treating Arrays of Antennas Printed on Protruding Dielectric Substrates," *IEEE/AP-S International Symposium Digest,* pp. 600-603, 1991.

[5]   Bayard, J-P. R., D.H. Schaubert and M.E. Cooley, "E-Plane Scan Performance of Infinite Arrays of Dipoles Printed on Protruding Dielectric Substrates: Coplanar Feedline and E-Plane Metallic Wall Effects," accepted for publication in the *IEEE Transactions on Antennas and Propagation.*

[6]   Bayard, J-P. R., "Analysis of Infinite Arrays of Microstrip-Fed Dipoles Printed on Protruding Dielectric Substrates and Covered with a Dielectric Radome" submitted for publication in the *IEEE Transactions on Antennas and Propagation.*

[7]   Bayard, J-P. R., "Infinite Arrays of Microstrip-Fed Dipoles with Bent Arms Printed on Protruding Dielectric Substrates", Final Report to be submitted to the Air Force Office of Scientific Research, December 1993.

[8]   Young, L., L.A. Robinson, and C.A. Hacking, "Meander-line Polarizer," *IEEE Transactions on Antennas and Propagation*, Vol. AP-21, pp. 376-378, May 1973.

[9]   Terret, C., J.R. Level, and K. Mahdjoubi, "Susceptance Computation of a Meander-line Polarizer Layer," *IEEE Transactions on Antennas and Propagation*, Vol. AP-32,

pp. 1007-1011, September 1984.

[10]   Chu, R-S., and K-M. Lee, "Analytical Model of a Multilayered Meander-Line Polarizer Plate with Normal and Oblique Plane-Wave Incidence," *IEEE Transactions on Antennas and Propagation*, Vol. AP-35, No. 6, pp. 652-661, June 1987.

[11]   Liu, C-C, J. Shmoys, A. Hessel, J. Hanfling, and J.M. Usoff, "Plane Wave Reflection from Microstrip-Patch Arrays - Theory and Experiment," *IEEE Transactions on Antennas and Propagation*, Vol. AP-33, No. 4, pp. 426-435, April 1985.

[12]   Balanis, C. A., *Antenna Theory: Analysis and Design*, Harper & Row, Publishers, New York, 1982, Sect. 2.12.1, pp. 51.

A MOLECULAR DYNAMICS SIMULATION OF ELECTROMIGRATION

H.F. Helbig
Professor
Department of Physics

T. Bartelt
Graduate Student
Department of Physics

Clarkson University
Potsdam, NY 13699

A MOLECULAR DYNAMICS SIMULATION OF ELECTROMIGRATION

H.F. Helbig
Professor
Department of Physics
Clarkson University

T. Bartelt
Graduate Student
Department of Physics
Clarkson University

Abstract

A flexible model of polycrystalline metallization on integrated circuits was developed, and the construction of a computer simulation to study electromigration in such structures has begun. This work was part of an ongoing effort to determine whether microcircuit failure due to electromigration can be reduced or eliminated. Experiments have revealed that void formations in aluminum interconnections on integrated circuits result from current-induced transport of metal atoms [1]. A computer model is being developed to simulate this effect. The model will permit variation of boundary conditions, including grain size and orientation, thermal effects, crystallite composition, as well as interatomic potentials. The roles of grain boundaries and interstitial atoms are of particular interest since these are parameters that can be controlled, to some degree, during fabrication. The computer code is not complete; specific results are not reported. However, progress was made in the development of the model, and significant portions of the code have been written. A commitment to completion endures regardless of further support.

A MOLECULAR DYNAMICS SIMULATION OF ELECTROMIGRATION

H.F. Helbig

T.Bartelt

Introduction

Microcircuit failure due to current-driven changes in the interconnections (traces) between circuit elements is a serious obstacle to reliable performance. Such failures are due to the transport of metal atoms away from their original, more or less uniform, distribution along the trace; a process called electromigration. Operating temperature, thermal gradients, mechanical stress, current density, grain size and structure, and defects (particularly vacancies and impurities) affect failure rate. Experimental studies to determine the effect of each of these parameters are challenging because of the difficulty of sample preparation and the destructive nature of both the experiment and measurement techniques. A realistic, three-dimensional, polycrystalline model that permits control over individual parameters can be pivotal to the understanding of this phenomenon.

If one represents the interactions between atoms by empirical potential functions (rather than doing *ab initio*, quantum mechanical, many body calculations), it is currently possible to handle the motions of thousands of atoms, in reasonable amounts of computing time, without resort to super-computers. Once the concepts described here are proven on commonly available machines (386/486 PCs and workstations), it will undoubtedly be desirable to move the code to one of the national super-computer facilities to study larger structures. The simulation code is being written in the C programming language so that it will be easy to port to a wide range of computers.

The primary interface to the program is a text file containing information about initial condition, including crystal structure and composition. The output will be positions and velocities of each of the atoms, directed to files at predetermined intervals. Additional modules will be used to analyze the output files to determine such things as diffusion coefficients and failure rates. A graphical interface would also be useful, and is being considered. Linking a graphical interface directly to the main program, however, would severely restrict portability.

The principal objective of this project is to study the migration of metal atoms in a polycrystalline conductor as they react to thermal and "electron wind" processes. That objective is to be accomplished in four steps proceeding, generally in the following sequence.

1. Completion of the simulation program, MDEM

2. Preparation of test sample configurations

3. Collection of simulation data

4. Comparison of simulation results and experimental data

The sections to follow describe these steps in detail.

Step 1. describes the simulation program by subheadings corresponding to the names of the major C-code modules from which MDEM is constructed. The functions that calculate the various forces that act on the atoms represent choices about the fundamental physical mechanisms believed to control atomic migration in a conductor. For that reason those functions contain more extensive discussion than those that attend mainly to bookkeeping chores.

Step 2. demands special comment as it includes an effort complementary to the simulation as originally conceived. In particular, we propose to simulate the deposition of the metallization onto its substrate. This will provide an alternative and, perhaps, more realistic starting configuration for the simulated conductor than so far provided by MDEM.

Step 3. describes the sorts of data that we plan initially to extract from the simulation.

Step 4. is the pivotal, feedback step. There is already a wealth of experimental data that document the onset and evolution of electromigration damage, e.g., void formation and hillock growth [1]. Although such data are microscopic in scale, the smallest features are still gross on the scale of atoms. The chief utility of the simulation will be to show the connection between processes occurring at the atomic level and the experimental data. We hope that the ability of the simulation to make this connection will suggest new lines of experimental effort at Rome Lab, and ultimately provide both fundamental and practical information that can be used to reduce circuit failures due to electromigration.

Technical Description

1. Completion of MDEM

The main functional modules of MDEM are listed below along with a description of the services they provide and an indication of their current status.

input_configuration   (outlined; under development)

This reads and parses the configuration input file provided by the user. The configuration file contains all the information about the atoms required for the simulation. Apart from data relevant to the entire sample (e.g., temperature), this information is organized as a set of crystallite descriptions. The data format is very general, utilizing a system of "tags" so that the configuration file can contain documentation that is ignored by the parser, and so that it is easy to allow for additional input parameters, should they become necessary, without invalidating earlier configuration files.

Parameters currently anticipated for the configuration file are the system temperature, and for each crystallite, atom species, impurity species and concentration, vacancy concentration, the shape, size, orientation and position of the crystallite, the character of each of its boundary planes (are the atoms near that plane free or pinned, and/or do they act as thermostats?), the lattice vectors defining the shape, size, orientation and position of the primitive unit cell, and the constants that define the interaction energy between pairs of atoms and between the atoms and the electron gas.

Choosing the parameters for the configuration file is the present solution to the "sample preparation" problem. This and an alternative solution, simulation of the film deposition process itself, are discussed in section 2, below.

make_crystallite   (code written)

This uses the information gleaned by input_configuration to initialize the atomic data array, crystallite by crystallite. The atomic data array keeps track of the positions and velocities of the entire set of atoms in the sample. This routine must do a substantial amount of bookkeeping and geometric analysis to assure that the user's input data is self-consistent. Its construction consumed much of the two month Summer Research Program.

modify_crystallite   (code outlined)

This is actually a sub-module of make_crystallite that reprocesses the atomic data array to create vacancies, impurities or to perform other operations that might be desired as part of the sample initialization.

monitor   (code to be written)

This is the module that calls for integration of the equations of motion and monitors the elapsed time or other cues that have been requested by the user to trigger the collection of data.

integrate   (code written)

This performs a numerical integration of Newton's equations of motion ($F_i = m_i a_i$) for each of the atoms in the sample using forces that are described under the next code module. An efficient algorithm (4th order Runge-Kutta with adaptive step-size) has been adapted for use in MDEM [2]. The integration routine takes the system from its current state (the positions and velocities of all the atoms at time t) to its state at time $t + \Delta t$ under the forces assumed to control the atomic motion.

Adaptive step-size controls the size of Δt so that the error of the numerical integration is maintained within acceptable bounds; small enough that the output is free of computational artifacts and large enough that the evolution of the system proceeds at a reasonable rate. It is expected that the natural time scale for the system motion will be on the order of the period of lattice vibrations, i.e., about 100 fs, so that Δt will necessarily be somewhat smaller than this.

Rather than include the force model in the integration routine, it is embodied in a separate routine so that new force models can be substituted easily.

emt_force   (code outlined)

This provides the force exerted on each atom according to the recently developed "effective medium theory. Forces associated with thermal control of the sample and with the electron wind force presumably responsible for electromigration will be supplied by routines similar to this, but are discussed under this module for compactness of presentation.

In order that a molecular dynamics simulation of a metal properly reproduce the elastic and thermal properties (e.g., Young's modulus, thermal expansion coefficient) characteristic of real metallic systems, it has been found necessary by several researchers [3,4,5,6,7] to describe the system energy by functions more sophisticated than pair potentials. This is because a major portion of the cohesive energy in metal systems arises from the interaction of the metal ions

with the "gas" of nearly free conduction electrons rather than from the direct interaction of the ions with their neighbors. On this account, we have begun to adapt the effective medium theory of Jacobsen et al.[3], as extended by Häkkinen and Manninen [6] to MDEM. Fortunately, this recent literature provides a background of work on aluminum and copper that will be directly applicable to the electromigration problem.

Preliminary tests of the code will be made using simple pair potentials of the Lennard-Jones or Morse type.

It is important to provide the simulation with a means to add or remove energy from the system. In nature, this is accomplished by exchanges of energy between the system and its environment, but simulations cannot afford the luxury of nearly infinite heat reservoirs. Hoover [8] has shown a simple technique for temperature control that properly preserves the fluctuations characteristic of the canonical ensemble distributions of statistical mechanics. This technique was employed by Valkealahti and Manninen [7] in their work on the melting of copper clusters.

In short, the idea is to endow some of the atoms in the simulation with an additional, velocity-dependent force that behaves like a friction force except that the friction coefficient may be either positive or negative. By linking the friction coefficient to the average system kinetic energy (temperature), energy may introduced or extracted from the system as required to stabilize the system temperature. The obvious location for "thermostat" atoms is at the face of the crystallite intended to simulate the substrate since that face would in nature serve as the main heat sink for the conductor.

For numerical experiments involving thermal effects alone, this thermostat mechanism can be used to maintain thermal equilibrium. For experiments also involving the I^2R heating associated with an electron wind, the thermostats will allow the maintenance of steady-state conditions including thermal gradients. Thus, the simulation may be able to complement the work by Rome Lab's Dr. Mark Levi on the importance of thermal gradients to the electromigration process.

Finally, the passage of an electric current through the sample will be simulated by adding random momentum increments (biased appropriately in the direction of the electron drift) to the metal atoms in the sample. It is anticipated that these momentum increments, when applied to atoms immediately upstream from vacancies, will prove to be the agent responsible for the preferential migration of metal atoms along the direction of the electron flow and of vacancies in the opposite direction.

It is difficult in laboratory experiments to discover whether this electromigration scenario is accurate. The reason is that in normal circuit operation the process is slow. In terms of the atomic picture, the significant collisions are rare, and they are accompanied by vast numbers of electron-phonon collisions that are responsible for Joule heating

but are relatively ineffectual as a cause of metal migration. Experimental attempts to accelerate the migration-stimulating collisions are accompanied by heating effects that alter the conditions under which electromigration occurs in practice.

The simulation offers the possibility of separating the effects of collisions between electrons and vacancy-proximate atoms from those that merely add heat to the lattice. It seems reasonable, at least during the nucleation stages of void formation, that these two mechanisms are independent and their effects additive. If this is so, it may be possible to accelerate this atom-plus-vacancy migration mechanism without materially increasing the Joule heating.

This could be done, for example, by applying a heavy dose of electron-wind to randomly selected atoms during each *time step*, *moving the atoms* according to Newton's laws, and then scaling the speed of each atom down to prevent the average kinetic energy (temperature) from rising. If atoms next to vacancies are, indeed, the primary transport objects, this method would reveal that fact without increasing the system temperature. The result will be to compress the time scale on which effects of this electron-wind model emerge while controlling the sample temperature independently.

Whether this artificial method of temperature control will produce the same migration effects as result from prolonged current flow at lower current densities is a question that can be explored with the simulation.

randn & gausdevn   (code completed)

These are (*pseudo*)random number generators, called upon by many routines. Although generic *linear congruential* random number generators, supplied with most compilers, might be adequate for some of the simulation's requirements (e.g., assigning random initial velocities and displacements to atoms in the system), they are always suspicious, and undoubtedly insufficient for electron wind-lattice interactions. The algorithms chosen here are adaptations of the work of Press *et al* [2]. Randn produces (*pseudo*)random numbers with uniform distribution, gausdevn yields a Gaussian distribution.

Additional routines that are not linked with MDEM include:

comb_data   (code to be written)

This combs through the atomic data array collecting information for such calculations as mean square displacements, radial distribution functions, and density profiles.

view3d (under development)

This presents a perspective view of the sample atoms so that the user may form visual impressions of the sample. Naturally, this is where portability breaks down since graphics standards vary with platforms. This important task, however, is not as computationally intensive as the simulation itself, so it will not be necessary to adapt it to every machine. A program that allows one to visually scan through the sample is being developed for some of the most popular operating systems.

2. Preparation of test sample configurations

The first step in simulating a conducting line is to create the line. In the manufacture of microcircuits the line is prepared, first by depositing a film of metal atoms onto a substrate, and then by etching away unwanted regions of the film. During the deposition, islands of metal grow around nucleation sites randomly located on the substrate. Each island may be thought of as a randomly oriented and imperfect crystallite or grain. The islands grow until adjacent grains meet, and the resulting interfaces become grain boundaries of a polycrystalline film. What remains after the etching stage is a polycrystalline conductor whose transverse dimensions are comparable in size with the grains.

Preparation of a simulated polycrystalline conductor may be accomplished in at least two ways. The starting configuration may be tailored to test various idealized arrangements of grain boundaries, vacancy and impurity concentrations. Alternatively, it is possible to simulate the island growth process itself.

Completed components of MDEM provide for the first alternative. The user of the program can assemble a polycrystalline sample by specifying the shape, position and orientation of each grain. Furthermore, each grain may be specified to contain atoms of a given species and be interspersed with vacancies and impurity atoms of other species. While most grains will contain "metal" atoms, some may be populated with atoms bound more tightly than those simulating metals, and be deployed as substrate and passivation structures.

Simulation of the deposition process may be of considerable value if it can provide more realistic starting configurations. We hope to be able to include this as an additional facility.

3. Collection of simulation data

The simulation will necessarily maintain a record of the current state of the system in microscopic detail; that is, the positions and velocities of all the atoms and of the time elapsed. In order to interpret these data as they evolve in time, it will be necessary to obtain periodic summaries of various macroscopic statistics. Preliminary parameters that will be calculated from the position/velocity data include the elastic moduli and thermal expansion coefficients of the modeled metal. Quantities more closely related to the electromigration process include system energy, density and temperature gradients and fluctuations, and diffusion coefficients.

4. Comparison of simulated and experimental data

The data collected from the simulation may be displayed as tables, graphs and visualizations. After ascertaining that the simulation properly reproduces the known mechanical and thermal properties of the metal, it will be of major interest to determine the effects of the orientation of grain boundaries, relative to the direction of current flow, on the transport of atoms and on the concentration of vacancies. Are these effects consistent with observed electromigration phenomena? We anticipate that graphics to present three dimensional visualizations will be crucial to these comparisons.

Final comment

The generality of this simulation scheme is noteworthy. In addition to the experiments already indicated, other applications are easily imagined. Studies of thermal and mechanical stress effects could be made in conjunction with electromigration or separately. Looking even farther afield, nothing inherently restricts the modeled system to the solid state. Studies of interfaces between (or among) any of the phases could easily be accommodated.

A project of this magnitude could not have been completed in the twelve weeks of the Summer Research Program. Consequently, specific results are not reportable. We have, instead, presented an outline of the project, and indicated the progress made toward completion. These accomplishments have led to a the negotiation of a contract to complete the simulation at Rome Lab between September, 1993 and July 1994. The results of preliminary studies are to be reported at the 1993 Fall Meeting of the Materials Research Society [9].

References

[1]   See, for example, *Phenomenological Observations on Electromigration*,
        R.W. Thomas and D.W. Calabrese,
        21st Annual Proceedings IRPS, p. 1, (1983).
        and the numerous micrographs obtained in association with this work.

[2]   *Numerical Recipes*,
        W.H. Press, B.P. Flannery, S.A. Teukolsky and W.T. Vetterling,
        Cambridge University Press.

[3]   *Interatomic Interactions in the Effective Medium Theory*,
        K.W. Jacobsen, J.K. Nørskov and M.J. Puska,
        Phys. Rev. B35, 7423 (1987).

[4]   *Monte Carlo Calculation of the Thermal Expansion Coefficient of Al*,
        P. Stoltze, K.W. Jacobsen and J.K. Nørskov,
        Phys. Rev. B36, 5035 (1987).

[5]   *Disordering and Melting of Aluminum Surfaces*,
        P. Stoltze, J.K. Nørskov and U. Landman,
        Phys. Rev. Lett. 61 440 (1988).

[6]   *The Effective-medium Theory Beyond the Nearest-neighbor Interaction*,
        H. Häkkinen and M. Manninen,
        J. Phys.: Condens. Matter 1 9765 (1989).

[7]   *Melting of Copper Clusters*,
        S. Valkealahti and M. Manninen,
        Computational Materials Science, 1, 123 (1993).

[8]   *Canonical Dynamics: Equilibrium Phase-space Distributions*,
        William G. Hoover,
        Phys. Rev. A31 1695 (1985).

[9]   *A Molecular Dynamics Simulation of Electromigration*,
        H.F. Helbig, T. Bartelt, L.H. Walsh and J.V. Beasock
        Submitted to MRS Fall Meeting, Boston MA, 29 Nov. - 3 Dec., 1993.

Estimating The Number Of Defects

Under Imperfect Environmental Stress Screen Levels

Lifang Hsu

Associate Professor

Department of Mathematics

Le Moyne College

Syracuse, NY 13214

Estimating The Number Of Defects

Under Imperfect Environmental Stress Screen Levels

Lifang Hsu

Associate Professor

Department of Mathematics

Le Moyne College

Abstract

A fixed sample size procedure is proposed to quantify the initial and refined estimates of the defect of electronics density for Environmental Stress Screening (ESS) plans. The idea of group testing, i.e., testing units in batches instead of individually, where each test indicates whether the test batch contains only good parts or whether it contains at least one defective, is applied to the problem of estimating the probability, π, of an arbitrary unit being defective. Five estimators are given with their root mean square error, or asymptotic variance. An example and table of procedure parameters are given to illustrate the proposed method.

Estimating The Number Of Defects

Under Imperfect Environmental Stress Screen Levels

Lifang Hsu

I. Introduction

This report proposes a statistical methodology to quantify the initial and refined estimates of the number of defects resident in electronic equipment subject to Environmental Stress Screening (ESS). ESS plans, which are applied during the development and production phases, can yield significant improvements in field reliability and reductions in field maintenance costs. One parameter important in the economical design of ESS plans is the degree of contamination; i.e., the proportion of parts with latent defects in an otherwise well designed equipment. This proportion governs the ESS process and determines the rate at which the purification proceeds. The ESS methodology, as described in MIL-HDBK-344 (1993) estimates the number of incoming defects based on the equipment complexity and the reliability levels of the various parts and processes. This is accomplished by describing the equipment in terms of the quantity of items within various part-process categories and multiplying these by an expected fraction defective for each of the part-reliability grades and process types. The fraction defectives are determined using lookup tables found in MIL-HDBK-217 (1991) and have different values depending upon the end application operating environment. Because MIL-HDBK-217 (1991) defect density data is generic, it may not be sufficiently current for certain programs. In this report, we propose a fixed sample size procedure to provide the estimates of: (1) part defect density, (2) equipment defect density, and the (3) proportion of part and manufacturing defects. Since the number of defects in equipment depends on the quantity and quality of parts and workmanship characteristics, we assume that there are k independent and identically distributed parts in the equipment (the procedure could also be used and generalized for equipment with multiple part types). The quality of parts is characterized by the probability, π, of a part being defective. The defective probability π is an unknown parameter and its value depends upon the end application operating environment. The proposed experiment is to apply base line screening tests with known sensitivity η and specificity θ to a given m equipments. The value η is the probability that an equipment is defective given that at least one part is defective. It is determined from the product of precipitation efficiency and detection efficiency. The precipitation efficiency for a given stress type, level, and duration is determined by using lookup tables or solving equations that are provided in MIL-HDBK-344 (1993). The test detection efficiency is determined based on the type of testing performed and whether testing is performed during exposure to stress. The value θ is the probability that the equipment is not defective given that all the parts are good. The value of θ is determined [Barlow, Bazorsky, and Wechsler

(1991)] by the equation $(T/(T+ t))^k$, where T is the expected life time of a good part and t is the screen duration. Based on an analysis of screening fallout data and subsequent failure analysis, an improved environmental stress screening level with a new sensitivity η′ and a new specificity θ′ will be generated. Note that the base line stress levels should always be higher than the application stress. To account for non-relevent type failures, i.e., false alarms, or non-operational failures, the defective equipments from the base line screening will then be subjected to the improved stress screening test. Since the majority of parts and workmanship operations are defect free, only some small fraction will contain flaws or defects that can be measured as a defect density in defects per million. The sum of the defects from parts and workmanship operations determines the total defects per equipment. The model and procedure developed here is similar to that arising in group testing. The ideas of group testing, i.e., testing parts in equipments instead of individually, where each test indicates whether the tested equipment contains only good parts or whether it contains at least one defect, is applied to the problem of estimating the probability π of an arbitrary part being defective. The ideas of group testing were first used by [Dorfman (1943)]. However, the original purpose of Dorfman's procedure was to minimizes the number of tests needed to identify all carriers of a disease in a large population. Another aspect of the group testing problem was in the estimation of the frequency of a disease or of some property, which was studied by [Sobel and Elashoff (1975)]. In that paper, they assume that the classification process is perfect. For this effort we assume that the classification process is imperfect.

This report is organized in the following manner: Section 2 describes the problem and mathematical model in detail, Section 3 investigates the estimation procedures and properties of the estimator, Section 4 gives an example and tables from procedure parameters to illustrate the proposed method.

II. Description of the problem and the mathematical method

When estimating the number of defects resident in an equipment, a preliminary estimate can be based on the results of screening tests. A random sample of m equipments taken from the production line are subject to a baseline stress screening test.The initial estimate of percentage defect can be derived by using the results of the base line stress screening test. Based on an analysis of the screening fallout data and failure analysis, an improved stress screening test will be developed. Those equipments classified as defective are given an improved stress screening test. The estimate can then be refined based on the results of both the base line stress screening and the improved stress screening tests.

Before proceeding with the description of the model, the parameters that determine the accuracy and the predictive value of the tests are defined:

k - the number of parts in an equipment;

m - the number of equipments to be tested;

π - the probability of a part being defective.

$B_i = 1$ if ith equipment is defective after base line stress screening test,
   0 otherwise;

$I_i = 1$ if ith equipment is defective after improved stress screening test,
   0 otherwise;

$C_i = 1$ if ith equipment contains at least one latent defect,
   0 otherwise;

$\eta = P(B_i = 1 \mid C_i = 1)$ - the probability that the latent defect will not escape from the
   screen, i.e. , the sensitivity of the base line stress screening test;

$\theta = P(B_i = 0 \mid C_i = 0)$ - the probability that a good part will survive the screen, i.e.
   the specificity of the base line stress screening test;

$\eta' = P(I_i = 1 \mid C_i = 1)$ - the sensitivity of the improved stress screening test;

$\theta' = P(I_i = 0 \mid C_i = 0)$ - the specificity of the improved stress screening test;

We assume the base line stress screening test and improved stress screening test are independent. Their sensitivity and specificity do not depend on the number of parts in the equipment. We base our inferences of the initial estimate on the statistic:

$$B = \sum_{i=1}^{m} B_i ,$$ the number of defective equipments on base line stress screening test.

The random variable B, has a binomial distribution:

9-5

$$f(b) = \binom{m}{b} p^b(1-p)^{m-b}, \quad b = 0,1,...,m, \quad 0 \leq p \leq 1. \tag{1}$$

where $p = P(B_i = 1) = P(B_i = 1, C_i = 1) + P(B_i = 1, C_i = 0)$

$$= P(C_i = 1)P(B_i = 1 \mid C_i = 1) + P(C_i = 0)P(B_i = 1 \mid C_i = 0) \tag{2}$$

$$= (1 - (1-\pi)^k)\eta + (1 - \pi)^k(1-\theta).$$

We base our inferences of the refined estimate on the following statistics:

$x = \sum\limits_{i=1}^{m} B_i I_i$, the number of defective equipment on both screening tests;

$y = \sum\limits_{i=1}^{m} B_i(1 - I_i)$, the number of defective equipment on base line stress screening test only;

$z = \sum\limits_{i=1}^{m} (1 - B_i)$, the number of defective free equipment on base line stress screening test.

The random variables x,y,z have a trinomial distribution:

$$f(x,y,z) = \binom{m}{x\,y\,z} p_1{}^x p_2{}^y p_3{}^z, \quad \sum_{i=1}^{3} p_i = 1, \ x + y + z = m \tag{3}$$

where $p_1 = P(B_i = 1, I_i = 1) = P(B_i=1, I_i=1, C_i=1) + P(B_i=1, I_i=1, C_i=0)$

$$= P(C_i = 1)P(B_i=1|C_i=1)P(I_i=1|C_i=1) + P(C_i=0)P(B_i=1|C_i=0)P(I_i=1|C_i=0)$$

$$= [1-(1-\pi)^k]\eta\eta' + (1-\pi)^k(1-\theta)(1-\theta'),$$

$$p_2 = P(B_i = 1, I_i = 0) = P(B_i=1, I_i=0, C_i=1) + P(B_i=1, I_i=0, C_i=0) \tag{4}$$

$$= P(C_i = 1)P(B_i=1|C_i=1)P(I_i=0|C_i=1) + P(C_i=0)P(B_i=1|C_i=0)P(I_i=0|C_i=0)$$

$$= [1-(1-\pi)^k]\eta(1-\eta') + (1-\pi)^k(1-\theta)\theta'.$$

$$p_3 = P(B_i = 0) = P(B_i=0, C_i=1) + P(B_i=0, C_i=0)$$

$$= P(C_i = 1)P(B_i=0|C_i=1) + P(C_i=0)P(B_i=0|C_i=0)$$

$$= [1-(1-\pi)^k](1-\eta) + (1-\pi)^k\theta.$$

The proportion of equipment being defective on the base line stress screening test is defined as

$$P(B_i = 1) = (1 - (1-\pi)^k)\eta + (1 - \pi)^k(1-\theta). \tag{5}$$

The proportion of part defects given that the equipment is defective on the base line stress screening test is defined as

$$P(C_i = 1 \mid B_i = 1) = P(C_i = 1, B_i=1)/P(B_i = 1)$$

$$= (1 - (1-\pi)^k)\eta /[(1 - (1-\pi)^k)\eta + (1 - \pi)^k(1-\theta)]. \tag{6}$$

The proportion of manufacturing defects given that the equipment is defective on the base line stress

screening test is defined as

$$P(C_i = 0| B_i = 1) = P(C_i = 0, B_i=1)/P(B_i = 1)$$
$$= (1-\pi)^k \theta /[(1 - (1-\pi)^k)\eta + (1 - \pi)^k(1-\theta)]. \qquad (7)$$

The proportion of equipment being defective on the improved stress screening test is defined as

$$P(I_i = 1) = (1 - (1-\pi)^k)\eta' + (1 - \pi)^k(1-\theta'). \qquad (8)$$

The proportion of part defects given that the equipment is defective on the improved stress screening test is defined as

$$P(C_i = 1| I_i = 1) = P(C_i = 1, I_i=1)/P(I_i = 1)$$
$$= (1 - (1-\pi)^k)\eta' /[(1 - (1-\pi)^k)\eta'+ (1 - \pi)^k(1-\theta')]. \qquad (9)$$

The proportion of manufacturing defect given that the equipment is defective on the improved stress screening test is defined as

$$P(C_i = 0| I_i = 1) = P(C_i = 0, I_i=1)/P(I_i = 1)$$
$$= (1-\pi)^k (1-\theta')/[(1 - (1-\pi)^k)\eta' + (1 - \pi)^k(1-\theta')]. \qquad (10)$$

Our inferences are based on the sensitivities (η,η') and specificities (θ,θ') of the base line stress screening and improved stress screening tests when applied to m equipments of k identical parts. For the equipment with multiple part types, the same procedure can be applied to different part types separately.

III. Estimation Procedures and Properties of the Estimator

Initial Estimation

While the probability of the m observed test results is a function of a number of parameters $(\eta,\theta,m,k,$ and $\pi)$, in the procedure developed here we assume all parameters except π are known. The probability distribution of the observation is the likelihood function $L(b|\pi)$ which equals the binomial distribution stated in (1). The maximum likelihood estimator (MLE) of π is easily determined since $L(b|\pi)$ is twice differentiable.

An initial estimator of π, π_{I1}, and its asymptotic variance are obtained by solving the following equations:

$$\frac{dlogL(b|\pi)}{d\pi}\Big|_{\pi_{I1}} = [(b/p)(dp/d\pi)] - ([m-b]/[1-p])(dp/d\pi) = 0 \qquad (11)$$

$$aVar(\pi_{I1}) = - \{ E [\frac{d^2logL(b|\pi)}{d\pi^2}] \}^{-1}$$

$$= \{E[(b/p^2)(dp/d\pi)^2 - (b/p)(d^2p/d\pi^2) + ((m-b)/(1-p)^2)(dp/d\pi)^2$$
$$+ ((m-b)/(1-p))(d^2p/d\pi^2)]\}^{-1} \tag{12}$$

where p is given in (2) and aVar denotes the variance of the asymptotic distribution of π_{I1} [Freeman (1963)]. The solutions to equations (11) and (12) are

$$\pi_{I1} = 1 - ([\eta - (b/m)]/(\eta+\theta-1))^{1/k} \tag{13}$$

$$aVar(\pi_{I1}) = \{[\eta - (\eta+\theta-1)(1-\pi)^k][1-\eta + (\eta+\theta-1)(1-\pi)^k]\}/\{mk^2(\eta+\theta-1)^2(1-\pi)^{2k-2}\} \tag{14}$$

For the binomial distribution it is known that the MLE is admissible with respect to the given loss [Johnson (1971)]. Hence π_{I1} is admissible with respect to the square error loss. In Table I values of initial estimate π_{I1} are listed for m = 100, η = .99, θ = .90, and k = 1,2,4,8,16,32,64,72, and 100. We note that the values for b (the observed number of defective equipment) given in Table I are greater than 10 and less than 99. Since π_{I1} in (13) exists only when $m-m\theta < b < m\eta$.

Another estimator π_{I2} can be obtained by taking the first term of the MacLaurin series of π_{I1}, expanded about b = 0.

$$\pi_{I1} = 1 - ([\eta - (b/m)]/(\eta+\theta-1))^{1/k} = 1 - (\eta/(\eta+\theta-1))^{1/k}(1 - b/(km\eta) -(k-1)b^2/2(km\eta)^2 -...)$$

$$\pi_{I2} = 1 - (\eta/(\eta+\theta-1))^{1/k}(1 - b/(km\eta)) \tag{15}$$

When k = 1, $\pi_{I1} = \pi_{I2}$. The expected value, bias, and variance of π_{I2} are

$$E(\pi_{I2}) = 1 - (\eta/(\eta+\theta-1))^{1/k}[((k-1)\eta + (\eta+\theta-1)(1-\pi)^k)/(k\eta)]$$

$$Bias(\pi_{I2}) = 1 - \pi - (\eta/(\eta+\theta-1)^{1/k}[((k-1)\eta + (\eta+\theta-1)(1-\pi)^k)/(k\eta)]$$

$$Var(\pi_{I2}) = \{(\eta/(\eta+\theta-1))^{2/k}[\eta - (\eta+\theta-1)(1-\pi)^k][1 -\eta + (\eta+\theta-1)(1-\pi)^k]\}/(mk^2\eta^2)$$

In Table II values of the root mean square error (RMSE) of π_{I2} and $(aVar(\pi_{I1}))^{1/2}$ are listed for m = 100, (η = .99 ,θ = .90),(η = .95 ,θ = .85), and (η = .99 ,θ = .99). We note that the RMSE associated with π_{I2} is smaller than the standard error for the MLE π_{I1} for small values of π.

The proportions $P_{BI1}(P_{BI2})$ of equipment being defective on the base line stress screening test can be estimated by replacing $\pi_{I1}(\pi_{I2})$ for π in (5). The solutions are:

$$P_{BI1} = (1 - (1 - \pi_{I1})^k)\eta + (1 - \pi_{I1})^k(1-\theta) = b/m \tag{16}$$

$P_{BI2} = (1 - (1 - \pi_{I2})^k)\eta + (1 - \pi_{I2})^k(1-\theta) = \eta[1 - (1 - (b/km\eta)^k]$ (17)

Similarly, the estimates of proportions of parts and manufacturing defects given that the equipment is defective on the base line stress screening test can be obtained by the following equations:

P_{BI1}(part defect) $= \eta(m\theta - m + b)/[b(\eta + \theta - 1)]$ (18)

P_{BI1}(manufacturing defect) $= [m(m\eta - b)(1 - \theta)]/[b(\eta + \theta - 1)]$ (19)

P_{BI2}(part defect) $= [(km\eta)^k(\eta + \theta - 1) - (km\eta - b)^k\eta]/[(\eta + \theta - 1)[(km\eta)^k - (km\eta - b)^k]]$ (20)

P_{BI2}(manufacturing defect) $= [(km\eta - b)^k(1 - \theta)]/[(\eta + \theta - 1)[(km\eta)^k - (km\eta - b)^k]]$ (21)

Refined Estimation

The joint probability of the observed test results is a function of $(\eta,\theta,\eta',\theta',m,k,$ and $\pi)$, we assume all parameters except π are known. The joint probability distribution of the observations is the likelihood function $L(x,y,z|\pi)$ which equals the trinomial distribution stated in (3).

The maximum likelihood estimator π_R and its asymptotic variance can be obtained by solving the following equations:

$$\left.\frac{d\log L(x,y,z|\pi)}{d\pi}\right|_{\pi_{I1}} = [(x/p_1)(dp_1/d\pi)] + [(y/p_2)(dp_2/d\pi)] + [(z/p_3)(dp_3/d\pi)] = 0 \quad (22)$$

$$\mathrm{Var}(\pi_R) = -\left\{ E\left[\frac{d^2\log L(x,y,z|\pi)}{d\pi^2} \right] \right\}^{-1}$$

$$= \{E[(x/p_1^2)(dp_1/d\pi)^2 - (x/p_1)(d^2p_1/d\pi^2) + (y/p_2^2)(dp_2/d\pi)^2 - (y/p_2)(d^2p_2/d\pi^2)$$
$$+ (z/p_3^2)(dp_3/d\pi)^2 - (z/p_3)(d^2p_3/d\pi^2) \}^{-1} \quad (23)$$

where p_1, p_2, and p_3 are given in (4).

The solution to equation (22) and (23) are:

$$\pi_R = 1 - \{[-b + (b^2 - 4ac)^{1/2}]/(2a)\}^{1/k} \quad (24)$$

where $a = -m(\eta+\theta-1)[(1-\theta)(1-\theta')-\eta\eta'][(1-\theta)\theta'-(1-\eta')\eta]$

$b = x[\eta(1-\eta')-\theta'(1-\theta)][(1-\theta)(1-\theta')(1-\eta)-\eta\eta'\theta] + y\{(1-\theta)(1-\theta')-\eta\eta'][\eta\theta(1-\eta')$

$\qquad -\theta'(1-\theta)(1-\eta)] - m\eta(\eta+\theta-1)[(1-\eta')[(1-\theta)(1-\theta')-\eta\eta'] + \eta'[(1-\theta)\theta'-\eta(1-\eta')]$

$c = \eta\{x(1-\eta')[\eta\eta'\theta-(1-\theta)(1-\theta')(1-\eta)] + y\eta'[\eta(1-\eta')\theta-\theta'(1-\theta)(1-\eta)] - m\eta\eta'(1-\eta')(\eta+\theta-1)\}$

$aVar(\pi_R) = \{mk^2(1-\pi)^{2k-2}[(\eta\eta'-(1-\theta)(1-\theta'))^2/(\eta\eta' -(\eta\eta'-(1-\theta)(1-\theta'))(1-\pi)^k) +$

$\qquad (\eta(1-\eta') -\theta'(1-\theta))^2/(\eta(1-\eta')-(\eta(1-\eta') -\theta'(1-\theta))(1-\pi)^k) +$

$\qquad (1-\eta-\theta)^2/((1-\eta) -(1-\eta-\theta)(1-\pi)^k)]\}^{-1}$ \hfill (25)

For the trinomial distribution it is known that the MLE is admissible with respect to the square error loss [Alam(1979)], hence π_R is also admissible.

The proportion P_R of equipment being defective on the improved stress screening test can be estimated by replacing π_R for π in (8). The solution is

$P_R(equipment) = (1 - (1-\pi_R)^k)\eta' + (1 - \pi_R)^k(1-\theta').$ \hfill (26)

The estimates of the proportion of part $P_R(part)$ and manufacturing $P_R(manufacturing\ defect)$ defects, given that the equipment is defective on the improved stress screening test can be obtained by the following equations:

$P_R(part\ defect) = (1 - (1-\pi_R)^k)\eta'/[(1 - (1-\pi_R)^k)\eta'+ (1 - \pi_R)^k (1-\theta')].$ \hfill (27)

$P_R(manufacturing\ defect) = (1-\pi_R)^k (1-\theta)(1-\theta')/[(1 - (1-\pi_R)^k)\eta'\eta + (1 - \pi_R)^k(1-\theta)(1-\theta')].$ \hfill (28)

We will assume $\eta'=1, \theta'=1$ to do the further analysis for the properties of the refined estimators. Under this assumption, an estimator π_{R1} and its asymptotic variance $aVar(\pi_{R1})$ are obtained as following:

$\pi_{R1} = 1 - \{ [-(m+y)(1-\eta)+(m-x)\theta]/2m(\eta+\theta-1)] - \{[[(m-x)\theta-(m-y)(1-\eta)]^2+4xy(1-\eta)\theta]/$

$\qquad [2m(\eta+\theta-1)]\}^{1/2}\}^{1/k}.$ \hfill (29)

$aVar(\pi_{R1}) = - \{ E[\underline{\dfrac{d^2 logL(x,y,z|\pi)}{d\pi^2}}] \}^{-1}$

$\qquad = \{E[(x/p_1^2)(dp_1/d\pi)^2-(x/p_1)(d^2p_1/d\pi^2)+(y/p_2^2)(dp_2/d\pi)^2-(y/p_2)(d^2p_2/d\pi^2)$

$\qquad +(z/p_3^2)(dp_3/d\pi)^2 - (z/p_3)(d^2p_3/d\pi^2) \}^{-1}$

$\qquad = \{mk(1-\pi)^{k-2}[(\eta[(k-1)+(1-\pi)^k])/(1-(1-\pi)^k) + (1-\theta) - [(\eta+\theta-1)[(k-1)(1-\eta)-$

$\qquad (\eta+\theta-1)(1-\pi)^k]]/[1-\eta+(\eta+\theta-1)(1-\pi)^k]\}^{-1}$ \hfill (30)

A simpler, moment kind of estimator, $\pi_{R2} = x/k m \eta$, can be obtained by noting that $E(x|m) = \eta[1-(1-\pi)^k]$, solving for π, and taking the first term of the MacLaurin series of $\pi = 1 - (1 - (x/\eta m))^{1/k}$, expanded about x=0. The expected value, bias and variance of π_{R2} are

$$E(\pi_{R2}) = [1-(1-\pi)^k]/k,$$

$$Bias(\pi_{R2}) = [1-k\pi-(1-\pi)^k]/k,$$

$$Var(\pi_{R2}) = [1-(1-\pi)^k][1-\eta(1-(1-\pi)^k)]/(k^2 m \eta).$$

In Table III, values of $(aVar(\pi_R))^{1/2}$ are listed for m = 100, (η = .99 ,θ = .90, η'=.95, and θ' =.95), and (η = .99, θ = .99, η' =.95, and θ' = .95). Values of the root mean square error(RMSE) of π_{R2} and $(aVar(\pi_{R1}))^{1/2}$ are listed for m = 100, (η = .99 ,θ = .90), and (η = .99 ,θ = .99). We note that the PMSE associated with simple estimator π_{R2} is larger then the standard error for the MLE π_{R1} for large values of π. However, for smaller π the simple estimator is quite good.

IV. Numerical Example

Consider a random sample of 100 equipments with 16 independent identical parts in each equipment. We will use the proposed procedure to provide the initial and refined estimates of : (1) part defect density, (2) equipment defect density, and (3) proportion of parts and manufacturing defects. Suppose the expected life time of a good part is 150 times the base line screening duration, and the base line screening performs according to the following factors:

(i) Temperature cycling screening is performed 15 cycles at 20°C/min over a 100°C range.

(ii) Functional and parametric type of testing is performed with detection value = .99.

(iii) Testing performed concurrently with stress; i.e. detection value is 1.0.

(iv) Probability of detecting, isolating and removing the defect is 1.0.

Then, precipitation efficiency = $1 - \exp[-(.0017(100+.6)^{.6}(\ln(20+2.718)]^3(15)]$

$$= .99999$$

sensitivity = η = .99999 x .99 x 1 x 1 $\approx$ .99

specificity = θ = $(150t/(150t+t))^{16}$ $\approx$ .90

Assume 30 equipments are observed defective, then from (13), (16), (18) and (19), we obtain:

the initial estimate of part defect density $\pi_{II} = .0157822$.

the initial estimate of equipment defect density P_{BI}(equipment) = .30.

the initial estimate of proportion of part defect density P_{BI}(part defect) = .74.

the initial estimate of proportion of manufacturing defect density

P_{BI}(manufacturing defect) = .26.

If 5 of the 30 defective equipments were observed during the first 4 cycles, then an improved environmental stress screening level will be generated with new precipitation efficiency .96293, new sensitivity .95, and new specificity .96. From (24),(26),(27) and (28), we have:

the refined estimate of part defect density $\pi_R = .0182053$

the refined estimate of equipment defect density P_R(equipment) = .28.

the refined estimate of proportion of part defect density P_R(part defect) = .86.

the refined estimate of equipment defect density P_R(equipment) = .14.

The proposed procedure allows the characterization of defect density to be expressed as a function of environmental stress screening level. It will be verified by the engineers at Rome Laboratory, then incorporated into the appropriate documents.

Acknowledgements

TABLE I

Initial Estimate π_{11} when m=100, η=.99, and θ=.90:

b	k=1	k=2	k=4	k=8	k=16	k=32	k=64	k=72	k=100
11	.011236	.005633	.002820	.001411	.000705	.000353	.000176	.000156	.000113
12	.022471	.011299	.05665	.002837	.001419	.000710	.000355	.000315	.000227
13	.033707	.016998	.008535	.004276	.002140	.001070	.000535	.000476	.000342
14	.044943	.022730	.011430	.005731	.002869	.001436	.000718	.000638	.000459
15	.056179	.028495	.014350	.007201	.003607	.001805	.000903	.000802	.000578
16	.067415	.034295	.017297	.008686	.004352	.002178	.001089	.000968	.000697
17	.078651	.040131	.020271	.010187	.005106	.002556	.001279	.001137	.000818
18	.089887	.046001	.023271	.011704	.005869	.002939	.001470	.001307	.000941
19	.101124	.051909	.026300	.013237	.006640	.003326	.001664	.001479	.001065
20	.112360	.057853	.029357	.014788	.007421	.003717	.001860	.001654	.001191
21	.123595	.063835	.032443	.016355	.008211	.004114	.002059	.001830	.001318
22	.134831	.069855	.035560	.017941	.009011	.004515	.002260	.002009	.001447
23	.146067	.075915	.038706	.019544	.009820	.004922	.002464	.002190	.001577
24	.157303	.082014	.041884	.021166	.010639	.005334	.002670	.002374	.001710
25	.168539	.088155	.045094	.022807	.011469	.005751	.002879	.002560	.001843
26	.179775	.094337	.048336	.024467	.012309	.006173	.003091	.002748	.001979
27	.191011	.100562	.051612	.026148	.013160	.006602	.003306	.002939	.002117
28	.202247	.106830	.054923	.027849	.014023	.007036	.003524	.003133	.002256
29	.213483	.113142	.058268	.029571	.014896	.007476	.003745	.003329	.002398
30	.224719	.119500	.061650	.031315	.015782	.007922	.003969	.003528	.002542
31	.235955	.125903	.065068	.033081	.016679	.008374	.004196	.003730	.002687
32	.247191	.132354	.068525	.034870	.017589	.008834	.004426	.003935	.002835
33	.258427	.138854	.072020	.036683	.018512	.009299	.004660	.004143	.002985
34	.269663	.145402	.075555	.038519	.019448	.009772	.004898	.004355	.003137
35	.280889	.152002	.079131	.040381	.020398	.010251	.005139	.004569	.003292
36	.292135	.158653	.082750	.042268	.021362	.010738	.005383	.004787	.003449
37	.303371	.165357	.086412	.044182	.022340	.011233	.005632	.005008	.003608
38	.314607	.172115	.090118	.046122	.023333	.011735	.005885	.005232	.003770
39	.325843	.178929	.093870	.048091	.024342	.012246	.006141	.005461	.003935
40	.337079	.185800	.097669	.050089	.025366	.012764	.006402	.005693	.004102
41	.348315	.192730	.101518	.052116	.026407	.013291	.006668	.005929	.004272
42	.359550	.199719	.105416	.054175	.027464	.013828	.006938	.006169	.004445
43	.370786	.206770	.109366	.056265	.028540	.014373	.007212	.006413	.004622
44	.382022	.213885	.113368	.058388	.029633	.014928	.007492	.006662	.004801
45	.393258	.221064	.117426	.060546	.030745	.015492	.007776	.006915	.004984
46	.404494	.228310	.121541	.062738	.031877	.016067	.008066	.007173	.005170
47	.415730	.235625	.125714	.064967	.033029	.016653	.008361	.007435	.005359
48	.426966	.243010	.129948	.067234	.034202	.017249	.008662	.007703	.005552
49	.438202	.250468	.134245	.069540	.035396	.017857	.008969	.007976	.005749
50	.449438	.258001	.138607	.071887	.036613	.018477	.009281	.008254	.005950
51	.460674	.265612	.143036	.074276	.037854	.019100	.009601	.008538	.006155
52	.471910	.273302	.147534	.076709	.039119	.019755	.009926	.008828	.006364
53	.483146	.281074	.152105	.079188	.040410	.020413	.010259	.009124	.006578
54	.494382	.288932	.156751	.081714	.041727	.021086	.010599	.009427	.006796
55	.505618	.296887	.161476	.084290	.043072	.021773	.010946	.009736	.007019

b	k=1	k=2	k=4	k=8	k=16	k=32	k=64	k=72	k=100
56	.516854	.304913	.166281	.086917	.044467	.022476	.011301	.010052	.007247
57	.528090	.313043	.171171	.089599	.045851	.023194	.011665	.010375	.007481
58	.539326	.321270	.176149	.092337	.047286	.023929	.012037	.010707	.007720
59	.550562	.329598	.181219	.095135	.048756	.024682	.012809	.011046	.007965
60	.561798	.338032	.186386	.097994	.050260	.025454	.013209	.011394	.008216
61	.573034	.346573	.191652	.100918	.051800	.026244	.013209	.011750	.008474
62	.584270	.355228	.197023	.103910	.053379	.027056	.013620	.012116	.008738
63	.595506	.364001	.202505	.106974	.054999	.027888	.014042	.012492	.009010
64	.606742	.372897	.208102	.110113	.056661	.028744	.014476	.012878	.009289
65	.617977	.381920	.213820	.113332	.058369	.029623	.014923	.013276	.009576
66	.629214	.391078	.219665	.116634	.060124	.030528	.015382	.013685	.009872
67	.640449	.400375	.225645	.120026	.061930	.031460	.015855	.014106	.010176
68	.651685	.409818	.231767	.123511	.063790	.032420	.016343	.014541	.010491
69	.662921	.419415	.238039	.127096	.065706	.033411	.016847	.014989	.010815
70	.674157	.429174	.244469	.130787	.067684	.034435	.017368	.015453	.011150
71	.685393	.439102	.251069	.134592	.069726	.035493	.017907	.015933	.011497
72	.696629	.449209	.257847	.138517	.071838	.036588	.018464	.016430	.011857
73	.707865	.459509	.264816	.142572	.074025	.037724	.019043	.016945	.012230
74	.719101	.470001	.271990	.146765	.076292	.038903	.019644	.017481	.012617
75	.730337	.480709	.279382	.151108	.078646	.040128	.020269	.018037	.013020
76	.741573	.491643	.287008	.155612	.081094	.041404	.020920	.018618	.013440
77	.752809	.502817	.284888	.160290	.083643	.042734	.021600	.019223	.013878
78	.764045	.514248	.303041	.165159	.086303	.044125	.022311	.019857	.014337
79	.775281	.525955	.311490	.170235	.089085	.045581	.023056	.020521	.014818
80	.786517	.537958	.320263	.175538	.092001	.047110	.023839	.021218	.015323
81	.797753	.550281	.329389	.181092	.095064	.048719	.024663	.021953	.015855
82	.808989	.562952	.338904	.186922	.098291	.050416	.025534	.022729	.016418
83	.820225	.576001	.348848	.193060	.101702	.052214	.026457	.023552	.017014
84	.831461	.589465	.359270	.199544	.105318	.054123	.027438	.024427	.017648
85	.842697	.603385	.370226	.206417	.109167	.056160	.028486	.025361	.018325
86	.853933	.617812	.381787	.213735	.113284	.058343	.029610	.026364	.019053
87	.865169	.632806	.394035	.221562	.117709	.060696	.030823	.027445	.019837
88	.876404	.648438	.407074	.229083	.122494	.063247	.032140	.028620	.020690
89	.887640	.664799	.421035	.239102	.127706	.066032	.033580	.029905	.021623
90	.898876	.682001	.436086	.249058	.133431	.069102	.035170	.031324	.022653
91	.910112	.700187	.452448	.260033	.139787	.072523	.036944	.032907	.023804
92	.921348	.719551	.470426	.272281	.146936	.076385	.038951	.034699	.025106
93	.932584	.740355	.490446	.286169	.155115	.080823	.041263	.036763	.026608
94	.943820	.762977	.513150	.302254	.164688	.086045	.043990	.039199	.028381
95	.955056	.788000	.539566	.321447	.176257	.092397	.047318	.042173	.030547
96	.966296	.816403	.571518	.345414	.190935	.100520	.051590	.045992	.033332
97	.977528	.850094	.612823	.377764	.211181	.111845	.057580	.051349	.037243
98	.988764	.894000	.674424	.429407	.244624	.130876	.067732	.060438	.043893

TABLE II
Comparison of errors associated with initial estimators when m=100:

π	k	RMSE(π_{12})	$(aVar(\pi_{11}))^{1/2}$	RMSE(π_{12})	$(aVar(\pi_{11}))^{1/2}$	RMSE(π_{12})	$(aVar(\pi_{11}))^{1/2}$
		$\eta=.99, \theta=.90$		$\eta=.95, \theta=.85$		$\eta=.99, \theta=.99$	
.2	1	.050338	.050338	.057811	.057811	.041268	.041268
	2	.040459	.034664	.047886	.038761	.032148	.030663
	4	.065978	.026554	.074147	.029590	.054959	.024518
	8	.105932	.024509	.112164	.028883	.097015	.023079
	16	.145351	.036706	.149131	.057585	.139843	.034473
.1	1	.043989	.043989	.052604	.052604	.031671	.031671
	2	.026057	.027683	.031083	.031883	.020893	.022512
	4	.025134	.018923	.030325	.021191	.018998	.016657
	8	.036288	.014342	.040827	.015965	.030102	.013209
	16	.054294	.012957	.057542	.015122	.049629	.012190
.08	1	.042324	.042324	.051265	.051265	.028966	.028966
	2	.024219	.025956	.028764	.030260	.018979	.020358
	4	.019909	.017233	.024329	.019448	.014981	.014834
	8	.025966	.012560	.029954	.011980	.020684	.011428
	16	.038754	.010541	.041738	.015913	.034514	.009867
	32	.053940	.012016	.055811	.084269	.051211	.011339
.05	1	.039505	.039505	.049037	.049037	.024043	.024043
	2	.021400	.023047	.025675	.027601	.015670	.016501
	4	.014098	.014460	.017327	.016677	.010735	.011714
	8	.013781	.009850	.016721	.011040	.010238	.008651
	16	.018912	.007431	.021289	.008268	.015659	.006835
	32	.027466	.006649	.029112	.007733	.025083	.006253
	64	.036543	.009056	.037519	.013416	.035113	.008523
.02	1	.036221	.036221	.046510	.046510	.017294	.017294
	2	.018407	.019604	.022794	.024590	.010942	.011217
	4	.010211	.011186	.012562	.013573	.007140	.007602
	8	.006501	.006837	.008111	.007984	.004834	.005334
	16	.005587	.004522	.006920	.005109	.004060	.003879
	32	.006928	.003280	.007999	.003646	.005499	.002979
	64	.009899	.002729	.010667	.003094	.008805	.002551
.01	2	.017280	.018287	.021818	.023485	.008590	.008720
	4	.009076	.009849	.011330	.012414	.005449	.005654
	8	.005121	.005637	.006377	.006849	.003565	.003830
	16	.003299	.003447	.004150	.004027	.002427	.002687
	32	.002844	.002278	.003529	.002575	.002057	.001954
	64	.003499	.001651	.004040	.001836	.002776	.001499
.001	16	.002064	.002266	.002642	.002927	.000997	.001021
	32	.001094	.001210	.001388	.001531	.000625	.000651
	64	.000610	.000677	.000769	.000831	.000406	.000435
	72	.000556	.000617	.000701	.000753	.000379	.000408
	100	.000439	.000481	.000554	.000577	.000312	.000342
	128	.000376	.000403	.000475	.000477	.000272	.000302

TABLE III

Comparison of errors associated with refine estimators when m=100:

π	k	$(aVar(\pi_R))^{1/2}$ $\eta=.99, \theta=.90$ $\eta'=.95, \theta'=.95$	$(aVar(\pi_{R1}))^{1/2}$ $\eta=.99, \theta=.90$ $\eta'=1.0, \theta'=1.0$	$RMSE(\pi_{R2})$ $\eta=.99, \theta=.90$ $\eta'=1.0, \theta'=1.0$	$(aVar(\pi_R))^{1/2}$ $\eta=.99, \theta=.99$ $\eta'=.95, \theta'=.95$	$(aVar(\pi_{R1}))^{1/2}$ $\eta=.99, \theta=.99$ $\eta'=1.0, \theta'=1.0$	$RMSE(\pi_{R2})$ $\eta=.99, \theta=.99$ $\eta'=1.0, \theta'=1.0$
.2	1	.041970	.040251	.040251	.040863	.040251	.040251
	2	.031433	.030235	.031386	.030564	.030235	.031386
	4	.025331	.024305	.053857	.024495	.024305	.053857
	8	.024083	.022929	.096092	.023074	.022932	.096092
	16	.036568	.034079	.139264	.034472	.034232	.139264
.1	1	.031814	.030167	.030167	.030794	.030167	.030167
	2	.022878	.021929	.020360	.022272	.021930	.020360
	4	.017965	.016414	.018436	.016598	.016414	.018436
	8	.013638	.013090	.029481	.013195	.013091	.029481
	16	.012709	.012112	.049144	.012187	.012111	.049144
.08	1	.028940	.027277	.027277	.027894	.027277	.027277
	2	.020619	.019712	.018415	.020053	.019712	.018415
	4	.015158	.014573	.014544	.014756	.014573	.014544
	8	.011766	.011309	.020164	.011410	.011309	.020164
	16	.010250	.009798	.034077	.009863	.009798	.034077
	32	.011923	.011259	.050925	.011338	.011269	.050925
.05	1	.023668	.021910	.021910	.022495	.021910	.021910
	2	.016566	.015699	.014966	.016028	.015699	.014966
	4	.011900	.011404	.010428	.011584	.011404	.010428
	8	.008860	.008522	.009912	.008619	.008522	.009912
	16	.007054	.006772	.015332	.006827	.006773	.015332
	32	.006516	.006211	.024835	.006251	.006212	.024835
	64	.009013	.008444	.034962	.008522	.008466	.034962
.02	1	.016258	.014072	.014072	.014597	.014072	.014072
	2	.010939	.010002	.009804	.010291	.010002	.009804
	4	.007589	.007146	.006752	.007309	.007146	.006752
	8	.005400	.005160	.004678	.005251	.005160	.004678
	16	.003963	.003809	.003925	.003858	.003809	.003925
	32	.003066	.002947	.005358	.002974	.002947	.005358
	64	.002651	.002534	.008692	.002552	.002535	.008692
.01	2	.008195	.007089	.007018	.007355	.007089	.007018
	4	.005512	.005039	.004891	.005185	.005039	.004891
	8	.003823	.003600	.003373	.003682	.003600	.003373
	16	.002720	.002599	.002347	.002645	.002599	.002347
	32	.001996	.001918	.001987	.001943	.001918	.001987
	64	.001543	.001483	.002704	.001497	.001483	.002704
.001	16	.000945	.000797	.000783	.000830	.000797	.000783
	32	.000628	.000566	.000548	.000583	.000566	.000628
	64	.000431	.000403	.000380	.000413	.000403	.000431
	72	.000406	.000381	.000356	.000390	.000381	.000356
	100	.000344	.000325	.000299	.000332	.000325	.000299
	128	.000304	.000290	.000262	.000295	.000290	.000262

References

Alam, K.(1979). Estimation of Multinomial Probabilities. The Annals of Statistics . Vol. 7. No. 2, 282-283.

Barlow, R. E., Bazovsky, I. and Wechsler, S.(1990). Classical & Bayes Approaches to Environmental Stress Screening (ESS): A comparison. 1990 Proceedings Annual Reliability and Maintainability Symposium, 81-84.

Dorfman, R. (1943). The Detection of Defective Members of Large Populations. Ann. Math. Stat. 14, 436-440.

Freeman, H. (1963) . Introduction to Statistical Inference. Addison-Wesley Publishing Company,Inc.,Reading, Mass.

Johnson, B. (1971). On the Admissible for Certain Fixed Sample Binomial Problems. Ann. Math. Statist 42, 1579-1587.

Mil-HDBK-344 (USAF) (1993). Revised Military Handbook: Environmental Stress Screening (ESS) of Electronic Equipment.

Mil-HDBK-217 (USAF) (1991). Reliability Prediction of Electronic Equipment.

Sobel, M. and Elashoff, R. M. (1975) Group Testing With A New Goal, Estimation. Biometrika 63, 181-193.

Characterization of Pure and Doped $Bi_{12}SiO_{20}$

Wallace B. Leigh,
Assistant Professor, Division of Electrical Engineering,
Alfred University
26N Main, Alfred, New York 14802

Final report for:
Summer Faculty Research Program

work performed at
Rome Laboratories, Solid State Directorate
RL/ERX, Hanscom AFB MA 01730

Sponsored by:
Air Force Office of Scientific Research
Bolling Air Force Base, Washington, D.C.

September, 1993

Characterization of Pure and Doped $Bi_{12}SiO_{20}$

Wallace B. Leigh,

Assistant Professor, Division of Electrical Engineering,

Alfred University

Abstract

This reports describes research performed at Rome Laboratories, Hanscom AFB, MA under a summer research program. Two separate areas of research were investigated. The first concerned defect studies of pure and doped $Bi_{12}SiO_{20}$ (BSO) grown at Rome, and the characterization of this material by way of photoconductivity and optical absorption measurements. This is part of an ongoing effort to understand the photorefractive properties of BSO, particularly the photorefractive response at longer (larger than 500nm) wavelengths and how to enhance this response. Photoconductivity measurements were made on undoped BSO grown by Czochralski (Cz) and Hydrothermal transported material, as well as material doped with various impurities. Undoped Cz BSO exhibited excellent photoconductive response under a wide spectral range. A peak was observed in the photoconductivity spectrum, identifying a resonance absorption at 510nm. Hydrothermal material, however, exhibited only minor photoconductive response only at a wavelength corresponding to the bandgap energy of BSO. BSO samples doped with transition metals were observed to lose the majority of their photoconductive response as the impurity apparently kills photo-conductivity. An attempt was made to change the charge state of transition metals by irradiation in an effort to revive the photoconductivity. Various degrees of success in enhancing photoconductivity in the red region of the spectrum was met by doping with Al and B, and co-doping these samples with V and Mn. Vastly different photoconductivity results were obtained between Cz and Hydrothermal material doped with the same impurity. Various photoconductive quenching was observed in many of the samples, particularly in the doped hydrothermal material. $Bi_{12}TiO_{20}$ (BTO) material transported by the hydrothermal technique was observed to have excellent photoconductive response, unlike hydrothermal BSO. The second area of research investigated at Rome under this program involved the study of optical waveguides in BSO. The refractive index of BSO grown by various techniques was measured, and the fabrication of waveguides using ion implantation and liquid phase epitaxy was investigated.

Characterization of Pure and Doped $Bi_{12}SiO_{20}$

Wallace B. Leigh,

I. Introduction

Photorefraction is a name given to a third-order nonlinear optical effect observable in certain insulators and semi-insulators. Photorefraction is a method of writing volume holograms which are dynamic; that is, volume gratings which erase after cessation of the writing beams. Time constants of the gratings may range from several milliseconds to several months. Thus photorefracting crystals can be used for a variety of suitable applications of non-linear mixing including active spatial filtering, phase conjugation by way of degenerate four-wave mixing, optical processing devices such as optical oscillators, and as a technique useful for non-destructive materials analysis.

In this study, photorefraction and general defect properties were observed in cubic $Bi_{12}SiO_{20}$ (BSO). Introductory studies of BSO on single crystals grown by Czochralski and by the hydrothermal method are a part of a large effort to relate defect properties of BSO to its photorefractive behavior.[1] Emphasis of the study is to isolate impurity/defect phenomena in respect to photorefractive quality and demonstrate the photorefractive technique as a method of nondestructive and contactless testing of this material.

Photorefraction is unique in that it is a nonlinear effect the sensitivity of which does not depend on the absolute intensity of the laser which writes the grating. Thus the technique should be observable with small (less than 100mW) power lasers. In, fact, what would be most desirable would be the ability to tailor a crystal for any desirable photorefraction application, for example applications involving low-power red or infrared sources. The advantages of using these sources for photorefraction applications are obvious. in terms of cost and ease of portability of the device.

Doping studies at Rome Laboratories of BSO were introduced as a method of altering the spectral dependence of absorption and photoconductivity. This is especially desirable for fabricating photorefractive samples from hydrothermal BSO, as undoped hydrothermal material is not normally photorefracting.

There is also an interest in preparing waveguides in photorefracting materials. Photorefracting waveguides are easier to interface into certain optoelectronic applications than bulk photorefracting devices. An example would be an application involving light-guided fiber optics. The speed of

photorefractive response should also be higher in photorefractive waveguides due to the higher optical field density for the same optical power.

II.   Photoconductivity

An optimum photorefractor should be fairly transparent at the wavelength of interest. to allow for the grating to be written in the full volume of the material, but at the same time not too transparent as phoconductivity is also dependent on the absorption. There is a trade-off. therefore to make use of extrinsic photoconductivity with the proper amount of absorption without severely attenuating the optical beam as it passes through the sample. To examine an elective sample for photorefraction requires a study of both the spectral dependence of absorption and photoconductivity.

Ohmic contacts for TSC and photoconductivity measurements were made by applying indium strips to the polished surfaces of samples 1 cm on a side. Samples were heated in air at 150°C for 15 minutes to alloy the contacts. Samples were then mounted on a sample holder kept at room temperature. Very low (typically 100 V/cm) electric fields were used in TSC and photoconductivity to minimize the influence of internal space charge generated electric fields on the electrical measurements.

Spectral photoconductivity and absorption measurements were made with a 1/4 m monochrometer with a 2 nm bandpass, and a 1000W Xenon arc lamp as a source. Spectral measurements were made from long to short and from short to long wavelengths to ensure no photochromatic transitions were taking place. Figure 1 shows spectral dependence of the DC photoconductivity for two crystals grown by the different processes. In both cases, the photocurrent flux has been normalized to the incident light power density which averaged ~5mW/cm^2. The Cz sample exhibits photoconductivity over a wide range, from 600nm to well over the band edge, which contributes to useful photorefraction over a wide range of pumping source wavelengths. A peak is observed in the DC photoconductivity for all undoped Cz samples, illustrating perhaps, an energy-dependent capture cross-section. In each case the peak. which represents an absorption resonance, is centered close to 510nm. The hydrothermal material is only slightly photoconducting at an energy which, from absorption data, is associated with the band-to-band transition. Even under intrinsic illumination, the photoconductivity of the hydrothermal material is still two orders of magnitude smaller than for Cz grown BSO.

We have also observed that not only the optically induced conductivity but also the dark conductivity is different in hydrothermal and Cz material. BSO is known to possess thermally activated current instabilities due to charge injection from contacts[2]. These instabilities are most often observed at temperatures above 100°C or at high applied fields. We have also observed a thermally activated dark

conductivity in both Cz and hydrothermal BSO with an activation energy of 1.2 eV for both material types. The thermally activated dark conductivity is, however, three orders of magnitude smaller in hydrothermal as in Cz BSO.

We observed significantly smaller optical- and thermal-induced conductivities in the hydrothermal material. A lower defect content also appears to inhibit the conduction processes for the hydrothermal material, in terms of missing traps responsible for a hopping conduction process. A hopping conduction process has been proposed as a conduction mechanism in BSO[3,4]. The hopping model assumes conduction takes place via a light induced mechanism from a filled to an empty neighboring trap rath via band transport from a photoexcited carrier. The identity of the traps involved in hopping conduc. in BSO is not yet known.

III. Photoconductivity of doped BSO and BTO.

Photoconductivity measurements were also undertaken to measure the spectral response of the photo-induced current of BSO doped with a variety of impurities. The purpose here is to investigate the possibility of changing the shape of the photoconductivity spectral response curve and enhancing the photoconductivity in specific areas of the response curve. Table I shows doped samples investigated for photoconductive response. Cz-BSO co-doped with Mn and Al appeared green in color. Sample used was full of veils but both sides were polished. Samples of Cz BSO doped only with Mn were reddish brown and clear, although not very transparent. Iron compound BFO is black and has shown no photoconductiviy.

Table I. Doped BSO used in photoconductivity analysis.

Sample	Impurity
BSO 110	none
BSO 160	Mn+Al
BSO 168	Mn only
BS45	Cr (hydrothermal)
BSO 128	Al+Cr
BSO 127	La
BSO150	Al

Table I. (cont)

BSO183	V+B
BSO139	V+Al
BSO 55	none (from hydro charge)
BT2	Hydrothermal BTO
	Ge implanted BSO
BFO	iron compound

Results

In all cases, doping BSO reduced the overall magnitude of the photoconductivity, as could be expected. Figure 2 shows results of selected samples of Cz BSO containing various dopants and co-dopants. Samples of undoped Cz BSO showed excellent photoconductivity , while those doped with transition metals show that doping has killed the pc in that material. A weak photoconductive shoulder appears in the CZ-BSO:Al,Mn sample. It is difficult to compare absolute scales between various samples, however, it appears that at least the Al and La doped material should be investigated again for photorefraction using red pump beams. Of the other samples in Table I, each exhibited only extremely weak photoconductivity.

Of the the samples, the co-doped Al-Mn sample appears to have the highest resistivity and is difficult to make ohmic contacts to. An effort may be undertaken to improve contacts to this material.

The four doped samples of Fig. 2 have been sent to be irradiated and will be irradiated with 10K initially of gamma rays and stored in dry ice. While irradiating samples does not always increase the photorefraction efficiency at longer wavelengths, It does not effect the efficiencies at shorter wavelengths and speeds of erasure can be enhanced for erasure by a long-wavelength probe.

Samples of BTO grown by hydrothermal transport, while not suitable for transmission measurements, could be used for photoconductivity analysis. Figure 3 shows a PC scan of a hydrothermal BTO sample. It is interesting to compare this spectra with the hydrothermal BSO of Fig, 1, which contains no color and little photoconductivity.

Evidence of photoconductive bleaching could be observed in chrome doped hydrothermal material. A PC spectra for sample BS 60 is shown in Fig. 4. While scanning into the blue and UV region of the spectrum, the photoconductivity would disappear. Heating the sample on a hot plate for a few minutes would restore the photoconductivity to the sample. Bleaching rates were quite high for this sample, and a time constant could not be measured with the scanning equipment used.

IV. Refractive Index Measurements

Refractive index measurements were made on various samples of BSO prepared by Czochralski and Hydrothermal transport. Motivation of this work is the lack of color in the hydrothermal material. Since the Cz BSO absorbs with a 500nm absorption edge and the hydrothermal does not, it is expected that the refractive index near the 500nm region may be higher in the Czochralski than in the Hydrothermal material. Thin films of yellow BSO on transparent hydrothermal substrates should make excellent

Table II Results of refractive index measurements of BSO. Measurements are estimated to be within ± 0.03

Wavelength	Cz BSO		Hydrothermal BSO	
	Sample 1 Nut for BSO50	Sample 2 BSO 110E	Sample 1 110h	Sample 2 BS 60A
480 nm	2.71	2.67	2.67	2.66
546 nm	2.62	2.59	2.59	2.59
620 nm	N/A	2.53	N/A	N/A

photorefractive waveguides. If this is the case, then the hydrothermal material should prove to be excellent substrate for the growth of thin films of yellow BSO by liquid-phase epitaxy.

Refractive index measurements were made using the minimum deviation of refracted angle of a prism.[5] Two prism samples of apex angle 9° were made in each of Czochralski and hydrothermal material. A Hg/Cd arc lamp was used as the source, and a high-resolution goniometer was used to detect the refracted angle. Care was taken to align the prism faces and several measurements were made of apex angle and refracted angle for each sample.

Results of these measurements are shown in Table II. Sample 1 of each material type were prisms made by the author at Rome while sample2 of each were made by a commercial supplier. Because the red line of the Hg/Cd lamp is the weakest line, measurements at 620nm could not always be made for all samples.

Measured refractive indexes are centered around 2.6, which is the value determined from absorption at infrared wavelengths. BSO does not show a large amount of energy dependent dispersion at the three optical energies used for these measurements. Contrary to what was predicted, not much difference is observed between the hydrothermal and Czochralski refractive index for the 480nm line. However, the blue line at 480nm and the green line at 546 nm may both be outside of the resonance line of 510nm as determined from photoconductivity, above. Further measurements of refractive index with a 510nm source are planned for the future.

V. Implanted BSO

Samples of Cz and Hydrothermal BSO were ion-implanted for two purposes: 1) As an attempt to introduce impurities that could not normally be introduced by melt during growth or by diffusion. The intent was again to alter the photoconductivity in such a way as to increase the photorefracting properties of the materials at longer wavelengths. 2) As a possible way to produce waveguides on BSO. By implanting a deep (at least 1000Å) distance into the sample, the intent was to prepare a low index damaged region with a range as deep as possible into the sample, which could be used to form a waveguide in the higher index material left undamaged. This is the same method as has been used previously to prepare photorefracting waveguides in $BaTiO_3$ and $KNbO_3$.

Implant conditions for BSO appear in Table III. Implanted samples were sent to a commercial laboratory for impurity profile analysis. Impurity profiles as determined by secondary ion mass spectroscopy (SIMS) is shown in Fig. 5. The results show that implanting is a viable method for introducing impurities in BSO. The data shows an implant range of $\sim$ 1000Å for Ge implanted into Cz BSO and only $\sim$ 100Å for the same impurity implanted into hydrothermal material. It is not known at this early stage why there is such a significant difference in the range.

Before and after photoconductivity analysis of the Cz sample demonstrated that the implant had only a slight affect on the photoconductivity spectrum. More studies, including large implant doses followed by impurity drive-in, are planned.

VI. Liquid Phase Epitaxy

Initial studies of liquid-phase epitaxy was prepared on some samples by growing $Bi_{12}TiO_{20}$ (BTO) on BSO substrates. This particular system was selected as an initial study of epitaxy as the melting temperature of BTO (860°C) are less than that for BSO (900°C). LPE growth runs were carried out in the same growth system used to grow Czochralski BSO. The charge was melted, supercooled. then a BSO

Table III. Implant conditions of BSO

Present Vaue Dose	2×10^{16} ions/cm^2
Set Value Dose	2×10^{16} ions/cm^2
Elapsed Time	1.75×10^6 sec.
Energy	150 kV
Beam Current	43 µA.

substrate was slowly lowered into the melt. The melt was supercooled ~30°C. The seed was kept in the supercooled melt for 30minutes.

Initial runs made demonstrated some growth of material on the BSO substrates. However, the quality of the films were not, as yet high enough for characterization studies. Future work is planned on enhancing the quality of the films by a polishing study of the substrates, and a more detailed refractive index study to look at alternative film compositions.

Bibliography

[1] W. B. Leigh, J.J. Larkin, M. T. Harris. "Characterization of Czochralski and Hydrothermal Grown $Bi_{12}SiO_{20}$" Submitted to *J. Appl. Phys.* September, 1993.

[2] R. Oberschmid, *phys. stat. sol. (a)* 89, (57 (1985).

[3] J. Feinberg, K. Heiman, A. R. Tanguay, and R. W. Hellwarth, *J. Appl. Phys.* 51, 1297 (1980).

[4] A. E. Attard. *J. Appl. Phys.* 69, 44 (1991).

[5] See for example: F. E. Jenkins, H. E. White, Fundamentals of Optics, Mcgraw-Hill, 1957, p 21.

List of Figures

Fig. 1

(a) Cz BSO
(b) Hydrothermal BSO

Net Photocurrent
Various doped Cz material

File manyScan
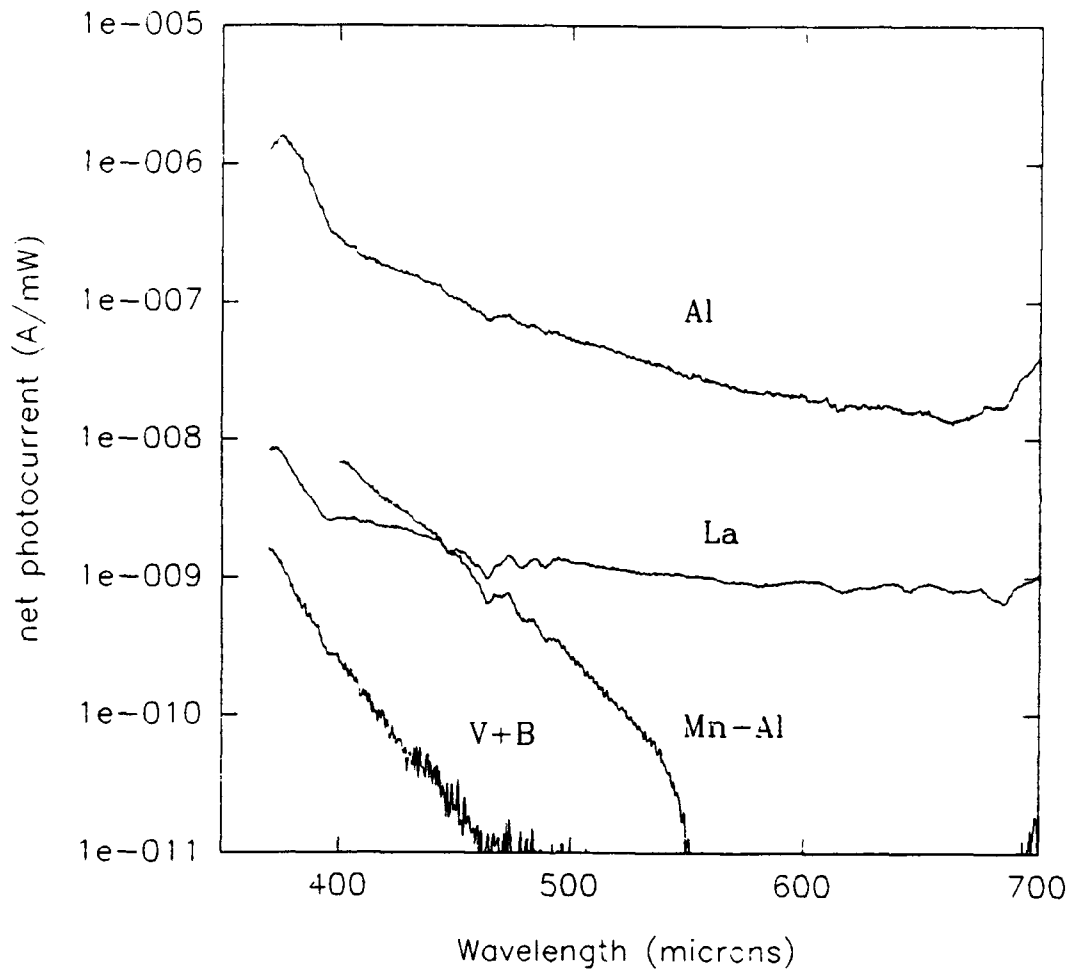
Fig 2.
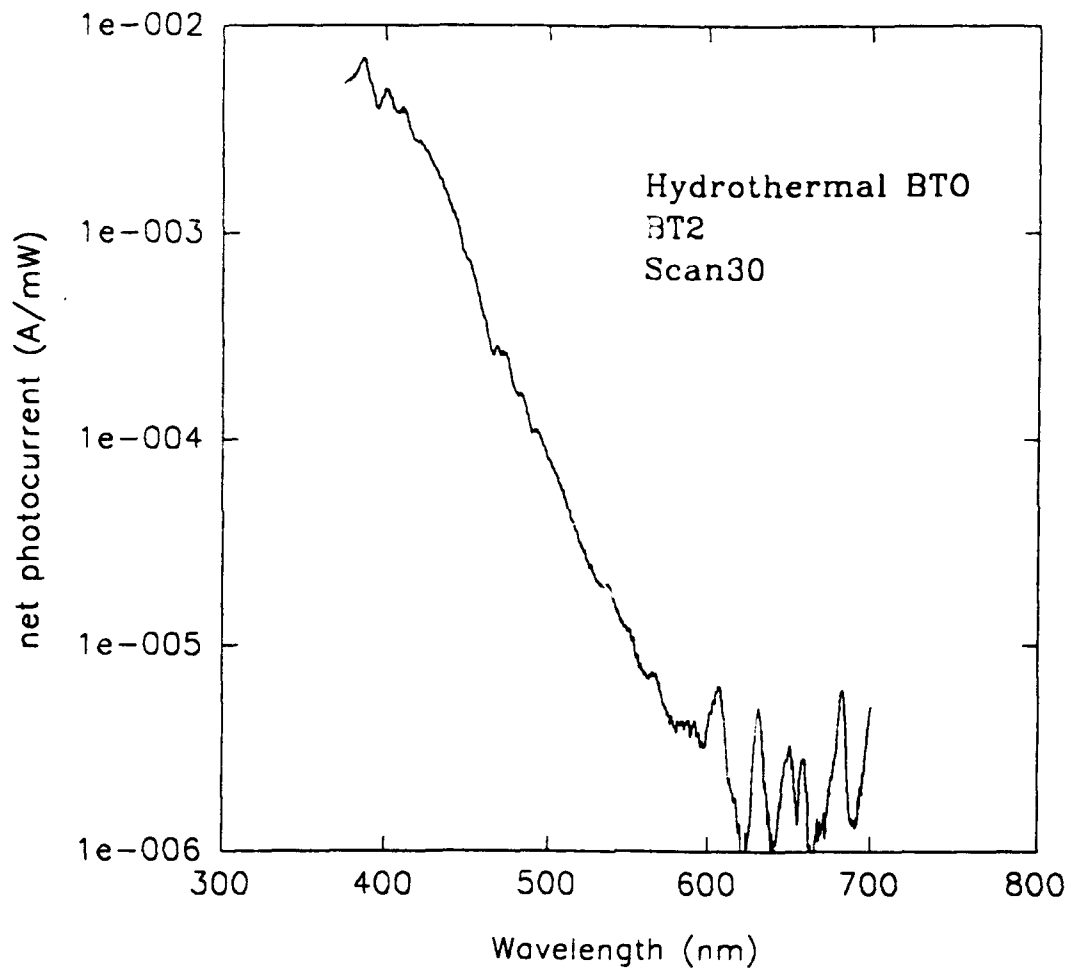
Fig 3.
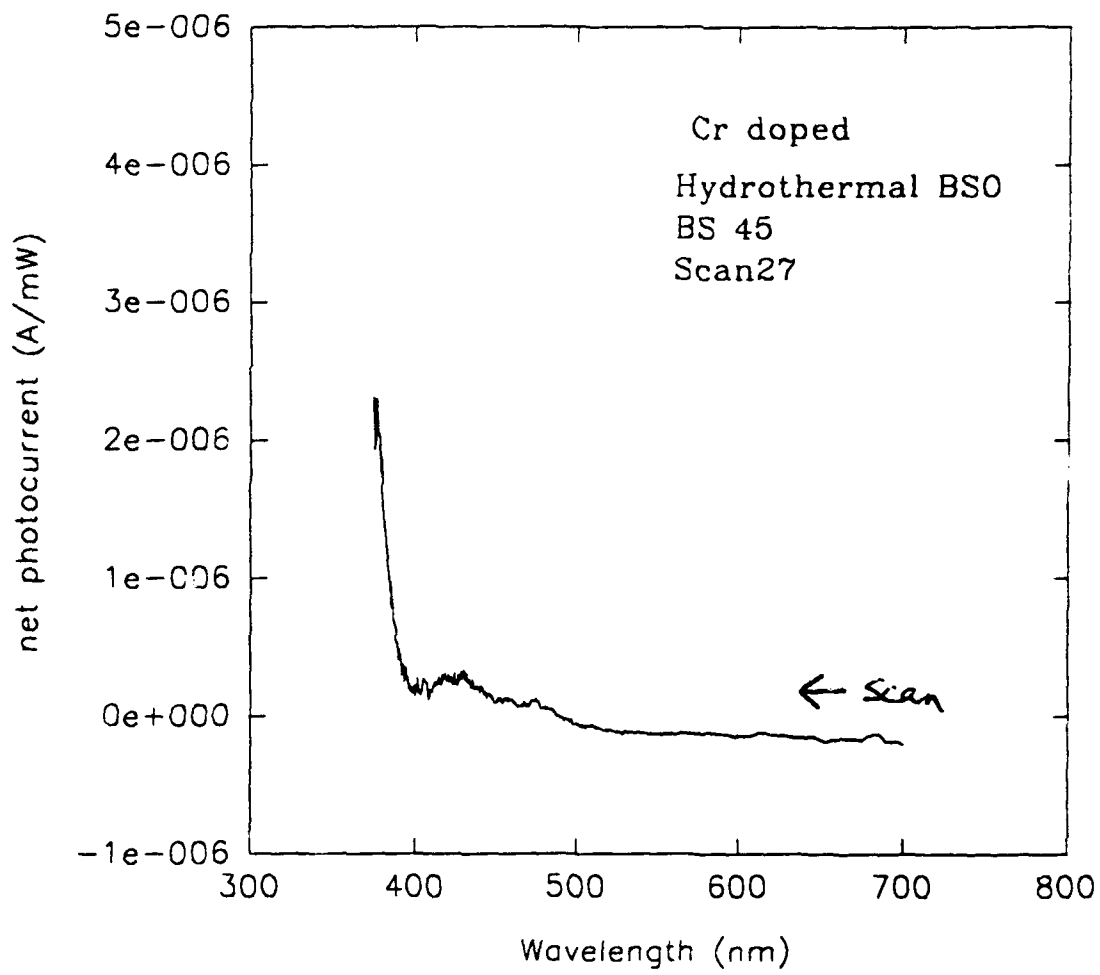
Fig. 4.
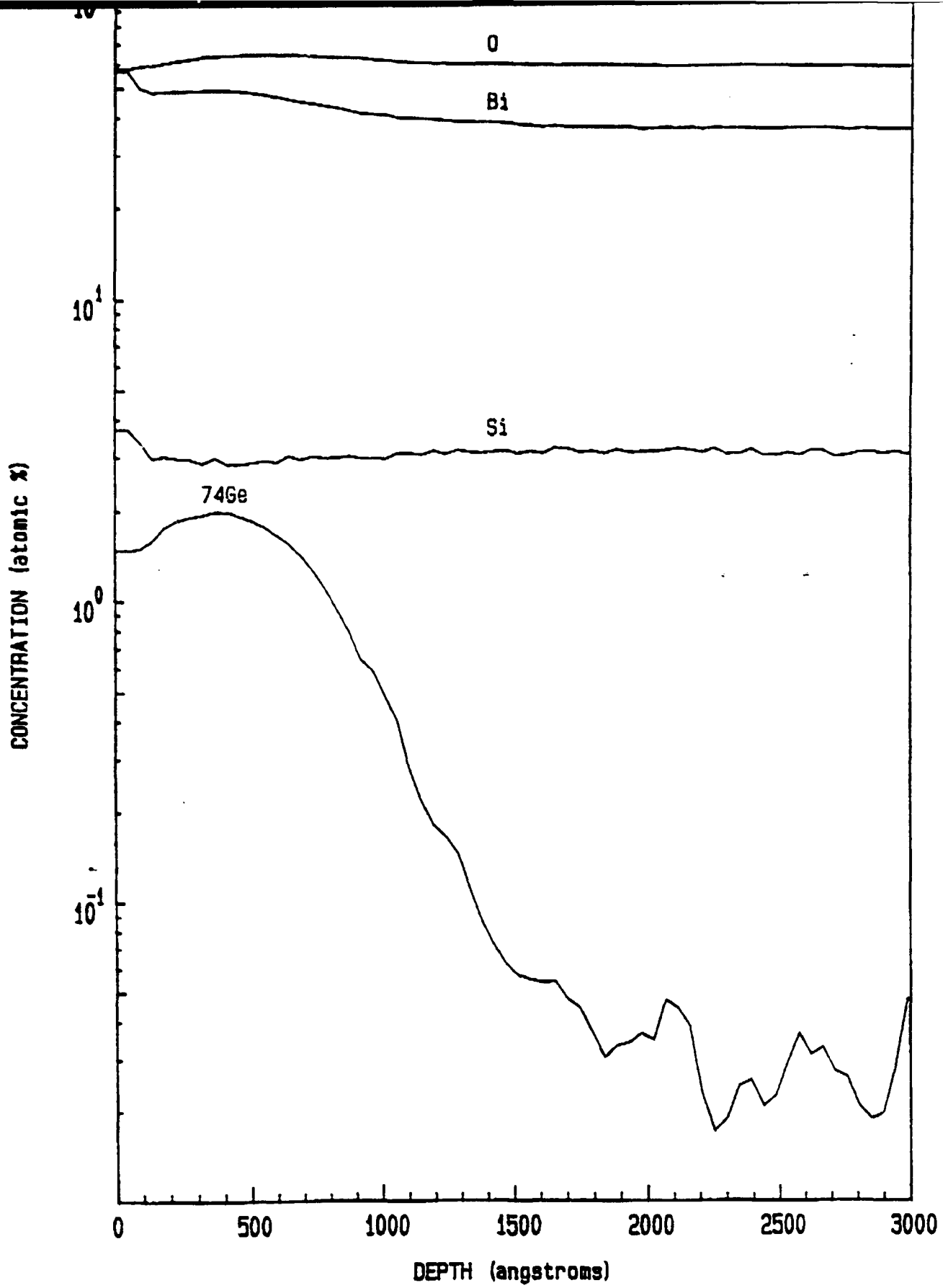
Fig. 5.
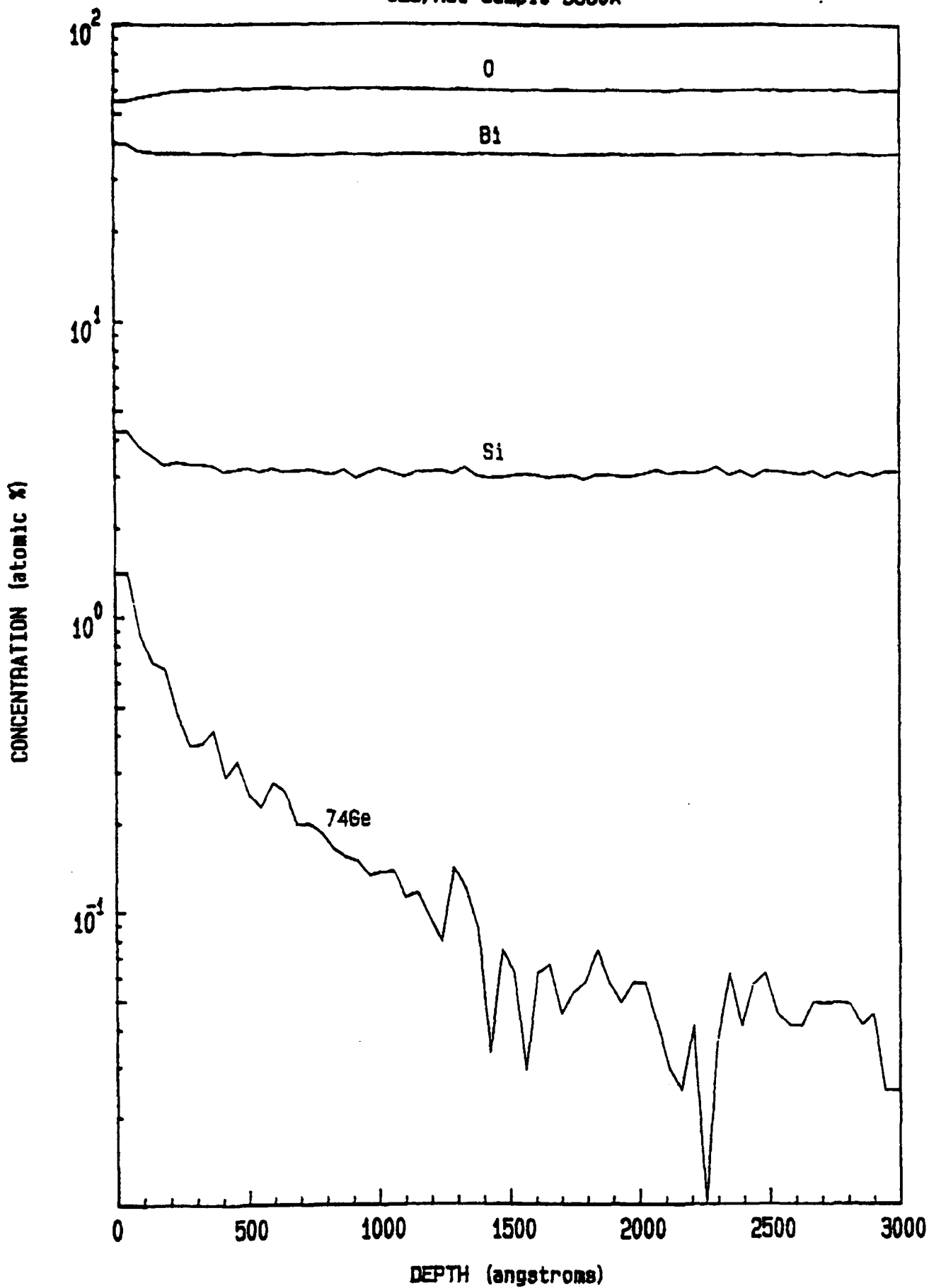
UES/Rai Sample BS60A

Fig.

10-16

CONDUCTED INTERFERENCE SIMULATION RESULTS FOR A
GENERAL ELECTRIC SOFT PART ANALOGOUS MODULE (SPAM)

Rick J. Levin

Research Engineer II

Electromagnetic Environmental Effects Laboratory

Georgia Tech Research Institute

347 Ferst St.

Atlanta, GA 30332-0800

CONDUCTED INTERFERENCE SIMULATION RESULTS FOR A GENERAL ELECTRIC SOFT PART ANALOGOUS MODULE (SPAM)

Rick J. Levin

Electromagnetic Environmental Effects Laboratory

Georgia Tech Research Institute

Abstract

The Soft Part Analogous Module (SPAM) [1] is a high speed 1-megabit RAM that was built by the General Electric (GE) Corporation to verify multi-chip-module (MCM) fabrication techniques and processes prior to full construction of radiation hardened MCM's. Conducted Electromagnetic Interference (EMI) measurements were performed on this MCM as well as on the individual integrated circuits (IC's) within the MCM [2]. The individual IC's were measured in order to determine if simpler and less expensive IC's could be evaluated prior to testing a more complex and costly MCM. Conducted EMI simulations for two of the MCM interface IC's are presented in this report. SPICE circuit analysis was used to simulate conducted EMI. The utilization of Harmonic Balance circuit analysis to simulate conducted EMI is discussed in the Appendix.

CONDUCTED INTERFERENCE SIMULATION RESULTS FOR A GENERAL ELECTRIC SOFT PART ANALOGOUS MODULE (SPAM)

Rick J. Levin

1.0   INTRODUCTION

The Soft Part Analogous Module (SPAM) [1] is a high speed 1-megabit RAM that was built by the General Electric (GE) Corporation to verify multi-chip-module (MCM) fabrication techniques and processes prior to full construction of radiation hardened MCM's.   Conducted Electromagnetic Interference (EMI) measurements were performed on this MCM as well as on the individual integrated circuits (IC's) within the MCM [2]. The individual IC's were measured in order to determine if simpler and less expensive IC's could be evaluated prior to testing a more complex and costly MCM. Conducted EMI simulations for two of the MCM interface IC's are presented in this report. SPICE circuit analysis was used to simulate conducted EMI. The utilization of Harmonic Balance circuit analysis to simulate conducted EMI is discussed in the Appendix.

The GE SPAM MCM contains the dies of four IC's: the Texas Instruments 74S00 NAND gate, 74S138 3-to-8 line decoder, 74S373 D-flip-flop, and Performance Semiconductor P4C164 8kx8 static CMOS RAM. In order to determine if circuit simulations of conducted EMI can accurately predict measured results, the Texas Instruments 74S00 and 74S138 IC's were simulated during this effort. Conducted EMI was simulated with a continuous wave (CW) single frequency interference waveform over the interference frequency range of 10 MHz to 800 MHz. The conducted EMI measurement results [2] showed that the 74S00 two inputs are equally susceptible and exhibited no unusual responses to conducted EMI.   The six 74S138 inputs

11-3

exhibited similar susceptibility levels up to approximately 90 MHz, while the two enable inputs exhibited a sharp and unusual increase in the signal level required to cause susceptibility at approximately 90 MHz. The conducted EMI waveforms were simulated as if injected on the 74S00 "A1" input and 74S138 "G2B" (enable) input.

2.0 SPICE Models

Circuit schematics for the Texas Instruments IC's were obtained from data books [3,4] and from the manufacturer [5]. The TI 74S series of IC's are Schottky technology, which makes extensive use of Schottky barrier diodes and Schottky-clamped transistors. The Schottky-clamped transistor is a transistor with a Schottky barrier diode attached from base to collector. Multiple emitter transistors were modeled as multiple transistors with the base and collectors tied together.

Detailed transistor and diode parameter models were not available for the TI 74S series of IC's, which is an old technology that is not supported by TI. The 74S was modeled by the following representative transistor and diodes: the 2N3932 (NPN) transistor, the 1N914 switching diode, and the 1N5711 Schottky barrier diode. The default parameter of 1 was used for the junction areas of all the transistors and diodes on the IC's.

The 74S00 contains four identical independent 2-input NAND gates. Each NAND gate contains six transistors and seven diodes. The single NAND gate illustrated in Figure 1 was used in the simulations. The functional (digital) input signals were represented by voltage sources set to correspond to a 1 MHz clock, 10 nsec rise and fall times, 0.4 Volts logic 0 (low), 2.4 Volts logic 1 (high), and the input binary patterns presented in the truth tables of the IC data sheets [3]. The IC output was terminated with a 1 kOhm resistor. The input CW interference waveform was simulated with a CW voltage source. A divide by two voltage divider was utilized to add (combine) the interference and digital input signals. To compensate for the division in voltage, the interference and digital source amplitudes (prior to the voltage divider) were doubled.
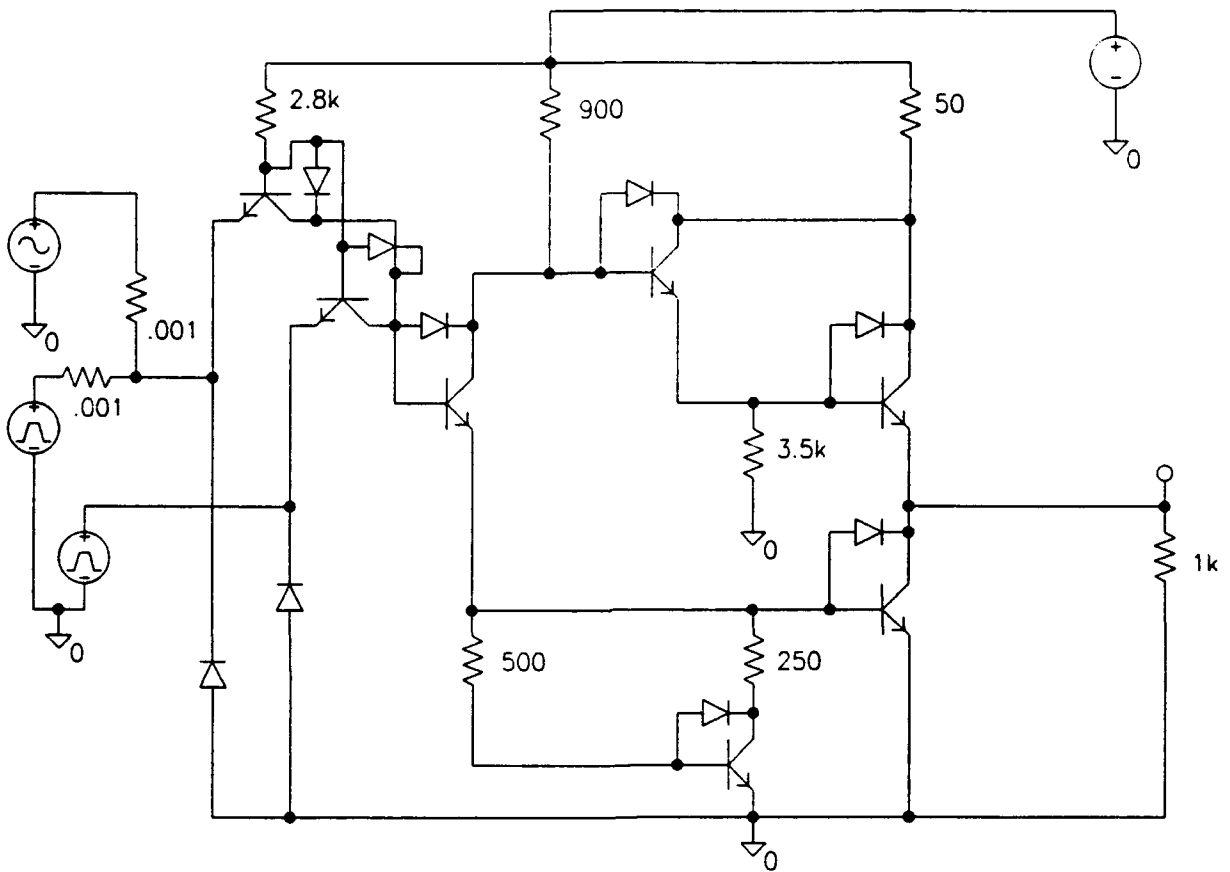
Figure 1. 74S00 NAND Gate Schematic

The 74S138 IC is a 3-line to 8-line decoder that contains over 100 transistors. The 74S138 circuit was partitioned into 3 input blocks, 1 enable block, and 8 output blocks, as illustrated in Figure 2. The input interference waveforms, input digital waveforms, and output terminations were simulated in the same manner as described for the 74S00.
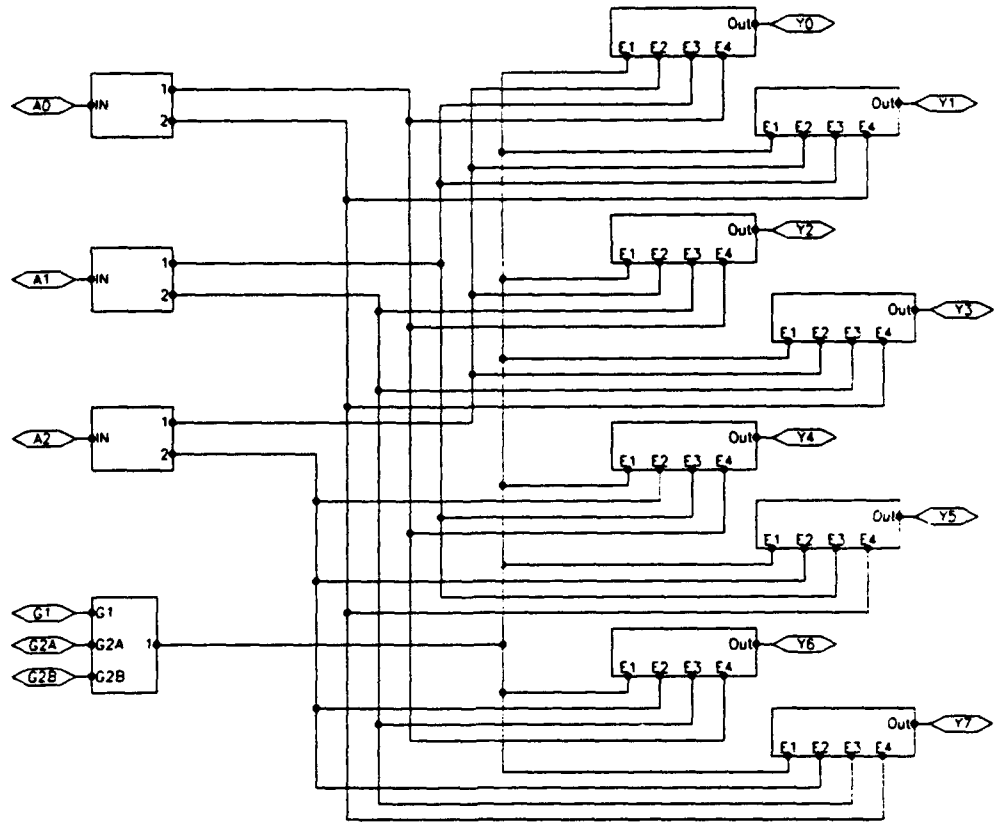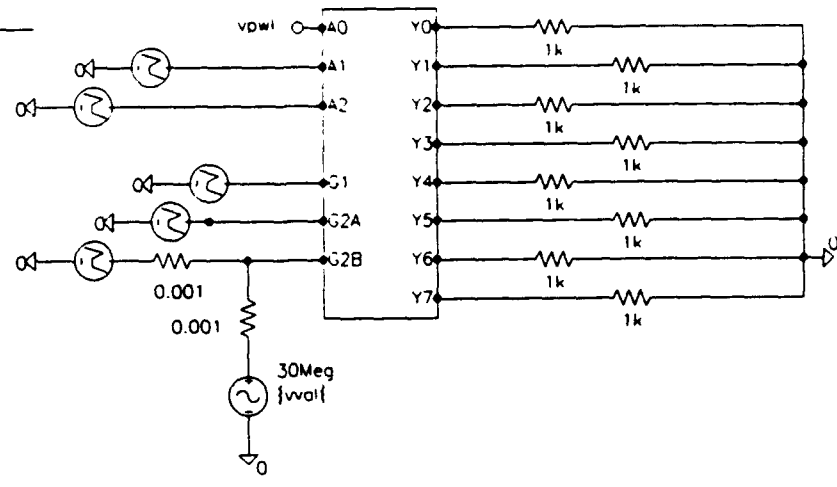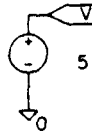
Figure 2. 74S138 3-Line to 8-Line Decoder Schematic (1/2)

11-6
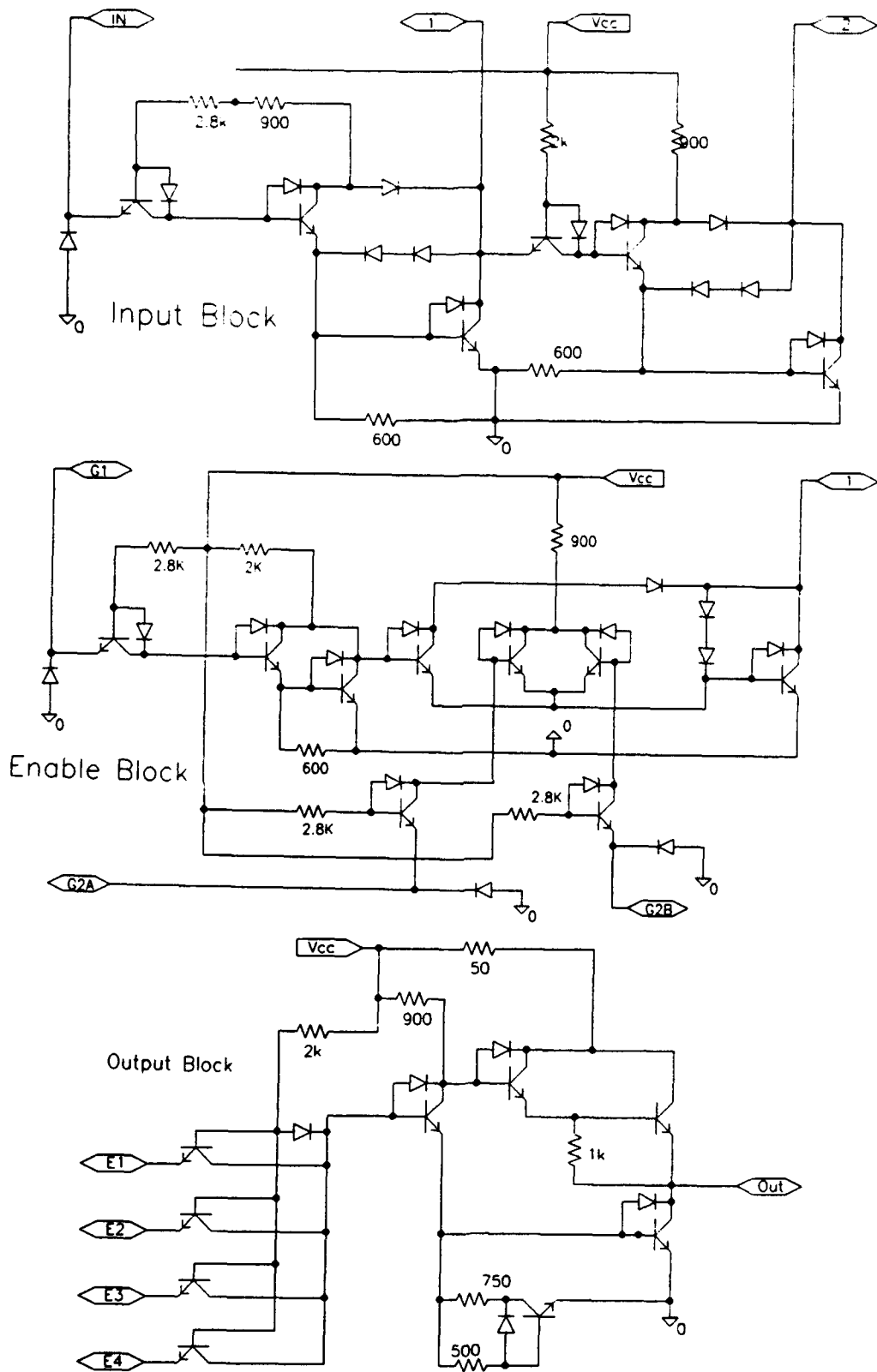
Figure 2. 74S138 3-Line to 8-Line Decoder Schematic (2/2)

3.0   SPICE Simulations

The SPICE simulations were performed with PSPICE [6] software on a 33 MHz 486 PC with 8 Mbyte of RAM.   Results of the 74S00 simulations were reviewed to determine the susceptibility levels at the different interference frequencies. The susceptibility level is the input interference voltage level that causes a false logic state change in the output (as compared to the IC output truth table [3]). A false logic state occurs when the output voltage of a logic 1 dips below 1.4 Volts or when the output voltage of a logic 0 rises above 1.4 Volts (which is the same as the measurement criteria). Additionally, the output waveform was sampled for false logic at mid-clock period (multiples of 0.5 μseconds) this corresponds to the sampling used in the measurements.   The simulation susceptibility voltage levels were converted to incident interference power levels expressed in dBm and plotted along with the measured susceptibilities of the 74S00 as illustrated in Figure 3. For interference frequencies less than approximately 300 MHz, the simulated and measured results compare well, +3.5/-1.0 dB.   The simulated susceptibilities leveled-off at approximately 11 dBm for frequencies greater than 300 MHz, while the measured susceptibility levels increased with frequencies above 300 MHz.   The poor comparison at high frequencies may be due: 1) the use of general purpose transistor and diode model parameter, 2) The effects of the IC package/layout (which was not modeled).

The simulation results were also reviewed to determine the EMI effect as the input interference voltage level was increased to the point of susceptibility. The dominant interference effect in the 74S00 IC simulations is that the output logic 1 is pulled to a logic 0. This is the same effect observed in the measurement results [2]. The 74S00 output voltage waveforms for 10 MHz input interference voltage waveforms with different input peak-to-peak voltage levels ranging from 1.0 to 1.6 Volts are shown in Figure 4. The 74S00 output voltage waveforms for 60 MHz input interference voltage waveforms with different input peak-to-peak voltage levels ranging from 1.5 to 2.5 Volts are shown in Figure 5.
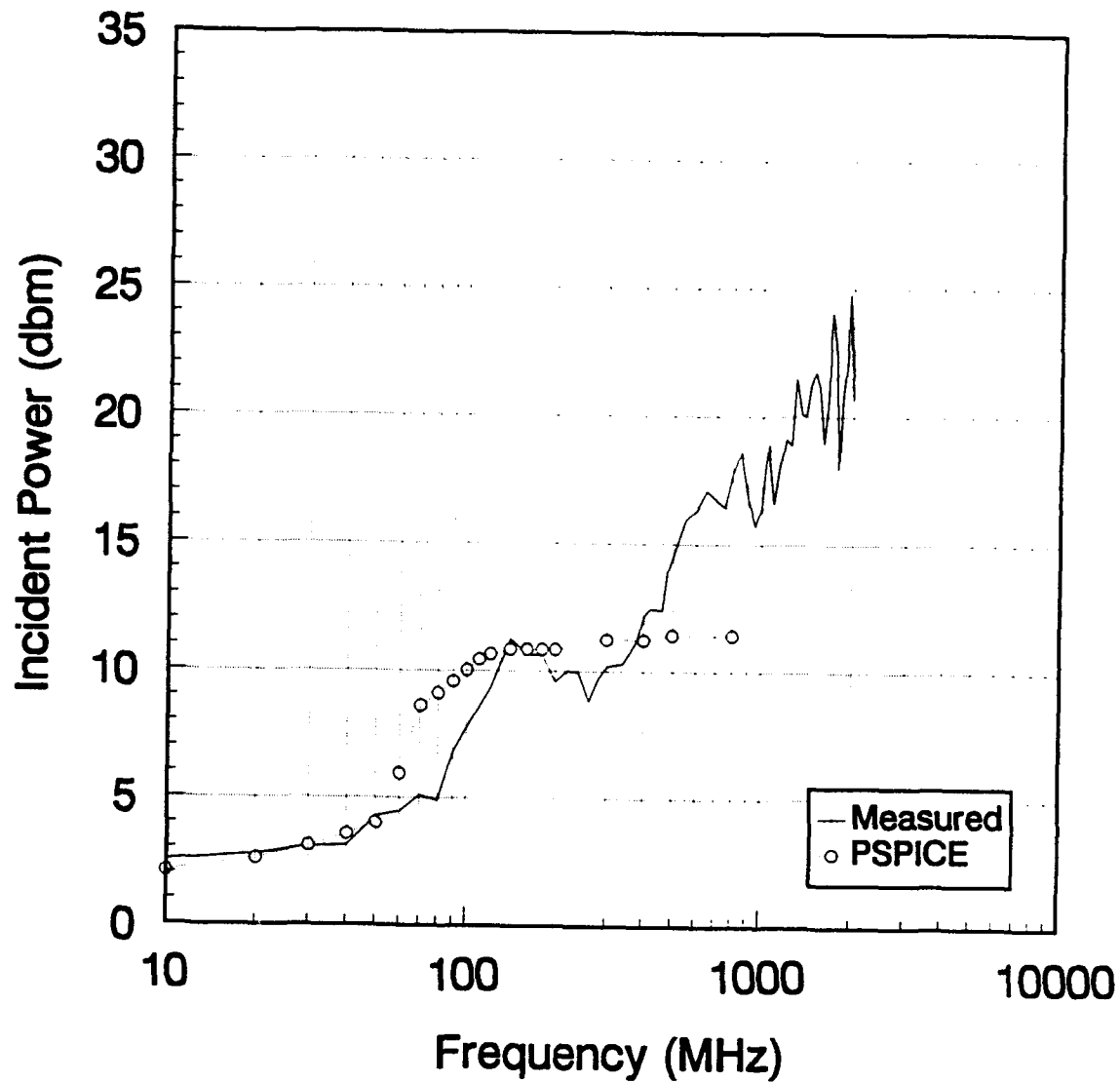
Figure 3. 74S00 Conducted EMI Susceptibility
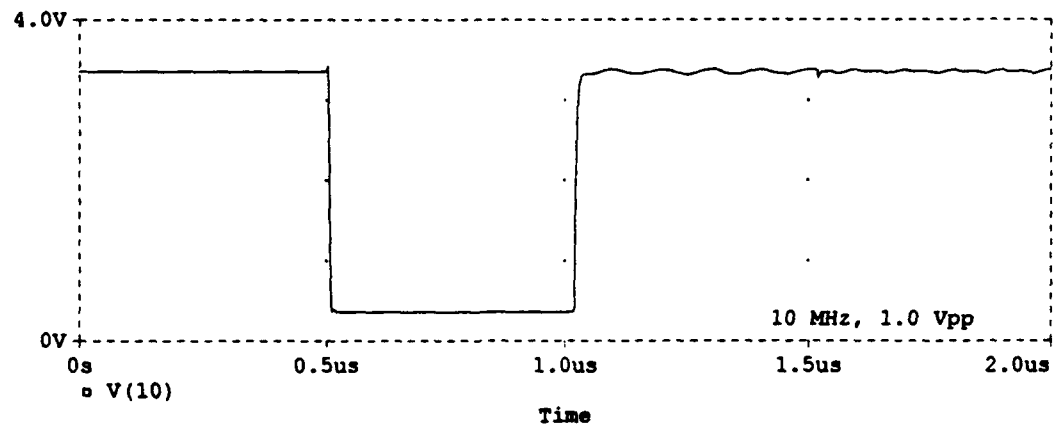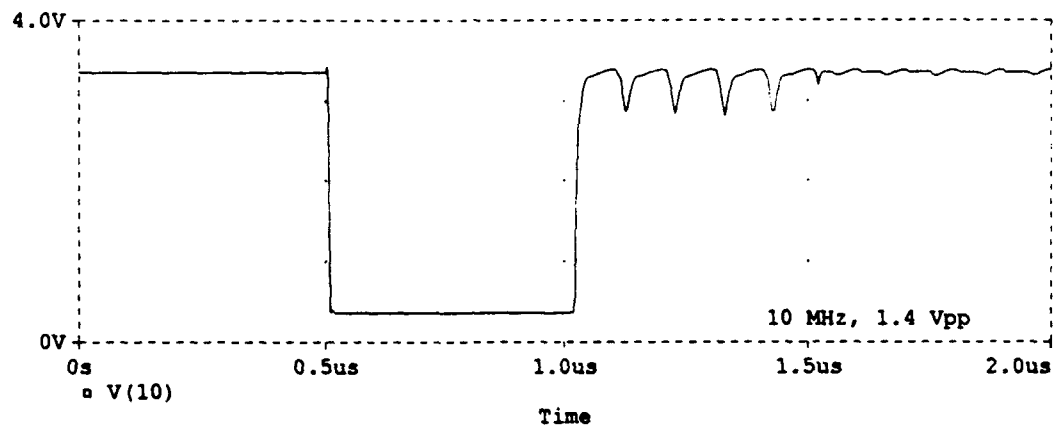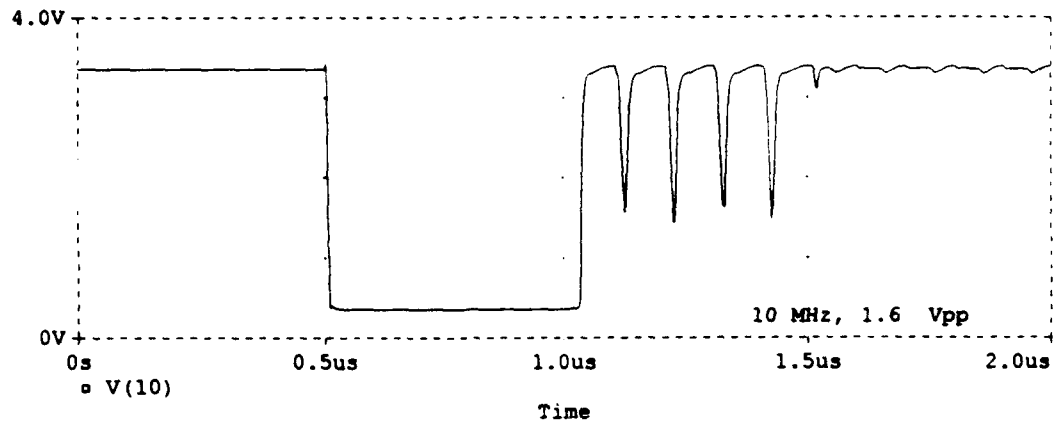
Figure 4. 74S00 Conducted EMI Effects for 10 MHz.
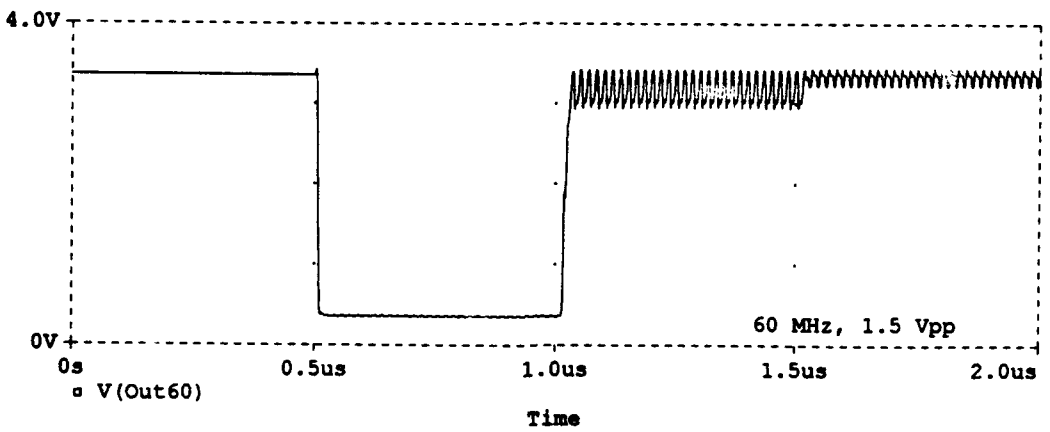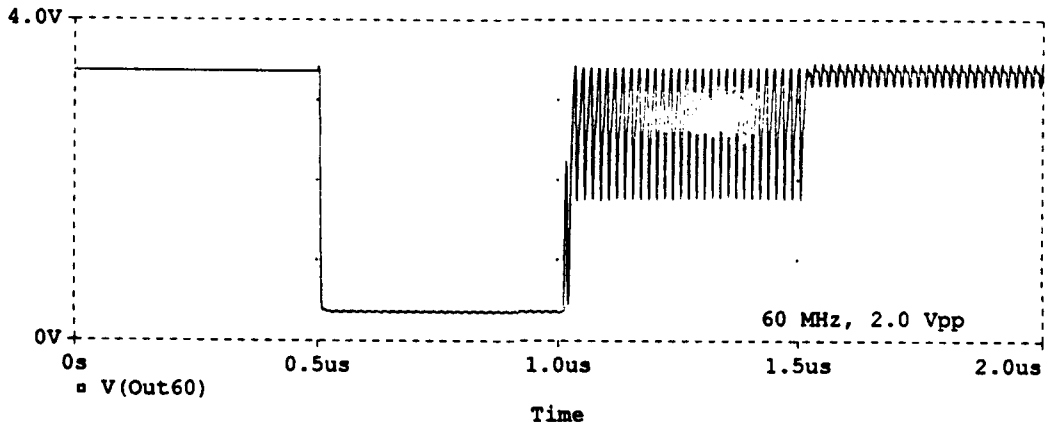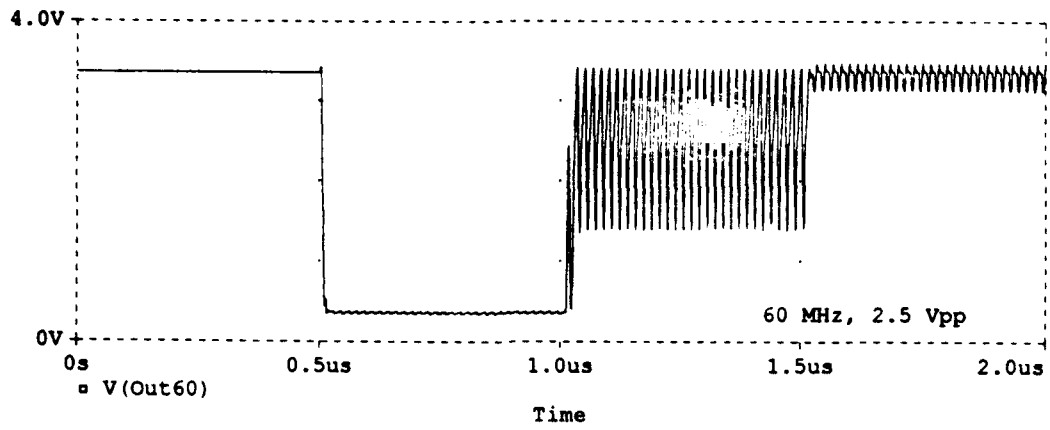
Figure 5. 74S00 Conducted EMI Effects for 60 MHz.

A 1.4 Volt output logic threshold and mid-clock period sampling were used to assess false logic states for the 74S138 simulations. The simulation susceptibility voltage levels were converted to incident interference power levels and plotted along with the measured susceptibility levels of the 74S138 as illustrated in Figure 6. The simulation results did not show the sharp increase in the input power level required to cause susceptibility, at approximately 90 MHz, that was observed in the measurements. The 2N3932 transistor model parameters were used to represent the 74S138 transistor model parameters, since the 74S138 transistor model parameters were not available. A few of the 2N3932 transistor model parameters were modified as follows:

Ideal Maximum Forward Beta	B_f	= 90
Ideal Maximum Reverse Beta	B_r	= 2.5
Zero-Bias Base Resistance	R_b	= 21
Collector Ohmic Resistance	R_c	= 26
Emitter Ohmic Resistance	R_e	= 1.31
Forward Early Voltage	V_{af}	= 90

The 74S138 simulations were repeated with the modified 2N3932 transistor model parameters. For interference frequencies less than approximately 100 MHz, the simulated and measured results compare well, +/- 2.5 dB and the sharp increase in the input power level required to cause susceptibility, at approximately 90 MHz, was simulated. The simulated susceptibilities started to level-off at approximately 100 MHz, while the measured susceptibility levels increased with frequencies above 100 MHz. The dominant interference effect in the 74S138 IC simulations is that the output logic 0 is pulled to a logic 1. This is the same effect observed in the measurement results [2]. The 74S138 output voltage waveforms for 10 MHz input interference voltage waveforms with different input peak-to-peak voltage levels ranging from 1.0 to 1.5 Volts are shown in Figure 7. The 74S138 output voltage waveforms for 60 MHz input interference voltage waveforms with different input peak-to-peak voltage levels ranging from 1.5 to 2.0 Volts are shown in Figure 8.

Incident Interference Thresholds for 74S138AN, Pin G2B.
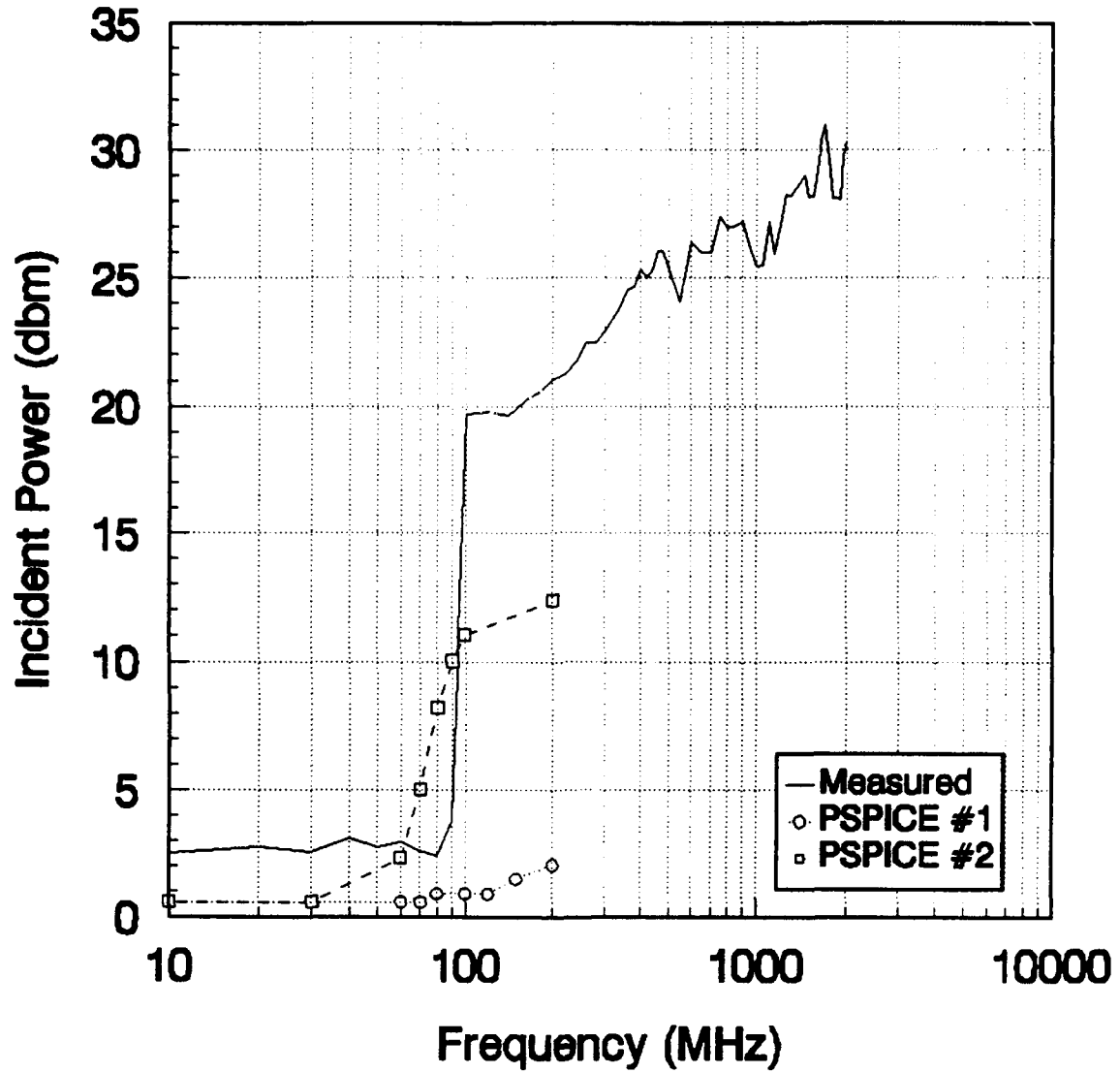
Figure 6. 74S138 Conducted EMI Susceptibility
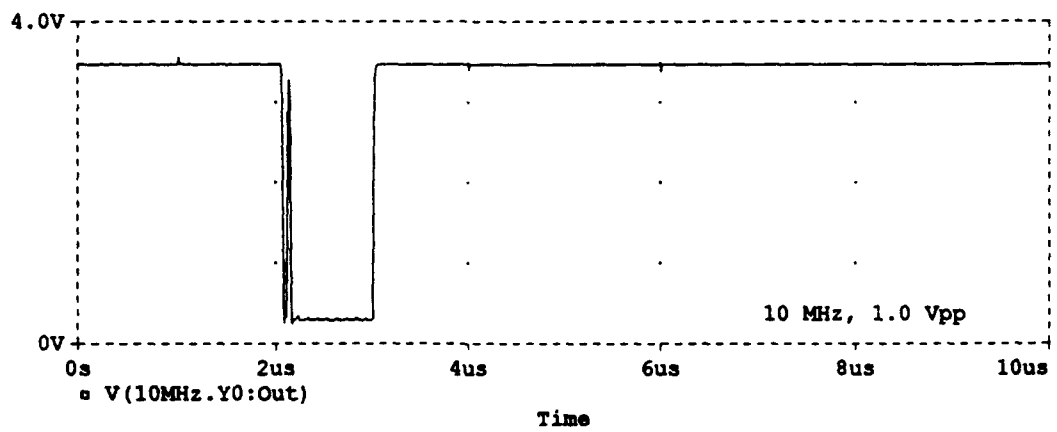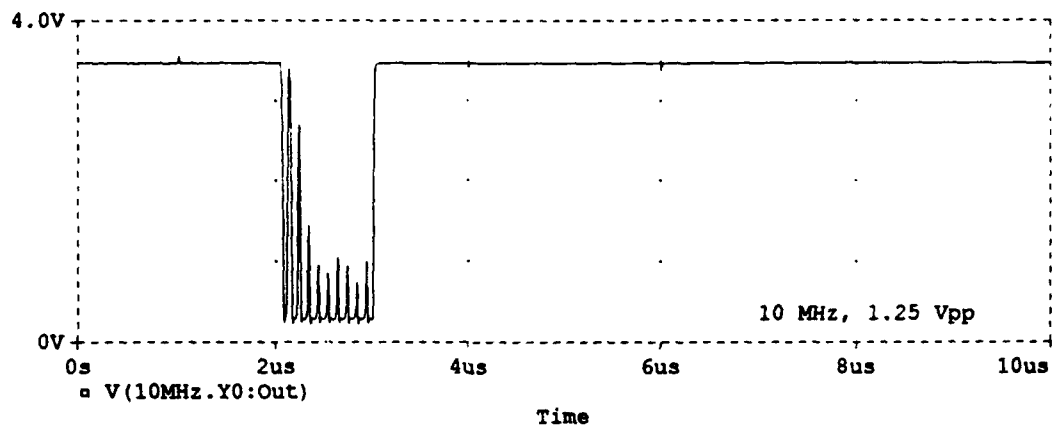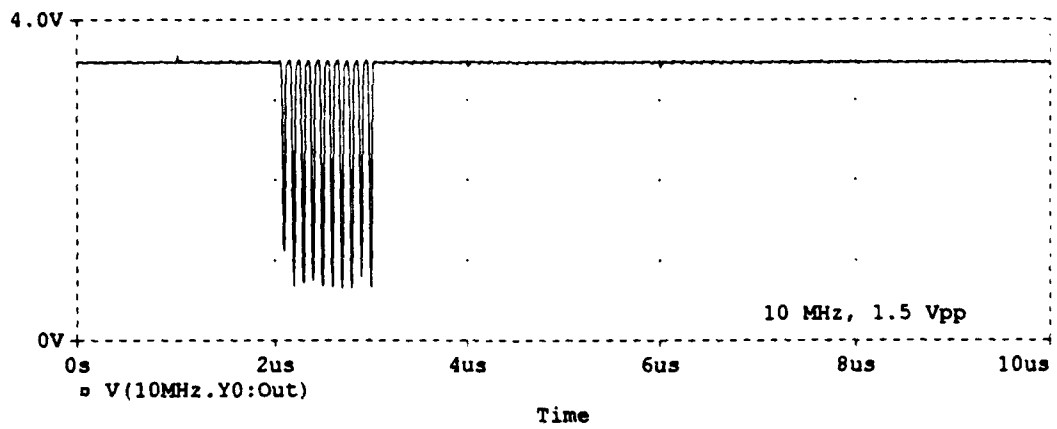
Figure 7. 74S138 Conducted EMI Effects for 10 MHz.
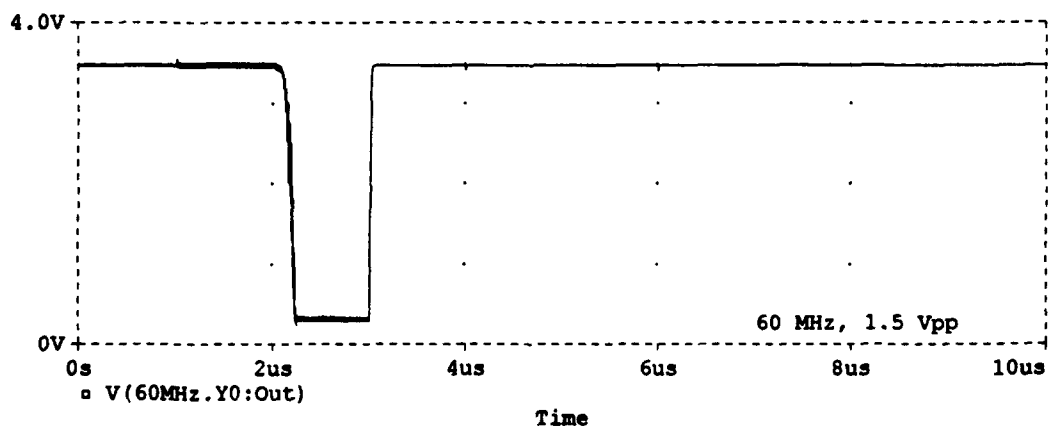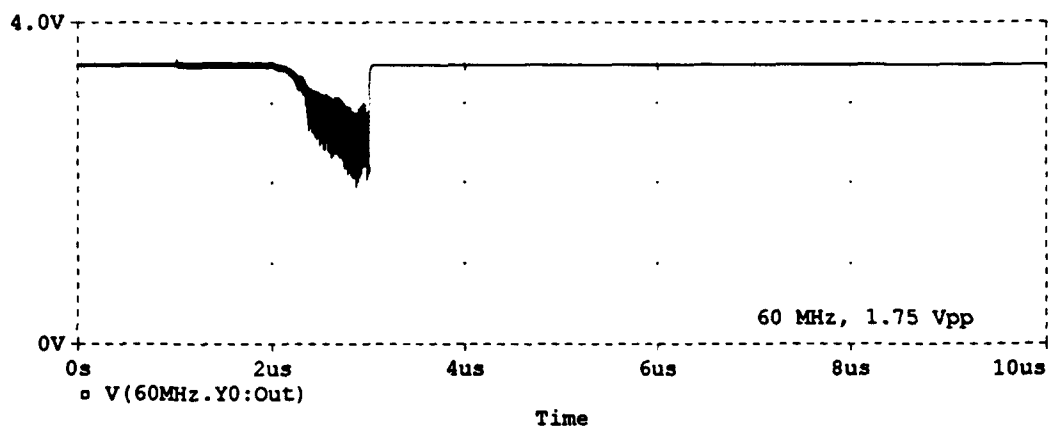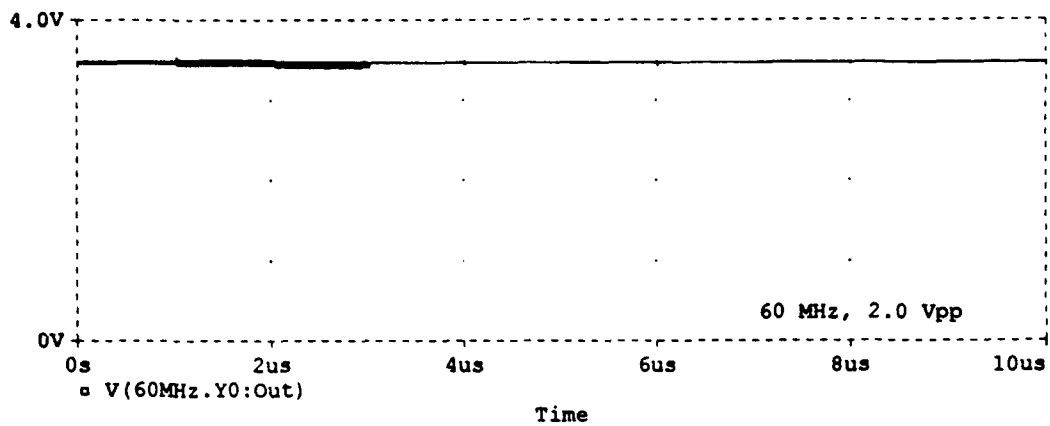
Figure 8. 74S138 Conducted EMI Effects for 60 MHz.

4.0 Conclusions and Recommendations

The conducted EMI effects and susceptibility levels of the 74S00 and 74S138 IC's within the MCM can be simulated with SPICE. The SPICE simulations were accurate within +3.5/-2.5 dB for frequencies less than 100 MHz. The correct transistor and diode model parameters may increase the frequency range at which the simulations provide accurate results.

It is recommended that this research effort be extended to include the following:

1) A comparison of conducted EMI susceptibility simulations to measurements for various technologies (e.g., AS, LS, ALS, and CMOS) of the 74 series of IC's.

2) A comparison of conducted EMI susceptibility simulations to measurements for IC's at different temperatures.

3) An investigation of IC reliability, through a comparison of internal IC power/voltage levels from parametric simulations with respect to input conducted EMI levels and IC temperature.

5.0 References

1. C. W. Eichelberger, et al., "Wafer Scale Integration Technology Demonstration, Final Report," Contract No. F29601-86-C-0020, WL-TR-89-56, November 1989.

2. J. P. Rohrbaugh, "Conducted Interference on Measurement Results for a General Electric Soft Part Analogous Module (SPAM)," 1993 AFOSR Summer Research Extension Program, Contract No. F49620-90-C-0076, July 1993

3. "The TTL Data Book, Volume 2," Texas Instruments, Dallas, Texas, 1985.

4.   "Supplement to TTL Data Book, Volume 3," Texas Instruments, Dallas, Texas, 1984.

5.   "74S138 and 74S373 Integrated Circuit Schematics," Facsimile from S. Spencer, Texas Instruments, Midland, Texas, to R. Levin, Georgia Tech Research Institute, Atlanta, Georgia, June 1993.

6.   PSPICE, Version 5.3, MicroSim Corporation, Irvine, California, January 1993.

7.   LIBRA, Version 3.5, EESof Corporation, Westlake Village, CA.

8.   J. P. Rohrbaugh, R. H. Pursely, "X-Band T/R Module Conducted Interference Simulation and Measurements," 1992 AFOSR Summer Research Extension Program, June 1993.

9.   S. A. Mass, Nonlinear Microwave Circuits, Artech House, Norwood, MA, 1988.

Appendix. Comments on Harmonic Balance Simulations.

Early in this effort, Harmonic Balance (HB) circuit analysis techniques were also considered for IC conducted EMI simulations. SPICE and HB simulations were conducted on an example circuit and compared to measurements. Libra [7] HB software and PSPICE [6] SPICE software were used in the simulations. A National Semiconductor DS8820/7820 differential line receiver IC was used in example simulations, since transistor model parameters, schematics, and measurements were available from a previous effort [8]. The DS8820/7820 IC contains ten 2N3932 transistors and no diodes.

The differential line receiver compares two input signals and outputs a digital signal based on the comparison. One of the two inputs was connected to ground for the simulations and a 1 MHz periodic pulse waveform and a CW interference waveform were both connected

to the other input. The PSPICE simulations converged and were similar to the measurements performed on the previous effort. The Libra simulations would not converge with the interference source connected. In order to have the simulation converge, the interference source was removed from the circuit and the libra parameters controlling convergence and accuracy were varied. After some doing the HB simulations (without interference) converged, but were not similar to the measurements (without interference) performed on the previous effort.

HB circuit analysis [9] is described in order to obtain insight into the HB convergence and accuracy during IC simulations. HB is a mixed domain circuit analysis technique that segments the circuit into linear and nonlinear elements. The linear elements form a multi-ported network described by S- or Y-parameter matrices. The nonlinear elements are modeled by their large-signal I/V or Q/V characteristics. The linear elements are analyzed in the frequency domain and the nonlinear elements are analyzed in the time domain. The HB technique satisfies Kirchhoffs current law at the port nodes separating the linear and nonlinear subcircuits. First, an initial guess is made of the time voltage waveforms at each of the port nodes. The time voltage waveforms are then Fourier transformed into the frequency domain components corresponding to the harmonics of the excitation frequency (including the DC term and fundamental). The linear sub-circuit is then solved in the frequency domain for the port node currents of each harmonic. The nonlinear subcircuit is analyzed using the initial time voltage waveforms. The resulting time current waveform is then Fourier transformed into the frequency domain components corresponding to the harmonics of the excitation frequency (including the DC term and fundamental). At each port node and for each harmonic of the excitation frequency (including the DC and fundamental) the addition of the linear and nonlinear current waveforms will equal 0 if the initial voltage waveforms were a good guess. If the addition of the linear and nonlinear currents are not within the error tolerance, then the process is repeated with new time voltage waveforms. Newtons-method is a popular algorithm for solving the time waveforms in successive iterations due to its good convergence properties and efficiency.

The DS8820/7820 differential line driver, which contains ten transistors, had HB convergence and accuracy problems. A combination of factors contribute to these problems: the

11-18

number of nonlinear elements, the number of harmonics required to adequately represent the input waveforms, and the number of harmonics required to adequately represent the nonlinearity of the circuit elements. These problems are further exacerbated when the fundamental excitation frequencies used to represent the functional and/or interference waveforms are not harmonically related. Multiple excitation frequencies will increase the number of frequency components that need to be balanced at each port node since each excitation frequency has different harmonics and the nonlinear elements will produce mixing products of the different excitation frequencies.

1993 USAF SUMMER FACULTY RESEARCH PROGRAM

FINAL REPORT

GHz MICROWAVE RADIATION BY PICOSECONDS OPTICAL PULSES

Sponsored by the

AIR FORCE OFFICE OF SCIENTIFIC RESEARCH

Prepared by: David Liu, Ph.D.

Academic Rank: Adjunct Assistant Professor

Department and   Department of Physics

University   Worcester Polytechnic Institute

                        Worcester, MA 01609

Research Location   Rome Laboratory/Electromagnetics & Reliability Directorate

                        Hanscom AFB

                        Lexington, MA 02173

USAF Researcher   J. Bruce Thaxter

Date: 25 September, 1993

GHz MICROWAVE RADIATION BY PICOSECONDS OPTICAL PULSES

by

David Liu

ABSTRACT

High power, directional 1~20GHz microwave radiation has been generated out of high resistivity by 50 picoseconds optical pulses. The radiation signal generated as well as the associated mechanisms were monitored directly on the sampling oscilloscope in real time. The phase, amplitude, and direction of the radiation can be effectively manoeuvered by optical method. The combination of optics and microwave of this innovative technique provides the potential of flexibility, simplicity and low cost in microwave applications.

ACKNOWLEDGMENTS

INTRODUCTION & TECHNICAL BACKGROUND

The advent of picoseconds laser pulses has made it possible to generate GHz microwave signals via the use of optical switching methods [1]. Photoconducting switches consist of normally insulating doped-semiconductor material between two electrodes. Illumination by a laser pulse free some electrons bound to the atoms of the material and enable them to conduct electrical current. Fast response time of the order of picoseconds has been achieved out of this principle. Thus, microwave signals can be normally generated by photoconductive shorting the charged coplanar microstrip transmission lines with short laser pulses. The electrostatic energy stored in the transmission lines is thus converted into the energy of microwave radiation.

The results of this technique give the frequency of millimeter-wave burst is approximately 55GHz (corresponding to a period of 18ps) by the measurements of Auston and coworkers [2]. Based upon this principle, a hybrid device, so called the frozen wave generator [3] for the radiation signal in the 5GHz frequency regime was developed. A schematic of a basic five-cycle frozen wave generator is illustrated in Fig. 1. Initially, as all the six switches are open, all the six elements of transmission line are charged to potentials $\pm V_o$ as shown. This static condition gives the "frozen wave". When all the switches are simultaneously closed, the frozen wave is free to propagate. If the switches are closed not simultaneously, but in a certain synchronous manner, a different output wave form will be produced. The adequate timing for closing the switches can be most effectively achieved by the optical path lengths adjustment in order to provide the desired modulated output signals. Lately, Thaxter [4] at Rome Laboratory, Hanscom AFB has demonstrated the success of frozen wave generator in the 5GHz regime by incorporating with single mode optical fibers.

The energy source of radiation previously discussed has been contributed by the electro-static energy stored in the microstrip transmission lines. Recently, Hu and coworkers [5] pioneered a new approach by utilizing photoconducting material itself as the energy source for emitting microwave radiation. By illuminating with colliding pulse, mode-locked (CPM) 75fs

short pulses, large planar photoconductors were found to radiate a directional electromagnetic pulse in space, which can be steered by varying the angle of incidence of the optical beam. The short photocurrent generated in a voltage biased photoconductor by the optical pulse serves as the radiation source. The photocurrent signal is a short pulse, whose frequency spectrum extends from dc to 1THz. It has a median frequency of ~600GHz, corresponding to a free-space wavelength of 500μm. Zhang and Auston [6] went further by optically inducing THz electromagnetic beams steered by controlling the pattern structure with two degrees of freedom. A semi-insulating InP wafer illuminated by the unfocused optical beam was used as the emitter. The temporal measurement was achieved using the technique of optical sampling by varying the time delay between the excited laser pulse illuminated on the semiconductor surface and the trigger laser pulse focused on the photoconducting detector.

By adopting the similar idea, this summer we utilized high power (peak power > 50KW), mode-locked, Q-switched 50ps laser pulses, instead the 75fs CPM pulses by Zhang and Auston mentioned earlier, to generate microwave pulse in the 10GHz regime. The uniqueness and main objectives of this work are outlined as follows:

(1) The frequency range of radiation we try to generate is of current use in radar communication. 1~20 GHz frequency range is most active in microwave communication technology today.

(2) The high power laser pulse and high quality semi-insulating InP materials available at Rome Laboratory, Hanscom AFB are ideal for us to conduct this research.

(3) Taking advantage of the 20GHz resolution of the our sampling oscilloscope, we are able to observe the microwave radiation profile directly on the scope screen. This allows us to analyze the data in a more effective way than the similar work previously reported.

(4) Again, the equipment in hand allows us to seek the answers as to the roles of conducting current and displacement current in microwave generation under this

scheme.

(5) Incorporating the attractive features of both frozen wave generator and large-aperture photoconducting antenna, the experiment setup provides flexibility and higher degree of freedom for generating directional, high powered, modulated microwave signals.

EXPERIMENTAL

The schematic diagram for the experimental setup is illustrated in Fig. 2, 3. The mode locked, Q-switched, frequency-doubled YLF laser system provides an output of $4\mu J$ pulse energy, 100KW peak power, 50ps pulse duration with a center wavelength at 527nm. The laser pulses were selectively chosen by a Pockel cell with a repetitive rate of 400Hz. The laser beam was split into two after the frequency doubler with approximately a 1:10 ratio. The weak beam was fed into an ultrafast photodetector for triggering the TEK11802 sampling scope. The main beam was positioned to pass through an optical path delay line of about 15m (equivalent to a 50ns time delay) before reaching the sample in order to bypassing the delay line on the scope for the best detecting temporal resolution of 20GHz. For investigating the nonlinear and interference effect, the main laser beam was divided equally into two and then be guided by two optical fibers. The electric pulses with an amplitude of 200V and width of $5\mu s$ were amplified by a TV transformer to come up a 10KV bias voltage across the sample. Standard S-band, X-band, K-band and self-made wide band wave guide transducers were used to measure the microwave radiation in real time. Microwave spectral analyzer was taken as the complementary tool for determining the spectral distribution for the radiation signal received. High quality Fe doped InP and Fe, Zn doped InP grown under stabilization magnetic field at Rome Laboratory were preferentially taken as the samples (microwave emitters) for this experiment.

RESULTS AND DISCUSSION

The radiated electric field due to the localized photoconducting current can be expressed as [7]

$$E = -E_b \frac{\sigma_s \eta_o}{\cos\theta_i} (\sigma_s \eta_o + \frac{1}{\cos\theta_i} + \frac{\sqrt{\epsilon}}{\cos\theta_t})^{-1} \qquad (1)$$

E_b is the bias field, η_o is the characteristic impedance of free space, θ_i is the angle of incidence the optical beam, θ_t is the angle of the inward propagating electric pulse, ϵ is the dielectric constant of the photoconductor, and σ_s is the surface photoconductivity, given by

$$\sigma_s(t) = \frac{e\mu(1-R)\cos\theta_i}{\hbar\omega} \int_{-\infty}^{t} dt' \cdot I_{op}(t') \exp^{\frac{(t-t')}{\tau_r}} \qquad (2)$$

where μ is the carrier mobility of the photoconductor, R is the optical reflectivity, $\hbar\omega$ is the photon energy, I_{op} is the optical intensity, and τ_r is the photocarrier decay time. From equation (1) we see that at low optical excitation, the electric field is proportional to the optical intensity.

For the purpose of avoiding signal contamination caused by the attached conducting wires and establishing more localized current source on the sample, the electrical contacts to the photoconductor are made as not ohmic.

Typical signal received by the wide band detector under the low optical excitation over the entire sample is shown in Fig. 4. Like a replica of the optical laser pulse, the microwave pulse with a temporal width of ~50ps was observed. The broad band nature of the radiation microwave pulse can be verified by using narrow band wave guide detectors. As shown in Fig 5-7, signals were received by S-band, X-band, K-band detector respectively. The respective peak frequency revealed the maximum efficiency of the combination of the wave guide spectral

efficiency and the signal spectral distribution. The signals were further investigated by using microwave analyzer, the peak frequency of about 12GHz was observed (not shown), of which the convolution is consistent with the pulse temporal width of 50ps.

As the illuminating beam was more focused on the spot near electrodes, a stronger radiation occurred. As predicted by Auston [8], a strong electric field near the electrodes will remain, which can have a significant influence on the transport properties of electrons and holes in the sample. The static approximation for E in this case can be determined by conformal mapping and theoretically can be expressed as

$$E(x,z=0) = \frac{2V_g}{\pi l} \frac{1}{\sqrt{1-(\frac{2x}{l})^2}} \qquad (3)$$

where V_g is the bias voltage and l is the length between the electrodes. It is a minimum at center of the gap, and increases to infinity at the metal electrodes. The experimental technique provides a powerful and convenient tool for mapping the static electric field distribution on the semiconductor surface.

As the illuminating beam was better focused on the sample, the excitation intensity was enhanced. The radiation amplitude was reduced by attenuating the laser beam intensity. However, the variation was not in a linear fashion, saturation and nonlinear behavior occurred, as shown in Fig. 7&8. This might suggest that the electric field on the sample has been depleted at large as the laser intensity is above certain value - that was approximately $5MW/cm^2$ for our measurement. As mentioned earlier, the radiation energy is due to the conversion of the static energy $(\epsilon E^2/2)$ in the sample. The sample in this sense can be considered as a combination of a capacitor and a resistor with varying resistance. The depletion of the electric field will meanwhile keep a low intrinsic resistance for a longer time duration. As a consequence, the signals will become more oscillatory (less damped). The observed larger "overshoot" signal under

12-8

higher optical illumination (Fig. 7) supports the qualitative description stated above. In addition, the short time constant of RC due to reduced R induced an unsymmetric microwave signal profile, of which the temporal width was even less than that of incident optical pulse.

The microwave radiation signal can be effectively modulated by optical means, which offers simplicity and low cost. Such a feature was demonstrated by using two optical sources guided by single mode fibers. Fig. 9 shows the radiation signal under single optical illumination (Fig. 9, (a)&(c)) and dual optical illumination (Fig. 9, (b)). Adjustment of the optical path length difference corresponds to the phase shift of the microwave signal. The superposition nature of output microwave radiation under dual illumination and the geometrical pattern illuminated on the InP sample by the optical signals provides the degrees of freedom to steer as well as modulate the radiation output.

SUMMARY

- 1~20GHz microwave radiation was successfully generated by picoseconds optical pulses. The output signal as well as the associated mechanisms were monitored for the first time by 20GHz sampling oscilloscope in real time.

- The energy source of radiation was contributed by the static electric energy not from the transmission lines, but from the sample. Nonlinear effect due to electric field depletion in the sample was observed.

- High quality Fe doped InP and Fe, Zn doped InP grown under stabilization magnetic field at Rome Laboratory were preferentially chosen as the radiation source due to material homogeneity and high dark resistivity ($>10^8\Omega$cm).

- The direction, phase and amplitude profile of radiation output were effectively controlled by optical means.

- The simplicity, flexibility and the low cost offered by this technique merit new application in radar communication as well as electronic testing device, such as, generation of microwave radiation in space, electronic field mapping on the semiconductor wafer..etc.

REFERENCES

[1] G. Mourou, W. H. Knox, and S. Williamson, "High-Power Picosecond Switching in Bulk Semiconductors", in Picosecond Optoelectronic Devices, pp. 219-248, ed. by C. H. Lee, Academic Press, Inc. (1984).

[2] D. H. Auston, "Picosecond Photoconductors: Physical Properties and Applications", in "High-Power Picosecond Switching in Bulk Semiconductors", in Picosecond Optoelectronic Devices, pp. 73-117, ed. by C. H. Lee, Academic Press, Inc. (1984).

[3] J. M. Proud and S. L. Norman, "High-Frequency Waveform Generation Using Optoelectronics Switching in Silicon", IEEE Transactions on Microwave Theory and Techniques, Vol. MTT-26, No. 3, 137 (1978).

[4] B. Thaxter, and R. Bell, "Photonically Activated Stored Energy Device Arrays for Microwave", Summer Topical Meeting on Optical Millimeter-Wave Interactions: Measurement, Generation, Transmission, and Control, LEOS Meeting, July (1991).

[5] B. B. Hu, J. T. Darrow, X.-C. Zhang, and D. H. Auston, "Optically Steerable Photoconducting Antennas", Appl. Phys. Lett. 56, (10), 886 (1990).

[6] X.-C. Zhang, and D. H. Auston, "Optoelectronic Measurement of Semiconductor Surfaces and Interfaces with Femtosecond Optics", J. Appl. Phys. 71, (1), 326 (1992).

[7] D. H. Auston, and X.-C. Zhang, "Large-Aperture Photoconducting Antennas", OSA Proceedings on Picosecond Electronics and Optoelectronics, Vol. 9, (1991), eds. Gerhard Sollner and Jagdeep Shah.

[8] D. H. Auston, "Impulse Response of Photoconductors in Transmission Lines", J. of Quantum Electronics, Vol. QE-19, No. 4, 639 (1983).

FROZEN WAVE GENERATOR
Five Period Frozen-Wave Generator

LASER PULSE ON
PHOTO-SWITCHES

+V

R.F. OUT

-V

+V/2

-V/2

TRAVELING WAVE OUTPUT
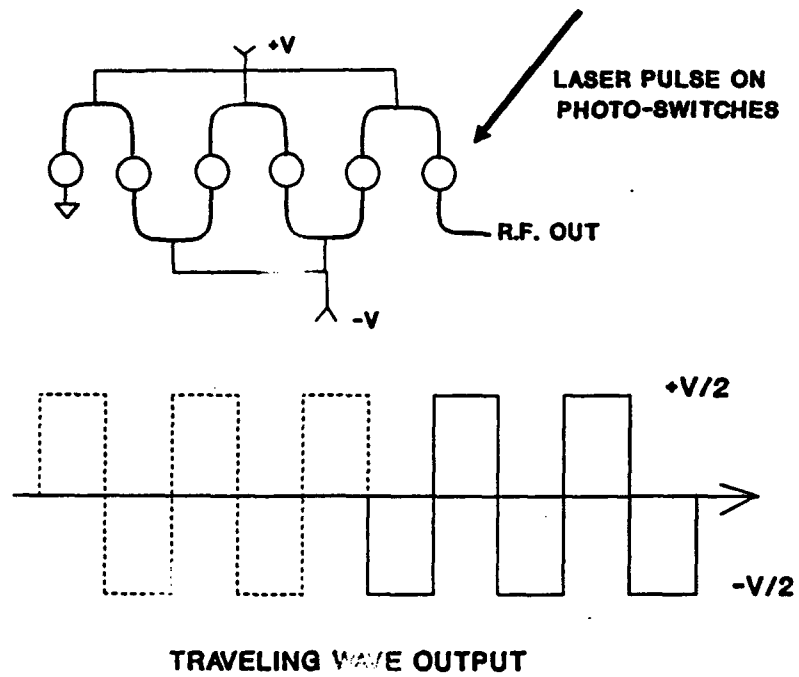
PHOTON4

Fig. 1 Frozen wave generator schematic.

Fig. 2 Schematic diagram for the experimental setup.

Wideband GHz pulse output

to pulsed bias supply

+

InP:Fe wafer

50 ps optical pulse input

waveguide adaptor

−

coax

optics to shape laser beam

to wideband preamplifier
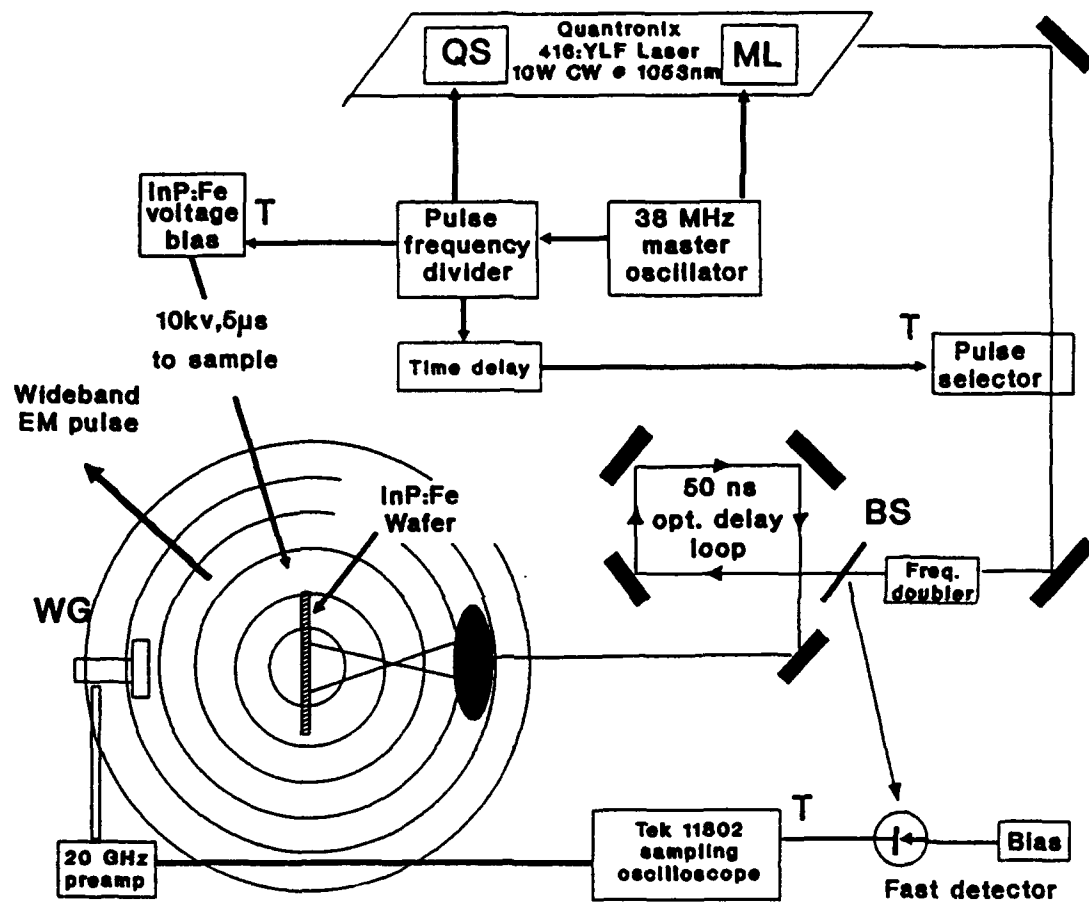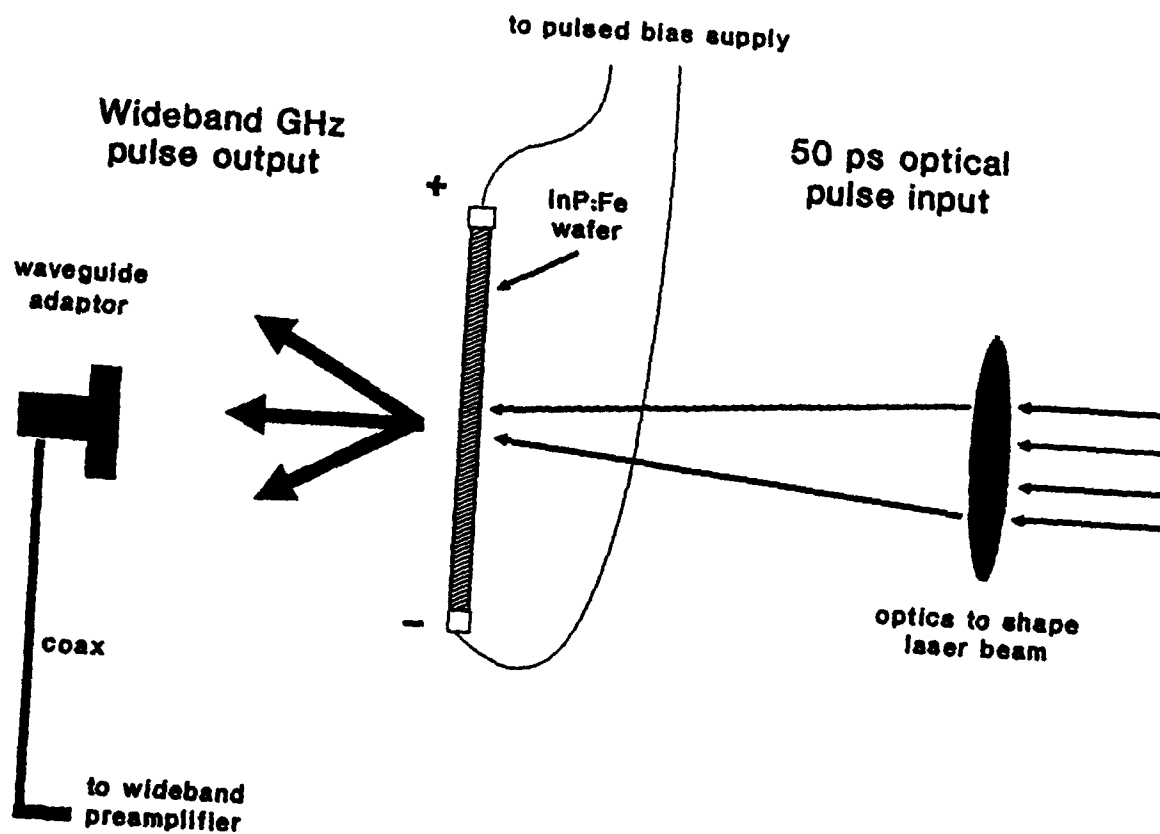
Fig. 3 Wideband GHz pulse radiation out of electric pulsed bias InP:Fe wafer.

Fig. 4 A 50 picosecond microwave pulse generated by 50 picosecond laser pulse.

Fig. 5 Microwave output signal received by S-band ridge waveguide transducer.

11802 DIGITIZING SAMPLING OSCILLOSCOPE
date: 19-AUG-93 time: 14:53:21
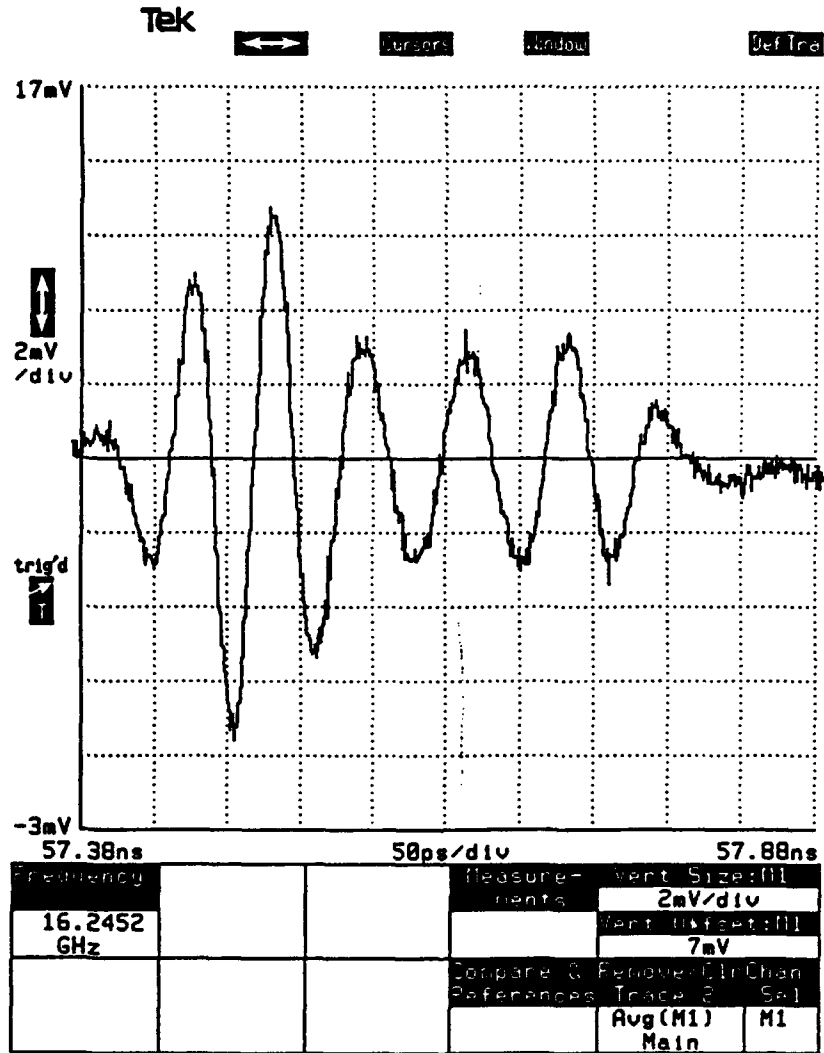
Fig. 6 Microwave output signal received by K-band ridge waveguide transducer.

12-17
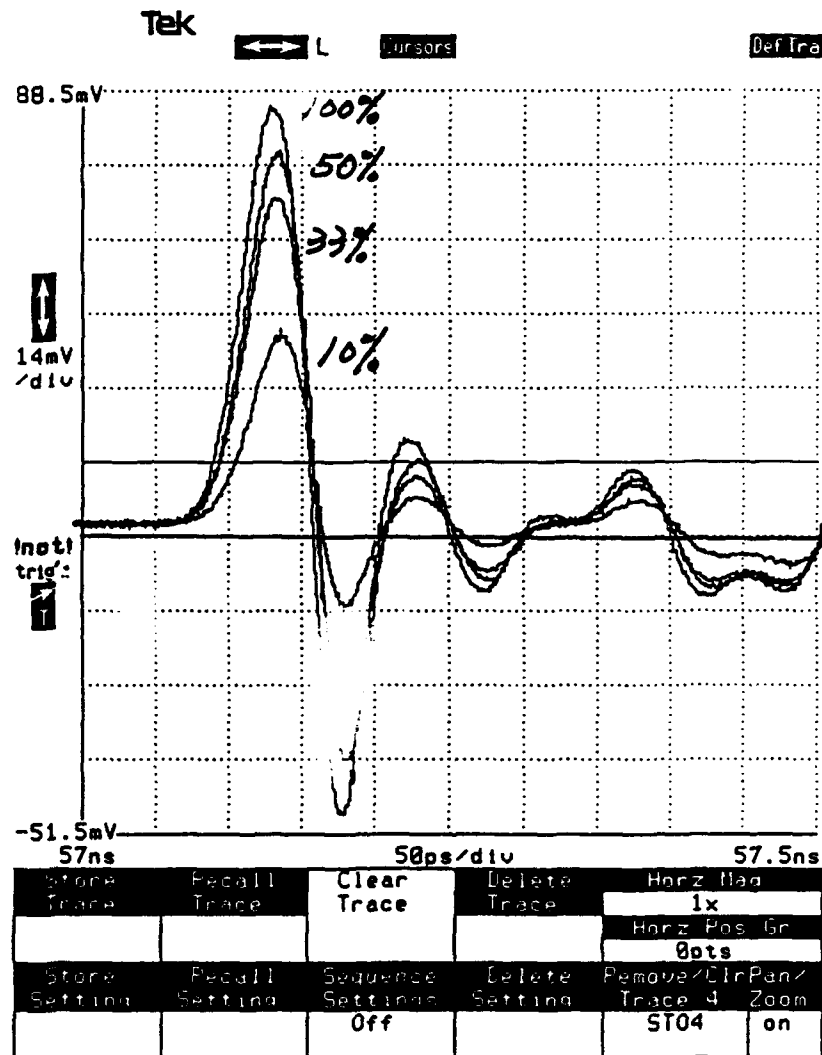
Fig. 7 Nonlinear effect due to the depletion of the electric field in InP wafer under intensive illumination.
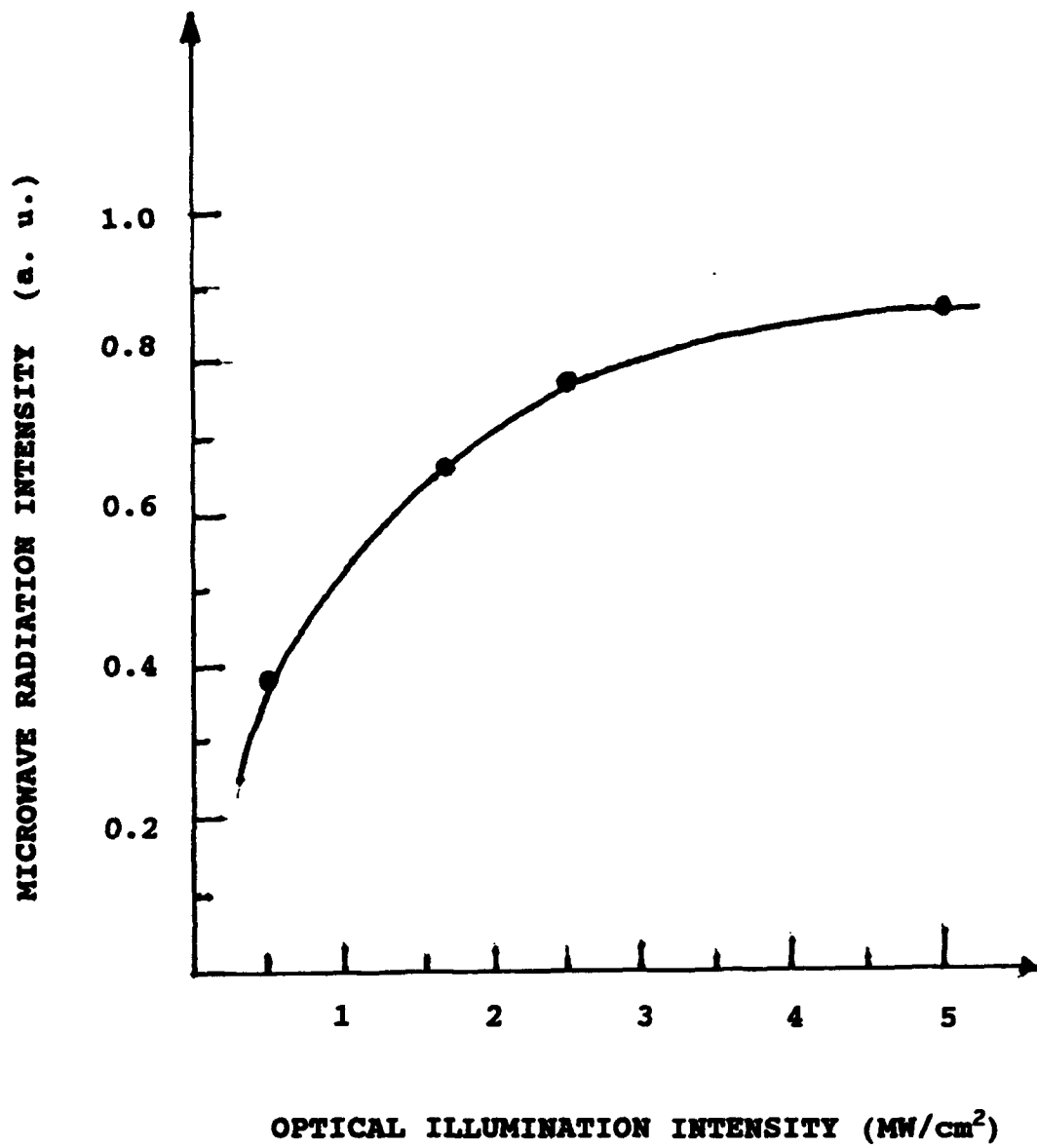
Fig. 8 Microwave radiation intensity vs. optical illumination intensity. Nonlinear behavior was observed. The solid line is a guide to the eyes.
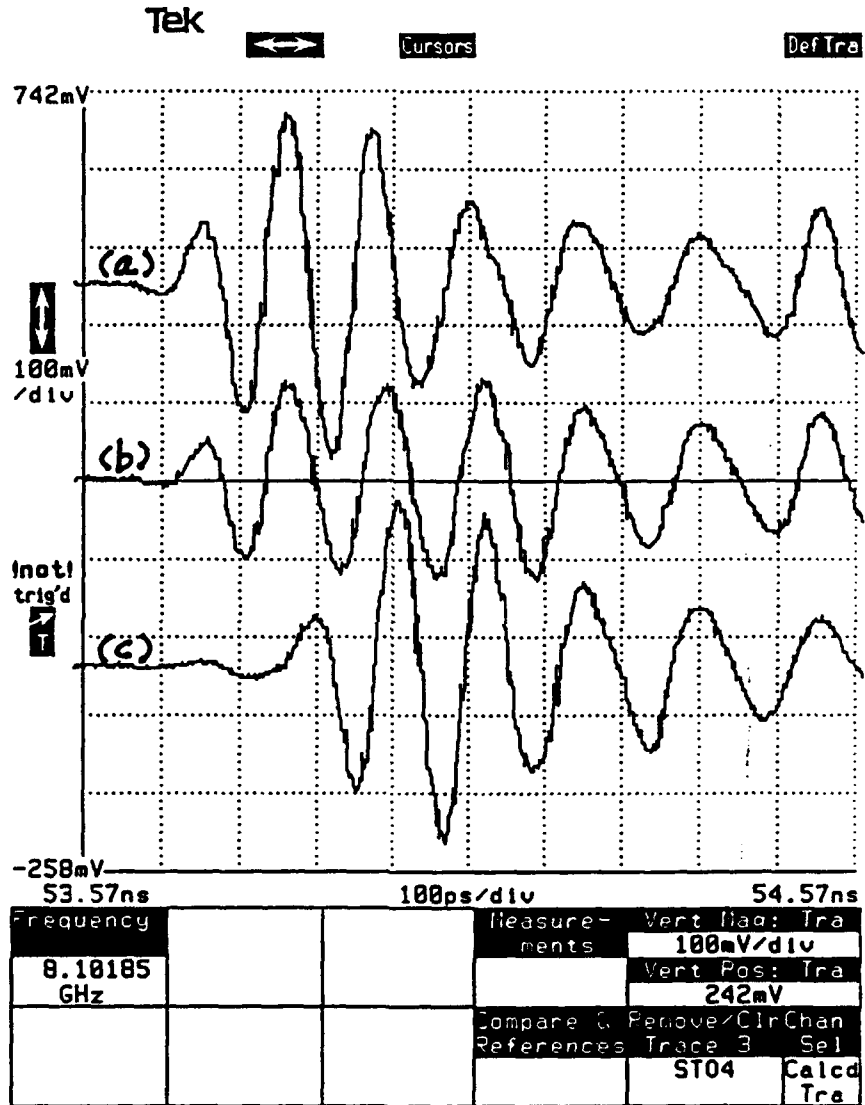
Fig. 9 Microwave signals generated by single illumination ((a)&(c)) and dual illumination (b).

AN EXPERIMENTAL AND NUMERICAL STUDY OF THERMAL CONDITIONS
IN A HIGH PRESSURE SYSTEM FOR INDIUM PHOSPHIDE CRYSTAL GROWTH

Vishwanath Prasad, Professor
Department of Mechanical Engineering
State University of New York, Stony Brook, NY 11794-2300

and

Andrew P. Anselmo[1], Doctoral Candidate
Department of Mechanical Engineering
Columbia University, New York, NY 10027

---

1. Present Address: Department of Mechanical Engineering
        State University of New York, Stony Brook, NY 11794-2300

AN EXPERIMENTAL AND NUMERICAL STUDY OF THERMAL CONDITIONS IN A HIGH PRESSURE SYSTEM FOR INDIUM PHOSPHIDE CRYSTAL GROWTH

Vishwanath Prasad
Department of Mechanical Engineering
State University of New York, Stony Brook, NY
and
Andrew P. Anselmo
Department of Mechanical Engineering
Columbia University, New York

Abstract

For one-step, in-situ synthesis of phosphorus vapor and indium melt, and liquid-encapsulated Czochralski growth of InP crystals to succeed and produce single crystals of uniform quality and at lesser cost, it is important to develop a basic understanding of the mechanics of heat transfer and gas flow in a high pressure crystal growth (HPCG) furnace. A series of experiments performed recently in order to characterize the temperature conditions at the graphite susceptor and crucible walls is reported here. These results demonstrate the variations in temperature profiles with the power input as well as with the crucible's vertical location. A computer model to study the gas flow in an HPCG furnace has also been developed. Numerical computations are performed to examine the gas flow and temperature fields with and without the presence of phosphorus injector inside the furnace. Complex recirculatory flows which become oscillatory at high Grashof numbers, are produced by the buoyancy forces. The temperature variations are generally very strong in the vicinity of the encapsulant surface, and weak in the outer region which agree qualitatively with the temperature measurements.

AN EXPERIMENTAL AND NUMERICAL STUDY OF THERMAL CONDITIONS IN A HIGH PRESSURE SYSTEM FOR INDIUM PHOSPHIDE CRYSTAL GROWTH

V. Prasad and A. P. Anselmo

INTRODUCTION

In order to grow single crystals of III-V compounds such as gallium arsenide, indium phosphide and so on, a high pressure crystal growth (HPCG) system is used. The mechanisms of energy transport in such furnaces are very different from that in the low pressure Czochralski puller for silicon crystals. While in a low pressure system, the energy is transferred to the melt and from the melt and crystal, primarily by conduction and radiation, gas convection plays an important role together with other modes of heat transfer in determining the thermal field within an HPCG puller. The buoyancy-driven convective flows in a high pressure chamber are turbulent and oscillatory, and the recirculating gas flow pattern is a strong function of the geometric configuration, temperatures of the r.f. coil, susceptor, melt, crystal and puller walls, and the gas properties. In addition, the convective heat transfer in an HPCG system is strongly coupled with the conduction in various components of this system and radiation exchange between the surfaces which can see each other.

The heat transfer mechanism is further complicated by the process employed to grow the single crystal. Motivated by the high cost of indium phosphide crystals grown by a two-step method - the synthesis of polycrystal by the horizontal Bridgman method and single crystal growth by the liquid-encapsulated Czochralski (LEC) method, a one-step operation has been proposed and investigated by several researchers [1-11]. It is basically an LEC method for pulling a single crystal from an "in-situ" synthesized melt of indium phosphide. Recently, magnetically stabilized liquid-encapsulated Czochralski (MLEC) and Kyropoulos (MLEK) growth of InP single crystals have also been reported [12,13].

For synthesis, the heat radiated by the melt is absorbed by the solid phosphorus for melting and/or sublimation. The convective heat transfer also helps. The temperature of the phosphorus can therefore be controlled by changing the vertical location of the injector. The ampoule is placed directly above the melt and the vapor is transferred to indium melt by a quartz tube whose length is another key variable in the "in situ" synthesis. The heat transfer phenomena during the in-situ synthesis is therefore highly transient. The movement of P-injector changes the temperature field significantly by modifying the radiation exchange between various surfaces and by changing the convective gas flow rate and its structure. The

energy generated into the melt due to the reaction of In and P, and the volume increase (ρ_{In} = 7.31 and ρ_{InP} =4.787) also affect the heat transfer and gas velocity.

For one-step, in-situ synthesis and growth process to succeed and produce InP crystals of uniform quality and at lesser costs, it is important to understand the mechanics of heat transfer and gas flow in an HPCG furnace. This can be achieved only by a well-coordinated experimental and numerical research program. During this summer, we developed a model to analyze the gas flow inside the HPCG furnace, and have performed simulations for a number of selected cases. The computed flow fields support the observed flow phenomena in the furnace [14,15]. Also, whenever a model is used to simulate the crystal growth process, a selection of suitable boundary conditions poses the biggest problem. Special experiments were therefore designed and conducted to determine the boundary conditions on the crucible wall as well as the relationship between the power input and the wall temperature variations as functions of the crucible's location.

DESCRIPTION OF THE HPCG FURNACE

The HPCG furnace (Fig. 1) used for ongoing research at Rome Laboratory uses a 96 mm i.d. quartz crucible or a PBN cup of 2 mm thick wall, placed in a 113 mm o.d. graphite susceptor. The susceptor is insulated from the r.f. coil by "Fiberfrax Lo-Con Felt" insulation placed in an annular space formed by two quartz cylinders. An opaque glass plate of 280 mm diameter separates the bottom portion of the furnace from its upper region. However, the gas can flow downward through a 2 mm gap between this plate and cold puller wall. The plate is placed on top of the quartz cylinders, 305 mm from the bottom surface of the puller, while the mean height of the upper tube of the r.f. coil is 286 mm. The graphite susceptor with crucible can be moved up or down, and can be rotated by a shaft. The shaft holds a boron nitride (BN) hollow cylinder which, in turn, supports the susceptor. A tungsten sheathed W26Re-W.5Re thermocouple probe passes through the shaft and measures temperature at the crucible bottom.

A 75 mm o.d., 100 mm long quartz ampoule is used for phosphorus storage and its vapor injection into the indium melt. This injector has an off-center tube of 12 mm i.d. for the vapor outflow. The injector can be hung from the top with the help of a 12 mm i.d. hollow tube through which a cooled seed shaft can pass. The injector can be moved up or down independent of the seed shaft. The gap (about 2 mm) between the hollow, support tube and the seed shaft can allow the cold gases to flow downward along the seed shaft. To insulate the phosphorus injector from heat losses, 8 mm Lo-Con felt insulation is placed between the injector and an inverted quartz cup (Fig. 1).
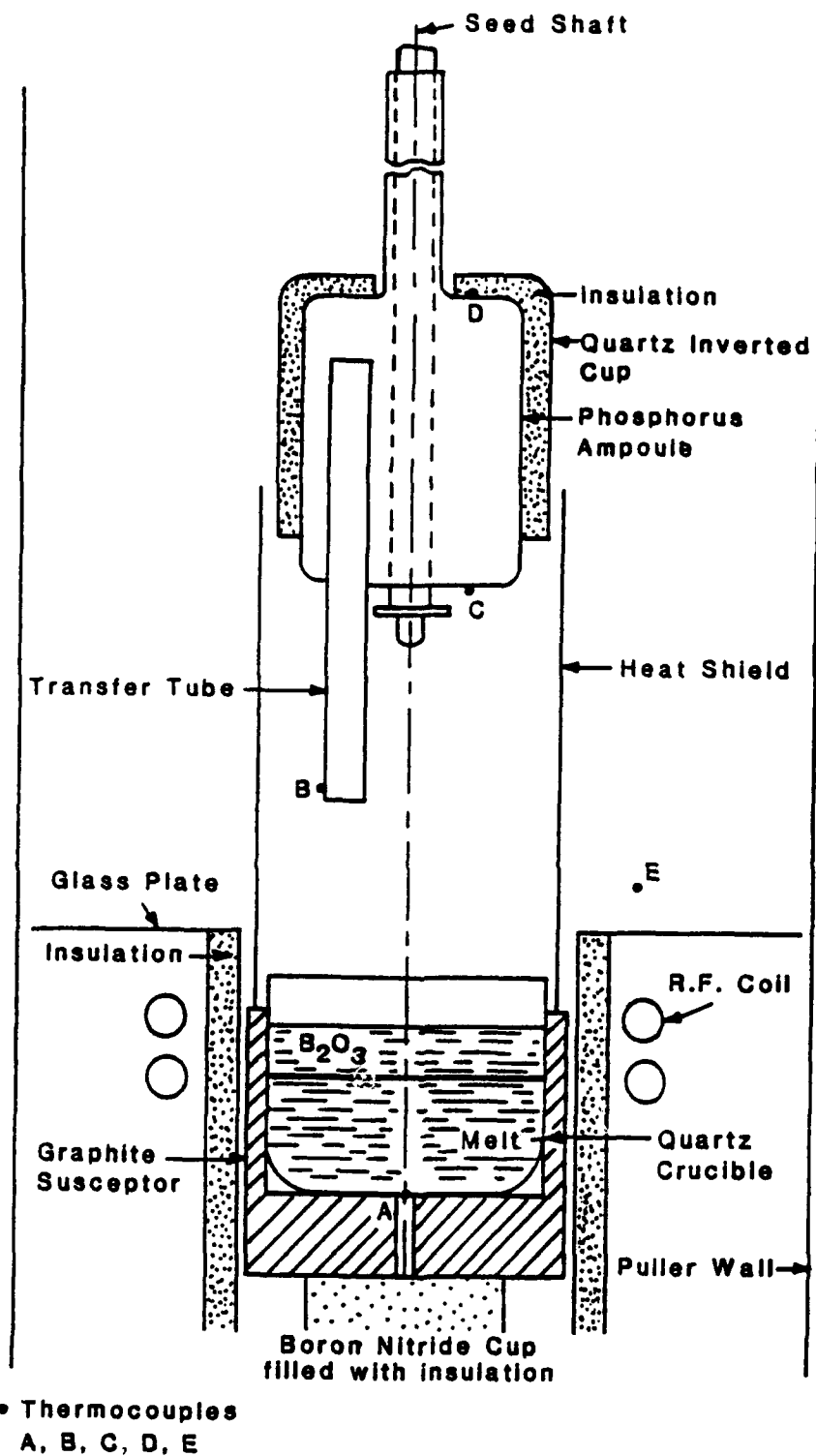
Figure 1. A schematic of the high pressure crystal growth furnace used for the on-going research on in-situ synthesis and MLEK growth of InP single crystals at Rome Laboratory.

A quartz cylinder of 103 mm i.d. is used as a heat shield. However, the heat shield cannot completely eliminate the buoyancy-induced flows - gas flows downward along the seed shaft and upward along the quartz shield - it can reduce the gas velocity significantly. The heat shield rests on the graphite susceptor and therefore can rotate with the crucible. Further details of the HPCG furnace may be found elsewhere [14,15].

There are two viewing ports in this HPCG puller, one is used for video monitoring and photography while the other helps in visual observation. Since the system is run at a high temperature (above 1063°C) and a high pressure (500-600 psi) at which the density of nitrogen is about six to fifteen times larger than at the atmospheric condition, it is possible to see the direction of flow whenever the gas flows over a step. Light reflections also seem to help in this visualization. Although only a small portion of the growth chamber is visible, it is possible to draw flow patterns qualitatively from the observed gas flow behavior [14,15].

EXPERIMENTAL WORK

A series of experiments to study the thermal conditions in this HPCG furnace was conducted earlier and has already been reported in the literature [15]. The purpose of the present experiment is to measure temperature variations on the crucible wall and the outer surface of the susceptor, and to determine their relationship with the power input as well as with the crucible's location. Several thermocouples were therefore placed outside the susceptor and inside the crucible as shown in Fig. 2. This was the first time that 11 thermocouples were used to record temperature distributions in this system. A conex fitting was used to carry eight thermocouple extension wires. However, this was not a simple job, because placing the thermocouples at right locations and holding them there during the experiments are not easy tasks. Inner thermocouples were placed inside thin quartz tubes attached to the crucible wall, to prevent them from damage from the melt as well as to hold them in place. In order not to alter the susceptor's characteristics, outer thermocouples were placed on the outside of the inner quartz cylinder. We also connected a personal computer to the existing Omega strip chart recorder to monitor and record temperature continuously. Software were developed to collect the temperature information and store them for further analysis. We were therefore able to add some permanent features to the existing system which can help in future experiments.

First, the crucible was held in its central location (@ 2 cm) and temperatures were recorded for three different power inputs. Next, the power was kept fixed and the crucible was moved up or down to study the effect of its location. Figure 3 presents the crucible's location with respect to the r. f. coil. Sufficient time was allowed after every change in either power or location, for the system to reach (quasi) steady-state. From the temperature data collected, it is
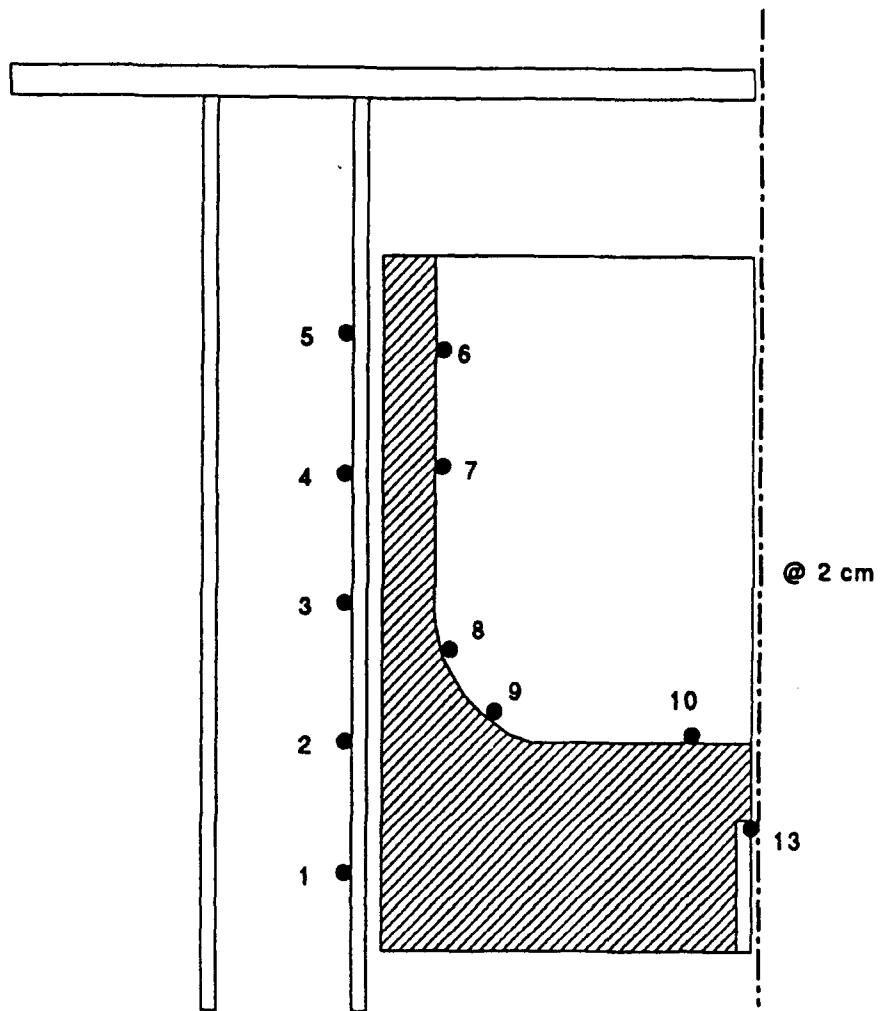
Figure 2. Thermocouple locations for temperature measurements on the inside of the crucible and outside of the graphite susceptor.
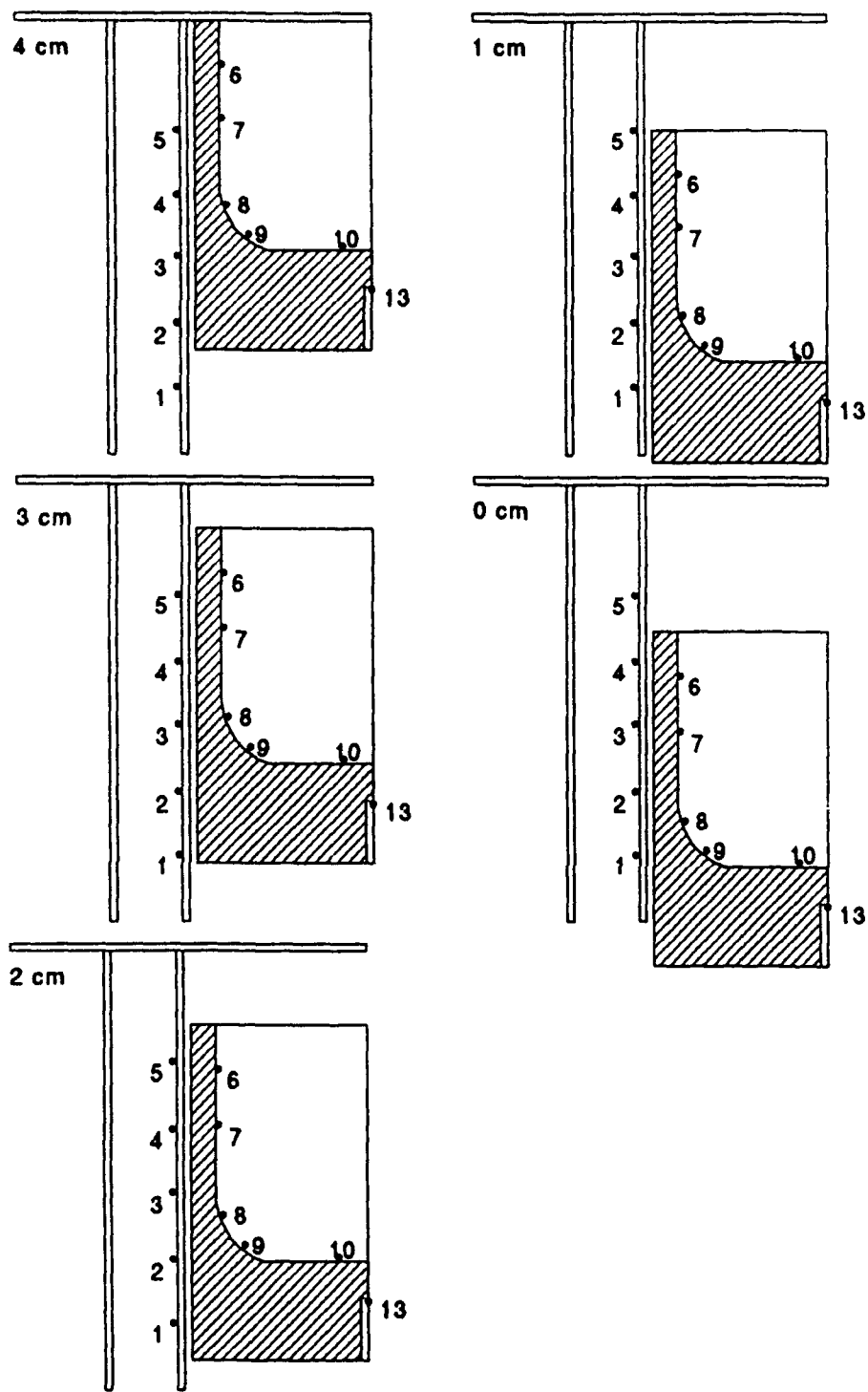
Figure 3. Crucible locations with respect to the upper quartz plate (Fig. 1).

possible to study the transients inside the HPCG furnace. However, this report will present temperatures only under steady conditions (Figs. 4 and 5).

We also designed and conducted two other sets of experiments. The objective of the first experiment was to study the effects of a graphite cover placed on top of the phosphorus injector. This was observed to suppress the temperature fluctuations [14,15] on the injector and temperature rise at the bottom and top of the injector was very smooth. However, the rate of phosphorus vaporization was slow which did not help the synthesis process. The second set of experiments was conducted to examine the effect of a reduction in radiation loss from the melt. The space between the furnace wall and the heat shield (146 mm dia. in this case) was filled with an insulation, placed between two concentric cylinders. This reduced the radiation loss significantly, and a larger temperature rise was observed at lower powers. A detailed analysis of these results will be presented later.

Figures 4(a) and 4(b) present the temperature rise with power. As can be seen the temperature increases monotonically with the power, and the nature of the curve does not change. Indeed the curves are almost parallel and support our earlier observation [14,15] that the melt temperature changes almost linearly with power. In Fig. 4(a), the thermocouple # 2 reads the largest temperature which is slightly higher than that at 1. The temperature, however, drops with the height, moving up from # 2 to # 5. This can be easily explained by considering the heat loss from the susceptor. Thermocouple #5 is in a position where the susceptor loses heat directly to the furnace walls and other components by radiation whereas the energy in the middle portion of the susceptor is transferred to the melt only by conduction. The temperature in the lower portion of the susceptor is smaller because of heat loss to the bottom portion of the furnace. Figure 4(b) confirms this behavior by demonstrating that the temperature is lowest for # 7 and largest for # 8. (Unfortunately, thermocouples 6 and 10 stopped working soon after the experiment was started.)

Figure 5 demonstrates the effects of the crucible's location (central location @2cm). It is observed that the temperature of the susceptor generally increases as it is moved up (Fig. 5a). The only exception is the bottom, thermocouple #1. Figure 5(a) further shows that the temperature at the top of the susceptor is much lower than that at its bottom when the susceptor is at its bottom most location, a temperature drop of 600°C. This temperature variation decreases as the susceptor is moved up, less than 200°C at the topmost location. This does not mean that the topmost location is the most desirable one. As shown in Fig. 5(b) by thermocouple # 7, the melt temperature may be lower when the susceptor is at its top location. It seems that a central location somewhere between 2 and 3 cm is better for the melt.
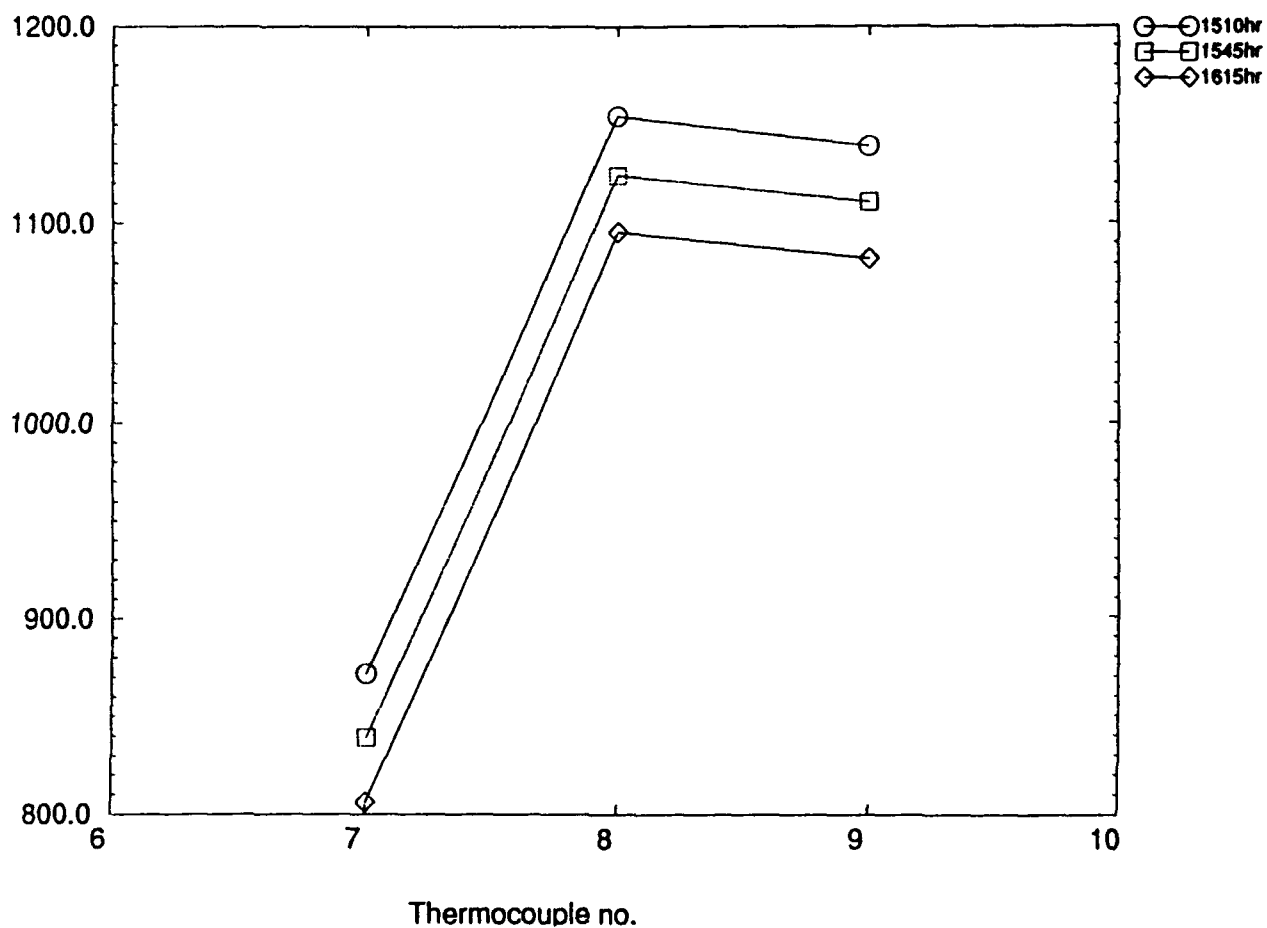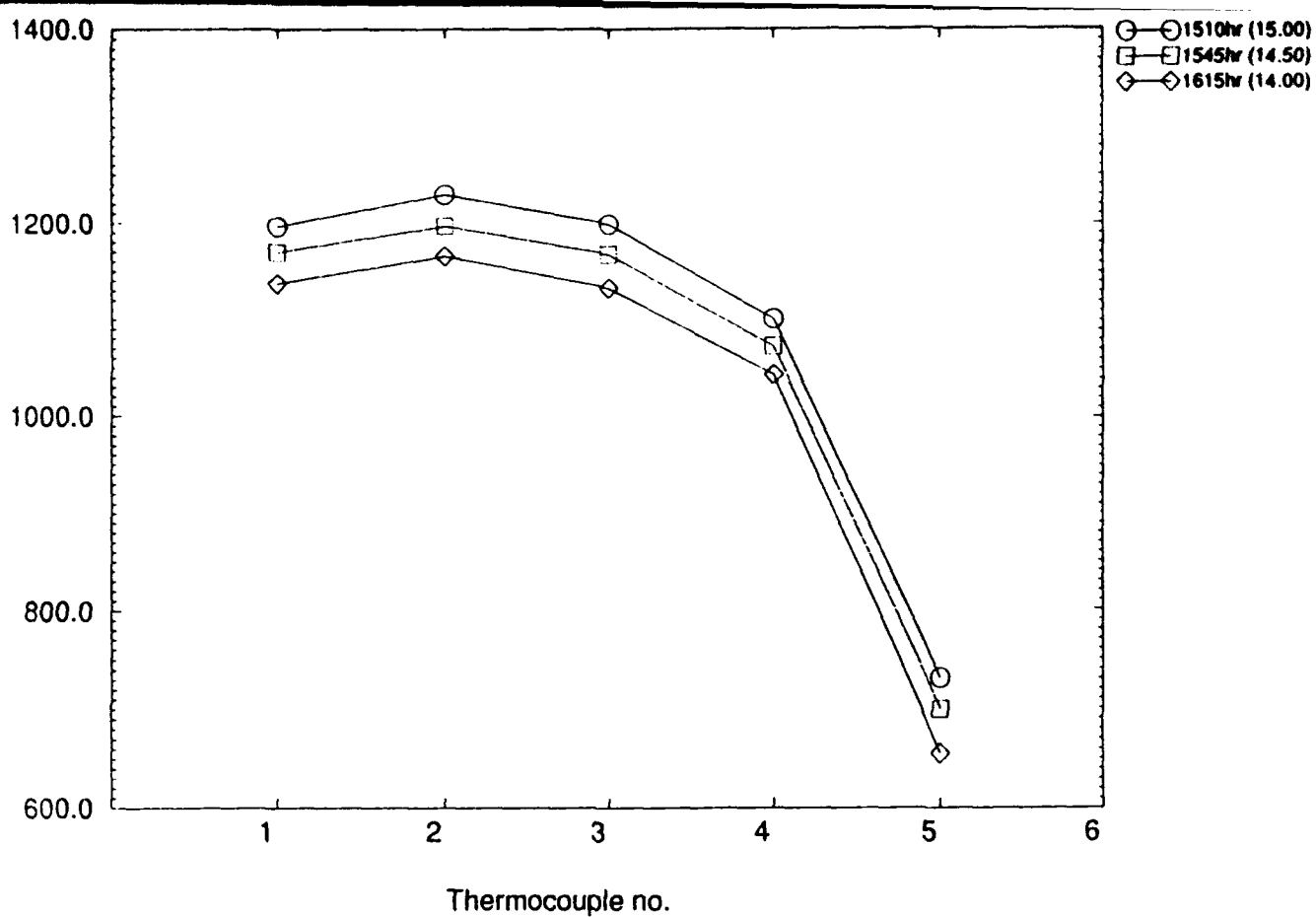
Figure 4. Temperature variation as a function of the power input. The power is expressed here in terms of the applied voltage. (a) temperature on the outside of the graphite susceptor and (b) temperature on the inside of the crucible wall.
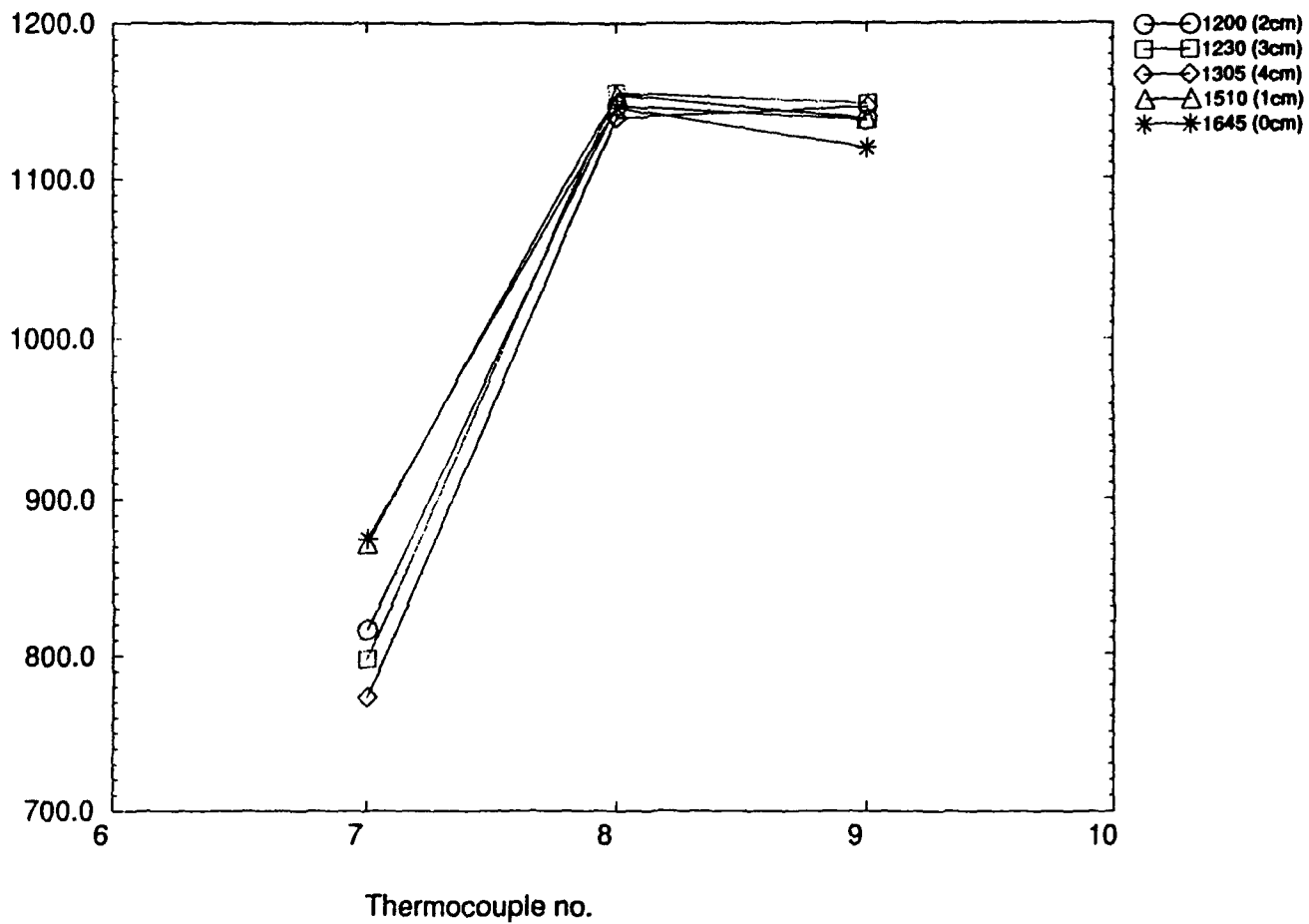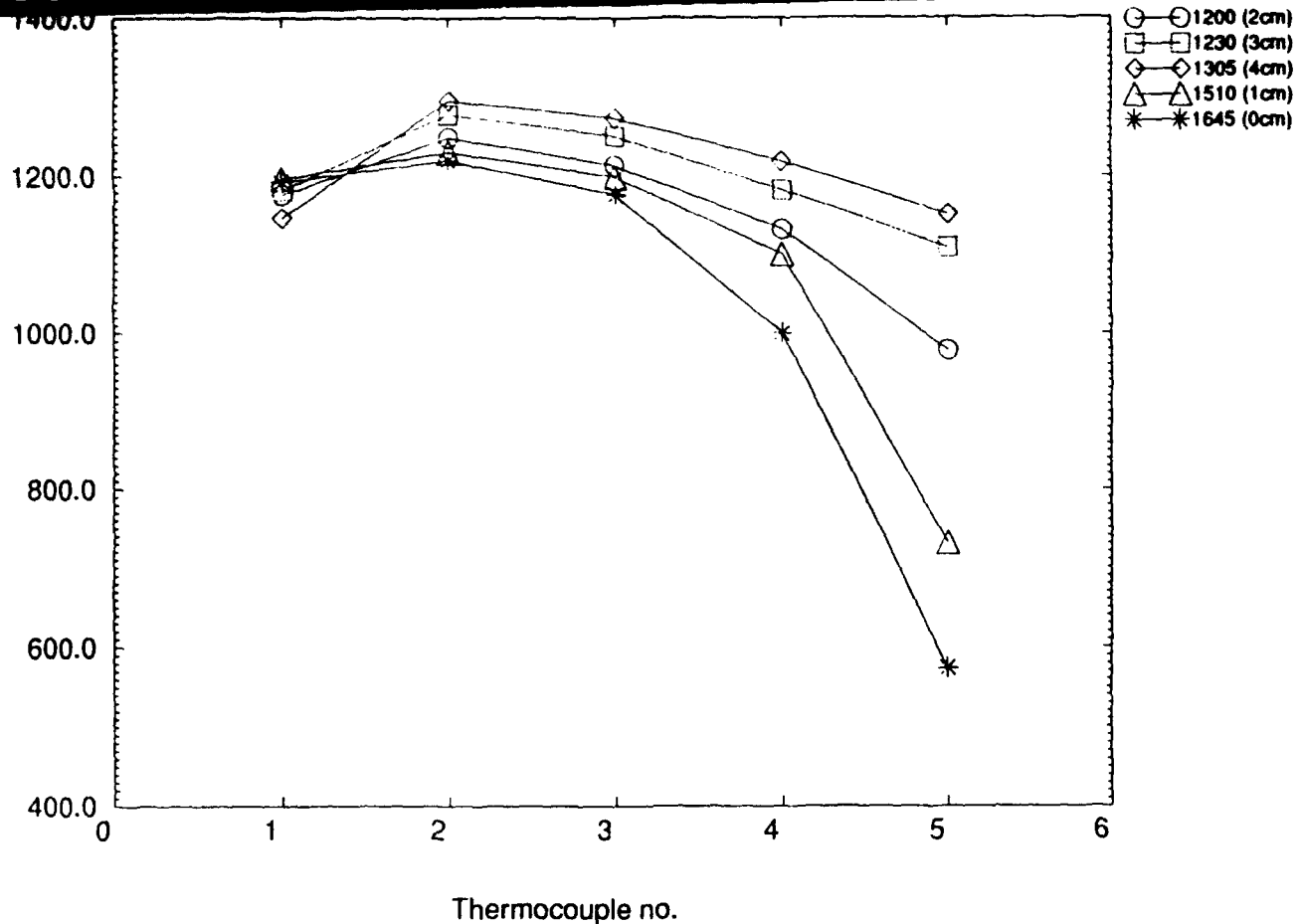
Figure 5. Temperature variation as a function of the crucible location. (a) temperature on the outside of the graphite susceptor and (b) temperature on the inside of the crucible wall.

NUMERICAL STUDY OF GAS FLOW IN AN HPCG FURNACE

As reported earlier [14,15], strong convective flows are induced in an HPCG furnace. The flow is oscillatory and turbulent, and has a complex pattern. A numerical research program was therefore initiated to study the gas flow phenomena in a high pressure system. **Governing Equations.** The model used here to analyze the gas flow assumes that the flow is incompressible and laminar (turbulent flows may be considered in the future), the Boussinesq approximation is applicable, and the viscous dissipation is negligible. The gas flow is considered to be axisymmetric, and therefore, only two dimensional calculations are performed. With these assumptions, the non-dimensional governing equations can be written as follows:

Continuity:

$$\frac{1}{r}\frac{\partial}{\partial r}(ru) + \frac{\partial w}{\partial z} = 0 \tag{1}$$

R-Momentum:

$$\frac{\partial u}{\partial t} + u\frac{\partial u}{\partial r} + w\frac{\partial u}{\partial z} = -\frac{\partial p}{\partial r} + \frac{1}{r}\frac{\partial}{\partial r}(r\frac{\partial u}{\partial r}) + \frac{\partial^2 u}{\partial z^2} - \frac{u}{r^2} \tag{2}$$

Z-Momentum:

$$\frac{\partial w}{\partial t} + u\frac{\partial w}{\partial r} + w\frac{\partial w}{\partial z} = -\frac{\partial p}{\partial z} + \frac{1}{r}\frac{\partial}{\partial r}(r\frac{\partial w}{\partial r}) + \frac{\partial^2 w}{\partial z^2} - Gr\Theta \tag{3}$$

Energy:

$$\frac{\partial \Theta}{\partial t} + u\frac{\partial \Theta}{\partial r} + w\frac{\partial \Theta}{\partial z} = \frac{1}{Pr}\left(\frac{1}{r}\frac{\partial}{\partial r}(r\frac{\partial \Theta}{\partial r}) + \frac{\partial^2 \Theta}{\partial z^2}\right) \tag{4}$$

which employ the following scales:

length: b, time: b^2/α , velocity: ν/b, and pressure: $\rho\nu^2/b^2$.

Here, the dimensionless velocities in radial (r) and axial (z) directions are represented by u and w, respectively, while p and t denotes the pressure and time. The dimensionless temperature, Θ, is defined as $(T - T_c)/(T_h - T_c)$, where T_h and T_c are the encapsulant surface and wall temperatures, respectively. Here, ν, α, and β are kinematic viscosity, thermal diffusivity and isobaric coefficient of thermal expansion, respectively. The crucible radius, b, has been chosen as the primary length dimension. The governing parameters Gr and Pr are defined as:

$$\text{Grashof number,} \quad Gr = g\beta b^3(T_h - T_c)/\nu^2 \tag{5}$$

$$\text{Prandtl number,} \quad Pr = \nu/\alpha \tag{6}$$

The flow boundary conditions are relatively well-defined since the gas occupies a specifically prescribed control volume with rigid boundaries except the encapsulant surface. For present calculations, the encapsulant surface has also been assumed to be rigid. No-slip conditions are therefore employed on all boundaries. However, the thermal boundary conditions are not as accurately known, since precise conditions within the real systems are not known. For present calculations, we consider $\Theta = 1$ at the encapsulant surface while the furnace walls are assumed to be at $\Theta = 0$. More realistic boundary conditions based on temperature measurements may be employed in future.

In this numerical algorithm, the solid region within the computational domain is introduced by imposing an extremely large artificial viscosity in that region so that no flow can take place in this area. Heat conduction is allowed to take place through the partitions walls/heat shields. This does not pose any difficulty since the energy equation (4) automatically reduces to the conduction equation when the velocities are zero. Note that the thermophysical properties can be allowed to vary from grid to grid [16,17].

Numerical Scheme. The governing equations (1)-(4) are discretized using the control volume integral approach and a staggered grid. It is Patankar's SIMPLER method which is used to solve the equations [18]. In this scheme, each term is integrated over its volume element. In a similar manner, the continuity equation is integrated over the same control element, then multiplied by the dependent variable of the equation being discretized. The discretized continuity equation is eventually subtracted from the discretized momentum or energy equation. This manipulation enables the flow field to always satisfy mass conservation. Two other equations, the pressure and pressure-correction equations are obtained by substituting the discretized momentum equations into the continuity equation. The latter has the task of correcting the velocities during iterations, while the former improves the pressure field. The SIMPLER method is based on a semi-implicit procedure. In the present algorithm, the convective fluxes are approximated by the power law scheme [16-18] which is one of the most robust algorithms. It approximates the central difference when velocities are small, and gradually mimics the upwind difference when velocities becomes large.

The discretized equations are underrelaxed and solved iteratively, within each time step to resolve the coupling and nonlinearity of the flow and energy equations, using a line-by-line tri-diagonal matrix algorithm. Sweeps are performed in both forward and backward directions so that the effects in one part of the computational domain may be felt throughout the entire domain without bias. Convergence at each time step is declared when the mass source and the residuals of the discretized equations are less than a specified absolute relative tolerance. Strict convergence within each time interval is crucial for the accuracy of the final solutions, particularly when the flow is oscillatory. Since the temperature gradients are generally strong

in the vicinity of the furnace walls, the quartz shields and the encapsulant surface, a suitable non-uniform grid distribution is used for the present computations. Only limited trials runs were carried out to optimize the grid distribution, convergence criteria and time step since our objective here is to obtain some qualitative information first and see how do they compare with the observed flows.

Numerical Results. Figures 6 and 7 present the flow and temperature fields in half of the cylindrical enclosure with a partition for Gr = 10^6 and 5×10^7, respectively. For these calculations, the gas properties are assumed to be constant. As can be seen in Fig. 6a, there exist two main recirculating cells, one on top of the encapsulant (rotating counter-clockwise) and the other on the outside of the partition wall extending to the top (rotating clockwise). The mechanism of formation of these cells is straight-forward. The gas is heated by the encapsualnt surface and moves up along the quartz shield since the cold gas flows downward along the seed rod which is at a lower temperature than the B_2O_3 surface (Fig. 1). On the outside of the quartz shield, the hot gas rises along its surface and flows downward along the cold furnace wall. This is a basic flow pattern which is induced by the thermal conditions in this HPCG furnace and agrees with the visualization reported earlier [14,15].

Figure 6(b) also shows that a large temperature gradient exists near the B_2O_3 surface and even temperature inversion is possible. The temperature variations in the region outside of the quartz shield and in the upper portion of the furnace are weak. However, a strong flow is induced in this region primarily because of the shear effects produced by the inner cell, and a strong buoyancy force, since the length scale is very large. Note that the Grashof number is proportional to the third power of the length (equation 5).

Figure 7 (Gr = 5×10^7) demonstrates the effect of an increase in the buoyancy force. Although the primary flow pattern remains the same, the convective flow oscillates at this Grashof number (Fig. 7a). Several secondary cells whose shapes and sizes change with time are produced and the flow becomes extremely complex. This supports our earlier observation that the flow in an HPCG furnace is oscillatory [14,15]. Note that this Gr is much lower than the real value encountered in an HPCG furnace, and at higher Grashof numbers, the flow can certainly become chaotic and turbulent. Figure 7b further shows that with an increase in Grashof number, the plume effect has been extended much beyond the vicinity of the B_2O_3 surfa· ·roducing large temperature gradients in other regions (compare with Fig. 6b).

· the above calculations, the presence of the phosphorus injector inside the furnace was not considered, as well as the thermophysical properties of the nitrogen gas were assumed to be constant. A set of calculations was therefore performed to examine the effects of these parameters. The phosphorus injector was placed at its topmost location which simulates the
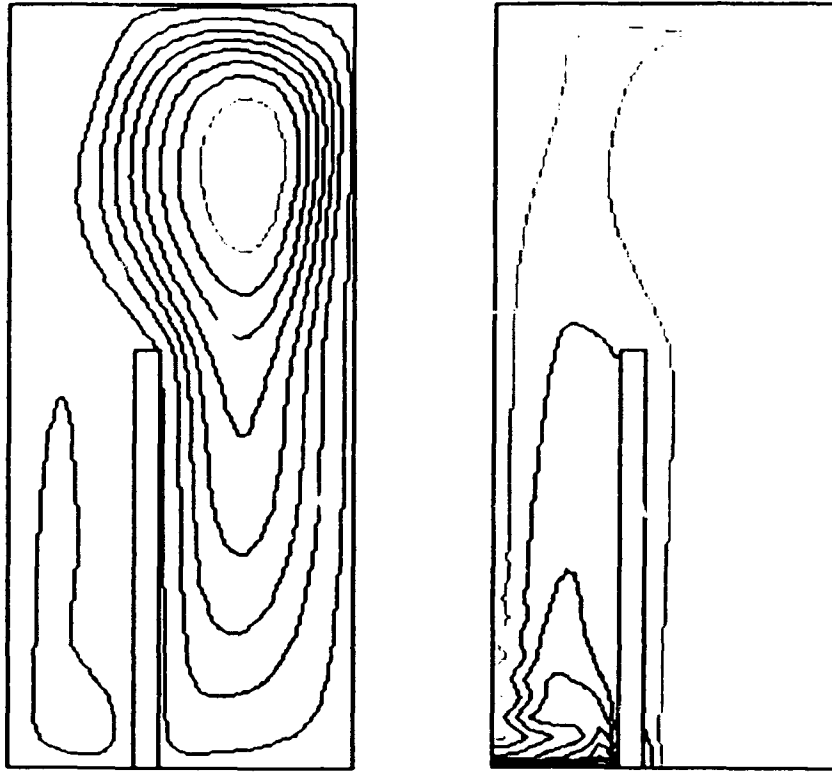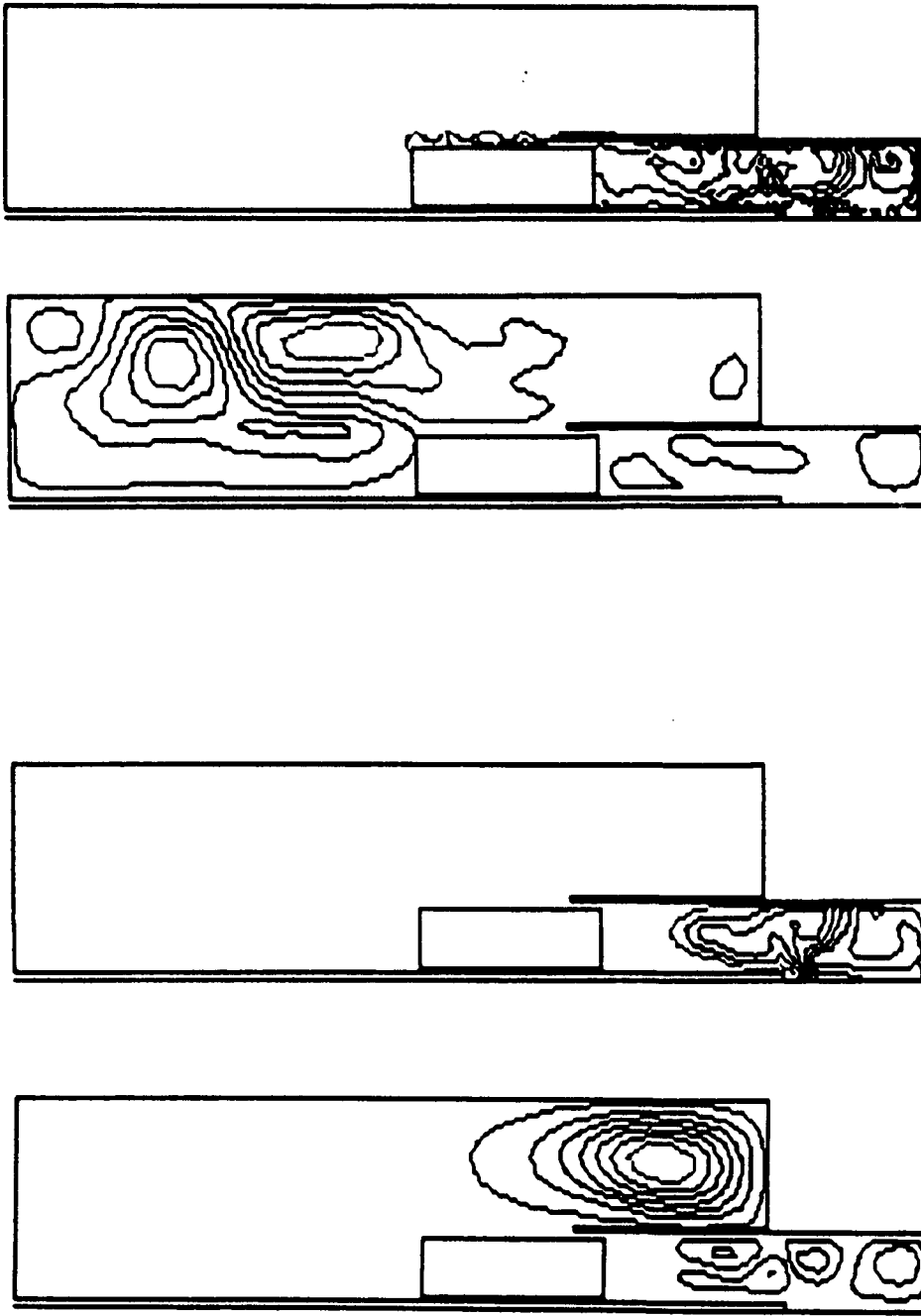
Figure 6. Predicted temperature and flow fields in right half of the enclosure for Gr = 10^6, the effect of a partition wall, (a) flow field and (b) temperature distribution.
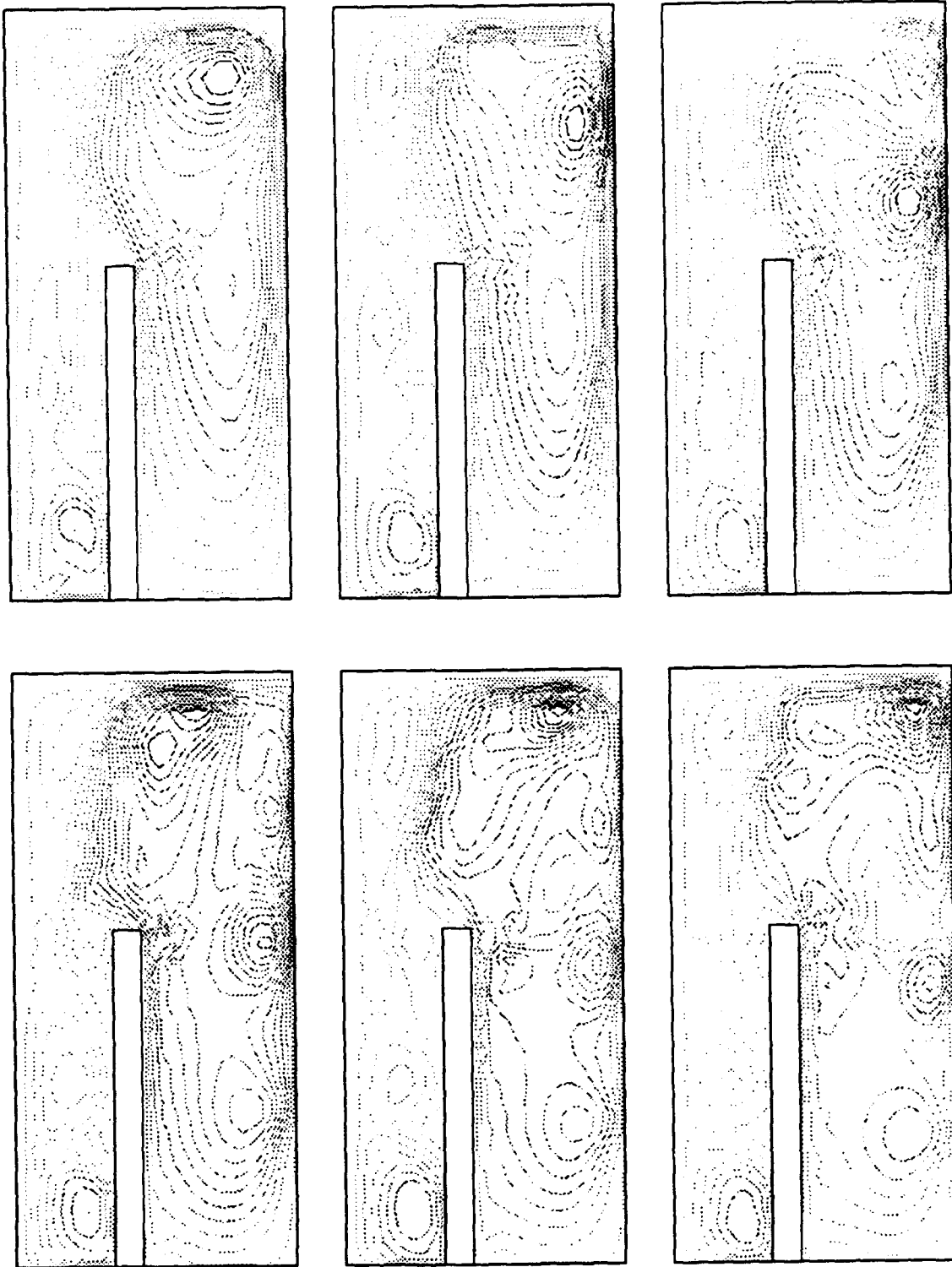
Figure 7a. Predicted flow fields in right half of the enclosure for Gr = 5×10^7, the effect of a partition wall.
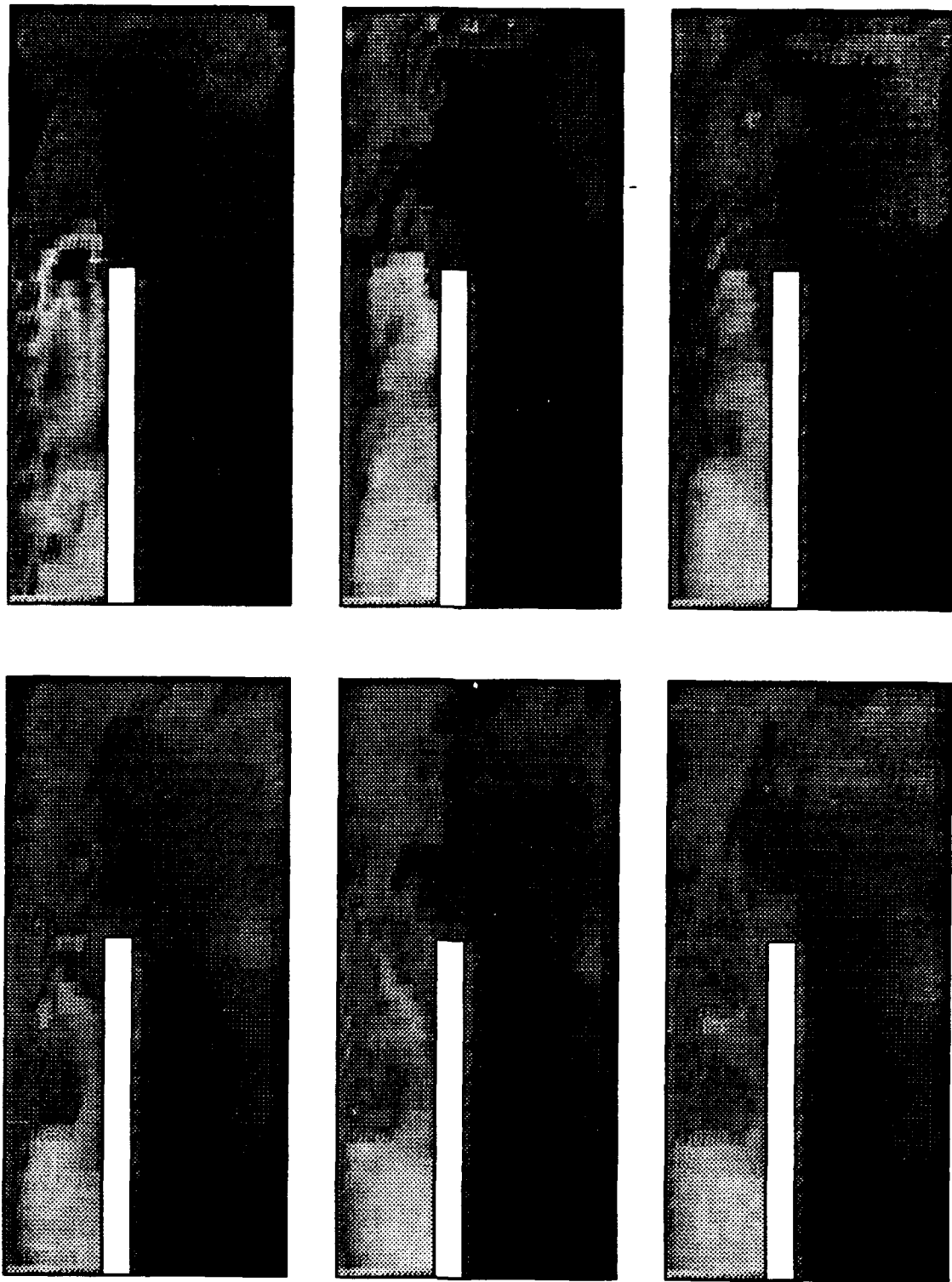
Figure 7b. Predicted temperature field in right half of the enclosure for Gr $= 5\mathrm{x}10^7$, the effect of a partition wall.

crystal growth conditions, and the gas properties were allowed to vary with temperature. These results are presented in Figs. 8-9 for Gr = 10^6, 5×10^7 and 5×10^8, respectively.

In comparison to Fig. 6a, it is now observed that several cells are produced in the melt region at Gr = 10^6 (Fig. 8a), one on top of the other (underneath the P-injector). This is primarily because the phosphorus injector restricts the flow passage, and the gas can go out only through a small passage between the injector and the heat shield. The flow in the outer region has also become weaker and does not extend to the top portion of the furnace as much as it did earlier. As a result the temperature gradient is also localized in the melt region (Fig. 8b).

An increase in Gr again complicates the flow, and two large cells are produced in the outer region (Fig. 9a). These two convective cells have resulted from the hot gases coming out through the gap between the heat shield and the injector, and getting cooled on the furnace side wall and top as well as by the seed rod. The top surface and seed rod provide negative buoyancy for the upper cell while the side wall produces a second cell rotating in the clockwise direction. Several secondary cells are produced when the Grashof number is high although the basic pattern of the flow remains the same. The flow at Gr = 5×10^8 is oscillatory (not shown here). It seems that the flow restriction has reduced the buoyancy effect in the outer region thereby suppressing the oscillatory behavior to some extent. Figure 9(b) demonstrates the complexity of the temperature fields at high Grashof numbers. The temperature fields reported in Figs. 6(b)-9(b) qualitatively agree with the temperature measurements reported earlier.

CONCLUDING REMARKS

In order to develop a successful process for one-step, in-situ synthesis of phosphorus vapor and indium melt and growth of InP crystals of large sizes, uniform properties and at lesser cost, it is extremely important to understand the mechanism of heat transfer and gas flow in a high pressure crystal growth system. A series of experiments and numerical computations have been performed to study the thermal conditions in an HPCG furnace. Temperature distributions have been measured for the first time on the outer surface of the graphite susceptor and the inner surface of the crucible. The effects of variation in power supply and the vertical location of the crucible have also been examined. The numerical results demonstrate interesting flow patterns and show that the flow becomes oscillatory at high Grashof number.

Even though these experiments and computations provide a much better understanding of the HPCG furnace for one-step, in-situ synthesis and growth of InP crystals, they are by no means complete. Further experiments and simulations are needed to characterize the heat

Figure 9. Predicted temperature and flow fields in right half of the enclosure for Gr = 5x10⁷, the effect of a partition wall and the phosphorus injector, (a) flow field and (b) temperature distribution.

Figure 8. Predicted temperature and flow fields in right half of the enclosure for Gr = 10⁶, the effect of a partition wall and the phosphorus injector, (a) flow field and (b) temperature distribution.

transfer and gas flow under the growth conditions. A simultaneous theoretical/numerical and experimental research program will further help in determining the optimized conditions for both the synthesis and the growth, and in suggesting the modifications in the existing system in order to achieve these conditions.

REFERENCES

1. J. P. Farges, *J. Crystal Growth*, 59, 665-668 (1982).

2. J. P. Farges, *2nd NATO Workshop on Materials Aspects of InP*, 1, 9.1-6 (1983).

3. G. A. Antypass, *2nd NATO Workshop on Material Aspects of InP*, 1, 8.1-9 (1983).

4. S. B. Hyder and C. J. Holloway, Jr., *J. Electron, Mater.*, 12, 575-585 (1983).

5. Y. Sasaki, J. Nakagawa and K. Kurata, *46th Aut. Meet., Jpn. Soc. Appl. Phys.* (1985).

6. S. B. Hyder and G. A. Antypass, *3rd NATO Workshop on Material Aspects of Indium Phosphide*, 1 (1986).

7. D. J. Dowling, R. A. Brunton, D. A. E. Crouch, A. J. Thompson and J. E. Wardill, *J. Crystal Growth*, 87, 37-41 (1988).

8. D. F. Bliss, R. M. Hilton and J. A. Adamski, *4th Int. Conf. on Indium Phosphide and Related Materials*, 262-265 (1992).

9. T. Inada, T. Fujii, M. Eguchi and T. Fukuda, *J. Crystal Growth*, 82, 561-565 (1987).

10. T. Inada, T. Fujii, M. Eguchi and T. Fukuda, *Appl. Phys. Lett.*, 50, 86-88 (1987).

11. K. Kohiro, K. Kainosho, H. Shimakura, T. Fukui and O. Oda, *4th Int. Conf. on Indium Phosphide and Related Materials*, B.5, 35-38 (1992).

12. S. Bachowski, D. F. Bliss, B. Ahern, R. M. Hilton, J. Adamski and D. J. Carlson, *2nd Int. Conf. on Indium Phosphide and Related Materials*, 30-34 (1990).

13. D. F. Bliss, J. A. Adamski, W. M. Higgins, V. Prasad and F. X. Zach, *Int. Conf. on Indium Phosphide and Related Materials, Paris* (1993).

14. V. Prasad, Thermal Characterization of In-situ Synthesis for LEC/MLEK Growth of InP Single Crystals, Final Report for Summer Research Program 1992, AFOSR.

15. V. Prasad, D. F. Bliss and J. A. Adamski, *J. Crystal Growth* (submitted).

16. A. Anselmo, V. Prasad, J. Koziol and K. P. Gupta, *J. Crystal Growth*, 131, 247-264 (1993).

17. A. Anselmo, V. Prasad, J. Koziol and K. P. Gupta, *J. Crystal Growth*, in press (1993).

18. S. V. Patankar, *Numerical Heat Transfer and Fluid Flow*, Hemisphere Publ. (1980).

CONDUCTED INTERFERENCE MEASUREMENT RESULTS FOR A GENERAL ELECTRIC CORPORATION SOFT PART ANALOGOUS MODULE (SPAM)

John P. Rohrbaugh

Senior Research Engineer

Electromagnetic Environmental Effects Laboratory

Georgia Tech Research Institute

347 Ferst St.

Atlanta, GA 30332-0800

CONDUCTED INTERFERENCE MEASUREMENT RESULTS FOR A GENERAL ELECTRIC CORPORATION SOFT PART ANALOGOUS MODULE (SPAM)

John P. Rohrbaugh

Electromagnetic Environmental Effects Laboratory

Georgia Tech Research Institute

Abstract

Conducted electromagnetic interference (EMI) measurements were performed on a General Electric (GE) Corporation Soft Part Analogous Module (SPAM) [1]. The SPAM is a high speed 1-megabit random access memory (RAM) that was built by GE to verify multi-chip-module (MCM) fabrication techniques and processes prior to full construction of radiation hardened MCM's. Measurements and simulations were also performed on the individual integrated circuits (IC's) within the MCM in order to determine if simpler and less expensive IC's could be evaluated prior to testing a more complex and costly MCM. This report discusses the conducted EMI measurements performed on the GE SPAM and the SPAM interface IC's while the simulation results are discussed in Reference 2.

CONDUCTED INTERFERENCE MEASUREMENT RESULTS FOR A GENERAL ELECTRIC CORPORATION SOFT PART ANALOGOUS MODULE (SPAM)

John P. Rohrbaugh

1.0   INTRODUCTION

Conducted electromagnetic (EM) interference measurements were performed on a General Electric Corporation Soft Part Analogous Module (SPAM) [1]. The SPAM is a high speed 1-megabit random access memory (RAM) that was built by GE to verify multi-chip-module (MCM) fabrication techniques and processes prior to full construction of radiation hardened MCM's. Measurements and simulations were also performed on the individual IC's within the MCM in order to determine if simpler and less expensive integrated circuits (IC's) could be evaluated prior to testing a more complex and costly MCM. This report discusses the measurements performed on the GE SPAM and the SPAM interface IC's while the simulation results are discussed in Reference 2.

The GE SPAM is shown in Figure 1. The SPAM is illustrated schematically in Figure 2. SPAM package pins are connected to Texas Instruments 74S00 NAND, 74S138AN 3-to-8 line decoder, 74S373AN D-flip-flop, and Performance Semiconductor P4C164 8kx8 static CMOS RAM integrated circuits (IC's). Only input data and control pins were evaluated on this effort and not +5 or output pins. Continuous wave (CW) single frequency interference measurements were performed over the interference frequency range of 10 MHz to 2 GHz.

2.0   Conducted Interference Test Setup

The MCM and IC conducted Interference test setup is illustrated in Figure 3. An HP8180A/8182A digital word generator and analyzer system was used as the functional signal source/analyzer. The HP8180A is a digital word generator having sixteen data, one strobe, and
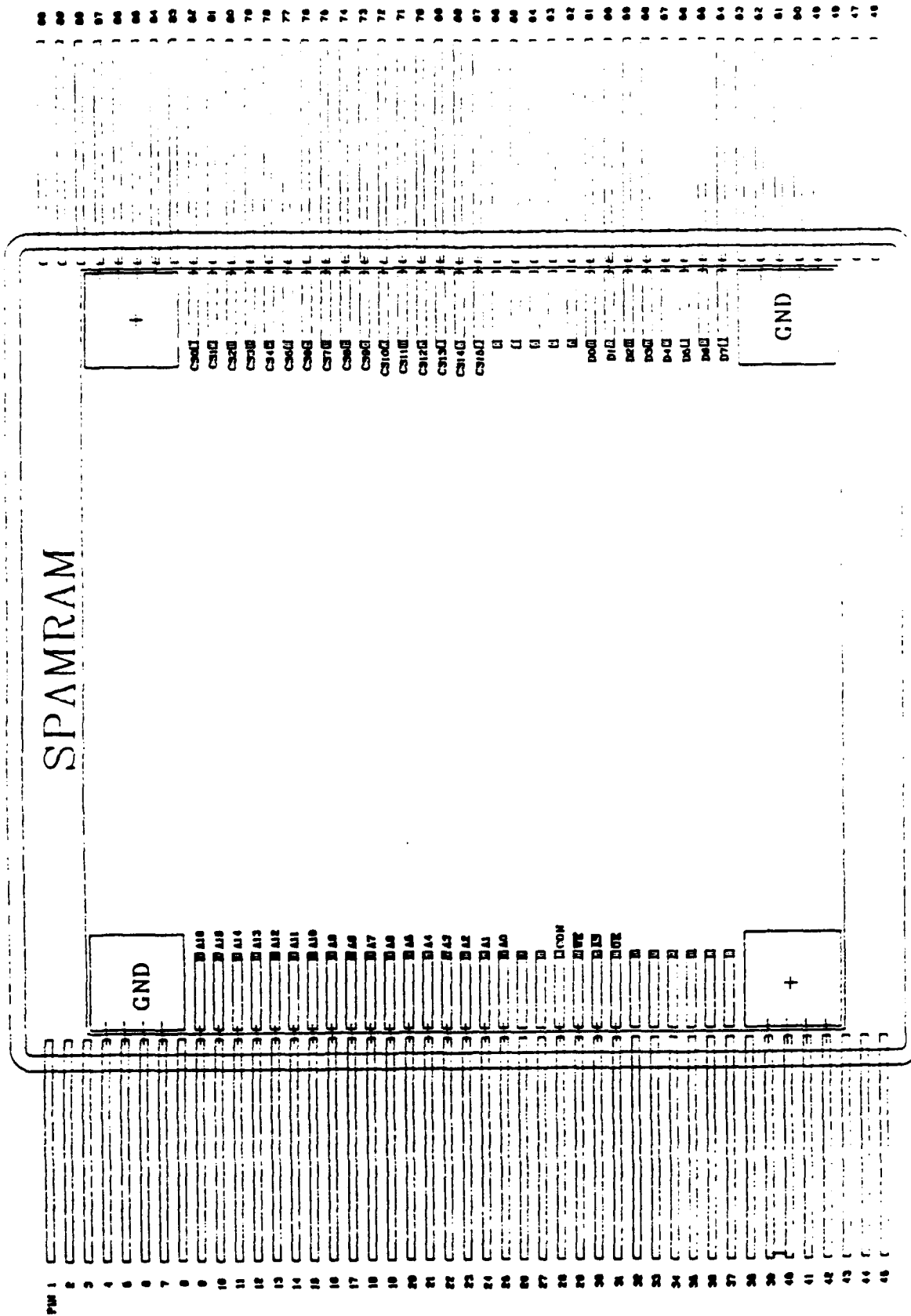
Figure 1.   GE SPAM.
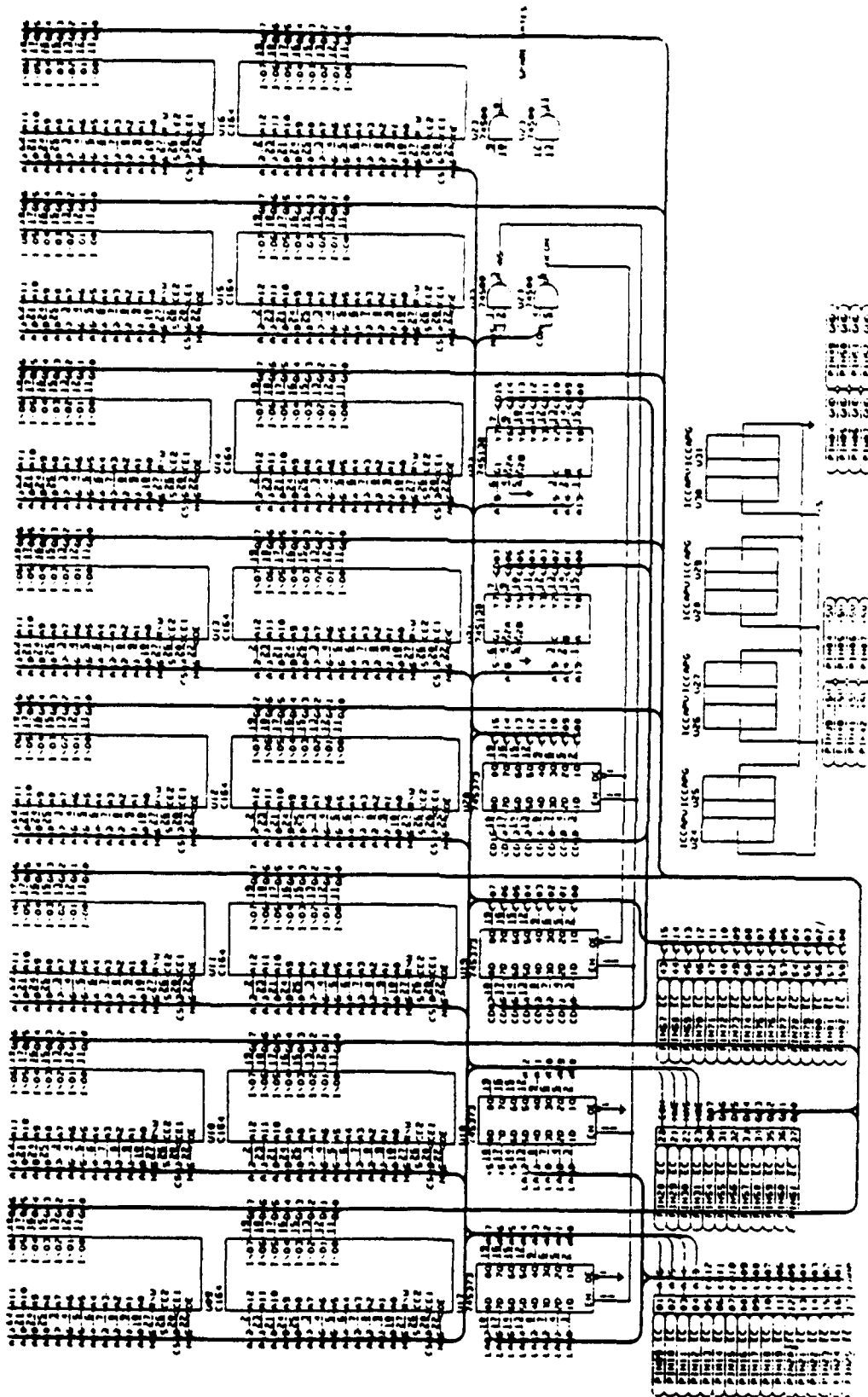
Figure 2. Schematic of GE SPAM.

14-5

Figure 3.   Conducted Interference Test Setup.

two clock outputs. One of the clock outputs was used as the external clock input to the HP8182A digital word analyzer. The strobe output was used to synchronize the HP8182A to the HP8180A for error analysis. The HP8182A was used to determine when an interference condition occurred by looking at the word error map display. When a word error occured, the word position was displayed in inverse video on the error map. The HP8180A output levels were set at 2.4 volts and 0.4 volts. The HP8182A was used as a single-threshold detector with a logic 0 to 1 transition threshold set at 1.4 volts. The HP8182A also has a timing diagram display that was used to view expected data timing patterns. An oscilloscope was used prior to all measurements to set timing, amplitude levels and to verify interference effects and thresholds.

Various combinations of signal generators and amplifiers were used to perform the conducted interference measurements depending upon the IC under test and the interference frequency. At frequencies less than 100 MHz (and greater than 100 MHz when performing measurements on the SPAM and the Performance Semiconductor RAM's) an HP8640B signal generator was used as the interference source. The output level and frequency of the HP8640B was verified to be accurate using independent measurements of power and frequency during calibration. A Mini-Circuits RF switch was used to gate interference signals into the RAM and SPAM during the write cycle only and not during the read cycle. Various amplifiers were used after the RF switch if the interference power level exceeded the RF switch's 1 db compression point of 18 dbm. An MCL 15022 RF Power Generator was used at frequencies greater than 100 MHz when testing the TI interface IC's. The MCL output frequency and power levels were monitored during all measurements. Reflected power levels were recorded when the reflected levels were greater than -30 dbm (the low power measurement limit of the power meter and detector used at the reflected power port of the HP778D dual directional coupler.) In order to more accurately control the output power level of the MCL RF Power Generator at power levels less than 20 dbm, a 10 or 20 db attenuator was sometimes used at the generator output.

Various digital and RF signal combiners were used to add an interference signal to a digital signal. At interference signal frequencies below 100 MHz, a high power op amp circuit was used as the signal combiner. Various dual quadrature hybrid combiners (DQHC) were used

14-7

to add the digital and RF signals for interference frequencies greater than 100 MHz. The signal combiners used on this effort were designed on previous GTRI efforts for Rome Laboratory and are described in detail in References 3 and 4. The op amp combiner design was modified on this effort with a schematic of the modified combiner presented in Appendix A.

The combined signals were routed to an IC or MCM pin using a 50 ohm micro-strip printed circuit (PC) board. The micro-strip PC board forms part of a Tester Interface Unit (TIU) that provides 32 controlled impedance paths to device pins-under-test up to frequencies of 12 GHz. The TIU is described in detail in Reference 3. A new upper aluminum PC board holder and micro-strip PC board were fabricated on this effort in order to test the GE SPAM. The upper and lower TIU aluminum PC board holder drawings shown on pages C-5 and C-6 of Reference 3 were found to be incorrect. The corrected drawings are given in Appendix B.

3.0   Measurement Results

The individual IC measurement results are presented in Figure 4. The 74S138AN 3-to-8 line decoder G2A and G2B pins exhibited an unusual susceptibility profile in that there was a 20 db increase in the power required to cause interference at frequencies greater than approximately 100 MHz. The transition region was measured to be only a few MHz and was very repeatable with other IC's. Simlations (see Reference 2) verified the transition, although the exact reason for the sudden increase is unknown.

The P4C164 RAM exhibited varying susceptibility thresholds and curves for various inputs and outputs. The most susceptible pin was the CE2 enable pin.

The interference thresholds for the GE SPAM are shown in Figure 5. Above approximately 300 MHz the MCM connector begins to resonate with power being reflected at the connector interface to the MCM. The interference thresholds do not compare well with the individual IC's above approximately 200 MHz because of the MCM connector.
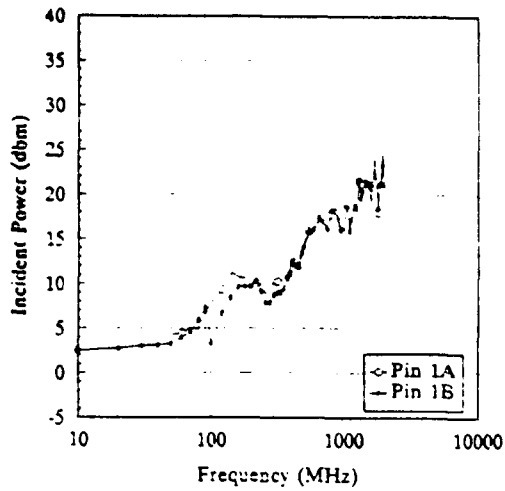
Incident Interference Thresholds for 74S00
2-Input NAND Gate.
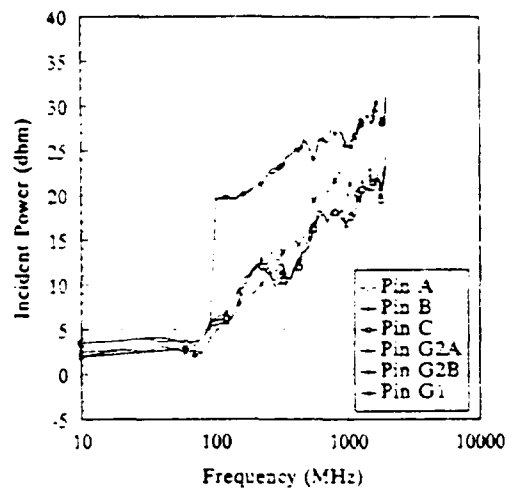
Incident Interference Thresholds for 74S138AN
3-to-8 Line Decoder.
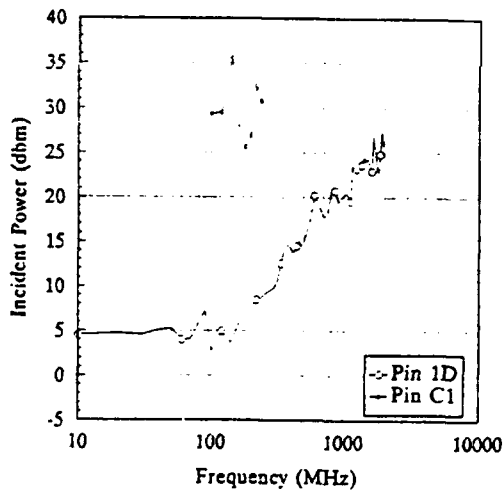
Incident Interference Thresholds for 74S373AN
D-Type Flip-Flop.
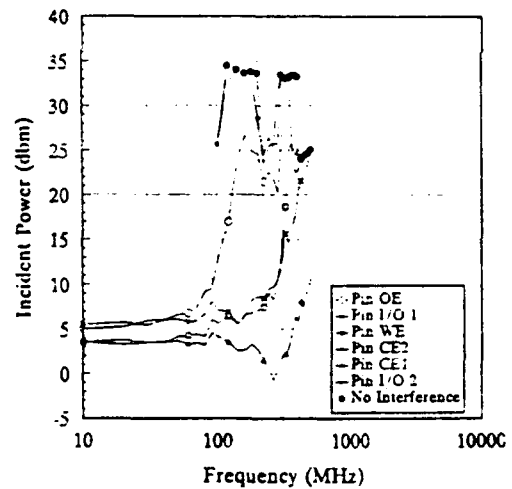
Incident Interference Thresholds for P4C164
8k by 8 Static RAM.

Figure 4. Individual IC Susceptibility Measurement Results.

14-9
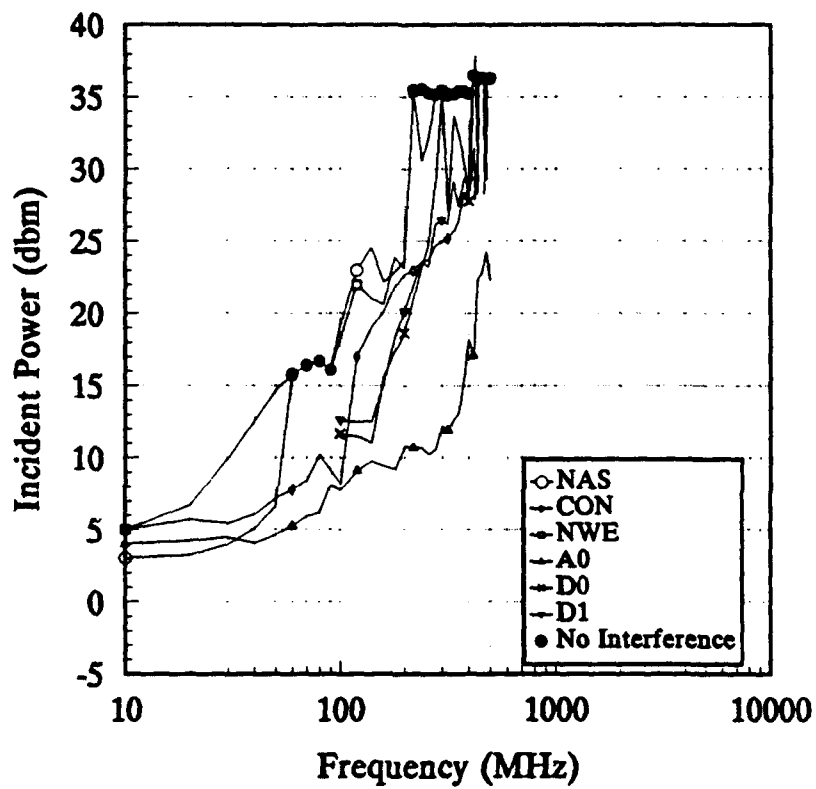
Incident Interference Thresholds for General Electric
Soft Part Analogous Module (SPAM).

Figure 5. GE SPAM Interference Measurement Results.

14-10

4.0   Vulnerability Assessment

The results of this effort indicate that the the GE SPAM module is susceptible to EM interference but not whether a vulnerability condition could exist. To perform a vulnerability assessment, an estimate was made of the coupled signal levels due to external EM threats. Radiated field levels from Reference 5 were used to determine if the modules could be vulnerable to upset or damage due to EM field exposure. It was assumed that each pin was connected to a tuned dipole for analysis purposes. Techniques from Reference 6 were used to calculate coupled signal levels given the threat source profile in Figure 6 (from Reference 5) and for separation distances of 1 and 10 km. Given the power density profile in Figure 6, the power received at an IC pin can be calculated using the following equation,

$$P_r = \frac{G_r P_D \lambda^2}{2\pi}$$

or in decibels as

$$P_r = G_r + P_D + 20\log\lambda - 7.98$$

where,

P_r = recieved power in dBm

G_r = receive antenna gain, which for a tuned dipole is 2.14 dBi

P_D = incident power density in dBm per square centimeter

λ = wavelength in centimeters

Figure 7 overlays the GE SPAM susceptibility profile over the calculations of coupled signal levels. Coupling to any of the pins could lead to vulnerability over the measurement frequency range of 100 MHz to 500 MHz for threat sources located at either 1 or 10 km. Additional filtering, limiting and shielding of up to 60 dB would be required to prevent

14-11
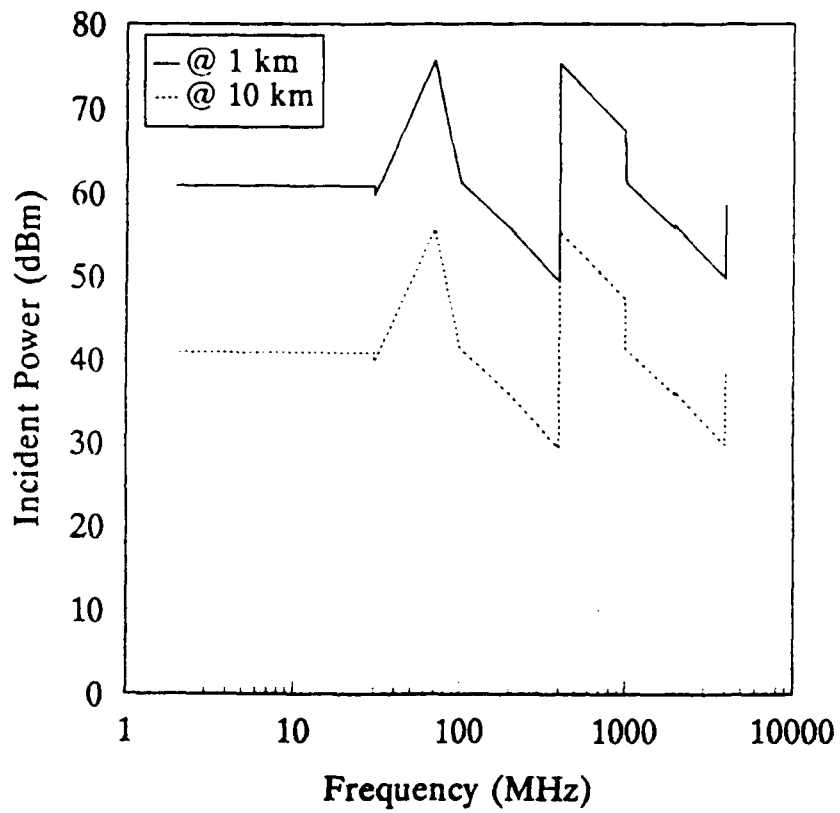
Figure 6. EM Power Density at a Distance of 1 km from Threat Source.
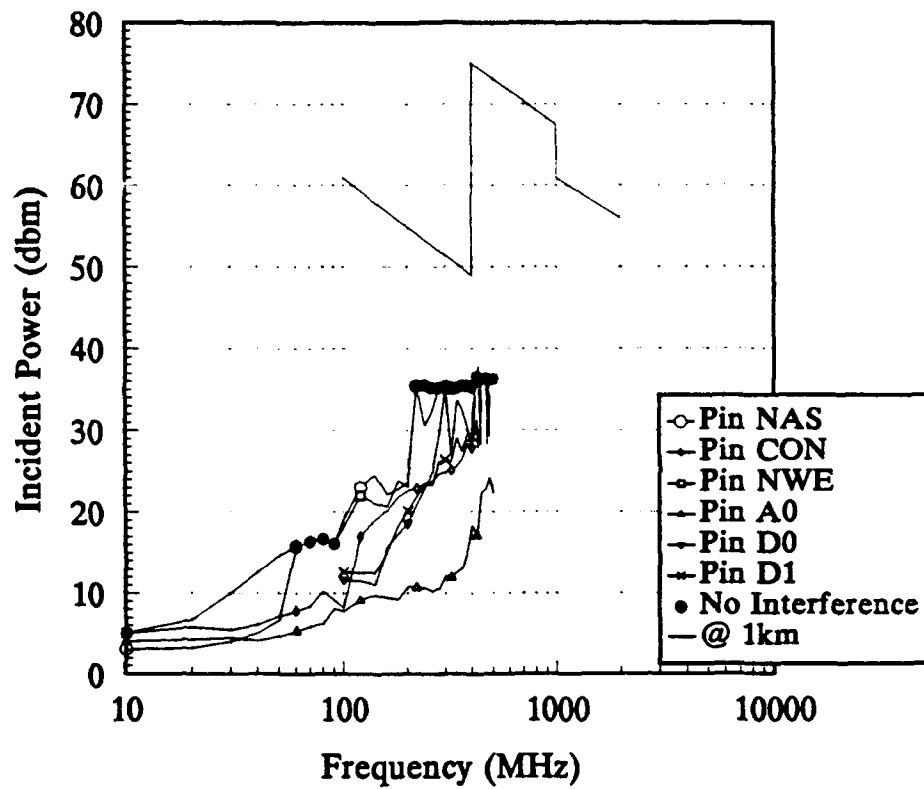
Figure 7. GE SPAM Susceptibility Thresholds and Calculated Threat Levels.

vulnerability.[1]

5.0   Conclusions and Recommendations

The GE SPAM and individual IC measurement results did not correlate well at frequencies greater than 200 MHz because of reflections that occured at the GE SPAM connector interface. In actual practice this connector would not be used. It is expected that the GE SPAM and individual IC measurement results would correlate better at high frequencies if the interface connector wer not used. Even with the interface connector, the GE SPAM could still be vulnerable to EM interference. Care must be taken to assure system vulnerability does not occur by adequately shielding and filtering the interconnect lines to the GE SPAM.

Based on the results of this effort and previous efforts for Rome Laboratory by GTRI, it is recommended that a Designer's Guide, a Designer's Handbook, and a short course be prepared for use by Multi-Chip Module developers. The above materials should discuss simulations, measurements, analyses, trade-offs, and EM mitigation techniques that can be used prior to full-scale development of an MCM.

6.   REFERENCES

1.   C. W. Eichelberger, et al., "Wafer Scale Integration Technology Demonstration, Final Report," Contract No. F29601-86-C-0020, WL-TR-89-56, November 1989.

2.   R. J. Levin, "Conducted Interference Simulation Results for a General Electric Soft Part Analogous Module (SPAM)"

---

[1] The threat profile given in Figure 6 does not considered classified sources, lightning, electro-static discharge, electronic warfare transmitters, nuclear electromagnetic pulses or high power microwave weapons. Consideration of the above sources could dramatically increase the vulnerability levels and required filtering, limiting and shielding.

3.   J. K. Daher, J. C. Santamaria, R. M. Herkert, and J. M. Goodroe, "Built-In Test Techniques for EMI Test Applications, Final Technical Report," Contract No. F30602-87-C-0061, RADC-TR-90-310, December 1990.

4.   J. K. Daher, J. P. Rohrbaugh, and J. G. Hotchkiss, "EMI Test Methodology for High Speed, High Density IC's, Final Technical Report," Contract No. F30602-85-C-0088, RADC-TR-86-223, February 1987.

5.   H. W. Denny, J. K. Daher, and J. P. Rohrbaugh, "Integrated Circuit Technology Assessment (ICTS) Project, Final Technical Report: Definition Phase," for AFEWC/SAX, San Antonio, Texas 78243, under Contract No. F41621-83-C-5015, prepared by the Georgia Tech Research Institute on GTRI Project A-3657, April 1984.

6.   J. P. Rohrbaugh, B. R. Farris, and P. C. Alford, "EM Performance Monitor," for Rome Laboratory, Griffiss AFB, NY 13441-5700, under Contract No. F30602-89-C-0144, on GTRI Project A-8426, October 1990.

Appendix A. Signal Combiners.

The schematic of the op amp combiner built on this effort is shown in Figure A-1. An Elantec EL-2009 buffer is used at the output of a Comlinear CLC-220 op amp.
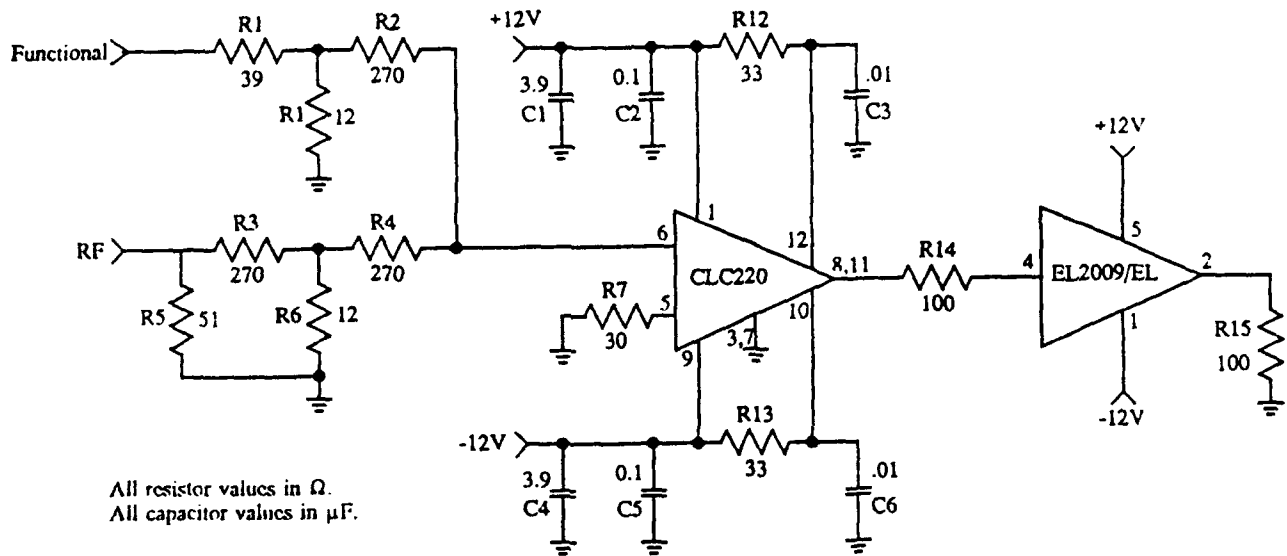
Figure A-1. Op Amp Combiner.

Appendix B. Tester Interface Unit Aluminum PC Board Holders.

The upper and lower aluminum PC board holder drawings for the Tester Inteface Unit are incorrect in Reference 3. Below is a corrected drawing for the upper PC board holder that was fabricated on this effort.
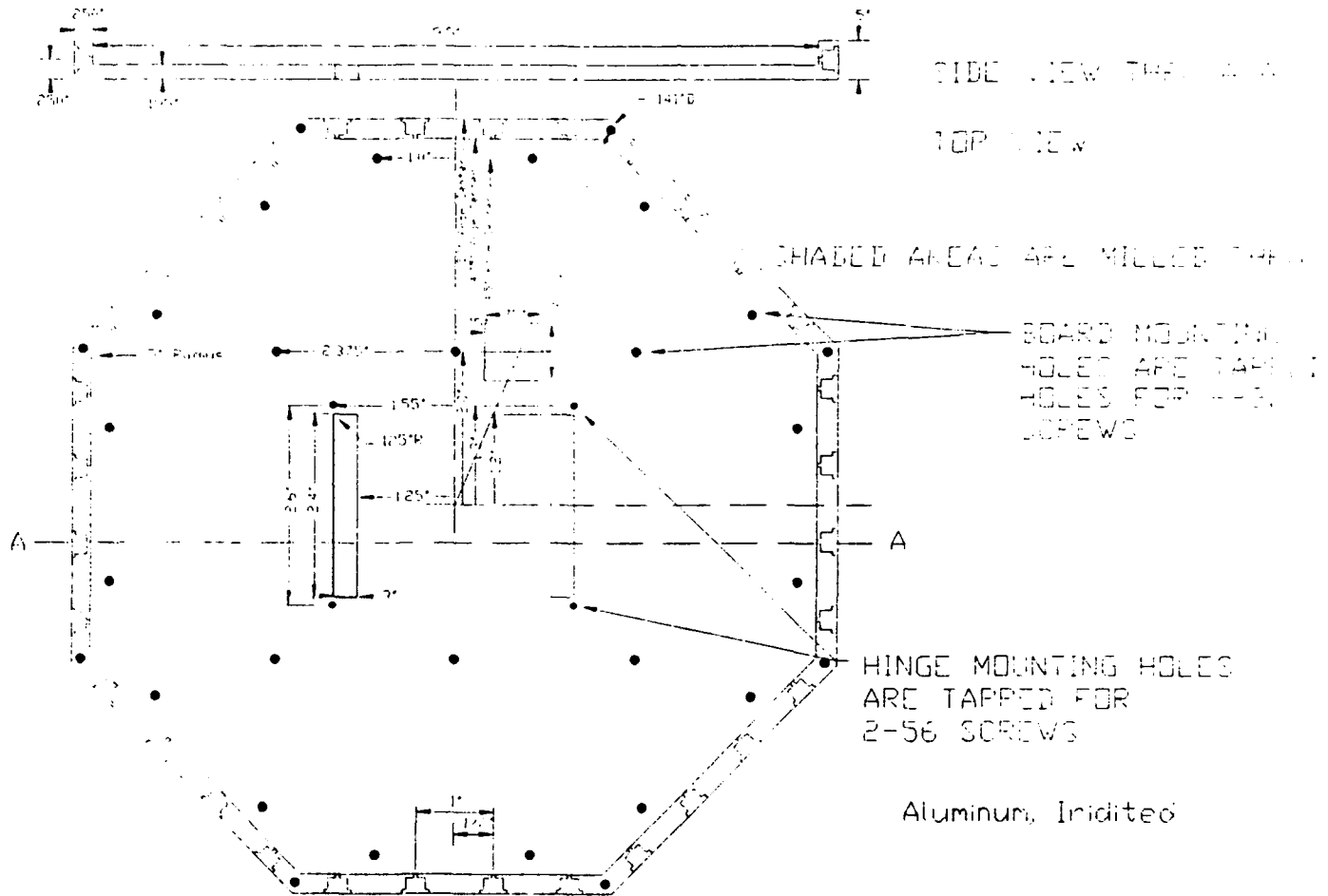
Near-Bandgap Second Order Optical Nonlinearities of Zincblende Crystals

X.-C. Zhang

Associate Professor
Physics Department
Rensselaer Polytechnic Institute
Troy, NY 12180-3590

Final Report for:

Summer Research Extension Program
Hanscom AFB

September 9, 1993

Second Order Optical Nonlinearity near the Bandgap of Zincblende Crystals

X.-C. Zhang

Associate Professor
Physics Department
Rensselaer Polytechnic Institute
Troy, NY 12180-3590

Abstract

We have studied the near-bandgap second order optical nonlinearities of several semiconductors possessing the zincblende structure. Specifically, we concentrated on difference-frequency generation (DFG) and sum-frequency generation (SFG). We simultaneously measured the DFG radiation field and the SFG intensity as a function of crystallographic orientation and incident photon energy. To perform the measurements, we select <100>, <110>, and <111> orientated samples of GaAs, InP and CdTe. Herein, the pronounced near-bandgap resonant behaviors of both DFG and SFG are compared for the first time.

Second Order Optical Nonlinearity near the Bandgap of Zincblende Crystals

X.-C. Zhang

Introduction

Recently, several different optoelectronic techniques have been developed to generate broadband electromagnetic pulses in free space by utilizing ultrafast laser pulses. These techniques include the use of high-speed photoconductors as ultrafast current sources for radiating antennas [1-5], and the use of electro-optic crystals for THz optical rectification media [6-8]. Optical rectification is a second order nonlinear process. Conventional optical rectification, which involves a monochromatic pump beam to generate a dc dielectric polarization, does not radiate electromagnetic waves. However, if the pump optical beam contains an ultrafast pulse train, the different components within the frequency broadening of the fundamental beam form a beating polarization [9]. This time-varying dielectric polarization produces a transient dipole which radiates electromagnetic waves [10]. The rectification radiation of electromagnetic pulses with a frequency range from GHz to THz has been demonstrated [5]. THz optical rectification radiation is preferable because of superior pulse duration and bandwidth. To date, the newly measured THz optical rectification of nonlinear organic materials provides the most intense THz radiation field among all of the natural, non-externally biased materials [11]. Besides optical rectification, second harmonic generation is another second-order process which has been well studied and widely used in many nonlinear crystals. However, due to the dispersion of second order susceptibility, an electro-optic material which produces intense second harmonic generation may not be suitable as an efficient source of THz radiation. It is important to further explore the relationship between sum-frequency generation (SFG) and difference-frequency generation (DFG) processes to understand the second order nonlinearities at a wider frequency range. During the AFOSR Summer Research Program, we studied second order optical nonlinearity: difference-frequency generation(DFG) and sum-frequency generation (SFG) radiations with the optical excitation near the bandgap of zincblende crystals [12]. The DFG field strength and the SFG intensity from GaAs, InP, and CdTe were measured simultaneously versus crystallographic

orientation and incident photon energy under several polarization schemes. Further, the pronounced near-bandgap resonant behavior of both SFG and DFG radiations are compared for the first time.

Experimental Set up

Fig. 1 schematically illustrates the experimental arrangement (side view) of an SFG and DFG spectroscope. A tunable femtosecond laser beam (a mode-locked Ti:sapphire laser) illuminates the sample at normal incidence. The optical pump beam is focused on the crystal with a spot diameter of 35 μm. During the photon energy tuning, the intensity was kept constant at 58 kW/cm^2 .
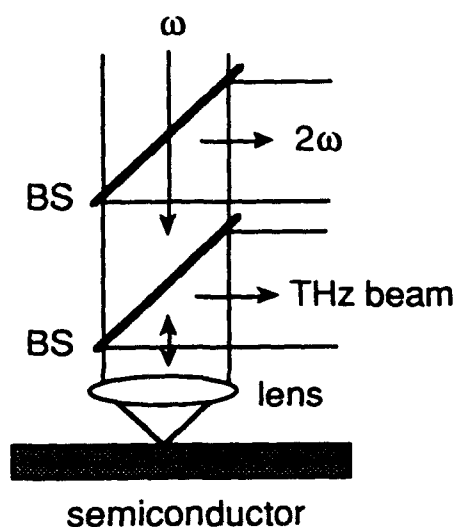
Fig. 1: Experimental arrangement for the measurements of SFG and DFG.

The zincblende crystals are semiinsulating GaAs, InP, and CdTe wafers. A dielectric optical beam splitter and a beam splitter using a thin metallic film on a glass plate are used to reflect the SFG light and the DFG field, respectively. The backward radiated SFG and DFG signals at different polarizations (parallel and perpendicular to the polarization of the optical excitation beam, respectively) are measured simultaneously. The peak value of the time-integrated SFG signal (light intensity) is detected by a photomultiplier attached to a one-meter spectrometer, and the peak value of the DFG signal (electric field) is detected by a picosecond photoconducting antenna. During the measurement of energy dispersion, which requires laser energy tuning, the spectrometer is scanned to find the peak value of the SFG signal. To reduce experimental error generated by the random fluctuation of optical power and temporal pulse duration of the fundamental beam, a quartz crystal (z-cut) is used as a reference sample to normalize the nonlinear radiation signals. The measurement is performed at room temperature.

Calculation

When a femtosecond laser pulse illuminates a <111> zincblende crystal with normal incidence, equations for DFG polarization, $P(\Omega)$, and SFG polarization, $P(2\omega+\Omega)$, can be derived. They are

$$P_{||}(\Omega) = \frac{4}{\sqrt{6}} d_{14}(\Omega; \omega+\Omega, -\omega) \sin(3\theta)E(\omega+\Omega)E^*(\omega) \qquad (1)$$

$$P_{\perp}(\Omega) = \frac{4}{\sqrt{6}} d_{14}(\Omega; \omega+\Omega, -\omega) \cos(3\theta)E(\omega+\Omega)E^*(\omega) \qquad (2)$$

$$P_{||}(2\omega+\Omega) = \frac{4}{\sqrt{6}} d_{14}(2\omega+\Omega; \omega+\Omega, \omega) \sin(3\theta)E(\omega+\Omega)E(\omega) \qquad (3)$$

$$P_{\perp}(2\omega+\Omega) = \frac{4}{\sqrt{6}} d_{14}(2\omega+\Omega; \omega+\Omega, \omega) \cos(3\theta)E(\omega+\Omega)E(\omega) \qquad (4)$$

where $P_{||}$ and $P_{\perp}$ are dielectric polarizations parallel and perpendicular to the pump beam, respectively, and d_{14} is a susceptibility tensor element. The azimuthal angle θ is measured with respect to the <1,1,-2> direction. The SFG beam intensity is proportional to the square of the dielectric polarization ($I(2\omega) \propto P(2\omega)^2$), and the DFG field strength E_r is proportional to the dielectric polarization ($E_r(\Omega) \propto P(\Omega)$). The measured $E_r(t)$ in time is the Fourier transform of $E_r(\Omega)$ over the frequency spectrum $\Delta\omega$ where $\Delta\omega$ is comparable to the spectrum broadening of the optical pump pulse.

For <110> oriented samples, two equations for DFG polarization, $P(\Omega)$ are:

$$P_{||}(\Omega) = \frac{3}{4} d_{14}(\Omega; \omega+\Omega, -\omega) [\cos(3\theta)-\cos(\theta)]E(\omega+\Omega)E^*(\omega) \qquad (5)$$

$$P_{\perp}(\Omega) = \frac{1}{4} d_{14}(\Omega; \omega+\Omega, -\omega) [3\cos(3\theta)+\cos(\theta)]E(\omega+\Omega)E^*(\omega) \qquad (6)$$

Experimental Results

Fig. 2 and Fig. 3 plot the peak values of second harmonic signal (intensity) and THz beam (field strength) versus θ, with the polarization of the detected signal perpendicular (Fig. 2) and parallel (Fig. 3) to that of the pump light (fundamental

beam), respectively. The dots are the experimental data and the curves are normalized plots from the calculations of $E_r(\Omega)$ and $I(2\omega)$.
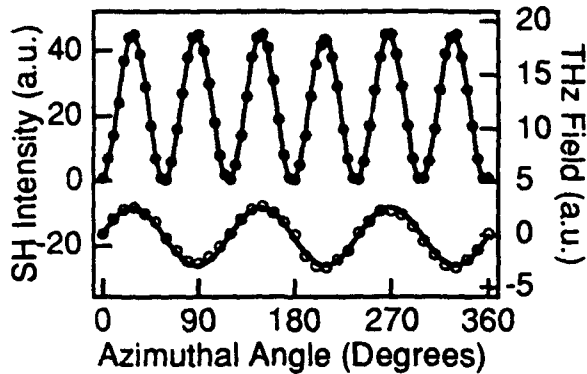
Fig. 2: Peak values of SH intensity (solid dots) and THz field (open dots) vs azimuthal angle for <111> GaAs; the polarization of the nonlinear signals is detected perpendicular to the fundamental light. The solid line is calculated from Equations (1) and (3).
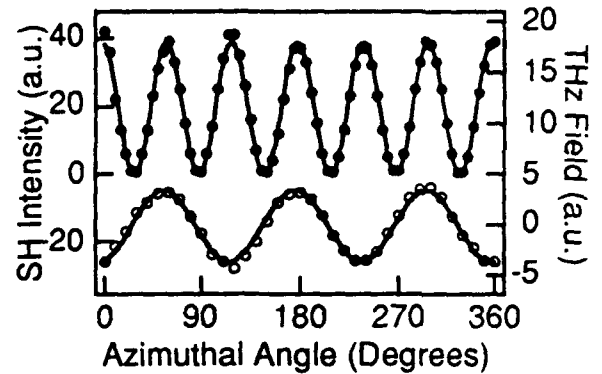
Fig. 3: Same as Fig. 2 except the polarization of the nonlinear signals is detected parallel to the fundamental light. The solid line is calculated from Equations (1) and (3).
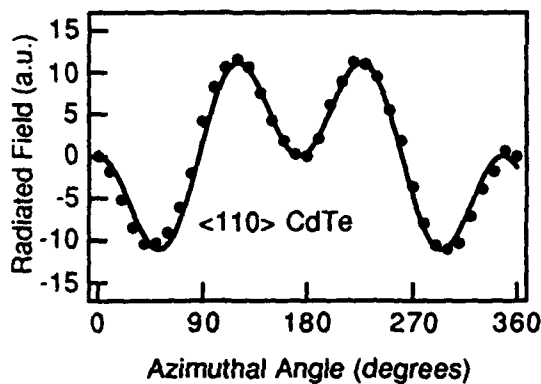
Fig. 4 Peak values of THz field (open dots) vs azimuthal angle for <110> CdTe; the polarization of the nonlinear signals is detected parallel to the fundamental light. The solid line is calculated from Equations (5).
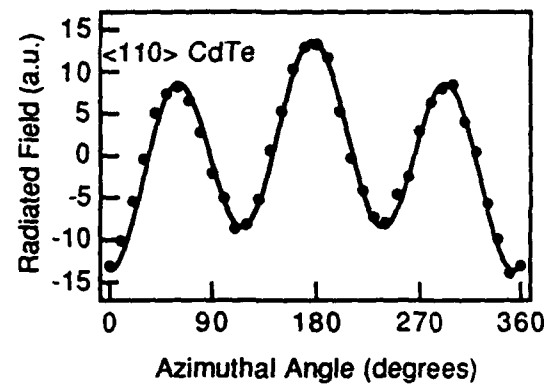
Fig. 5 Same as Fig. 4 except the polarization of the nonlinear signals is detected perpendicular to the fundamental light. The solid line is calculated from Equations (6).

As we expected from the calculations, the THz field shows a three-fold rotation symmetry ($\sin(3\theta)$ and $-\cos(3\theta)$), and the second harmonic intensity shows a six-fold rotation symmetry ($1 \mp \cos(6\theta)$). A similar angular dependence was observed in a <111> oriented CdTe sample. We also measured the THz field from a <110>

oriented zincblende crystals (GaAs, InP and CdTe) with near bandgap optical excitation. The THz signals, plotted in Fig. 4 and Fig. 5, showed $P_{||}(\Omega) \propto \cos(3\theta)$ - $\cos(3\theta)$ and $P\perp(\Omega) \propto \cos(\theta) + 3\cos(3\theta)$ measured from <00-1> direction, consistent with calculations for second order nonlinearity in a <110> crystal [13]. Excellent agreement between the experimental data and the calculations from second-order nonlinearity has thus been found for both <111> and <110> oriented zincblende crystals.

It should be noted that when the focusing spot of the fundamental beam is comparable with the wavelength of the DFG radiation (nearly one millimeter), the plane wave approximation is not valid. A simple estimate shows that at the tightest focusing point (a few μm), the SFG intensity reaches a maximum while the strength of the DFG field drops to a minimum. We have confirmed this experimentally. This consideration does not affect qualitative comparisons between DFG and SFG in crystal orientation and energy dispersion measurements.

We observed resonance enhancement and sign reversal of the nonlinear susceptibility near the bandgap of zincblende crystals by using a THz optical rectification technique [8]. When the laser photon energy was tuned 70 meV lower than the GaAs bandgap, the rectified DFG signal was nearly unchanged for small energy tuning. When the laser was tuned to the bandgap, the amplitude of the DFG signal increased, reaching a peak when the laser energy was just above the bandgap. Further tuning of the laser energy to the higher energy side results in a polarity change of the radiation signal. This dramatic change of THz radiation in <111> GaAs is due to the resonant nonlinear susceptibility. The resonance enhancement near the electronic resonance states has been confirmed in other samples. Fig. 6 shows the DFG signal from a <111> InGaAs/GaAs superlattice sample versus optical excitation energy at normal incidence. In addition to the resonance due to GaAs (barriers) at 1.45 eV, an additional resonance, which is due to the bound states in the InGaAs quantum wells, is observed at 1.40 eV. The origin of a small feature at 1.53 eV is not clear yet. During the laser energy tuning, the temporal duration of the rectified field remained essentially unchanged. We also observed similar resonant behavior from <111> oriented CdTe samples. Both the resonance enhancement and sign reversal near the bandgap of CdTe (E_g is about 1.50 eV) are observed, as shown in Fig. 7. The strong radiation signal around 1.4 eV

may be due to the impurity states in CdTe. Photoluminescence measurement has shown intense emission from impurity states in this CdTe crystal.
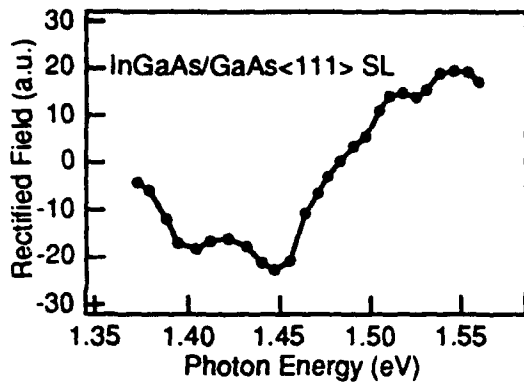

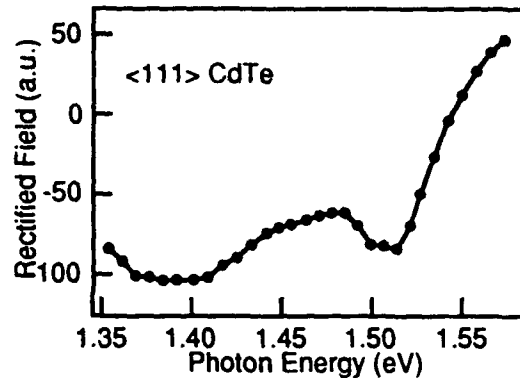Fig. 6   Peak value of the DFG signal (dots) vs laser energy from a <111> CdTe. Solid line is guided for eye.

Fig. 7:   Peak value of the DFG signal vs laser energy from a <111> InGaAs/GaAs superlattice.

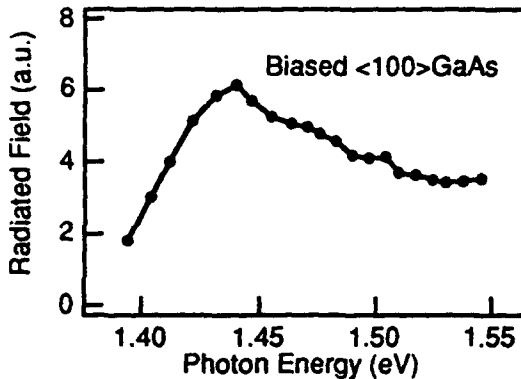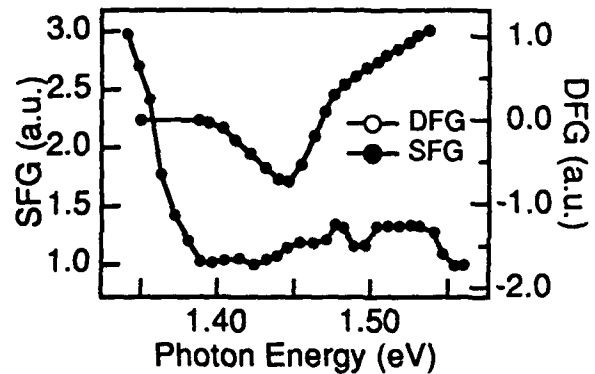Fig. 6   Peak value of the electromagnetic radiation signal vs laser energy from a biased <100> GaAs.

Fig. 7   Peak values of the integrated SFG light intensity and the DFG field strength from a GaAs sample versus the fundamental photon energy.

We have also calculated the nonlinear polarization from a perfect <100> oriented GaAs bulk sample. The calculation showed, regardless of the azimuthal rotation of the crystal, no DFG signal in the forward direction under normal incidence. This calculated result was confirmed by our experiment. Since <100> oriented GaAs can not emit a forward THz beam, we fabricated a pair of parallel planar electrodes on a <100> GaAs wafer to apply an external bias. The forward radiation from a biased <100> GaAs sample (pure transient photocurrent) versus photon energy is plotted in Fig. 6. This is a good comparison of the forward radiation driven by the transient photocurrent in the biased external field and the

forward radiation generated by ultrafast optical rectification. Clearly, no sign reversal is measured from the biased <100> GaAs in Fig. 6.

From an anharmonic oscillator model, when the fundamental photon energy $\hbar\omega$ is close to bandgap E_g, the singularities in the principal value of the integral of susceptibility provide resonance behavior for both SFG and DFG. Fig. 7 is a plot of peak values of the time-integrated SFG intensity and DFG field from a <111> GaAs sample (the same sample we used for azimuthal angle measurements) versus the fundamental photon energy. The dispersive feature near the bandgap $E_g = 1.42$ eV is clear for both second-order signals. However, unlike the optical rectification signal, the second harmonic signal does not show an expected minimum at the position where the DFG signal crosses the zero-line; instead, it decreases as the photon energy is tuned above the bandgap. This second harmonic dispersion of GaAs near the bandgap was observed previously [14]. The second harmonic nonlinearity is purely electronic since its frequency is well above the lattice mode frequencies. The optical rectification nonlinearity, on the other hand, is ionic as well as electronic, since the frequency lies below the optical lattice mode frequencies. Currently the discrepancy of the dispersion curves between the SFG and DFG signals is not fully understood. One possible reason may be the different absorption behaviors of SFG and DFG signals in the GaAs crystal.

Conclusion

We report the experimental results of sum-frequency generation (SFG) and difference-frequency generation (DFG) from <100>, <110> and <111> oriented zincblende crystals. The simultaneous measurement of near-bandgap resonant SFG intensity and DFG field versus crystallographic orientation and incident photon energy are presented for the first time.

Acknowledgment

References:

[1]   P.R. Smith, D.H. Auston, and M.C. Nuss, IEEE J. Quantum Electron., **24**, 255 (1988).

[2]   A.P. DeFonzo, M.Jarwala and C. Lutz, Appl. Phys. Lett., **50**, 1155, (1987).

[3]   Ch. Fattinger and D. Grischkowsky, Appl. Phys. Lett., **53**, 1480 (1988).

[4]   Y. Pastol, G. Arjavalingam, J.-M. Halbout and G.V. Kopcsay, Electron. Lett., **24**, 1318 (1988).

[5]   B.B Hu, J.T. Darrow, X.-C. Zhang, D.H. Auston and P.R. Smith, Appl. Phys. Lett., **56**, 886 (1990).

[6]   D.H. Auston, and M.C. Nuss,IEEE J. Quantum Electron., **24**, 184 (1988).

[7]   B.B. Hu, X.-C. Zhang, D.H. Auston and P.R. Smith, Appl. Phys. Lett., **56**, 506 (1990).

[8]   X.-C. Zhang, Y. Jin, K. Yang and L.J. Schowalter, Phys. Rev. Lett. **69**, 2303 (1992).

[9]   T. Yajima and N. Takeuchi, Japanese Journal of Applied Physics, **10**, 907 (1971).

[10]   R.Y. Shen, "The Principles of Nonlinear Optics," John Wiley & Sons Inc., New York, (1984).

[11]   X.-C. Zhang, X.F. Ma, Y. Jin, T.-M. Lu, E. P. Boden, P. D. Phelps, K. R. Stewart and C. P. Yakymyshyn, Appl. Phys. Lett., **61**, 3080 (1992); X.-C. Zhang, Y. Jin, and X.F. Ma, Appl. Phys. Lett., **61**, 2764 (1992).

[12]   X.-C. Zhang, Y. Jin, X.F. Ma, K. Ware, A. Rice, D. Bliss, J. Larken, and M. Alexander, Submitted to Appl. phys. Lett., (1993).

[13]   A. Rice, Y. Jin, X.F. Ma, X.-C. Zhang, D. Bliss, J. Larken, and M. Alexander, to be submitted to .

[14]   F.G. Parsons and R.K. Chang, Optics Communications, **3**, 176 (1971).

DESIGN OF AN INTERFACE BETWEEN THE GENERIC INTELLIGENCE PROCESSOR (GIP) AND A NATURAL LANGUAGE UNDERSTANDING SYSTEM

Pradip Peter Dey
Associate Professor
Computer Science Department

Hampton University
Hampton, VA 23668
Email: dey@cs.hamptonu.edu
Fax: (804)727-5390

DESIGN OF AN INTERFACE BETWEEN THE GENERIC INTELLIGENCE PROCESSOR (GIP) AND A NATURAL LANGUAGE UNDERSTANDING SYSTEM

Pradip Peter Dey
Associate Professor
Computer Science Department
Hampton University

ABSTRACT

The goal of this document is to specify the design of an interface between a data extraction system called the Generic Intelligence Processor (GIP) and a natural language understanding (NLU) system called the Probabilistic Language Understanding Model (PLUM). The interface will provide a mechanism for processing natural language fragments through PLUM in the GIP environment. The central design strategy for this interface is to make little or no changes to the existing systems, namely, GIP and PLUM.

DESIGN OF AN INTERFACE BETWEEN THE GENERIC INTELLIGENCE PROCESSOR (GIP) AND A NATURAL LANGUAGE UNDERSTANDING SYSTEM

Pradip Peter Dey

1. INTRODUCTION

The goal of this document is to specify the design of an interface between a data extraction system called the Generic Intelligence Processor (GIP) and an NLU system called PLUM. The interface will provide a mechanism for processing natural language fragments through PLUM in the GIP environment. It is desirable that an appropriate version of PLUM is selected for this interface since several versions of PLUM are available and not all versions are equally suited for this task. GIP has two distinct functional roles: as an application builder, and as a run-time message processing application. One of them have to be selected for this interface. There are several other design decisions that have to be made during the design process.

When used with NLU components, GIP would be a complicated system requiring enormous computing power. Efficient execution of GIP is possible only by clever utilization of computing resources around the GIP environment. In order to achieve this, parallel and distributed execution of GIP modules will be necessary. With this point in mind the proposed interface will execute PLUM on a remote site.

The general approach to the design and development of the proposed interface system is rapid prototyping (Pressman 1992, Boar 1984, Cieslak et al. 1989). This approach has many advantages for developing a large class of software (Luqi 1989). Boehm, Gary and Seewaldt (1984) found that software products developed using prototyping performed as well as those developed using other traditional techniques.

In addition, 45% less effort was expended and 40% fewer lines of code were generated by the developers who used the prototyping paradigm.

The specific design method followed in this document is known as the Data-Flow oriented design (Pressman 1992).

2. GENERIC INTELLIGENCE PROCESSOR (GIP)

GIP and PLUM are not described in this document except for some key elements that are directly referenced by the proposed interface. A detailed description of GIP is available in a Software Design Document written by the Sterling IMD, Inc. (Sterling 1993). The main goal of GIP is to extract information from formatted and unformatted messages and transmit the results to downstream databases and processes such as expert systems. GIP is a toolkit for developing, testing, and delivering message processing applications. When fully developed GIP will provide the following capabilities (a) user selectable input sources, (b) automatic message parsing, (c) automatic/user assisted information extraction, (d) automatic output formatting for development systems, (e) utilities for developing new algorithms. For processing messages with substantial natural language texts user assistance will be crucial for GIP, because, natural language processing technology is not mature enough for fully automated information extraction in an operational environment. However, for the demonstration interface the user assistance facility has been suppressed in order to achieve appropriate speed-up. The GIP program components are reproduced in Figure-1.
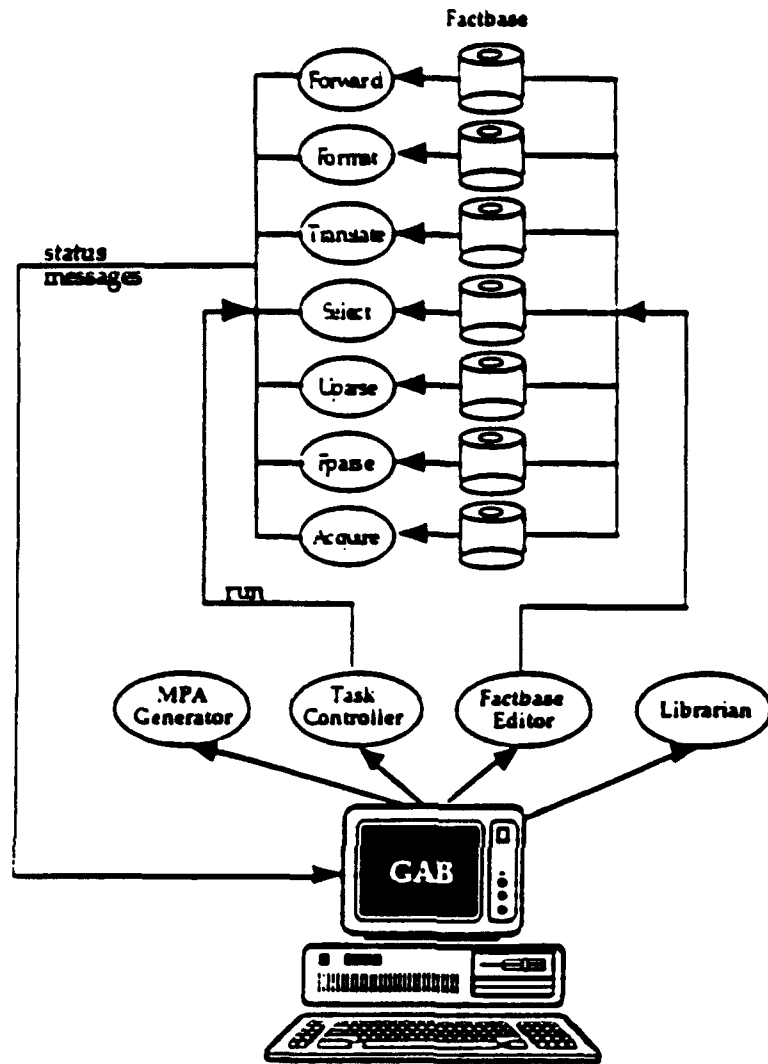
Figure-1: GIP Program Components (From Sterling 1993)

The most crucial GIP module for the interface is the UPARSE component. UPARSE allows manual data extraction as well as automatic data extraction through NLU systems. A candidate NLU system is PLUM. Since PLUM does not meet all the requirements that GIP imposes on a NLU system, this interface is designed to fill the gap between the two. A natural strategy for this design would therefore be to meet all the requirements through the interface that are imposed by GIP but lacking in PLUM.

3. PLUM

PLUM is a state-of-the-art NLU system for data extraction from NL texts. It is intended to be robust and scalable. Besides lexical, morphological, syntactic, and semantic components PLUM has a statistical learning module that enhances its robustness and scalability. A detailed description of PLUM is ava: ble in an article entitled "BBN PLUM: MUC-4 Test Results and Analysis" (Weischedel et al. 1992, Weischedel et al. 1993) and some other BBN reports (BBN et al. 1993). The MUC-4 version of PLUM is selected for this interface for the reasons described in Section-5.1. This version can be run in the client-server mode as described at the end of this section.

Since we do not intend to modify PLUM, its internal structure is not important for our purpose. Input to PLUM is a text-file containing a free text message like the one given in Figure-2. The output from PLUM is a text-file containing a set of templates like the one given in Figure-3. (These examples are taken from PLUM environment, although they appear to come from MUC-3.) PLUM tries to fill as many fields as possible. When it cannot fill a field it marks it with a "-" , following the MUC convention.

DEV-MUC3-0016 (NOSC)

BUENOS AIRES, 10 JAN 90 (NA) -- [TEXT] A UCR [RADICAL CIVIC UNION] BUENOS AIRES PROVINCE COMMITTEE SPOKESMAN TODAY REPORTED THAT A UCR DISTRICT HEADQUARTERS IN BUENOS AIRES PROVINCE WAS "COMPLETELY DESTROYED BY A BOMB EXPLOSION." THE DESTROYED UCR HEADQUARTERS IS IN THE MORENO DISTRICT OF BUENOS AIRES.

THE SPOKESMAN ADDED THAT NO ONE WAS INJURED AND THAT LEOPOLDO MOREAU, THE UCR BUENOS AIRES PROVINCE LEADER, HAS TRAVELED TO MORENO.

IT IS EXPECTED THAT UCR BUENOS AIRES PROVINCE BOARD WILL MEET AND THAT THEY WILL ASK THE PROVINCIAL GOVERNMENT AND THE INTERIOR MINISTRY TO INVESTIGATE THE INCIDENT.

Figure-2: A MUC-3 Message

```
0.  MESSAGE: ID                        DEV-MUC3-0016 (NOSC)
1.  MESSAGE: TEMPLATE                   1
2.  INCIDENT: DATE                      10 JAN 90
3.  INCIDENT: LOCATION                  ARGENTINA: BUENOS AIRES PROVINCE (PROVINCE)
4.  INCIDENT: TYPE                      BOMBING
5.  INCIDENT: STAGE OF EXECUTION        ACCOMPLISHED
6.  INCIDENT: INSTRUMENT ID             -
7.  INCIDENT: INSTRUMENT TYPE           -
8.  PERP: INCIDENT CATEGORY             -
9.  PERP: INDIVIDUAL ID                 -
10. PERP: ORGANIZATION ID               -
11. PERP: ORGANIZATION CONFIDENCE       -
12. PHYS TGT: ID                        "A UCR DISTRICT HEADQUARTERS"
13. PHYS TGT: TYPE                      ORGANIZATION OFFICE: "A UCR DISTRICT HEADQUARTERS"
14. PHYS TGT: NUMBER                    1: "A UCR DISTRICT HEADQUARTERS"
15. PHYS TGT: FOREIGN NATION            -
16. PHYS TGT: EFFECT OF INCIDENT        DESTROYED: "A UCR DISTRICT HEADQUARTERS"
17. PHYS TGT: TOTAL NUMBER              -
18. HUM TGT: NAME                       -
19. HUM TGT: DESCRIPTION                -
20. HUM TGT: TYPE                       -
21. HUM TGT: NUMBER                     -
22. HUM TGT: FOREIGN NATION             -
23. HUM TGT: EFFECT OF INCIDENT         -
24. HUM TGT: TOTAL NUMBER               -
```

Figure-3: The TEMPLATE Produced by PLUM from the Message of Figure-2

The MUC-4 version of PLUM can be run in several modes; the most appropriate for this interface being the Client-Server mode. It reads a single message from an input-file named .to_plum and writes output to .from_plum. Multiple messages are processed by copying messages from /home/plum/TIPSTER/msg to .to_plum and copying out-put from from .from_plum to the same directory. The PLUM server is currently activated by performing the following 3 actions in the given order:

(1) giving the command "run-muc" from UNIX; this will start LISP,

(2) loading a file into LISP by "(load "demo-server-patch.lisp")"

(3) executing "(file-message-server)" in LISP.

This sequence of 3 actions makes the server ready for processing messages. When the server is ready, the client process is activated by the command "serv_test" from a UNIX shell. Once the client establishes connection with the server the messages are taken one by one from /home/plum/TIPSTER/msg directory for processing. Under this directory input messages are in msg-inX files and after each message is processed the output is written to a corresponding msg-outX file in the same directory. Currently serv_test.c is written in such a way that maximum of 5 messages are processed in a session; after that the client and the server continue to run without processing any messages. This can be easily changed by modifying serv_test.c. The client and the server can be stopped by a signal such as Ctrl-Z.

4. REQUIREMENTS ANALYSIS

The software design presupposes software requirements analyses. The requirements that GIP imposes on its NLU components are described in Sterling (1993: 3-5). GIP is supposed to interface to NLU components via files stored in a Network File System (NFS) mounted file system as well as through interprocess communication messages sent via the Event Manager. "All input data for the NLU will be stored in a specified NFS mounted file system which the NLU has access to. This data includes the free text from the messages, the templates available for filling by the NLU, and any formatted information that has been extracted from the message, such as message header data. GIP will then notify the NLU application of the input data location via a message posted with Event Manager. Templates filled by the NLU are likewise written to an NFS mounted file system which can be accessed by GIP. The NLU will post a message for GIP via the Event manager that contains the location of NLU processing results..." (Sterling 1993: 3-5). Figure-4, taken from (Sterling 1993) illustrates the requirements that GIP imposes on the NLU.
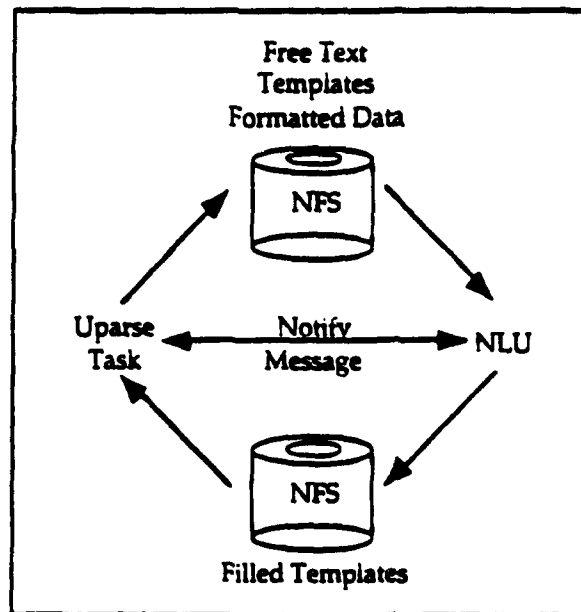
Figure-4: NLU Interface (From Sterling 1993)

Flow of information is an important aspect of data-flow oriented analysis. A Level-0 data-flow diagram given in Figure-5 presents the flow of information in the proposed interface system (Pressman 1992). Input to PLUM comes from the UPARSE component of GIP. Normally, free text messages and their associated blank templates would be input to PLUM. However, there is really no need to transmit the blank templates from GIP to PLUM for this interface version. Because these templates are already available to PLUM in the expected form. We have chosen a version of PLUM that deals only with MUC-4 templates. As long as the same set of templates are used by GIP for this type of messages there would not be any problem. The output from PLUM has to go back to the UPARSE component of GIP with some modifications.

These modifications must be made by the interface system.
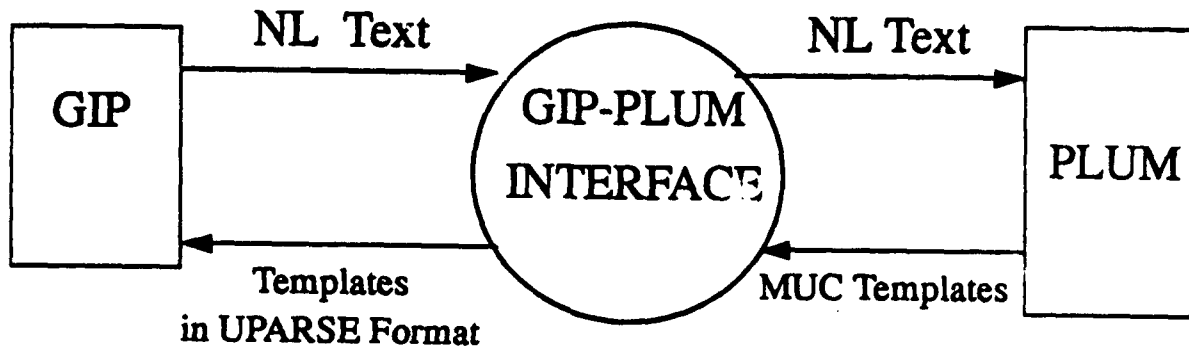
Figure-5: Level-0 Data-Flow Diagram

Certain other requirements of the proposed interface are given below:

(1) The interface must provide a mechanism for execution of PLUM as a logical component of GIP(UPARSE) that can be used for at least one type of messages.

(2) PLUM should be executed on a remote site for efficiency considerations.

(3) The interface should not place any extra burden on the user.

5. INTERFACE DESIGN

The main strategy for this design is to make little or no changes to the existing systems, namely, GIP and PLUM. The interface should handle each transformation of data required by one system from the other.

5.1 Design Decisions

For any design usually a number of design decisions have to be made. The following design decisions are made with the justifications stated therewith.

1. Select a version of PLUM: The MUC-4 version of PLUM is selected because it is recommended by BBN on the basis of its performance. This version works well in the client-server mode bypassing the x-window based user interface. The client-server is important for our purpose, because we want to run the server on one machine and the client on another machine. More specifically, we want to activate the client process from the interface system. This version is currently activated by run-muc and loading demo-server-patch.lisp into LISP as described in Section-3.

2. Select a mode from GAB and MPA: GAB is selected because an MPA is indirectly generated from GAB whereas GAB is directly available through compilation of source codes.

3. Select a communication media from Event Manager, Cronus, remote copy and NFS mounting and a mixture of these: A mixture is selected because Event Manager is used by GIP and Cronus is used by PLUM and these can not be easily eliminated or substituted for the other. NFS mounting of NLP_INTERFACE_DIR is required by the UPARSE component of GIP.

4. Select a Start-up sequence: The PLUM processes can be started either from UPARSE_CONTROLLER or from the interface system or independently. PLUM should be started independently for two main reasons: (1) That's the easiest way. That's the way PLUM works now. (2) PLUM should not be started from UPARSE_CONTROLLER, so that existing GIP operations are least likely to be altered in the processes of experimental development process.

5.2 Procedural Design

In the GIP environment, UPARSE_CONTROLLER usually creates NLU Processes. However, a better strategy for this interface is to start PLUM independently. In any case, PLUM processes should be able to communicate with the two UPARSE processes, namely, nlu_writer and nlu_reader. Since PLUM will be hard to modify, this interface system will mediate the communication. As soon as the interface process is created it should be registered with the Event Manager in order to receive messages from UPARSE. This can be done by sending an ACK message to UPARSE_CONTROLLER. The ACK message contains the standard GIP message header fields, followed by the tag field ACK!!!. The format of the ACK message is as follows (Sterling 1993: 4-14):

[[SOURCE NAME]]   <<Category of process sending the message.>>

[[HOST MACHINE]]   <<Name of the machine on which the process is running.>>

[[MESSAGE NAME]]   <<Name of message being built.>>

[[ACK!!!]]   <<Name of process publishing this message.>>

The nlu_writer is normally responsible for assigning messages to NLU processes and load balancing (Sterling 1993:4-37). However, it would be hard to modify PLUM so that it receives messages directly from nlu_writer. At this stage, it would be easier to assign messages to PLUM and balance the load from the interface system. The following procedural description is developed for the proposed interface.

begin

1 Send ACK message to UPARSE_CONTROLLER and Wait for a pathname_message

2 REPEAT

3 Extract pathname from the pathname_message

   /* Alternatively a default pathname can be assumed for this version   */

4   Count the number of UN_PROCESSED PLUM_TYPE_MESSAGES from NLP_INTERFACE_DIR

   /* NLU_INTERFACE_DIR : An NFS mounted directory in the GIP environment, usually,

```
            /home/gip/GIP_LIBRARY/UPARSE_WORKSPACE                              */

        /* UN_PROCESSED_MESSAGE: No file named  PROCESSED exists under the message

            directory, usually,  /home/gip/GIP_LIBRARY/UPARSE_WORKSPACE/plum/msgXX        */

        /* PLUM_TYPE_MESSAGES : Messages usually stored under

            /home/gip/GIP_LIBRARY/UPARSE_WORKSPACE/plum                         */

5    If the number is 0  sleep for 30 seconds and go to step 4

6    For every 1- 4 PLUM_TYPE_MESSAGES create a PLUM_PROCESS on a remote site

     and assign the messages to the processes and mark the messages PROCESSED.

     /* For this version only 1-4 messages are expected */

7    Check /home/plum/TIPSTER/msg   directory for output from PLUM and

     TRANSLATE  PLUM output, if any, and write to NLP_INTERFACE_DIR

     /* TRANSLATE: For each message, it reads from a single output file in the PLUM

        environment (usually /home/plum/TIPSTER/msg/msg-outX ) and writes each template

        to a distinct file in the GIP environment                              */

8    Publish a message for UPARSE giving the pathname of the results.

     /* Alternatively a default pathname can be assumed for this version        */

9 UNTIL (halt flag set)

end.
```

6. ESTIMATION OF SPEED-UP

GIP is usually executed in a distributed environment where several computers are networked together for sharing resources. The model of computation for this environment is known as the client-server model. The architecture is generally known as MIMD (Multiple Instruction Multiple Data stream). In order to take full advantage of available resources in the GIP environment its modules are designed for distributed execution. Since data extraction from free text needs substantial computing power, distributed execution of the NLU module is highly desirable. The most important

potential benefit from distributed execution of GIP is speed-up. Unless the execution of UPARSE with its associated NLU modules is speeded-up the subsequent processes such as SELECT will starve under certain input conditions. Under the proposed interface PLUM will be executed in a distributed manner in order to minimize the starvation of the subsequent processes. The exact amount of speed-up depends on the speed of the involved processors and various overhead costs. The amount of speed-up is usually sublinear due to overhead costs. The types of expected overheads are:

(1) Process Creation Overhead: Extra time required for creating additional processes.

(2) Interprocess Communication Overhead: Extra time required for communication between processes.

(3) Synchronization Overhead: Extra time required for waiting for certain events.

PLUM takes about 42 seconds on Sun Sparc Station-2 for processing the message given in Figure-2. For four messages of this type it took about four times longer. If PLUM executes these 4 messages on four machines how fast can it finish? The current version of PLUM is not yet ready for distributed execution. Therefore it is not possible to measure the exact speed-up of distributed execution of PLUM. However, modeling PLUM's behavior in some programs that ran on 4 Sun workstations it is found that PLUM is expected to process this type of messages about 3 times faster utilizing four machines.

References:

BBN et al. 1993. Software Requirements Specification for the Natural language Understanding Shell. BBN Systems and Technologies, Cambridge: MA.

Boar, B. 1984. Application Prototypes, Wiley-Interscience.

Boehm, B.W., T. E. Gray, and T. Seewaldt, 1984. "Prototyping Versus Specifying: A Multiproject Experiment," IEEE Transactions on Software Engineering, Vol 10(3).

Cieslak, R. et al. 1989. "The Programmable Network Prototyping System", Computer, Vol 22(5).

Dey, P. and Hayashi, Y. 1990. "A multiprocessing model of natural language processing," Theoretical Linguistics, 16, 11-23.

Luqi. 1989. "Software Evolution through Rapid Prototyping", Computer, Vol 22(5).

Maldovan, D. et al. 1992. " Parallel Processing applied to AI", Computer, Vol.25(5).

Morell, L. 1990. "A theory of fault-based testing," IEEE transactions on Software Engineering, 844-857.

MUC-3. 1991. Third Message Understanding Conference Proceedings.

MUC-4. 1992. Fourth Message Understanding Conference Proceedings.

Pressman, R. S. 1992. *Software Engineering*, McGraw-Hill.

Sterling, IMD, Inc. 1993. Generic Intelligence Processor (GIP): Software Design Document

Weischedel, Ralph, et al 1992. "BBN PLUM: MUC-4 Test Results and Analysis," Technical Report, BBN Systems and Technologies, Cambridge: MA.

Weischedel, R.M. et al. 1993. Coping with Ambiguity and Unknown words through probabilistic Models," *Computational Linguistics*, Vol.19(2).

THE GLOTTAL PULSE:
POSSIBLE APPLICATIONS TO SPEAKER IDENTIFICATION

Dr. Beth L. Losiewicz

Assistant Professor

Experimental Psychology

Colorado State University

Fort Collins, Colorado

THE GLOTTAL PULSE:
POSSIBLE APPLICATIONS TO SPEAKER IDENTIFICATION

Dr. Beth L. Losiewicz

Assistant Professor

Experimental Psychology

Colorado State University

Abstract

One of the major current thrusts of the Speech Processing Lab at Rome Labs is speaker identificiation. There is evidence that the vocal fold vibrations (the glottal pulse) may provide unique information capable of differentiating between speakers. If this is true, glottal pulse information could be used to substantially improve current speaker identification algorithms. An in-depth literature review of what is known about the glottal pulse waveform cooberates this evidence. Recommendations are made about appropriate equipment to use in future investigations of glottal pulse waveforms in speaker identification.

THE GLOTTAL PULSE:
POSSIBLE APPLICATIONS TO SPEAKER IDENTIFICATION

Dr. Beth L. Losiewicz

Introduction

Voiced speech can be characterized as resulting from a glottal wave (source) passed through the vocal tract (filter). On the whole, speaker identification algorithms have not attempted to analyze the glottal wave 'source' separately from the overall speech signal in which the effects of 'source' and 'filter' are compounded. Briesman et. al., (1987) suggest that such a division of the speech waveform into subcomponents with unique physiological origins, (i.e. glottal 'source' and vocal tract 'filter') could provide a larger set of descriptors for use in speaker identification tasks. Similar suggestions have been made by other researchers, (e.g., Miller, 1959; Sondhi, 1975; Monsen et. al., 1977; Childers and Lee, 1991), but few such attempts are reported in the literature (e.g., Curtis, 1974; Wolf, 1972; Carrell, 1984).

Evidence that the glottal pulse may be an essential component in human perception of speaker differences comes from work by Holmes (1973) with speech synthesis. In an attempt to model a given speaker as closely as possible with synthesized speech, he found that if the excitation source was an estimate of that speaker's (inverse-filter derived) glottal pulse, the resulting synthesized speech was judged as more natural than if the excitation source was an idealized pulse shape (e.g., combinations of cosine segments). Klatt (1987) also reports that glottal pulse characteristics are of "considerable importance to speaker identification," and models glottal variability in open quotient, spectral tilt and breathiness noise in

17-3

his Klatttalk speech synthesizer. Yegnanarayan, Naik & Childers (1984) also report that glottal pulse shape has a large role in quality of synthetic speech, more so than either pitch period or choice of vocal tract modelling parameters.

The Glottis

The glottis is the opening between the vocal folds through which pulmonary air pressure passes during both breathing and speech. These folds consist of muscle and mucous membrane tissue which stretch between the thyroid cartilage and the arytenoids. During breathing the glottis is fully open, allowing air to pass through freely. In voiced speech, however, the glottis is partially or completely closed. Subglottal air pressure causes periodic vibration of the vocal folds, resulting in the strong periodic excitation that drives voiced speech. The speaker, by controlling the shape and tension of the vocal folds, can, within limits, control this excitation source. The periodic pulse generated in the glottis passes through the pharyngeal cavity to the mouth, (and, if the nasal passages are open, into the nasal cavity as well). By varying the mouth cavity and the various articulators (tongue, teeth, soft palate, etc.) the speaker shapes the glottal wave, augmenting some frequencies and attenuating others, yielding the complex waveforms of speech.

The Glottal Pulse

The moment of glottal closure coincides with the peak excitation of the vocal tract (Miller, 1959), although excitation can occur without complete glottal closure (Holmes, 1962; cited in Rosenberg, 1970). Dampening of the excitation occurs during the succeeding closed-glottis phase, as a result of energy absorption by the vocal tract. Secondary excitation occurs at the point of glottal re-opening (Miller, 1959; Childers, et. al., 1991).

The source-filter model of the vocal apparatus is often simplified to exclude results of interaction between the source and the filter, and the idealized glottal

pulse is represented as a smoothly varying signal except for discontinuous slopes at the endpoints. This is not completely accurate. In fact Bickley and Stevens (1986) report significant individual differences in the effect of vocal tract loading on the glottal waveform. Rothenberg (1985) reports that "The low frequency inertance of the vocal tract . . . can cause a skewing of the glottal flow pulse to the right." Monsen & Engebretson (1977) reports dips in the waveform at the fourth, fifth and sixth harmonics, presumably resulting from the interaction of the glottal airflow with the acoustic loading of the vocal tract (Milenkovic, 1986). Klatt and Klatt (1990) report "ripple components" at the F1 frequency due to pharyngeal pressure, and Fant (1985) reports "superposition of formant ripple from previous glottal periods," which varies with closed phase duration, being most prominent after short closed phases. Sub-glottal and supra-glottal resonances also influence glottal pulse shape (Scordilis & Gowdy, 1990; Fant, 1985), and glottal pulse shape can reflect out-of-phase vibration of the top and bottom surfaces of the vocal folds (Klatt, 1987).

Sources of GLottal Pulse Variability

The glottal pulse can vary on a number of different parameters: pulse width, pulse skewedness (ratio of duration of open and closed phases), closure abruptness, symmetry of pulse, shape of pulse peak, rms intensity, pulse phase, source spectrum slope, turbulent noise component, etc. (Rosenberg, 1970; Miller, 1959; Childers, et. al., 1991; Wolf, 1972; Klatt & Klatt, 1990; Monsen & Engebretson, 1977; Scordilis & Gowdy, 1990).

This variance is caused by complex interactions of physiological and motor control determinants, including shape and size of the glottal opening, subglottal resonances, subglottal air pressure, vocal fold elasticity and thickness, phase relations of upper and lower portions of vocal fold, and certain supra-glottal

characteristics (e.g., of the trachea and supra-glottal vocal tract). Although physiological determinants are relatively static within a given speaker (e.g., sub-glottal resonance characteristics, vocal fold elasticity, etc.), most motor control parameters have an effective range of intra-speaker variance. The speaker can, and does, control the various motor parameters during speech, both individually and in complex interactions. Intonation, syllable stress, phonation type (e.g., creaky voice, breathy voice, falsetto, and normal voice), vowel type and amplitude intensity all have glottal, and hence glottal waveform implications.

If glottal pulse characteristics are to be usable as cues to speaker recognition, those aspects of the glottal pulse which have greater inter- than intra-speaker variability need to be identified. Only a handful of studies have attempted to distinguish between characteristics that are inter- versus intra- speaker variable, mostly focusing on male/female differences. A brief review of known sources of inter- and intra-speaker variance in glottal pulse characteristics follows.

Inter-Speaker Variability: Male/Female Differences

Although it has long been known that there are mean F0 differences between male and female speakers, only a handful of studies have investigated other glottal pulse characteristics of male versus female speech. Monsen and Engebretson (1977) found several such glottal pulse attributes. First, the shape of the glottal pulse for females was, on the whole, more symmetrical than the male pulse, with the male pulse often evincing a pronounced 'hump' in the opening portion of the wave. They hypothesized that this results from a "slight out-of-phase movement of the upper and lower vocal fold." As the F0 of a male speaker rises, this 'hump' becomes less prominent, and the pulse becomes more symmetrical. Intensity also affects pulse symmetry. Soft (i.e., not loud) male articulations also tend to lose the characteristic "hump."

17-6

Not surprisingly, Monsen and Engebretson also found that average rms intensity is lower for female than male voices, with an average drop of -6 dB. The most striking difference they found between male and female glottal pulses, however, was a difference in harmonic relations, namely that the amplitude attenuation slope at high frequencies was steeper for females than for males. While the average fall-off rate for males was approximately -10 dB per octave, the fall-off rate for female voices averaged -15 dB per octave. Martony (1965) and Wolf (1972) also found significant inter-speaker differences in the high frequency slope of the source spectrum. The range of intra-sex variance in slope in the Monsen study, however, was fairly large, especially in connection with intensity differences. Steeper declines in the spectrum slope occurred during soft (as opposed to normal or loud) articulation (intra-speaker).

The results of Monsen and Engebretson also hint at the possibility that the mean F0 change for rising and for falling intonations may be different for males and females.

Klatt and Klatt 1990 found male/female differences in the propensity to different phonation types. Although there was large inter-speaker variability within sex, female speech was more apt to be characterized by breathy voice, while creaky voice was more likely to occur in male speech. Instances of breathy voice also increased for unstressed syllables, utterance-final syllables, and at the margin of voiceless consonants.

Intra-Speaker Variability

Higher level linguistic factors can condition changes in the glottal waveform within speakers. Sentence- and discourse-level intonation contours depend on F0 changes. Interrogative prosody is characterized by a sharp final-syllable rise in F0, while the final syllable of a declarative utterance, as well as stressed syllables, are

characterized by falling F0. Syllable and word stress patterns, also affect the
glottal wave shape.

Speakers can also vary glottal characteristics to achieve variations in vocal
quality. Some languages exploit phonation differences as contrast ive linguistic
parameters (Klatt & Klatt 1990), but this is not the case in English. Thus in English
phonation type is free to signal individual voice characteristics, sex of speaker, or
pragmatic information. There is also evidence that the glottal waveform changes
with the vowel being vocalized (Cranen and Bovis, 1985; Ananthapadmanabha and
Fant, 1982; Fant, 1985).

Glottal Pulse Variables in Speaker Identification

In spite of the large number of parameters on which glottal source
characteristics can differ within the utterances of a single speaker, there is reason
to believe that such variability may be sufficiently constrained to allow inter-
speaker differences to be used in speaker identification.

Miller (1959) claimed that individual speakers tend to keep pulse shape and
width constant while varying closure period. "This keeps the frequency-energy
distribution essentially constant as the pitch varies, thus presumably having less
effect on the formant values." If this is the case, pulse shape and width might be
candidate parameters for speaker identification algorithms. Milenkovic (1993), in
contrast, emphasizes the variability of glottal open time within speakers.

The degree of F0 rise due to linguistic stress, on the other hand, may not
provide good inter-speaker differentiation. Wolf (1972) claimed that in his data set
(21 adult male speakers) the range of intra-speaker variation on this parameter
was so great as to make it an unlikely candidate for distinguishing between
speakers. He did predict that average F0, on the other hand, would be a good

differentiator between speakers, and Atal (1972) claims that pitch contour is a usable parameter in speaker identification.

Same Effect, Different Cause: Possible Speaker Identification Parameters

There are several known instances in which a single perceptual result can be caused by more than one type of glottal waveform. Monsen and Engebretson (1977), for example, found that creaky voice phonation could result from two different types of glottal activity. One type was characterized by slack vocal folds, low subglottal air pressure and wide, random, variations in pulse period (for one subject, three adjacent pulses had periods of 33 ms, 11 ms, and 18 ms). The other type of creaky voice was produced by double pulses of unequal duration. Hamlet (1971) also reports more than one type of creaky voice. It is possible that characteristic use of creaky voice, as well as type of creaky voice used (perhaps interacting with other factors, such as linguistic or intonation context) could be a usable parameter for voice recognition, although one that would presumably be susceptible to intentional deception (i.e., voice disguise).

Another case of a similar perceptual effect arising from different glottal patterns arises in F0 changes. Monsen and Engebretson (1977) found that F0 change was either characterized by 1) an envelope shift in frequency and amplitude, with a concomitant maintenance of harmonic relations, or 2) a change in harmonic relations with concomitant stability of the frequency and amplitude envelope. They found that when the F0 rise was associated with interrogative pitch contour, the spectral envelope retained its shape (as the harmonic relations become steeper) whereas the (smaller) rise in F0 associated with syllable stress was associated with a shift in amplitude and frequency, maintaining harmonic relations. The fall in F0 associated with a declarative pitch contour was accompanied by the same glottal wave changes as the F0 rise due to syllable stress. They concluded that different

types of glottal changes characterized different types of F0 change. It might be worthwhile to investigate whether this distinction holds across speakers, or whether speakers show a preference for one type of F0 shift mechanism over the other. If they do, this might be exploited in speaker identification algorithms.

<u>Measuring (Estimating) The Glottal Pulse</u>

Measuring (or, more commonly, estimating) the glottal pulse is not trivial. Direct measures, usually rather invasive, include high speed photography (Childers, Mott and Moore, 1980), transillumination, electromyography, ultrasound (Hamlet, 1971), or direct measure of the glottal air flow. Simulations have been carried out with excised human and canine larynges, and with computer models of the vocal fold oscillation. Sondhi (1975) and Monsen & Engebretson (1977), directly measured the glottal pulse using a reflectionless metal tube as a pseudo-infinite extension of the vocal tract.

Indirect measurements are accomplished through inverse filtering techniques that attempt to factor out the vocal tract contribution, leaving the glottal pulse as a residual (Briesman, et. al., 1987; Matausek & Batalov, 1980; Milenkovic, 1987; Milenkovic, 1993; Rosenberg, 1971; Alku & Laine, 1989; Isaksson & Millnert, 1989; Schoentgen, 1990; Strube, 1974; Ananthapadmanabha & Fant, 1982). On the whole these indirect estimates have correlated well with the results of more direct measures, although careful attention to filter adjustment is crucial. Even with an optimal filter, there is a large potential for confusion of glottal wave and formant oscillations for vowels with low F1,[1] and nasalized vowels are not amenable to this type of inverse filtering (which only models the effect of the *vocal* tract). Milenkovic (1986) reports filter-induced artifactual mimicking of glottal non-

_____

[1] But see Cranen and Bovis (1985) for an alternate explanation of this difficulty. Their suggestion that low vowels have a different glottal waveform might explain this difficulty in obtaining a 'good' glottal pulse for low F1 vowels by inverse filtering.

closure. Briesman, et. al. (1987) suggest testing the inverse filter on a waveform with a known (synthesized) glottal waveform before experimentation.

The set of glottal waveform measurements proposed by Fant (1985) are illustrated in Figure 1.

<u>Recommended Methods for Further Research</u>

Several possible avenues for investigating the usefulness of glottal pulse information in speaker identification were considered: Electroglottograph (EGG) signals; a software inverse filter; a Sondhi tube; and an analog (hardware) inverse filter with a Rothenberg Mask (Rothenberg, 1977).

The Air Force Academy has provided a database to the Speech Processing Lab which contains parallel speech and electroglottograph (EGG) signals from a variety of speakers. Although the two signals were intended to be time-aligned, they are not in fact so aligned, being offset by approximately 25 msec. Since the glottis-to-microphone travel time should only be about 1-2 msec, this asynchrony was presumably caused by transmitter characteristics. Although the signals could be time-aligned retrospectively, this is a less than optimal solution.

This EGG data was not chosen as the best method for investigating the glottal pulse for a slightly different reason, however. The EGG is a measure of vocal fold contact area, and as such fails to give any detailed information about airflow during the open period of the glottal pulse. This is reflected in flattened peaks in the signal. Since inverse filtering offers more detailed information, and since it is more likely to be applicable to signals obtained from existing communication channels, it was deemed to be a preferable technique for present purposes.

A Sondhi Tube (Sondhi, 1975) was also rejected as a method for obtaining glottal pulses, primarily because it is not certain what effect the tube has on the speaker's articulation.

We were unable to locate a pre-programmed software inverse filter to estimate the glottal pulse. Since the literature reports that filter adjustment is critical, we decided not to venture into the business of developing and programming our own filter.

An analog, hardware, inverse filter is available commercially from Glottal Enterprises in Syracuse, New York. This filter was developed by Rothenberg (1977), and is marketed with a volume velocity flow mask ~~which~~ and has been accepted by the scientific community as a reliable way to obtain the airflow to be inverse filtered. (Its main advantage is that it obviates the need for an expensive low-frequency response microphone needed to obtain accurate low frequency glottal pulse information from a pressure wave.) The mask and filter units are inexpensive (approximately $2,300) and it was decided that it provided the best cost/reliability ratio for the proposed research.

It should be noted that the waveform obtained from the volume velocity airflow contains more accurate glottal pulse information than is available from the signals generally found in real-life speaker identification applications. AC microphones seriously distort the low frequency information of the speech signal, thus a pristine glottal source waveform is not obtainable with speech signals as transmitted by most current communications equipment. However, it was decided that it would be preferable to begin an investigation with the 'best case' scenario, investigating whether, in principle, the glottal pulse information can differentiate between speakers. Then, if we find that it _does_ differentiate, further work could develop more direct applications. If we fail to find differentiating parameters, we would be confident that we had made our best attempt to discover any that might exist.

Conclusions:

Although sparse, the available information about inter-speaker differences in the glottal pulse waveform suggests that it may be a useful parameter for speaker identification algorithms. It is recommended that the airflow mask and inverse filter developed and marketed by Glottal Enterprises in Syracuse, New York be used in future glottal pulse research originating from this lab, as the most cost effective and accurate way to obtain the glottal waveform for speaker identification research.

REFERENCES

Ananthapadmanabha, T. and G. Fant. (1982). Calculation of true glottal flow and its components. Speech Communication, 1, 167-184.

Atal, B. (1972). Automatic speech recognition based on pitch contours. Journal of the Acoustical Society of America, 52, 1687-1697.

Alku, P. & U. Laine. (1989). A new glottal LPC method for voice coding and inverse filtering. IEEE International Symposium on Circuits and Systems, vol. 3, 1831-1834.

Bickley, C. & K. Stevens. (1986). Effects of vocal-tract constriction on the glottal source: Experimental and modelling studies. Journal of Phonetics, 14, 373-382.

Briesman, N., C. Thorpe & R. Bates. (1987). Nontactile estimation of glottal excitation characteristics of voiced speech. IEE Proceedings, 134, 887-813.

Carrell, T. (1984). Contributions of fundamental frequency, formant spacing and glottal waveform to talker identification. Speech Research Lab Progress Report 5, Indiana University, Bloomington.

Childers, D. & C. Lee. (1991). Vocal quality factors: Analysis, synthesis and perception. Journal of the Acoustical Society of America, 90, 2394-2410.

Childers, D., J. Mott & G. Moore. (1980). Automatic parameterization of vocal cord motion from ultra high speed films. Proc. ICASSP, 1, 65-68.

Cranen, B. and L. Boves. (1985). Aerodynamic aspects of voicing: Glottal pulse skewing revisited. ICASSP, Proc. of the IEEE Int'l Conf. on ASSP, 1085-1088

Curtis, T. (1974). Inter speaker versus intra speaker variability of glottal pulse shapes. Journal of the Acoustical Society of America, 55, 462.

Fant, G. (1985). The voice-source theory and acoustic modeling. In I. Titze & R. Scherer, eds., Vocal Fold Physiology: Biomechanics, Acoustics & Phonatory Control. The Denver Center For the Performing Arts, Denver, Co., 453-464.

Geisler, C. D., & S. Silkes. (1991). Responses of "lower-spontaneous-rate" auditory nerve fibers to speech syllables presented in noise. II: Glottal-pulse periodicities. Journal of the Acoustical Society of America, 90, 3140-3148.

Hamlet, S. (1971). Location of slope discontinuities in glottal pulse shapes during vocal fry. Journal of the Acoustical Society of America, 50, 1561-1562.

Holmes, J. (1973). The influence of glottal waveform on the naturalness of speech from a parallel formant synthesizer. _IEEE Transactions on Audio and Electroacoustics, AU-21,_ 298-305.

Isaksson, A. & M. Millnert. (1989). Inverse glottal filtering using a parameterized input model. _Signal Processing, 18,_ 435-445.

Klatt, D. (1987) Review of text-to-speech conversion for English. _Journal of the Acoustical Society of America, 82,_ 747-793.

Klatt, D. & L. Klatt. (1990). Analysis, synthesis, and perception of voice quality variations among female and male talkers. _Journal of the Acoustical Society of America, 87,_ 820-857.

Marton, J. (1965). Studies of the voice source. Speech Transmission Lab, Royal I   Jte of Technology, Stockholm, Quarterly Progress Status Report 1, 4-9.

Matausek, M. & U. Batalov. (1980). A new approach to the determination of the glottal waveform. _IEEE Transactions on Acoustics, Speech, and Signal Processing, ASSP-28,_ 616-622.

Milenkovic, P. (1986). Glottal inverse filtering by joint estimation of an AR system with a linear input model. _IEEE Transactions on Acoustics, Speech and Signal Processing, ASSP-34,_ 28-42.

Milenkovic, P. (1993). Voice source model for continuous control of pitch period. _Journal of the Acoustical Society of America, 93,_ 1087-1095.

Miller, M. and M. Sachs. (1984). Representation of voice pitch in discharge patterns of auditory-nerve fibers. _Hearing Research, 14,_ 257-279.

Miller, R. (1959). Nature of the vocal chord wave. _Journal of the Acoustical Society of America, 31,_ 667-677.

Monsen, R. & M. Engebretson. (1977). Study of variations in the male and female glottal wave. _Journal of the Acoustical Society of America, 62,_ 981-993.

Ricart, R., J. Cupples & L. Fenstermacher. 1993.

Rosenberg, A. (1970). Effect of glottal pulse shape on the quality of natural vowels. _Journal of the Acoustical Society of America, 49,_ 583-590.

Rothenberg, M. 1977. Measurement of airflow in speech. _Journal of Speech and Hearing Research, 20,_ 155-176.

Rothenberg, (1985). Source-Tract Acoustic Interaction in Breathy Voice. In I. Titze & R. Scherer, eds., _Vocal Fold Physiology: Biomechanics, Acoustics & Phonatory Control._ The Denver Center For the Performing Arts, Denver, Co., 155-165.

Schoentgen, J. (1990). Non-linear signal representation and its application to the modeling of the glottal waveform. _Speech Communication, 9,_ 189-201.

Scordilis, M. and J. Gowdy. (1990). Effects of the vocal tract shape on the spectral tilt of the glottal pulse waveform. _Proceedings of the IEEE,_ Session 2E2, 86-89.

Sondhi, M. 1975. Measurement of the glottal waveform. _Journal of the Acoustical Society of America, 57,_ 228-232.

Strube, J. (1974). Determination of the instant of glottal closure from the speech wave. _Journal of the Acoustical Society of America, 56,_ 1625-1629.

Wolf, Jared. (1972). Efficient acoustic parameters for speaker recognition. _Journal of the Acoustical Society of America, 51,_ 2044-2056.

Yegnanarayana, B., J. Naik, & D. Childers. (1984). Voice Simulation: Factors Affecting Quality and Naturalness. Tenth International Conference on Computational Linguistics, Stanford, California.

FIGURE [1] **: Suggested measurement parameters for glottal pulse From Fant, 1985.**
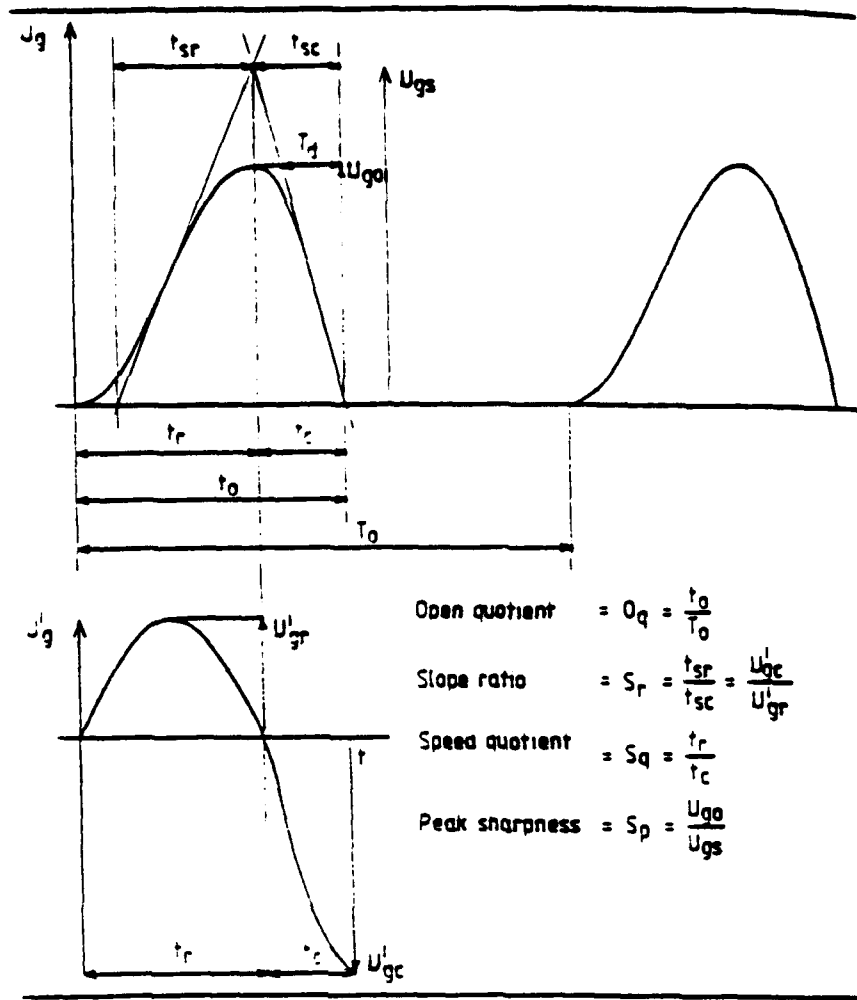
$$\text{Open quotient} = O_q = \frac{t_o}{T_0}$$

$$\text{Slope ratio} = S_r = \frac{t_{sr}}{t_{sc}} = \frac{U'_{gc}}{U'_{gr}}$$

$$\text{Speed quotient} = S_q = \frac{t_r}{t_c}$$

$$\text{Peak sharpness} = S_p = \frac{U_{go}}{U_{gs}}$$

ARTIFICIAL NEURAL NETWORK INVESTIGATION
IN AUTO SOURCE UPDATE PROGRAM

Mohamad T. Musavi   Walter P. Sweeney Jr.
Associate Professor   Graduate Student

Department of Electrical & Computer Engineering

University of Maine
5708 Barrows Hall
Orono, ME 04469-5708
Phone : (207) 581-2243
Fax: (207) 581-2220
E-mail: musavi@eece.maine.edu

ARTIFICIAL NEURAL NETWORK INVESTIGATION
IN AUTO SOURCE UPDATE PROGRAM

Mohamad T. Musavi   Walter P. Sweeney Jr.
Associate Professor   Graduate Student
Department of Electrical & Computer Engineering
University of Maine

Abstract

An investigation of artificial neural networks (ANN) in the candidate selection of auto source update (ASU) program was conducted. Among many types of ANNs the emphasis was given to the probabilistic neural network (PNN) architecture. As compared to other types of ANNs, PNN has proved to be reliable and superior in terms of speed of operation and simplicity of adaptation process. A PNN network was designed and implemented to find the best match and its confidence estimate for a given message among several possible candidates. Different experiments were conducted on a set of messages and candidates from the Defense Mapping Agency (DMA) databases to check the performance of the PNN. The results have been successful and promising. Future enhancement of the proposed PNN and other ANN methodologies in ASU program has also been presented.

ARTIFICIAL NEURAL NETWORK INVESTIGATION IN AUTO SOURCE UPDATE PROGRAM

Mohamad T. Musavi and Walter P. Sweeney Jr.

1.   INTRODUCTION

The objective of this project was to investigate application of artificial neural networks (ANN) in support of the Auto Source Update (ASU) program which is currently under development by the Grumman Data Systems Corporation, Woodbury, New York. The ASU is a prototype software capability for maintaining the accuracy and currency of vectorized geographical information using Defense Mapping Agency (DMA) data [1] and other source material as input.

1.1   Auto Source Update (ASU)

The accuracy and currency of the DMA databases prove to be very critical in accurately identifying different segments in geographical regions of interest. The accuracy issue depends primarily on the original DMA databases and the currency issue concerns rapid and dynamic changes in a geographical area due to sudden events during time of conflict. Some changes occur so rapidly that the MCG&I (Mapping, Charting, Geopositioning and Imagery) database supplied by DMA are altered significantly in a matter of minutes or hours. Under these conditions, one can not solely rely on the original DMA database for planning purposes. An updating system is required to incorporate new changes to be used with the original database in a time efficient manner. Dependence of a large number of Air Force systems on the cartographic information, signifies the importance of an updating system.

The objective of the ASU program [2, 3] is to create such an updating environment for the vectorized information supplied by DMA. From an external input-out point of view, the ASU program can be viewed as a black box that accepts inputs from two different sources of information: (1) the update message data and (2) the original database. The message data is an update request obtained from the dynamic source materials. The original database can be any vectorized data from the DMA databases. The output of the ASU is the appropriate correction and/or update of the original database for the given message. The ASU internal organization consists of three main building blocks: (1) scenario generation, (2) candidate retrieval, and (3) candidate selection. Central to the ASU design is the ASU database which serves as a data depository for different operations and contains data from different external sources in Neutral Update Format (NUF). NUF is a format used by the Grumman Data System in the ASU project.

The scenario gener   lock provides a simulation environment for generation of update messages to be used in t   ing and testing of the ASU program. It consists of a message generator and message handler. Both will work v   data in Neutral Update Format (NUF). The candidate retrieval block will accept update reques s input   will produce a set of candidates for the given message. The candidates are retrieved from the A J database. The candidate selection block, which is the focus of this study, will accept the message and its associated candidates and identify the most appropriate candidate for the given message.

1.2 Candidate Selection

The candidate selection block of the ASU program requires intelligence and adaptation process to select the best possible candidates among all given candidates. The objective of this research is to investigate an optimal artificial neural network architecture that can effectively be utilized in   task.

2. PROJECT DESCRIPTION

The objective of this project is to apply artificial neural network (ANN) technology in candidate selection of the ASU program.

2.1 Message and Candidates

The candidate selection (CS) module should accept message data and candidates' data as input and then find the best match for the given message among all possible candidates. The message data is extracted from dynamic update sources such as evaluated intelligence products, Electronic Chart Updating Manual (ECHUM), raw imagery (e.g. LANDSAT TM, panchromatic SPOT, scanned NHAP, infrared RADAR, SAR, and etc.), native cartographic source materials (e.g., paper road maps), intelligence databases, and any other update source within the Air Force. These update messages are normally in varying United States Message Text Format (USMTF) types (e.g., RECCEXREP, IIR, etc.). The ASU program will reformat the information into the Neutral Update Format (NUF) before submitting it to the candidate selection.

A message data in NUF is normally a set of points, given in latitude (LAT) and longitude (LON) degree coordinates, from segments such as roads, runways, lakes, buildings, and etc. in a geographical area of interest. Each message consists of one of four features: (1) point, (2) line, (3) polygon, or (4) area. Each feature can have both numerical and categorical attributes associated

with it. These attributes include feature attribute coding system (FACS) identifier, surface material category (SMC), predominant height (HGT), width (WID), and etc. For example, for a forest polygon FACS = 5C030 (i.e. woodland), SMC = 12 (i.e. trees), and HGT = 15 meters above ground level (AGL). While the attributes of a bridge can have FACS = 1Q040 (i.e. bridge/overpass/viaduct), SMC = 2 (i.e. part-metal), HGT = 20 meters AGL, and WID = 10 meters. Feature attributes are normally given in the beginning of a NUF message for identification purposes. The appendix at the end of this report gives a print-out of a NUF message and Figure 1 presents the same message points plotted as a curve.

The candidates' data for a given message are provided by the candidate retrieval. The candidate retrieval extracts appropriate candidates from the ASU database based on the NUF message. The candidates also are in NUF and have the same structure as the message. A set of candidates for the message of Figure 1 is shown in Figure 2. In this specific example there are 11 different candidates (numbered from 0 to 10). The candidate selection has to find the candidate that best matches the given message.
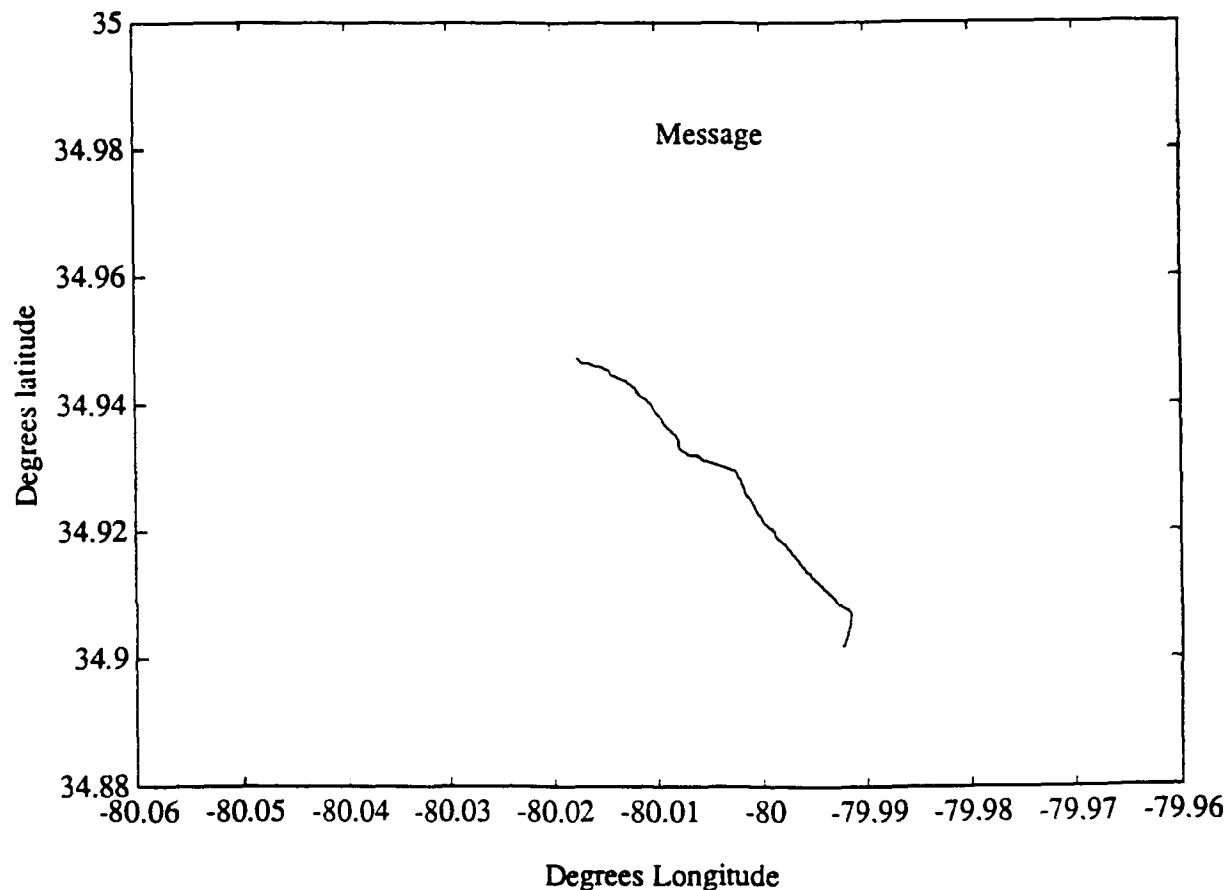
Figure 1. A NUF message plotted by connection of message points.
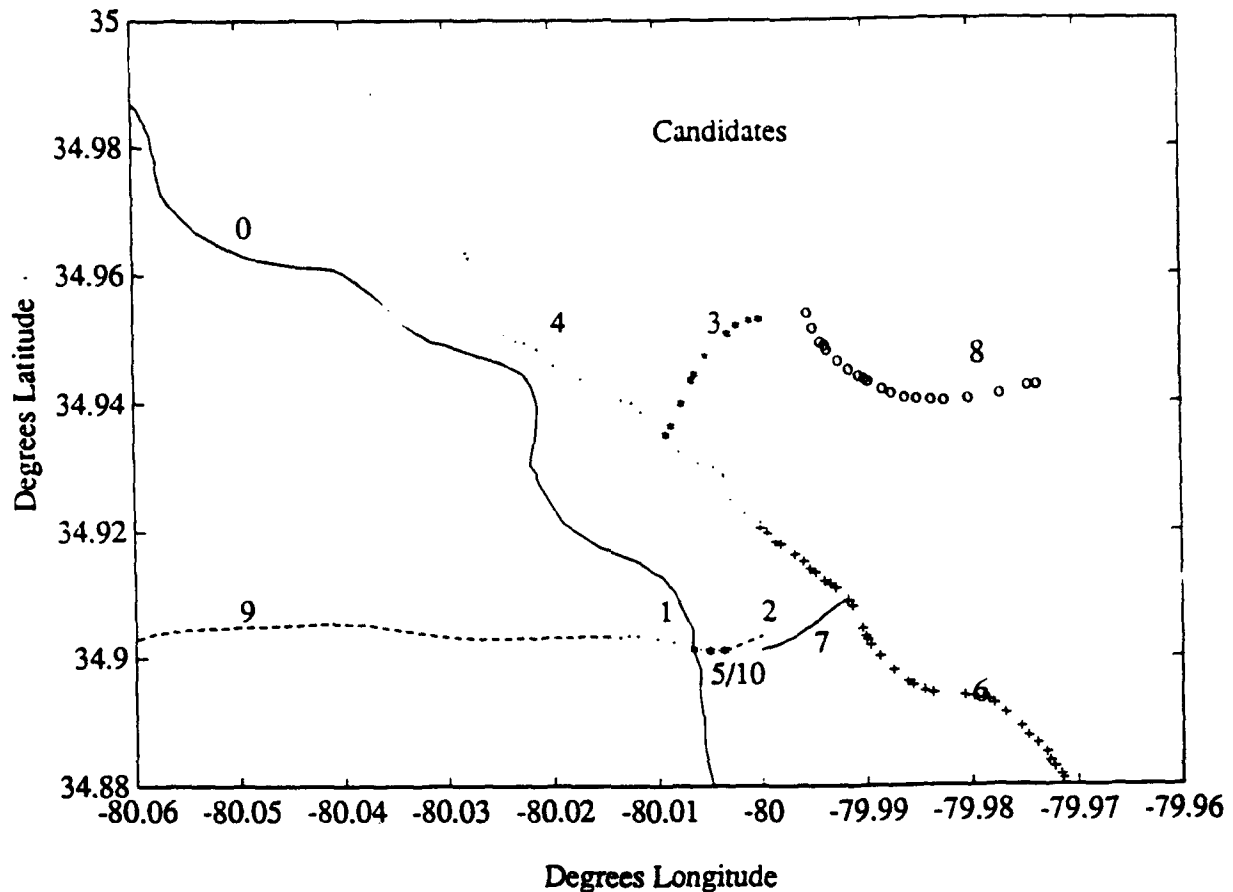
Figure 2. Eleven different candidates associated with the message of Figure 1.

2.2 Probabilistic Neural Network (PNN) Architecture

Our experience with the probabilistic neural network (PNN) [4, 5, 6, 7] has indicated certain advantages of this network over other types of artificial neural networks. At the lower level of architectural design, PNN would be sufficient to act as an independent building block. However, for higher level decision making and integration of individual blocks in the overall system design, more sophisticated architecture and learning paradigm may be needed.

The PNN which has its origin in Specht's earlier work [8] has been recently recognized as a viable alternative in dealing with different classification problems. PNN [9, 10] is the combination of a kernel based estimator for estimation of probability densities and the Bayes rule

for classification decision. For example in a two class (A and B) problem the probability densities are found by:

$$f_A(x) = \frac{1}{T} \sum_{n=1}^{T} \Phi_n \left(\|x - c_{an}\| \right) \tag{1a}$$

$$f_B(x) = \frac{1}{T} \sum_{n=1}^{T} \Phi_n \left(\|x - c_{bn}\| \right) \tag{1b}$$

where T is the total number of training points, Φ_n (‖.‖) is a local kernel function, x is the input to the network, and c_{an} and c_{bn} are the training data from class A and B respectively. Equations (1a) and (1b) measure the closeness (not necessarily Euclidean) of input x to the training data and then a simple comparison of the two determines if x belongs to class A or B. Similar strategy can be adopted for more than two classes of data.

The training process in PNN is that of finding a set of appropriate kernels Φ_n (‖.‖) and there is no weight adaptation process. To simplify the training process, Specht makes the following three assumptions:

i)   All kernels are the same. In other words,

$$\Phi_n \left(\|x - c_n\| \right) = \Phi \left(\|x - c_n\| \right). \qquad \text{for} \quad n = 1, 2, \ldots\ldots, T \tag{2a}$$

ii) The kernel is a Gaussian function given by:

$$\Phi \left(\|x - c_n\| \right) = (2\pi)^{-M/2} |\Sigma|^{-1/2} \exp\left[-\frac{1}{2}(x - c_n)^T [\Sigma]^{-1} (x - c_n) \right]. \tag{2b}$$

Where M is the dimension of the input space and Σ is the covariance matrix.

iii) And that the covariance matrix is diagonal and has equal eigenvalues ($\Sigma = \sigma^2 I$),

$$\Phi \left(\|x - c_n\| \right) = (2\pi)^{-M/2} \sigma^{-M} \exp\left[-\frac{\|x - c_n\|^2}{\sigma^2} \right] \tag{2c}$$

Using the above assumptions the problem of training PNN is simply reduced to selecting parameter σ that is referred to as the smoothing parameter. This parameter is normally found by

trial and error or the nearest neighbor criterion. Musavi et al. [4] have recently presented a technique for optimal selection of all covariance matrices. In our future studies, this technique will be utilized to enhance the accuracy of PNN network.

The significant advantages of PNN classifier are its speed and training process. First, the training process is one-pass and there is no need for weight adaptation, hence yielding great processing speed as compared to the back propagation (BP), radial basis function (RBF), and other types of neural networks. Second, the network generalizes to the new incoming patterns without having to repeat the training process. These characteristics are ideal for real time applications [11, 12, 13]. The architecture of PNN is very simple, thus, software/hardware implementation of the network on conventional or parallel computers is easy. The processing speed of PNN is achieved at the expense of increased memory size. This is due to the fact that the training data set has to be available for classification of every incoming datum. Specht in defense of his networks argues justifiably that memory is abundant and affordable.

2.3   PNN in Candidate Selection Module

Accurate selection of a candidate, among many candidates, to best match a given message relies on many attributes. Some of these attributes are proximity, orientation, shape, FACS ID, width, hight and etc. A robust system should take advantage of all available attributes to make the best possible decision.

To apply artificial neural networks in the design of candidate selection, PNN will be used as an individual building block. One PNN will be designed for each attribute. The following two sections will discuss structures of proximity PNN (PPNN) and orientation PNN (OPNN). Similar structures can be designed for shape PNN and other attributes.

2.3.1   Proximity PNN (PPNN)

For the proximity attribute, a network like that of Figure 3 is constructed. In this network, the input vector is two dimensional consisting of latitude (LAT) and longitude (LON) coordinates. The output is a scalar giving a numerical value presenting the closeness of the input point to the message under consideration. The points of the message (training data) are set to be the centers of the Gaussian functions. Therefore, the number of nodes in the network equals the number of points in the message. In case of excessive message points, it is possible to use some kind of clustering algorithm without significantly affecting the generalization ability of the network. The smoothing parameter, σ, can be either entered by the operator using trial and error, or found automatically by the nearest neighbor criteria.

The following procedure is followed to find a measure of confidence on the closeness of each candidate to a given message. A block diagram of the procedure has also been given in Figure 4.

`Procedure`:

Step 1. Set up the PNN network for the given message.

Step 2. Select a candidate for the given message.

Step 3. Input each point of the candidate to the PNN and calculate the output.

Step 4. Add the output to the previous output.

Step 5. Repeat Steps 3 and 4 until all points of the selected candidate are covered. The total summation value at Step 4 is a measure of confidence on the closeness of the selected candidate to the given message.

Step 6. Repeat Steps 2 though 5 until all candidates of the selected message are covered.

Step 7. Perform a normalization on the total summations of Step 4 for different candidates. Comparison of these normalized values give a measure of confidence on each of the candidates.

Step 8. Repeat Steps 1 through 7 for a different message.
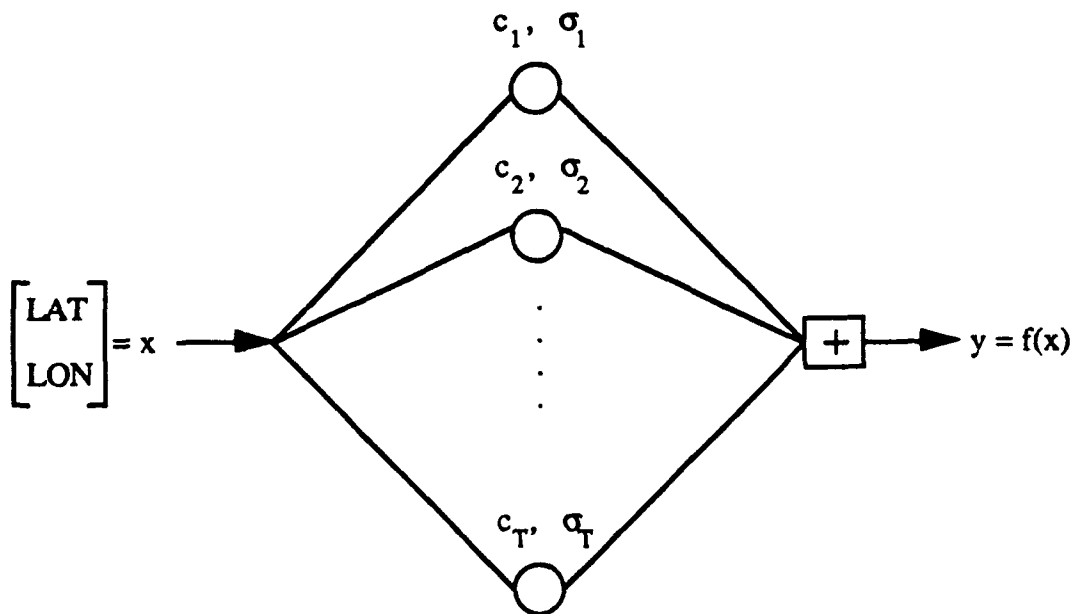
Figure 3. The PNN architecture used in the candidate selection block.
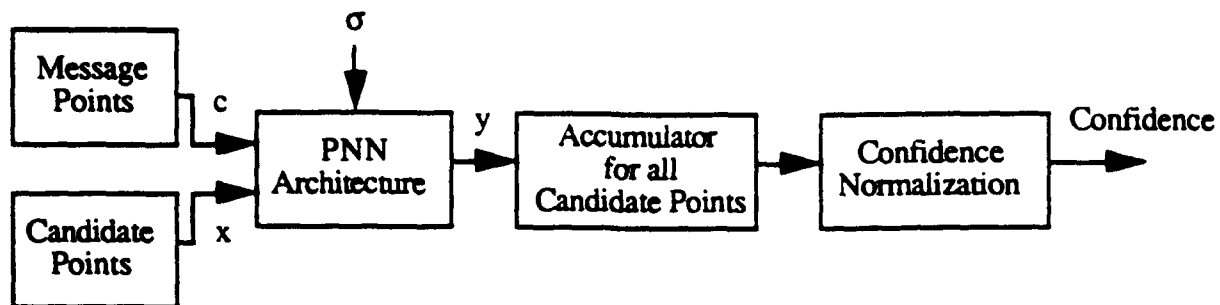
Figure 4. A block diagram of the confidence generator for each given candidate.

2.3.2 Orientation PNN (OPNN)

A PNN similar to the one given in Figure 3 can also be used for orientation attribute (OPNN). Note that in this case the input to the network is one dimensional representing the orientation of the input candidate object. The centers of the Gaussian nodes are the orientations of different segments constructing the message object. The output of the OPNN is a measure of similarity between the orientations of the message and candidate objects.

2.3.3 Candidate Selection Architecture

The overall intelligent system for candidate selection module is built by the integration of PNN blocks for different attributes. Figure 5 presents a block diagram of the overall candidate selection system design.
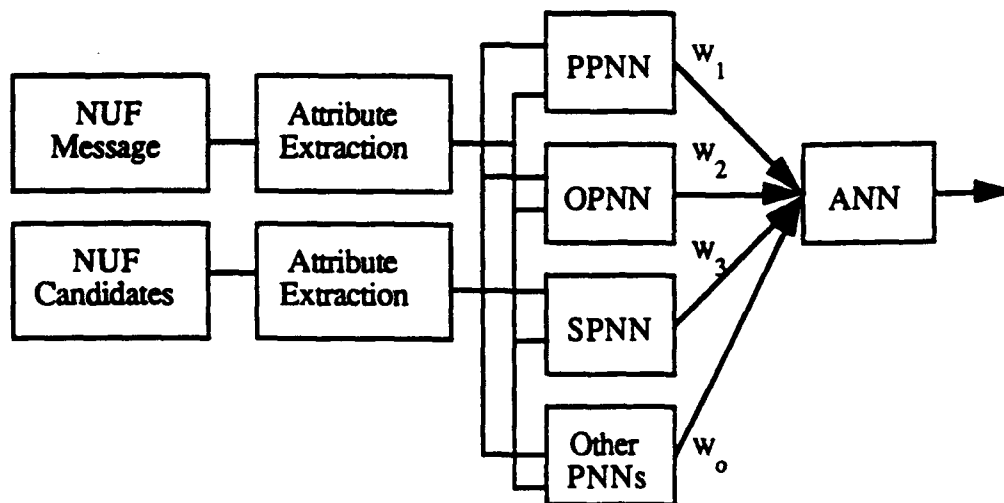
Figure 5. The overall system design for candidate selection module.

3.   TEST RESULTS

A set of messages and their associated candidates were obtained from Grumman Data System for testing the methodology presented in Section 2. The message file consisted of 19 different messages and the candidate file consisted of 76 different candidates for the 19 messages. The 19 messages and 76 candidates are shown in Figure 6, the messages are in solid and the candidates are in dotted lines. Since all the messages and candidates have been plotted on the same graph the beginning and end of a message and its corresponding candidates are not clearly identified. A message with its corresponding candidates are shown in Figures 1 and 2 respectively. Another message with its corresponding candidates are shown in Figure 7.

Table 1 presents the results of our experiments with the given messages and candidates using only proximity PNN. The first column gives the message number, the second column gives the associated candidates for the message, and the last column presents the confidence of the PNN in selecting each of the candidates.
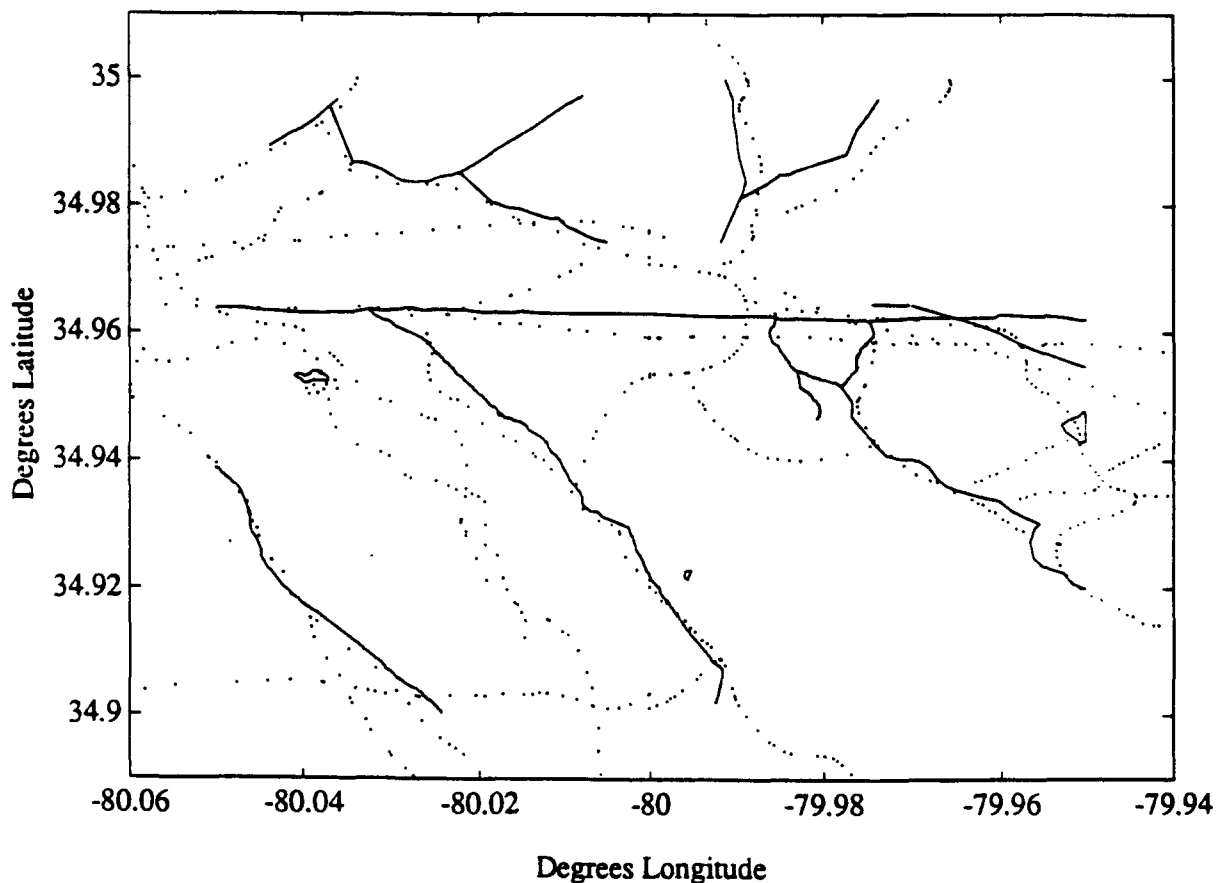
Figure 6. Nineteen messages and their corresponding candidates.

All programs for this project were written in C on a SUN SPARCstation IPC. It should be mentioned that for all the 19 messages and 76 candidates the program generated the confidence measures of Table 1 in under 16 seconds. The smoothing parameter for the PNN network was selected to be 0.002.
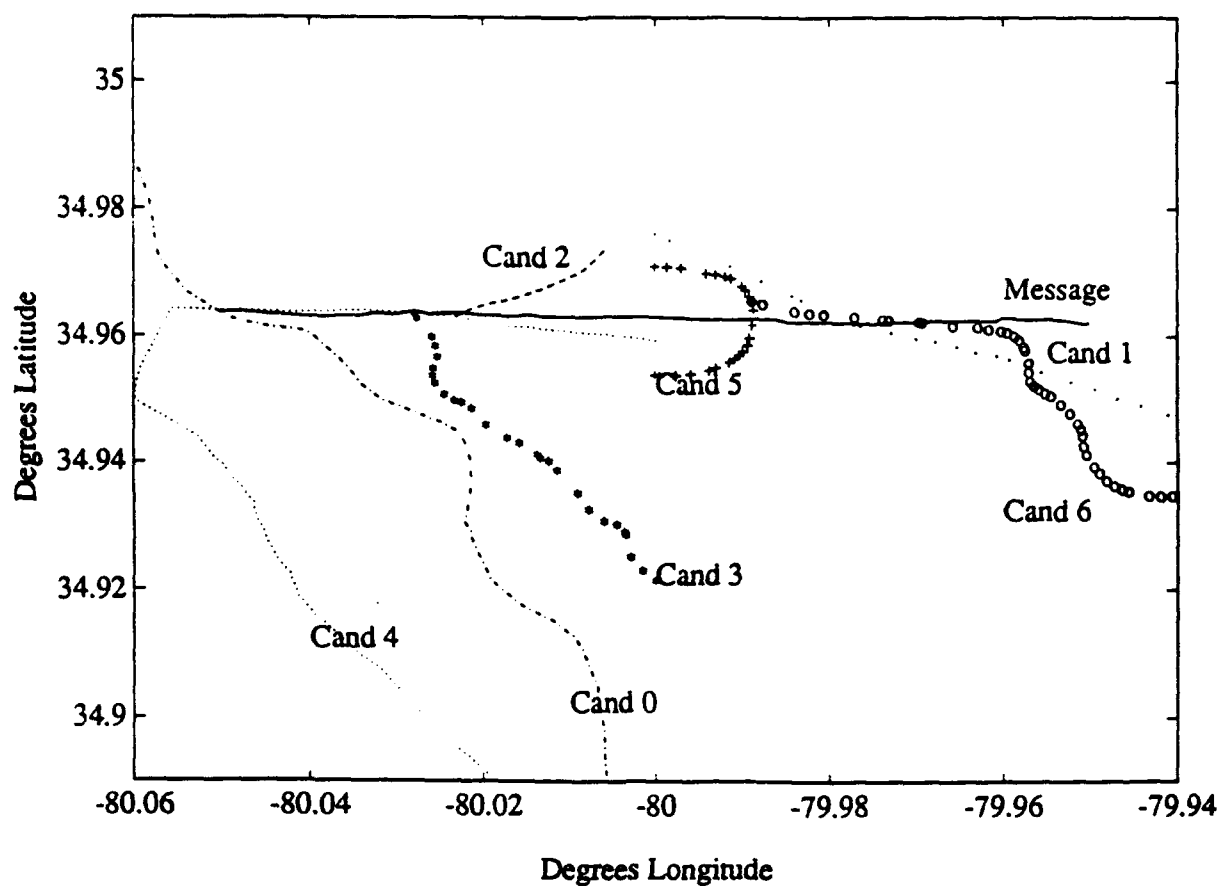
Figure 7. A messages and its corresponding candidates.

Message	Candidate	Confidence Level
1	1	90 %
	0	9 %
	2	1 %
2	1	54 %
	0	46 %
3	2	81 %
	3	18 %
	1	0 %
	0	0 %
4	6	48 %
	4	36 %
	7	10 %
	3	7 %
	5	0 %
	8	0 %
	9	0 %
	0	0 %
	2	0 %
	10	0 %
	1	0 %
5	4	48 %
	6	23 %
	2	12 %
	3	12 %
	5	5 %
	0	0 %
	1	0 %
6	1	83 %
	2	13 %
	0	5 %
7	4	61 %
	6	26 %
	5	8 %
	2	5 %
	3	0 %
	7	0 %
	0	0 %
	1	0 %

Table 1-a. The results of the PPNN candidate selection on the test messages.

Message	Candidate	Confidence Level
8	2	46 %
	1	29 %
	3	25 %
	0	0 %
9	2	71 %
	1	29 %
	0	0 %
10	1	72 %
	2	28 %
	0	0 %
11	No Candidates	Available
12	No Candidates	Available
13	No Candidates	Available
14	0	75 %
	1	25 %
15	2	76 %
	1	16 %
	0	8 %
16	1	86 %
	2	14 %
	0	0 %
17	3	92 %
	4	7 %
	1	0 %
	2	0 %
	5	0 %
	6	0 %
	0	0 %
18	0	100 %
19	0	80 %
	1	20 %

Table 1-b. The results of the PPNN candidate selection on the test messages.

IV. CONCLUSION and FUTURE WORK

5.1 Conclusion

In this study, the probabilistic neural network (PNN) architecture was successfully applied to the candidate selection part of the ASU program. At the present time, the candidate selection results are solely based on the proximity criteria. However, the proposed architecture should be tested with more test cases and other attributes should be clued in for system robustness.

5.2 Future Work

To enhance the candidate selection program further investigation needs to be conducted. The following subject areas can be considered.

- Inclusion of Feature Attributes
- Shape Description
- Hardware Implementation

5.2.1 Inclusion of Feature Attributes

An important enhancement of the proposed work reported here is the inclusion of feature attributes. Additional artificial neural network (ANN) modules can be designed to handle these attributes. Each module can be designed to work internally as an independent component and externally as an integral part of the overall system. The ANN design depends of the complexity and specifications of the feature. Radial basis function (RBF) and probabilistic neural networks (PNN) can be investigated in this phase.

5.2.2 Shape Description

Although inclusion of attribute information is important for more accurate identification of the candidates, the information might sometimes be unknown, incomplete, or even wrong to be of any use. The overall system design should therefore be able to handle conflicting scenarios in a self organizing manner. One of the strong means for achieving this objective is object identification through shape analysis. Therefore a shape descriptor algorithm needs to be devised and implemented. The algorithm has to be size and rotation invariant. The design of the shape descriptor requires a supervised neural network. However, its integration in the overall candidate

selection design has to be self-organized and based on an unsupervised network. The radial basis function (RBF) and probabilistic neural network (PNN) can be utilized for this purpose.

5.2.3 Hardware implementation

For real-time application of the candidate selection program a hardware implementation of the proposed ANN methodology is necessary. A commercial hardware platform that has recently been designed for implementation of PNN and RBF networks can be utilized for this investigation. The result of our investigation may lead into development of a portable intelligent hardware to be used by the Air Force.

ACKNOWLEDGMENT

REFERENCES

[1]   Digitizing the Future, Third Edition, Defense Mapping Agency, Fairfax, Va.

[2]   Draft Software Design Document for Auto Source Update: Part I. Prepared for Rome Laboratory Intelligence and Reconnaissance (IRRP) by Grumman Data Systems Corporation, 7 August 1992.

[3]   Draft System/Segment Specification for Auto Source Update. Prepared for Rome Laboratory Intelligence and Reconnaissance (IRRP) by Grumman Data Systems Corporation, 9 January 1992.

[4]   Musavi, M.T., Kalantri, K., Ahmed, W., & Chan, K.H. (1993). A minimum error neural network (MNN), *Neural Networks*, Vol. 6, 397-407.

[5]   Sweeney, W.P., & Musavi, M.T. (1993). Probabilistic Neural Networks as Chromosome Classifier. submitted to *Cytometry*.

[6]   Musavi, M.T., Chan, K.H., Hummels, D.M., Kalantri, K., & Wahid, A. (1992). A probabilistic model for evaluation of neural network classifiers. *Pattern Recognition*, Vol. 25, No. 10, 1241-1251.

[7]   Musavi, M.T., Kalantri, K., & Ahmed, W. (1992). Improving the Performance of Probabilistic Neural Networks. Proc. of Int. Joint Conf. on Neural Networks (IJCNN), Vol. I, pp. 595-600, Baltimore, MD, June 7-11.

[8]   Specht, D.F. (1967). Generation of polynomial discriminant functions for pattern recognition. *IEEE Trans. on Electronic Computer*, vol. EC-16, 308-319.

[9]   Specht, D.F. (1990a). Probabilistic neural networks. *Neural Networks*, vol. 3, 109-118.

[10]   Specht, D.F. (1990b). Probabilistic neural networks and the polynomial adaline as complementary techniques for classification. *IEEE Trans. on Neural Networks*, vol. 1, no. 1, 111-121.

[11]   Maloney, P.S. (1988). An application of probabilistic neural networks to a hull-to-emitter correlation problem. Washington: 6-th Annual Intelligence Community AI Symposium.

[12]   Maloney, P.S., & Specht, D.F. (1989). The use of probabilistic neural networks to improve solution times for hull-to-emitter correlation problems. San Diego: International Joint conference on Neural Networks, I, 289-294.

[13]   Washburne, T.P., Okamura, M.M., Specht, D.F., & Fisher, W.A. (1991). The Lockheed probabilistic neural network processor. Seattle: International Joint conference on Neural Networks, I, 513-518.

APPENDIX

The following is the coordinate information and partial attribute information of a NUF message.

```
Message #4
SCAL = 50000
HAC  = 50.000000
CONF = 90.000000
UTC  = 2
FACS = 1P030
TYPE = L

34.9637 ,-80.0499
34.9638 ,-80.0471
34.9634 ,-80.045
34.9633 ,-80.0431
34.9631 ,-80.0413
34.963  ,-80.0398
34.963  ,-80.0384
34.9631 ,-80.037
34.9631 ,-80.0356
34.9632 ,-80.0342
34.9636 ,-80.0326
34.9634 ,-80.0314
34.9634 ,-80.0304
34.9636 ,-80.0294
34.9639 ,-80.0282
34.9638 ,-80.0275
34.9634 ,-80.0264
34.9636 ,-80.0254
34.9636 ,-80.0237
34.9636 ,-80.022
34.9633 ,-80.0202
34.9632 ,-80.0184
34.9631 ,-80.0163
34.9634 ,-80.015
34.9631 ,-80.0136
34.963  ,-80.0067
34.963  ,-79.9996
34.9626 ,-79.9933
34.9627 ,-79.9885
34.9627 ,-79.9861
34.9622 ,-79.9847
34.9623 ,-79.9828
34.9622 ,-79.9803
34.962  ,-79.9755
34.9624 ,-79.969
34.9624 ,-79.9645
34.9624 ,-79.9609
34.9629 ,-79.9602
34.9626 ,-79.9567
34.9627 ,-79.9548
34.9625 ,-79.9531
34.9622 ,-79.9518
34.9619 ,-79.9506
34.962  ,-79.9502
```

IPToolkit: An Image Processing Environment
for the X Window System

Robert R. Snapp
Assistant Professor
Department of Computer Science and
Electrical Engineering

University of Vermont
Burlington, VT 05405

IPToolkit: An Image Processing Environment
for the X Window System

Robert R. Snapp
Assistant Professor
Department of Computer Science and
Electrical Engineering
University of Vermont

Abstract

A prototype for an image processing subroutine library, tailored to the X Window System, is presented. This library, called the IPToolkit, is designed so that a comprehensive selection of image processing, visualization, and analysis operations can be integrated into larger software systems with minimal cost and effort. This package currently contains three modules: an input/output interface to grayscale and 24 bit color TIFF images (IOManager), an image processing module (IPRoutines), and a visualization module that interfaces with the X Window System (VPManager).

IPToolkit: An Image Processing Environment
for the X Window System

Robert R. Snapp

Introduction

The IPToolkit is an extendable library of computer subroutines that can be used to add image handling capabili-

ties to a variety of software applications with minimal cost and effort. The toolkit consists of three main modules. The

Input-Output Manager allows the toolkit to read digital images from data files stored in the widely used TIFF[1] format.

In addition, processed images can be stored in TIFF data files. The Viewport Manager allows an application to dis-

play an arbitrary portion of a digital image on a computer display that is running the X Window System under the

Motif Window Manager. This module also provides a number of tools that allow the application to change the appear-

ance of the image on the display. Basic routines are provided for resize, pan, zoom, and rotation operations. Other

routines collect information interactively from the user. For example, the getRectangle function allows the applica-

tion to apply an arbitrary function on a rectangular portion of the image determined by the user as the application is

running. In order to minimize the effort involved in adding these capabilities to a new or existing application pro-

gram, most of these operations are performed as callback routines and event handlers that are automatically placed

under the control of the X Windows event manager. Finally, a library of Image Processing Routines contains a variety

of useful operations to enhance, modify, and extract features from digital images. This module is described more

completely in the companion report "Image Processing Toolkit," by Robert L. Stevenson on pages 20-1 through 20-

12 of this volume.

In the following we give a brief overview of the Input-Output and Viewport Managers, and two Image Process-

ing Routines. More detailed information can be found in the computer files that comprise the toolkit. Almost every

toolkit subroutine is described in a UNIX manpage. Other information can be found in the source code itself. We

_____

1. TIFF, which stands for Tagged Image File Format, is a trademark of Aldus Corporation.

would first like to emphasize, however, that although this software may function more or less as described, it is not sufficiently robust or efficient to be released. The programs and subroutines developed therefore represent only a first effort. Further efforts will be needed to enhance its efficiency and functionality. At the very least, the IPToolkit, in its current state, demonstrates the viability of the concept of a comprehensive image processing environment.

The Input-Output Manager

Two toolkit routines allow digital images to be read from a TIFF file and loaded into an IMAGE data structure (see page 20-4), and the reciprocal operations. These are:

loadTiff()	reads an image from a TIFF file
dumpTiff()	writes an image to a TIFF file

At present, only 8 bit grayscale and 24 bit, RGB, color images are supported. Both of these routines call functions from the libtiff subroutine library. Libtiff is public domain software and can be obtained by the ftp program from the internet host sgi.com. The source code for these routines can be found in the subdirectory IOManager. Future tools will include routines to read and write FEATURE data structures, graphics data, and training set data.

The Viewport Manager

This is the most complex part of the toolkit. In addition to the raster data, an application must know what portion of the image should be displayed (i.e. the viewport), how this visible portion should be oriented and magnified, where is should appear on the display, where the converted image data is stored, etc. The viewport manager takes care of all of these details, and more. To do so requires a comprehensive data structure which we call an IPTXProject. The IPTXProject has fields for the IMAGE structure returned by the loadTiff subroutine, a viewport structure, and X image structure, a pixmap identification number, a list of widgets used to display and scroll the viewport, and some other miscellaneous fields. The first task then, will likely be to convert an IMAGE structure to an IPTXProject. Instead, we provide a routine that reads a TIFF file directly into a Project structure:

IPTXloadProject()	reads a TIFF image into an IPTXProject structure

Before any imagery can be rendered on the display, it is necessary to initialize the colormap. Currently images

can only be rendered with a gray scale.

IPTXinitColormap()	Initializes the gray scale colormap and the X Window visual

The highest level routines create composite Motif widgets that can be used to display a digital image:

IPTXcreateSimpleViewingShell()	creates a shell widget, a frame widget, a simple menu bar, and a managed scroll area widget.
IPTXcreateProjectScrollAreaWidget()	creates an unmanaged scroll area widget for viewing an image, including horizontal and vertical scroll bars, and a drawing area.
IPTXcreateProjectDrawingAreaWidge()	creates a drawing area widget for viewing an image.

Normally, an application needs to call only one of these for each image area desired. For example, to display the image in the TIFF file pretty.tif within a simple viewing shell, a program might insert the following segments.

```
#include <stdio.h>
#include <IPTdatatype.h>
#include <IPTio.h>
#include <IPTvp.h>
. . .
Widget topLevel, shell;
IPTXProject *project;
IPTXProjectLink *link;
IPTXProjectLink *projectList;
IPTXListHeader listHeader = IPTX_LIST_HEADER("examples");
. . .
projectList = IPTXallocProjectLink((IPTXProjectLink *) NULL, &listHeader,
                                    (IPTXProjectLink *) NULL);
topLevel = XtAppInitialize(&app, "IPToolkit", NULL, 0, &argc, argv, NULL, NULL, 0);
IPTXinitColormap(topLevel);
project = IPTXloadProject(topLevel, TIFF_FILE, "pretty.tif");
link = IPTXappendProjectLink(IPTXgetLastLink(projectList), project);
shell = IPTXcreateSimpleViewingShell(link);
. . .
```

This example is perhaps more elaborate than is necessary: Here a list of simple viewing shells is maintained so that the application can manage more than one simple viewing shell simultaneously. The routines that create the scroll area and drawing area widget allow an application to invoke the visualization module at a slightly lower level. Using IPTXcreateProjectScrollAreaWidget() for example, an application can insert the same scroll area widget used by

IPTXcreateSimpleViewingShell() into its own Motif form, frame, or row-column widget. Note that the scroll area widget created by **IPTXcreateProjectScrollAreaWidget()** is unmanaged, i.e. the X window manager has not yet calculated where the scroll area will appear on the screen. Consequently, the application must also call **IPTXmanageProjectScrollArea()** before the scroll area widget is realized and visible on the screen. Using **IPTXcreateProjectDrawingArea()** similarly creates an image drawing area only. When these routines are invoked, the widgets that they create are assigned default callback functions. For the scroll bars used by the scroll Area widget, these are **IPTXhorizontalScrollBarCB()** and **IPTXverticalScrollBarCB()**. These two routines allow the user to pan the viewport across the digital image. An auxiliary routine **IPTXadjustScrollBars()** is used to modify the appearance of the scroll bars after the viewport has been changed. The amount of overlap (in pixels) that is maintained during a scroll increment or decrement operation is maintained by the internal variable `scrollOverlap`. Its value can be changed using **IPTXsetScrollOverlap()**.

A number of callbacks have also been developed for the drawing area widget. (This drawing area is occasionally referred to as the imageArea in some of the man pages, as the digital image is rendered on this widget.) The default callback function for the drawing area created all of the routines in the previous table is **IPTXdrawingAreaCB()**. It manages motif expose (XmCR_EXPOSE) and resize (XmCR_RESIZE) events. After an expose event, the pixmap that contains the visible portion of the image is copied to the display[1]. After a resize event, the dimensions of the viewport are adjusted to agree with the new dimensions of the drawing area widget. Three special event handlers have also been developed to acquire geometric information from the user interactively. These event handlers are:

IPTXelasticRectangeEH()	Collects rectangle information in the form "\<row\> \<col\> \<height\> \<width\>"
IPTXelasticSegmentEH()	Collects line segment information in the form "\<row1\> \<col1\> \<row2\> \<col2\>"
IPTXpixelStatusEH()	Collects pixel information in the form "\<row\> \<col\> \<intensity\>"

After a `ButtonPress`, `MotionNotify`, or `ButtonRelease` event in the appropriate drawing area, these event handlers will, if appropriate, update a graphical overlay on the display, save the geometric information about the

---

1. Efficiency can be gained in future editions of the toolkit by setting the background pixmap of the drawing area to the pixmap of the project, or by writing the image directly to the display.

overlay in the current IPTXProject structure, and call the appropriate auxiliary event handler assigned to the IPTX-Project. The routine **IPTXelasticRectangleEH()**, for example, writes a colored rectangular boundary over the display. One corner of this rectangle is fixed on the window where the pointer was when the `ButtonPress` event was registered; the other (opposite) corner follows the pointer as it moves across the screen with the button pressed (`MotionNotify`). After releasing the button (`ButtonRelease`), the rectangle is erased and the event handler removes itself from the event handler list. After each of these events a character string is reallocated that can be referenced from the data field of the IPTXProject structure, or by calling the routine **IPTXgetProjectData()**. This string contains the four fields indicated in the preceding table that represent the window coordinate of the upper left corner of the rectangle and its height and width (in window coordinates). **IPTXelasticSegment()** and **IPTXpixelSta-tusEH()** function similarly, and are described in the toolkit's man pages.

Normally, the application will not call these event handlers directly. Instead, each has a corresponding routine that adds it to the event list, along with an application specific routine that should parse the data field of the project and take appropriate action.

IPTXgetRectangle()	Construct and process a rectangular portion of the image defined by the user.
IPTXgetSegment()	Construct and process a line segment defined by the user
IPTXgetPixel()	Select and a pixel defined by the user.

Thus, for example, **IPTXgetRectangle()** can be used to allow an application to process an arbitrary rectangular portion of the image interactively. This function is especially useful for clipping operations and for constructing a rectangle in a graphical overlay. **IPTXgetSegment()** can be used to interactively extract distance information from an image.

Viewport Geometry

Before describing the viewport manipulation routines, it is helpful to understand how the geometry of the viewport is

maintained. The following table illustrates the three coordinate systems that are used to render images on the display.
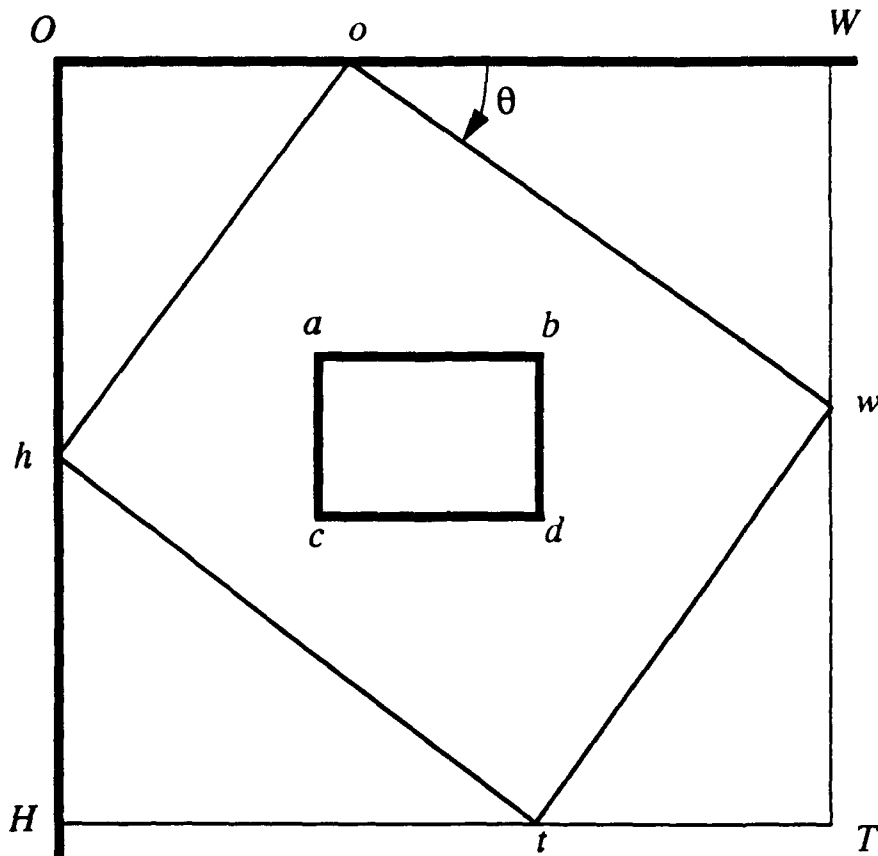
In the above, rectangle *howt* represents the entire image raster, which is assumed to have *h* pixel rows and *w* pixel columns. Rectangle *abdc* represents the visible portion of the image, viz. only the pixels within this smaller area will be rendered in the project's drawing area widget. We usually call this rectangle the project's viewport. When we pan the viewport, e.g., by incrementing the scroll bar widgets, we are in effect moving viewport *abdc*, while preserving its rectilinear orientation. In addition, the position of the viewport is constrained so that *abdc* always lies entirely within the larger rectangle *HOWT*. We call the latter, the global viewport. In this representation, we regard the orientations of *abdc* and *HOWT* as fixed: ray *OH* is always oriented vertically and ray *OW* always horizontally. However, we will allow the orientation of the image to vary. In the above illustration, for example, the image (*abdc*) is inclined by an angle θ with respect to *HOWT*. (Here $\theta < 0$, as it falls in quadrant IV). We will call θ, the viewport angle. The global viewport, then is defined to be the smallest rectangle in the given orientation that completely encloses the project's image for the current viewport angle. As θ varies, *howt*. will maintain is rectilinear orientation, but will shrink and stretch so that it exactly encloses the full extent of the image. After the viewport is modified, the image pixels that it

contains are mapped into an XImage structure that conforms to the dimensions of the current drawing area. We refer to point O in the above figure as the origin of the Global Viewport Coordinate System, and point o, as the origin of the Image Coordinate System. We call point a the Viewport Origin.

Four basic operations are used to manipulate the viewport and consequently modify the appearance of the displayed image. The translation operation changes the location of the viewport in the manner described above. The rotation operation changes the viewport angle in such a way so that image appears to rotate about the point at the center of the viewport. The magnification, or zoom operation, makes changes the rate at which the pixels are sampled when the viewport is mapped to the XImage structure. An increase in the magnification factor, without a commensurate increase in the dimensions of the drawing area, will implicitly reduce the size of the viewport. Finally, the window resize operation changes the size of the project's drawing area. A window resize operation will implicitly modify the dimensions of the viewport. To avoid unwanted interference between these four operations, the viewport structure maintains the image coordinates of its center, the viewport angle, the magnification factor, and the dimensions of the project drawing area. In addition to the previously described scroll bar callback functions, the following operations can be used to manipulate the position of the viewport without changing the other viewport parameters::

IPTXmoveViewportAbs()	Translates the viewport origin so that it coincides with a specified global viewport coordinate.
IPTXmoveViewportRel()	Moves the viewport origin relative to its current location in the global viewport coordinate system
IPTXgetViewportOriginGVC()	Returns the location of the viewport origin within the global viewport coordinate system.
IPTXgetViewportOriginIC()	Returns the location of the viewport origin within the image coordinate system.

The routine IPTXadjustOffset() will ensure that the viewport lies entirely within the Global Viewport Frame: rectangle $HOWT$ above. Routine IPTXgetGlobalViewportRange() returns the dimensions of the Global Viewport Frame, and IPTXfromGVCtoIC() and IPTXfromICtoGVC() convert pixel locations between the Global Viewport and Image Coordinate Systems.

The following routines can be used to change the orientation of the image with respect to the viewport:

IPTXgetViewportAngle()	Returns the current viewport angle
IPTXrotateViewportAbs()	Sets the viewport angle
IPTXrotateViewportRel()	Adds or subtracts to the viewport angle
IPTXrotateViewportForwardCB()	Rotates the image by the `rotationIncrement` in the clockwise sense
IPTXrotateViewportBackwardCB()	Rotates the image by the `rotationIncrement` in the counter-clockwise sense
IPTXgetRotationIncrement()	Returns the `rotationIncrement`
IPTXsetRotationIncrement()	Sets the `rotationIncrement`
IPTXnullViewportAngleCB()	Sets the viewport angle to 0

The following routines modify the magnification factor:

IPTXsetViewportMagnification()	Sets the viewport magnification
IPTXgetViewportMagnification()	Returns the viewport magnification
IPTXzoomInCB()	Multiplies the magnification by `zoomFactor`
IPTXzoomOutCB()	Divides the magnification by `zoomFactor`
IPTXnormalViewportMagnificationCB()	Sets the magnification to unity
IPTXsetZoomFactor()	Sets the `zoomFactor`
IPTXgetZoomFactor()	Returns the `zoomFactor`

Image Processing Module

The image processing module is described in detail in the following report "Image Processing Toolkit". Here, however, we describe two new image processing routines.

IPCannyEdge()	Detects edges in an image according to Canny's algorithm
IPMarrHildrethEdge()	Detects edges in an image according to the algorithm proposed by Marr and Hildreth.

Applications

Three preliminary applications were developed to help debug portions of the IPToolkit and also demonstrate

some of its features. The program ip applies a single image processing operation to the image contained in a TIFF file, and stores the processed image in TIFF format in a new file. As this is batch program, only the IOManager and IP Library are used.

A second application, called IPView uses the viewport manager to display an arbitrary number of TIFF images simultaneously. Here, extensive use is made of the routine IPTXcreateSimpleViewingShell().

A third application, called ipt_test integrates many of the functions of the IPToolkit with the IE2000 imagery server developed at Rome Laboratory.

Conclusion

Although this version of the IPToolkit, is preliminary, it demonstrates the feasibility of a comprehensive subroutine library for manipulating and displaying digital images in the X windows environment. In its current state, the IPToolkit should provide a useful starting point for future efforts.

IMAGE PROCESSING TOOLKIT

Robert L. Stevenson
Assistant Professor
Department of Electrical Engineering

University of Notre Dame
Notre Dame, IN 46556

IMAGE PROCESSING TOOLKIT

Robert L. Stevenson
Assistant Professor
Department of Electrical Engineering
University of Notre Dame

Abstract

For effective exploitation of digital imagery data it is essential to process the data using a variety of techniques. The algorithms through which the data needs to be run depends on the source of the data, the environment in which it was collected and the goals of the exploitation task. If the data is noisy, filtering is needed. For better visualization of the imagery, enhancement is needed. For characterization of data, features needs to extracted. In order to segment the image into regions of interest, classifying routines are needed. Thus there is great need for a collection of image processing routines which can easily and effectively used on a variety of data. This project entailed the design, creation and documentation of an image processing toolkit. The basic form of the toolkit was established, basic image processing routines were implemented and flexibility was added so that additional routines can be added as they are developed.

IMAGE PROCESSING TOOLKIT

Robert L. Stevenson

Introduction

For effective exploitation of digital imagery data it is essential to process and to visualize the data using a variety of techniques. The algorithms through which the data needs to be run depends on the source of the data, the environment in which it was collected and the goals of the ex oitation task. If the data is noisy, filtering is needed. For better visualization of the imagery, enhancement is needed. For characterization of data, features needs to extracted. In order to segment the image into regions of interest, classifying routines are needed. For visualization, routines are needed to display, pan, zoom, in addition to other operations. Thus there is great need for a collection of image processing and visualization routines which can easily and effectively be used on a variety of data. The overall project entailed the design, creation and documentation of an image processing toolkit. The toolkit consists of three essential components.

1. Image Processing Routines,

2. Visualization Routines, and

3. Input/Output Routines.

The input/output routines provide the capability to read and write image data. They currently can read and write image data in the Tiff 6.0 format. The visualization routines create, maintain and process a set of X motif based widgets for the visualization of image data. Current capabilities include the display, magnification, rotation and scrolling of imagery. The image processing routines provide basic processing of the image data.

This part of the project centered on the design and implementation of the image processing routines. The basic form of the toolkit was established, basic image processing routines were implemented and flexibility was added so

that additional routines can be added as they are developed.

Implementation

In image processing there are three basic types of routines.

1. routines which process the image and output a modified image (e.g. filtering routines),

2. routines with extract some metric from the image (e.g. find the maximum of the image), and

3. routines which transform the image data in order to extract information (e.g. Fourier transform or an edge detector).

The input to each of these type of routines is an image data structure. The output of the first type of processing is also an image data structure. The output of the second type of processing is a number (or array of numbers). The output of the third type of processing has the same dimensions of an image but quit often requires a higher intensity resolution then that needed to represent the image data. In order to support the different basic resolution needs of the data types, the following two structures were defined.

```
typedef struct {
    int fmt;
    u_long h;           /* height                                    */
    u_long w;           /* width                                     */
    u_long p;           /* #planes, e.g. 3 for RGB, 1 for Grayscale */
    PIXEL ***data;      /* raster                                    */
                        /* data[0][0] points to the beginning of a  */
                        /* contiguous raster of h*w*p pixels;        */
                        /* data[k][0] points to the beginning of    */
                        /* the k-th plane (or color);                */
                        /* data[k][i] points to the first pixel in  */
                        /* the i-th row of the k-th plane.           */
    PALETTE *palette;   /* Only used for palettized color images     */
} IMAGE;

typedef struct {
    u_long h;           /* height                                    */
    u_long w;           /* width                                     */
    u_long dim;         /* number of planes                          */
    float ***data;      /* data, orgainized as in IMAGE              */
} FEATURE;
```

The important difference between the two data structures is in the resolution of the data variable. In the FEATURE structure, data is a float, where as in the IMAGE structure, data is a PIXEL. PIXEL is currently defined to be an unsigned char (8 bits), but can be easily changed to support higher resolution imagery.

Each routine in the image processing toolkit is passed an input IMAGE and any other necessary parameters. The image processing routine allocates the necessary space for the output data structure, processes the input image and returns a pointer to the output. If the routine fails (due to running out of memory or incorrect parameters) an error message is processed by Error() and the routine returns a NULL pointer. For example, to perform a 5 by 5 square median filtering operation on the image InImage, the following call is made

```
IPSquareMedian(InImage,5,5);
```

If the routine is successful a pointer to the processed image data is returned, if unsuccessful NULL is returned.

Routines Implemented

This section contains a list of the implemented routines, grouped by the type of processing they perform. The routines can also be grouped by the type of data that they return. Most routines either return a pointer to a FEATURE or IMAGE structure. Space for processed data is allocated within the routine. All of the Image Handling, Image Enhancement, Image Filtering, and Image Segmentation routines allocate and return a pointer to an IMAGE structure. In addition the routines IPAddBitError(), IPAddGaussian(), IPAddImpulsive(), IPAddUniform(), IPImageToFeature() and allocImage() return IMAGE pointers. All of the Feature Handling (except IPImageToFeature()) and Feature Extraction routines (except IPCoOccurrence()) allocates and returns pointers to FEATURE structures. In addition allocFeatureInit() returns a FEATURE pointer. The remaining routines, IPImageHistogram(), IPImageMax(), IPImageMin(), IPImageMoments(), IPImageStdDev() and IPCoOccurrence(), all return information about the image generally in some multidimensional floating point array. See their respective manual pages for more details.

Image Handling Routines:

IP3GrayToColor()	creates a color image by copying planes from three grayscale images
IPAddConstant()	add a constant value to an image
IPAddImage()	add two images together
IPCopyImage()	creates a copy of an image
IPCropImage()	create smaller image by cropping a piece from a larger image
IPImageFlipHorizontal()	create the mirror image

IPImageFlipVertical()	flip image around horizontal axis
IPImageRotate90()	rotate image by increments of 90 degrees
IPImageScale()	resizes an image by a scale factor
IPImageToColor()	creates a color image by copying three image planes from the original
IPImageToGray()	creates a grayscale image by selecting one of the image planes
IPImageToImage()	maps one image structure to another with a possible reordering of planes
IPMultConstant()	multiplies an image by a constant value
IPMultImage()	multiply two images together
IPSubImage()	subtract one image from another

Image Enhancement Routines:

IPCenterMean()	adjusts the mean of the image
IPConstrastAdjust()	stretch or compress the image contrast
IPGammaAdjust()	adjust the image gamma
IPHistogramEqual()	do contrast enhancement by histogram equalization
IPIntensityMap()	perform a mapping of the intensity values in the image
IPInvert()	invert the intensity values of an image
IPStretchRange()	stretch the range of the image values
IPUnSharpMask()	enhance an image using an unsharp mask operator

Image Filtering Routines:

IPATrimmedCrMean()	filter an image with a alpha-trimmed cross mean
IPATrimmedSqMean()	filter an image with a alpha-trimmed square mean
IPAverage()	filter an image with an averager
IPConvolution()	filter an image by convolving image with kernel
IPCrossMedian()	filter an image with a cross median
IPGaussianSmooth()	filter an image by convolving image with a Gaussian kernel
IPSquareMedian()	filter an image with a square median

Image Statistical Routines:

IPAddBitError()	add an impulsive noise signal to an image
IPAddGaussian()	add an Gaussian noise signal to an image
IPAddImpulsive()	add an impulsive noise signal to an image
IPAddUniform()	add an uniform noise signal to an image
IPImageHistogram()	return the histogram of an image
IPImageMax()	return the maximum of an image
IPImageMean()	return the mean of an image
IPImageMin()	return the minimum of an image
IPImageMoments()	return the moments of an image
IPImageStdDev()	return the standard deviation of an image

Image Segmentation Routines:

IPThreshold()	threshold an image to create a bi-level image

Feature Handling Routines:

IPCombineFeatures()	combines two feature lists, deleting originals
IPDeleteFeaturePlane()	removes a feature plane from a feature structure
IPFeaturetoImage()	convert an feature image to a intensity image
IPImageToFeature()	convert an intensity image to a feature image
IPMergeFeatures()	combines two feature lists

Feature Extraction Routines:

IPAboveThreshold()	counts the number of pixels above a threshold value
IPBelowThreshold()	counts the number of pixels below a threshold value
IPCoOccurCluster()	computes the cluster tendency of the co-occurrence probability matrix
IPCoOccurContrast()	computes the contrast of the co-occurrence probability matrix
IPCoOccurCorrelation()	computes the correlation of the co-occurrence probability matrix
IPCoOccurEnergy()	computes the uniformity of the energy of the co-occurrence probability matrix

IPCoOccurEntropy()	computes the entropy of the co-occurrence probability matrix
IPCoOccurHomogeneity()	computes the homogeneity of the co-occurrence probability matrix
IPCoOccurInverseMoment()	computes the inverse difference moment of the co-occurrence probability matrix
IPCoOccurMax()	computes the maximum of the co-occurrence probability matrix
IPCoOccurrence()	compute the co-occurrence probability matrix
IPFeatureConvolution()	create feature by convolving image with kernel
IPFreiEdge()	performs edge detection using the Frei and Chen operator
IPKirschEdge()	perform a Kirsch edge detection
IPPrewittEdge()	perform a Prewitt edge detection
IPRobertsEdge()	perform a Roberts X edge detection
IPRobinsonEdge()	perform a Robinson edge detection
IPSobelEdge()	perform a Sobel edge detection
IPWindowMean()	creates feature image based on mean of a window
IPWindowMoments()	creates feature images based on moments of an image
IPWindowStdDev()	creates feature image based on standard deviation of a window

* Memory Handling Routines:

allocFeatureInit()	initializes the image feature structure
addFeatureImages()	to add feature data to existing feature structure
freeFeature()	free feature structure
deleteFeatureImage()	delete feature images
allocImage()	initialize the image structure
freeImage()	frees the image structure
freeImageData()	delete the image data

Adding New Routines

One of the considerations in the design of the toolkit was to allow new routines to be easily added. This flexibility was added by providing an organized and easily understood file structure, providing Makefiles which simplify the compiling and the inclusion of new routines into the library and finally by providing useful internal subroutines to simplify the implementation of common image processing techniques. Adding a new routines consists of the follow-

ing basic steps:

1. Decide on the appropriate subdirectory under IPRoutines for the new routine.

2. Create the new source code, IPNewRoutine.c.

3. Create a man page for the routine, IPNewRoutine.3IP.

4. Edit Makefile. Add IPNewRoutine.o to the definition of OBJECT at the top of the Makefile.

5. Edit the header file in the subdirectory to include the new routine's function prototype.

6. Type make to compile.

7. In the top level directory type, "make clean; make" to add the new routine to the library.

To help with steps 2 and 3 templates and several subroutines have been written.

Many image processing routines are based on the concept of either a point operation or a window operation. For a point operation the output at a pixel is based only on the input pixel value. For a window operation the output is based on a small neighborhood of values centered at the pixel location. For both of these types of operations the output is computed by scanning through the image. This scanning process has been automated through the use of several subroutines. These routines all begin with the word Process, and mainly differ in the type of data inputted or outputted. Their common approach is to be used after the called subroutine has initialized and setup any necessary data structures. They are called with parameters for the input image (or feature) and a function pointer which points to a function to do the processing at each node. The easiest way to explain the use of these subroutines is by examining a sample routine. The toolkit routine IPUnSharpMask() is a window operator which sharpens image edges by adding a weighted highpass version of the original. The code using the ProcessWindow() routine is as follows,

```
#include <IPTdatatype.h>
#include <IPInternal.h>

static long lWindowSize;
static float fWeightParam;
static long lHeightOrder;
static long lWidthOrder;

IMAGE *IPUnSharpMask(IMAGE *pimageIn, u_long ulHeight,
                                        u_long ulWidth, float fWeight)
{
    IMAGE *pimageOut;
    static PIXEL ComputePoint();
```

```
    lWindowSize = ulHeight*ulWidth;
    fWeightParam = fWeight;
    lHeightOrder = ulHeight/2;
    lWidthOrder = ulWidth/2;

    pimageOut = ProcessWindow(pimageIn,ulHeight,ulWidth,ComputePoint);

    return (pimageOut);
}

static PIXEL ComputePoint(IMAGE *pimageWindow)
{
    PIXEL *ppixelData;
    PIXEL ulAverage;
    long lEnhanceValue;

    ppixelData = pimageWindow->data[0][0]
    ulAverage = pixelAvg(ppixelData);
    lEnhanceValue = (1.0+fWeightParam)*
                        pimageWindow->data[0][lHeightOrder][lWidthOrder]
                        - fWeightParam*ulAverage;
    return(CLIP(lEnhanceValue));
}
```

The routine **ProcessWindow()** scans through the image pimageIn. For each pixel value a subimage of height ulHeight and width ulWidth is extracted, put into the image structure pimageWindow, and passed to the function ComputePoint() for processing. All the called routine does is set up some global variables, and the call **ProcessWindow()** to handle scanning through the image. The function ComputePoint() uses only the window of passed data to compute a single pixel output value. This value is returned by ComputePoint(). Thus writing a new routine only requires the implementation of two simple subroutines. The toolkit level routine is only used to initialize global variables and to call the appropriate "Process" routine. The processing routine only needs to process output value for the passed window.

Internal Routines: The routines listed below are provided for internal use by toolkit routines. In addition to the "Process" routines described above, several common and useful processing tasks have been included. To use in new routines, include the header file IPInternal.h in your source code. Details of their use can be found by looking at their source code.

CoOccurrence()   fill the co-occurrence matrix

Error()	print out error message
ProcessFeaturePoint()	compute feature from image point
ProcessFeatureWindow()	compute feature from image window
ProcessFeatureWindowFeature	compute feature from feature window
ProcessMultFeatureWindow()	compute multiple features from image window
ProcessPoint()	compute image from image point
ProcessWindow()	compute image from image window
floatAvg()	average vector of floats
floatMax()	find maximum of a float vector
floatMin()	find minimum of a float vector
floatSort()	sort a vector of floats
noise()	generate a random number
pixelAvg()	average vector of pixels
pixelMax()	find maximum of a pixel vector
pixelMin()	find minimum of a pixel vector
pixelSort()	sort a vector of pixels

Conclusion

The Image Processing Toolkit was conceived and implemented to ease the implementation of high-level user applications. An integral part of this toolkit is the image processing routines which provide basic image processing to the high-level application programmer. The objective of this initial work was to provide for three essential components for image processing, they are:

1. Easy to understand and use data structures and file structures so that the toolbox routines can be used by an application programmer.

2. Implementation of a basic set of image processing routines. This provides an example set of routines on which future work can build.

3. Implementation of a mechanism so that the typical image processing routine can be quickly implemented.

This initial work has reached these goals. Simple but flexible image and feature structures have been defined, over 70 basic image processing routines have been implemented, tested, and documented, and finally through the use of subroutine calls using function pointers, a mechanism for the simple implementation of pointwise and window operators has been included.

TERRAIN-SCATTERED RADAR CLUTTER SUPPRESSION USING SIGNAL RESTORATION

John F. Doherty
Assistant Professor
Department of Electrical Engineering and Computer Engineering

Iowa State University
Coover Hall
Ames, IA 50011-1045

TERRAIN-SCATTERED RADAR CLUTTER SUPPRESSION USING SIGNAL RESTORATION

John F. Doherty
Assistant Professor
Department of Electrical Engineering and Computer Engineering

Abstract

This report presents research results on a new method for the suppression of terrain-scattered clutter due to intentional jamming of the radar footprint. The new method applies signal restoration processing on the conventional beamforming output. The temporal processing of the received radar signal attempts to restore the known properties of the transmitted radar waveform. This approach relies on the transmitted radar signal having coded phases, such as a discretized chirp or polyphase waveform. The properties of the code are used to distinguish the desired radar return from the jamming and clutter interferences. Because of the assumed prior knowledge of the transmitted waveform, it is not necessary to have an auxiliary record of the jamming signal. The signal processing is also iterative, requiring no sensor correlation matrix formation or inversion.

TERRAIN-SCATTERED RADAR CLUTTER SUPPRESSION USING SIGNAL RESTORATION

John F. Doherty

1 INTRODUCTION

The radar signal processing problem considered in this report is the suppression of terrain-scattered jamming (clutter) in the main beam of the radar array response. The clutter is usually distributed such that spatial nulling in the main beam results in a significant loss in target detection [1]. The alternative approach is to temporally process the sensor outputs by estimating the clutter delay profile and subsequently subtracting the clutter estimate [1,2]. These approaches are limited by the requirement of a clutter-free record of the jamming signal. This usually assumes an auxiliary antenna directed at the jammer. In addition, there is either an explicit or implicit calculation of the sensor matrix and its inverse. This may limit the applicability of such approaches to problems of small dimension, for example, arrays with a small number of sensors. The performance gains of such space-time adaptive approaches to experimental airborne pulsed radar data was recently demonstrated for systems with relatively low processing complexity [3]. The new approach differs from these in three ways: it does not rely on a clean look at the jamming signal, it does not require correlation matrix calculation or inversion, and it operates on the uncompressed pulse.

The new approach to clutter suppression is essentially one of signal property restoration based upon known properties of the desired signal. Undesired signals which may be present include direct path jamming, jamming via multipath clutter, clutter returns due to the radar, and ambient thermal noise. The "art" of the signal restoration approach is to determine, or construct, the *unique*

properties of the desired signal which enable suppression of the undesired signals.

The class of transmitted signals studied are the polyphase coded pulse compression waveforms. This class encompasses the direct-sequence and discretized chirp signals. An important distinction of the new approach is that the signal processing occurs before the pulse compression. This allows greater latitude in utilizing the desired signal properties to enhance the suppression process.

The discrete-time signal that is used for analysis can be derived from the general transmitted pulse signal

$$s(t) = a(t) \cos(2\pi f_c t + \theta(t))$$ (1)

where $a(t)$ represents the amplitude modulation function (assumed constant for the remainder of this report), f_c is the carrier frequency, and $\theta(t)$ is the phase modulation function. The low pass equivalent representation of $s(t)$, i.e., the complex baseband signal, is given by

$$\bar{s}(t) = a(t)\big(\cos(\theta(t)) + j\ \sin(\theta(t))\big)$$ (2)

The pulse has duration denoted by T time units. The phase function has the form

$$\theta(t) = \sum_{n=1}^{N} \exp\big[j\phi_n\big]\, p(t - n T_c)$$ (3)

where the minor pulse duration is $T_c = T/N$. The pulse $p(t)$ is zero outside the interval $0 \le t \le T_c$. The output samples of a matched filter (matched to $a(t)\, p(t)$) sampled at the rate $1 / T_c$, are given by the constants.

$$v_k = \exp[j\phi_k] \qquad (4)$$

It should be noted here that pulse compression has not yet occurred. Pulse compression can only be achieved by multiplication by the phasors v_k.

1.1 Received signal model

The received signal at the output of the kth sensor matched filter at time $t = nT_c$ is represented by

$$r_k(n) = v_k(n) + q_k(n) + c_k(n) + w_k(n) \qquad (5)$$

where the disturbances are $q_k(n)$, the jammer signal, $c_k(n)$, the terrain-scattered clutter signal, and $w_k(n)$, the wideband thermal noise. In general, all the signal samples will be complex valued. The jammer is assumed time uncorrelated and sensor correlated. The clutter is time correlated over a pulse duration and sensor uncorrelated. The thermal noise is time and sensor uncorrelated. These properties will be used to discriminate between the desired signal, $v_k(n)$, and the disturbances.

1.2 Space-time signal model

The space-time signal matrix will have the form

$$D(n) = \begin{bmatrix} r_1^T(n) \\ r_2^T(n) \\ \vdots \\ r_K^T(n) \end{bmatrix} = \begin{bmatrix} r_{1,n}^T & r_{1,n-N_r}^T & \cdots & r_{1,n-MN_r}^T \\ r_{2,n}^T & r_{2,n-N_r}^T & \cdots & r_{2,n-MN_r}^T \\ \vdots & \vdots & \ddots & \vdots \\ r_{K,n}^T & r_{K,n-N_r}^T & \cdots & r_{K,n-MN_r}^T \end{bmatrix} \qquad (6)$$

where $r_{k,n-mN_r}^T = \left[r_k(n-mN_r) \; r_k(n-1-mN_r) \; ... \; r_k(n-N-mN_r) \right]$ is the complex received sample

vector for the kth sensor during the mth pulse period. The pulse repetition period is $T_r = N_r T_c$.

1.2.1 Target signal vector component

The target embedded in $r_k(n)$ will be at a spatial angle θ_v with power P_v and Doppler shift f_d, so
that the desired signal vector is given by

$$v_k(n) = \sqrt{\frac{P_t}{2}} \begin{bmatrix} \exp\{-j2\pi(k-1)d_s\sin\theta_v\}\exp\{j2\pi\,0f_d\}\exp\{j\phi_{n\,\mathrm{mod}N-1}\} \\ \exp\{-j2\pi(k-1)d_s\sin\theta_v\}\exp\{j2\pi\,1f_d\}\exp\{j\phi_{n\,\mathrm{mod}N-2}\} \\ \vdots \\ \exp\{-j2\pi(k-1)d_s\sin\theta_v\}\exp\{j2\pi(N-1)f_d\}\exp\{j\phi_{n\,\mathrm{mod}N-N}\} \end{bmatrix} \tag{7}$$

The autocorrelation function of $v_k(n)$ will depend on both the spatial index k and the time index

n.

1.2.2 Jammer signal vector component

The jammer signal portion of the received vector at spatial angle θ_q with power P_q is represented

by

$$q_k(n) = \sqrt{\frac{P_q}{2}} \begin{bmatrix} \exp\{-j2\pi(k-1)d_s\sin\theta_q\}\{q_{rk}(n)+jq_{ik}(n)\} \\ \exp\{-j2\pi(k-1)d_s\sin\theta_q\}\{q_{rk}(n+1)+jq_{ik}(n+1)\} \\ \vdots \\ \exp\{-j2\pi(k-1)d_s\sin\theta_q\}\{q_{rk}(n+MN)+jq_{ik}(n+MN)\} \end{bmatrix} \tag{8}$$

where $q_{rk}(n)$ and $q_{ik}(n)$ are i.i.d. Gaussian random sequences with zero mean and unit variance.

Thus, the sequence $q_k(n)$ will exhibit only spatial correlation.

1.2.3 Clutter signal vector component

The terrain clutter vector component, $c_k(n)$, will be formulated as the response of a discrete-time linear filter to an i.i.d. Gaussian random sequence.

$$c_k(n) = \sqrt{\frac{P_c}{2}} \begin{bmatrix} c_{rk}(n)+jc_{ik}(n) \\ c_{rk}(n+1)+jc_{ik}(n+1) \\ \vdots \\ c_{rk}(n+MN)+jc_{ik}(n+MN) \end{bmatrix} \tag{9}$$

where P_c sets the power of the clutter. The filtering will result in the output process having a

Gaussian autocorrelation function that specifies the relative Doppler frequency, f_d, and relative

bandwidth, B_d, of the clutter power spectral density, viz.,

$$\rho_c(m,k') = E\{c_k(n)c_{k'}(n+m)\} = \begin{cases} \delta(k-k') \, \exp\{-j2\pi f_d m\} \, \exp\{-2[\pi B_d m]^2\} & |m| < N \\ 0 & |m| \geq N \end{cases} \quad (10)$$

where $\delta(k)$ is the Kronecker delta function which equals unity when $k = 0$, otherwise it equals zero. The clutter is not correlated from pulse to pulse.

1.2.4 Thermal noise component

The thermal noise will be uncorrelated in both time and space and will have power P_w,

$$w_k(n) = \sqrt{\frac{P_w}{2}} \begin{bmatrix} w_{rk}(n) + j w_{ik}(n) \\ w_{rk}(n+1) + j w_{ik}(n+1) \\ \vdots \\ w_{rk}(n+MN) + j w_{ik}(n+MN) \end{bmatrix} \quad (11)$$

where $w_{rk}(n)$ and $w_{ik}(n)$ are i.i.d. Gaussian random sequences with zero mean and unit variance.

2 METHODOLOGY OF SIGNAL RESTORATION APPROACH

The received signal vector, $r_k(n)$, belongs to a vector space of dimension $M \times N$. The desired signal vector will be restricted to a subspace of this vector space. Thus, any components in the received signal vector that are outside the desired signal subspace can be discarded without a loss

in the fidelity of the desired signal. The restoration approach relies on performing operations on the received signal vector which attempt to retain only the desired signal components.

The process of signal restoration used is iterative, where each iteration results in a vector which is closer to the desired signal vector. The iterative implementation avoids such problems as construction and inversion of the received signal correlation matrix. The updates are usually a mix of linear and non-linear operations. The non-linear updates are guaranteed to converge if they are *convex*, e.g., they describe spheres in the vector space. A weaker condition is that the update be non-expansive, i.e., the updated vector is guaranteed to have finite length. The non-expansive condition only guarantees that the updates will not diverge. Some properties of the desired signal that are used to formulate the update process are amplitude (time and frequency), energy, and correlation.

2.1 Signal properties used for updates

A set of update equations are needed which selectively suppress the undesired components of the received signal. Each update can be supplied sequentially, converging to the desired target signal estimate. The update equations will rely on using known propertied of the desired received signal which are not generally descriptive of the undesired disturbances.

2.1.1 Amplitude

The desired signal may be bounded in amplitude in either the time or frequency domain. Any estimate can be constrained to adhere to this condition using the update

$$\hat{v}_{l+1}(n) = \begin{cases} v_{\max} & \text{if } \hat{v}_l(n) > v_{\max} \\ \hat{v}_l(n) & \text{if } \hat{v}_l(n) \leq v_{\max} \end{cases} \tag{12}$$

where $v_{\max}$ is the expected maximum for the desired signal vector.

2.1.2 Energy

If the desired signal can be bounded in energy, then the following update is appropriate

$$\hat{v}_{l+1} = \begin{cases} \sqrt{\dfrac{\varepsilon_{v.\max}}{\hat{v}_l^H \hat{v}_l}}\ \hat{v}_l & \text{if } \hat{v}_l^H \hat{v} > \varepsilon_{v.\max} \\ \hat{v}_l & \text{if } \hat{v}_l^H \hat{v}_l \leq \varepsilon_{v.\max} \end{cases} \tag{13}$$

where $(\cdot)^H$ is the complex conjugate (Hermitian) transpose operation.

2.1.3 Linear updates

The previous updates are considered non-linear. A linear update can be achieved using the formula

$$\hat{v}_{l+1} = \hat{v}_l + \mu \left[d - x^H \hat{v}_l \right] \frac{\hat{v}_l}{\hat{v}_l^H \hat{v}_l} \tag{14}$$

where the scalar d and the vector x are chosen to correspond to some property of the vector v_k.

The scalar μ will determine how well the estimate satisfies the conditions. For example, if we

know that $\sum v(n) = v_\Sigma$, then the update vector is given by $x = \begin{bmatrix} 1 & 1 & \dots & 1 \end{bmatrix}$ and the estimate

$$\hat{v}_{l+1} = \hat{v}_l + \left[v_\Sigma - x^H \hat{v}_l \right] \frac{\hat{v}_l}{\hat{v}_l^H \hat{v}_l} \tag{15}$$

will result in $\sum \hat{v}_{l+1}(n) = v_\Sigma$.

All the preceding updates can be applied to the received data iteratively. In general, it will take only one pass through all the updates to provide reasonable clutter suppression performance.

2.2 Polyphase codes

Pulse compression based upon polyphase waveform transmission is assumed. A major departure from current techniques is that signal processing occurs before pulse compression takes place (see Figure 1). The pre-compression processing allows use of the phase code properties in suppressing the clutter. That is, the pre-compression waveform has structure that can be used before it is lost in the compression operation. There are several possible polyphase waveform that can be used in pulse compression radar. Two possibilities are direct sequence codes and Frank codes [4]. Frank polyphase codes are of particular interest because they represent discrete approximations to linear FM waveforms. The remainder of this report will assume the use of Frank codes, although the principles of the signal restoration processing apply to any polyphase waveform.

The Frank polyphase codes can be derived from the complex exponentials used in the discrete Fourier transform (DFT). Given the DFT of length N, the Frank code is given by

where the codes, p_k, are the elements of the DFT matrix of dimension N^2.

$$p_k = \exp\{-j2\pi \bmod(k,N-1) \bmod(k/(N-1),N-1)\} \quad k = 1,2,...N^2 \tag{16}$$

2.3 Clutter suppression using temporal decorrelation

The model of the terrain-scattered jamming clutter is that it is temporally correlated, due to the multiple scattering of the ground, up to a delay equal to the PRI. The transmitted polyphase waveform exhibits strong correlation only at delay intervals equal to multiples of the PRI. This property leads to the "thumbtack" ambiguity function for polyphase waveforms. A conclusion is that temporal correlation, at delays other than multiples of the PRI, in the received radar signal is primary due to the terrain-scattered clutter. Thus, applying a decorrelation filter prior to pulse compression will remove a significant portion of the clutter energy (see Figure 1). Of course, the polyphase waveform is also affected, however, to a lesser degree. The decorrelation filter length should be less than the length of the polyphase code (PRI) to avoid code cancellation. This condition is easily satisfied in most situations. The decorrelation filter can be a simple linear predictive structure

$$\hat{v}_k + \hat{w}_k = \left[c_k + v_k + w_k\right] - \sum_{n=1}^{N_r} h_n \left[c_{k-n} + v_{k-n} + w_{k-n}\right] \tag{17}$$

where the bracketed terms are the available data. The error in the prediction process is actually an estimate of the radar return plus noise, since these components are not predictable compared to the clutter. It should be noted that the prediction filter weights, h_n, can be determined by an appropriate adaptive algorithm without the need for an external reference signal. That is, an advantage of processing the signal prior to pulse compression is that the desired polyphase component appears uncorrelated and is unaffected by the decorrelation filter.

3 RESULTS

A set of simulation experiments were conducted which demonstrate the performance improvements using signal restoration processing. The adjustable system parameters are the number of polyphase codes per pulse, pulses available for processing, and linear array of sensor elements. The performance crite. ion of primary interest is the output signal-to-residual-interference (SINR) power ratio. The residual interference is defined as the sum total of all the direct path jamming, terrain-scattered jamming, and thermal noise that remains after processing, at the input of the detector. Other parameters of the simulations are the direct path jamming power, the direct path jamming direction, the clutter bandwidth, the clutter power, the clutter mean Doppler frequency, and the target Doppler frequency. The power levels are determined relative to the target power, assumed unity for convenience. The Doppler frequencies are determined relative to the center frequency of the radar and are in the units of cycles-per-sample. The target direction is assumed to be orthogonal to the array, i.e., at boresight.

Simulation 1. A first look at the signal restoration process is given in Figure 3. This figure shows the power spectral density (PSD) before and after clutter suppression. The clutter parameters are center frequency 0.4Hz, bandwidth 0.1Hz, and relative power 20dB with respect to the target signal. The number of pulses processed is eight (8) with 32 polyphase codes per pulse. The direct path jamming is assumed to be zero for this simulation. The PSD of the processed signal shows better registration with the desired signal PSD than does the unprocessed signal. This is the contributing factor in the subsequent demonstrations of output SINR improvement.

Simulation 2. The next simulation consists of 32 pulses, 256 polyphase codes/pulse, and 8 array sensors. The clutter bandwidth is 0.1 Hz with power 20dB. The jammer is at 45 degrees from the array boresight with power 40dB. The target Doppler frequency ranges from zero to a maximum of

0.01 cycles/sample. This maximum Doppler is a typical value for maximum velocity, minimum wavelength, and low bandwidth conditions [1]. The output SINR improvement is shown in Figure 4.

Simulation 3. The parameters of this simulation are identical to those of Simulation 2, except that the clutter bandwidth is reduced to 0.03 Hz. The results are shown in Figure 5.

Simulation 4. In this simulation, the number of pulses is 128, the number of codes/pulse is 64, and the number of sensors is again eight (8). The results are shown in Figure 6.

4 CONCLUSIONS

A new method for terrain-scattered jamming suppression is reported. This new method relies on processing a coherent pulse train of polyphase coded waveforms prior to pulse compression. The pre-compression signal properties are used for decorrelation and signal restoration. The average increase in SINR is approximately 6dB across Doppler frequency. The signal processing used does not involve correlation matrix calculation or inversion. Also, each pulse can be processed separately, then combined prior to detection. This makes the new approach amenable to parallel processing architecture implementation. Future extensions of this work can be the use of the partial correlation properties of the polyphase codes and the analysis of existing pulse compression radar data containing terrain-scattered clutter.

REFERENCES

[1] Brennan,L., Doyle,W., and Reed, I., "Adaptive Cancellation of Scattered Interference," Naval Air Systems Command Final Report, AD-A141 566, March, 1984.

[2] Clark, C., Woods, D., and Jai, R., "Scatter Cancellation Experiment," Rome Laboratory Final Report, I91-0079, February, 1992.

[3] Brennan,L., Piwinski,D., and Staudaher,F., "Comparison of space-time adaptive processing approaches using experimental airborne radar data," *Proceedings of the IEEE Radar Conference*, pp. 176-81, 1993.

[4] Eaves,J. and Reedy,E., Principles of modern radar, Van Nostrand Reinhold, 1987.
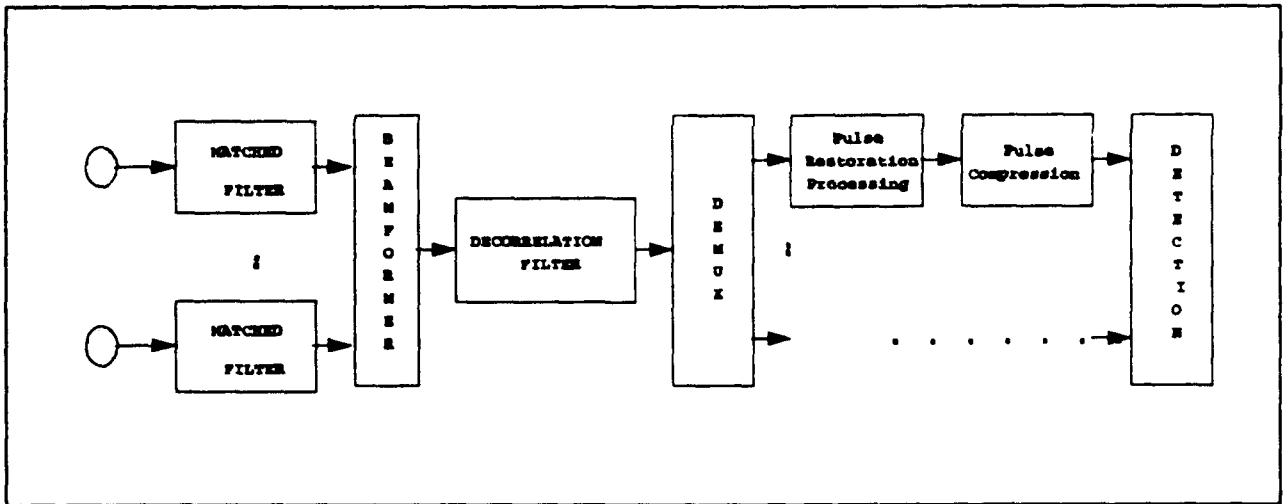
Figure 1 System block diagram showing major signal processing functions.
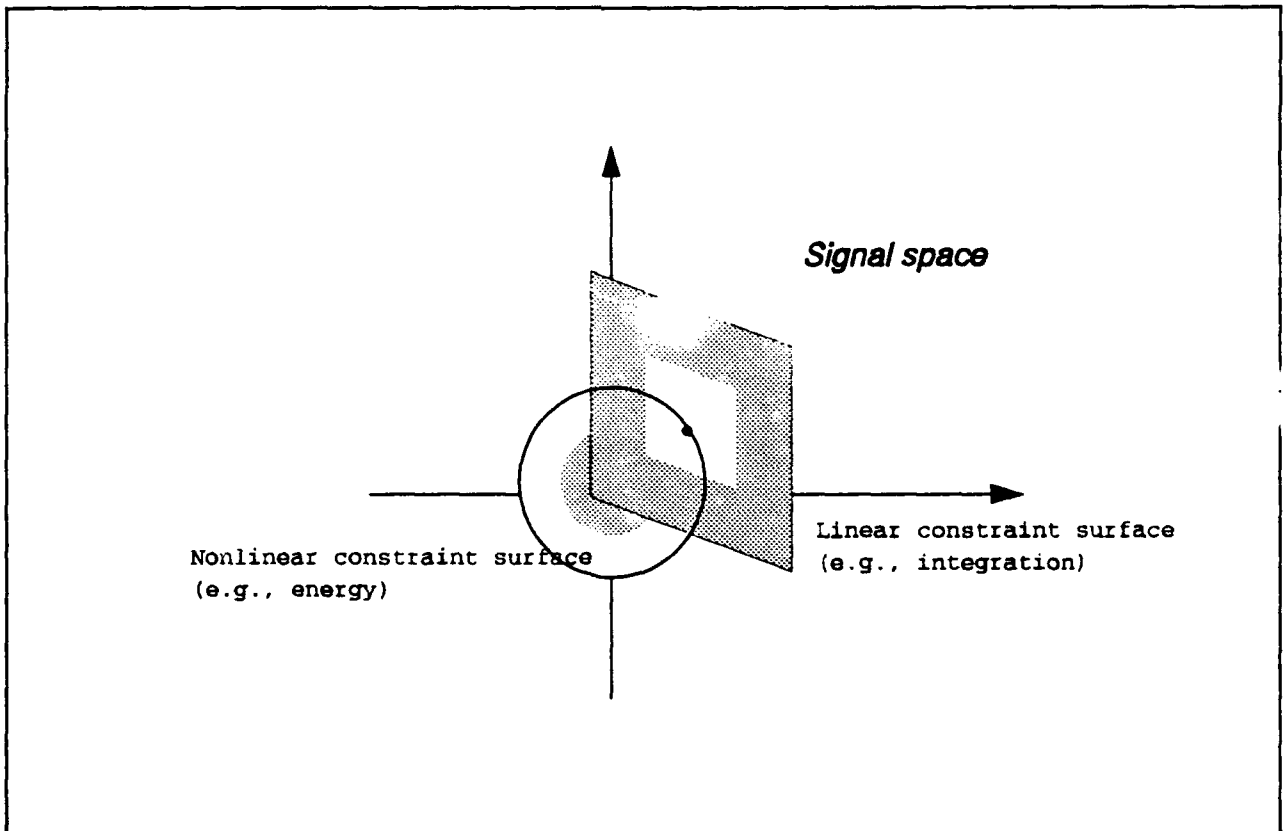
Figure 2   Signal properties can be translated into projection surfaces. A sequence of projections onto these surfaces converges to an intersection, describing the desired signal.
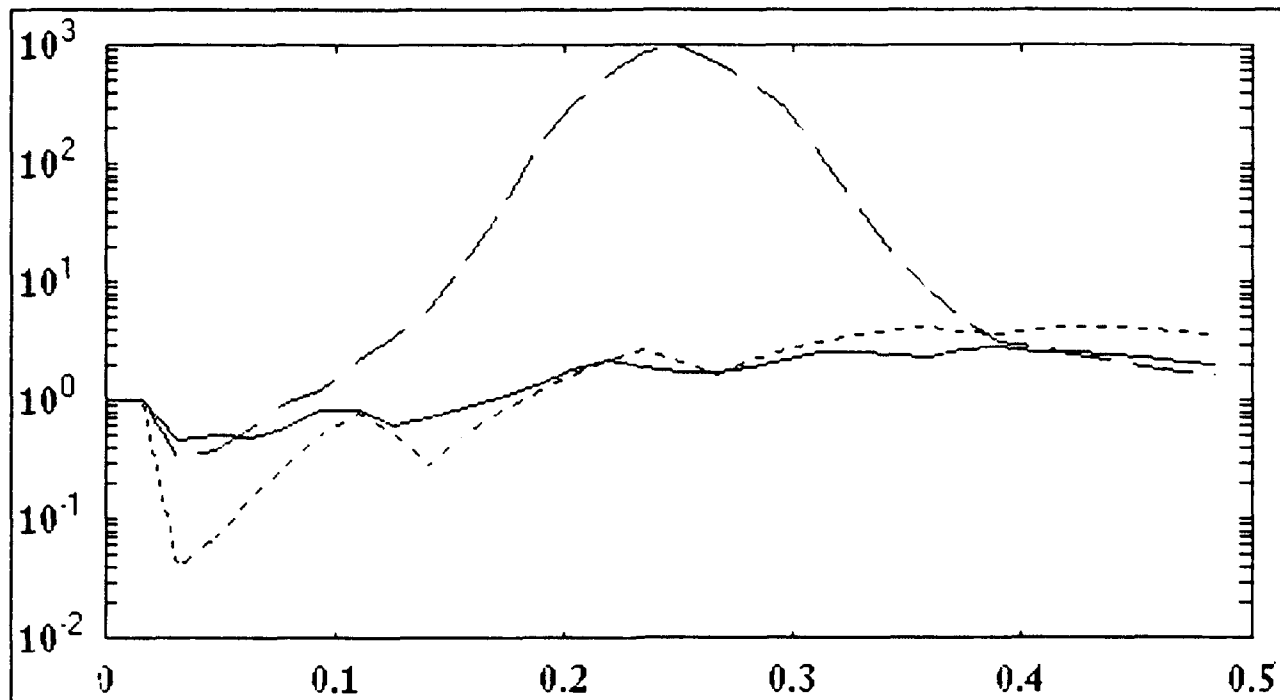
Figure 3 The power spectral density comparison. The true PSD is given by '- -', the clutter + signal PSD '-- --', and the restored PSD '--'.
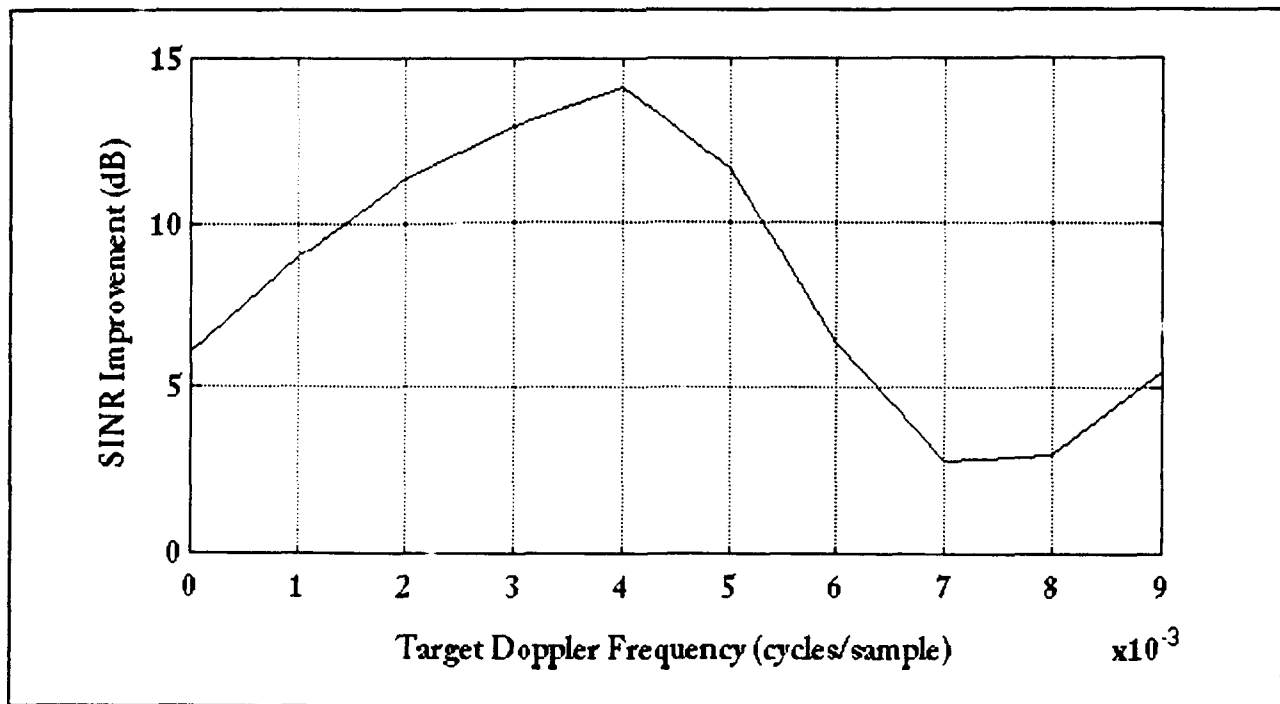
Figure 4 Output SINR improvement of new approach compared to matched filter performance. System parameters: 32 pulses, 256 codes/pulse, 8 sensors. Clutter bandwidth is 0.1 Hz.
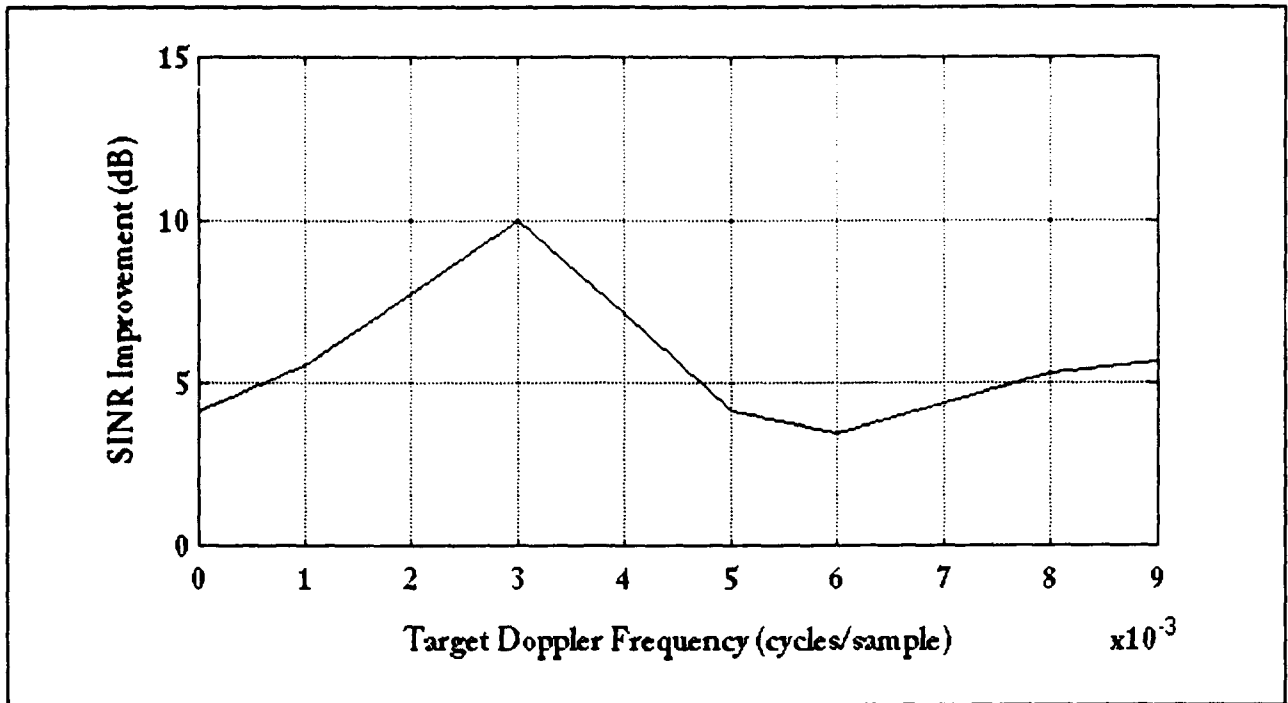
Figure 5 Output SINR improvement of new approach compared to matched filter performance. System parameters: 32 pulses, 256 codes/pulse, 8 sensors. Clutter bandwidth is 0.03 Hz.
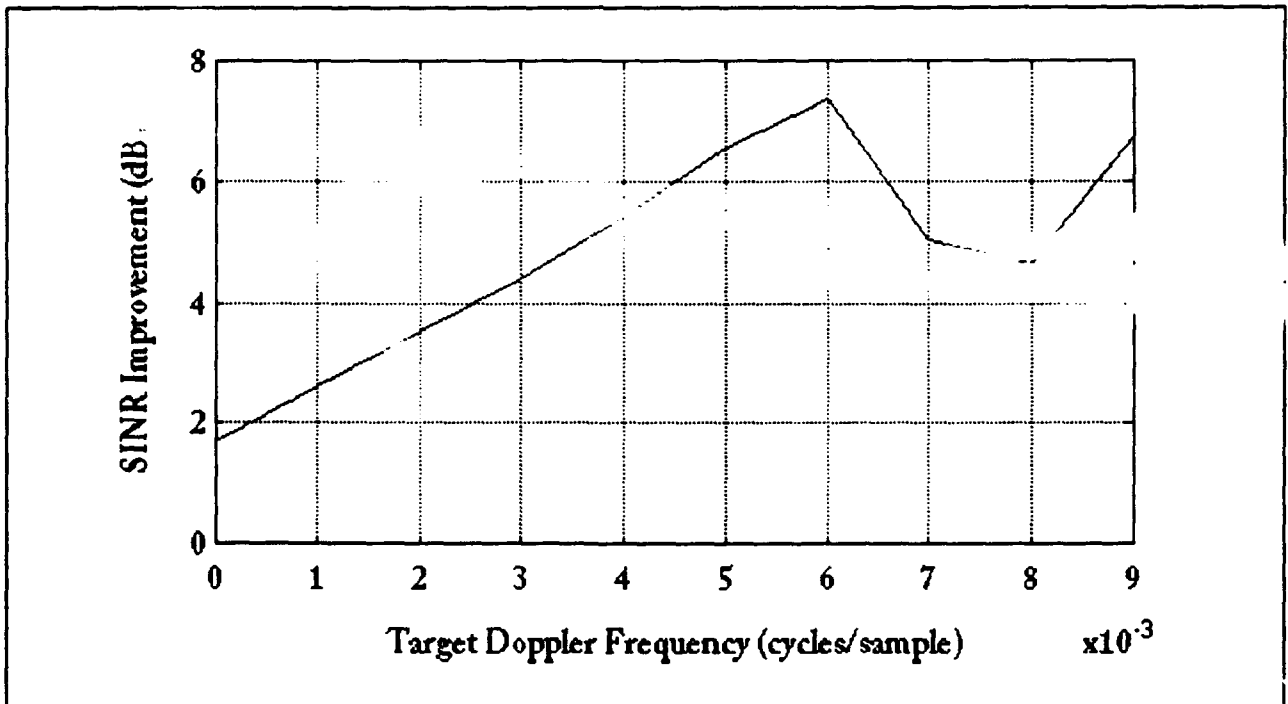
Figure 6 Output SINR improvement of new approach compared to matched filter performance. System parameters: 128 pulses, 64 codes/pulse, 8 sensors. Clutter bandwidth is 0.1 Hz.

Characterization Of A CdTe-Doped Fiber and The Design of A Wave-Shaping Circuit for Optical TDMA Network Implementation.

Eric Donkor
Assistant Professor
Department of Electrical and Systems Engineering

University of Connecticut
260 Glenbrook Road
Storrs, CT. 06269-3157

Final Report For:

Summer Faculty Research Program
Rome Laboratory

September 1993

Characterization Of A CdTe-Doped Fiber and The Design of A Wave-Shaping Circuit for Optical TDMA Network Implementation.

Eric Donkor

Assistant Professor

Department of Electrical and Systems Engineering

University of Connecticut

Abstract

A cadmium telluride (CdTe) optic fiber, and a fast electronic switching circuit, were constructed and studied for use in an Optical Time-Domain Multiple-Access (OTDMA) network. The fiber was to be used in constructing a broad-band optical amplifier. The switching circuit was integrated into a lithium niobate electro-optic carrier modulator.

The fiber core had a CdTe-glass hyperlattice structure. The diameter of the glass-core was 20 microns surrounded by a CdTe cylindrical ring of thickness 20 armstrongs. The absorption and transmission spectra of the fiber were characterized. The results were compared with those of bulk CdTe with remarkable difference between the two. The absorption spectra for the fiber was broad-band and was red-shifted in comparison with the bulk.

The switching circuit had fast rise- and fall-times of 2 nanoseconds and converted TTL logic gate levels (as inputs) to 10 volt, 200 milliamp output levels for the electro-optic modulator.

Characterization Of A CdTe-Doped Fiber and The Design of A Wave-Shaping Circuit For Optical TDMA Network Implementation.

Eric Donkor

I. Introduction

Optical time-division multiple-access (OTDMA) networks and packet switching architectures are currently being investigated and implemented, at the Photonic Research Center of Rome Labs, for high-speed information transfer and distribution in multi-user environment with intended applications in integrated systems digital networks, local area and micro area networks. A five gigabit/second 50-channel optical time-division multiple-access interconnect has already been demonstrated (see R. K. Boncek et. al., Optical Engineering, pp 2442, Nov '92). Efforts to implement even faster architectures are under investigation. The speed of operation is currently limited by the performance of the electronic devices and circuits that are used to implement some of the various subsystems of these architectures.

Two approaches are being researched at Rome Labs to circumvent such electronic bottlenecks. In one approach, research is directed at the design and implementation of all-optical network architectures. Consequently, several projects are under way to produce optical materials, devices, and circuits that will ultimately be used for such all-optical time-division multiple-access network implementation. They include photostable ultra-fast optical switches and switching networks, tunable optical delay devices, high bandwidth optical modulators, and novel semiconductor-glass composite fiber optic amplifiers.

Another approach, that already has produced promising results, is directed at the design and implementation of hybrid electronic/photonic TDMA architectures. In this hybrid approach optical techniques are used to time-division multiplex signals from all users unto a shared optical link. The multiplexed signal is

broadband broadcasted to all receivers. The data transmission rate typically run in the multi-gigabit range. Consequently, conventional electronics will be inadequate to directly process these signals at the receiving ends.

Thus at each receiver, optical techniques are employed to demultiplex and extract the desired baseband data from the broadband signal. The baseband signal can then be processed with electronic devices and circuits. Critical devices required to implement this architecture include tunable electro-optic modulators and photoconductive device that can be used to perform optical correlation functions, and fast pulse-shaping electronics.

This summer, July 5 to September 3, I participated in tw research projects at Rome Labs. One was to characterize the optical properties of a cadmium telluride-glass composite fiber. In particular we were interested in the occurrence of quantum size effect phenomena and other optical nonlinear effects in such fibers. In the second project, a fast electronic switching and pulse-shaping circuit was implemented. It was intended to be integrated into a tunable electro-optic modulator subsystem for a hybrid TDMA architecture.

This report summarizes my research activities at Rome Labs. It is divided into four sections, Section I to Section IV, of which this introduction part is Section I. Section II reports on work relating to the CdTe-glass composite fiber, and Section III describes the implementation of the electronic subcircuit for the electro-optic modulator subsystem of the hybrid TDMA. The last section, Section IV covers the conclusions of the work.

II. Optical Characterization of CdTe-Glass Fiber.

A1. Description of The Fiber Structure

The CdTe-glass fiber has a composite CdTe-glass core and a glass cladding. The preform was fabricated by first depositing a CdTe film on the entire outer diameter of a pyrex glass rod at elevated temperatures. This was then placed inside another pyrex

WHITE LIGHT

SLIT   LENS M1   LENS M2   MOUNT   LENS M3

OPTICAL SPECTRUM ANALYZER

OPTICAL BENCH
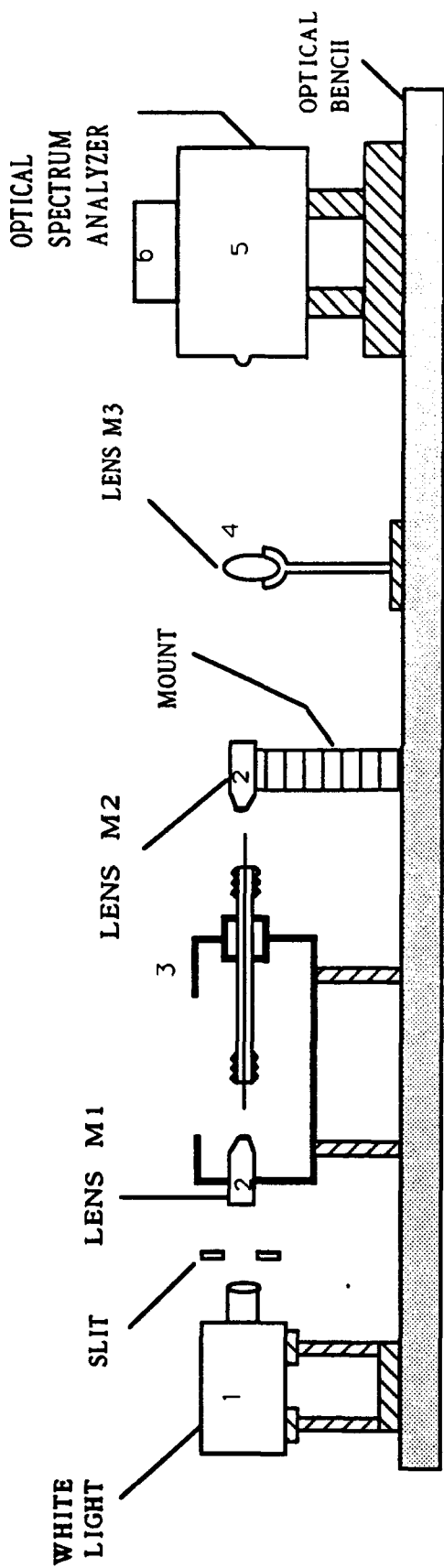
1. 100 Watts White Light Source

2. Microscope Objective (f20/0.35)

3. Newport MF916 Fiber Holder

4. Convex Lens KBX064

5. Optical Spectrum Analyzer AQ1425

6. A Thermal Printer (Axiom)

Fig. 1 Setup for Measuring Optical Characteristics of CdTe–Doped Fiber

glass tube and shrunk to produce a preform. The preform was about 9mm in total diameter. The inner glass core of the preform was about 4mm in diameter. The CdTe (circular) film has a thickness of 0.15μm and the outer glass has a thickness of 2.5mm. A fiber was pulled from the preform. The fiber core has an inner glass rod of diameter 30μm surrounded by a 15-20 armstrongs thick CdTe cylindrical ring (or film). The cladding was about 20μm thick. The CdTe film has a higher index of refraction than the surrounding cladding and as a result much of the incident laser beam is confined near the core region.

A2. Experimental Procedure

Experiments were conducted to measure the transmission and absorption characteristics of both the composite fiber and the .15μm CdTe ring in the preform. The set-up used for the measurements is shown in Fig.1. A 100 watt white light was used as the source. A slit was placed in front of the source in order to control the width of the emerging beam.

The device (fiber) under test was placed between the two microscope objectives M1 and M2, each objective has a numerical aperture of 0.35 and a magnification index of 20. A converging lens (KBX 064) was used to focus the light from M2 unto the detector of a wide-band optical spectrum analyzer (Ando AQ-1425). Two ends of the composite fiber were cleaved and mounted in a Newport MF 916 fiber holder. The total length was 10cm. The mounted fiber was then inserted between M1 and M2. The various components of the set up were adjusted till a maximum reading was displayed and recorded as the measured data. The experiment was repeated with the fiber now removed. The resulting display was recorded as the reference data. The transmission and absorption spectra were extracted from these measurements.

A3. Results and Discussion

Fig.2 shows the transmission spectra response of the 10cm CdTe-fiber over a wave-length interval of 380nm to 1800nm. A broad
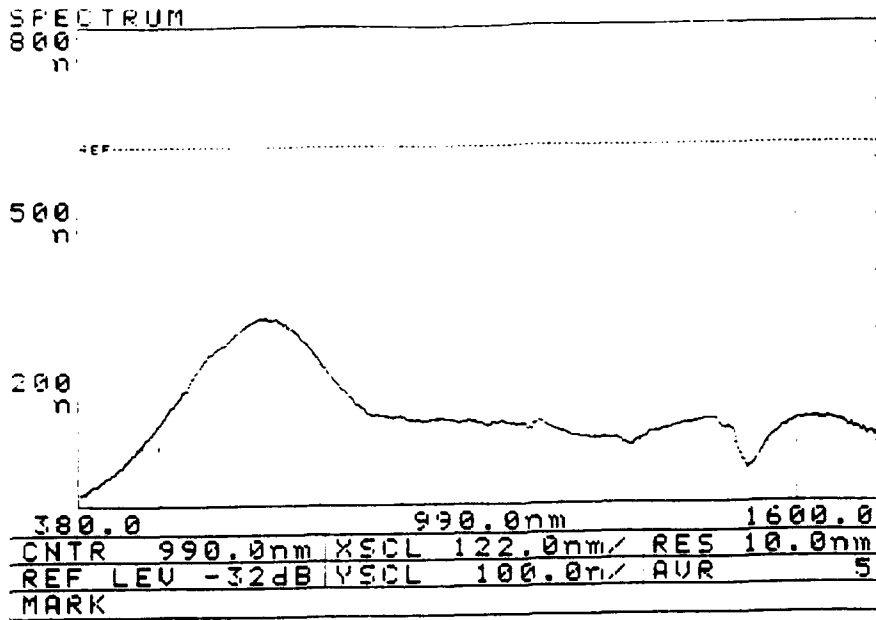
Fig. 2 Optical Spectra of CdTe Fiber
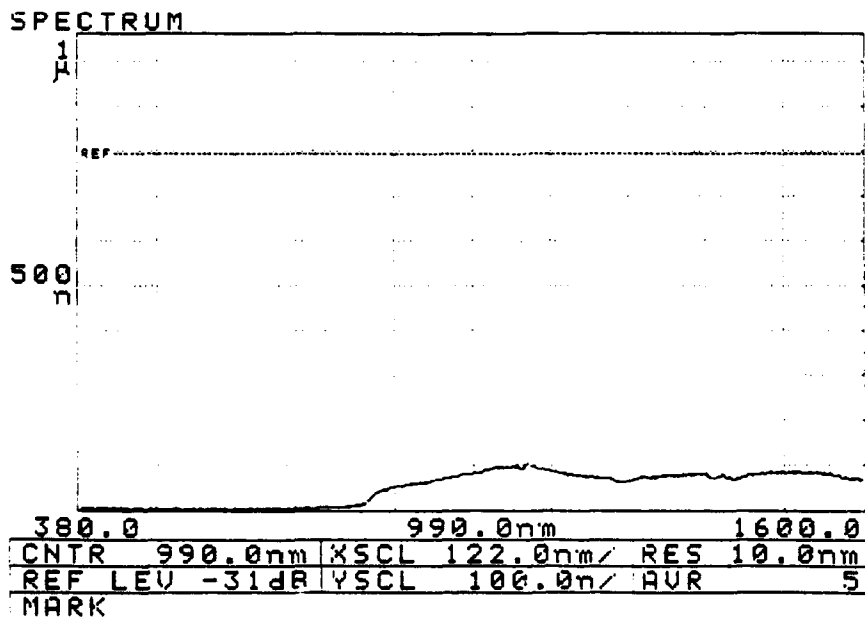
Fig. 3 Optical Spectrum of 0.15um thick CdTe Ring

22-6
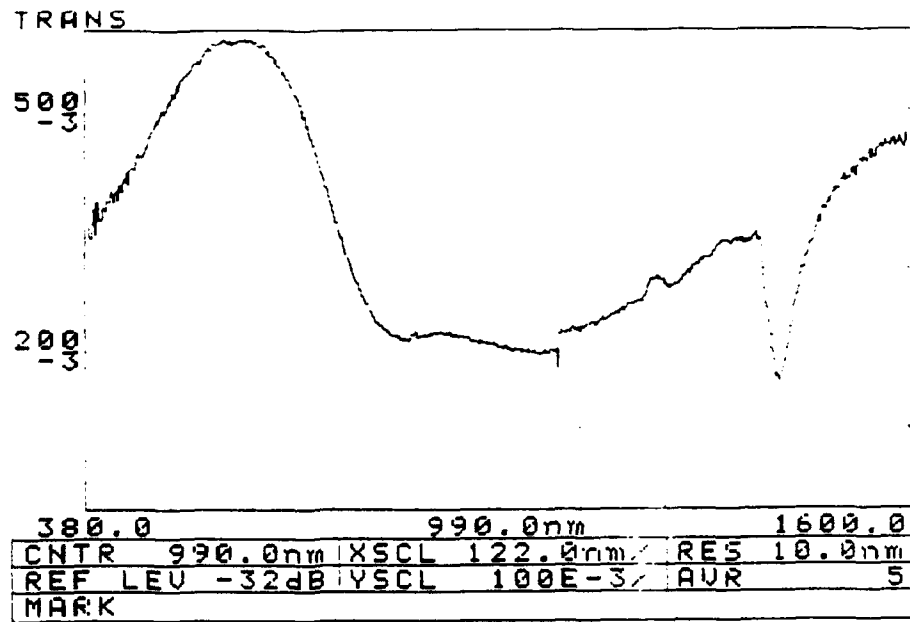
Fig. 4 Optical Transmission in CdTe Fiber.   (Fiber length 10cm)
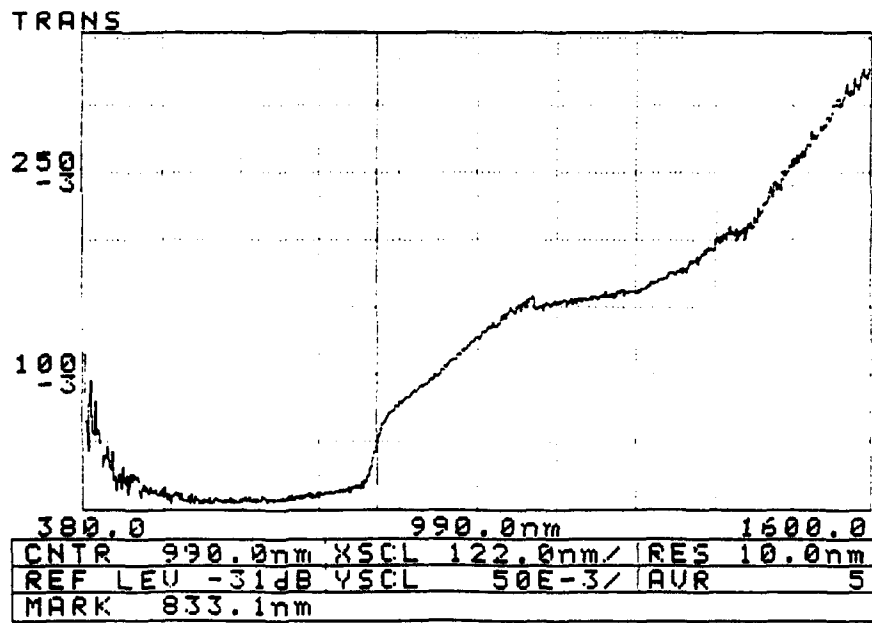
Fig. 5 Transmission of 0.15um thick CdTe Ring

peak occurs at 664 nm. The dip at 1400nm is believed to be due to OH⁻ absorption. A similar spectral response for the 0.15μm CdTe film in the preform is shown in Fig 3. It has very low response at wavelengths between 380nm and 807nm. and a flat response between 807nm to 1800nm.

The absorption spectra for the composite fiber and the CdTe film are shown in Fig.4, and fig.5 respectively. In fig.4 we observe a broadband high absorption region for the fiber in the wavelength interval between 800nm to 1400nm. Fig.5 depicts a high absorption region for the CdTe film in the region between 380nm to 860nm and transmission beyond 900nm.

The response of the 0.15μm CdTe film is analogous to that of bulk CdTe. However, the results obtained for the fiber is remarkably different with a number of peculiarities. In particular, the composite fiber shows absorption at wavelength higher than what would be expected in the bulk or thin film. The red-shift in the absorption spectra could be due to quantum size effect or nonlinear optical effects, arising from the generation of polaritons or plasmon waves. Further experimentation will be needed in order to reveal the origin or mechanisms that give rise to the red-shift in the absorption spectrum.

III. Wave-Shaping Circuit For Modulator Subsytem of TDMA.
    B1.   A Block Diagram of the Hybrid TDMA Architecture.

A simplified description of the time domain multiple access network is given here. Fig.6 gives a block diagram of the TDMA network. The mode-lock laser generates a train of pulses, whose width and repetition rate defines the maximum and baseband data transmission rate of the architecture. The output of the laser is distributed by a 1XN splitter to fixed N-1 delay lines. Each user is dedicated one of the N-1 delay lines. A fixed delay exists between successive lines. The last(N-th) laser source is also routed to a 1XN splitter. The output of the second splitter are routed directly to the receivers to be used as clocking signals.

The dedicated lines serve as carriers to be modulated with
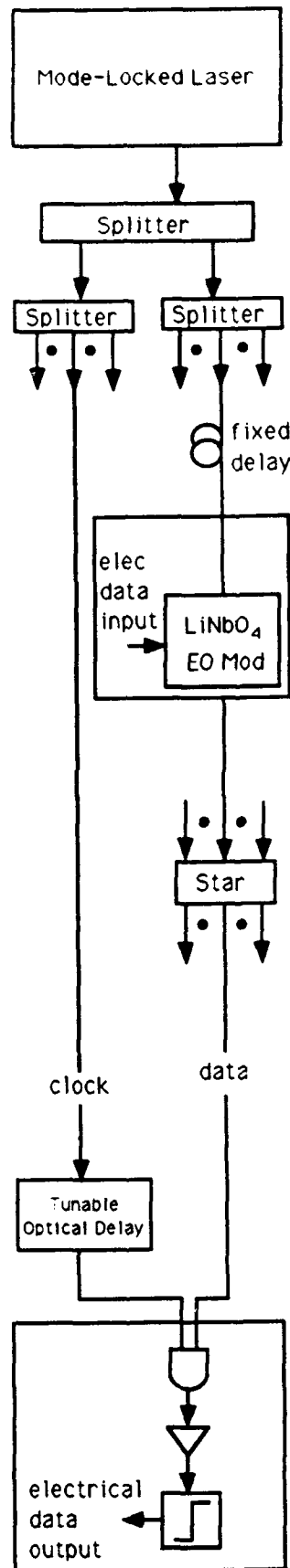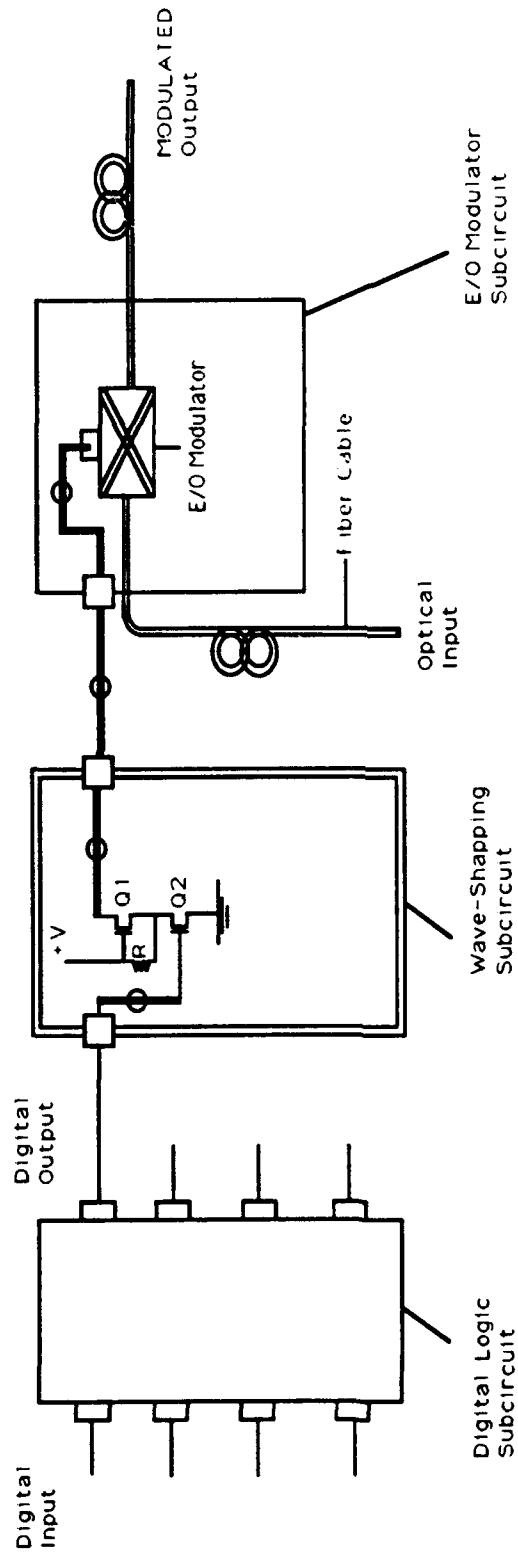
Fig. 6 Block Diagram of TDMA

Fig. 7   Electro-Optic Modulator Subcircuit

user baseband signals. The modulated signals from users are multiplexed unto a shared transmission link. The multiplexed signals together with the clocking signal are distributed to all receivers. A transmitter is tuned in at a given receiver by optical means. Optical demultiplexing recovers the baseband signal which are then photodetected and processed elect onically.

B2. Description of the Electro-Optic Modulator Subcircuit.

Modulation of the carrier with baseband signal is achieved by electro-optic techniques.The key element is a lithium niobate electro-optic modulator. Typical drive signals are 8-12 volt and 200 mA into a 50 ohm impedance. However the logic circuits and systems, that generate baseband signals, can only output up to 4 volts and source 10-50mA. A pulse shaping and switching circuit was therefore constructed to up-convert logic output levels to the desired voltage and current levels for the lithium niobate electro-optic modulator.

The pulse-shaping circuit is shown in fig 7. The transistors Q1 and Q2 are enhancement mode FETs with threshold voltages of 2.5 volts. Input signals for the circuit are either address encoding signals or user data signals. These signals are fed to the gate of Q1.

When an input signal is at logic high it turns on Q1. In this case the voltage at the source of Q2 will be pulled to ground through Q1 and therefore the output at Q2 will be low. Suppose the input now makes a transition from the high state to a low state, Q1 will be turned-off. Now the voltage at the source of Q2 will be the same as the drain to source voltage of Q1. Resistor, R, is chosen such that the source-to-drain voltage of Q1 is 10volts, adequate to actuate the lithium niobate modulator.

B3. Results and Discussion.

Fig 8 shows a typical reponse of the wave-shapping and switching circuit of fig.7. The lower trace represents the input and the upper trace the output of the circuit. The input was a 0-2.5 volt 50% duty cycle square wave.The output is an inverted square pulse with voltage swing of 0-10 volt. The rise time of the output was measured as 20 nanoseconds the fall time as 5ns. The rise and fall times of the input were 4 nanaseconds.
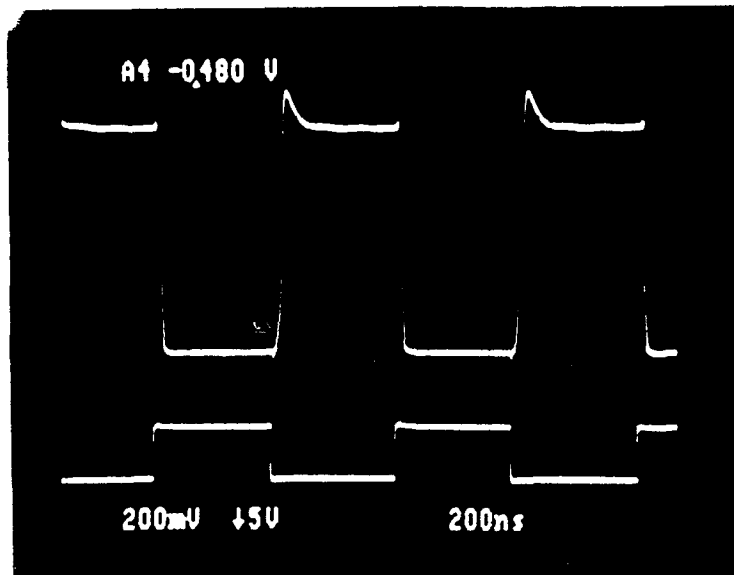
Fig. 8. Reponse of The Wave-Shapping Circuit.

An overshoot is observed in the rising edge of the output signal. We were able to eliminate this overshoot by increasing the value of resitor, R1. However this was achieved as a trade-off for lower output voltage and slower rise and fall times. Also the overshoot could be reduced by lowering the applied bias.

III. Conclusions.

The measured absorption and transmission spectra of CdTe-glass composite spectra were remarkably different from bulk CdTe. The difference appears to originate from quantum size effects. Further measurements, such as photoluminence should help to reveal the source of this discrepancies.

The switching circuit designed for the electro-optic modulator had rise time of 20ns and fall time of 5ns. The response time was not affected by the duty cycle of the input signal. The circuit could convert an input square wave with a swing of 0-2.5 volt to a square wave output having a voltage swing of 0-10 volt and current of 200mA.

FORM AND IMPLICATIONS OF THE NONLINEAR DEPENDENCE OF PHASE ON FREQUENCY FOR AN ACOUSTO-OPTIC BEAMFORMER

Evelyn H. Monsay
Associate Professor
Department of Physics

Le Moyne College
1419 Salt Springs Road
Syracuse, New York 13214

FORM AND IMPLICATIONS OF THE NONLINEAR DEPENDENCE
OF PHASE ON FREQUENCY FOR AN ACOUSTO-OPTIC BEAMFORMER

Evelyn H. Monsay
Associate Professor
Department of Physics
Le Moyne College

Abstract

Accurate, low-noise, wideband phased array radar antennas depend on the use of true time delays between microwave elements. A photonic means of generating the required element-to-element phase shifts was developed by Toughlian and Zmuda for systems operating in the VHF frequency range, and extended by Monsay and Caccuitto for operation in the radar C band. The photonic beamformer is based on an acousto-optic (AO), heterodyne optical system, in which the reference beam acts as a probe of the acoustic wave in the AO cell. The time delay of the acoustic waveform "read out" by the optical probe from various locations along the length of the AO cell can then be imposed directly on the microwave elements of the radar beamformer, providing the correct phase for each element at whatever frequency drives the AO cell.

It is apparent that the benefits of this photonic system rely greatly on the ability of the probe beam to pick out just the right phase shift/time delay from the acoustic waveform in the AO cell. It was suggested in last summer's report that laser instability resulting in small changes in beam direction would have an impact on radar system performance because of this dependence. In the interim, it became clear that a potentially more basic limitation to the system performance could come from intrinsic diffraction effects due to the finite beamwidth of the probe in the AO cell. The latter effect has been studied in detail and its implications for design and performance of the photonic beamformer are discussed here.

FORM AND IMPLICATIONS OF THE NONLINEAR DEPENDENCE
OF PHASE ON FREQUENCY FOR AN ACOUSTO-OPTIC BEAMFORMER

Evelyn H. Monsay

I. INTRODUCTION

Within the past few years, Toughlian and Zmuda [1-4] have developed an
RF true time delay phase shifter, based on a heterodyne optical system, which
can act as a beamformer for high performance, wideband phased array radar
systems. Sumberg [5] and Baldwin [6] have investigated means for integrating
the optical system. In Monsay [7] and Monsay and Caccuitto [8], the results
of using a dichromatic laser, demonstrated the potential of the photonic
beamformer for providing true time delays for high frequency (C band) radar
systems.

Various potential operational problems were also considered [7]. Since
the photonic delay line is based on a heterodyne optical system, some laser
nois̱e suppression is automatically built in. In low-frequency (VHF) systems,
both reference and signal beams carry the same noise disturbances which can be
made to cancel upon coherent interference. The reference and signal beams in
the dichromatic laser or coherent laser system required for high-frequency
(C band, etc.) operation will, to the degree of coherence exhibited by the
particular laser or laser system, also tend to suppress laser jitter and
drift.

However, it was suggested [7] that the most important potential problem
for the photonic delay line would arise from pointing errors of the laser beam
along the acoustic wave in the AO cell. Such pointing errors could arise from
mode hopping in the laser, or from mechanical dithering of the rotating mirror
which directs the probe beam. In addition, small, but not negligible,
oscillations in the data of phase versus frequency were observed in both low-
and high-frequency photonic delay lines, potentially exaggerating the effect
of small deviations in pointing angle on the accuracy of the final radar
system. These "wiggles" in the data proved to be highly reproducible; they
were apparently not random noise, but some true physical effect requiring
further study of the optical system.

The study of the diffraction of the optical probe beam, presented in
this report, has provided a theoretical understanding of the "wiggles" in the
data. This derivation, along with the modeling of the effects of the detector
aperture, will allow for a thorough determination of the impact of laser and
mirror pointing error on the associated radar system performance.

In Section II, the basic operation of the photonic true time delay line

23-3

is described, and the data on both low- and high-frequency demonstration systems are presented and discussed. The modeling of the diffraction of the AO cell probe beam is presented in Section III, with results and a comparison to data. In Section IV, the finite aperture of the photodetector is explicitly included in the equations for the system and a preliminary evaluation of its impact derived. A final discussion of this work and recommendations for future work are presented in Section V.

II. BASIC PHOTONIC DELAY LINE THEORY

Figure 1 presents the architecture of the basic photonic true time delay line, using a dichromatic laser as for a high-frequency radar system. The optical configuration is a standard heterodyne system with signal and reference beam frequencies of f_s and f_R, and amplitudes A_s and A_R, respectively. A lens of focal length F transforms the point-like probe illumination in the AO cell into a plane wave. The AO cell is used in the Bragg mode of operation. With AO cell RF frequency offset f_M, the resulting optical beams are

$$E_{SIGNAL} = A_S \exp\left[j\left(2\pi\left(f_S + f_M\right)t + f_x x - \frac{\pi x^2}{\lambda F} + \phi\right)\right] \tag{1}$$

$$E_{REFERENCE} = A_R \exp\left[j2\pi f_R t\right] \tag{2}$$

where ϕ is an optical phase shift representing the accumulated phase difference of the two beams as they propagate through the system. In Equation (2), f_x is the spatial frequency of the heterodyned output, where there is a unique identification of spatial frequency with mirror position, and so with the location of the probe beam in the AO cell. The spatial frequency f_x equals the mirror position angle θ divided by optical wavelength λ, and is uniquely associated with a particular mirror position, and so a unique time delay in the acoustic time waveform. The heterodyned output, ie, the coherent addition of the two optical beams, has the units of optical power and is given by the square of the sum of the two complex beam amplitudes. This operation results in a constant dc background illumination plus the system output signal with frequency dependence given by

$$I_S(t) \sim A_R A_S \cos \left[2\pi \left(f_x x + [\Delta f + f_M] \, t \right) - \frac{\pi x^2}{\lambda F} + \phi \right] \qquad (3)$$

In Equation (3), the self-heterodyne frequency of the laser output, $\Delta f = (f_S - f_R)$, appears, modulated by the RF frequency f_M. Hence, the system operates in a band defined by lower frequency Δf and upper frequency $(\Delta f + f_{M(max)})$. Note that any additional phase shift imposed on either beam, here given by

$$\Phi = 2\pi \left(f_x x + [\Delta f + f_M] \, t \right) + \phi \qquad (4)$$

comes through directly in the final detected optical signal.

Figure 2 indicates the selective action of the system optics within the Bragg cell, where a specific phase shift can be "picked off" from the acoustic wave in the cell. The rotating mirror will establish a location, and so a particular time delay, along the acoustic wave relative to its launch point in the cell. As, f_M changes, the phase of the acoustic wave at that fixed point in the Bragg cell will also change, such that a linear dependence of optical phase on RF frequency - the hallmark of the true time delay phase shift - is established. Hence, for a wideband RF signal with upper and lower frequencies f_U and f_L, respectively, a true time delay phase shift for each frequency component of the RF signal will be available with varying magnitude dependent on which particular point within the Bragg cell is chosen by one, or more (for multiple antenna elements), rotating mirror(s).

The previous discussion is based on the assumption that the optical probe of the AO cell is performed by a point-like beam. The resulting dependence of read-out phase Φ on system frequency $f = (\Delta f + f_M)$ is then perfectly linear:

$$\Phi = \frac{2\pi x f}{v} \qquad (5)$$

However, the data on $\Phi(f)$ for fixed x from demonstrations of both low-frequency (Figure 3) [4,5] and high-frequency (Figure 4) [7,8] photonic delay lines show very regular oscillations superimposed on the correct [9] linear dependence. Additional study of the photonic delay line architecture with a wide range of focal lengths, laser frequencies, and other parameters indicated that the oscillations were relatively independent of the parameter values over

a sizeable range [10].

Two candidate effects could possibly create these oscillations: the windowing effect of the finite aperture photodetector, and the diffraction from a finite-sized (non-infinitesimal) probe beam. Both effects were studied and found to contribute to nonlinear behavior in Φ. The following sections present a detailed understanding of these effects.

III. EFFECTS OF A FINITE-WIDTH PROBE BEAM

The original analysis of the photonic delay line assumed an infinitesimal, point-like probe beam reading out the phase of the acoustic wave in the AO cell. However, realistically, the ability to focus the probe, beam is limited by diffraction effects. For unfocussed beam diameter d and lens of focal length F, the *finite* spot size of the probe beam in the AO cell is given by the function

$$p(x) = \frac{1}{\pi x} \sin(\frac{x}{d_0})$$ (6)

where $d_0 = (\lambda F)/d$. The Fourier transform of the probe function is

$$P(k) = rect(kd_0)$$ (7)

where $k = 2\pi/\Lambda$ and Λ is the acoustic wavelength. The space and time dependence of the acoustic wave in the AO cell is given by

$$\cos[2\pi f(t - \frac{x}{v})] = \cos[\beta x - \omega t],$$ (8)

with $\beta = \omega/v$, v being the acoustic velocity in the AO cell, and using the identity $\cos(-\chi) = \cos(\chi)$. The acoustic wave will be illuminated by the signal beam over the range $-a \leq x \leq a$, ie, by the aperture function

$$w(x) = rect(\frac{x}{a}).$$ (9)

Hence, the illuminated portion of the acoustic wave in the AO cell can be expressed as

$$\cos(\beta x - \omega t) \cdot rect(\frac{x}{a}) \tag{10}$$

with spatial transform

$$\frac{2\sin((k-\beta)a)}{(k-\beta)} e^{-j\omega t} + \frac{2\sin((k+\beta)a)}{(k+\beta)} e^{j\omega t}. \tag{11}$$

Then, for probe position x_0, the system response can be expressed as

$$h(x_0, t) = \int_{-\infty}^{\infty} rect\frac{x}{a}\cos(\beta x - \omega t) p(x - x_0) dx \tag{12a}$$

$$= rect\frac{x_0}{a}\cos(\beta x_0 - \omega t) \star p(x_0) \tag{12b}$$

where $\star$ denotes the convolution of the probe function with the illuminated portion of the acoustic time waveform in the AO cell. Since the Fourier transform of the convolution of two functions is the product of their Fourier transforms, it is easiest to evaluate the system response from the form

$$h(x_0, t) = \mathscr{F}^{-1}(\mathscr{F}[rect\frac{x_0}{a}\cos(\beta x_0 - \omega t)]\mathscr{F}[p(x_0)]) \tag{13}$$

where $\mathscr{F}$ indicates the Fourier transform. Using the expressions for the Fourier transforms given in Equations (7) and (11) leads to the integral expressions

$$h(x, t) = \frac{1}{2\pi}\int_{-\infty}^{\infty} (\sin\frac{[(k-\beta)a]}{(k-\beta)} e^{-j\omega t} + \sin\frac{[(k+\beta)a]}{(k+\beta)} e^{j\omega t}) rect(kd_0) e^{jkx} dk \tag{14a}$$

$$= \frac{1}{2\pi} e^{-j\omega t} \int_{-\frac{1}{d_0}}^{\frac{1}{d_0}} \sin\frac{[(k-\beta)a]}{(k-\beta)} e^{jkx}dk + \frac{1}{2\pi} e^{j\omega t} \int_{-\frac{1}{d_0}}^{\frac{1}{d_0}} \sin\frac{[(k+\beta)a]}{(k+\beta)} e^{jkx}dk. \quad (14b)$$

The integrals over k in Equation (14b) can be simplified by defining $u = (k-\beta)$ in the first integral, and $u = (k+\beta)$ in the second integral. Then, for both integrals, $du = dk$, and the limits of integration become $(-1/d_0-\beta)$ and $(1/d_0-\beta)$ for the first integral, and $(-1/d_0+\beta)$ and $(1/d_0+\beta)$ for the second integral. The limits of integration on the two integrals can be made the same; let $u \rightarrow -u$ in the first integral, providing the same integration limits as in the second integral with only a change in the sign of the argument of ' the exponential. Hence, the two integrals can be combined, with the sum of the exponentials of the two parts combining via the identity $2 \cdot \cos(z) = [\exp(jz) + \exp(-jz)]$. So, Equation (14b) becomes

$$h(x,t) = \frac{1}{\pi} \int_{-\frac{1}{d_0}+\beta}^{\frac{1}{d_0}+\beta} \sin\frac{(ua)}{u} \cos(\beta x - ux - \omega t) \, du \quad (15)$$

Expanding the cosine term via the trigonometric angle sum rule changes Equation (15) to

$$h(x,t) = \frac{1}{\pi} \cos(\omega t) \int_{-\frac{1}{d_0}+\beta}^{\frac{1}{d_0}+\beta} \frac{\sin(ua)}{u} \cos[x(\beta-u)] \, du \quad (16a)$$

$$+ \frac{1}{\pi} \sin(\omega t) \int_{-\frac{1}{d_0}+\beta}^{\frac{1}{d_0}+\beta} \sin\frac{(ua)}{u} \sin[x(\beta-u)] \, du, \quad (16b)$$

which has the form

$$h(x,t) = A(x,\omega) \cos(\omega t) + B(x,\omega) \sin(\omega t) = \sqrt{A^2 + B^2} \cos[\omega t - \arctan\frac{B}{A}]. \quad (17)$$

Hence, the effect of a realistic, finite aperture probe beam is found from the factor

$$\Phi(x,\omega) = atan\left[\frac{\sin(\beta x)\int_{-\frac{1}{d_0}+\beta}^{\frac{1}{d_0}+\beta}\frac{\sin(au)}{u}\cos(xu)\,du - \cos(\beta x)\int_{-\frac{1}{d_0}+\beta}^{\frac{1}{d_0}+\beta}\frac{\sin(au)}{u}\sin(xu)\,du}{\sin(\beta x)\int_{-\frac{1}{d_0}+\beta}^{\frac{1}{d_0}+\beta}\frac{\sin(au)}{u}\sin(xu)\,du + \cos(\beta x)\int_{-\frac{1}{d_0}+\beta}^{\frac{1}{d_0}+\beta}\frac{\sin(au)}{u}\cos(xu)\,du}\right]$$

(18)

Figure 5 shows a comparison of $\Phi(x,\omega)$ versus ω for several closely spaced, fixed values of x, for realistic laser frequency and beamwidth, AO cell and lens parameters (see Table I). The results of the calculations displayed in Figure 5 are comparable to the data of Figure 3.

Figure 6 shows a comparison of $\Phi(x,\omega)$ versus ω for two largely separated values of x, and should be compared with Figure 4. In Figure 4, time delay is the measured value of the slope of the Φ versus ω lines (ignoring the small oscillation behavior), and is equal to 1.67×10^{-7} seconds for the maximum slope curve. The minimum slope curve in Figure 4 is assumed to have zero slope. The predicted value for the maximum slope curve, assuming a full $2°$ turn in the rotating mirror relative to its initial position and using the expression $\Delta T = 2\Delta\theta_m F/v$, is 1.74×10^{-7} seconds, with the values $F = 0.5$ inches and $v = 5.1$ km/sec (Indium phosphide AO transducer) used in the experiment [11]. Since ΔT is also given by $\Delta T = \Delta x/v$, the expected value of Δx would be 8.9×10^{-4}m. Figure 6, which shows remarkable similarity to the data of Figure 4, was calculated for $x_1 = 0.01 \times 10^{-4}$m and $x_2 = 10.41 \times 10^{-4}$m, ie, for $\Delta x = 10.3 \times 10^{-4}$m, a deviation of only 16% from the experimental value. This is a favorable comparison, considering the accuracy with which the mirror deflection in the experiment was measured is.

It was mentioned in Section II that the oscillations in the data were found to be relatively insensitive to changes in laser and optical parameters [10]. This behavior was also reproduced by the calculation of $\Phi(x,\omega)$ presented here. The key parameters all enter into the single variable $d_0 = \lambda F/d$, the Rayleigh width of the probe beam, hence, if one key parameter is systematically varied, the analogous effect of varying any of the other parameters is immediately apparent.

The parameter which was varied in this work was the reference beam width d. As d becomes infinitely large, the probe beam diameter (which can be viewed as the focussed reference beam) becomes infinitesimally small. The reference beam width was varied from a minimum of 0.0012 m to a maximum of 0.01 m, over a factor of eight variation. The results of this variation can be seen in Figures (7a,b,c,d), in which d = 0.0012m, 0.0024m, 0.0036m, and 0.01m, respectively. Notice that for the initial factor of three increase in beam diameter, as seen in Figures (7a) - (7c), the change in Φ is negligible. Only in Figure (7d) is the approach of Φ to a purely linear behavior seen, as expected for an infinite plane wave focussed to a point-like probe. When d = 0.01m, the reference beamwidth, before focussing, is over four times that of the signal beam.

Note that the minimal effect of varying reference beamwidth over a large range of values could also be claimed as the result of maintaining d at its original value and varying F or λ. The focal length F could be viewed as changing by a factor of two increase (up to F = 25.4mm), or down in size by 66 percent without changing the appearance of the nonlinear oscillations in Φ. A reduction in F to over 25 percent of its original value, ie, from 12.7 mm to 3.0 mm) is required to produce the approach to linear behavior seen in Figure (7d). Laser wavelength could be viewed as ranging from 0.7 microns to 2.12 microns without showing a change in the small oscillations.

IV. EFFECTS OF A FINITE-APERTURE PHOTODETECTOR

Although, there will be diffraction effects in the output signal of the photonic delay line due to the finite aperture of the photodetector, it can be shown that these effects are constant with respect to frequency, once x is fixed. Hence, these effects would be scaled out of the data on $\Phi(x,\omega)$ versus ω once the mirror position is fixed, and so would not be useful in explaining the data of Figures 3 and 4.

To understand the conclusion presented above, consider the full expression for the intensity of the time-varying signal incident on the photodetector surface, Equation 3. This signal (in which, for clarity here, the effects of a finite probe beam have not been included), must be integrated over the width of the photodetector aperture, x_p [10]. (It is natural for this system, in which a one-dimensional "fan" of optical beams leaves the AO cell, to consider only the x-dimension throughout). Hence,

$$I_s(t) \sim A_R A_s \int_0^{x_{pmax}} \cos[2\pi(f_x x + ft) - \frac{\pi x_p^2}{\lambda F} + \phi] \, dx_p, \tag{19}$$

where $f = (\Delta f + f_M)$ as before. Expanding the cosine so as to separate out the time variation of the argument yields

$$I_s(t) \sim A_R A_s [\cos(2\pi ft) \int_0^{x_{pmax}} \cos(2\pi f_x x - \frac{\pi x_p^2}{\lambda F} + \phi) \, dx_p - \sin(2\pi ft) \int_0^{x_{pmax}} \sin(2\pi f_x x - \frac{\pi x_p^2}{\lambda F} + \phi) \, dx_p] \tag{20}$$

which can be rearranged in the form $I_s(t) \sim I_{s0} \cos(2\pi ft - \Phi)$, where

$$I_{s0} \sim A_R A_s \sqrt{(\int_0^{x_{pmax}} \cos(2\pi f_x x - \frac{\pi x_p^2}{\lambda F} + \phi) \, dx_p)^2 + (\int_0^{x_{pmax}} \sin(2\pi f_x x - \frac{\pi x_p^2}{\lambda F} + \phi) \, dx_p)^2} \tag{21}$$

and

$$\Phi = atan[\frac{\int_0^{x_{pmax}} \sin(2\pi f_x x - \frac{\pi x_p^2}{\lambda F} + \phi) \, dx_p}{\int_0^{x_{pmax}} \cos(2\pi f_x x - \frac{\pi x_p^2}{\lambda F} + \phi) \, dx_p}]. \tag{22}$$

From Equation (22), it is clear that, once the probe location in the AO cell (ie, x) is fixed, variations in the RF frequency driving the AO cell (ie, f) will not affect the value of Φ. Hence, the effect of the photodetector aperture on the phase output of the system is only to add an overall constant to Φ for a fixed value of x. This effect would not, then, be relevant to the data taken in References 3 and 7, displayed in Figures 3 and 4.

V. CONCLUSIONS AND RECOMMENDATIONS

In this paper, it has been shown that in applications of the photonic delay line, such as a beamformer for wideband phased array radar systems, care must be taken due to the effects of finite apertures in the optical system.

The linear dependence of output phase on the signal frequency driving the AO cell is only approximate. The finite, rather than point-like, spot size of the probe in the AO cell due to diffraction of the optical beam introduces non-negligible oscillations in the read-out phase. Additional effects on Φ are introduced due to the finite aperture of the photodetector in the optical system.

In order to evaluate the photonic delay line for use in a radar system, the real behavior of the output phase as a function of RF frequency must be considered. The oscillations in output phase may have a major role in evaluating the impact of laser mode hopping on the radar system. The pointing error of a shifting laser beam will be compounded by, in essence, the existence of a range of values for Φ in each frequency bin. Detailed calculations are required in order to decide whether care in constructing the optical system can overcome the added hurdle due to the aperture effects established here. Radar system beam squint and pointing accuracy are at risk.

ACKNOWLEDGMENTS

REFERENCES

[1]   Toughlian, E.N. and Zmuda, H., "A Photonic Variable RF Delay Line for
         Phased Array Antennas", _J. Lightwave Technol._, vol. 8, no. 12, pp.1824-
         1828, 1990.

[2]   Toughlian, E.N., Zmuda, H., and Kornreich, P., "A Deformable Mirror-
         Based Optical Beamforming System for Phased Array Antennas", _IEEE
         Photon. Technol. Lett._, vol. 2, no. 6, pp. 444-446, 1990.

[3]   Zmuda, H. and Toughlian, E.N., "Variable Photonic Delay Line for Phased
         Array Antennas and RF/Microwave Signal Processing", RL-TR-91-120, Final
         Technical Report, June 1991.

[4]   Zmuda, H. and Toughlian, E.N., "Adaptive Microwave Signal Processing: A
         Photonic Solution", _Microwave Journal_, vol. 35, no. 2, 1992.

[5]   Sumberg, David A., "An Integrated Photonic Delay Line for Phased Array
         Antenna Applications", RL-TR-93-54, Final Technical Report, May 1993.

[6]   Baldwin, Kevin C., "Computer Aided Design and Simulation of an
         Integrated Photonic Delay Line System for Phased Array Antenna and Other
         Microwave Signal Processing Applications", Thesis for degree of Master
         of Science in Electrical Engineering, Rochester Institute of Technology,
         August 1993.

[7]   Monsay, Evelyn H., "Photonic Delay Line for High-Frequency Radar
         Systems", Final Report, Air Force Office of Scientific Research Summer
         Faculty Research Program, August 1992.

[8]   Monsay, Evelyn H. and Caccuitto, Michael, "Photonic Delay Line for High-
         Frequency Phased Array Systems", PSAA-III Symposium on Photonic Systems
         for Antenna Applications Proceedings, January 1993.

[9]   Private communication from Prof. Henry Zmuda.

[10]   VanderLugt, Anthony, _Optical Signal Processing_, John Wiley & Sons, Inc.,
         New York, N.Y., 1992, pgs. 374-383.

TABLES

Table 1:   Realistic parameters used in calculations of $\Phi(x,\omega)$. Parameters
            correspond to data in Reference 7.

FIGURES

Figure 1:   Photonic true time delay phase shifter for high-frequency
            applications: optical layout.

Figure 2:   Delay as a function of position of the optical probe beam along
            the acoustic waveform in the Bragg cell.

Figure 3: Φ versus f data from low-frequency (55 - 80 MHz) photonic delay
            line from Reference 3.

Figure 4: Φ versus f data from high-frequency (1.29 - 1.31 GHz) photonic
            delay line from Reference 7.

Figure 5: Φ (labelled "p") versus $\omega = 2\pi f$, calculated for realistic
            parameters (see Table 1), for small changes in probe location x,
            where each curve is for a different fixed value of x: solid line:
            x = 2.3mm; dash-dot: x = 1.6mm; dotted line: x = 0.8mm; dashed
            line: x = 0.1mm.

Figure 6: Φ (labelled "p") versus $\omega = 2\pi f$, calculated for realistic
            parameters (see Table 1), for a large change in probe location x,
            where the dashed curve is for x = 0.001mm, and the solid curve is
            for x = 1.041mm. Note that the curve of maximum slope undergos
            several 2π phase shifts.

Figure 7: Φ (labelled "p") versus $\omega = 2\pi f$, calculated for realistic
            parameters (see Table 1), for probe location x = 0.1mm, in order
            to illustrate the slow dependence of Φ on changes in system
            parameter d, for (a) d = 1.2mm; (b) d = 2.4mm; (c) d = 3.6mm;
            (d) d = 10mm.

Table 1

==

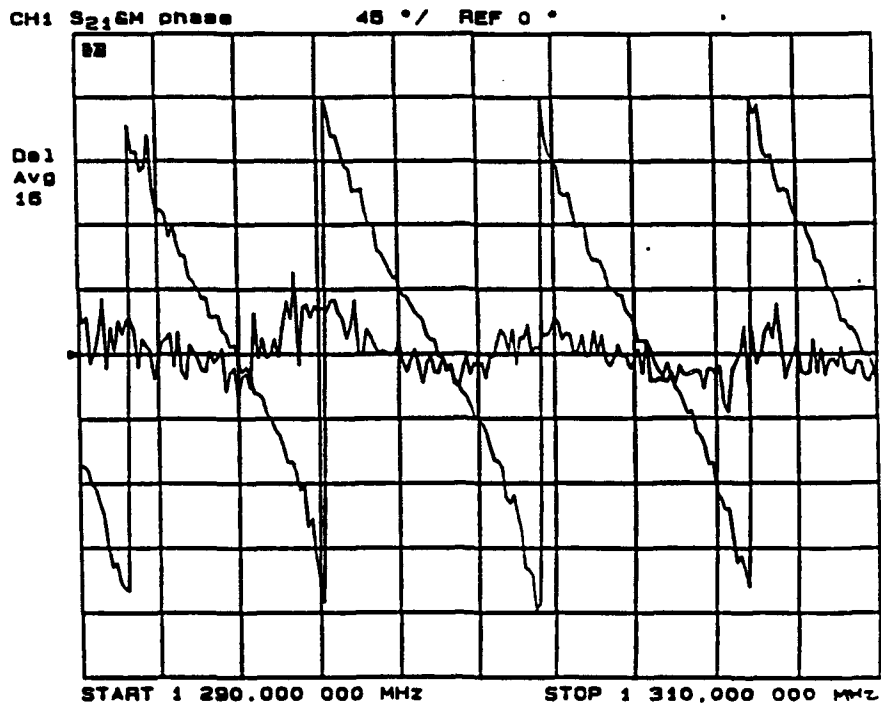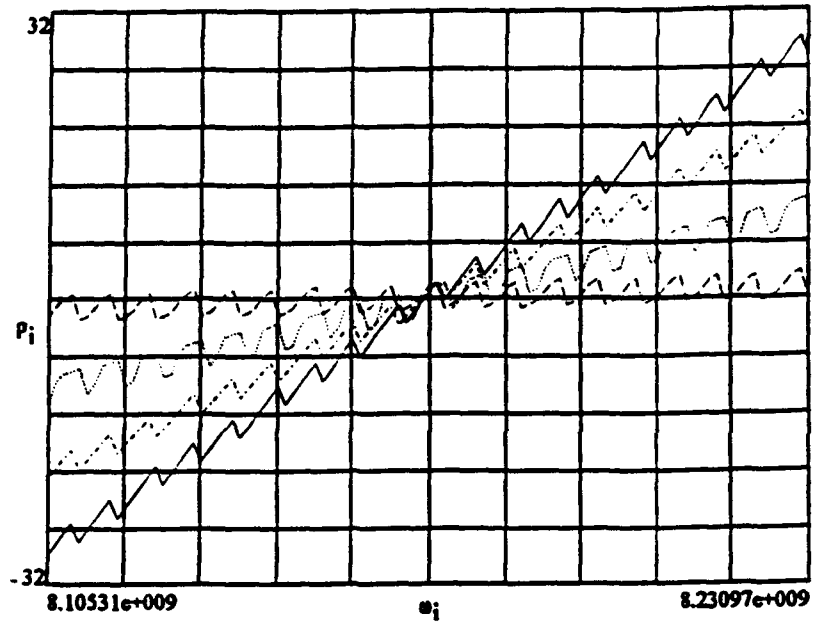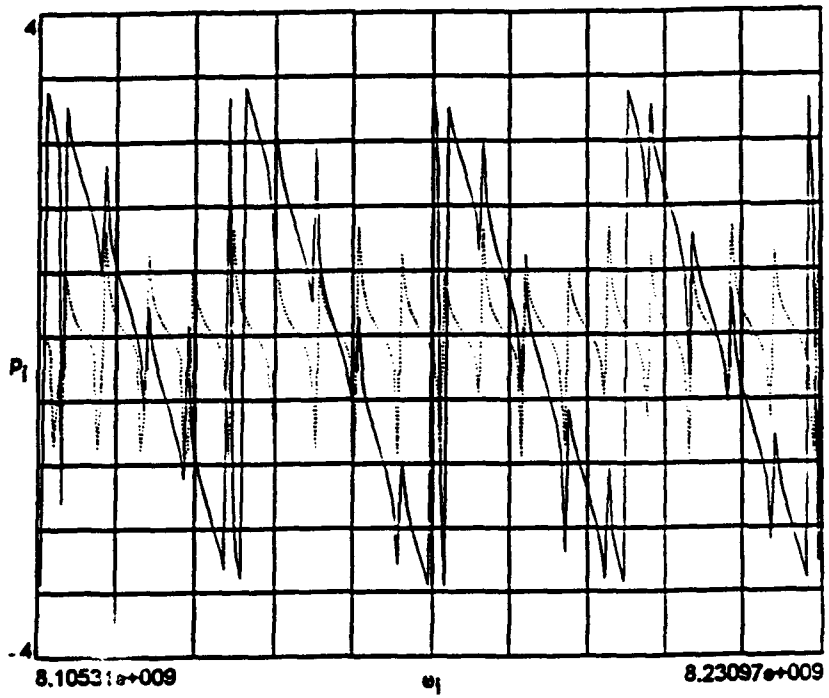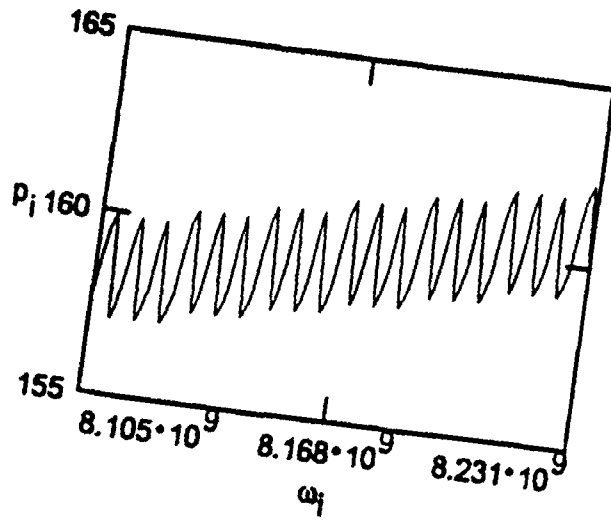| Symbol	Parameter	Value
λ	Laser Wavelength	1.06 μ
F	Lens Focal Length	12.7 mm
a	Signal Beamwidth	2.4 mm
d	Reference Beamwidth	2.4 mm
v	Sound Speed in AO Cell	5120 m/s
x_{pmax}	Photodetector Width	0.015 mm
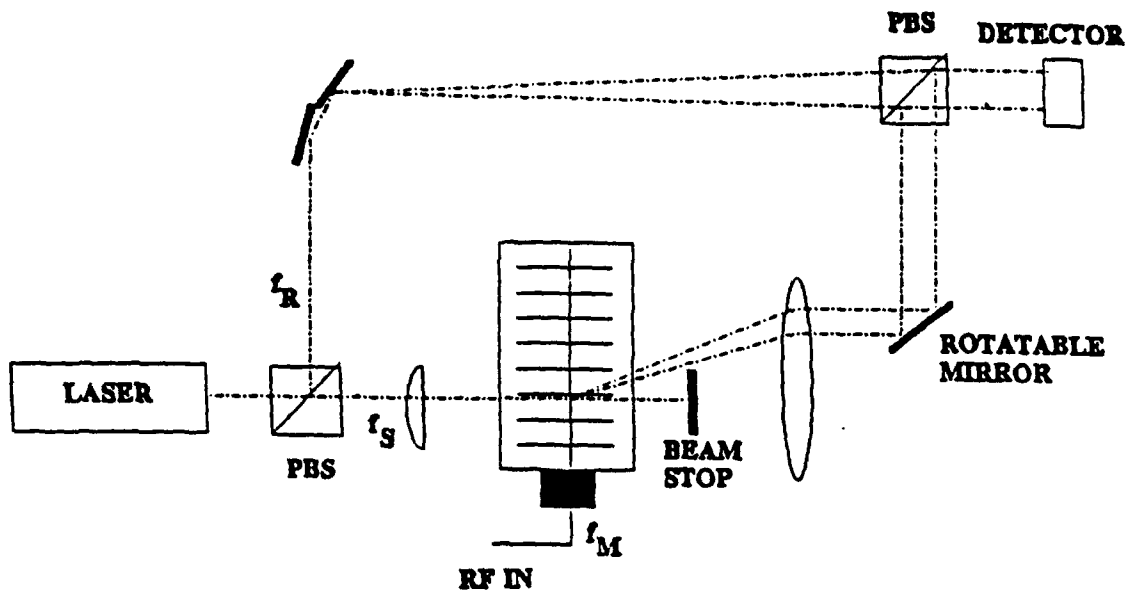
Figure 1
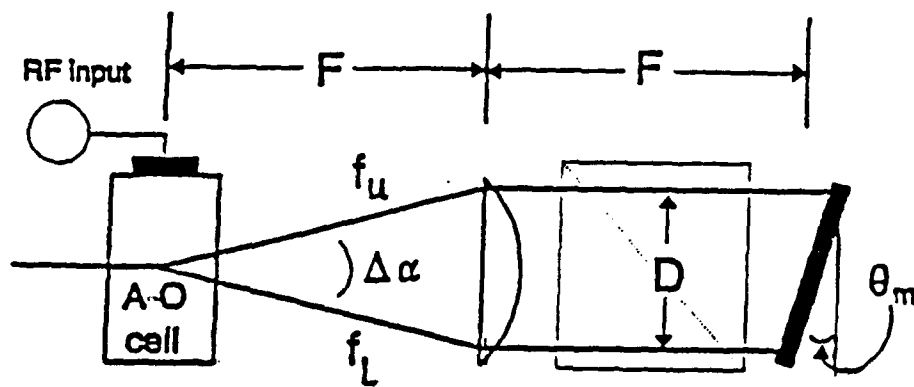
Figure 2
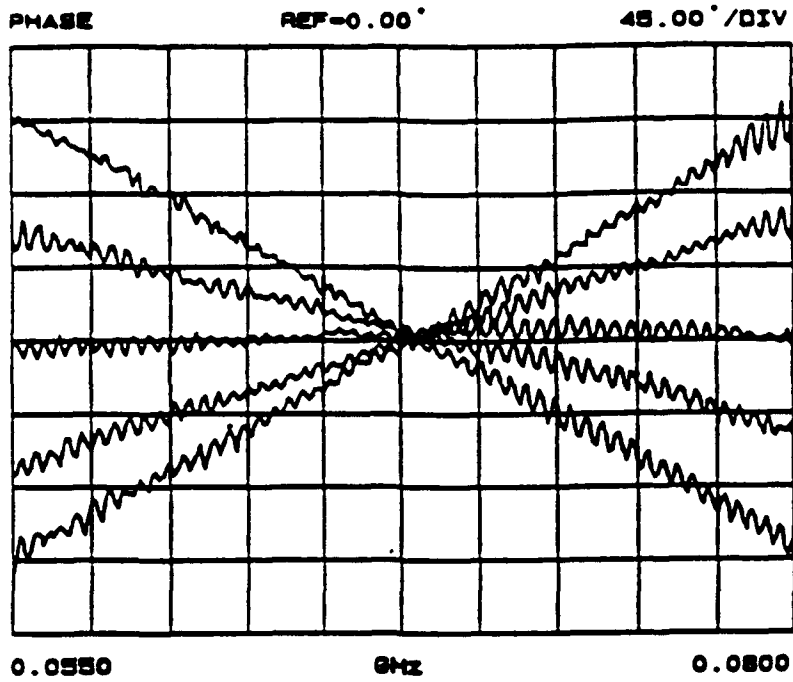
Figure 3

Figure 4

Figure 5

Figure 6

23-18
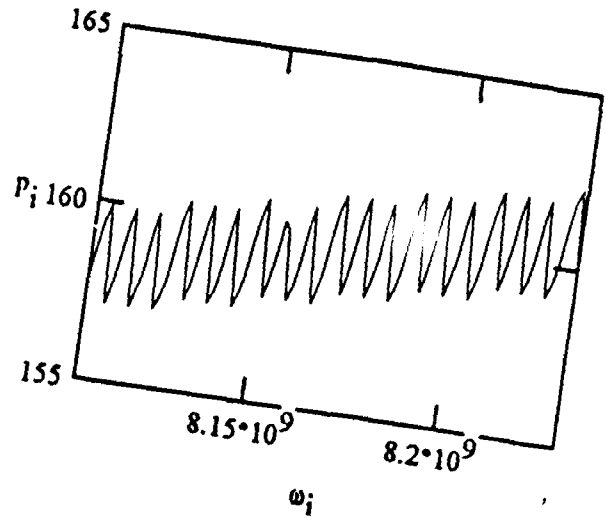
Figure 7a

Figure 7b
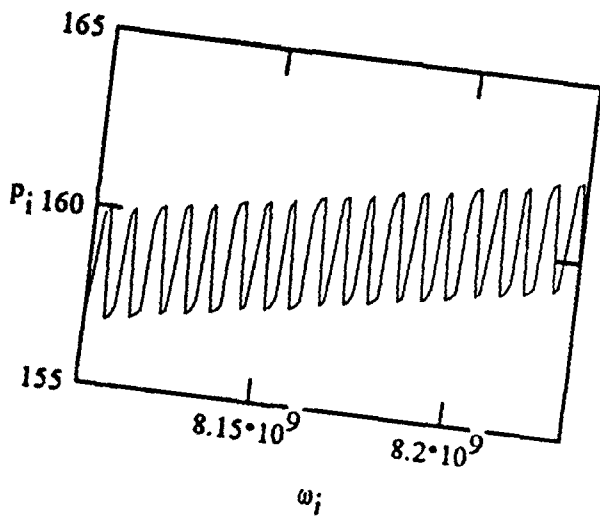
Figure 7c
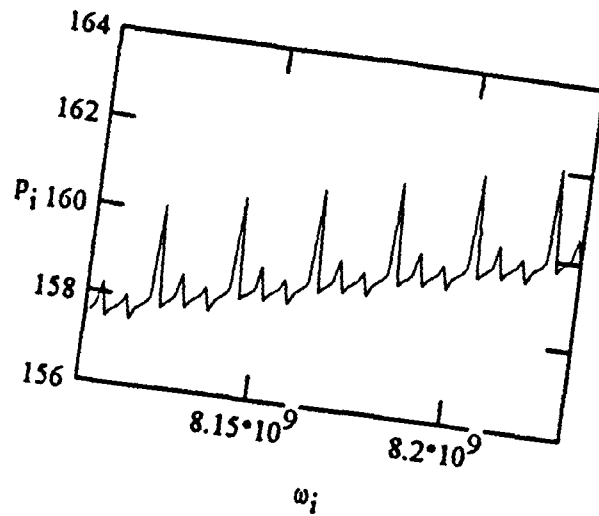
Figure 7d

23-19

AN INTERFACE INTEGRATED CIRCUIT

FOR A DIGITAL SIGNAL PROCESSOR

MULTI CHIP MODULE

Myron E. Sveum

Assistant Professor

Electronic Engineering Technology Department

Metropolitan State College of Denver

Mail Stop 29

Post Office Box 173362

Denver, Colorado 80217-3362

AN INTERFACE INTEGRATED CIRCUIT
FOR A DIGITAL SIGNAL PROCESSOR
MULTI CHIP MODULE

Myron E. Sveum
Assistant Professor
Electronic Engineering Technology Department
Metropolitan State College of Denver

Abstract

An interface Integrated Circuit (IC) was partially designed using VHDL. The IC worked within an "element", an element containing two memory ICs and two processor ICs. This IC interfaced an element to an external host processor via a futurebus, a data bus from external sensors and a bus internal to the element. Elements are packaged within a Multi-Chip Module (MCM) containing either four or sixteen elements. The system supports boundary scan testing.

The MCMs are a digital signal processing system to be used for fire control, space, Kalman filtering and fast Fourier transforms applications [1].

AN INTERFACE INTEGRATED CIRCUIT FOR A
DIGITAL SIGNAL PROCESSING MULTI CHIP MODULE

Myron E. Sveum

Introduction

Digital Signal Processing (DSP) has uses in fire control, radar antenna sidelobe suppression, target recognition, and space applications. Fast Fourier Transforms (FFT) and Kalman filtering are two methods used in these applications, which require fast multiplications techniques. These techniques are often implemented in integrated circuits designed around fast multiplication algorithms.

Signals from radars and infra-red sensors often range widely in amplitude. In the system described here this problem is attacked by using floating point digital signal processors.

In real systems several DSP problems can be computed simultaneously, or processed in parallel. This system uses massively parallel processing to speed the throughput [2].

The Integrated Circuit (IC) or chip discussed in this paper is to interface system "elements" to a common futurebus.

Element

An element contains six integrated circuits or "chips."[2] See Figure 1. The six integrated circuits are four memory elements, and two Floating Point Application Specific Processors (FPASP), or floating point digital signal processors. These ICs are interconnected by two address busses, two data busses and a memory control bus. The ELement InterFace (ELIF) chip ties these element internal buses together with a futurebus and a data bus.

Boundary scan testing is supported by the ELIF and FPASPs. The Joint Test Action Group (JTAG) first created this test specification. This group recognized that as ICs grew larger and more complex, special testing techniques must be designed and specified. The result is IEEE specification 1149.

Data Bus

Sensor data is received via optical fiber and receiver. This data link and "Hot Rod" receiver uses gallium arsenide (GaAs) technology for high speed data rates. The "Hot Rod" data link system is made by the Tri-Quint company. The sensor data rate is 40 Mbits/sec over a serial optical fiber link. At the Hot Rod receiver the serial data is converted to a parallel 40 bit word. Only 32 bits of this 40 bit word are used by the ELIF. The 32 parallel data word consists of two 16 bit words, each word being the output of Analog to Digital (A/D) converters. The A/D output words are not required to be 16 bits, but can be less, and the unused bits will be ignored by the FPASPs.

The Hot Rod system used 4B/5B encoding and the receiver will output an error bit if an invalid 4B/5B code is received. A 34 bit deep First In - First Out (FIFO) storage register is used to prevent data loss while the ELIF is handling futurebus transactions.

The Hot Rod receiver gets a 40 MHz clock signal from the ELIF.

Futurebus

Futurebus specifications are contained in IEEE ????.1. The futurebus connects the host processor to either four or sixteen elements. See Figure 3. The futurebus address/data bus is 64 bits wide. The ELIF has a three deep FIFO data register for the futurebus address/data bus to prevent data loss and increase throughput. The host processor is the centralized arbiter and therefore distributed arbitration is not needed. Table 1 shows the Future bus signals.

AD* - 64 bits - bidirectional Address & Data bus

GR* - 2 bits - ELIF to host GRant & host to ELIF GRant

RQ* - 2 bits - bidirectional ReQuest lines

AS* - 1 bit - bidirectional Address Strobe

AK* - 1 bit - bidirectional Address acKnowledge

AI* - 1 bit - bidirectional Address acknowledge Inverse

DS* - 1 bit - bidirectional Data Strobe

DK* - 1 bit - bidirectional Data acKnowledge

DI* - 1 bit - bidirectional Data acknowledge Inverse

ET* - 1 bit - bidirectional End of Tenure

GA - 5 bits - output - geographical address

Futurebus Lines to ELIF

Table 1

Internal Buses

The element internal buses (see Figure 1) are four data, two address busses and a memory control bus. These busses communicate between the ELIF, FPASPs and the memory chips. See Table 2.

The ADD0 address bus services the memories MEM_U0, MEM_L0 and FPASP0, while address bus ADD1 handles MEM_U1, MEM_L1 and FPASP1. Each FPASP communicates with its respective memories as well as with the other FPASP via the four data busses. Each memory chip has three lines controlling data direction, memory select and data bus tri-stating.

ADD0 - ADDress bus 0 to FPASP0 and memories 0.

Bit 21 specifies either MEM_L0 or MEM_U0.

ADD1 - ADDress bus 1 to FPASP1 and memories 1.

Bit 21 specifies either MEM_L1 or MEM_U1.

LD0 - Lower Data bus 0 - 32 bit used by memories 0.

UD0 - Upper Data bus 0 - 32 bit used by memories 0.

LD1 - Lower Data bus 1 - 32 bit used by memories 1.

UD1 - Upper Data bus 1 - 32 bit used by memories 1.

OE_bar - Output Enable - Controls tristating of memories.

CS_bar - Chip Select - selects individual memories.

WE_bar - Write Enable - selects either read or write mode for each memory.

Operate - the ELIF authorizes each FPASP to perform it's program.

BA - Bank Authorization - Tells each FPASP which memory bank it has authorization to access.

WD - Watch Dog - tells if either FPASP is in the watchdog mode, in which one FPASP checks the other's computations.

DONE - done - FPASP indicates to the ELIF that the FPASP is finished with it's computations, often a request for a futurebus service.

BA - Bank Authorization - indicates to FPASP which memory bank it has access to.

Element Buses & Control Signals

Table 2

Element Interface Integrated Circuit (ELIF)

The ELIF (see figure 2) interfaces with the futurebus, data bus and internal element busses, and does some housekeeping duties.

The Clock Generator receives a 40 MHz clock from the host, and outputs a single phase clock to the Hot Rod receiver, and a two phase clock to the FPASPs. It also receives test information from the JTAG entity and outputs Testmode signals to the FPASPs.

The JTAG entity enables all chips within the Element to be tested using JTAG standard protocols.

The data FIFO receives 32 bit parallel data word from the T quint Hot Rod receiver and puts two 32 bit words into a 64 bit wide FIFO. The FIFO is used to prevent data loss during futurebus transactions. The first data word contains the address of element memory where the data is to be put. This is stored in the Data Address Register. The Data Address Register is incremented after each data transfer to Element memory. Occasionally an invalid code is received by the Hot Rod receiver and the Data Error bit is asserted. The corrupt data addresses are stored in element memory, and this is controlled by the Error Address Register.

The ELIF futurebus portion gets arbitration signals from the central arbiter, which is the host computer. Any element can request access to the address/data bus, but the central arbiter decides which element will have access. The element status is stored in the futurebus Status Register, and is available to the host upon request. The Geographical Address, or physical address

(physical location) of an element is how the host differentiates between elements. A reset line resets the ELIF and element to their initial conditions.

MultiChip Module

Either four or sixteen elements are packaged in a Multichip Module (MCM). A MCM is several ICs interconnected on a common supporting substrate, and packaged as an interconnected group. The substrate conductors often are formed in multiple layers separated by insulating material. Vias connect various layers. Circuit densities are much greater than with previous packaging techniques[3].

Figure 3 shows a four element MCM electrical block diagram with the data busses, and futurebus connecting the host to the MCM.

Conclusion

An interface IC was partially designed for tying three busses together using VHDL (Very high speed integrated circuit Hardware Description Language). The busses were a data bus, a futurebus connection all elements and a host computer, and a bus internal to each element. Regretfully there was not sufficient time this last summer to complete the project.

References

1. Kohler, R. L. Jr., Linderman, R. W., "4.8 Gigaflop Wafer Scale Vector Processor for Fire Control Applications", AIAA 1991 Fire Control Symposium Digest of Papers.

2. Linderman, R. W., Kohler, R. L., "Designing a Wafer-Scale Vector Processor Using VHDL", GOMAC 1991 Digest of Papers, pp 65 - 68.

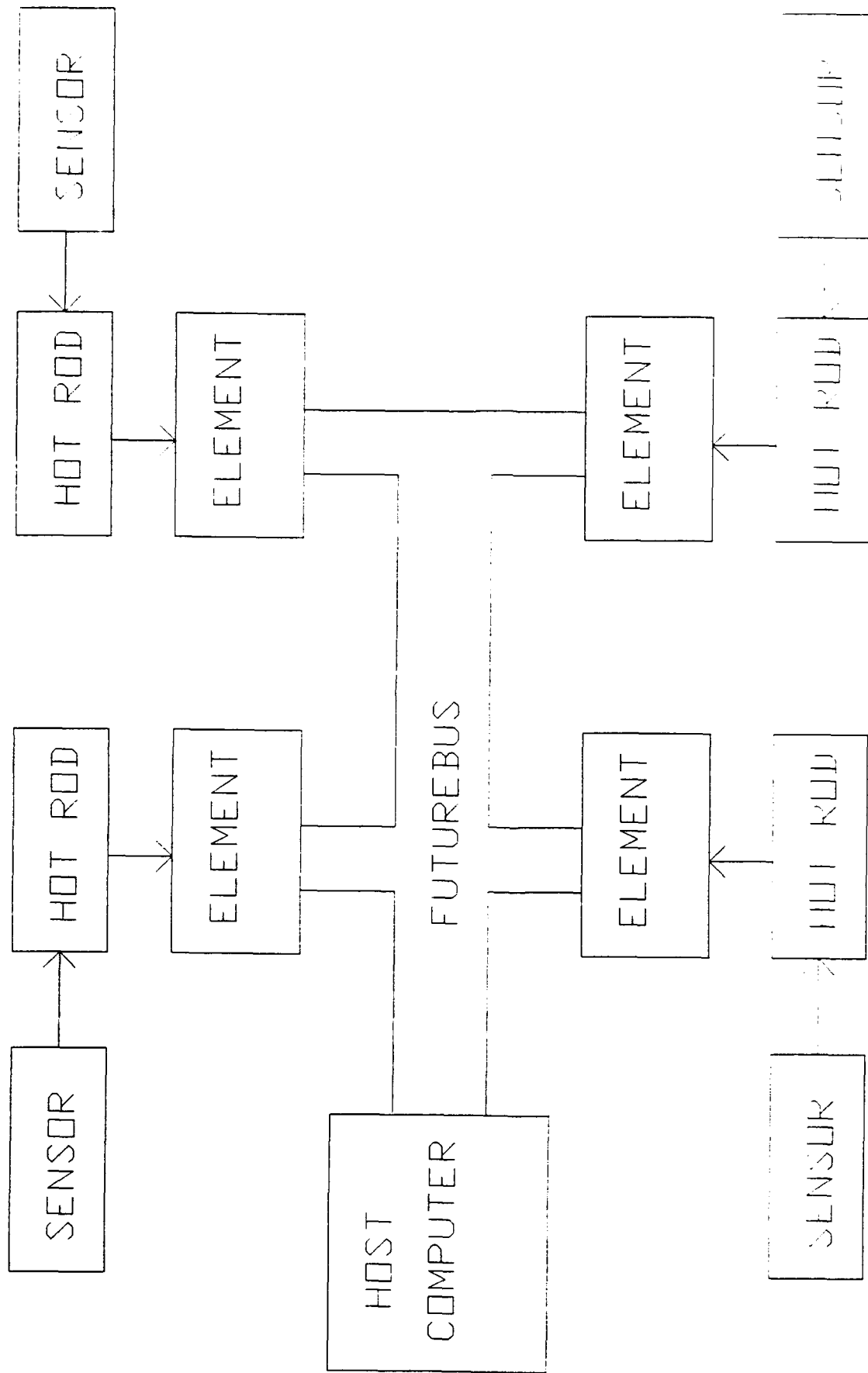3. Lall, P., Bhagath, S., "An Overview of Multichip Modules", Solid State Technology, September 1993 pp 65 - 76.
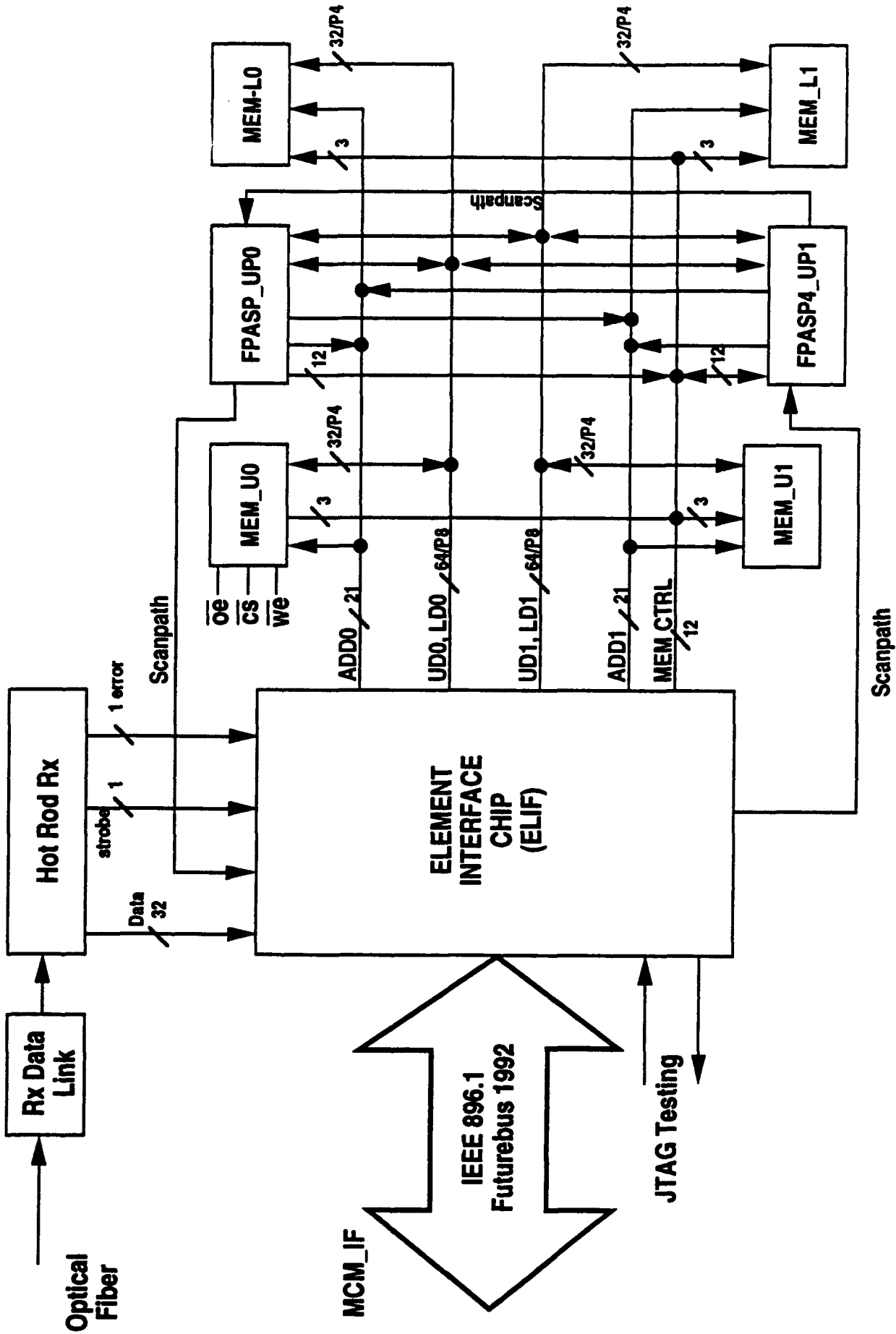
ELEMENT BLOCK DIAGRAM
Figure 1

24-11
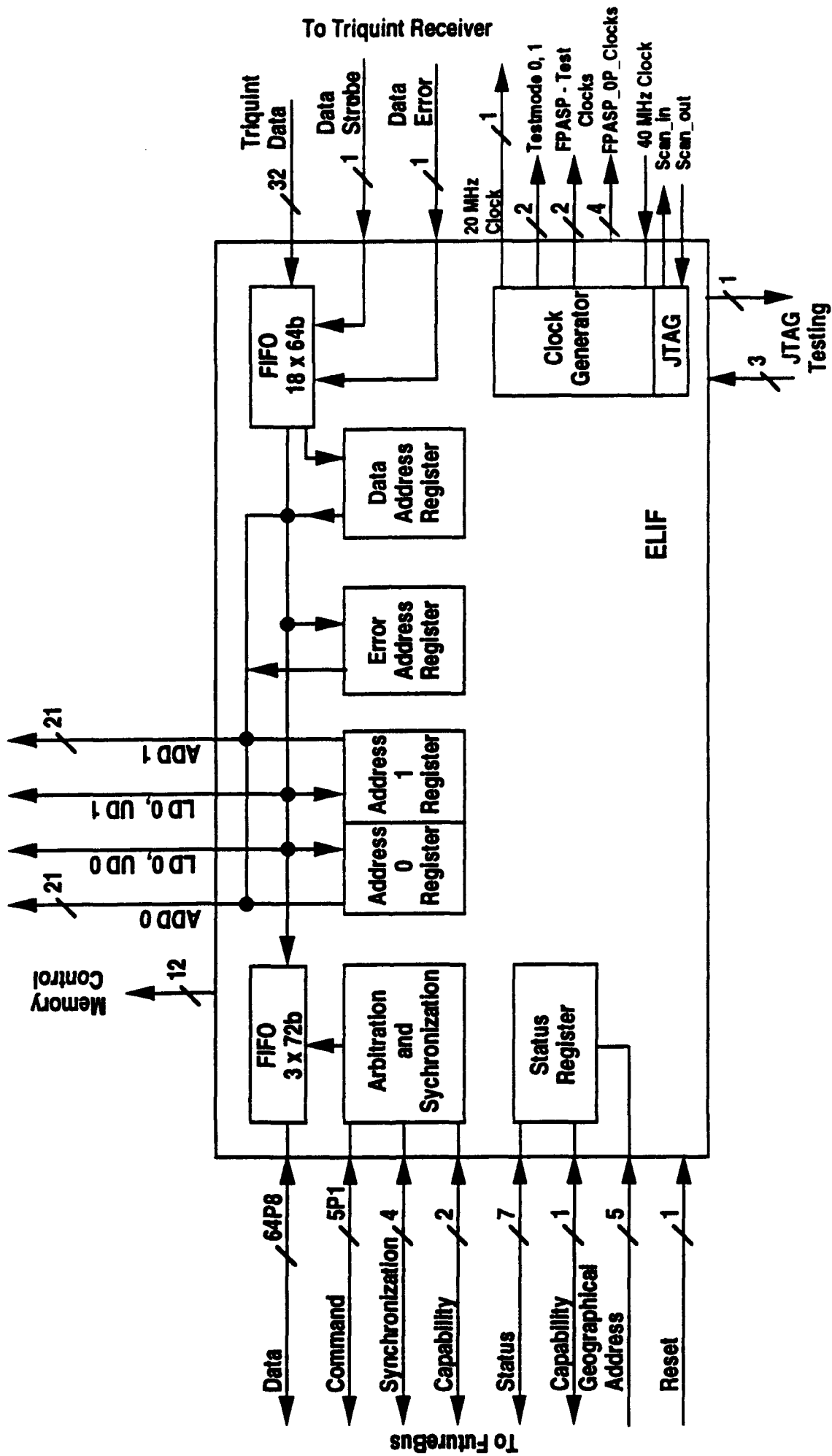
ELEMENT INTERFACE (ELIF) INTEGRATED CIRCUIT
Figure 2

Wafer Scale Vector Processor

Figure 3

CASCADABLE OPTICAL LOGIC GATES

BASED ON

DETECTOR DRIVEN Q-SWITCHED LASERS

Paul D. Swanson

Post Doctoral Associate

School of Electrical Engineering

Cornell University

Phillips Hall

Ithaca, NY 14853

M.A. Parker, S.I. Libby, J.S. Kimmet

Rome Laboratory

Griffiss AFB, NY 13441

CASCADABLE OPTICAL LOGIC GATES
BASED ON
DETECTOR DRIVEN Q-SWITCHED LASERS

Paul D. Swanson
Post Doctoral Associate
School of Electrical Engineering
Cornell University

M.A. Parker, S.I. Libby, J.S. Kimmet
Rome Laboratory
Griffiss AFB, NY 13441

Abstract

Optical OR and NOR gates were developed using Q-switched GaAs/AlGaAs diode lasers driven directly by photo detectors. The Q-switched lasers were designed and fabricated. Both optical logic functions were demonstrated. In the OR gate, an on-off ratio of ~1000:1 was observed using a multi-mode Q-switched laser, and an on-off ratio better than 10:1 was observed for single mode Q-switched lasers. The NOR gate on-off ratio was significantly less for the multi-mode Q-switched lasers. The power required to switch the single mode Q-switched lasers was less than one twentieth the lasers' output power.

CASCADABLE OPTICAL LOGIC GATES

BASED ON

DETECTOR DRIVEN Q-SWITCHED LASERS

Paul D. Swanson, M.A. Parker, S.I. Libby, J.S. Kimmet

Introduction

Logic gates with coherent optical inputs and outputs are the basic building blocks for optical switching and signal processing. Q-switched semiconductor lasers provide the ideal output for such gates due to their high on-off ratios and abrupt switching characteristics.[1] Previous efforts have developed NOR gates using high intensity input beams to quench the gain section within the laser cavity, thus Q-switching it off.[2] Unfortunately such devices cannot by themselves be cascaded since the input intensity must be larger than the lasing intra-cavity light, and the output intensity will always be smaller than the lasing intra-cavity light. OR gates that use input beams to saturate an intra-cavity absorption section suffer from the same flaw. The research presented in this paper demonstrates a means of Q-switching a laser diode with significantly less power than the laser diode's output. This is accomplished by voltaicly changing the absorption within a very small modulator section of the laser cavity. The voltage swing required to turn off and on the laser can be easily provided by the photo-voltaic response of a photo detector. Both OR and NOR functionality can be achieved by varying the orientation and biasing of the detector(s).

Methodology

The Q-switched lasers used a graded index, multiple quantum well laser diode heterostructure. Such material can be used as an optical amplifier, electro-absorptive modulator, or photo-detector, depending on how the diode is biased.[3,4,5] A forward-bias current produces gain, while reversing the bias increases both the optical absorption and the resulting photocurrent. The Q-switched laser optical cavity consisted of a long gain section and a very short modulator section.

Figure 1 shows the lasing threshold current of the gain section as a function of modulator bias for a laser consisting of a 200 μM by 20 μM gain section and a 20 μM by 20 μM modulator.
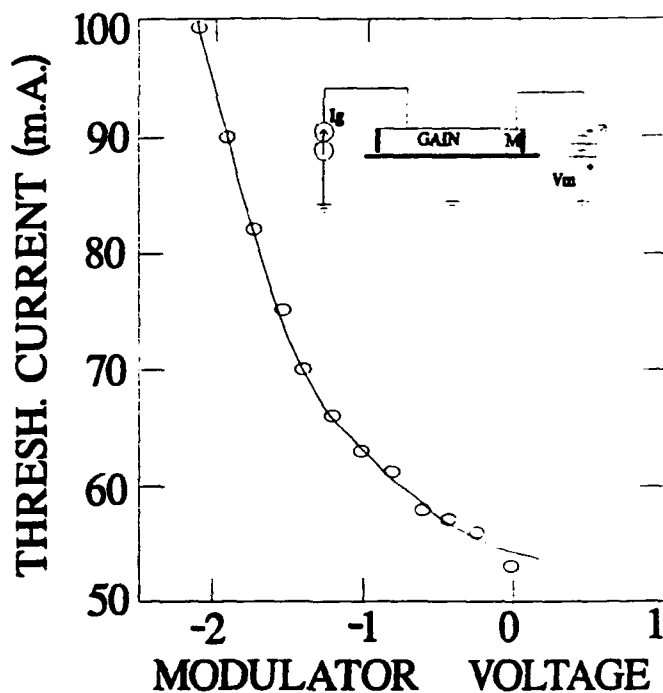

Figure 1. Threshold current of Q-switched laser as a function of the intra-cavity modulator voltage.

25-4

These data show that the laser can be turned off by reverse-biasing the modulator, even when the gain section is biased significantly above the threshold current required for lasing when the modulator is not reverse-biased. The amount of current required to maintain reverse bias on the modulator is limited to the photocurrent caused by spontaneous emission since stimulated emission in the gain section ceases when the laser is turned off. When the laser is turned on, the modulator photo current is still negligible due to the modulator's lack of absorption in forward bias.

Figure 2 shows the laser/detector circuit design for the implementation of the OR function. The current source biasing the modulator and detectors is designed to reverse-bias the modulator in the absence of detector photocurrent. Thus the sourced current should be set equal to the spontaneous emission photocurrent of the modulator when the laser is in the off state. When the input detectors' photocurrent becomes sufficient to satisfy the source current, the modulator voltage will swing positive and the laser will turn on. When input light is terminated, the modulator voltage will swing negative and the laser will turn off.
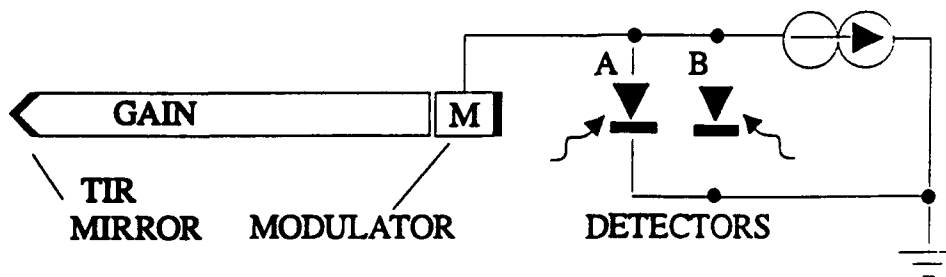

Figure 2. Schematic for the OR gate.

Figure 3 shows the laser/detector circuit required to achieve NOR functionality. In this design, the modulator voltage remains positive in the absence of input light. When the photocurrent of the detectors becomes larger than that of the current source, the modulator current will reverse direction, causing a negative modulator voltage swing, turning the laser off. Required switching power should decrease with smaller sourced currents, while the laser output power should increase with larger forward-bias modulator currents. For this reason, maximum gain conditions should occur at a critical biasing current.
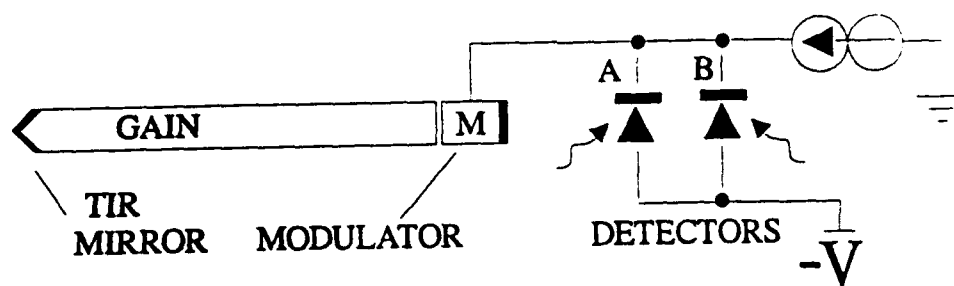

Figure 3. Schematic of the NOR gate.

The detectors for either design can be either external discrete photo detectors, or integrated in waveguides on the same substrate as the Q-switched laser.

Fabrication

A variety of two section etched ridge lasers with and without monolithically integrated waveguides was fabricated from a standard

multiple quantum well laser heterostructure, shown in Figure 4. The heterostructure consists of quantum wells centered in a p-i-n diode superimposed on a planar optical waveguide (high-index core surrounded by a low-index cladding).
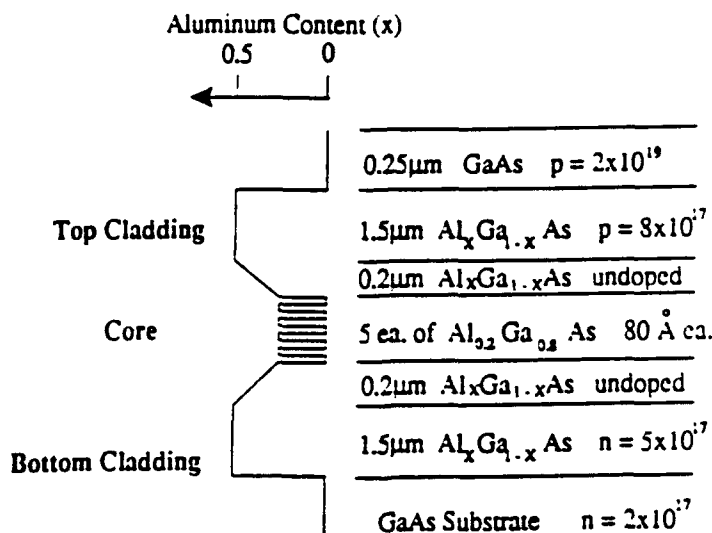
Aluminum Content (x)

0.5   0

Top Cladding | 0.25μm GaAs   p = 2x10^{19}

                    | 1.5μm Al$_x$Ga$_{1-x}$As   p = 8x10^{17}

                    | 0.2μm AlxGa$_{1-x}$As undoped

Core | 5 ea. of Al$_{0.2}$Ga$_{0.8}$As   80 Å ea.

                    | 0.2μm AlxGa$_{1-x}$As undoped

Bottom Cladding | 1.5μm Al$_x$Ga$_{1-x}$As   n = 5x10^{17}

                    | GaAs Substrate   n = 2x10^{17}

Figure 4. A standard epitaxially-grown laser heterostructure, utilizing multiple quantum wells in an active region centered within a graded-index waveguide.

The lasers require etched regions of two different depths: a deep etch that extends well into the lower cladding region for the laser mirrors, and a shallow etch to delineate the waveguides. In order to create an effective lateral index difference, the shallow etch should be within 100 nm of the top of the planar waveguide core.[6] Mirror-quality vertical walls were etched using chemically assisted ion beam etching (CAIBE).[7] Chrome, silicon dioxide or photo-resist all can be used as CAIBE etch masking materials; however, of the three, only chrome stands up well enough to produce good quality laser mirrors. Originally chrome and

silicon dioxide were used to mask the two different etch depths, but due to charging problems in the CAIBE, the silicon dioxide etch mask was replaced with photo-resist. The chrome doubled as the top metal for the p-type ohmic contact, so it did not require removal after processing.

The devices were etched twice in the CAIBE. In the first etch only the regions to be deep etched were not masked. The depth of this etch was that of the difference of the two desired etch depths. After the silicon dioxide (or photo-resist) mask was removed, leaving only the chrome mask, a second etch was performed. The depth of the second etch was that of the desired shallow etch.

After the two CAIBE etches, oxygen was implanted at 60 KeV, 120 KeV, and 180 KeV at a dose of 10^{12} /cm^2 for electrical isolation between laser sections. The p-contact metallization (20 nm of titanium, 20 nm of platinum, 300 nm of gold and 170 nm of chrome) was used to mask the oxygen implant. Finally, the wafers were lapped down to 250 μM thick, and the backs were metallized with 10 nm of nickel, 40 nm of germanium, 80 nm of gold, 100 nm of silver and 70 nm of gold for the n-type ohmic contact. The contacts were alloyed at 360°C for one minute. The wafers were then cleaved, mounted and tested.

Figure 5 shows cross sections and top views of the processing of a pair of two-section lasers. Cleaving down the center of the finished wafer yields two lasers, each with one cleaved facet mirror and one total internal reflection mirror (TIR). The laser output would exit the cleaved facet mirror, on the modulator side of the laser.
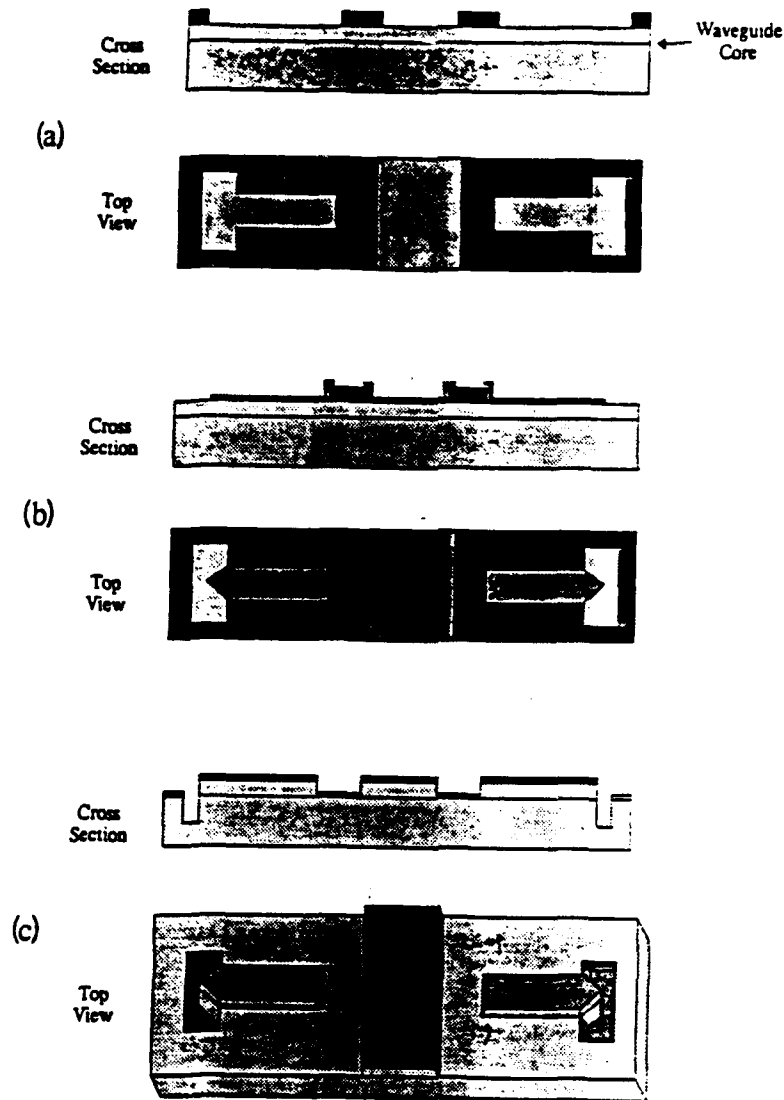
Figure 5. Cross sections and top views of a pair of two-pad lasers during progressive stages in fabrication: (a) After depositing and patterning the SiO_2; (b) After the patterning of the ohmic contact / oxygen implant mask / chrome CAIBE mask; (c) After both CAIBE etches and the oxygen implant.

The devices were tested using a fiber optic / electronic probe station at the Photonics Laboratory at Griffiss Air Force Base. A pulse generator, used as a clock for the gates, pulsed the gain sections of the lasers while discrete PIN detectors were connected as shown in Figures 2 and 3 to implement the OR and NOR gate, respectively. A low-power helium-neon laser was used as optical input beams. Because of the design of these gates, the input light wavelength does not affect the gates' operation (within the limits of the sensitivity of the detectors used). Though fabricated, the gates with monolithically integrated wave detectors were not ready to be tested by the conclusion of the research program. Therefore, only the discrete tests are presented here.

Results

Two sizes of Q-switched lasers were used to test the gates. The first consisted of a 200 μM by 20 μM gain section and a 20 μM by 20 μM modulator, separated by a 2 μM shallow etched (and oxygen implanted) gap. The second consisted of a 200 μM by 4 μM gain region and a 4 μM by 4 μM modulator, again separated by a 2 μM etched gap. Before the oxygen implant, the isolation trench between the gain section and the modulator provided resistances varying between 300 and 1000 ohms. After the implant, the pad-to-pad resistance of the 20 μM wide devices was ~1.7 Meg ohms, while the 4 μM wide pad-to-pad resistance was even higher. This resistance was crucial for the performance of the gates, since the currents

determining the bias on the modulator were orders of magnitude smaller than the pump currents driving the gain section.

OR Gate

The OR function was demonstrated by directing the helium-neon laser onto two PIN detectors, which were connected to a Q-switched laser as shown in Figure 2. Both 20 μM wide and 4 μM wide Q-switched lasers successfully performed the OR function, with the multi mode (20 μM) lasers yielding a higher on-off ratio and the single mode (4 μM) lasers yielding higher gain. For each case, the current source was set to the photocurrent of the modulator section when its bias voltage was approximately -4 volts. This current was 0.7 mA for the 20 μM square modulator, and 0.002 mA for the 4 μM square modulator. For the latter case, an input power of 3.95 μW switched on the gate, producing 83 μW of output power, and thus providing a power gain of 21. The 20 μM wide Q-switched lasers did provide a gain above unity.

Figure 6 shows the emission spectrum for an OR gate using a 20 μM wide Q-switched laser. Both the logic 1 output state and the logic 0 output state are shown. From this data, the on/off ratio is determined to be approximately 1000:1. The 4 μM wide lasers yielded similar results with an on/off ratio of better than 10:1.
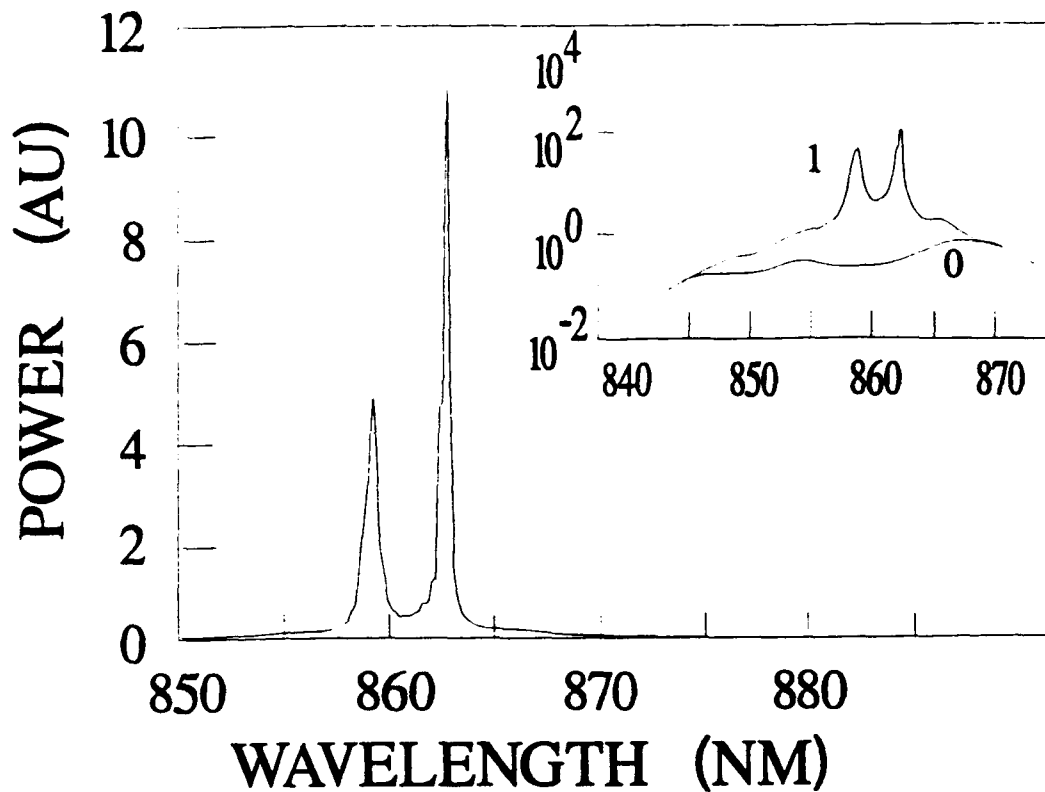
Figure 6. The emission spectrum of an OR gate using a 20 micron wide Q-switched laser for both the logic 0 and 1 output states.

NOR Gate

The NOR function was successfully demonstrated by connecting the Q-switched laser and PIN detectors as shown in Figure 3. The negative voltage bias on the detectors was set at -3 volts. As anticipated, increasing the sourced current to the modulator increased the output and switching power; however, the switching power increased at a much faster rate than the output power. For this reason a zero-mA source current yielded the best gain. Figure 7 shows the emission spectrum of a NOR gate using a 20 μM wide Q-switched laser. Both the output logic 1 and logic 0

state are shown for the current source set to zero mA. Note that at these
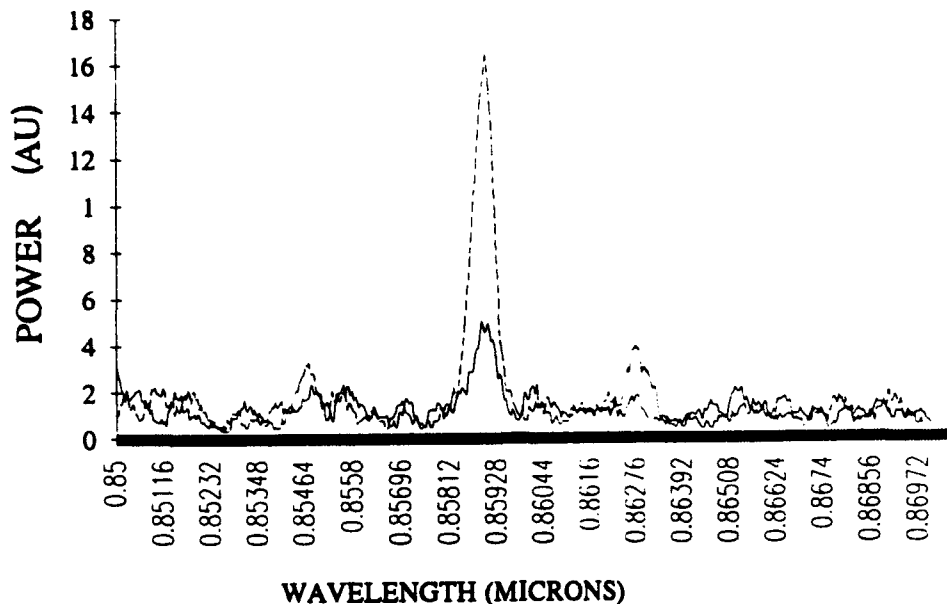
bias levels the on/off ratio is only 3.4:1.

Figure 7.   The emission spectrum of a NOR gate using a 20 µM wide Q-

switched laser for both the logic 0 and logic 1 output states.

Conclusion

Both the OR gate design and the NOR gate design were validated,

using discrete detectors and various-sized Q-switched lasers.   Only gates

using single mode lasers with very small area modulators demonstrated gains

capable of allowing the devices to be cascaded to the input of a similar

gate.   Fully integrated single mode Q-switched lasers and detectors were

fabricated; however, time constraints prevented test results for these

devices from being presented in this report.

References

1. C. Harder, K.Y. Lau, A. Yariv, "Bistability and Pulsations in Semiconductor Lasers with Inhomogeneous Current Injection", IEEE J. Quant. Electr. QE-18, 1351 (1982)

2. W.J. Grande, C.L. Tang, "Semiconductor laser logic gate suitable for monolithic integration", Appl. Phys. Lett., Vol. 51, p.1780, Nov. 1987

3. P.D. Swanson, "Characteristics of Semiconductor Optical Waveguides Fabricated by Impurity Induced Layer Disordering", Ph.D. thesis, University of Illinois, Urbana-Champaign, 1989

4. K.P. Jackson, C. Harder, P. Buchmann, and K. Datwyler, "High-Speed Characterization of a Monolithically Integrated GaAs-AlGaAs Quantum-well Laser-Detector". IEEE Photon. Technol. Lett. ,Vol .2, p832, 1990

5. C.M. Herzinger, P.D. Swanson, K.T. Tang, T.M. Cockerill, L.M. Miller, M.E. Givens, T.A. DeTemple, J.J. Coleman, and J.P. Leburton, "Electroabsorption properties of a single GaAs quantum well", Phys. Rev. B, Vol. 44, Dec. 1991, p.13478.

6.   C.F. Lin, "A New Technique for Monitoring Etched Depth in the Fabrication of Ridge-Waveguide Lasers", M.S. Thesis, Cornell University, May 1989.

7.   W.J. Grande, J.E. Johnson, and C.L. Tang, "Characterization of etch rate and anisotropy in the temperature-controlled chemically assisted ion beam etching of GaAs", J. Vac. Sci. Technol. B, Vol. 8, p. 1075, Sept/Oct 1990

MASTERMIND: Modeling and Simulation
Technology Enhancement for Research in
Multimedia Intelligent Network Domains

Scott E. Spetka
Assistant Professor
Department of Computer Science

State University of New York
Institute of Technology at Utica/Rome
Utica, New York 13504-3050

Final Report for
Summer Research Program
Rome Laboratory

September 1993

MASTERMIND: Modeling and Simulation
Technology Enhancement for Research in
Multimedia Intelligent Network Domains

Scott E. Spetka

Assistant Professor

Department of Computer Science

State University of New York

Institute of Technology at Utica/Rome

ABSTRACT

This paper introduces new concepts in query processing needed to support construction
of models from existing component submodels which are stored in a distributed model
database management system (MDBMS). Dynamic execution of submodels provides the
basis for evaluation of global model constraints specified as part of the model database
query or global model specification. The paper describes a network service approach to
modeling and simulation which was developed to support the evolution of standard
interfaces and component model implementations required by a MDBMS. The MDBMS
research direction presented in this paper is part of a strategy that the Modeling and
Simulation Office at Rome Laboratory is pursuing to address the problems of model
interoperability, reusability and construction of models that operate with varying
degrees of fidelity.

MASTERMIND: Modeling and Simulation Technology Enhancement for Research in Multimedia Intelligent Network Domains

Scott E. Spetka

## 1) Introduction - Evolution of Standards

The problems of interoperability, reusability, and fidelity are related by their potential solution through dictation of standards for implementation of model component interfaces. There is a simple reason why this approach is inappropriate at this time. Modeling and simulation technology, especially in the area of object-oriented modeling is still under development. The areas of model interaction and hierarchical modeling for varying fidelity are currently the subject of research in a variety of diverse problem domains. Much of the current research involves artificial intelligence, distributed processing and multimedia. The approach of modeling and simulation technology enhancement for research in a multimedia intelligent network domain (MASTERMIND) is to enhance existing and developing modeling and simulation technology in order to provide an environment in which the modeling and simulation community can evolve standards which facilitate building new models from a distributed database of existing models.

In section 2, we briefly consider the parameters that govern existing modeling environments. We also consider environments that are currently under development in which standards will evolve. The MASTERMIND environment is described in section 3. It is based on expected advances in the technology described in section 2. Section 4 introduces the concept of a Community Research Network Resource which is an integral component of a plan to facilitate the evolution of standards for modeling and simulation and to provide additional benefits from sharing of technical ideas at all levels. The concluding section discusses directions for future research.

2) Current Modeling Environments

Modeling environments have developed over the past 25 years in which some networking is used and in which object-oriented programming techniques are applied. Most of these systems have been developed in the past 5 to 10 years. The growth of distributed modeling environments has paralleled the growth of local area networks and the development of smaller and more powerful processors. This trend continues, with new modeling and simulation technology, such as object-oriented modeling being driven by the increasing availability of processing resources growing up around a maturing national digital network.

The technologies that will drive new developments in modeling and simulation are new and faster processors, improved networking and advances in object-oriented systems. It is important in any research program aimed at system development in a broad area of application that the target for design be an architecture that is expected to be affordable upon completion of the project so that software developed that can take advantage of expected gains in hardware. Research projects that build software for today's expensive workstations help to drive down the cost of hardware and make it affordable, by increasing demand. The diagram below shows integrated modeling environments, loosely coupled through the Internet.
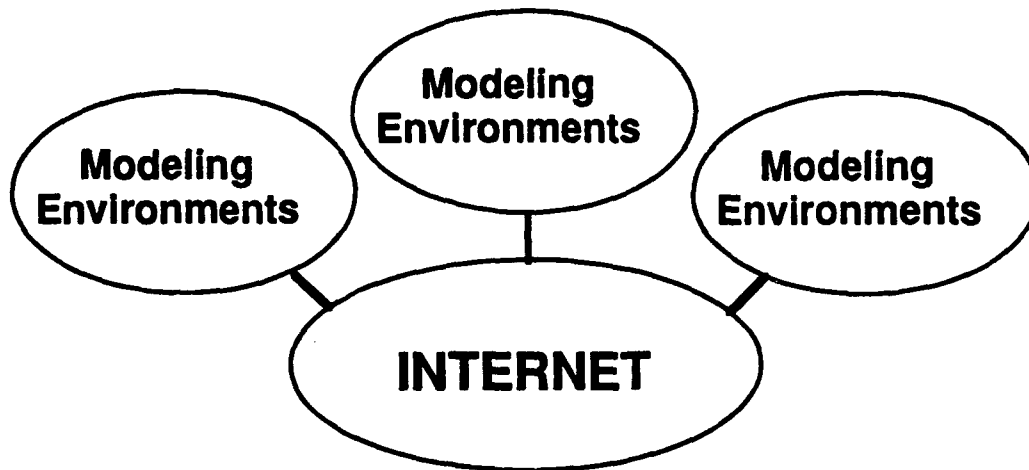
2.1) The Internet

The potential of increased access to processing resources through public and private networks will be a critical factor in modeling and simulation technology development.

Although some systems currently use networks to implement distributed processing, the interfaces to distributed function interfaces are often proprietary, special purpose, or subject to change. They have not been used to provide access to the functions that exist. It is safe to say that even within companies, government research laboratories, the degree of sharing and reuse of model components has been disappointing, given the availability of the Internet over the past 10 years.

Much of the problem has been associated with the monolithic nature of many systems developed over the last 10 years. Systems were not constructed to provide convenient interfaces that could be generalized to provide access to component models in a complex environment for use in the construction of new models. The development of object-oriented techniques for system design has lead to significant improvement in this area. The lack of sufficient bandwidth in the Internet also prohibited the degree of sharing that might otherwise have been possible over this period. Distributed models and simulations that were developed relied on high-speed local area networks for service. Increasing bandwidth in the Internet along with object-oriented technology are expected to solve many of the technical problems preventing distributed modeling in a truly interoperable environment.

Communication within the modeling and simulation community must improve for increased sharing and development of object-oriented models that are useful to the point that developers may reuse them in their models. Services available on the Internet provide simple file retrieval and are used to share access to every form of software available. Technical articles, bitmaps, system source code and binary applications, and more are routinely distributed through the Internet today. These services can be efficiently provided using database indexing techniques often depend on machines which are financed by government programs. As object-oriented systems are developed, their component models can be distributed through the existing mechanisms. Applications that can be used for search and retrieval on the Internet include *Gopher, Archie, World-Wide-Web,* and *Hytelnet* [Kehoe 92] [Marine 93].

2.2) Modern Workstations

Modern Workstations are driving the implementation of models and simulations that would not have been possible 10 years ago. Application are being developed that depend on time consuming access to knowledge bases and the application of other processor-

intensive techniques from the field of artificial intelligence. These approaches are possible due to the introduction of a new generation of micro- and mini-computers. The DEC Alpha workstation, for example is a 64 bit machine that runs at 200 MHz. Several models are available at under $15,000. Fully networked UNIX systems are also available for Intel 80386/486 based systems. A 33 MHz machine costs around $1,500.

Advances in hardware and software are adding to the quality of models while supporting improved communication within the modeling and simulation community. Multimedia cards are inexpensive and color graphics is also affordable for most users. Software products, like DEC's MediaImpact and Adobe Premier provide easy interfaces to include live video or computer stored video recordings into models. Multimedia hardware can be used, along with the Internet, to transmit video and audio for technical exchange. For example, *Phone* is a free application, available through anonymous FTP which allows a workstation to become a telephone, but with no toll charges. The Internet *talk radio* is a system that uses the Internet as a radio broadcast channel. CDROMs are also used to distribute information in all fields of research. The DEC Alpha workstation has an ISDN port which can be used to access a new worldwide network that may replace the Internet when it becomes widely available. A modern networked workstation environment provides a user with access to the types of software depicted in the diagram below.
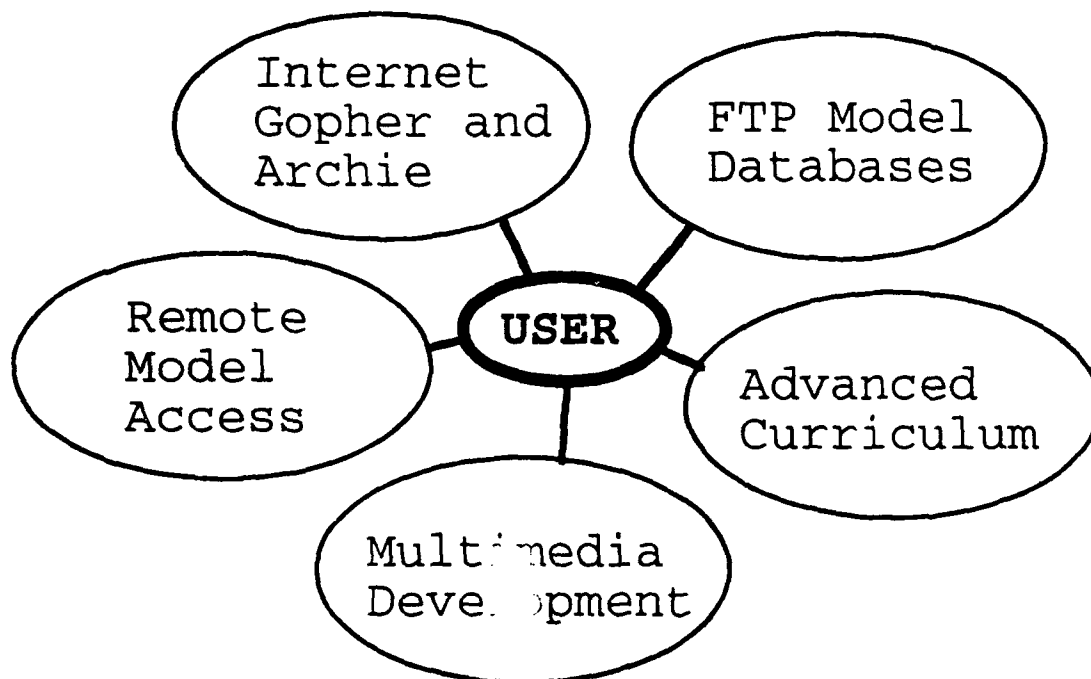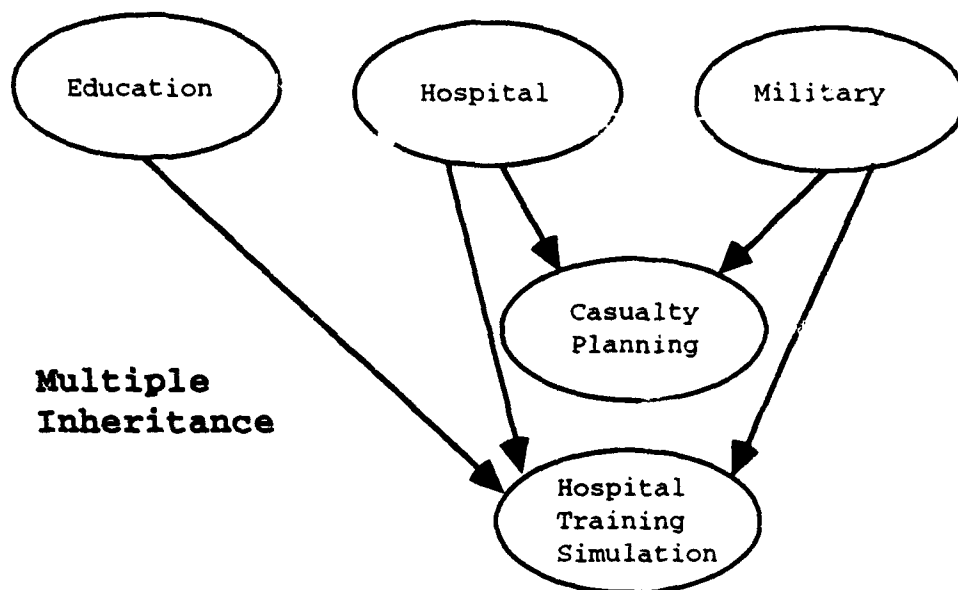
2.3) Object-Oriented Models

Object-oriented systems are an important software development tool. Their main advantage is that data and executable functions that access the data are packaged together in *objects*. Access to objects is performed by sending *messages* to invoke the functions implemented by the object on its associated data. Objects can be used in the definition of new objects through a mechanism called *inheritance*. The diagram below describes the set of object types defined through inheritance, starting with the root Model object type. All objects declared by a programmer would normally inherit the data structures and functions associated with the Model object. For example each object in the hierarchy could inherit a model type data element and a function which could be used to identify it as Military, Government, Hospital, etc. The figure below shows a class hierarchy for a system which involves sectors of our society that may be subject to modeling and simulation.
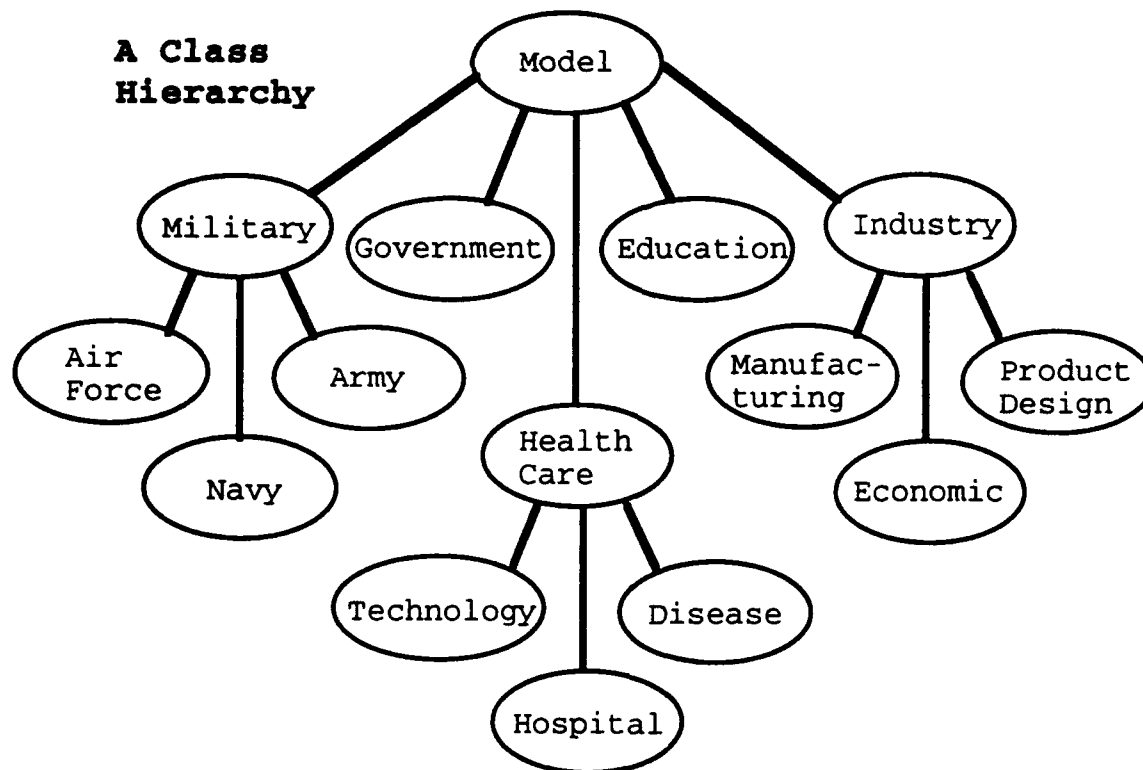
A Class Hierarchy

Multiple Inheritance is a mechanism that allows new object types to inherit their definitions from objects in the class hierarchy that are independently defined as shown

in the diagram below. For example, a model involving Hospitals and Military would define objects that inherit their definitions from objects that have only, perhaps, the Model type in common. This facility allows flexible models to be defined in specialized domains, using objects of any type. This facility can be used to take advantage of the functions that have been developed and the data structures that have been designed to support reusability and interoperability. It also promotes the development of component models that can be implemented in systems providing multiple levels of fidelity, to facilitate the construction of models involving component types that are already implemented. The system designer can focus on the problem of implementing variable fidelity with less concern for implementation of details governing object behavior.

Object-oriented database systems [Chorafas 93] provide a mechanism for persistent storage and access of objects. They support definition of new data models as well as the evolution of existing models to support diverse and changing storage structure and processing requirements. They provide a natural mechanism for integration of network communication, multimedia support functions, and object-specific processing, including displaying, storing and processing images, voice, and other data.

3) MASTERMIND - The Future Environment

MASTERMIND can take advantage of increasingly available processing resources that are being developed for the Internet. Most Internet access today is being used for file transfer and for simple point-to-point communication channels, usually to exchange

audio or video data. Distributed services, such as a modelbase management system usually require a "critical mass" of users before they are widely adopted. MASTERMIND is a system for access to models in a distributed model database. It will provide an incentive for developers to provide component models that implement varying degrees of fidelity and make it easy to use existing component models in the construction of new models.

Mastermind will allow a user to easily:

- Find the component models that produces the best results
- Find the input parameters that would produce that result
- Produce a model for a required degree of fidelity

MASTERMIND is a system that supports a generalized notion of modeling and simulation. It considers most computer-based applications to be models of "real" systems that are used to provide output to users or to connect directly to a device that controls a real-time process based on predictions or decisions that are generated by a model. A generalized concept of query processing is applied to a "model base" or collection of models. A new query processing paradigm allows selection of models, based on their characteristic attributes and based on the results of model execution, given a set of input parameters. It also allows determination of appropriate model parameters, given a set of inputs and a required result.

The generalized query processing paradigm goes beyond the most advanced concepts in query processing associated with logic programming and object-oriented databases. In addition to searching the database for specific "matches" to query inputs, a model database management system (MDBMS) is expected to derive parameters from, possibly continuous, distributions associated with model parameters. This approach allows a user, querying the modelbase to find the set of component models which, when integrated will produce an output that is closest to the desired output. Models are often used to verify expected results and show that a system should be built before its actual implementation. Mastermind will also serve to adjust input parameters to improve the result when directed to do so.

In the long-term, MASTERMIND will develop into a facility that extends beyond anything that is currently envisioned by experts in either the modeling and simulation or the

database communities. Advanced MDBMS query processing will model initialization parameters for input, but also provide for specification of model output as input to the query processor. The system will then execute potentially useful combinations of component models to determine which composite models return the best results.

3.1) MASTERMIND Architecture:

Sever mechanism and functions characterize the MASTERMIND architecture:

• A set of models that can be used as examples in coursework at all levels. A model for counting sheep may help a first grader to develop mathematical skills, without knowing how to actually build a model. A graduate researcher could use MASTERMIND to try a new queuing technique in a model implementation.

• Models that can be executed by researchers without concern for implementation details along with functions for the update of stored models.

• A mechanism for interfacing models which provides the capability to build new models that use existing models.

• A facility to store interface "models" that allow reuse of interfaces designed to connect models.

• Access to information about all models in the modelbase including technology used to develop the model and other descriptive information that can be used by users at all levels, from beginning to expert.

• A general query capability that provides access to all information, from access to model descriptions to execution of appropriate models to solve a problem.

3.2) MASTERMIND Queries

MASTERMIND queries provide a generalized facility for building models from existing models. Given a model description, including input parameters, initialization data and required output, the system automatically builds and executes a model that best solves the problem, given existing technology. The system can also report on other possible

approaches to building a model that would require additional interfaces to be developed. MASTERMIND provides a dynamic querying environment based on model execution, in addition to providing a static query capability that would allow selection of models or model components based on their static characteristics.

The MASTERMIND approach requires development of new query processing technology as well as development of a modelbase to support the system. Instead of searching for models that would support the expected types of input and output parameters, the system searches for the best model execution to produce a specific set of output parameters, given specific input.

Models in the database can be designed to accept variable numbers of input parameters. Variable input parameter models use default parameters when user inputs are not specified. For example, an F16 model may produce a number of targets capable of being acquired, given the number of F16s and a rate of target acquisition per F16. Specifying only the number of F16s in a model would result in use of the default target acquisition ratio. Accessing models with variable numbers of parameters is supported by standard object-oriented database technology.

When component model input and output parameters match, a model created by pipelining the result of one component to the other may satisfy user requirements. At the other extreme, a user finding that there are no models in the database that satisfy a problem statement would be required to build component models and implement their interface. We believe that many user requirements could be satisfied by developing new interfaces to existing models. But, for this approach to be successful, it is necessary that interface standards for modeling and simulation be developed, in order to avoid an exponential explosion of interface modules.

MASTERMIND will encourage development of reusable model components. Many of the models that have been developed incorporate internal implementations of submodels that could be made publicly available if a system such as MASTERMIND were available.

3.3 Processing Requirement for Modelbase Queries

MASTERMIND processing requirements will address many of the issues that are common for distributed database systems. In developing techniques to support the dynamic model

execution paradigm for query processing, the system must use techniques to maximize parallelism by predict results which can allow dependent stages of processing to be precomputed based on projected outcomes while producing reasonable approximations. Many of the issues that are raised in the area of query decomposition strategies appear to be similar to those that are addressed in [Spetka]. Generalized procedures for query decomposition allow component models to be processed in arbitrary order.

MASTERMIND query optimization will take into account:

- Need to execute queries to determine when to select a model

- Need for greater parallelism and increased computing power

- Increased opportunities for parallelism but reduced pipelining

3.4) Comparison to RDBMS Query Processing

Mastermind queries are significantly different from relational database queries. As the diagrams below show, in an RDBMS, the database scheme is defined and a database instance is installed. Queries are then submitted to search the database to look for existing relationships. Simple text comparison is used to find matching entries from tables involved in a query to produce a result. Indexing techniques can be applied to make processing very efficient. In the example shown below, a match of entries in the tables can easily produce a listing of names of courses taught by a particular professor.

|	
Smith	CS430
Spetka	CS430
Spetka	CS500
Thomas	CS430

Professor Relation

CS300	Fortran
CS430	Modeling
CS500	Queueing
CS600	Seminar

Course Relation

In a model base, it is not the end result of the model that is important but the models used to produce the result. This suits most classical modeling needs since it allows production of a model that can best produce a result. Query input parameters define the models that are accessed by the query to dynamically configure the component model to find the best component attributes or to meet the specification of a problem.

In addition, a modelbase query has to express the processes that are needed by the model. It may be possible for two completely independent sets of detailed models to produce the same output. In the diagram below, Models 1 and 2 can be used to produce a required output. The diagram also shows that the query also produces 2 other distinct models of higher fidelity, involving component models 3 and 4. Models 3 and 4 could be alternative implementations for the same functional model. Note that a search of the modelbase could be restricted to include only model types 1 and 2 if higher fidelity models are not desired.
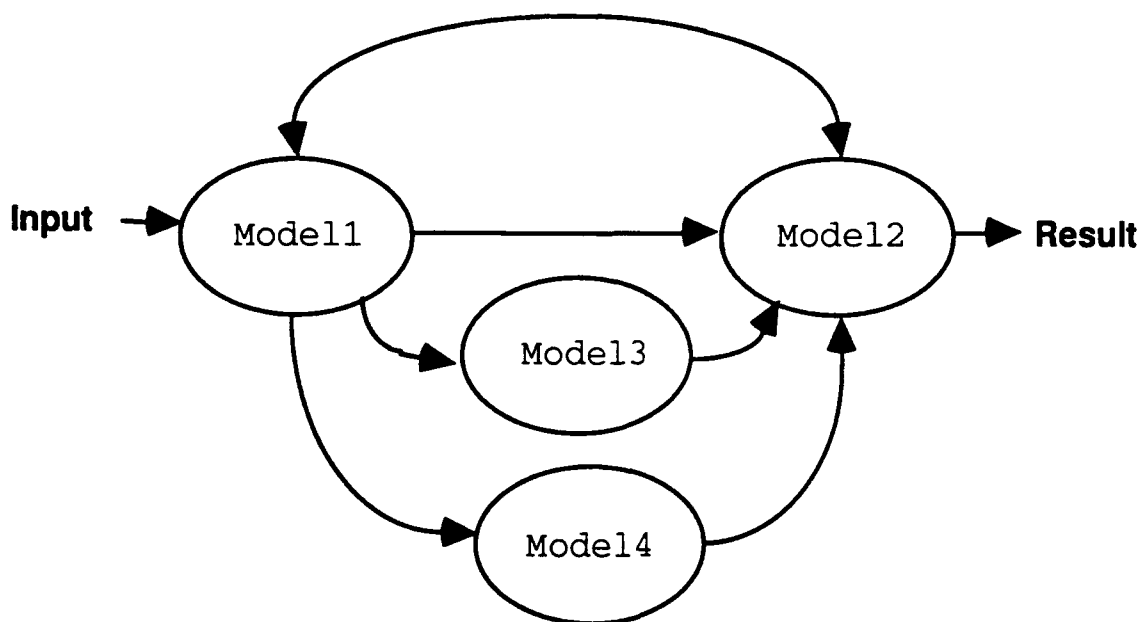
4) A Community Research Network Resource

The Rome Laboratory Modeling and Simulation Community Resource Network Resource (CRNR) addresses the need to improve interaction of researchers and educators in all sectors of the modeling and simulation community: government, university and industry. The vision of a CRNR calls for collaboration in the community to advance all critical

technologies through effective use of modeling and simulation. The CRNR will evolve through contributions from community members in both software and expertise.

The CRNR is designed as a conduit for the flow of expertise and knowledge to benefit all members of the community. It is a flexible mechanism designed to support the needs of top experts in the field and novices struggling to build their first model.
The CRNR provides a layer of multimedia tools for intelligent access to modeling resources through the CRNR network. The CRNR provides broad access functionality to support cooperative development of models by researchers distributed throughout industry, university and government laboratories. In addition to providing the basic tools needed by experts to work in a specific problem area, the system provides mechanisms to facilitate education and research in modeling and simulation at all levels within the modeling and simulation community.

4.1) Modeling Simulation and Analysis Research Laboratory

The Modeling Simulation and Analysis Research Laboratory (MSARL) will serve as the hub of the CRNR. A laboratory is needed in the CRNR to provide resources for remote model execution, for example to support MASTERMIND, and to encourage the use of object-oriented modeling techniques that will foster interoperability, reusability and variable fidelity. Researchers from all sectors of the community will be anxious to provide component models that are able to interoperate with existing models to help define interfaces. Interfaces will evolve to become de facto standards when they are accepted as the premier interface for a heavily used component. Object-oriented technology will of course provide for changes in the implementation of a component model after its interface is established. Component models that are inefficient or provide an inconvenient interface may be dismissed for neglect. It is essential that the government support the initial development of the CRNR to encourage development of facilities that extend into the community, in addition to MSARL The diagram below shows MSARL playing the role of the hub in the CRNR.
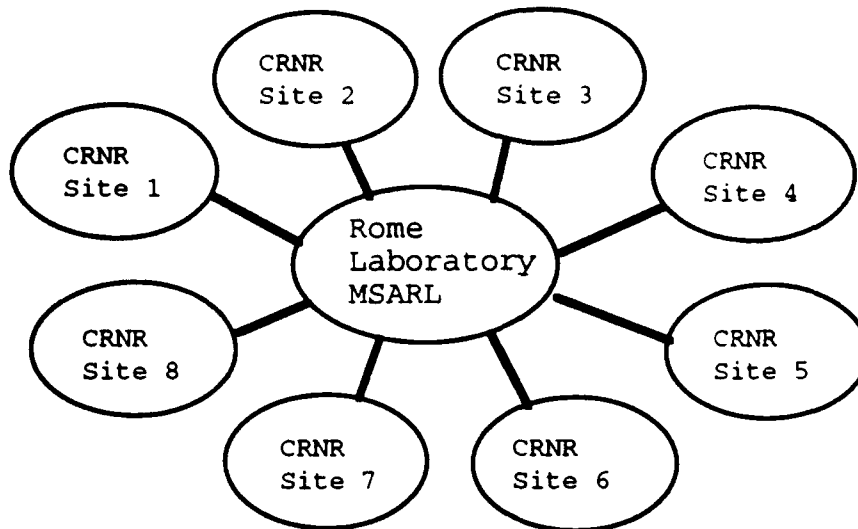
MSARL as Hub of CRNR

4.2) Anonymous FTP Model Description Database

For simple inquiries regarding availability of models with particular characteristics, Internet access should prove acceptable. In fact, a system to support this level of model access has been implemented at Rome Laboratory as a first step in CRNR development. The mechanism uses anonymous FTP for access to descriptions of Rome Laboratory models and simulations. Other interfaces, such as *Gopher* and *NFS mounting* can be used to "export" publicly available information to the modeling and simulation community in electronic form. NFS can make remote files appear as if they were part of a local disk. In addition to model descriptions, technical papers and discussion of technical issues can be shared through USENET News service and other developing systems.

4.3) Distributed Classroom

The CRNR will bring together experts from the modeling and simulation community. Videoconferencing is an important technology for experts to develop new ideas and to interact with students at all levels of study. The nature of the CRNR demands a flexible network configuration. Experts will at times require connection to many groups of "students". However, experts may become students in some cases to learn from other experts. The diagram below shows a possible configuration for a videoconference in support of a structured distributed classroom.
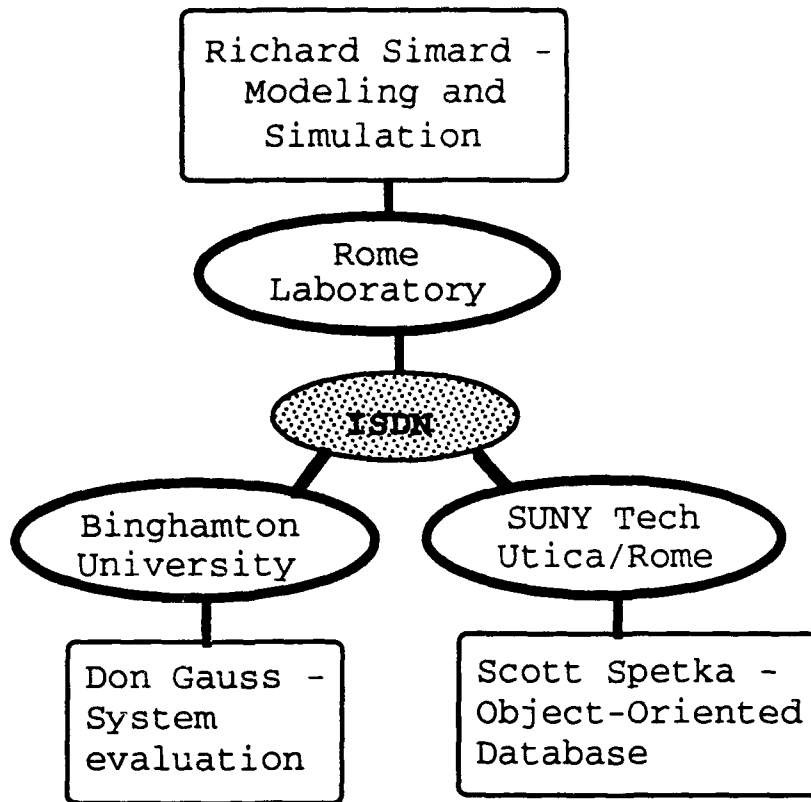
The CRNR will be used experimentally in a structured classroom environment at SUNY Institute of Technology at Utica/Rome, CSC555, a course in Models and Metrics for Computer System Performance Evaluation will be offered in Spring 1994 to test the capabilities of the developing CRNR and take advantage of initial tools and information resources provided by the Rome Laboratory MSARL. In addition, the expertise of the Office of Modeling and Simulation will contribute technical support in the development and offering of the course. Initial plans for the collaborative effort began during the period of the Summer Research Program.

Initial CRNR contributions to the distributed classroom:

- Network access to MSARL resources
- Experts to participate in classroom
- Develop resources for use in classroom
- Develop curriculum for CSC555
- Introduction to modeling and simulation concepts - Stella®

- Modeling Tools and Language -
    CACI: Network II, Simscript, Modsim II,Mathematica

4.4) A Remote Workstation Server Interface

It is important that as many members of the modeling and simulation community as
possible be networked into the CRNR, to provide momentum and encourage the sharing of
ideas that will drive the development of the CRNR. Early in the project an inexpensive
interface system will be developed to give access to members who cannot afford a
machine that will be typical of the CRNR model execution sites, like MSARL. The system
must provide a graphical interface and be capable of supporting the remote model access
protocols initially developed for the CRNR. A system is being developed that will
demonstrate the feasibility of an initial remote workstation server on an Intel
80386/DX platform running the 386BSD operating system. The software developed is
expected to be portable to the next generation of inexpensive platforms, based on the
Intel Pentium chip.

4.5) ISDN Network

The communication pathways needed by the system are as diverse as the mechanisms
they support. A fully functional CRNR will require flexibility not available through the
Internet, for videoconferencing and distributed modeling environments. A major
problem that must be addressed is the ability to provide sufficient communication
bandwidth to meet these requirement. Integrated services digital network (ISDN)
[Smouts 91] is a network being developed around the world which will provide the
improved services needed to support the CRNR proposal. The diagram below shows the
access paths for component models through the ISDN network to support an
implementation of MASTERMIND.
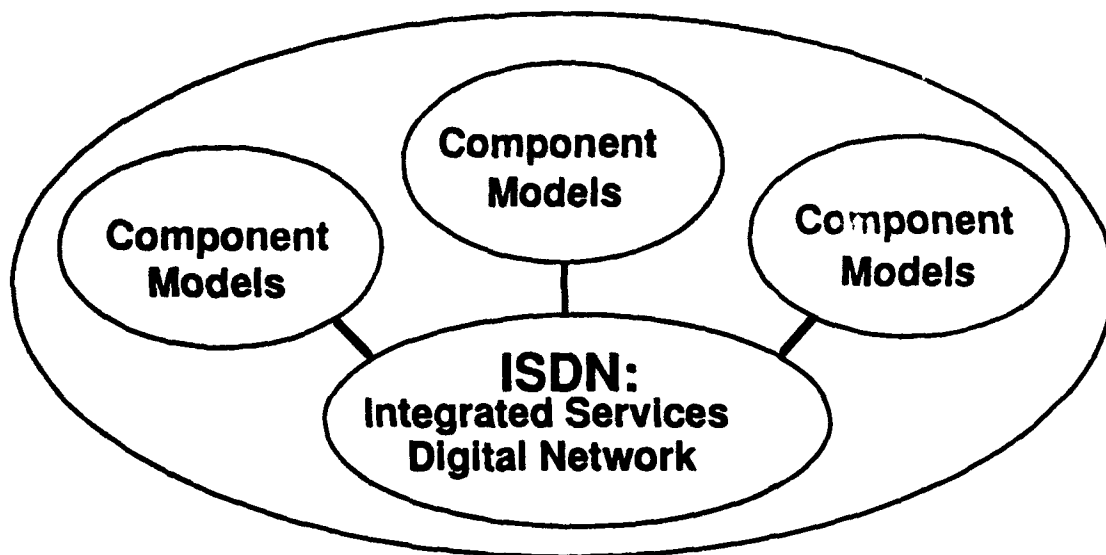
4.6) A CRNR Decision Aid

Interoperability of models and model construction from reusable components requires understanding relationships between models. In addition to MASTERMIND, interactive, graphical user interface (GUI) tools must be given to system users to facilitate a search process for component models that might interoperate to produce a new model. An interactive GUI interface would help to identify opportunities to exploit existing models when no apparent useful interfaces can be automatically located. The interactive decision aid can identify modules which might be useful if fuzzy logic techniques can be applied to adapt interfaces to conform to existing interfaces on other models. A prototype decision aid was built over the summer in the Rome Laboratory Office of Modeling and Simulation [Dobransky 93].

5) CONCLUSION

The Summer Research Program lead to a new concept in query processing and an integrated, evolutionary approach to solving the problems of interoperability, reusability and variable fidelity. The concepts that developed were the result of expert leadership in the Office of Modeling and Simulation and exposure to a broad range of modeling efforts both in Rome Laboratory and at other laboratories in the government, private industry and academics. In addition to exploring technical articles and books in the modeling and simulation field, the Summer Research Program implemented a microcosm of the Community Research Network Resource which we sought to implement. Our efforts validated many of our hypothesis regarding the need for cooperation and

sharing to provide advances in modeling and simulation and provide an environment in which researchers will continue to flourish and maintain technical leadership in the area. The paper concludes by presenting the research and development issues which remain to be addressed to make the CRNR vision become a reality.

CRNR Development:

- Interaction with modeling and simulation community
- Development of on-line model standards for CRNR access

    In addition to running a model, expert information about
    the model is needed. Internet protocol for model access.

- Develop ISDN access to CRNR.
- Monitor community interest in RL models through the FTP database.
- Develop graduate course to utilize CRNR.
- Develop query processing techniques for CRNR access, including decision aid
    and MASTERMIND.
- Develop distributed simulation techniques

Research Areas:

Parameter conversion functions and model interfaces will require research in the following areas:

- Fuzzy Logic
- Knowledge-Based Rules
- Neural Nets/Petri-Nets
- Object-Oriented Systems - Operator Overloading/Polymorphism

REFERENCES

[Chorafas 93]   Chorafas, Dimitris, Steinmann, Heinrich, "Object-Oriented
                  Databases", ISBN 0-13-491804-5, PTR Prentice-Hall 1993.

[Dobransky 93]   Dobransky, Mary, "Prototyping a Modeling and Simulation
                  Information Network", Air Force Summer Research Program
                  Report, Air Force Office of Scientific Research, August 1993.

[Kehoe 92]   Kehoe, B., ed., "Zen and the Art of the Internet: A Beginner's Guide
                  to the Internet", Anonymous FTP, pub/zen, ftp.cs.widener.edu,
                  1992.

[Marine 93]   Marine, April, Kirkpatrick, Susan, Neou, Vivian, Ward, Carol,
                  "INTERNET: Getting Started", ISBN 0-13-327933, PTR
                  Prentice-Hall, 1993.

[Smouts 91]   Smouts, Michel, "Packet Switching Evolution from Narrowband to
                  Broadband ISDN", ISBN 0-89006-542-X, Artech House, 1991.

[Spetka 92]   Spetka, Scott, "A Decomposition Algorithm for Distributed Hash
                  Join Query Processing", 2nd International Workshop on Research
                  Issues on Data Engineering: Transaction and Query Processing
                  (RIDE-TQP), Phoenix, Arizona, February 1992.